UNIVERSITY OF BIRMINGHAM

Street canyon atmospheric composition: Coupling dynamics and chemistry

Vivien Bianca Bright

A thesis submitted to the University of Birmingham
for the degree of Doctor of Philosophy

School of Geography, Earth and Environmental Sciences

September 2012

Abstract

Street canyons, formed by rows of buildings in urban environments, are associated with high levels of atmospheric pollutants emitted primarily from vehicles, and substantial pollutant exposure. Within the canyon environment, the prevailing atmospheric chemistry is highly non-linear, and the canyon mixing and predominant chemical reaction timescales are comparable, the combined impacts of dynamics and chemistry must therefore be considered to quantify these effects.

A new model for the simulation of street canyon atmospheric chemical processing has been developed, by integrating an existing Large-Eddy Simulation (LES) dynamical model of canyon atmospheric motion with a detailed chemical reaction mechanism, the Reduced Chemical Scheme (RCS), comprising 51 chemical species and 136 reactions, based upon a subset of the Master Chemical Mechanism (MCM).

The combined LES-RCS model is used to investigate both the effects of mixing and chemical processing upon air quality within an idealised street canyon. The effect of the combination of dynamical (segregation) and chemical effects is determined by comparing the outputs of the full LES-RCS canyon model with those obtained when representing the canyon as a zero-dimensional box model (*i.e.* assuming mixing is complete and instantaneous).

The LES-RCS approach predicts lower (canyon-averaged) levels of NO_X, OH and HO_2, but higher levels of O_3, compared with the box model run under identical chemical and emission conditions. Chemical processing of emissions within the canyon leads to a significant increase in the O_x flux from the canyon into the overlying boundary layer, relative to primary emissions, for the idealised case and a number of pollution scenarios considered. These results demonstrate that within-canyon atmospheric chemical processing can substantially alter the concentrations of pollutants injected into the urban canopy layer, compared with the raw emission rates within the street canyon and that such variations have a considerable effect on average within canyon concentrations and the flux of pollutants out of the canyon into the urban background environment.

The work included in this thesis represents a substantial analysis into the spatial and temporal variability of pollutants within the canyon, providing a detailed assessment of the likely exposure of receptors to harmful pollutants within the canyon.

Big whorls have little whorls,
That feed on their velocity,
And little whorls have lesser whorls
And so on to viscosity.

- Lewis Fry Richardson (1922)

Acknowledgements

I would like to thank a number of people and associations. **Bill Bloss** and **Xiaoming Cai** who have provided excellent PhD supervision. Bill for his first-rate direction and knowledge that have given me a keen interest in atmospheric chemistry. Xiaoming for many interesting discussions concerning numerical modelling, data analysis and dynamics. The **University of Birmingham** for award of a **PhD scholarship** and the University's **BlueBear HPC** service that was used to perform the computations included in this thesis and provided a huge amount of data storage. **Chris Kidd**, **Lee Chapman**, **Lesley Batty**, **Juana Maria Sobborit**, **Ruth Merrifield**, **Cat Muller**, **Duick Young, Martin Widmann** and **Stuart Harrad** for their encouragement. **Sandy Milner** and **Tom Dunkley Jones** for providing me with a quiet sanctuary for writing up. **Jamie Peart, Gretchel Coldicott** and **Steve Swoffer** for providing me with the resources needed to complete a PhD. The **atmospheric chemistry group** including **Marie Camredon**, **Juan Najera**, **Suad Al Kindi, Shana Saha** with special thanks to **Salim Alam**, **Kate Faloon** for providing me with guidance in both atmospheric chemistry and PhD survival. **Jonathan Eden** for his support in numerical modelling and shared interest in atmospheric science. **Anneley**, **Richard**, **Sahana**, **Tatiana** and **office 412**. **Charlie** for making the whole PhD a far more enjoyable experience, offering guidance and welsh cakes from the beginning. The **fourth floor** who have made lunchtimes and Friday evenings at the pub something to look forward to namely **Ian**, **Megan**, **Matt**, **Deb**, **James**, **Libby**, **Adam**, **Jill**, **Liz**, **Cath**, **Ruth**, **Rob**, **Ian**, **Jon**, **Simon** and **Jolyon**. **RMetS**, **AGU, RSC**, **UoB** and **NCAS** for providing me with the funds to attend conferences, awards and inclusion in conference committees. **Emma** for being a great friend, housemate and peer giving me excellent food, delicious cakes and support when I most needed it. **Colleagues** at the **University of Cambridge** including the **Rod Jones group**, **Alex** and **Clare** for pushing me to submit this thesis. Met Office friends: **Mark**, **Lucy**, **Jackie**, **Laura**, **Phil** and **James** for encouraging me to embark on a PhD in the first place. Close friends: **Vics**, **Jess**, **Vicky**, **Lee** and **Dave** for providing thesis respite, their friendship and patronage. **Ed** for proof reading, listening, his support, encouragement and putting up with me in difficult times. Finally, **my family** particularly my **Mum** and **Dad**, **Nanna** and **Grampy** for their continuous support and financial assistance not only during this PhD but throughout my life, I can't thank you all enough.

Declaration

The research included in this thesis was carried out in collaboration with Dr William Bloss and Dr Xiaoming Cai. The Common Representatives Intermediates mechanism version 2-R5 was provided by Dr Mike Jenkin and Professor Dudley Shallcross. The LES model used in this research was developed by Dr Cai with the FORTRAN code of the chemical subroutine extended by the author to include the full chemistry of the developed RCS mechanism. Chapter 5 presents analysis and discussions that include input from both Dr Bloss and Dr Cai. A number of figures included in this thesis were produced by the author by modifying R code written by Dr Cai. Statistical analyses included in Chapter 6 were carried out by the author. The use of other material from additional sources has been acknowledged in full elsewhere within this thesis.

List of symbols

Atmospheric chemistry

c	Concentration of chemical species
$\bar{c}$	Mean concentration of chemical species within the canyon
c_B	Background concentration of chemical species
$\overline{c_B}$	Mean background concentration of chemical species above the canyon
Da	Damköhler number
δ_{ps}	Photostationary state defect
H	Characteristic length of the atmospheric box model [m]
h	Height of atmospheric box model [m]
I_S	Intensity of segregation
j	Photolysis rate coefficient
k	Reaction rate coefficient
k_{eff}	The effective rate of chemical reaction
k'	Pseudo-first-order rate constant for removal [s^{-1}]
k'_{OH}	Total OH reactivity [s^{-1}]
L_i	Loss term in which i is the reactant
M	Mass of pollutants in the system
P_i	Production term in which species c_i is a product
Q	Mass emission rate of chemical species [molecules s^{-1}]
q	Emission rate of species per unit time and surface [molecules cm^{-2} s^{-1}]
R	Chemical production rate of species [molecules cm^{-3} s^{-1}]
$[R]$	Canyon averaged chemical reaction rate
R_M	Mass of pollutant removed per unit time
S	Removal rate of species [molecules s^{-1}]

S_i	Total photochemical source or loss term for species *i*
τ	Atmospheric lifetime [s]
τ_r	Residence time of air over the area of the box model [s]
ν_d	Deposition velocity of species
σ_A	*A*bsorption cross section of a molecule
ϕ_A	Photolysis quantum yield for dissociation
[X]	Concentration of chemical species, *X* [molecules cm^{-3}]
ω_t	Transfer velocity [m s^{-1}]

Constants

C_S	Smagorinsky constant
g	Acceleration due to gravity 9.81 ms^{-2}
k	Von Kármán's constant 0.41
R^*	Ideal gas constant 8.31451 J K^{-1} mol^{-1}
R	Specific gas constant 287 J kg^{-1} K^{-1}
N_A	Avagadro's constant 6.0221367×10^{23} molecules mol^{-1}

Meteorology

Γ_d	Dry adiabatic lapse rate 9.8 K km^{-1}
Γ_{env}	Environmental lapse rate [K km^{-1}]
H_S	Scale height
ρ	Density of air [1.2 kg m^{-3}]
p_0	Standard reference pressure [Pa]
p	Pressure [Pa]
T	Temperature [K]
τ	Surface drag per unit area

u	Instantaneous horizontal velocity [m s^{-1}]
u_{BL}	Average wind speed of the CBL [m s^{-1}]
$\overline{u}$	Mean horizontal velocity [m s^{-1}]
u'	Fluctuating component of horizontal velocity [m s^{-1}]
u_*	Friction velocity [m s^{-1}]
v	Lateral velocity component [m s^{-1}]
V_g	Geostrophic wind
w	Vertical velocity component [m s^{-1}]
z_i	Inversion height [m]

Other

γ	Longitude
Δt	Time step [s]
Δx	Increment of x
δ_s	Solar declination
θ_z	Solar zenith angle
I	Intensity of the solar flux
λ	Wavelength
N	Number of grid points
n	Natural frequency
n_{max}	Spectral peak
ϕ	Latitude
ψ	Local elevation angle
S_x	Spectral energy
t	Time [s]
t	Mass in tonnes
z	Altitude [m]

Statistics

n	Number of entities in sample
$P(a'b')$	Normalised joint probability density functions
R^2	Coefficient of determination
sk	Skewness
σ	Standard deviation

Urban

D_S	Sub-grid scale eddy diffusivity
d	Zero plane displacement height [m]
e, k	Turbulent kinetic energy [J]
ε	Turbulent dissipation rate [J]
δ_{ij}	Kronecker symbol
$F_{adv} = \langle w \rangle \langle c_i \rangle$	Vertical advective flux [ppb m^{-2} s^{-1}]
F_c	Pollutant flux at roof level [ppb m^{-2} s^{-1}]
F_{total}	Total resolved-scale vertical flux [ppb m^{-2} s^{-1}]
$F_{turb} = \langle \tilde{w}\tilde{c}_i \rangle$	Resolved-scale vertical turbulent flux [ppb m^{-2} s^{-1}]
H	Canyon height [m]
h	Mean height of the roughness elements [m]
h_c	Mean canopy height [m]
$h_i^{(\phi)}$	Kinematic sub-grid scale flux
l	Turbulent characteristic length scale [m]
$L_{x,\,y}$	Length of the canyon in the x or y axis [m]
Re	Reynolds number
$\overline{S}_{ij}$	Rate of sub-grid scale deformation
τ_{ij}	Sub-grid scale stress tensor

U_{max}	Free stream velocity at the top of the domain [m s^{-1}]
ν	Dynamic viscosity
ν_s	Sub-grid scale turbulent viscosity
W	Canyon width [m]
z_*	Height of the roughness sublayer [m]
z_i	Height of the UBL [m]
z_0	Surface roughness length [m]

List of acronyms

ABL	Atmospheric boundary layer
ACH	Air exchange rate
AGANET	Acid gases and aerosols network
AQEG	Air Quality Expert Group
AQG	Air Quality Guidelines
AQM	Air quality management
AQMS	Air quality management system
AURN	Automatic urban and rural monitoring network
CBM	Carbon Bond Mechanism
CBL	Convective boundary layer
CFCs	Chlorofluorocarbons
CFD	Computational fluid dynamics
CRI	Common representatives Intermediates mechanism
DALR	Dry adiabatic lapse rate
Defra	Department for Environment, Food and Rural Affairs
DFT	Department for Transport
DU	Dobson Units
ECMWF	European Centre for Medium-Range Weather Forecasts
ELR	Environmental lapse rate 6.5 K km^{-1}
EU	European Union
EZ	Entrainment zone
FT	Free troposphere
GECKO-A	Generator for Explicit Chemistry and Kinetics of Organics in the Atmosphere
GEIA	Global Emissions Inventory Activity

GHGs	Greenhouse gases
GPM	Gaussian plume model
GRS	Generic reaction set
HC	Total hydrocarbons
HPC	High performance computing
IQR	Interquartile range
JPDFs	Joint probability density functions
LES	Large eddy simulation
LEZs	Low emission zones
MCM	Master chemical mechanism
MEK	Methyl Ethyl Ketone
ML	Mixed layer
Mph	Miles per hour
NAEI	National Atmospheric Emissions Inventory
NAME	Numerical Atmospheric-dispersion Modelling Environment
NBL	Nocturnal boundary layer
NWP	Numerical weather prediction
OSPM	Operational street pollution model
PAN	Peroxyacetyl nitrate
PCH	Pollution exchange rate
POCP	Photochemical ozone creation potential
ppb	Parts per billion (10^9), by volume
ppm	Parts per million (10^6), by volume
ppt	Parts per trillion (10^{12}), by volume
PSS	Photochemical steady state
PSSD	Photostationary state defect
PTM	Photochemical trajectory model

QSSA	Quasi-steady state approximation
RACM	Regional Atmospheric Chemistry Mechanism
RAMS	Regional atmospheric modelling system
RANS	Reynolds Averaged Navier Stokes
RCS	Reduced chemical scheme
RH	Reactive hydrocarbons
SARs	Structure activity relationships
SF	Stochastic fields
SGS	Sub-grid scale
SL	Surface layer
SZA	Solar zenith angle
TKE	Turbulent kinetic energy
TORCH	Tropospheric organic chemistry experiment
TUV	Tropospheric ultraviolet and visible
UBL	Urban boundary layer
UKMO	UK Meteorological Office
veh	Vehicles
v/v	Volume of gas per volume of air
VOCs	Volatile organic compounds
WHO	World Health Organisation

Contents

1: Introduction

The introductory chapter of this thesis describes the structure and composition of the atmospheric boundary layer (ABL) with particular focus on the urban boundary layer (UBL). The dynamical and chemical processes of importance in terms of this research are also discussed here.

1·1 The atmosphere

1·1·1 Vertical structure

The vertical structure of the atmosphere[*] can be described in terms of the variation in pressure, density and temperature with height. Most commonly the atmosphere is divided up into different layers according to the variation in temperature with altitude (Figure 1·1).

The **troposphere** is a layer of the atmosphere that contains approximately 90 % of the earth's atmospheric mass. It extends from the earth's surface to a height of between 9 and 16 km that varies depending on latitude and season (Arya, 1999).

Pressure (p) decreases exponentially with height (z), assuming the atmosphere is **isothermal**[†] and varies according the **hydrostatic equation**:

$$p = p_0 \exp\left[-z/H_S\right], \qquad (1·1)$$

where p_0 is a standard reference pressure (*e.g.* standard atmospheric pressure — 1.013×10^5 Pa), $H_S = RT/g$, is known as the **scale height**, R is the specific gas constant

[*] The gaseous envelope that surrounds the earth's surface.

[†] Temperature remains constant with height *i.e.* there is zero 'lapse rate' (rate of fall of temperature with height) (UKMO, 1991).

(287 J kg^{-1} K^{-1}), T is temperature (K) and g is acceleration due to gravity (9.81 ms^{-2}). Where $z = H_S$, the pressure is $1/e$ of that at the surface.

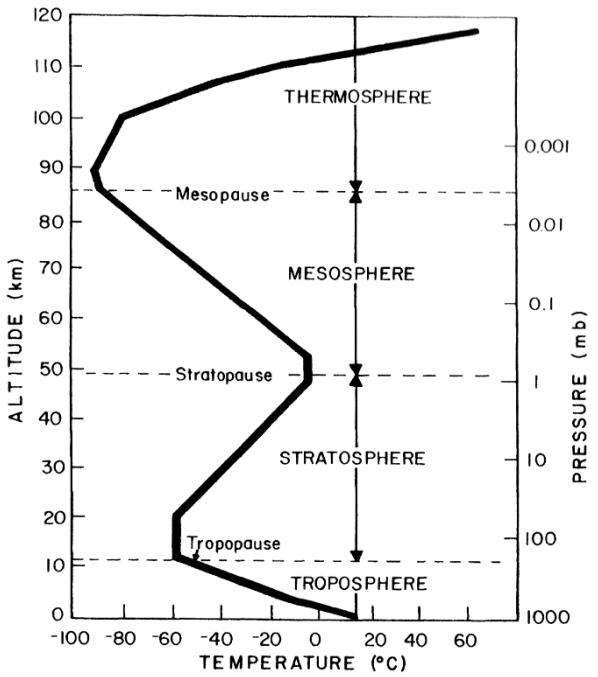

Figure 1·1 - *The average temperature profile through the atmosphere, indicating the different atmospheric layers (Arya, 1999).*

Temperature decreases with height in the troposphere at a rate of approximately 6.5 K km^{-1}, known as the **environmental lapse rate** (**ELR**). The highest temperatures are observed at ground level due to the sun's radiation which heats the earth's surface. Heat energy is then transferred away from the surface through convection and long-wave radiation. Vertical convection means that gases present in the troposphere are well mixed, enhanced by the horizontal and vertical transfer of heat energy, moisture and momentum. The troposphere is that region of the atmosphere that is of interest in terms of this thesis therefore the succeeding layers of the atmosphere will not be discussed further here.

1·1·2 Composition

The present-day troposphere is primarily composed of nitrogen (78 %), oxygen (21 %) and a number of noble gases including argon (≈ 1 %). These gases, known as **fixed gases**, have remained relatively constant in terms of both their temporal and spatial variation. Gases whose volume mixing ratios[‡] vary over time and space are known as **variable gases** and show a marked variation depending on the nature of the environment considered (Table 1·1).

Table 1·1 - *Volume mixing ratios of variable gases in troposphere of clean and polluted environments (Jacobson, 2002).*

Gas	Chemical formula	Clean troposphere	Polluted troposphere
Inorganic		*Volume mixing ratio / ppb*	
Water vapour	H_2O	3,000 — 4.0×10^7	5.0×10^6 — 4.0×10^7
Carbon dioxide	CO_2	365,000	365,000
Carbon monoxide	CO	40 — 200	2,000 — 10,000
Ozone	O_3	10 — 100	10 — 350
Sulphur dioxide	SO_2	0.02 — 1	1 — 30
Nitric oxide	NO	0.005 — 0.1	0.05 — 300
Nitrogen dioxide	NO_2	0.01 — 0.3	0.2 — 200
Organic			
Methane	CH_4	1,800	1,800 — 2,500
Ethane	C_2H_6	0 — 2.5	1 — 50
Ethene	C_2H_4	0 — 1	1 — 30
Formaldehyde	HCHO	0.1 — 1	1 — 200
Toluene	$C_6H_5CH_3$	-	1 — 30
Xylene	$C_6H_4(CH_3)_2$	-	1 — 30

Pollutants may be gaseous or in particulate form and are either **emitted** directly into the atmosphere from their source (**primary pollutants**) or are formed through

[‡] The number of moles of a species X per mole, expressed in units of volume of gas per volume of air since the volume occupied by an ideal gas (obeyed to within 1 % in the atmosphere) is proportional to the number of molecules (Jacob, 2000). Measured in parts per million, ppm (1 ppm = 10^{-6} v/v), parts per billion, ppb (1 ppb = 10^{-9} v/v), or parts per trillion (ppt) (1 ppt = 10^{-12} v/v).

chemical reactions (**secondary pollutants**) and may emanate from **anthropogenic** (manmade) and **biogenic** (natural) sources (Harrison, 2001a).

Following their emission or chemical production, gases undergo **transport**, **diffusion**, **chemical reaction**, **transformation**[§] and **deposition**[+] in the atmosphere, thus determining the concentration of pollutants at any one point.

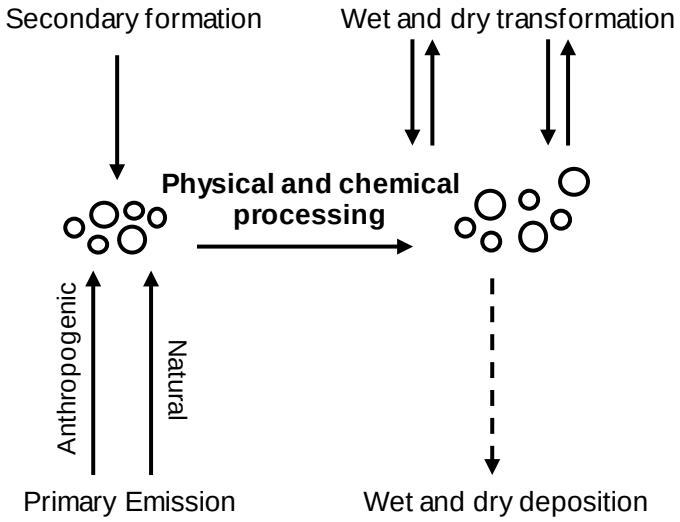

Figure 1·2 - *Primary emission, secondary formation, atmospheric processing and sinks of atmospheric pollutants. Adapted from (Harrison, 2001a).*

The atmospheric **lifetime**, τ, of atmospheric pollutants vary considerably, ranging from seconds, to millions of years, depending on the efficiency of the removal processes or atmospheric sinks and is defined as:

$$\tau = \frac{M}{R_M} = \frac{1}{k'} \qquad (1\cdot2)$$

where M is the mass of pollutants in the system, R_M is the mass of pollutant removed per unit time and k' is the pseudo first order rate constant for removal.

[§] Pollutants may be removed through *dry transformation processes* in which one chemical species is converted chemically into another.

[+] Including: *Dry deposition* — removal of pollutants at land and sea surfaces without precipitation; *Wet deposition* — removal of pollutants by precipitation, involving either *rainout* in which pollutants are incorporated into the cloud layer or *wash out* by falling raindrops (Harrison, 2001a).

1·2 The atmospheric boundary layer

The **atmospheric boundary layer** (**ABL**) is the term used to describe the lowest layer of the atmosphere, usually around 1 km deep in mid-latitudes however this can vary from 100 m to 3 km. The earth's surface exerts an influence on the ABL, on timescales of a day or less, through friction and heat flux. Turbulence generated by wind shear and thermal convection characterises the ABL, a result of the increasing wind profile in which the wind is approximately **geostrophic**[*] at the top of the ABL and zero at the surface (Figure 1·4).

1·2·1 Atmospheric stability

The state of the atmosphere in terms of its stability can be inferred from vertical temperature profiles that give the environmental lapse rate, Γ_{env}, (Figure 1·3). When the atmosphere is unsaturated the change in temperature of an air parcel[×] with height follows the **dry adiabatic lapse rate** (**DALR**), Γ_d, cooling takes place at a rate of 9.8 K km^{-1}.

An increase in the observed temperature with altitude (temperature inversion) indicates that the atmosphere is very **stable**. In this case a dry parcel of air that is initially the same temperature as its surroundings will cool at a faster rate than the environment. If, when reaching a new (lower) pressure level the parcel finds itself colder than its environment, negative buoyancy will result in the parcel returning to its original pressure level *i.e.* vertical displacements are **stable**.

If the temperature of an unsaturated air parcel with height decreases (super-adiabat) at a rate slower than the environment and the parcel finds itself warmer than its

[*] The horizontal equilibrium wind (V_g) that blows at right angles to the pressure gradient and represents an exact balance between *pressure gradient force* and *Coriolis force* (UKMO, 1991).
[×] A hypothetical volume of air that can be tracked as it moves through the atmosphere (Stull, 2000).

environment at a new pressure level, positive buoyant forces will result in the parcel continuing its vertical ascent *i.e.* vertical displacements are **unstable**.

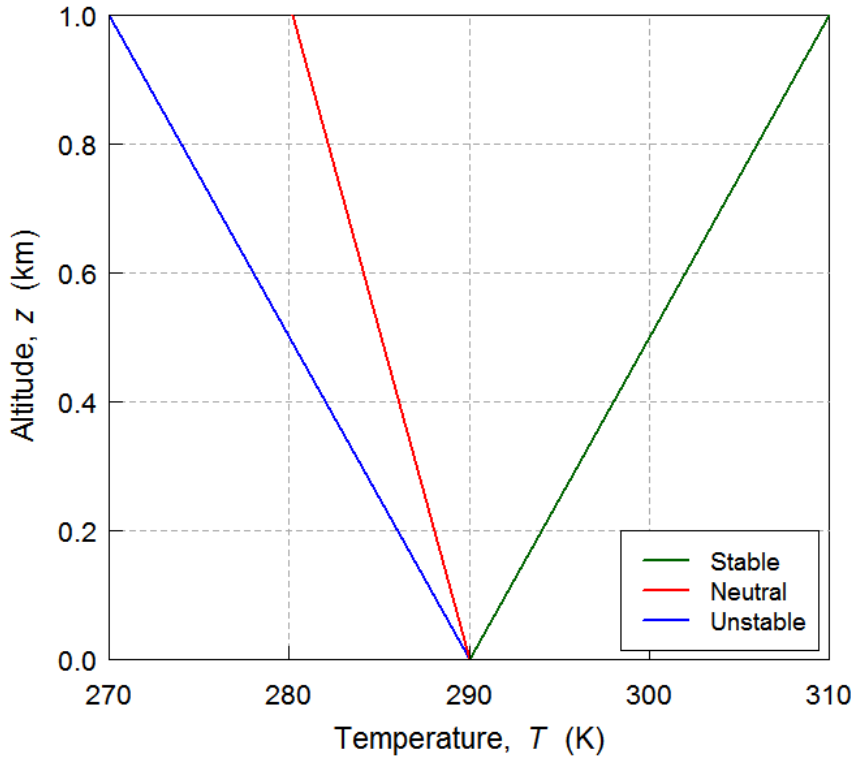

Figure 1·3 - *Vertical temperature profiles, Γ_{env}, under stable, neutral and unstable atmospheric conditions.*

Under **neutral conditions**, the rate at which unsaturated air cools is equal to that of the surrounding atmosphere *i.e.* cooling follows the DALR. If, when reaching the new pressure the unsaturated air parcel finds itself at the same temperature as its environment, the parcel will experience no buoyant force and the parcel will remain at this new level *i.e.* vertical displacements are **neutral**.

1·2·2 The daytime convective boundary layer

Under neutral conditions, the daytime **convective boundary layer** (**CBL**) can be described in terms of a number of characteristics observed in the profiles of atmospheric variables within each layer. A number of sublayers of the daytime CBL

can be identified (Figure 1·4). The bottom layer of the CBL is known as the **surface layer** (**SL**) and is typically 10 % of the CBL (~ 100 m thick). Variables including wind, temperature and pollutant concentrations change rapidly with altitude in this layer due to the strong interaction with the surface. Turbulence is acutely influenced by the surface characteristics of this layer and fluxes of heat, moisture and momentum in the vertical remain approximately constant with height as a result of strong turbulent mixing. At the lowest level of the surface layer lies a shallow **laminar sublayer** (a few millimetres in depth) in which the flow is smooth and parallel to the solid surface. The transport of heat and momentum perpendicular to the direction of flow takes place by molecular diffusion.

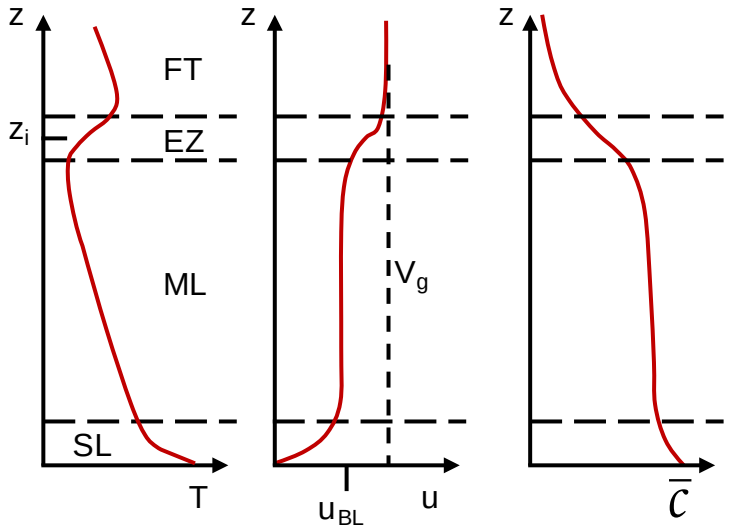

Figure 1·4 - *Typical daytime vertical profiles of temperature (T), wind speed (u) and pollutant concentration ($\overline{c}$). The structure of the CBL is illustrated by vertical profile of T, that consists of the surface layer (SL), the mixed layer (ML), the entrainment zone (EZ) and the free troposphere (FT). Geostrophic wind is represented by V_g and u_{BL} represents the average wind speed of the CBL. Height is represented by z and inversion height by z_i. Adapted from Stull (1988, 2000).*

The earth's rotation becomes significant within the convective **mixed layer** (**ML**), causing wind direction to veer with height. Rising buoyant plumes (thermals) that arise in the surface layer due to thermal convection and associated turbulence

(mechanical convection) cause quantities (*e.g.* the concentration of pollutants) to remain relatively constant with height within this layer (Figure 1·4).

At the top of the mixed layer is the **entrainment zone** (**EZ**) or **capping inversion** within which temperatures increase with altitude. This layer forms a boundary between the free troposphere and the CBL and often caps the daytime convective boundary layer, inhibiting mixing. This capping inversion is very important in terms of air pollution particularly under a strong inversion when pollutants are trapped in the mixed layer and can build up to harmful levels. If the inversion occurs closer to the ground (*e.g.* during anticyclonic conditions) elevated concentrations of pollutants near the surface can result.

Above the CBL lies the **free troposphere** (**FT**) in which there is an observed decrease in temperatures with height. The **nocturnal boundary layer** (**NBL**) that forms at night following radiative cooling near the ground is beyond the scope of this thesis and therefore will not be considered here.

Within the surface layer, wind speed increases with altitude as the effects of friction diminish. Under neutral conditions the change in wind speed with height can be expressed as:

$$\frac{\partial u}{\partial z} = \frac{u_*}{kz}, \tag{1·3}$$

where u is wind speed, z is altitude, k is von Kármán's constant (0.41) and u_* is the **friction velocity**[**] that may be determined as:

$$u_* = \sqrt{\frac{\tau}{\rho}}, \tag{1·4}$$

[**] The reference velocity employed in the study of fluid flow over a rough surface, increasing with surface roughness and mean wind speed (UKMO, 1991).

where τ is the surface drag per unit area and ρ is the density of air. Subsequent to integration of Equation 1·3 it follows that wind speed within the surface layer follows a **logarithmic profile** and may be expressed as:

$$u(z) = \frac{u_*}{k} \ln\left(\frac{z}{z_0}\right), \qquad (1{\cdot}5)$$

where z_0 is the surface roughness length[††]. Equation 1·3 approximates the change in wind speed with height well within the surface layer provided that there is steady flow, the boundary layer is well developed and the atmosphere is neutrally stable. Neutral conditions alone are considered within this thesis therefore modifications to wind profiles that may be applied under stable and unstable conditions according to Monin-Obukov similarity theory (*e.g.* Stull (1988), Garratt (1992), Arya (1999)) are not discussed further.

1·3 The urban boundary layer

The urban surface is very different from its rural counterparts due to the presence of roughness elements such as buildings. As the boundary layer flows from a rural to an urban area, its properties (including wind speed, temperature and turbulence characteristics) are altered resulting in the development of the **urban boundary layer** (**UBL**). This layer of the atmosphere, illustrated in Figure 1·5, is of particular importance in terms of air pollution as it is the place where the majority of pollutants are released; undergo transport, dispersion, chemical changes and removal processes.

[††] Aerodynamic roughness of a surface over which a fluid is flowing, often assumed to be a fraction of the height of roughness elements (Raupach *et al.*, 1980). z_0 ranges from 0.001 m over short grass (Barlow, 2009) to ≥ 2 m over cities (Stull, 2000).

An empirical adjustment may be made to Equation 1·5 in the case of the UBL, where densely packed buildings within the urban canopy cause the mean flow to be displaced upwards, thus the logarithmic wind profile becomes:

$$u(z) = \frac{u_*}{k} \ln\left(\frac{z-d}{z_0} \right), \qquad (1{\cdot}6)$$

where d is the **zero plane displacement height** and approximates to 2/3 h_c, where h_c is the mean canopy height (Barlow, 2009). Equation 1·6 however represents an oversimplification when applied to the urban boundary layer, as the zero plane displacement height and surface roughness length may vary substantially due to the heterogeneous nature of the urban canopy.

Both z_0 and d are governed by the density, distribution and characteristics of individual surface roughness elements including buildings and trees (Grimmond and Oke, 1999). Table 1·2 illustrates the variability in the roughness characteristics of the urban surface for a number of homogeneous zones within the urban canopy (Grimmond and Oke, 1999).

Table 1·2 - *Typical values of zero-plane displacement height (d) and surface roughness length (z_0) for a number of homogeneous zones within urban areas (Grimmond and Oke, 1999).*

Urban surface form	d **(m)**	z_0 **(m)**
Low height and density Residential — one- or two-storey single houses, gardens and small trees. Mixed houses and small shops. Warehouse, light industrial, few trees.	2 - 4	0.3 - 0.8
Medium height and density Residential — two- and three-storey large or closely spaced semidetached and row houses, large trees. Less than five-storey blocks of flats with open surroundings. Mixed houses with shops, light industry, churches and schools.	3.5 - 8.0	0.7 - 1.5
Tall and high density Residential — closely spaced < six-storey row and block buildings or major facilities (factory, university etc.), town centre.	7 - 15	0.8 - 1.5
High-rise Urban core or suburban nodes with multi-storey tower blocks in dense urban surroundings. Major institutional complexes.	> 12	> 2.0

The UBL can be subdivided into the **mixed layer** and the **urban surface layer**. As per the convective mixed layer (described in §1·2·2), the flow within the mixed layer is relatively unaffected by frictional forces and the surface whilst turbulence is assumed to be independent of surface roughness.

Within the urban surface layer (lowest 10 % of the UBL), frictional forces and surface roughness are both important in determining the characteristics of flow whilst the effects of Coriolis force[‡‡] are negligible. This layer can be further sub-divided into the **inertial sublayer** and the **roughness sublayer** (Raupach *et al.*, 1991).

The inertial sublayer is the outermost layer of the urban surface layer, overlying the roughness sublayer. Within the inertial sublayer, the principle length scale considered to affect the flow is height above the surface (z). Turbulence characteristics and airflow within this layer are characterised by the average effect of all roughness elements and Monin-Obukhov similarity theory (beyond the scope of this thesis) can be applied to determine turbulence statistics and fluxes within this layer (Fiegenwinter *et al.*, 1999).

The roughness sublayer is the lowest part of the surface layer within which air flow is directly influenced by individual roughness elements and turbulence is strongly affected by the geometric features of the canopy (Kaimal and Finnigan, 1994).

[‡‡] An apparent acceleration, which air possesses by virtue of the earth's rotation with respect to axes fixed in the earth (UKMO, 1991).

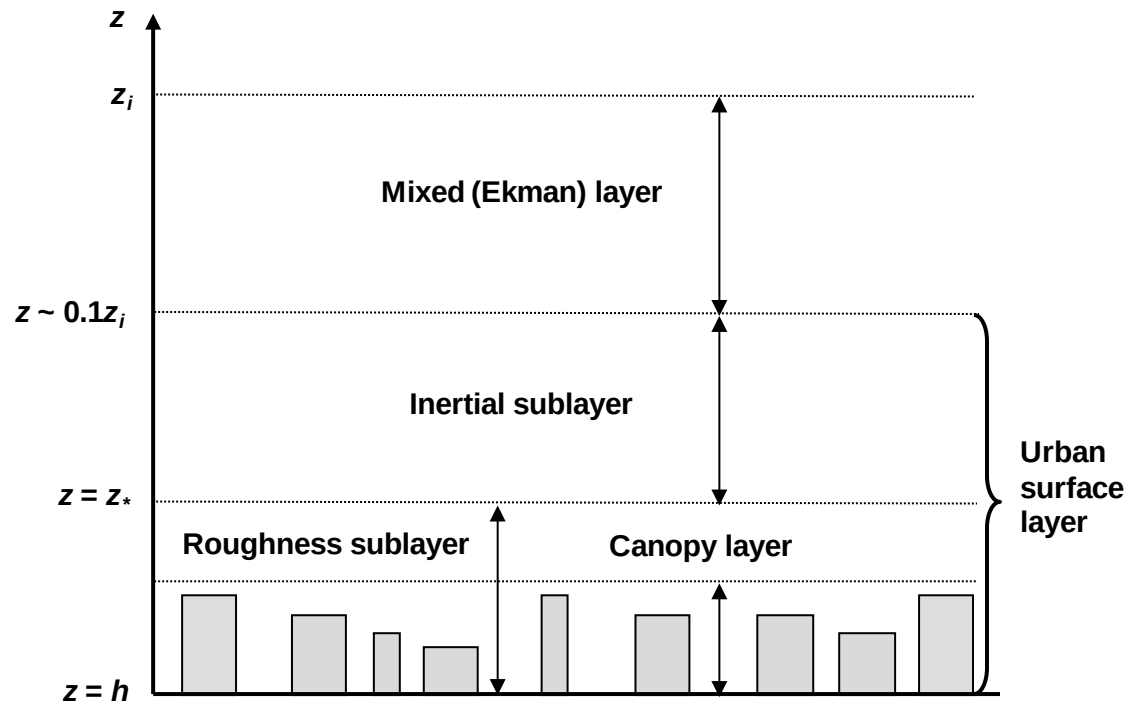

Figure 1·5 - *A schematic diagram of the structure of the daytime convective urban boundary layer (UBL). Where h is the mean height of the roughness elements, z_* is the height of the roughness sublayer and z_i is the height of the UBL.*

The **canopy layer** is the lowest part of the roughness sublayer that extends from the surface to the mean building height (that approximates to the zero-plane displacement height (Oke, 1987)). Mean airflow within this layer is significantly channelled by the geometry of roughness elements and turbulence is likely to be dominated by coherent structures that are of the same scale as the height of the canopy (Christen, 2005).

The vertical mixing of pollutants within the UBL can take place on timescales of minutes to hours. Within the canopy layer, the vertical transport of pollutants by turbulent processes may occur over shorter timescales ranging from seconds to minutes.

1·4 Turbulence

Moving away from the earth's surface, above some critical speed, the flow becomes **turbulent** in nature with inherently random fluctuations in both time and space. Turbulence within the UBL encompasses a wide spectrum of eddies that range in size from the molecular length scale to the larger synoptic scale. Energy is passed down across the spectrum in an "energy cascade" from large energy containing eddies, responsible for a significant proportion of turbulent transport, to smaller eddies that dissipate turbulent kinetic energy (TKE) into heat by viscosity. Turbulence spectra[§§] can be divided into three regions (Kaimal and Finnigan, 1994) as shown in Figure 1·6 that include:

- The **energy-containing range** in which the production of TKE occurs due to buoyancy and mechanical shear. This is the range of the large scale eddies and the spectral peak is found within this region.
- The **inertial subrange** is the range in which TKE is neither produced nor dissipated but is passed down from larger scales to smaller ones.
- The **dissipation range**, in which TKE is converted to heat by molecular viscosity.

At the lower end of the turbulence spectrum, separated from the synoptic scale eddies (that vary over timescales ranging from hours to days) by a **spectral gap**, are the turbulent scale eddies that vary over periods ranging from seconds or less to minutes, and span molecular length scales to tens of metres.

[§§] Specification of the character of turbulence in terms of the partition of kinetic energy between eddies of various sizes usually frequently obtained using Fourier analysis (UKMO, 1991).

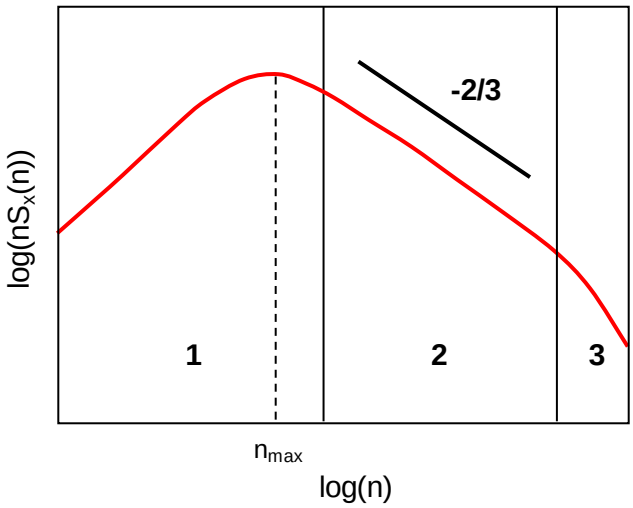

Figure 1·6 - *A schematic representation of the turbulence energy spectrum illustrating: (1) the energy containing range, (2) the inertial subrange and (3) the dissipation range. n represents the natural frequency, nS_x represents the spectral frequency multiplied by spectral energy and n_{max} is the spectral peak. Adapted from Christen (2005).*

In order to separate these components and provide a statistical representation of turbulence, **Reynolds decomposition** is often applied where:

$$u(t) = \overline{u} + u'(t) \ . \tag{1·7}$$

Hence, the instantaneous wind speed (u) at any given point is partitioned into the mean wind speed ($\overline{u}$) and a turbulent fluctuation (u').

In terms of the turbulent transport of other quantities such as heat, moisture and atmospheric pollutants (c), Reynolds decomposition can also be applied where for the concentration of pollutants (neglecting reactions), similarly:

$$c(t) = \overline{c} + c'(t) \ . \tag{1·8}$$

This gives an average of any fluctuating component (a) of zero, *i.e.* $\overline{a'} = 0$ and for the product of two variables, a and b:

$$\overline{ab} = \overline{\overline{a}\,\overline{b}} + \overline{a'b'} \ . \tag{1·9}$$

where the term, $\overline{a'b'}$ is known as the **covariance**.

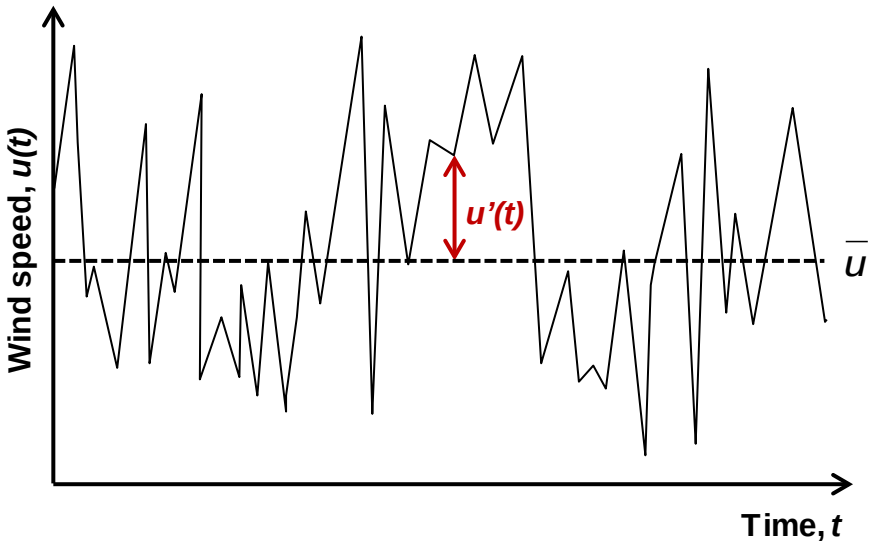

Figure 1·7 - *A schematic representation of the change in wind speed (u) over time (t) illustrating Reynolds decomposition where u' represents a turbulent fluctuation from the mean wind speed ($\bar{u}$).*

The street canyon acts to modify airflow and generate turbulence which differs in characteristics to that found over a homogenous surface typical of rural areas beyond the city. The flow and turbulence characteristics that occur within the urban canyon layer (and are of prime importance within this thesis) will be explored further in Chapter 2.

1·5 Atmospheric pollution

Air pollution[++] in cities, where a majority of people live and work, is fast becoming a problem of major concern. A rapidly increasing urban population witnessed in recent decades (*e.g.* Fenger (1999)) has led to an increase in the amount of congestion on roads, an increase in the density of housing and the number of receptors exposed to atmospheric pollutants in urban areas thereby exacerbating the problem. In 2011, 78 % of the population of developed regions lived in urban areas with this figure at 47 % of in developing countries, with this figure continuing to

[++] An atmospheric condition in which substances that arise from anthropogenic activities are present in concentrations at a sufficiently higher amount than their normal ambient levels to result in a measurable effect on humans, animals, vegetation, or materials (Seinfeld and Pandis, 1998).

increase (World Urbanization Prospects, 2011). The potential threat of the release of harmful material due to terrorist activity has also lead to an increase in effort to understand air pollution in urban areas that are particularly vulnerable to such events due to their concentrated populations (Belcher, 2005).

1·5·1 Causes and effects

The urban environment represents a major source of air pollution that has existed for centuries (*e.g.* Brimblecombe (1987), (1999)). The major cause of air pollution in urban areas occurs as a result of the **combustion** of fossil fuels (*e.g.* coal and natural gas for industry and domestic purposes) and more importantly the combustion of fuel for transport, particularly on roads.

Vehicle exhaust emissions[***] of; **carbon monoxide** (**CO**: 54 %) (Defra, 2008b), the **oxides of nitrogen** (**NO_X**[**]: 32 %) (Defra, 2008c) and a number of **volatile organic compounds**[××] (**VOCs**: 14 %) (Defra, 2008d) currently represent a major anthropogenic source of air pollution[†††].

VOCs

VOCs are of particular interest in terms of air pollution as they form precursors to photochemical ozone (O_3)[‡‡‡] production and the formation of other secondary pollutants. There are a large number of VOCs that can be identified and whilst the VOC OH sink is dominated by CH_4 and CO in the free troposphere, within urban areas larger VOCs dominate resulting in a greater contribution to the formation of

[***] Numbers in parenthesis refer to the percentage contribution of road transport to the 2008 total UK emissions (by source category) of that pollutant.
[**] The sum of nitric oxide (NO) and nitrogen dioxide (NO_2).
[××] Any carbon-containing compound present in the atmosphere, excluding elemental carbon, carbon monoxide, and carbon dioxide (Derwent, 1995).
[†††] All Defra statistics taken for the year 2008.
[‡‡‡] The triatomic form of oxygen (O).

secondary pollutants. Figure 1·8 shows the composition of VOC species emitted by road transport in 2006 (Defra, 2008d).

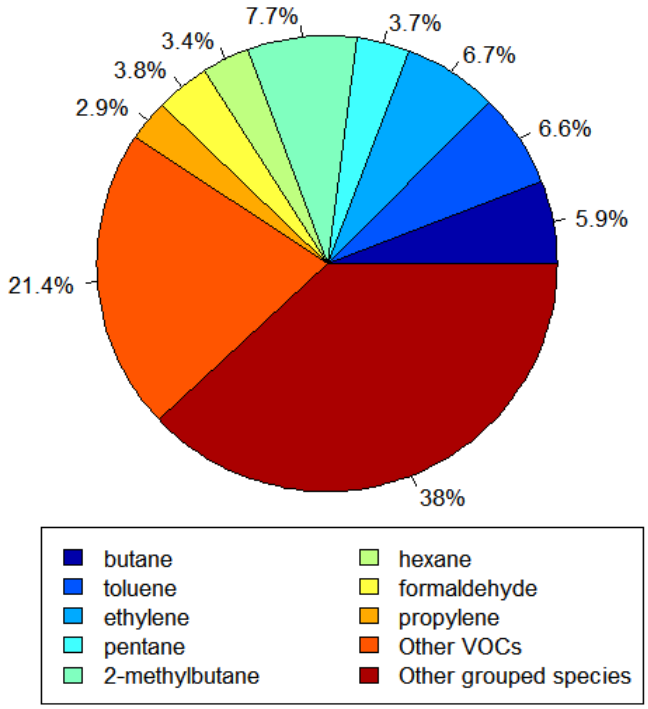

Figure 1·8 - *The estimated percentage mass emissions of VOC species from UK road transport in 2006. Data taken from Defra (2008d). Other grouped species represent unspeciated VOCs, hydrocarbons and similar groups whilst other VOCs represent total remaining speciated VOCs.*

The most abundant VOCs estimated to be emitted from UK road transport in 2006 include 2-methylbutane, ethylene and toluene. The ability of certain VOCs to react and form O_3 varies considerably and has given rise to a number of ways of classifying hydrocarbons (discussed further in §3·9·2). The simplest classification is to quantify VOCs by measuring their abundance although this method can result in an underestimation of their potential to produce O_3.

NO_X

The oxides of nitrogen, produced predominantly from vehicle exhaust emissions, dominate gas phase chemistry in urban environments. NO_X emissions have decreased over the past decades due to improvements in technology. However, NO_2

levels have shown a smaller decrease than NO due to the advent of diesel cars and other technologies that have increased the relative proportion of NO_2 emissions.

Effects

Air pollution has a wide range of impacts, the most concerning of which are those that relate to human health and well-being. Accidental releases of pollutants from storage tanks and industrial activities can result in high levels of mortality or cause serious injury. Pollution episodes can lead to the advent of disease, extreme discomfort, or even death in the vulnerable proportion of the population. Long term (chronic) exposure to low concentrations of air pollutants can cause respiratory problems, cardiovascular disease or exacerbate other conditions such as asthma (Arya, 1999).

Ozone can cause cellular damage, impairment of cell defences, a reduction in lung function during exercise (over 1 hour duration), cause headaches ($[O_3] > 150$ ppb), chest pains ($[O_3] > 250$ ppb), or a cough and sore throat ($[O_3] \geq 300$ ppb). Exposure to elevated levels of O_3 over several hours can also result in damage to the lining of the airways (Defra, 2012).

NO_2 is a key atmospheric pollutant (WHO, 2006) that has adverse impacts on human health. As a result of short-term (1 hour or less) exposure to NO_2 concentrations greater than 261 ppb (500 µg m^{-3}) a number of toxicology studies have observed acute (immediate) health effects, however bronchial responsiveness in asthmatics is known to increase from 105 ppb (200 µg m^{-3}) upwards (WHO, 2006).

Short-term exposure to high mixing ratios of NO_2 can also increase respiratory infections and cause inflammation of the lungs at high levels (1 - 1.5 ppm) (Frampton *et al.*, 1991, Walters and Ayres, 2001, Jacobson, 2005), with those greater

than 80 ppb known to increase the onset of illness and absence from school (Pilotto *et al.*, 1997, Jacobson, 2002).

In terms of the health effects that arise due to the long term exposure of individuals to NO_2, epidemiological studies have demonstrated an increase in bronchitic symptoms of asthmatic children in association with annual NO_2 concentrations (*e.g.* McConnell *et al.* (2003), Gauderman *et al.* (2005)) in addition to adverse effects on lung function growth (WHO, 2006). NO_2 may trigger asthma by damaging, irritating and sensitising the lungs making people more prone to allergic response in the presence of indoor allergens (Jones, 1999).

Whilst NO has no adverse effects on human health at typical ambient concentrations it may be rapidly converted to NO_2 through VOC oxidation chemistry, in addition to its role as an ozone precursor.

Such effects of air pollution on human health are one of the main concerns in terms of regulating urban air quality. It is therefore of prime importance to determine the extent to which people may be exposed to measured or modelled pollutant levels. For most cases pollution exposure is assessed according to unrealistic assumptions, *e.g.* that levels observed at a single monitoring station are representative of the exposure of the full urban population (Fenger, 1999). The effect of pollutants may be extremely rapid (resulting from a few minutes exposure) or arise due to the prolonged or repeated exposure to air pollutants taking place over a period of years (Walters and Ayres, 2001).

Air quality targets

In order to abate the health effects associated with atmospheric pollution, legislation and guidance relating to air quality has been developed ranging from the global to local scale.

To develop a robust guideline that ensures absolute safety, in depth knowledge of dose-response relationships in individuals in relation to all sources of exposure, the types of toxic effect elicited by specific pollutants or their mixtures, the presence or lack of "thresholds" for specific toxic effects, the importance of interactions, and the variation in sensitivity and exposure levels within the population is required (WHO, 2006). Such comprehensive data are often unavailable and quantitative relationships uncertain, thus expert judgement (often based on the weight of evidence available) plays a significant role in establishing guidelines to be used to establish acceptable levels of population exposure (WHO, 2000).

At the global scale, a number of Air Quality Guidelines (AQG) have been developed by the World Health Organisation (WHO) to inform worldwide air quality policy (*e.g.* WHO (2000); (2006)). The latest update of the WHO AQG was made in 2005 with the prime focus on O_3, NO_2, SO_2 and particulate matter (WHO, 2006).

The European Union (EU) has also developed an extensive body of legislation that establishes health based standards and objectives for a number of atmospheric pollutants. As part of the EU, the UK is required to report air quality data on an annual basis under the Council Directive on ambient air quality and cleaner air for Europe (2008/50/EC) and the Fourth Daughter Directive (2004/107/EC) within the Air Quality Framework Directive (1996/62/EC). Directive 2008/50/EC incorporated pre-existing EU regulation and air quality standards as well as introducing a framework for assessing $PM_{2.5}$. Such directives are designed to, amongst other objectives; reduce human exposure to air pollution.

In addition to the statutory requirements (enforced by the EU Directives outlined above) that the UK has in order to address air pollution, such legislation has also been used to inform a number of the UK's own Air Quality objectives. Following the

Environment Act in 1995, the UK Air Quality Strategy was published in March 1997, establishing objectives for 8 main atmospheric pollutants (Defra, 2012). These objectives were informed by epidemiology and are based on the best available medical and scientific understanding of the effects of such pollutants on health (in addition to accounting for recent developments in the EU and WHO). In some cases the targets imposed under the national air quality objectives are more stringent than those of the EU Directives.

Table 1·3 illustrates the range of air quality standards outlined above which may be applied over a series of averaging periods to account for the health impacts associated with the various atmospheric pollutants, with toxicity a complex function of the interaction between the concentration of pollutant and duration of exposure (WHO, 2000).

Atmospheric pollutants may result in acute adverse health effects following peak exposure for a short period or incapacitating effects after prolonged exposure to lower concentrations. In general when short term exposures result in harmful effects, short term averages are recommended (WHO, 2000). Under such conditions, the use of a longer-term average would be misleading since the typical pattern of repeated peak exposures is diminished as a result of the averaging process and the risk manager would have some difficulty in developing an effective strategy (WHO, 2000).

In the case of exposure to SO_2, for example, the associated health effects (including respiratory irritation and constriction of the airways) can result very rapidly, thus making short-term peak concentrations important with levels averaged over 15 minute, 1 hour and 24 hour intervals (Table 1·3). As outlined above, in the case of NO_2, health effects may be attributed to both short term exposure to high levels of

NO_2 and longer term exposure to lower levels of the pollutant. For CO and O_3, an 8 hour running mean is defined as the period over which concentrations are averaged as their associated health effects arise as a result of exposure to elevated levels of these pollutants over several hours. In some cases, knowledge of the dose-response relationship may be sufficient to allow recommendation of a longer averaging period, as is often the case whereby chemicals accumulate in the body over time resulting in adverse effects (WHO, 2000).

Table 1·3 - *Global (WHO), European (EU) and UK National Air Quality (UK N.A.Q.) standards for the protection of human health (shown for a number of selected pollutants). Numbers in parenthesis refer to the number of exceedences permitted annually excluding the EU guidelines for O_3 that represents those permitted over a 3 year period.*

Pollutant	Averaging period	WHO[§§§]	EU[****]	UK N.A.Q.[††††]
SO_2 (ppb)	10 min	188	-	-
	15 min	-	-	100 [35]
	1 hour	-	131 [24]	131 [24]
	24 hour	8	47 [3]	47 [3]
NO_2 (ppb)	1 hour	105	105 [18]	105 [18]
	Annual	21	21	21
O_3 (ppb)	8 hour	50	60 [25]	50 [10]
CO (ppm)	1 hour	25	-	-
	8 hour	10	9	9
PM_{10} (µg m^{-3})	24 hour	50	50 [35]	50 [35]
	Annual	20	40	40
$PM_{2.5}$ (µg m^{-3})	24 hour	25	-	-
	Annual	10	25	25

A number of air quality monitoring sites exist across the UK that comprise a series of monitoring networks. One such network is the Automatic Urban and Rural Network (AURN), the largest automatic monitoring network (103 stations,

[§§§] WHO (2000); (2006).
[****] Defra (2007); EU (2008).
[††††] UK N.A.Q. refers to the UK's National Air Quality objectives (Defra, 2007).

November, 2012) within the UK. Such measurements constitute a large proportion of the monitoring evidence base and are used in the annual assessment of air quality and compliance with legislation within the UK (Defra, 2012).

Within the UK, compliance with CO and SO_2 air quality standards was observed across the country in 2011 (with the targets for these pollutants not breached in recent years) however, a number of exceedences of the EU air quality standards occurred for NO_2 during the same year, the majority of these being in urban areas. Hourly mean limits set for NO_2 of 105 ppb (200 µg m^{-3}) were exceeded on more than the permitted 18 occasions during 2011 in the Greater London and Glasgow urban areas as well as the South East, whilst the limit value set for the annual mean (21 ppb) was exceeded in 40 of the 43 zones included in the UK air quality assessment (Defra, 2012).

Exceedences were also reported for the long term ozone objective (maximum daily 8-hour mean within a calendar year not exceeding 60 ppb) for human health in all 43 zones however target values (maximum daily 8-hour mean of 60 ppb not to be exceeded on more than 25 days averaged over three years) were met by all. In terms of O_3 there is also an additional target based on the AOT40 statistic (expressed in µg m^{-3} .hours) that represents the sum of the difference between hourly concentrations greater than 40 ppb (80 µg m^{-3}) and 40 ppb over a given period using only the one-hour values measured between 08:00 and 20:00 Central European Time each day (EU, 2008). In this case, all 43 zones achieved the target value determined using the AOT40 statistic.

Air pollution events

Particular attention to the air pollution problem has been gained through events such as that which occurred in London in 1952 during which up to 12,000 people

died due to **smog**[××] (Bell *et al.*, 2004) and resulted in the introduction of the UK clean air act (1956)[‡‡‡‡]. This event occurred due to sulphur dioxide (SO_2) emitted from coal-fired power stations within the city (forming a sulphuric acid mist) and unfavourable anti-cyclonic conditions that trapped the smog below a stable surface inversion layer (*e.g.* Figure 1·3).

Equally as harmful to health is **photochemical smog** that results from the build up of O_3 and other species *e.g.* peroxyacetyl nitrate (PAN). A number of severe photochemical smog episodes during which O_3 levels have exceeded 400 ppb (Harrison, 2001b) have been observed in Los Angeles, caused by the build up of NO_X and VOCs (that lead to the production of O_3 through a series of photo-chemical reactions (§1·6·1)) exacerbated by a strong sea breeze and the surrounding topography of the region.

Photochemical smog is less severe in the UK by comparison, although the UK heat wave of 2003 resulted in elevated O_3 concentrations particularly across the south east of England where concentrations ranged between 80 to 110 ppb (Figure 1·9), contributing to in excess of 200 additional deaths as a direct result (Stedman, 2004).

[××] A fog in which smoke, or any other form of atmospheric pollutant, plays an important role in formation or increase in density (UKMO, 1991).

[‡‡‡‡] That included SO_2 emission reduction measures such as the use of low sulphur fuels and a minimum height to be imposed for chimney stacks.

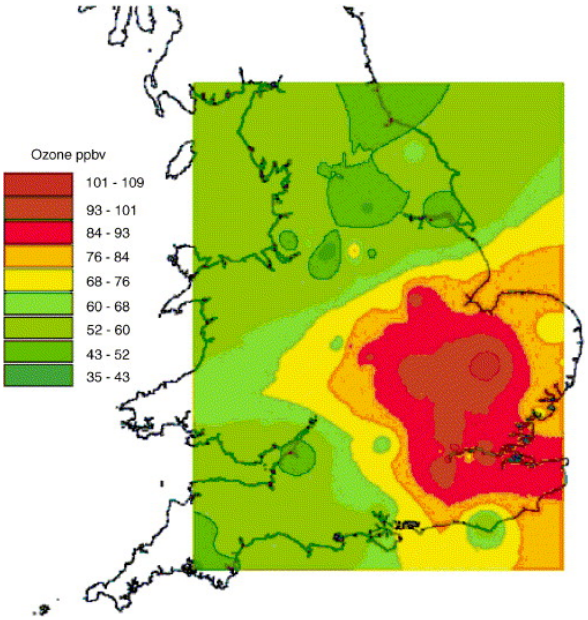

Figure 1·9 - *The distribution of ozone on 6th August 2003 across the UK, illustrating the harmful levels of ozone over a large proportion of southeast England (Lee et al., 2006).*

Spatial and temporal scales of air pollution

The atmospheric lifetime of species can be linked with certain characteristic spatial transport scales, illustrated in Figure 1·10 resulting from intricate coupling between chemical lifetimes of principal species and the atmospheric scales of motion (Seinfeld and Pandis, 1998). Long-lived, stable species such as methane (CH_4) and chlorofluorocarbons (CFCs) can reside in the atmosphere for decades or even centuries becoming uniformly mixed over the entire globe and as such are only of interest on the synoptic (10^2 to 10^3 km) or global scale (> 5 x 10^3 km).

Britter and Hanna (2003) define four different spatial scales in the urban context that include the; regional, city, neighbourhood and street canyon domains. The **regional scale** (up to 100 or 200 km) is the largest affected by an urban area that may represent a perturbation which acts to deflect and decelerate the flow. In terms of atmospheric composition, the pollutants of interest on such scales may include moderately long lived species such as CO.

On the **city scale** (up to 10 or 20 km) variations in flow and dispersion associated with individual roughness elements, such as buildings, have been averaged out. At the **neighbourhood scale** (up to 1 or 2 km), horizontal averaging over a large enough area of the city continues to filter out street scale flow although variations in building type and density across the city are now resolved. At this scale it is desirable to understand and model flow within the urban canopy. Moderately long lived chemical species including O_3, NO_X and some VOCs (*e.g.* propene (C_3H_6) and isoprene (C_5H_8)) become important on such scales.

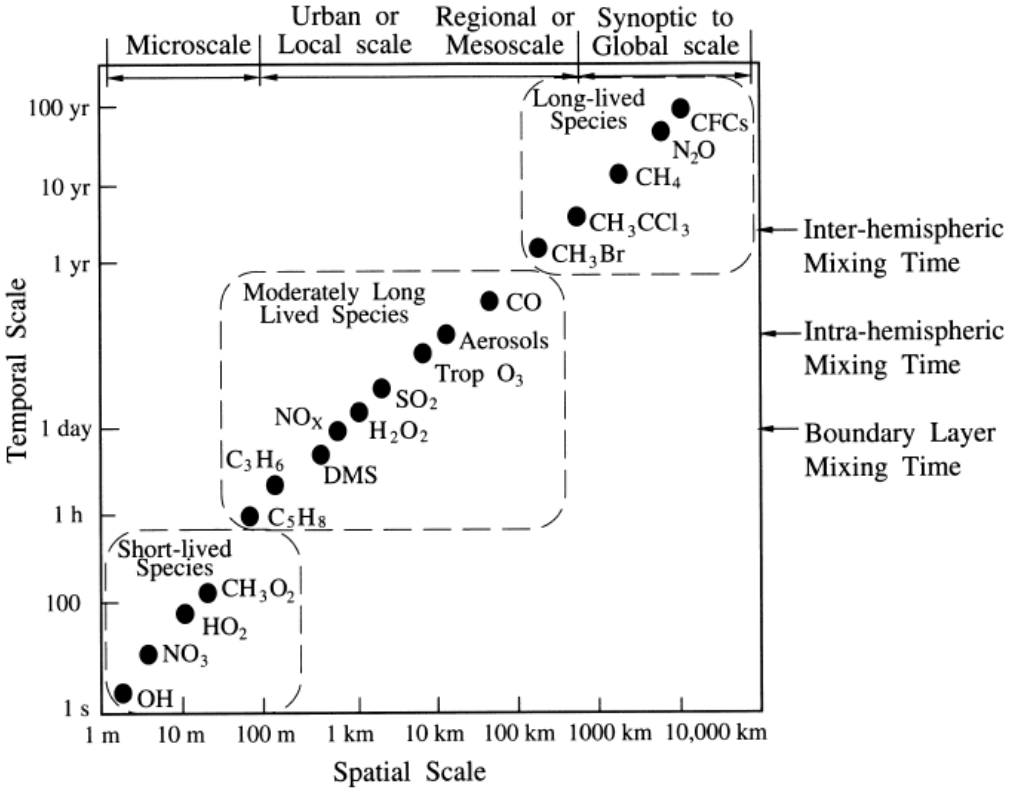

Figure 1·10 - *Spatial and temporal scales of the variability in atmospheric species (Seinfeld and Pandis, 1998).*

At the smallest scale is the **street canyon** formed by a road running between two rows of buildings; this scale (less than ~ 100 to 200 m) concerns flow and dispersion within and near a single street, around individual buildings, or intersections. Inhomogeneities at this scale strongly affect the characteristics of the flow. It is

important to study atmospheric composition on the street canyon scale as they are the place in which a large percentage of the population live and work.

Short-lived species have relatively small spatial scales *i.e.* the hydroxyl radical (OH) (τ_{OH} ≈ 0.1 to 2 seconds) or the hydroperoxy radical (HO_2) (τ_{HO_2} ≈ 10 seconds). These species as well as moderately long lived species *i.e.* NO_X (τ_{NO_X} ≈ 1 day) are of particular interest on the urban and microscale and provide the main focus of the following section.

1·6 Tropospheric chemistry

As highlighted in Table 1·1, there is a large difference between the **chemical composition** of "clean" and polluted environments. The chemical reactions that take place within the urban troposphere also differ from those of unpolluted environments. Increased emissions from local and anthropogenic sources as well as the varied morphology of the urban landscape can result in a decrease in the mixing and dispersion of pollutants leading to an increase in their concentrations. It is important to understand the chemical processes that occur in urban areas in order to control and reduce the impacts of air pollution within the vicinity or downwind of such conurbations. The **gas-phase chemistry** of the **urban troposphere** provides the main focus of this research.

1·6·1 HO_X chemistry

The troposphere is an oxidising environment in which the chemistry is dominated by the highly reactive gas phase radicals[§§§§] (known as the tropospheric oxidants, HO_X (OH and HO_2)). OH, represents a major sink for many pollutants in the

[§§§§] Compounds with a free electron (Jacobson, 2002).

atmosphere. Molecular oxygen (O_2 – the most abundant oxidant in the earth's atmosphere) is largely unreactive in the troposphere as it requires short-wave radiation (< 240 nm) to photolyse, the availability of which is limited to the stratosphere.

The concentrations of important **greenhouse gases** (**GHGs**) such as CH_4 and pollutants including CO, NO_2 and VOCs are dependent on their removal from the atmosphere through the process of oxidation[*****]. These processes are particularly important within the troposphere where pollutants are primarily emitted and subject to atmospheric processing. In polluted urban air, levels of the hydroxyl radical (OH) are strongly dependent on chemical cycling, which in turn is dependent on levels of NO_X.

In addition to a number of additional sources, OH is produced through a series of reactions that are initiated by the photolysis of O_3 to produce an electronically excited oxygen atom $O(^1D)$ (1·10). These excited state oxygen atoms collide predominantly with nitrogen or oxygen molecules (known as a third body, M[+++]) and stabilise to give the ground state oxygen atom $O(^3P)$ (1·11) that may then react with molecular oxygen (O_2) to reform O_3 (1·24). Alternatively, $O(^1D)$ may react with water vapour (approximately 10 %) to form two OH radicals (1·12).

$$O_3 + h\nu \longrightarrow O(^1D) + O_2; \quad (1{\cdot}10)$$

$$O(^1D) + M \longrightarrow O(^3P) + M; \quad (1{\cdot}11)$$

$$O(^1D) + H_2O \longrightarrow OH + OH. \quad (1{\cdot}12)$$

It is these series of reactions (1·10 - 1·12), initiated by O_3 photolysis, that represent a major source of atmospheric OH, thereby providing the driving force for daytime

[*****] The combination of oxygen with an element or compound during chemical reaction (Jacobson, 2002).

[+++] A third molecule which is involved in collision, but is not changed by the chemical reaction (Bloss, 2009).

tropospheric chemistry (particularly in remote regions). OH reacts readily with hydrocarbons*** (*e.g.* CH_4) initiating their degradation and ultimate removal from the atmosphere thus determining their lifetime. CH_4 and CO are major sinks of tropospheric OH with approximately 30 % reacting with CH_4 and 70 % with CO in unpolluted environments (Wayne, 1991). Due to its very short lifetime, the abundance of OH is highly variable, responding rapidly to changes in the processes that affect its production and removal.

Reactions of VOCs with OH can lead to the production of organic peroxy radicals (RO_2), *e.g.* the methyl peroxy radical, CH_3O_2 in the case of CH_4 (1·14) that follows the production of the methyl radical, CH_3 (1·13) that reacts with O_2.

$$CH_4 + OH \longrightarrow CH_3 + H_2O; \quad (1{\cdot}13)$$

$$CH_3 + O_2 + M \longrightarrow CH_3O_2 + M; \quad (1{\cdot}14)$$

$$CO + OH \longrightarrow CO_2 + H; \quad (1{\cdot}15)$$

$$H + O_2 + M \longrightarrow HO_2 + M. \quad (1{\cdot}16)$$

Hydroperoxy radicals (HO_2) are produced via reaction of CO and OH (1·15; 1·16) that produces carbon dioxide (CO_2) and a hydrogen atom (H) with H then reacting with O_2 to produce HO_2. Thus, the following reactions represent the oxidation of VOCs:

$$OH + VOC \longrightarrow H_2O + R; \quad (1{\cdot}17)$$

$$R + O_2 + M \longrightarrow RO_2 + M. \quad (1{\cdot}18)$$

The fate of peroxy radicals is dependent upon the concentration of NO_X in the surrounding environment.

*** Organic compounds that contain only hydrogen (H) and carbon (C).

Under low NO_X conditions (*e.g.* unpolluted environments) the peroxy radicals (HO_2 and RO_2) are consumed through a number of reactions including self reaction (1·19 - 1·21) that result in peroxides, aldehydes and alcohols being formed:

$$RO_2 + HO_2 \longrightarrow ROOH + O_2; \quad (1{\cdot}19)$$

$$HO_2 + HO_2 + M \longrightarrow H_2O_2 + M; \quad (1{\cdot}20)$$

$$HO_2 + O_3 \longrightarrow OH + 2O_2. \quad (1{\cdot}21)$$

These species remain relatively stable within the troposphere with lifetimes in the order of days, dissolving readily into cloud droplets prior to removal by precipitation. If NO_X levels are sufficiently low this process represents the terminal stage of the reaction chain that began with O_3 photolysis (1·10) with the net effect of reactions resulting in the destruction of O_3. In unpolluted environments, HO_2 may react with O_3 regenerating OH (1·21). As such, a fast null cycle links NO, NO_2 and O_3 in which there is no net source of O_3, known as **photochemical steady state** (**PSS**):

$$NO + O_3 \longrightarrow NO_2 + O_2; \quad (1{\cdot}22)$$

$$NO_2 + h\nu \longrightarrow NO + O; \quad (1{\cdot}23)$$

$$O + O_2 + M \longrightarrow O_3 + M. \quad (1{\cdot}24)$$

Thus, neglecting other processes *e.g.* $RO_2 + NO \longrightarrow RO + NO_2$, the concentration of ozone, $[O_3]$, is determined by NO_X levels and the intensity of sunlight *i.e.*:

$$[O_3] = \frac{j_{NO_2}[NO_2]}{k_{NO+O_3}[NO]}. \quad (1{\cdot}25)$$

Within the polluted urban environment where NO_X[×××] and VOCs are abundant, a very different series of reactions can occur following the formation of peroxy radicals (1·14 & 1·16) known as **radical propagation** that can result in the formation of secondary pollutants such as O_3. In polluted environments HO_2 reacts

[×××] If levels of NO emitted from car exhausts are high enough the recombination of NO occurs via the termolecular reaction: $NO + NO + O_2 \longrightarrow 2NO_2$.

rapidly with NO to form NO_2, regenerating OH in the process (1·26). RO_2 can react with NO to form an alkyl radical, RO (*e.g.* the methoxy radical (CH_3O) in the case of CH_4), and NO_2 (1·27). RO can then go on to react with O_2 to form a HO_2 and an aldehyde, R'CHO (*e.g.* formaldehyde (HCHO) in the case CH_4 oxidation). HO_2 can then go on to react with NO (1·26) *i.e.*:

$$HO_2 + NO \longrightarrow OH + NO_2; \quad (1{\cdot}26)$$

$$RO_2 + NO \longrightarrow RO + NO_2; \quad (1{\cdot}27)$$

$$RO + O_2 \longrightarrow R'CHO + HO_2. \quad (1{\cdot}28)$$

The cycle of reactions (outlined above) that occur during the oxidation of hydrocarbons is illustrated in Figure 1·11 with the additional reactions that take place in polluted environments indicated by the red arrows.

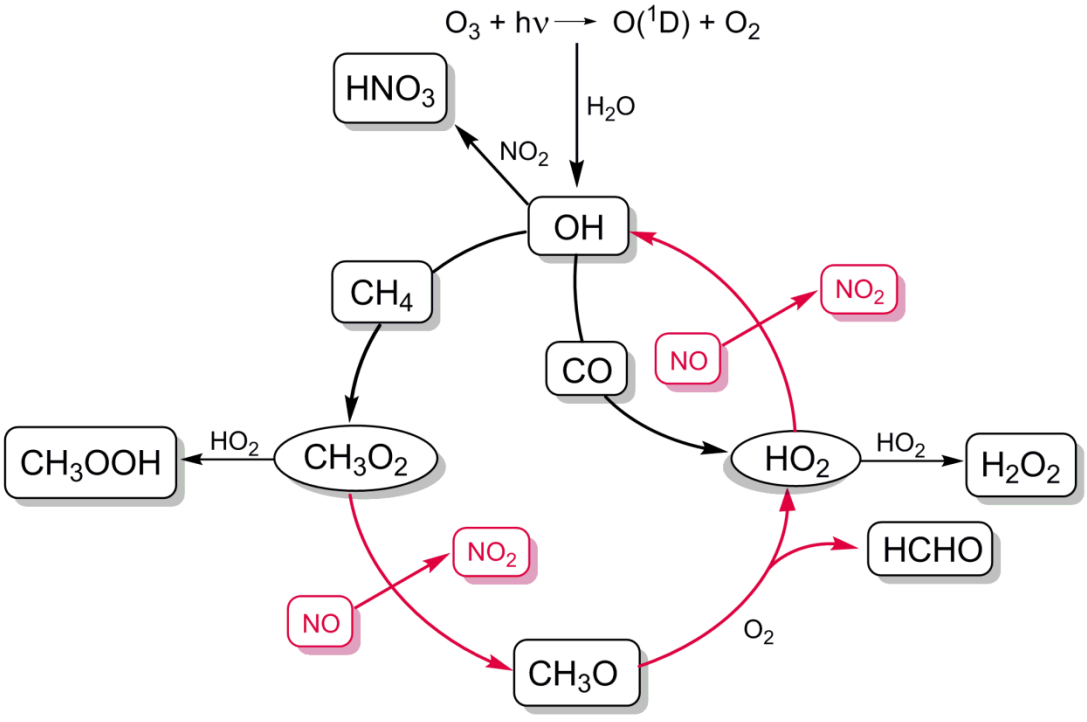

Figure 1·11 - *The reaction cycle involved in the oxidation of hydrocarbons using methane (CH_4) as an example with the additional processes that occur in the polluted environments (red arrows). Adapted from Bloss (2009).*

Thus, in a high NO_X environment, the oxidation of hydrocarbons leads to NO_2 production and an increase in OH that leads to a subsequent increase in oxidation. NO_2 can be photolysed via Reaction 1·23 and go on to form O_3, hence hydrocarbon oxidation in the presence of NO_X leads to the production of O_3 via Reactions 1·22 - 1·24. NO is therefore converted to NO_2 without destroying O_3 as in Reaction 1·23. The cycle rapidly interconverts OH, RO_2 and HO_2 and results in the net production of O_3.

The radical propagation cycle is limited by the removal of NO_2 through termination reactions such as reaction of OH and NO_2 to form nitric acid (HNO_3):

$$OH + NO_2 + M \longrightarrow HNO_3 + M. \qquad (1{\cdot}29)$$

This represents the principal removal mechanism for NO_X in urban environments as HNO_3 is highly soluble and is subsequently lost to cloud, fog and aerosols.

Peroxyacetyl nitrate (PAN - $CH_3C(O)OONO_2$) is an important product of oxidation, formed by the reversible reaction between NO_2 and peroxyacetyl radicals ($CH_3(CO)OO$). PAN forms a reservoir of NO_X that is much less soluble than HNO_3 and is particularly important in terms of transboundary air pollution (as the reaction of NO_2 and the peroxyacetyl radical is highly temperature dependent). Formed in favourable tropospheric conditions, PAN can be cooled upon its ascent in the atmosphere becoming stable at higher altitudes. In this way PAN can be transported over large distances from polluted environments to the remote atmosphere where, upon descent warming occurs and NO_X is released. PAN is also very important from an impacts perspective as it forms a key component of photochemical smog and is extremely harmful to human health.

Night time chemistry and the NO_3 radical

At night OH production through photolysis of O_3 and NO_2 ceases. The cycle of O_3 production is replaced by a series of reactions in which NO and NO_2 are converted to the nitrate radical (NO_3) and subsequently dinitrogen pentoxide (N_2O_5). N_2O_5 is hydrolysed readily by water on wet surfaces and the surface of aerosol particles yielding HNO_3. At night NO_3 acts in a similar way to OH as it is responsible for the oxidation of hydrocarbons via hydrogen abstraction in the case of aldehydes or addition reactions in the case of alkenes. This thesis concerns the photo-chemical reactions that occur within the troposphere in the presence of sunlight therefore night time chemistry will not be discussed further at this point.

During the day, NO_3 undergoes rapid photolysis therefore is not present in significant concentrations *i.e.*:

$$NO_3 + h\nu \longrightarrow NO + O_2; \quad (1{\cdot}30)$$

$$NO_3 + h\nu \longrightarrow NO_2 + O(^3P). \quad (1{\cdot}31)$$

The lifetime of NO_3 is approximately 5 seconds under clear conditions and with the sun at its highest point in the sky (Monks, 2005).

The diurnal variation in key pollutants

The diurnal variation in the concentration of NO, NO_2 and O_3 along with other pollutants in heavily polluted urban areas often follow the characteristic pattern illustrated in Figure 1·12 (Harrison, 2001b).

A peak in NO and other hydrocarbons tends to coincide with peak rush hour traffic with a lag in peak NO_2 of a couple of hours whilst NO emissions become oxidised more efficiently. At this point the ratio of NO_2 to NO has increased significantly to increase the rate at which O_3 is formed. The maximum concentration of O_3 occurs during the early afternoon coinciding with the maximum intensity of sunlight. As

solar radiation decreases during the afternoon, the rate of photolysis slows and O_3 is destroyed (1·10) as the rate at which NO_2 is photolysed diminishes (1·23).

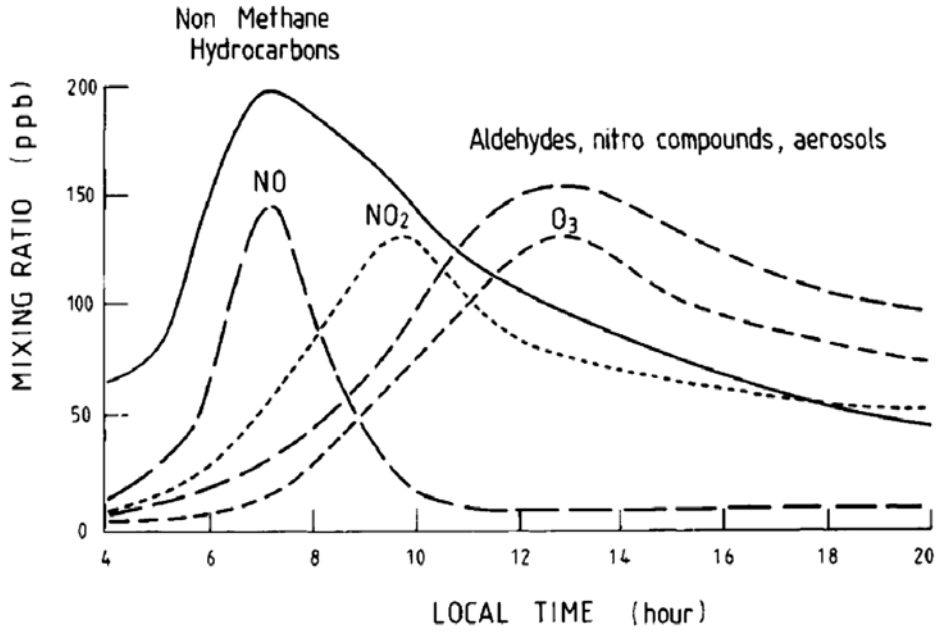

Figure 1·12 - *The diurnal variation in the mixing ratio of a number of pollutants in the heavily polluted urban atmosphere (Harrison, 2001b).*

1·6·2 Limits to ozone production

In polluted environments both NO_X and VOCs are required for significant O_3 production to occur with non-linear relationships existing between precursors and O_3 formation. An understanding of the change in O_3 production as a result of a change in either NO_X or VOCs is therefore important in mitigating pollution problems through the reduction of emissions (Finlayson-Pitts and Pitts Jr, 2000).

The production of O_3 is often observed to increase up to a certain point with increasing NO_X, subsequently decreasing with an increase in NO_X as a result of HNO_3 formation that acts as a radical sink *i.e.* Reaction 1·29 becomes predominant in OH removal and O_3 production decreases. The point at which this occurs can vary locally due to the availability of both VOCs and solar radiation.

The shape of the surface shown in Figure 1·13 can be used to establish whether the control of NO_X or VOC emissions is most effective in controlling O_3 production. It must be noted that the concentration of O_3 included on the *y* axis reflects that after a certain period of time and not instantaneous amounts. Point A represents a high VOC to NO_X ratio, and decreasing VOC alone at constant NO_X (along line AB) results in only a small reduction in the concentration of O_3 produced over time.

Decreasing NO_X at constant VOC however (along line A to C) leads to a significant reduction in the concentration of O_3, known as a **NO_X limited** case, whereby a reduction in NO_X is the most effective method of reducing O_3 production. Such conditions occur at locations where NO_X levels are low *e.g.* sub-urban or rural locations downwind of urban areas (Figure 1·14).

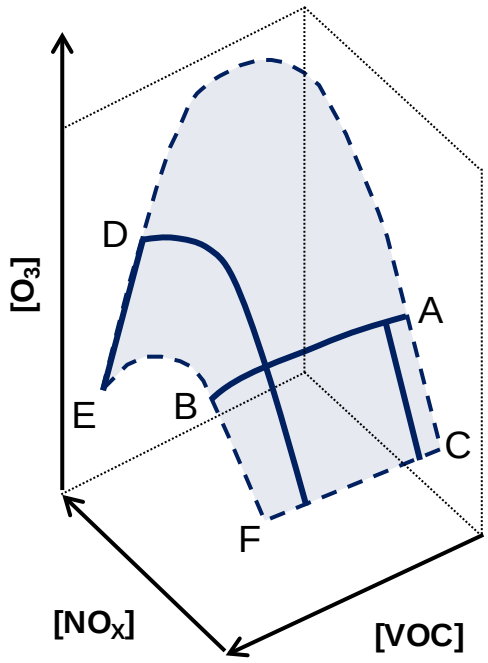

Figure 1·13 - *A three-dimensional (3-D) representation of ozone (O_3) isopleths generated from initial mixtures of VOC and NO_X in air. Point D represents the VOC-limited region (highly polluted city centres) and point A represents the NO_X limited region typical of locations downwind of city centres. Adapted from Finlayson-Pitts and Pitts (2000).*

A low VOC to NO_X ratio (point D) occurs at locations where NO_X levels are relatively high *e.g.* polluted city centres and represents **VOC limited** conditions. In this case, a reduction in VOC at a constant NO_X level (line DE) results in a substantial decrease in the concentration of O_3 over a certain period. Conversely, decreasing NO_X in this case at constant VOC (line DF) causes O_3 concentration to increase initially until a certain point is reached after which the concentration of O_3 then begins to decrease; these conditions again represent the NO_X limited case.

Figure 1·14 illustrates the effect of moving downwind from the source region (*e.g.* city centre) to a remote region (*e.g.* rural area) on O_3 and NO_X concentrations. O_3 levels are relatively low above the city centre due to the prevalence of VOC limited conditions in this region. The concentration of O_3 reaches a peak downwind of the city centre where conditions are neither NO_X nor VOC limited despite rapidly decreasing NO_X levels as a result of significantly lower emissions.

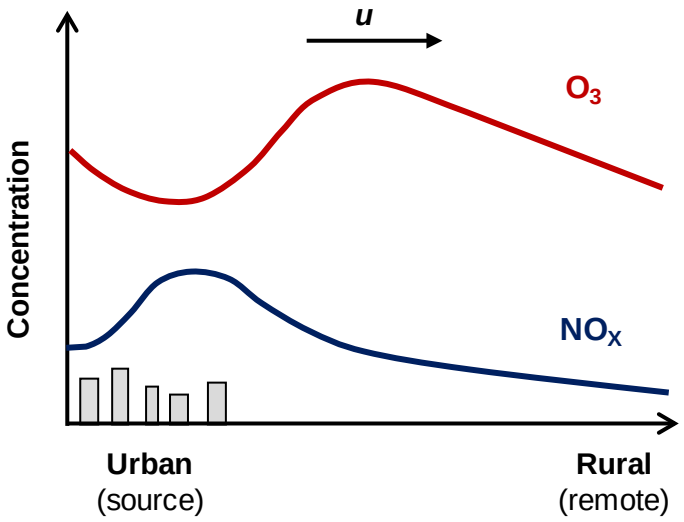

Figure 1·14 - *An idealised diagram showing the variation in the concentration of O_3 and NO_X moving downwind from an urban emission source (e.g. city) to a remote region (e.g. rural area) illustrating the transition from VOC-limited to NO_X-limited conditions. The prevailing wind direction is illustrated by u.*

Following a peak in O_3 levels, concentrations decrease significantly with decreasing NO_X upon the approach to remote regions where NO_X limited conditions prevail.

1·6·3 Alternative radical sources in polluted environments

As discussed in section 1·6·1 the main source of radicals in the free troposphere comes from the photolysis of O_3 and the subsequent reaction of $O(^1D)$ with H_2O. In polluted environments many additional sources of HO_X radicals can be identified, the most important of which occurs through the photolysis of **nitrous acid** (**HONO**), **alkene ozonolysis** and **aldehyde photolysis**. These processes can be summarised as follows:

$$HONO + h\nu \longrightarrow OH + NO; \quad (1{\cdot}32)$$

$$HCHO + h\nu \longrightarrow H + HCO \longrightarrow 2HO_2 + CO; \quad (1{\cdot}33)$$

$$Alkene + O_3 \longrightarrow OH + HO_2 + RO_2 + Products. \quad (1{\cdot}34)$$

HONO is an important pollutant that is more abundant in the urban atmosphere than the background troposphere and is formed through the termolecular reaction of OH with NO *i.e.*:

$$OH + NO + M \longrightarrow HONO. \quad (1{\cdot}35)$$

Alternatively HONO may be formed through the reaction of NO_2 on various surfaces or through a number of heterogeneous pathways (Monks, 2005). HONO can be emitted directly into the atmosphere by vehicles or formed overnight and increases through Reaction 1·35 to reach levels of several ppb (Bloss, 2009). HONO photolyses rapidly in the presence of sunlight (via Reaction 1·32) to give OH and NO therefore its daytime concentrations are low. HONO therefore provides an early morning source of OH in urban areas, initiating daytime chemistry before other sources of OH become established. The lifetime of HONO ranges from 10 minutes at noon to 1 hour in the early morning (Seinfeld and Pandis, 1998).

Recent observations of HONO during the day have revealed levels that reach up to 200 ppt with much uncertainty surrounding daytime sources (Finlayson-Pitts and

Pitts Jr, 2000, Bloss, 2009). Within the urban troposphere, high daytime concentrations of HONO may be explained by NO_2 to HONO conversion.

A recent study by Langridge *et al*. (2009) has also shown that a strong daytime source of HONO within the urban environment stems from the use of self-cleaning window glass and other building materials such as paints and cements. These materials are coated with titanium dioxide (TIO_2), specifically intended to remove pollutants such as NO_X and organic molecules from the atmosphere. TIO_2 however, instead of acting as a NO_X sink, actually leads to the production of HONO having serious implications in terms of OH production and formation of secondary pollutants. The use of TIO_2 coated materials can therefore affect atmospheric composition and cause the degradation of air quality in urban areas.

1·7 Management of urban air quality

There are a number of components that determine air quality in an urban area (Figure 1·15). The first component of the system stems from the source of pollution *e.g.* **emissions** into the atmosphere. Following emission, pollutants are subject to **diffusion**, **transport**, **chemical processing**, **chemical transformation** and **removal** within the atmosphere (Figure 1·2).

In order to improve air quality an understanding of how the atmosphere responds to pollutant emissions must be gained. **Monitoring** and **modelling** techniques may be employed to determine the level of **pollutant exposure** and determine local "**hot-spots**" in which pollutant concentrations are significantly higher. One of the latter components of the system involves the **response of receptors** (*e.g.* humans) following their exposure to atmospheric pollution. Such effects may in turn trigger

risk assessment, legislative action and the implementation of an air quality management system (AQMS) including the control of source emissions*.

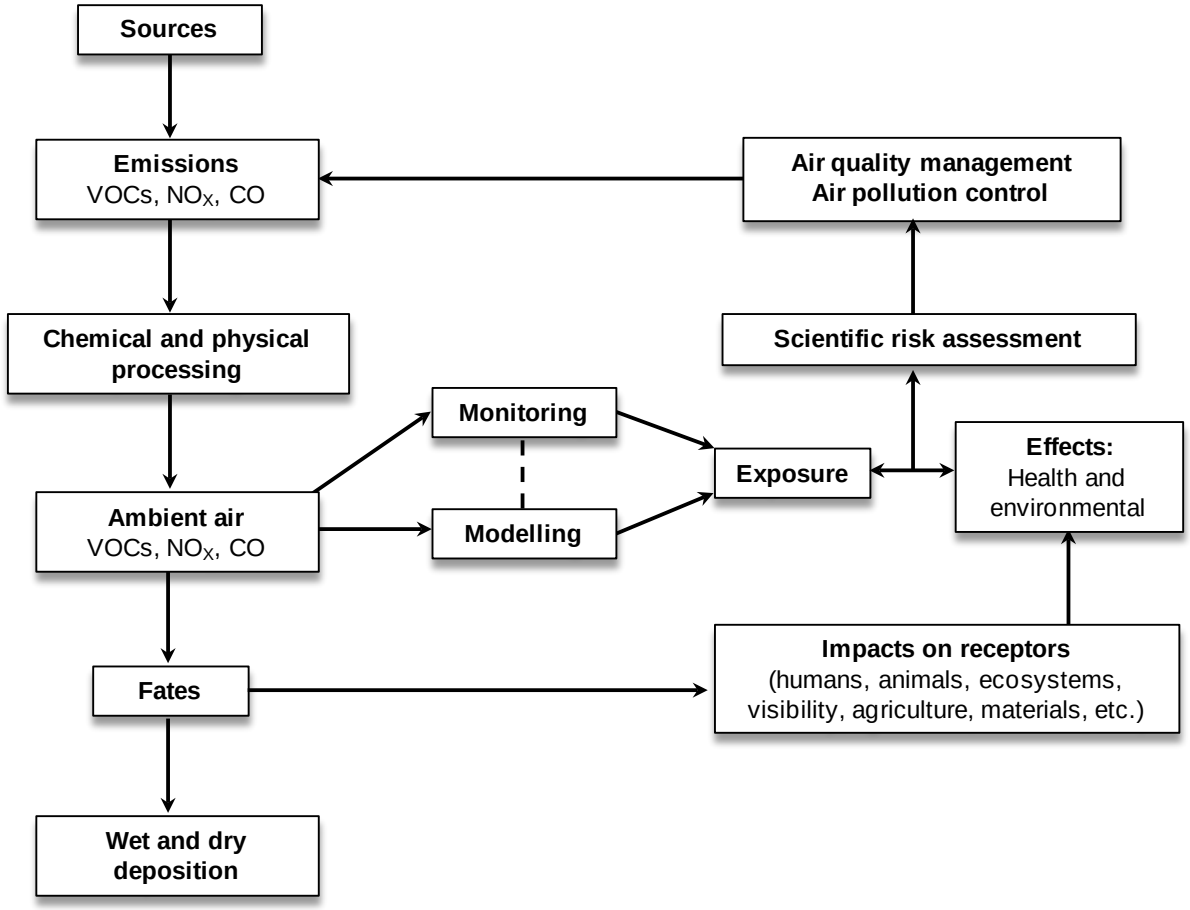

Figure 1·15 - *A schematic diagram of the various components of the air pollution system on the local scale (Finlayson-Pitts and Pitts Jr, 2000).*

Numerical modelling of air pollution can prove vital in understanding the likely causes and impacts of air pollution. Air pollution models may include vehicle emissions as well as the transport and chemical processing once released in the atmosphere. It is this aspect of local air quality management (AQM) that this thesis is concerned with.

* Measures may include the use of cleaner technologies such as catalytic converters on vehicles; reducing the volume of traffic (*e.g.* by introducing Low Emission Zones (LEZs)) or imposing limits industrial activity.

1·8 Research motivation and thesis outline

This research is concerned with the study of **street canyon atmospheric composition** (*i.e.* on the microscale (< 100 - 200 m)) where the residence time of pollutants is in the order of a few minutes. The chemical and dynamical processes that occur on the street canyon scale coupled with localised emissions can result in large differences between the compositions of air within the street canyon when compared to the overlying background atmosphere. Complex interactions between the chemistry and canyon fluid dynamics can also result in large spatial and temporal variations in pollutant levels within the canyon that may be significant in terms of local AQM. In general, street canyons are subject to increased emissions and poor ventilation which can lead to the build up of pollutants to potentially harmful levels with serious implications for public health, vegetation and the built environment (Vardoulakis *et al.*, 2003, Bright *et al.*, 2011).

Primary pollutants such as NO, NO_2 and VOCs are often found to be present in significantly higher concentrations within the street canyon when compared to the overlying background atmosphere, as expected considering proximity to (traffic) emission sources. Within such canyons, O_3 levels are often reduced compared with the overlying air due to titration with primary NO, an effect known as the "urban decrement" (AQEG, 2009).

As outlined in (§1·6·1) in the presence of sunlight, NO_X chemistry is governed by photochemical steady state chemistry in which NO, NO_2 and O_3 establish equilibrium. Interactions with HO_X radicals lead to additional NO-to-NO_2 conversion and result in the net production of O_3. As such, it is valuable to assess the extent of pollutant pre-processing prior to their emission into the wider urban atmosphere in order to gain an insight into the oxidative environment of the street canyon (Bright *et al.*, 2011). The associated key chemical processes are highly non-linear with time-

scales equivalent to that of the turbulent mixing (from seconds to a few minutes), leading to complex interactions between chemistry and fluid dynamics (Bright *et al.*, 2011). Long lived pollutants such as CO and VOCs are unlikely to show a substantial variation in concentration within the street canyon due to chemical processing alone with their distributions governed near-exclusively by canyon dynamics. Chemical processing of NO_X and O_3 which have shorter chemical lifetimes occurs down to similar timescales to those of the key dynamical processes within the urban canopy layer, thereby causing these species to exhibit a marked variation within the canyon. Very short lived species, such as OH and HO_2, with atmospheric lifetimes of seconds or less, are highly variable within the canyon and respond rapidly to changes in chemical composition on the canyon scale.

Atmospheric composition within street canyons is determined by the composition of **background air** mixed in from above the canyon, **advection** of air into and out of the canyon, **vehicle exhaust and other emissions** from within the street, together with the **mixing and chemical processing** of pollutants within the canyon. The interaction of these factors determines both the pollutant concentrations experienced within the canyon, their spatial and temporal variation, the extent to which emissions are pre-processed within the canyon and the resulting flux of such emissions out of the canyon (Bright *et al.*, 2011).

The study of canyon fluid dynamics and atmospheric composition has been the subject of a number of field measurement campaigns, wind tunnel experiments and numerical modelling investigations (Chapter 2). However relatively few studies have integrated the mixing and chemical processing of pollutants on the street canyon scale thereby limiting our understanding of atmospheric composition within such domains.

The main aim of this thesis is to investigate chemical-dynamical coupling and atmospheric composition on the street canyon scale. A computationally affordable reduced chemical scheme that includes an accurate and detailed representation of the chemical processes that occur within the canyon will be developed. Through the combination of this reduced scheme with emissions and dynamics simulated by a **Large Eddy Simulation** (**LES**) model, the dominant processes in determining canyon atmospheric composition will be investigated. As the key chemical processes and canyon dynamics occur on comparable time scales, the combined LES dynamics-chemistry approach is therefore necessary to study this interaction.

The key questions that form the main objectives of the thesis are as follows:

- *How different is the air quality within the street canyon from the overlying background atmosphere and how does this depend upon the dynamics?*
- *What is the spatial and temporal variation in pollutant levels within the street canyon and what are the implications in terms of pollutant exposure?*
- *To what degree are pollutants processed within the street canyon before they escape to the wider atmosphere?*
- *What are the short term (in the order of seconds) pollutant levels experienced within street canyons and how do these compare with hour long single point averages typically recorded at monitoring stations?*
- *What are the potential effects of changing the nature of emissions on atmospheric composition within the canyon?*

A review of the models and mechanisms used in modelling tropospheric chemistry is given in Chapter 2. In addition, recent advances and methods used in modelling dynamics, dispersion and chemical processing on the street canyon scale are discussed.

Chapter 3 describes the development and evaluation of the reduced chemical scheme to be implemented into the LES model. Subsequently, the formulation of a number of emission scenarios to be investigated using the developed model is outlined. The LES-RCS model, developed via the implementation of the reduced chemical scheme into the LES model, its configuration and validation is discussed in Chapter 4.

Chapter 5 investigates coupling dynamics, chemistry and atmospheric pre-processing on the street canyon scale using the combined model. Statistical analysis of model output is conducted in Chapter 6 to further investigate atmospheric composition, with particular attention paid to the potential exposure of receptors to pollutants within the canyon. Finally Chapter 7 includes discussion, conclusions and the potential scope of future work.

2: Modelling street canyon atmospheric composition

Simulating atmospheric composition involves two main types of model: **chemical models** and **dynamical / dispersion models**. The modelling techniques used to study tropospheric chemistry are considered in section 2·1 whilst those used to model street canyon dynamics and dispersion processes are explored in section 2·2. A major aim of this research is to combine these two modelling approaches in order to accurately simulate street canyon atmospheric composition. Another advantage of models is that they allow us to test our understanding, and (if found satisfactory) to predict atmospheric behaviour without having to make measurements.

2·1 Modelling tropospheric chemistry

Tropospheric chemistry modelling can be a useful tool in furthering our understanding of the chemical processes and transformations important in air pollution of the troposphere. It also allows us to study the response of the atmosphere to the release of pollutants and to develop effective pollution control strategies. Models may prove advantageous over field campaigns as they are relatively inexpensive in comparison and ensuing to their development they provide high resolution data, allow a number of scenarios to be investigated and parameters can be updated with relative ease.

Laboratory studies provide details on specific atmospheric processes and can be used to determine model input parameters (*e.g.* rate constants), however these studies provide limited insight into tropospheric chemistry as a whole due to the simplification of the system and limitation of the time scales studied.

It is possible to define atmospheric chemistry models according to their **domain** size (Table 2·1). These range from the microscale to the global scale (*i.e.* (usually) from high to low spatial resolution).

Table 2·1 - *Classification of atmospheric chemistry models according to their domain size (Seinfeld and Pandis, 1998).*

Model	Typical domain scale	Typical resolution
Microscale	200 x 200 x 100 m	5 m
Mesoscale (urban)	100 x 100 x 5 km	2 km
Regional	1000 x 1000 x 10 km	20 km
Synoptic (continental)	3000 x 3000 x 20 km	80 km
Global	65,000 x 65,000 x 20 km	5^{o} x 5^{o}

Although the typical resolution of microscale models is represented as 5 m in Table 2·1, street canyon models, for example, may be of considerably higher resolution where Δx and Δy are in the order of ≥ 0.3 - 0.5 m and Δz = 1.0 m within the canyon (*e.g.* the LES model presented within this thesis; Baker *et al*. (2004); Grawe *et al.* (2007) Kim *et al.* (2012); Kwak and Baik (2012)).

Atmospheric chemistry models may also be classified according to their spatial dimensionality (number of cells or grid boxes: Figure 2·1), alongside the time dimension. Column (1-D) models take into account the variation in concentrations in the vertical and with time whilst pollutant concentrations (c_i) remain homogenous in the horizontal, *i.e.* $c_i(z, t)$.

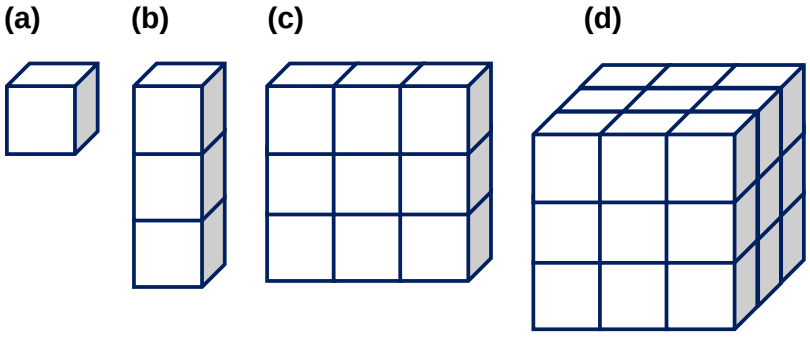

Figure 2·1 - *A schematic to show the classification of atmospheric chemistry models according to their spatial dimensionality (alongside the time dimension) including: (a) box (0-D), (b) column (1-D), (c) two dimensional (2-D) and (d) three dimensional (3-D) models. Adapted from Seinfeld and Pandis (1998).*

Increasing in complexity, two dimensional (2-D) models allow the simulation of chemical species in two dimensions. Therefore concentrations may vary in the horizontal, vertical and with time *i.e.* $c_i\,(x, z, t)$. Such models are often used to study atmospheric chemistry on the global scale by assuming pollutant concentration is a function of latitude and altitude (zonal) but not longitude (as longer lived species are usually well-mixed longitudinally).

The most complex of the models considered here is the three-dimensional (3-D) models in which pollutant concentrations vary longitudinally, latitudinally, vertically and over time *i.e.* $c_i\,(x, y, z, t)$. The chemistry in such models is often simplified, limited by computing power, and concentrations may be far lower than those observed during a regional pollution event through not including, for example, detailed oxidation chemistry (Emmerson and Evans, 2009).

There are two main types of model coordinate system used to simulate changes in chemical composition of an air parcel namely: **Eulerian** models and **Lagrangian** models. The concentration of species in Eulerian models is simulated within an array fixed in space whilst Lagrangian models simulate the continuous movement

(advection) of an air parcel with the wind field[*]. Table 2·2 lists examples of a number of models used in atmospheric chemistry.

Zero-dimensional (0-D) box models are the simplest form of atmospheric chemistry model (Figure 2·1) in which the atmosphere is represented by a single box. For an Eulerian box model a number of assumptions are made *i.e.*:

- Air within the box is well mixed
- The source of emissions are uniformly distributed
- Emissions are mixed instantaneously
- Pollutant concentrations are homogenous and therefore a function of time alone, $c_i(t)$.

Table 2·2 - *A selection of examples of atmospheric chemistry models.*

Model	Classification	Description
MOZART	3-D global CTM.	Simulates tropospheric chemical and transport processes and is driven by standard meteorological fields output from any number of meteorological centres including the European Centre for Medium-Range Weather Forecasts (ECMWF).
STOCHEM	3-D global Lagrangian model.	A Lagrangian model that works in a 3-D domain and incorporates chemistry as well as dynamical and dispersion processes.
NAME	Regional Lagrangian model.	Developed following the Chernobyl incident by the UK Met Office (UKMO). Treats pollutants as particles released into wind, temperature and rainfall fields from the UK Met Office's numerical weather prediction (NWP) model.
Photochemical Trajectory Model (PTM)	Lagrangian trajectory model.	Describes the chemical evolution and ozone production taking place within air parcels that arise from the oxidation of VOCs as they follow a certain trajectory.

The change in concentration of atmospheric species, *c,* over time within the box is determined by **emissions** (amount of pollutant emitted per unit time and surface of

[*] Also known as trajectory models.

the box), the **deposition** of species within the box (proportional to the concentration), the **advection** of species into and out of the box and finally the **ventilation flux** which represents the exchange of air from within the box with air above the box. The model is based on the conservation of the mass of species within the box of volume, $\Delta x \cdot \Delta y.h$

A mass balance for the concentration, c, of species within the box is given by the following equation:

$$\frac{d}{dt}(c\Delta x\Delta yh) = Q + R\Delta x\Delta yh - S + uh\Delta y(c_B - c), \qquad (2\cdot1)$$

where Q is the mass emission rate of chemical species (molecules s^{-1}), S is the removal rate of species (molecules s^{-1}), R is the chemical production rate of species (molecules cm^{-3} s^{-1}), c_B is its background concentration and u is the exchange velocity of species due to advection (m s^{-1}).

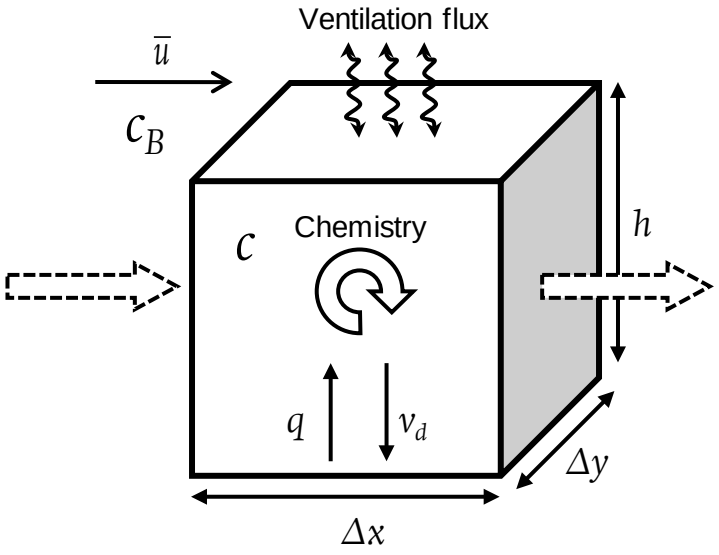

Figure 2·2 - *A schematic diagram to show the main components of an Eulerian box model. The concentration of species within the box is given by c whereas c_B represents the background concentration of pollutants. The exchange velocity of species due to advection (m s^{-1}) is represented by $\bar{u}$, emissions by q, and deposition by v_d. The advection of air into and out of the box is represented by the dashed arrows.*

Dividing Equation 2·1 by $\Delta x \cdot \Delta y$, assuming a constant height, h and describing the removal rate using the deposition velocity of species, v_d (with the total amount deposited per unit time equal to $v_d \cdot \Delta x \cdot \Delta y \cdot c$), Equation 2·1 can be simplified to:

$$\frac{dc}{dt} = \frac{q}{h} + R - \frac{v_d}{h}c + \frac{u}{\Delta x}(c_B - c), \qquad (2\cdot2)$$

where q is the emission rate of species per unit time and surface of the box (*e.g.* molecules cm^{-2} s^{-1}). The fourth term in Equation 2·2 represents the advection of species into the box from the surrounding environment and the transport of species out of the box. In order to consider the vertical exchange of air from within the box with air above the box, an additional term must be added to Equation 2·2 to give:

$$\frac{dc}{dt} = \frac{q}{h} + R - \frac{v_d}{h}c + \frac{u}{\Delta x}(c_B - c) + \frac{\omega_t}{h}(c_B - c), \qquad (2\cdot3)$$

where ω_t is the transfer velocity that represents the average speed of ventilation.

The residence time, τ_r, of air over the area of the box is given by the ratio of the length of the box to the exchange velocity of species due to advection *i.e.*:

$$\tau_r = \frac{1}{u/dx + \omega_t/h}. \qquad (2\cdot4)$$

Within **Lagrangian models** there is usually no mass exchange between the parcel and its surroundings. The change in chemical species is determined by emissions and the build up of primary and secondary pollutants it is subjected to as it moves along its trajectory. There is no dispersion in the horizontal and species are not removed from the box by mixing or dilution. For a Lagrangian box model the mass balance can be represented by the first three terms of Equation 2·2 (neglecting the advection term) assuming there is no change in the height of the box, h, over time.

2·1·1 Chemical mechanisms

As outlined in Chapter 1, the urban atmosphere is extremely complex in terms of its chemical composition where many hundreds of different species are present, emitted at varying rates, each possessing different rates of reaction and associated degradation chemistry. As such, the chemical processes taking place must be simplified to be represented within chemical mechanisms, fundamentally to be understood and characterised, of tractable size and complexity (Carslaw and Carslaw, 2001), which vary considerably.

The most complete representation of gas-phase tropospheric chemistry can be achieved through the use of a **near-explicit chemical mechanisms** such as the **Master Chemical Mechanism** (**MCM -** `http://mcm.leeds.ac.uk/MCM/`) (Jenkin *et al.*, 1997a) or the Generator for Explicit Chemistry and Kinetics of Organics in the Atmosphere (GECKO-A) (Aumont *et al.*, 2005).

The MCM (version 3.1) describes the degradation of 135 VOCs including the major UK anthropogenic emissions and biogenic species including isoprene and the monoterpenes α- and β-pinene, several including over 5,900 chemical species and 13,500 chemical reactions (Jenkin *et al.*, 1997a, Jenkin *et al.*, 2003, Saunders *et al.*, 2003, Bloss *et al.*, 2005b, Rickard *et al.*, 2006). The MCM has been evaluated using high quality datasets obtained from experiments carried out in large outdoor environmental reaction chambers and against ambient field observations *e.g.* Hynes *et al.* (2005), Bloss *et al.* (2005a), Pinho *et al.* (2006), (2007).

Data obtained using theoretical, semi-empirical and laboratory studies on the chemical kinetics and mechanism of reactions relevant to VOC oxidation are utilised within the MCM. However, there are still some major uncertainties that exist in a number of details of such mechanisms *e.g.* radical yields due to alkene

ozonolysis, daytime sources of HONO and the treatment of aromatic species (Jenkin and Clemitshaw, 2000, Carslaw and Carslaw, 2001, Bloss, 2009)

Although a large proportion of those chemical reactions relating to VOC chemistry included within the MCM have been studied, a number of unstudied reactions remain. These reactions may be defined on the basis of analogy to the studied reactions of a smaller subset of similar chemical species or using structure activity relationships (SARs *e.g.* Kwok and Atkinson, (1995)) to estimate otherwise unknown parameters (Saunders *et al.*, 2003, Rickard *et al.*, 2006, MCM, 2012).

The MCM can be subdivided into several component parts concerning the complete degradation of VOCs (*e.g.* Saunders *et al*. (2003)). The first stage in the process relates to the **initiation reactions** through photolysis, OH, NO_3 or O_3 reactions. The initiation reactions can result in the formation of **intermediates** including RO and RO_2 radicals, a Criegee intermediate[†] species or the direct production of an oxygenated product.

The reactions of intermediates, as well as initiation reactions involving O_3, can result in the formation of a number of **products** including alcohols, ketones and aldehydes. A number of oxygenated products may also be formed including complex carbonyls, hydroperoxides, percarboxylic acids, carboxylic acids, nitrates, PAN, and CO. The degradation process continues until eventually CO_2 is formed or another organic product or radical is generated for which the chemistry is represented in the MCM (Saunders *et al.*, 2003).

Despite the MCM being highly detailed it does include three general simplifications to limit its ultimate size: i) reaction routes of a low probability are excluded; ii)

[†] A carbonyl oxide that possesses excess vibrational energy and is unstable (*e.g.* Criegee (1975)).

simplification of the degradation process of minor reaction products and those in which the chemistry is not fully understood; and iii) reactions of the peroxy radicals (RO_2) with each other are parameterised (without which approximately half a million would need to be included). These simplifications make the MCM formally a near-explicit chemical mechanism (Saunders *et al.*, 2003).

2·1·2 Mechanism reduction

Near explicit chemical mechanisms such as the MCM are well suited for application in zero-dimensional box models that include a simplistic representation of dynamical processes. However, as a result of limitations in computational resource, near-explicit mechanisms such as the MCM, cannot be applied in complex atmospheric models such as 3-D dynamical models, thus the development of simplified chemical mechanisms is essential (Watson *et al.*, 2008).

A number of techniques are used to simplify near-explicit mechanisms to develop suitably reduced chemical schemes. These methods may be broadly classed as reduction through the removal of chemical species and reactions, reduction through species lumping and reduction through the use of surrogate species. Due to its near explicit nature, there is almost no empirical lumping or use of surrogate species within the MCM (Jenkin et al., 2002).

Reduction through the removal of chemical species and reactions may be achieved through the application of sensitivity analysis. The use of such techniques may allow redundant species and corresponding reactions to be excluded from the chemical scheme (*e.g.* Heard *et al.*, (1998)) whilst those that are significant in terms of accurately simulating key chemical species must be retained.

Redundant reactions may be identified through the investigation of local rate sensitivities that measure the effect of a perturbation in a rate parameter on the rate of production of an important / necessary species (Heard *et al.*, 1998, Whitehouse *et al.*, 2004a). Redundant species may be revealed through the inspection of normalised Jacobian elements that provide information relating to the influence of the change in concentration of species, *i*, on the rate of production of an *N*- membered group of important species (Whitehouse *et al.*, 2004a, Nagy and Turányi, 2009).

Principal component analysis (PCA) can be used to determine the effect of varying parameters such as rate constants on the concentration of a number or group of chemical species. Thereby PCA provides a means of selecting a reaction set from sensitivity data through the consideration of reaction interactions and elimination of groups of reactions that have little or no effect on the concentration of important or necessary species (Whitehouse *et al.*, 2004a).

Mechanism reduction might also be achieved via the application of time-scale based methods (as outlined in Whitehouse *et al*. (2004a)). These methods demonstrate that the long-term behaviour of a chemical mechanism may be accurately represented through the assumption that faster time-scales equilibrate with respect to slower ones, thus the dimension of the system may be reduced.

One such (time-scale based) method is achieved through the application of the Quasi-Steady-State Approximation (QSSA). This technique involves the identification of those short-lived chemical species *e.g.* radicals that may be assumed to be in equilibrium with respect to slower species and in which their rates of production and loss are near equal (Whitehouse *et al.*, 2004a). This method allows the number

of reactions included within the scheme to be reduced and also reduces its numerical stiffness (§3·3) (Whitehouse *et al.*, 2004a).

Following the application of sensitivity analysis and QSSA in mechanism reduction, after which the processes that occur over shorter and longer time scales have been removed, chemical schemes species that react on intermediate time-scales often remain (Whitehouse *et al.*, 2004b).

In order to reduce such mechanisms further, species lumping must be applied whereby a group of chemical species may be represented by one variable alone (Whitehouse *et al.*, 2004b). Within large / explicit chemical mechanisms there are often a large number of VOCs and associated chemical reactions included. Thus, species lumping is often applied to VOCs whilst the explicit representation of inorganic chemistry is often maintained.

Species lumping may be achieved through the definition of surrogates whereby the chemistry of one VOC is used to reproduce a number of VOCs that have similar chemical properties / reactivity and where the rate coefficient for reaction is determined by taking a mole-fraction-weighted average of the reaction rates of each species in the lumped group (Jacobson, 2005, Watson *et al.*, 2008).

An alternative approach to species lumping can be applied whereby a number of reactions with a similar molecular structure (*e.g.* those related to different VOC classes - alkenes, alkanes and aromatics) are grouped together.

A structural approach may also be employed in which organic species are grouped together depending on their bond type where reactions that include an equal number of carbon bonds are assumed to have similar chemical lifetimes and reactivities (Whitehouse *et al.*, 2004b).

Watson *et al*. (2008) implemented VOC emission lumping by incorporating minor VOCs emitted within suitable surrogate species whilst maintaining their chemical properties through inclusion within a number of VOC groups. This method allowed the potential of redistributed VOCs to form ozone to be retained through consideration of the Photochemical Ozone Creation Potential (POCP) discussed further in §2·1·3.

This method of reduction was applied to the CRI v2 mechanism to produce three further reduced chemical schemes namely the CRI v2-R1, CRI v2-R2 and CRI v2-R3. A second method of VOC emissions lumping was also applied to the CRI v2 by Watson *et al*. (2008) independently that resulted in the derivation of two additional reduced schemes: CRI V2-R4 and CRI V2-R5. This involved utilising the Global Emission Inventory Activity (GEIA) non-methane VOC groups to implement a higher level of emissions lumping reduction whilst considering the POCP of each emitted species in their redistribution. Table 2·3 illustrates a number of chemical mechanisms used to model atmospheric chemistry.

Table 2·3 - *Examples of chemical mechanisms used in atmospheric chemistry.*

Mechanism	Type	Reactions	Species
Master Chemical Mechanism (MCM)	Near-explicit	13,500	5,900
Common Representatives Intermediates mechanism - version 1 (CRI v1)	Species lumped	570	250
Common Representatives Intermediates mechanism - version 2 (CRI v2)	Species lumped	1183	434
Common Representatives Intermediates mechanism - version 2-R5 (CRI v2-R5)	Lumping of emissions	196	555
Carbon Bond Mechanism (CBM-IV)	Species lumped	82	33
Regional Atmospheric Chemistry Mechanism (RACM)	Species lumped	237	77

2·1·3 The Common Representative Intermediates (CRI) mechanism

Developed as a subset of the MCM, the **Common Representative Intermediates** (**CRI**) **mechanism** (Jenkin *et al.*, 2008b, Watson *et al.*, 2008) is a simplified chemical mechanism, used to describe the oxidation of VOCs and their resultant O_3 production. The most recent version, CRI v2, represents a significant reduction in the number of C≈ 91 %) and chemical species (≈ 93 %) included in the full MCM v3.1 (Table 2.3). The mechanism describes the degradation of methane and 115 VOCs including major anthropogenic emissions as listed in the National Atmospheric Emissions Inventory (NAEI) and important biogenic species including isoprene and monoterpenes (α- and β-pinene) (Jenkin *et al.*, 2008b). The first version of the CRI developed included a smaller number of reactions and species when compared to CRI v2, however significantly underestimated the formation of O_3 arising from the oxidation of aromatic hydrocarbons on short timescales, displaying under-reactivity in highly polluted conditions (Jenkin *et al.*, 2008b).

As per the MCM (§2·1·1) the complete degradation of VOCs to produce CO_2 results in the formation of intermediate oxidised products and radicals that lead to the formation of O_3, the amount of which is related to the number of NO-to-NO_2 conversions that occur. The amount of O_3 formed from OH initiated and NO_X catalysed oxidation of VOCs to CO_2 is equivalent to the number of reactive bonds (C-C and C-H) that the parent molecule possesses (Jenkin *et al.*, 2008b). In the case of the degradation of CH_4 (Figure 2·3), the overall result of the reactions involved can be represented by the following reaction in which 4 molecules of O_3 are produced:

$$CH_4 + 8O_2 \longrightarrow CO_2 + 2H_2O + 4O_3. \qquad (2{\cdot}5)$$

Reaction of CH_4 with OH initiates the degradation process (§1·6·1; Chapter 1), resulting in the formation of the intermediate formaldehyde (HCHO) and represents the first generation of products. Subsequent reaction of HCHO yields a second

generation product, CO. This then undergoes further chemical processing to form CO_2 which represents the end of the degradation process. There are 4 NO-to-NO_2 conversions that occur during this process (a result of reaction of NO with peroxy radicals) with the number of NO-to-NO_2 conversions corresponding to the amount of O_3 produced and the number of reactive bonds. This forms the basis for the CRI mechanism and provides a suitable index for the number of NO-to-NO_2 conversions with a number of generic intermediates defined and used to mediate the breakdown of larger VOCs (Jenkin *et al.*, 2002). A large set of intermediates possessing the same index may then be grouped together via a representative intermediate thereby simplifying the chemistry of larger VOCs.

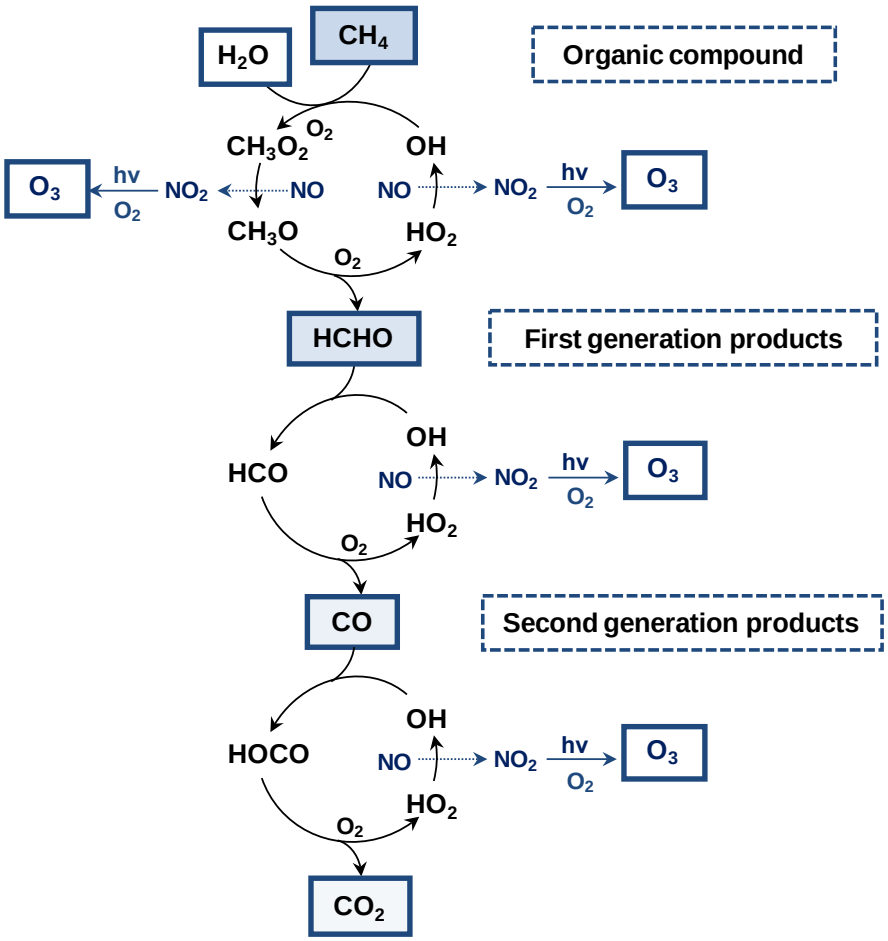

Figure 2·3 - *Stages in the OH-initiated, NO_X catalysed oxidation of CH_4 to CO_2 and H_2O. Adapted from Jenkin et al. (2008b).*

Irrespective of the CRI v2 mechanism representing a significant reduction in the complexity of the MCM v3.1, further simplification is needed before such mechanisms can be incorporated into detailed dynamical models. The performance of CRI v2 compares well with the MCM v3.1 over a wide range of conditions used in box model simulations with this level of agreement providing a good basis for further reduction. The CRI v2 was simplified further using systematic lumping techniques for anthropogenic emissions. This involves the redistribution of emitted anthropogenic VOCs on the basis of their chemical class and **Photochemical Ozone Creation Potential** (**POCP**)[‡] relative to VOC speciation included in the NAEI (Watson *et al.*, 2008).

Anthropogenic speciation is an important component of the mechanism as over 80 % of the chemistry in CRI v2 is related to the degradation of anthropogenically emitted VOCs. Biogenically emitted VOCs form a small proportion of the mechanisms and already represent a substantial simplification of reality. Reduction of CRI v2 in this way has given rise to 5 derived chemical mechanisms the smallest of which is the **CRI v2-R5** that represents a 53 % and 55 % reduction in the number of reactions and species respectively when compared to the CRI v2 and retains a good level of overall agreement with the more detailed mechanism.

The CRI v2-R5 mechanism was developed by testing a number of additional interim mechanistic variants (Watson, 2007, Watson *et al.*, 2008). This mechanism includes 19 emitted anthropogenic VOCs to represent full speciation, 196 chemical species and 555 reactions. To develop the CRI v2-R5, emissions included in the more detailed CRI mechanisms were lumped into groups (Table 2·4) similar to those included in the Global Emissions Inventory Activity (GEIA) which includes 25 groups into which VOCs are split (*see* Watson *et al.* (2008)).

[‡] Devised by Derwent *et al*. (1996) and discussed further in section 3·4·4 of Chapter 3.

CRI v2-R5 has also been compared with the CRI v2 using a photochemical trajectory model (PTM) to further investigate its ability to simulate ozone formation using conditions of the Tropospheric Organic Chemistry Experiment (TORCH) campaign carried out 25 miles to the north east of central London in during the summer of 2003 (Lee *et al.*, 2006).

Table 2·4 - *The treatment of VOCs included in the CRI v2-R5 mechanism. Adapted from Watson et al. (2008).*

Chemical species	**CRI v2-R5 representation**
Ethane	Ethane
Propane	Propane
Butanes	Butane
Pentanes	
Hexanes and higher alkanes	
Ethene	Ethene
Propene	Propene
Other alkenes	*trans*-2-butene
Acetylene	Acetylene
Benzene	Benzene
Toluene	Toluene
Xylenes	o-Xylene
Trimethylbenzenes	
Other aromatics	
Formaldehyde	Formaldehyde
Other aldehydes	Acetaldehyde, propanal
Ketones	Acetone, butanone
Alcohols	Methanol, ethanol
Ethers	
Isoprene	Isoprene
Monoterpenes	α-pinene, β-pinene

An identical version of the PTM model that included the CRI v2-R5 was used to simulate chemical changes in the boundary layer through trajectories made over a

96 hour period reaching the observation site. Figure 2·4 shows the simulated ozone mixing ratios achieved and forms a comparison of the CRI v2 and the CRI v2-R5 mechanisms in which both are in excellent agreement throughout (on average to within 0.3 %) (Watson *et al.*, 2008). Agreement between these mechanisms was observed over a wide range of conditions in which relative and absolute amounts of VOCs and NO_X were varied, therefore the CRI v2-R5 is suitable for inclusion in more complex dynamical models (Watson *et al.*, 2008).

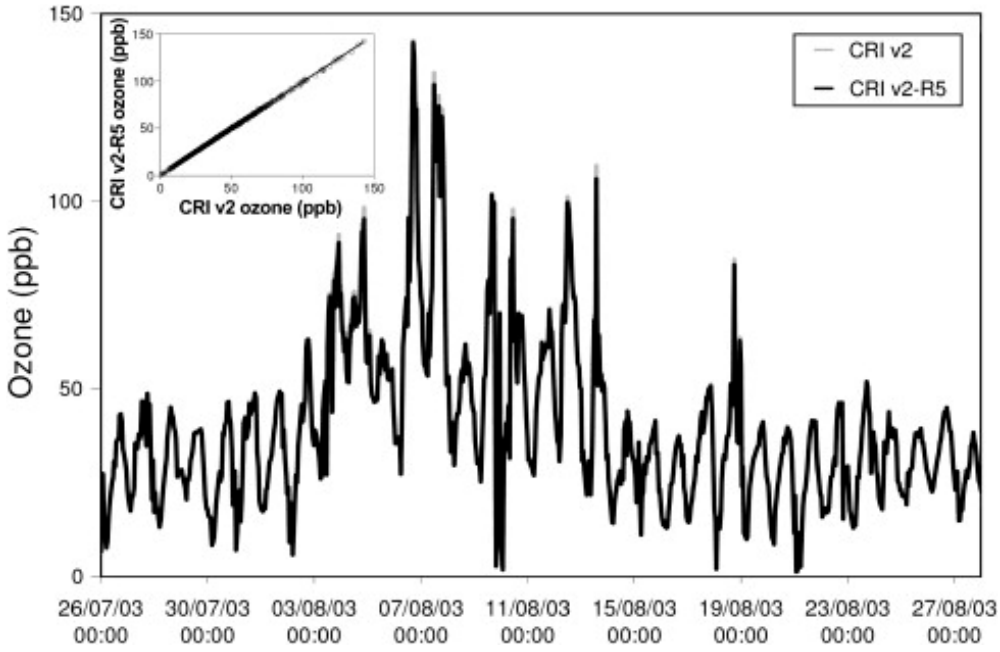

Figure 2·4 - *A comparison of hourly mean O_3 mixing ratios simulated using the PTM containing the CRI v2 (with a speciation of 112 anthropogenic VOCs) and CRI v2-R5 (with a speciation of 19 anthropogenic VOCs) for the entire TORCH campaign. In both mechanisms biogenic emissions are represented by isoprene, α -pinene and β -pinene (Watson et al., 2008).*

The reduced form of the CRI has been evaluated in comparison to the MCM and other mechanisms and found to replicate well both integrated ozone production on timescales of days, and (of more relevance here) OH levels on timescales of hours under polluted (industrial) conditions (Emmerson and Evans, 2009).

2·2 Modelling street canyon dynamics

The representation of chemical reactions in the atmosphere is only one aspect of a complex system. One of the major obstacles to overcome in order to improve our understanding of the dispersion of pollutants in urban areas occurs due to the complex nature of air flow and turbulence characteristics that arise as air flows over the urban canopy. Flow within the canyon is modified to a greater extent than that of the inertial sublayer (§1·3) as a result of individual roughness elements such as buildings.

2·2·1 Street canyon dynamics

The characteristics of the canyon dynamics are dependent on both wind direction and canyon geometry. In the most simple case, when the direction of the prevailing wind is **perpendicular** to the canyon and the street canyon **aspect ratio** (defined as the ratio of canyon height (H) to canyon width (W)) is approximately unity (H/W = 1) **skimming flow** (Figure 2·5) is observed in which a large proportion of the flow does not enter the canyon and instead skims over the top of buildings (Oke, 1987). This flow regime results in the formation of a large primary canyon vortex, the effect of which this has on pollution dispersion is discussed in §2·2·3.

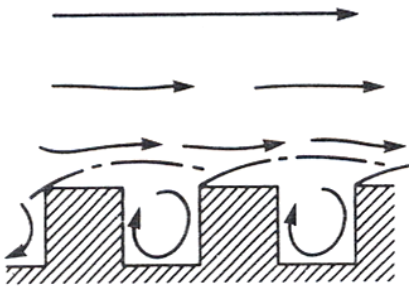

Figure 2·5 - *Skimming flow (Oke, 1987).*

Isolated roughness flow occurs when the distance between adjacent buildings is relatively large *i.e.* $H/W < 0.3$. The pattern of flow within this regime appears to be similar to that which occurs around an isolated building as adjacent flow fields do not interact. If buildings are more closely spaced ($0.30 < H/W < 0.65$), wake interference flow arises from the interaction between the wake of the upstream building with that downwind.

When the wind blows parallel to the street canyon, flow becomes channelled along the canyon axis. Wind speeds within such channelled flow can be greater than those in an open area (Oke, 1987) and therefore result in favourable conditions in which to effectively disperse pollutants from their sources within the canyon.

When the airflow approaches the canyon axis at an oblique angle, a spiral vortex develops along the length of the canyon. As a result of the along-street wind component, due to channelling, the flow is "reflected" at a greater angle than when it entered the canyon (Nakamura and Oke, 1988, Belcher, 2005).

2·2·2 Turbulence characteristics within an urban street canyon

Roughness elements can have a considerable impact on the nature of turbulence generated within an urban street canyon. Despite this, relatively few full-scale urban measurement campaigns have been conducted in order to assess turbulence characteristics within an urban street canyon (Rotach, 1993, Rotach, 1995, Feigenwinter *et al.*, 1999, Louka *et al.*, 2000, Kastner-Klein and Rotach, 2004, Longley *et al.*, 2004). Based on the results of an extensive urban measurement campaign known as the Basel Urban Boundary Layer Experiment (BUBBLE), Christen (2005) proposed a conceptual division of the roughness sublayer on the street canyon scale to include:

- The **above-roof layer** in which the mean wind velocity follows the logarithmic profile and turbulent statistics are similar to those of the inertial sublayer;
- The **roof layer**, where strong gradients exist in the profiles of turbulent statistics and (in the case of skimming flow) an inflection point in the mean wind profile is observed, from which instabilities evolve producing a large amount of turbulent kinetic energy, e[§];
- The **canopy layer** where turbulence is highly intermittent and dominated by large coherent structures. Vehicles at street level within this layer can act to enhance the mechanical production of turbulence (Britter and Hanna, 2003).

The **plane mixing layer / shear layer** forms when two fluids moving at different velocities and separated by a plate are allowed to merge downstream (Finnigan, 2000). Such a layer forms within the roof layer (Figure 2·6) which increases in depth with distance downwind from the upstream roof from which it is shed.

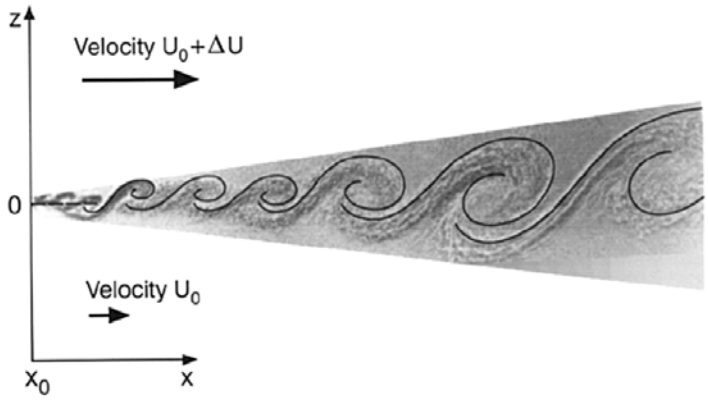

Figure 2·6 - *The growth of the plane mixing layer (Raupach et al., 1996).*

A characteristic of the shear layer is a point of inflection between the logarithmic wind velocity profile observed above the roof layer and the exponential profile of

§ Defined as: $e = \frac{1}{2}\left(\overline{u'^2} + \overline{v'^2} + \overline{w'^2}\right)$.

the canyon itself (Figure 2·7). As a result of the inflection point in the mean wind profile, Kelvin-Helmholtz instabilities may evolve causing turbulent flow within the canyon to become intermittent (Finnigan, 2000).

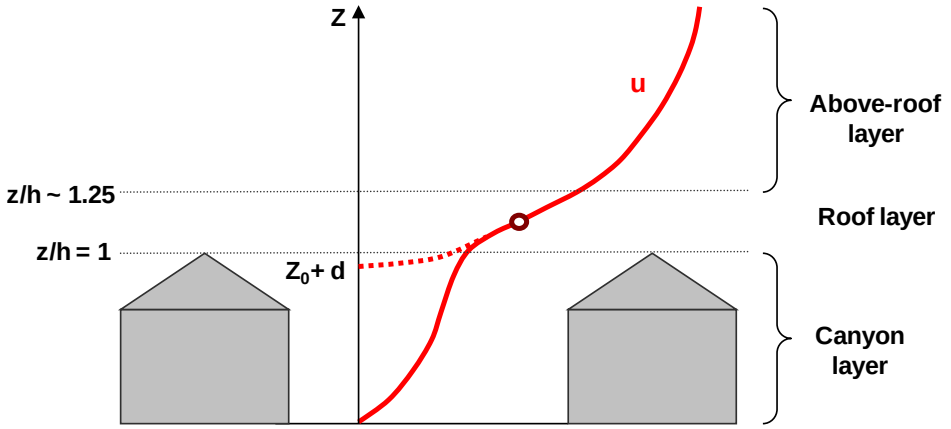

Figure 2·7 - *The inflected mean wind profile of the urban roughness sublayer. The dashed line represents the extrapolated logarithmic wind profile. Adapted from Christen (2005).*

Strong intermittency in the street canyon re-circulation was observed using roof level measurements by Louka *et al.* (2000) who concluded that the mean flow within the canyon was merely a residual of an unsteady turbulent re-circulation. It was proposed that the strong intermittency observed in the recirculation may be due to the intermittent nature of the mechanism that couples the flow within the canyon with that above *i.e.* the shear layer at roof level (Figure 2·8). Kelvin-Helmholtz instability can cause fluctuations in the vertical position of the shear layer to occur (Figure 2·8) *i.e.* "flapping" of the shear layer takes place (Louka *et al.*, 2000).

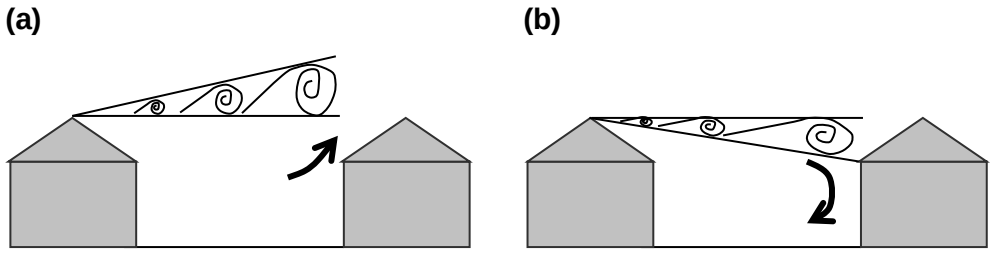

Figure 2·8 - *A schematic representation of shear layer movement where: (a) the canyon air is effectively flushed out due to the upward position of the shear layer and (b) re-circulation is prominent in the canyon due to the trapping of air by the downward movement of the shear layer.*

As a result, flow within the canyon will be directly affected by this process and canyon air will be intermittently flushed out. This provides an effective ventilation mechanism allowing air to escape and efficient mixing to occur when the shear layer moves to an upward position. Conversely, when the shear layer moves to a downward position reaching the upwind wall of the downwind building, air is effectively trapped within the canyon and recirculates.

Turbulent transport

Within and above urban canopies, large scale coherent structures are found to dominate turbulence (*e.g.* Christen (2005)). These structures are largely responsible for the turbulent transport of heat, momentum and other quantities *e.g.* pollutants within and above urban street canyons.

The role of such features in turbulent transport may be studied using a technique known as quadrant analysis (Figure 2·11) with four different events characterised, namely: outward interactions, ejections, inward interactions and sweeps. Sweep events are those in which air moves downwards at high velocities ($u' \geq 0$, $w' \leq 0$; Q4). Ejection events represent the upward motion of low velocity air, represented by Q2 where $u' \leq 0$, $w' \geq 0$. Outward interaction events (represented by Q1; Figure 2·9) are those in which air moves at a high velocity air moves in an upward motion from

near the surface ($u' \geq 0$, $w' \geq 0$) whilst inward interactions represent the downward movement of low velocity air ($u' \leq 0$, $w' \leq 0$; Q3).

Figure 2·10 illustrates the time variation of the horizontal and vertical velocity fluctuations, u' and w' respectively, the instantaneous Reynolds stress, $-u'w'$ and temperature fluctuation, θ', measured at two different heights above a suburban canopy (Oikawa and Meng, 1995). The arrows included in the figure represent sweep and ejection events. It is also clear from Figure 2·12 that $-u'w'$ is positive on average over the period, thus sweep and ejection events (that contribute to turbulence production) are dominant over inward and outward interaction events in terms of turbulent transport (that contribute to the destruction of turbulence).

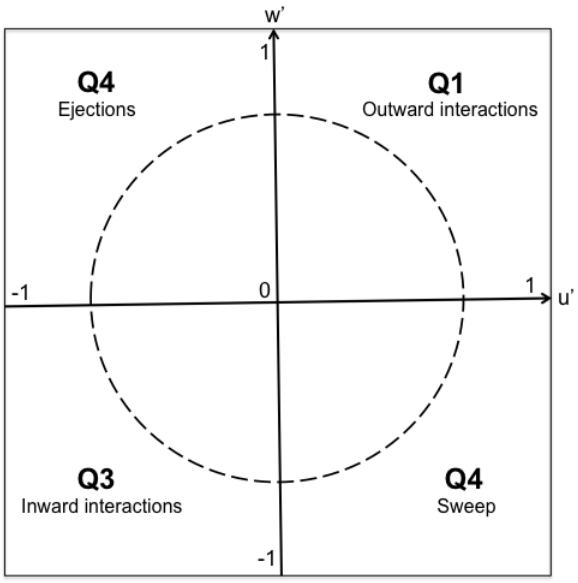

Figure 2·9 - *A schematic diagram illustrating the definitions applied to quadrant analysis of momentum flux.*

It is evident that during a sweep event ($u' > 0$ and $w' < 0$) a negative temperature fluctuation occurs. A number of studies (*e.g.* Feigenwinter *et al.* (1999); Christen (2005); Feigenwinter and Vogt (2005)) have shown that these events are the dominant transport mechanism observed within and immediately above the urban

canopy in which fast downward moving gusts penetrate the canopy, bringing cooler air from above.

During an ejection event ($u' < 0$ and $w' > 0$), a positive fluctuation in temperature is observed as warm air is brought up from the relatively warm canyon below by relatively slow upward motions. These events have been found to be the predominant mechanism of transport at greater height above the canopy (Oikawa and Meng, 1995, Feigenwinter *et al.*, 1999, Christen, 2005, Feigenwinter and Vogt, 2005).

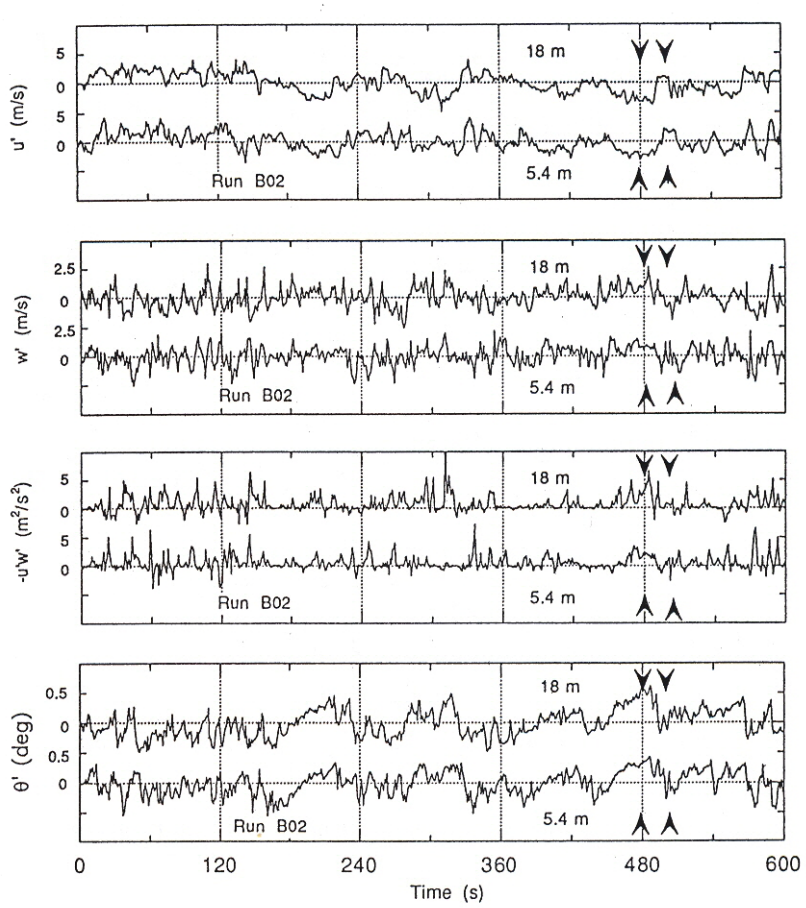

Figure 2·10 - *Time series of fluctuating u', w', -u'w' and θ' measured at two heights within a suburban roughness sublayer. Sweep and ejection events are represented by the arrows on the above time series (Oikawa and Meng, 1995).*

In contrast to those studies discussed above, Cui *et al*. (2004) demonstrated, using the results of a LES, that ejection events dominate turbulent processes just below roof level of the canyon. The largest contribution to total momentum flux however was found to occur as a result of sweep events with this influence greater than the sum of that due to the three remaining processes, and these findings in agreement with the urban experimental data of Oikawa and Meng (1995).

Cheng and Liu (2011) also found upward momentum transport within the shear layer to be dominated by ejection (greater than 50 %) and sweep events (30 %) when compared to the negligible contributions of inward and outward interactions (≈ 10 %). This study showed that within the canyon there is an increase in the complexity of vertical momentum transport. Ejection events dominate toward the leeward wall of the canyon with sweep events (to a lesser extent) also contributing to the upward transfer of momentum. In contrast, toward the windward side of the canyon momentum is transport downwards toward the centre of the street primarily through inward interactions, with momentum transferred from the sheer layer at roof level transported to other regions of the canyon, thus driving primary circulation.

Sweep and ejection events transfer a significant amount of horizontal momentum from above the canyon into the canyon, increasing drag force over the urban surface.

In the same way that turbulent events are important in transferring heat and momentum within the urban canopy, they are also responsible for the transport of pollutants within and above the street canyon. By studying the relative importance of sweep and ejection events at roof level (where vertical mean velocity is low) the amount of background air entering the canyon from above in the case of the former

and more polluted canyon air escaping from the canyon for the latter may be determined (Cheng and Liu, 2011).

Cheng and Liu (2011) also investigated the relative importance of each event in transporting pollutants within and above street canyons using LES. This work demonstrated that pollutants emitted within the canyon are transported upwards in the opposite direction to the transport of momentum (acting downwards). In addition, their results showed sweep and ejection events to be the dominant processes in the turbulent transport of pollutants (with that due to sweep events slightly greater) with that as a result of inward and outward interactions found to be negligible. Sweeps were also found to be particularly dominant towards roof level and the windward wall of the canyon indicating a large degree of the entrainment of background air and an increase in mixing within this region of the canyon.

Intermittency in street canyon flow may be studied by considering the skewness, a higher order moment (defined in Chapter 6) of both horizontal and vertical velocity (denoted as sk_u and sk_w respectively) that can be related to sweep and ejection events. Cui *et al.* (2004) showed that in close proximity to roof level within the canyon the skewness of u and w are both large in magnitude and are of equal and opposite sign (where sk_u is positive and sk_w is negative) indicating the dominance of ejection events within this region of the canyon (*i.e.* $u' < 0$ and $w' > 0$, thus $u < \overline{u}$ and $w > \overline{w}$). Conversely, for sweep events the reverse is true where sk_u is negative and sk_w is positive.

2·2·3 Pollutant dispersion on the street canyon scale

Pollutant dispersion within the canyon is dependent on the rate at which the street exchanges air vertically with the above roof level atmosphere and laterally with connecting streets (Vardoulakis *et al.*, 2003). Skimming flow, characterised by a

single primary vortex (§2·2·1), can lead to the decoupling of air within the canyon from that above. This gives rise to a low level of ventilation and is relatively ineffective in removing pollutants (*e.g.* vehicle emissions from within the street) resulting their build up to levels which may be harmful to human health (Hunter *et al.*, 1992, Vardoulakis *et al.*, 2003, Baker *et al.*, 2004).

The influence of the street canyon on the flow and dispersion of pollutants can be seen in Figure 2·11. In the case of a narrow street canyon (Figure 2·11a) the exchange of air from within the street with air above is restricted compared with (Figure 2·11b) where the presence of the canyon vortex permits street-level flushing (Oke, 1987).

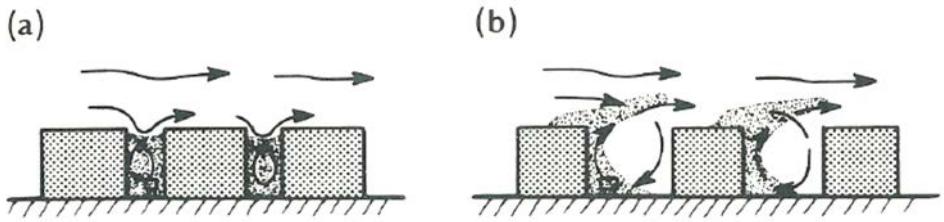

Figure 2·11 - *The influence of street canyons on flow and pollutant dispersion (Oke, 1987).*

As traffic represents the main source of pollutants within the street canyon, in situations where a single primary vortex forms, a large gradient of pollutant concentration is observed across the street with the highest concentration of pollutants evident toward the leeward wall (Figure 2·12).

The increase in the level of and the spatial variability in pollution within street canyons together with a larger number of individuals that are exposed to pollutants highlight the importance of the study of pollution on this scale with serious implications for public health.

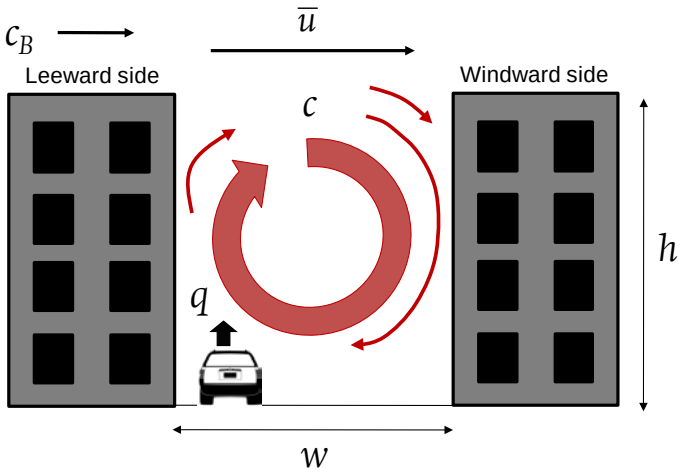

Figure 2·12 - *Schematic representation of the main dynamical processes that affect the dispersion of pollutants within a typical street canyon. The pollutant emission source is represented by q. Adapted from Dabberdt et al. (1973).*

A number of field studies have shown that the concentration of pollutants on the leeward side of the street can be significantly greater than that on the windward side and that a vertical decrease in concentration on both sides of the street is observed (DePaul and Sheih, 1985, Berkowicz *et al.*, 2002, Xie *et al.*, 2003, Baker *et al.*, 2004, Tomlin *et al.*, 2009).

Although important in terms of dynamical model validation, field studies are often relatively sparse in terms of their resolution and can be influenced considerably by the prevailing meteorological conditions and complex geometry of the surrounding urban environment. A number of reduced scale models (wind tunnel experiments) have also been used to study pollutant dispersion and canyon dynamics and have provided evidence for significant horizontal and vertical gradients in the concentration of passive pollutants within and above the canyon (Kastner-Klein and Plate, 1999, Pavageau and Schatzmann, 1999, Boddy *et al.*, 2005, Gromke *et al.*, 2008, Salizzoni *et al.*, 2009, Tomlin *et al.*, 2009).

The high spatial and temporal resolution of observations required for full understanding, that measurements may struggle to obtain, may be acquired

utilising models. Parameters can also be set easily and conditions varied in order to study the effect of changing conditions on atmospheric composition.

2·2·4 Dispersion modelling on the street canyon scale

Dispersion models can be used to investigate the physical and chemical processes that govern the dispersion and transformation of atmospheric pollutants (Table 2·5), a number of which are discussed in the comprehensive review of Vardoulakis *et al.* (2003). Numerical models are the focus of this thesis therefore this classification of dispersion model (not included in Table 2·5) are discussed further in the following sections.

Table 2·5 - *A selection of models used in atmospheric dispersion.*

Model type	Description
Gaussian plume models (GPM)	A relatively simple model used to describe the 3-D spatial concentration of pollutants usually emitted from a point source. Meteorological conditions and atmospheric stability play a vital role in governing the dispersion of pollutants in such models. Advanced Gaussian plume models that have been adapted to simulate dispersion within street canyons *e.g. ADMS-Urban*, *DREAM* and *CALINE4* models (Vardoulakis *et al.*, 2003, Holmes and Morawska, 2006).
Box models	Simplistic models that capture the essential features of canyon dispersion (*e.g.* Nicholson (1975), Hassan and Crowther (1998)). Model inputs may include wind speed, direction, turbulence parameters and pollutants emitted in the lower boundary of the box (Johnson and Hunter, 1995). *STREET-SRI* (*e.g.* Johnson *et al*. (1973), Berkowicz (2000)) is another example in which pollutant concentrations are determined by two components: Urban background concentration and the concentration due to vehicle emissions within the street.
Street canyon models	Parametric models that include an empirical representation of, for example, wind generated and vehicle induced turbulence, on the street canyon scale. Examples include: The *Danish Operational Street Pollution Model (OSPM)* (*see* Buckland (1998); Berkowicz (2000)) - a basic parameterised semi-empirical model used to calculate hourly pollution concentrations and one of the most validated. *AEOLIUS Full* — that calculates hourly pollutant concentrations at a receptor location and can be used to estimate the maximum concentration of vehicle emissions within the street canyon (*e.g.* Buckland and Middleton (1999); Derwent and Middleton (1996); Vardoulakis *et al*. (2007)). *ADMS urban* - used to calculate pollutant concentrations using two different chemistry options *i.e.*: empirical functions or using a chemical scheme known as the Generic Reaction Set (GRS) - a semi-empirical model that simplifies photochemical reactions using a set of parameters derived from observations (Vardoulakis *et al.*, 2007).

2·2·5 Computational Fluid Dynamics (CFD)

Numerical simulations can provide high-resolution results on both spatial and temporal scales to give a more complete picture of canyon dynamics and dispersion

when compared to those models discussed in the preceding section (Cui *et al.*, 2004). 3-D numerical models provide a powerful tool to study air pollution within street canyons however such models are computationally expensive, thus their employment is usually restricted to research applications.

Computational fluid dynamics (**CFD**) is a numerical modelling technique that can be used to describe the fluid dynamics, thermal effects, heat transfer, chemical reactions and turbulence that influence the dispersion and transformation of pollutants on the street canyon scale (Murena *et al.*, 2009). CFD is an example of an Eulerian model that uses flexible fine scale grids, particularly useful in simulating complex boundary conditions (Vardoulakis *et al.*, 2003). There are three main elements contained in CFD codes, including:

- The **pre-processor** that generates a grid of the computational domain; includes all necessary input parameters (*e.g.* chemical and physical phenomena) and where appropriate boundary conditions must be defined;
- The **solver** that includes the approximation of unknown flow variables and subsequent numerical discretization which transforms partial differential equations into discrete numerical equations. Numerical values for variables throughout the flow domain are then determined using the discrete numerical equations.
- The **post-processor** this includes model visualisation through *e.g.* the display of the grid and domain geometry, vector plots, contour plots and animation of results.

The numerical solutions of the dispersion and fluid flow equations form the basis of CFD models. These equations can be derived from the basic transport and conservation principles *i.e.*: the **continuity equation;** the **Navier Stokes** equations

and the **transport equation** for the concentration of pollutants (Vardoulakis *et al.*, 2003).

To simulate turbulent processes, there are two main types of turbulence models used, that include: those based on **Reynolds Averaged Navier Stokes** (**RANS**) flow equations (*e.g.* the k-ε models where k is the turbulent kinetic energy and ε is the turbulent dissipation rate) and the **large-eddy simulation** (**LES**) models (see §2·2·6). The main differences between these models are concerned with the methods used in discretization and approximation of flow variables. CFD allows a high level of detail to be modelled in the domain through the introduction of roughness coefficients for various surfaces *e.g.* cars and vegetation. Pollution concentration fields and other physical quantities such as turbulent kinetic energy (TKE) can be reproduced using these models.

CFD modelling studies that have included representations of the chemical reactions that occur on the street canyon scale are discussed in section 2·3. CFD codes including PHOENICS (*e.g.* Crowther and Hassan (2002)), FLUENT (*e.g.* Murena *et al.* (2009, Liu *et al.*, 2011)), MISKAM (*e.g.* Ziehn and Tomlin (2008); Benson *et al.* (2008)) and MIMO (*e.g.* Assimakopoulos *et al.* (2003)) have been used to simulate the flow and dispersion above 2-D and 3-D street canyons.

The impact of changing street canyon characteristics (*e.g.* the addition of a low boundary wall) on the exposure of pedestrians to pollutants within an urban street canyon has also been investigated using CFD (Assimakopoulos *et al.*, 2003, McNabola *et al.*, 2009).

One disadvantage of CFD applications based on Reynolds averaged equations is that they are unreliable in the prediction of unsteadiness and intermittency in flow (Cui *et al.*, 2004). Such models assume gradient transport which is not likely to be the

case for pollutant removal and re-entry at roof level of the street canyon (Cai *et al.*, 2008).

2·2·6 Large-eddy simulation (LES)

An increasing number of studies focussing on high resolution modelling of canyon fluid dynamics and pollutant transport / dispersion processes have utilised RAMS models such as LES to simulate the canyons' turbulent flow and associated pollutant dispersion; a number of these are reviewed in Li *et al.* (2006). Most research has involved the simulation of the dispersion of a non-reactive tracer species (referred to hereafter as a passive scalar) (Liu and Barth, 2002, Liu *et al.*, 2004, So *et al.*, 2005, Cai *et al.*, 2008, Li *et al.*, 2008, Li *et al.*, 2009, Cheng and Liu, 2011, Salim *et al.*, 2011). Studies by Ca *et al.* (1995) and Cai (2012a, Cai, 2012b) have used LES to model the thermal properties of a street canyon and effects of differential heating on the flow characteristics and dispersion.

Cui *et al.* (2004) developed an LES model based on the regional atmospheric modelling system (RAMS) to simulate the turbulent flow within and above a real scale street canyon of aspect ratio ≈ 1. The model used was adapted to represent the urban canopy layer through the explicit treatment of the effect of building obstacles on the flow field. A major objective of this research was to validate the model by comparing the results gained (including mean velocities and turbulence statistics such as TKE, skewness and kurtosis) with wind-tunnel measurements of street canyon dynamics and to investigate the nature of coherent structures inherent in the canyon flow. Their findings showed that results gained using the LES were comparable to those obtained from wind-tunnel experiments. Quadrant analysis showed that momentum exchange was unevenly distributed over sweep and ejection events. Although weak ejection events ($u > \overline{u}$ and $w > \overline{w}$) were more

frequent, sweep events ($u < \overline{u}$ and $w < \overline{w}$) were much stronger and contributed most to momentum transfer (where u and w represent the instantaneous, across canyon and vertical wind components, averaged over a given time period to give $\overline{u}$ and $\overline{w}$). A corner eddy next to the windward wall of the canyon was also found to be a permanent feature of the canyon flow.

Using LES, Liu *et al.* (2004) and Liu *et al.* (2005) have conducted detailed studies on flow, turbulence characteristics, pollutant transport and exchange at roof level for a range of *H*/*W* ratios. Their results, in agreement with Cui *et al.* (2004), also indicated the presence of a corner eddy near the canyon's windward wall. Pollutant removal was found to occur through turbulent transport at the windward roof level for all of the aspect ratios studied with the highest concentrations of pollutants observed on the leeward side of the street (where *H*/*W* = 0.5 and 1.0). Conversely, where *H*/*W* = 2.0, the highest concentrations were observed toward the windward corner of the street where concentrations were higher than the previous instances and ground level air quality was inferior.

Liu *et al.* (2005) have demonstrated the suitability of the LES in determining ventilation rates and its application in investigating the processing and transport of pollutants once they are emitted or enter the canyon from the background atmosphere. The air exchange rate (ACH) and pollutant exchange rate (PCH) for a range of street canyons of varying *H*/*W* ratios were determined. ACH was shown to increase with decreasing aspect ratio indicating that canyons with a smaller aspect ratio are better ventilated and therefore have lower levels of pollutants accumulating inside the street.

Cai *et al.* (2008) have applied the LES model to determine the wind fields, turbulence, scalar concentration and flux on the street canyon scale. Both line and

area sources of emissions of a passive scalar were applied to the model to study its dispersion characteristics.

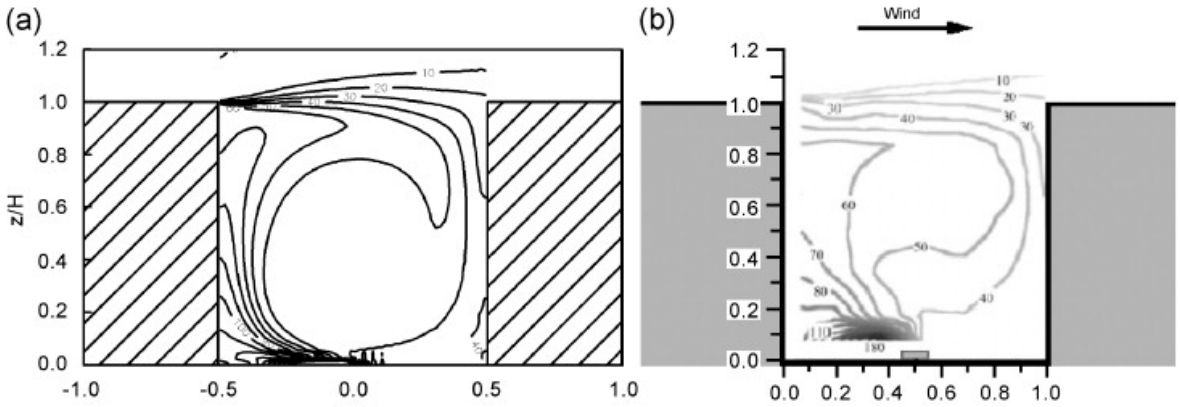

Figure 2·13 - *Spatial distribution of a normalised passive scalar: (a) using LES results and (b) using wind tunnel experimental results (Cai et al., 2008).*

The results gained using the LES are comparable to those gained using the wind tunnel data (Figure 2·13) although a disparity is observed toward the leeward corner of the canyon, likely to be the result of different initial emission discharge velocities used in each case.

More recently, Li *et al.* (2009) employed LES in order to study the flow and transport characteristics of scalar quantities within deep urban street canyons of large *H/W* ratios (3, 5 and 10) that were shown to develop a number (3, 5 and 8 respectively) of overlying primary vortices in the vertical. In such cases the wind speed at ground level was very low effectively trapping pollutants at ground level. Large gradients in the concentration of pollutants existed between the re-circulation and the shear layer at roof level and vertical turbulent transport at this level formed the main mechanism of pollutant removal.

Limitations of CFD models remain however as these represent idealised models that may deviate from those conditions experienced in reality. In the real world there may be more complex geometries and heterogeneous roughness elements within

the urban canopy which may be oversimplified in their representation within numerical models. Boundary and prevailing meteorological conditions in addition to thermal and buoyancy effects (Li *et al.*, 2006) as well as vehicle generated turbulence and the location and nature of emissions are also likely to be inadequately represented within models. A constant wind speed and direction in addition to a logarithmic wind profile, for example, may be assumed for modelling purposes whilst in reality these parameters are likely to be highly variable and also effect mean recirculation within the canyon itself.

Xie and Castro (2009) used LES to investigate flow and dispersion for a real world scenario within the urban domain of the DAPPLE campaign site (Dobre *et al.*, 2005) that included 50 or more building obstacles. A realistic representation of inlet boundary conditions was incorporated within the LES model through the application of an inflow generator with the importance of an adequate representation of the mean and fluctuating velocities highlighted. The mean velocity and Reynolds stresses applied at the inlet were determined by fitting measured data obtained from wind tunnel experiments (conducted as part of DAPPLE). This work also demonstrated that the flow characteristics within and immediately above the canopy layer are largely governed by the size and distribution of local individual geometric features and that the mean and fluctuating concentrations in the near field < 0.1 km are highly dependent on the location of sources and the local characteristic of the urban canopy.

Xie (2011) also highlighted the importance of local meteorological conditions on flow and dispersion at the DAPPLE site through the comparison of simulations made when the wind blows perpendicular to the site to that when the wind is at an oblique angle, the latter simulated by Xie and Castro (2009). The research of Xie (2011) also included more realistic wind conditions by incorporating wind data

measured at 190 m on the top of the BT Tower (central London) into the LES model simulations. Through the inclusion of such data, dispersion simulated by the LES was significantly improved in comparison with field measurements when compared to the case where steady wind conditions were used.

This work also included an investigation into the effect of varying wind direction on dispersion as simulated by an LES model through the variation of wind direction between -51.4^{o} and -90^{o} *i.e.* at an oblique angle and perpendicular to the windward faces of the buildings. Neutral conditions were also assumed within this study, as is the case in much LES research (*e.g.* Baker *et al.* (2004) and Cui *et al.* (2004)) however this is another assumption that may not provide an adequate representation of real world conditions as weakly unstable conditions are often those found within the urban canopy of large European cities (Wood *et al.*, 2010).

The effects of thermal stratification on dispersion within urban areas were further investigated by Xie *et al.* (2013) using a LES model, wind tunnel experiments and field measurements. This study demonstrated that within urban areas (in this case London), stratification effects on dispersion under weakly unstable conditions are not negligible and in addition to this that further effects (*e.g.* small scale roughness elements and heat transfer on the local scale) must be considered to improve the accuracy of LES simulations.

2·3 Combined chemistry and dynamics

In contrast to the range of applications of the LES to study flow and the dispersion of a passive scalar, relatively little attention has been given to modelling the dispersion of reactive pollutants with most practical applications tending to focus on the dispersion of a passive scalar, or including only a limited number of

chemical reactions (Baker *et al.*, 2004, Baik *et al.*, 2007, Garmory *et al.*, 2009, Wang and Mu, 2010, Kikumoto and Ooka, 2012). As the computational power available increases, dynamical models are increasingly able to consider a larger number of chemical reactions (Carslaw and Carslaw, 2001).

Baker *et al.* (2004) investigated the turbulent dispersion and transport of reactive pollutants within a street canyon using a large-eddy simulation model with simple NO_X-O_3 photochemistry (Reactions 1·22 to 1·24 included in Chapter 1) applied. This study found the spatial variation of pollutants to be significant and that these variations were in agreement with a field study and previous studies of dispersion of passive pollutants (Xie *et al.*, 2003).

A measure known as the **photostationary state defect** (**PSSD**), δ_{ps}, that indicates the deviation from chemical equilibrium is found to be a sensitive indicator of reactive mixing taking place within the canyon, defined by Baik *et al.* (2007) as:

$$\delta_{ps} = \frac{k_{NO+O_3}[NO][O_3]}{j_{NO_2}[NO_2]} - 1. \qquad (2{\cdot}6)$$

The highest values of the PSSD and therefore greatest deviation from chemical equilibrium, were observed well above the canyon ($z/H \approx 1.3$) corresponding the outer extent of the escaping canyon plume — *i.e.* where polluted canyon air meets less polluted background air flowing over the canyon (Figure 2·14). A significant variation in the photostationary state defect within the canyon was also found to occur, with the highest 'within canyon' values observed downwind of the emission source and toward roof level on the windward wall due to entrainment of air by the canyon vortex. The lowest values of the passive scalar co-emitted with NO_X were observed in the centre of the canyon vortex. The same modest reaction scheme was subsequently used by Grawe *et al.* (2007) to investigate the effect of local shading on pollutant concentrations. This however neglects the impact of more detailed

atmospheric chemistry, for example, peroxy-radical mediated NO-to-NO_2 conversion and O_3 or total oxidant (O_X) production, upon the steady state NO_X levels.

Figure 2·14 illustrates the clear existence of a primary vortex within the street within which there is a local minimum of NO and NO_2 and a maximum concentration of O_3. Traffic emissions are entrained by the outer edge of the canyon vortex whereas O_3 is entrained along the windward wall. As a result of wind transport, dispersion and reaction, the leeward side is higher in NO and NO_2 and lower in O_3 than toward the windward wall.

Baik *et al.* (2007) used the same simple representation of the photochemistry to study the dispersion of reactive pollutants within the street canyon however in this case the canyon dynamics were simulated using a RANS based dynamical model. This study also found a similar variation in the photostationary state defect with the largest deviation from chemical equilibrium found above roof level where within canyon air meets background air and the region closest to equilibrium to be the within the canyon vortex.

Although a number of studies have investigated the dispersion of reactive pollutants by applying a simple photochemical scheme to a dynamical model, relatively few have included more detailed chemical schemes. Due to limitations in computing power it is impossible to include the vast number of chemical species and reactions that occur in the urban atmosphere, particularly when combined with computationally expensive dynamical models such as LES. Explicit representation of the oxidation processes taking place within the canyon may contain several thousand chemical species and over 20,000 reactions (Dodge, 2000). Owing to the computational expense of such models it is even impracticable to include near explicit chemical schemes as a true representation of the canyon

chemistry. As a result a number of reduced chemical mechanisms, including those reviewed by Dodge (2000), have been developed that accurately represent the chemical environment of urban canyons and may be effectively applied to photochemical / dynamical models.

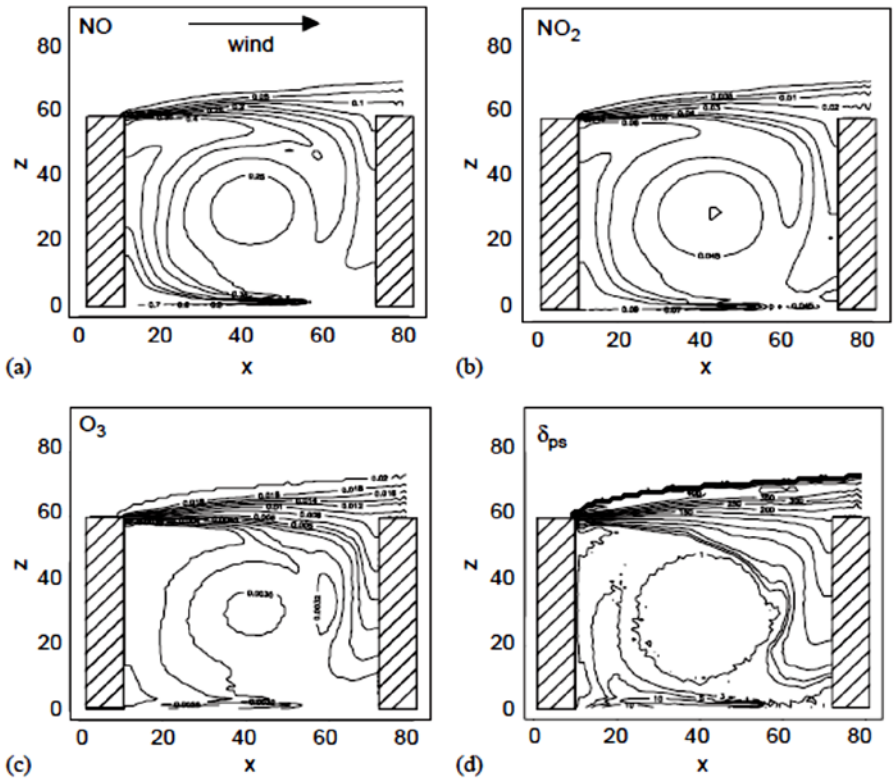

Figure 2·14 - *Contour plots illustrating the spatial distribution of (a) NO, (b) NO_2, (c) O_3 concentration and (d) photostationary state defect (δ_{ps}) at t = 90 min (Baker et al., 2004).*

The work of Garmory *et al.* (2009) used the Stochastic Fields (SF) method to simulate turbulent reacting flows and the dispersion of reactive scalars within the street canyon. This research applied the same simple chemical scheme as Baker *et al.* (2004) and Baik *et al.* (2007) and utilised a number of statistical methods to study atmospheric processes and composition within the canyon.

The results of this initial study were in close agreement with those of Baker *et al.* and Baik *et al.*, with the lower values of photostationary state defect located within the canyon and maxima observed just above roof level, within the mixing layer, the

region in which the variance of a number of chemical species was also found to be highest. In addition to the simple scheme the more detailed Carbon Bond Mechanism (CBM-IV) (Gery *et al.*, 1989) was used. Comparing both mechanisms, the effect of segregation was investigated by calculating the Damköhler number, *Da*, defined as the ratio of the mixing timescale to the chemical timescale.

A value of $Da >> 1$ indicates that the chemistry / dynamical interaction is important and that segregation effects must be accounted for (Krol *et al.*, 2000, Garmory *et al.*, 2006). If $Da << 1$, species become well mixed much more rapidly than undergoing chemical reaction as the chemical processes are relatively slow when compared to the turbulent timescales and hence segregation effects are minimal.

For intermediate and long lived species, including important species such as O_3 and NO, the effect of segregation was found to be minimal. For a number of the shorter lived radical species, however, the CBM-IV results demonstrated that there are significant differences in their predicted concentration in the mixing region above the top of the canyon when segregation effects are considered.

A reaction scheme that included six chemical species was applied to both a box model and an LES model by Krol *et al.* (2000). However in this case, the simulation was applied to the photochemical processes that occur on the larger atmospheric boundary layer scale. Akin to Garmory *et al.* (2009) this research investigated the deviation from chemical equilibrium, as a result of the turbulent nature of the convective boundary layer, in terms of the intensity of segregation. The volume-averaged concentrations of all chemical species simulated using the LES model were found to be in close agreement with those simulated using the box model. The results also demonstrated that when assuming emissions of reactive hydrocarbons are instantaneously mixed the atmospheric lifetime of such chemical species may

be underestimated. It was found that turbulence inherent in the convective boundary layer results in large concentration fluctuations and these indicate a divergence from chemical equilibrium in contrast to that obtained using box model calculations.

When species are emitted uniformly the volume averaged concentrations are found to deviate only slightly from the box model concentrations. When reactive hydrocarbons are emitted non-uniformly, segregation effects are increased and volume averaged LES model results show that the rate of destruction of reactive hydrocarbons (RH - that represents all reactive hydrocarbons and intermediate species) may be reduced by up to 30 % when compared to that calculated using the box model. It was also found that if both the turbulent timescale and the chemical timescale of a compound are comparable, the integrated flux of RH through the RH-OH reaction will be reduced due to the chemistry-turbulence interaction.

Pugh *et al.* (2011) have also investigated segregation effects using field measurements taken above a tropical rainforest in South-East Asia. The effect of segregation on the reaction of OH and isoprene was determined using high temporal resolution isoprene concentration data. It was found that the reduction in the effective rate constant for the reaction of isoprene with OH due to segregation effects was typically less than 15 %. The intensity of segregation was found to be considerably lower than that needed to explain observed inconsistencies between measured and modelled concentrations of OH produced by global and box models of atmospheric chemistry.

Segregation effects were also deemed important in determining concentrations of isoprene averaged over the boundary layer above the Amazon rainforest by Ouwersloot *et al.* (2011). Concentrations of isoprene were found to increase by up to

12 % as a result of incomplete mixing and consequent reduction in the rate of chemical reaction.

Although studies such as these have used modelling techniques to simulate the chemical reaction and transport of pollutions within the street canyon, the chemistry used is very limited with only a few chemical reactions included. Chemical reactions play a vital role in determining the atmospheric composition within street canyons therefore this research aims to combine complicated dynamics through models such as the LES with more complex and realistic chemical reaction schemes.

Recent studies by Kwak and Baik (2012) and Kim *et al.* (2012) have both involved the application of more detailed chemical schemes (CBM-IV and GEOS-Chem respectively) to RANS based CFD models, then used to investigate the dispersion of reactive pollutants within the street canyon domain where $H/W = 1$.

A number of emission scenarios were considered by Kwak and Baik (2012) in which investigation into OH reactivity was also included. One of the main findings of this investigation was that O_3 sensitivity (response to increasing emissions) within the canyon differs from that of the wider urban area where the NO-to-NO_2 ratio is relatively low, resulting in a higher level of NO titration of O_3 when compared to NO_2 photolysis. This study also demonstrated the canyon itself to be a negatively NO_X-sensitive regime where the concentration of O_3 is negatively correlated with increasing NO_X emissions (possibly indicative of NO_X saturated conditions where the ratio of NO to NO_2 is high). In line with a number of the studies discussed above, mixing ratios of NO and NO_2 were observed to be highest toward the leeward wall of the canyon for the base scenario ($VOC/NO_X = 1$) applied. In contrast to previous

studies however, O_3 concentrations were observed to be greatest toward the leeward wall.

Kim *et al.* (2012) carried out an extensive evaluation of their combined CFD-chemistry model using field measurements and found modelled NO levels to be significantly higher (3 ×) than observations. The importance of photochemistry that had a significant effect on the concentration of NO_2 and O_3 was also highlighted through their research. The spatial variation of pollutants within and above the canyon was in agreement with those discussed previously in spite of the application of the more detailed chemistry to the model. Sensitivity analysis demonstrated that by increasing the complexity of the chemical scheme applied to the CFD, a significant difference in the simulated peak concentration of O_3 (at 2pm for July) toward both the leeward and windward walls of the canyon was observed, with higher levels for the full chemistry case over a range of emission rates.

* * * * *

The work within this thesis will include the development of a more detailed and representative chemical mechanism (in comparison to Baker *et al.* (2004)) that will be combined with the canyon dynamics simulated by the LES. A more extensive chemical scheme allows further investigation into the spatial and temporal variation of various chemical species, in particular of short lived species such as OH which have received relatively little attention in the previous studies discussed here.

3: Development of a Reduced Chemical Scheme (RCS)

3·1 Background

In order to develop a suitable model to study street canyon atmospheric composition a representation of the chemistry to be applied within the LES dynamical model needed to be developed. This chapter describes the development of this **Reduced Chemical Scheme** (hereafter referred to as **RCS**) and its subsequent validation. The RCS was based upon a subset of the near explicit chemical mechanism, the MCM discussed in the preceding chapter. The final RCS includes **51 chemical species** and **136 reactions**. In addition to mechanism development, the input parameters used in the box model are discussed here. Finally the quantification of emissions and scenarios modelled using the RCS are described.

3·2 Chemical mechanism development

The most accurate representation of gas-phase tropospheric chemistry can be achieved through the use of near-explicit chemical mechanisms such as the MCM (§2·1·1). This mechanism is too large to incorporate directly into the LES due to its high computational expense. As a result, a subset of the MCM, the Common Representative Intermediates mechanism version CRI v2-R5 (Jenkin *et al.*, 2008b, Watson *et al.*, 2008) that includes 19 emitted anthropogenic VOCs to represent full speciation, 196 chemical species and 555 reactions, was used as a basis for further scheme reduction (the development and evaluation of which is discussed in §2·1·3; Chapter 2) (Bright *et al.*, 2011). The derived RCS mechanism was then compared with the full MCM simulation, the latter providing the standard for evaluation of the new scheme. To carry out evaluation of the chemical scheme, **version 3.1** of the

MCM was employed (§2·1·1) with the equivalent parent VOCs to that of the full CRI v2-R5 included. Thus the full MCM used for comparison therefore included 1220 chemical species and 3634 reactions.

3·3 A zero-dimensional (0-D) photo-chemical box model

A simple, **zero-dimensional** (**0-D**) box model of atmospheric chemistry (§2·1) was used to develop and assess the accuracy of a reduced chemical reaction scheme, referred to hereafter as **box model A**. Concentrations within the box model are assumed to be homogeneous (*i.e.* the volume of air is assumed to be well mixed).

3·3·1 Box model configuration

Box model A included three main input components; a chemical reaction scheme, a photolysis scheme and a physical parameterisation scheme. Figure 3·1 illustrates the model framework of box model A.

3·3·2 Chemical reaction scheme

An integral part of the box model is the chemical mechanism which comprises a set of chemical reactions that determine alongside physical processes the change in atmospheric composition over time. Fundamentally the chemical mechanism is a set of numerically stiff differential equations that relate to the production and loss terms for each chemical species included in the model reaction scheme.

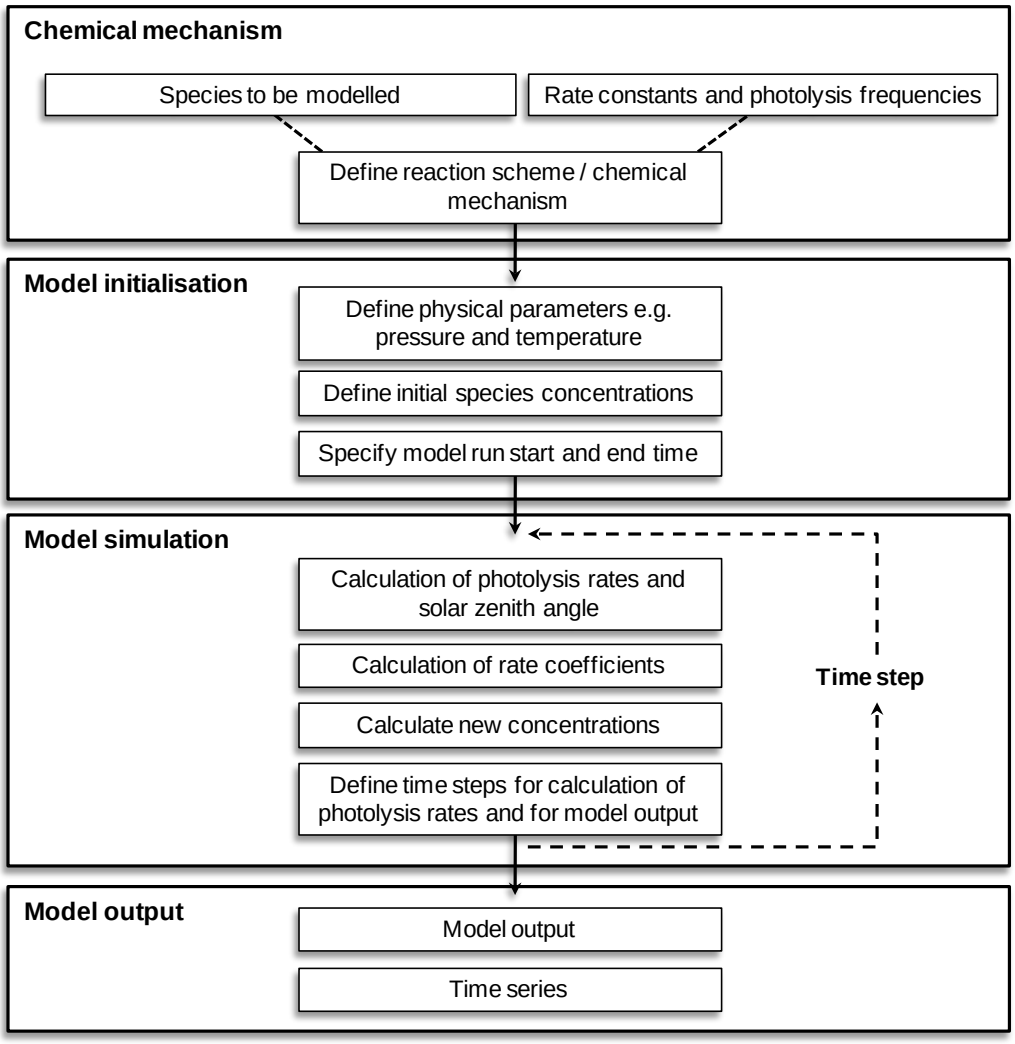

Figure 3·1 - *A schematic illustrating the model framework of box model A.*

Deposition, background mixing and emissions were not included in (the closed) box model A; therefore the concentration of each species was governed by chemical processes alone. In this case the rate of change in the concentration of chemical species, i, (where c_i represents its concentration) is determined by the total sum difference between the production and loss terms for each reaction, *i.e.* the continuity equation is simplified to Equation 3·1.

$$\frac{d[c_i]}{dt} = P_i - L_i = S_i \,, \qquad (3\cdot1)$$

$$i = 1, 2, \ldots, N \,,$$

where P_i is the production term in which species i is a product, L_i is the loss term in which i is the reactant and S_i is the photochemical source or loss term for species i. These terms may be further expanded to:

$$P_i = \sum_{j,l} k_{jl}[c_j]\cdot[c_l] \ , \tag{3·2}$$

$$L_i = [c_i]\sum_{l} k_{il}[c_l], \tag{3·3}$$

where k_{jl} and k_{il} are the rate constants for the production or loss of species i, whilst $[c_j]$ and $[c_l]$ are the concentrations of the reactants j and l. Thus the rate of change in the concentration of a chemical species, i, where c_j reacts with c_l and c_i reacts with c_l is determined through the integration of Equation 3·1 at each time step, Δt.

Non-linear differential equations included in chemical reaction schemes often possess a degree of numerical stiffness as a result of the range in magnitude of rate coefficients included. As a result, the integration routine can often be a lengthy process for which a suitable algorithm must be applied in order to solve such equations accurately and efficiently.

3·3·3 FACSIMILE solver

The **FACSIMILE** solver used in this work to develop a suitably reduced chemical scheme employs variable order Gear's method of FACSIMILE (Curtis and Sweetenham, 1987), a predictor-corrector technique that can be used efficiently to solve stiff differential equations. The predictor-corrector technique involves firstly predicting the values of the solution vector at the end of the step, and then correcting these values to satisfy the differential equations by a limited number of Newton-Raphson iterations (`http://www.mcpa-software.com/facsimile.html`). This method of integration combines the simplicity of explicit schemes with the more stable implicit counterparts and has a higher degree of computational efficiency

when compared to alternative fully implicit integration schemes however, these may be less numerically stable when compared to the latter.

3·4 Box model initialisation

To allow the direct comparison of each chemical scheme, a number of common initial input parameters were defined. These included **physical parameters** such as temperature and pressure (Table 3·1) as well as **initial chemical conditions** such as background and near tailpipe concentrations.

3·4·1 Physical input parameters

A number of physical parameters were applied to the box model and are listed in Table 3·1 below. Firstly, the latitude, longitude and date (Day/Month/Year) were specified in order to calculate solar zenith angle (SZA), θ_z (Figure 3·2), a function of solar declination, δ_s, and calculated at each model time step. Solar declination is defined as the angle between the plane of the Earth's equator and the ecliptic determined by latitude (ϕ), longitude (γ) and the local elevation angle (ψ). The local elevation angle is determined using the date and time parameters specified and is equal to 0 ^{o} at the equator. SZA is given by:

$$\cos(\theta_Z) = \cos(\delta_S)\cos(\phi)\cos(\psi) + \sin(\delta_s)\sin(\phi), \tag{3·4}$$

The rate of photolysis can be defined as the integral over all wavelengths (λ) expressed as:

$$j_A = \int_{\lambda_1}^{\lambda_2} \sigma_A(\lambda,T)\phi_A(\lambda,T)I(\lambda)d\lambda\,, \tag{3·5}$$

where σ_A is the absorption cross section of the molecule, ϕ_A is the photolysis quantum yield for dissociation and I is the intensity of the solar flux (Seinfeld and Pandis, 1998).

Photolysis rates are calculated in the model as a function of SZA and are derived using a two stream isotropic scattering model for clear sky conditions and at an altitude of 0.5 km as described by Hough (1988) and Jenkin *et al.* (1997b). The variation in photolysis rate coefficients (j) with SZA can be expressed well by the following expression:

$$j = l(\cos\theta)^m \exp(-n.\sec\theta), \qquad (3{\cdot}6)$$

where parameters l, m and n have been optimised for each reaction (Jenkin *et al.*, 1997b).

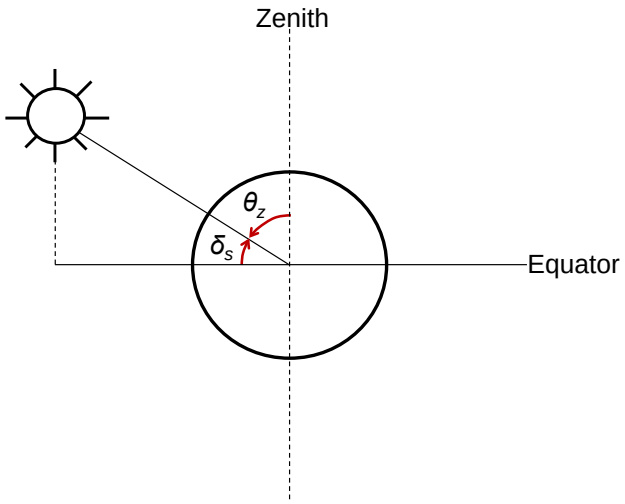

Figure 3·2 - *A schematic illustrating solar zenith angle (SZA) and the angle of declination used to calculate box model photolysis rates.*

Latitude and longitude were defined for the city of Birmingham, UK (52 ^{o} 29' N, -1 ^{o} 54' W) (Figure 3·3) and the time and date was set to 12.00 UTC on August, 1st, 2010 (representative of daytime summer conditions when photochemical ozone formation is prevalent). Standard mean sea level pressure of 1013.25 hPa was applied to the model whilst temperature was set to 293 K (≈ 20 ^{o}C) *i.e.* typical of midday temperatures in August. The model initialisation in which the initial photolysis and complex (non-Arrhenius) rate coefficients (*i.e.* those that have a pressure dependence are calculated) are compiled for 12.00 UTC over one time step prior to the start of the main simulation that is 12.00 UTC.

Table 3·1 - *Initial physical parameters applied to the photo-chemical box model.*

Physical parameter	Box model input
Latitude (ϕ)	52 ^{o} 29' N
Longitude (λ)	-1 ^{o} 54' W
Day	1
Month	8
Year	2010
Time	12.00 UTC
Temperature (T)	293 K
Pressure (p)	1013.25 hPa
Ideal gas constant (R^{*})	8.31451 J K^{-1} mol^{-1}
Avagadro's constant (N_A)	6.0221367×10^{23} molecules mol^{-1}
[M]	2.50×10^{19} molecules cm^{-3} (3 s.f.)
Molecular nitrogen (N_2)	78.09 %
Molecular oxygen (O_2)	20.79 %
Water vapour (H_2O)	2 % (volume - 1 s.f.)

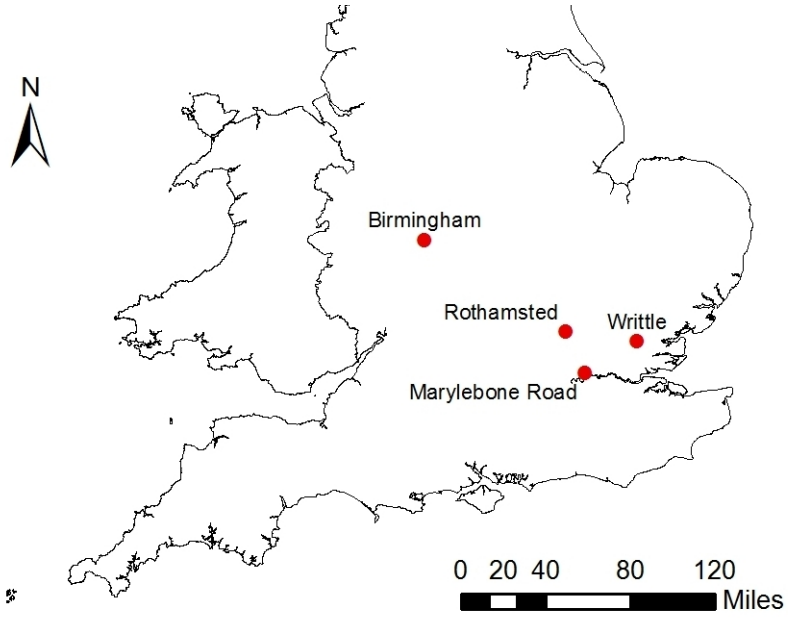

Figure 3·3 - *Site locations of selected monitoring stations from which observations have been used in determining initial inputs, pollutant concentrations and emissions to be applied to the box model. Locations include: Bristol Road, Birmingham (52 ^{o} 29' N, -1 ^{o} 54' W) - the location of study and traffic data; Rothamsted (51 ^{o} 80' N -0.37' W) - HNO_3 data; Writtle, Essex (51 ^{o} 44' N, 0 ^{o} 25' E) - TORCH data; Marylebone Road, London (51 ^{o} 52' N -0 ^{o} 15' W) - air quality data.*

3·4·2 Initial concentrations: The Tropospheric ORganic CHemistry experiment (TORCH)

The initial concentrations of pollutants to be used in the development of a reduced chemical scheme were determined using observations taken during the **Tropospheric ORganic CHemistry experiment** (**TORCH**) field campaign carried out in suburban London from 1—30 August, 2003 (Lee *et al.*, 2006).

During the campaign, measurements were taken at a college located in Writtle, Essex (Figure 3·3), approximately 25 miles to the North East of central London and over 2 miles from the nearest busy road to the south. The location of the Writtle observation site is suitable for determining the background concentrations of pollutants typical of suburban areas and is appropriate for the study of air pollution events when the prevailing conditions allow the transport of air from the relatively heavily polluted London conurbation.

Throughout the measurement campaign the predominant air mass affecting the region was of Atlantic origin with south to southwesterly winds bringing air from the south of the UK and across London toward the measurement site. Wind speeds mainly ranged between 5 and 8 m s^{-1} although higher wind speeds were observed from 13-24 August with peak speeds up to 14 m s^{-1} and the wind direction observed to be west or northwesterly. During this time temperatures generally ranged from 17 to 25 ^{o}C.

From an air pollution perspective the most interesting period to note during the campaign occurred between 6-10 August. During this interval high pressure was dominant across the UK bringing heatwave conditions and maximum temperatures ranging from 26-37 ^{o}C combined with light, variable winds (0.5-5 m s^{-1}). Figure 3·4 illustrates the synoptic conditions affecting the UK during heatwave conditions. A

blocking anticyclone caused air to effectively stagnate across the UK allowing the build up of pollutants; a result of the accumulation of secondary pollutants formed through photochemical processes combined with reduction in the dispersion of emitted primary pollutants.

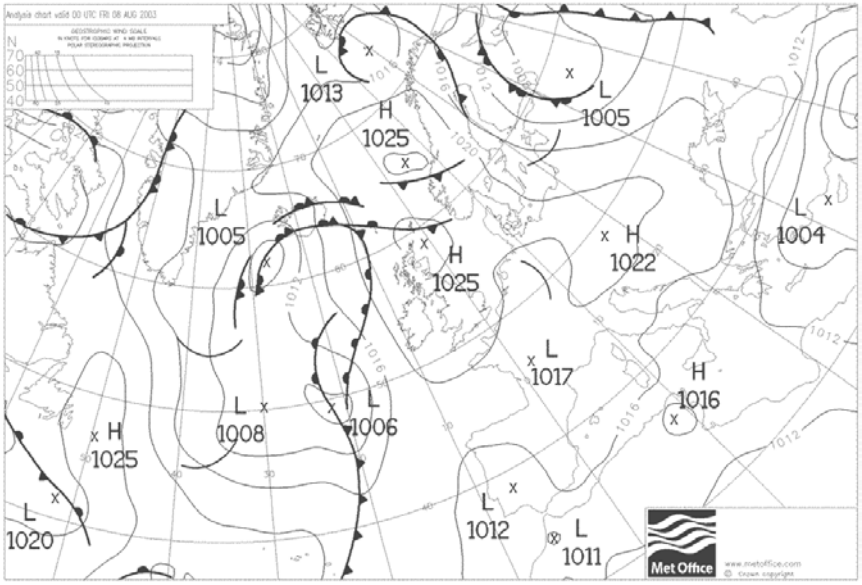

Figure 3·4 - *A surface pressure chart for 00 UTC on August 8th, 2003 illustrating the blocking Anticyclonic conditions affecting the UK during the heatwave period of the TORCH campaign.*

In order to intercompare the full MCM v3.1 and the CRI v2-R5 mechanisms over a range of ambient conditions, initial concentrations of chemical species first had to be determined. To test the sensitivity of the chemical schemes to changing NO_X levels and to ensure adequate representation of chemical processes in such cases, a range of test scenarios were developed. Firstly, a low NO_X case representative of typical urban background conditions was determined using averaged TORCH data in which mean daytime NO_X levels during non-heatwave conditions were in the order of 10 to 15 ppb (Figure 3·5). NO_X levels in this low NO_X case are set to 15 ppb and represented initially as NO_2 only.

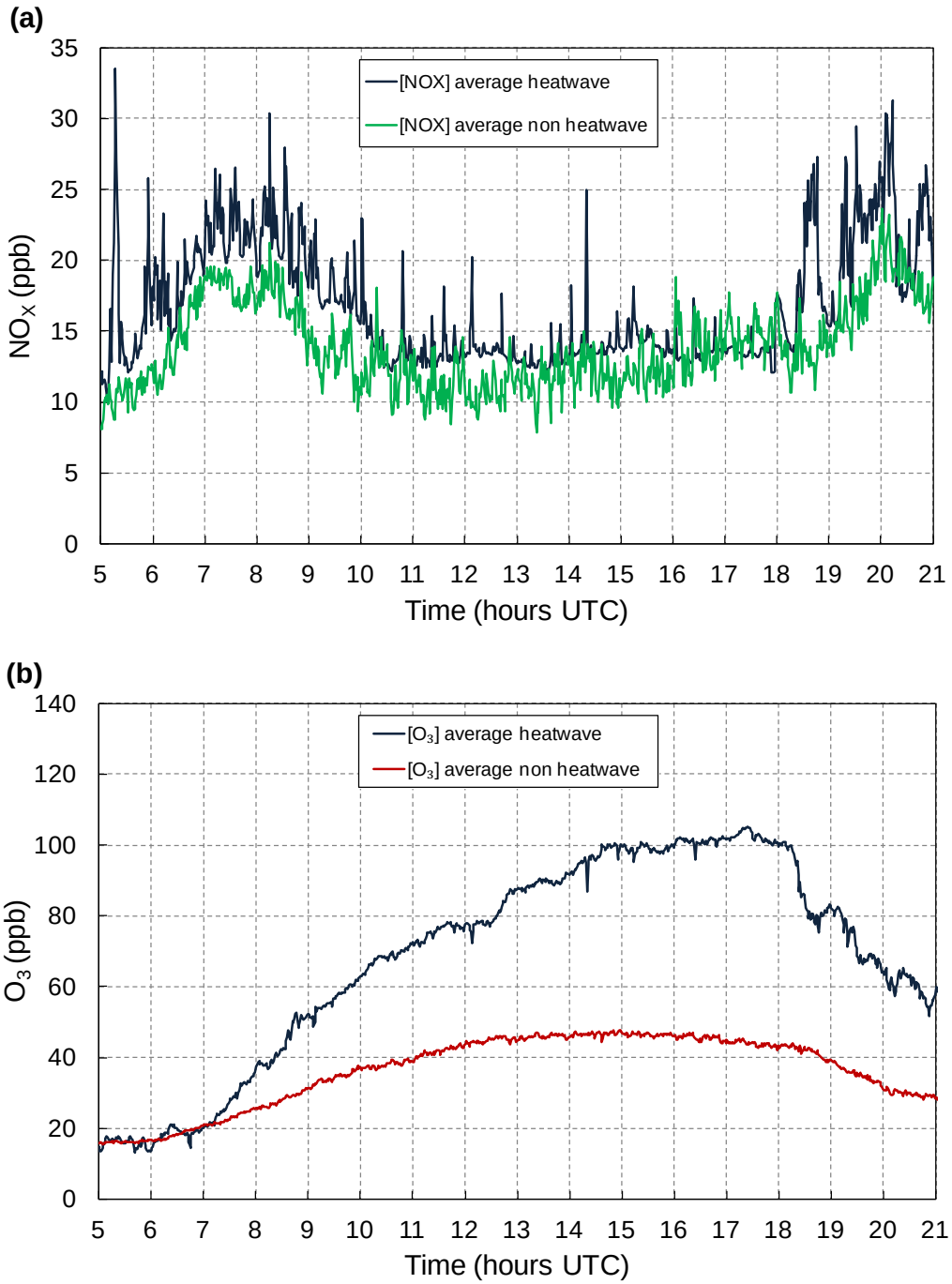

Figure 3·5 - *Diurnal profiles of (a) NO_X and (b) O_3 during heatwave (6 - 10 August) and non heatwave conditions (1 – 30 August excluding the heatwave period). Time series generated using raw 1 minute TORCH measurements averaged at each time point over each defined period above. Measurements from 11th and 22nd of August are omitted from the non- heatwave average due to incomplete data. Data is also excluded for 6th August from the O_3 average taken for the heatwave period. Data from BADC (2004).*

To determine typical NO_X levels for an intermediate (polluted) scenario, data was obtained for a typical kerbside site using the Marylebone Road (Figure 3·3) air

quality monitoring station that forms part of the Defra Automatic Urban and Rural monitoring Network (AURN). Available NO_X data was taken over the same time as the non- heatwave period of the TORCH campaign (Figure 3·6).

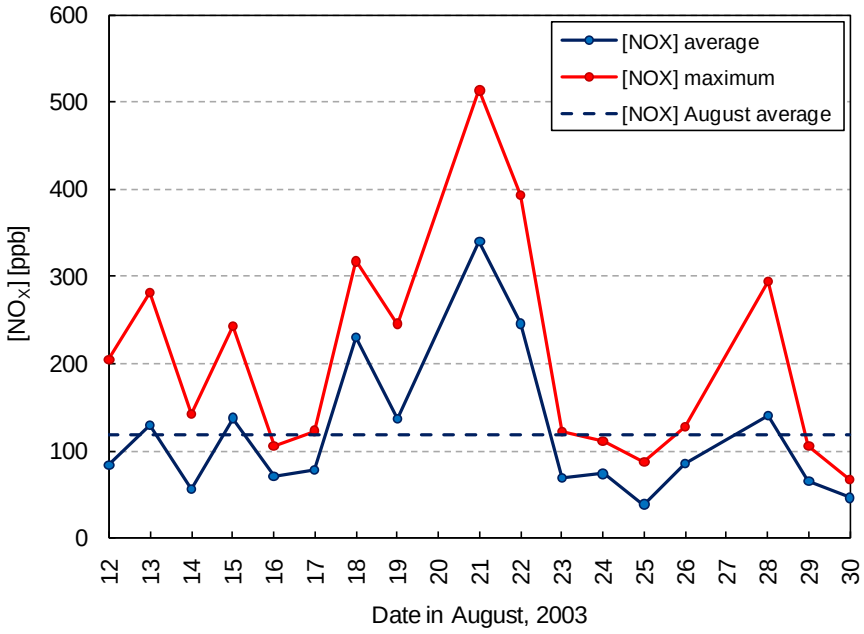

Figure 3·6 - *Maximum, average daily and monthly mean concentrations of NO_X observed during August, 2003 at the Marylebone Road, kerbside air quality monitoring site. Available data was used to calculate averages that coincide with the non-heatwave period of the TORCH campaign. Observations are omitted for 20th and 22nd of August due to incomplete measurements. Data from Defra (2003).*

Average daytime NO_X levels (05.00-21.00 UTC) were averaged over the period to give intermediate NO_X levels of 120 ppb (2 s.f.) referred to hereafter as the intermediate case for the polluted Marylebone Road site and the street canyon in general. Over the same time, maximum daily NO_X levels were also deduced with a peak of 513 ppb reached on August, 21st. This maximum was then taken to be the high NO_X case to further assess the sensitivity of each chemical scheme.

A suitable concentration of O_3 to be applied to the box model simulations was determined using TORCH data with average non-heatwave daytime concentrations of 40 ppb (Figure 3·5b). The concentration of CO was also obtained using TORCH results with an average non-heatwave concentration of 200 ppb applied.

3·4·3 Initial concentrations: CH_4, H_2O and HNO_3

The initial concentration of CH_4 and the percentage volume of H_2O were taken as those typical of the troposphere and are included in Table 3·2.

HNO_3 was not measured during TORCH and as such a suitable concentration had to be determined through other means. Very limited HNO_3 measurements exist for urban locations across the UK. Therefore a mean monthly value for August, 2003 of 2 ppb (1 s.f.) was obtained using monthly observations taken from the Rothamsted Experimental Station which forms part of the Defra Acid Gases and Aerosols network (AGANET) (Defra, 2008e). The site is located approximately 20 miles to the north-north-west of London and is a suitable representation of urban background HNO_3 concentrations. The 2 ppb mixing ratio is also in good agreement with the mean daytime value of 2.32 ppb averaged across a number of measurement sites located in south-east England observed by Kitto and Harrison (1992).

3·4·4 Representation of Volatile Organic Compounds (VOCs)

The simplest way of quantifying VOCs is by measuring their abundance nonetheless this can fail to fully quantify their role in O_3 production. The potential of certain VOCs to produce O_3 provides a more suitable metric in terms of air pollution in urban areas, *e.g.* Photochemical Ozone Creation Potential (POCP) devised by Derwent *et al.* (1996) (Bright *et al.*, 2011).

The individual contribution of each VOC to the formation of O_3 is related to their concentration and chemical reactivity, in general with OH. Total OH reactivity provides a suitable measure of the potential for VOC oxidation and subsequent formation of organic peroxy radicals and hence O_3 formation under more polluted

conditions. Total OH reactivity (k'_{OH}) is defined as the sum of the product of the OH reaction rate coefficient ($ppb^{-1}\ s^{-1}$) and the concentration of each VOC (ppb) *i.e.*:

$$k'_{OH} = \sum k_{1(OH+VOC_1)}[VOC]_1 + k_{2\left(OH+VOC_2\right)}[VOC]_2 + k_{3\left(OH+VOC_3\right)}[VOC]_3 \ldots \quad (3{\cdot}7)$$

Expressing VOC concentrations as OH-reactivities gives a better measure of the potential of a VOC to produce O_3 than its concentration alone. Physically the OH reactivity of a VOC represents the inverse of the lifetime of OH due to loss by reaction with a VOC (Bright *et al.*, 2011).

The concentrations of the common VOCs included in both the MCM and CRI v2-R5 mechanisms were then set to their measured concentrations obtained during the TORCH campaign. To achieve an accurate representation of the measured VOCs, a scaling factor was then applied to each remaining parent VOC abundance included in each mechanism to maintain the total OH reactivity of 3.396 s^{-1} *i.e.* that observed during the non-heatwave conditions of the measurement campaign. The concentration of VOCs included in the full MCM and CRI v2-R5 mechanisms are included in Table 3·2.

3·4·5 Representation of Biogenic Volatile Organic Compounds (VOCs)

The monoterpenes alpha and beta pinene were not measured during the TORCH campaign. Such biogenic species are important in terms of their POCP and potential to form oxidation products via their reactions with O_3 and OH (Calogirou *et al.*, 1999, Yu *et al.*, 1999, Saunders *et al.*, 2003). Such species should therefore be included within the VOC representation. There are very limited measurements of monoterpenes that exist for urban areas of the UK. However a mixing ratio for α-pinene equal to 10 ppt has been measured in the city of Leeds (Hassoun *et al.*, 1999). Assuming that half of this concentration is β-pinene the concentration of

both α and β pinene were set to 10 ppt each in the full MCM and CRI v2-R5 mechanisms following scaling. By adding these monoterpenes to the VOC set to be modelled total OH reactivity increased slightly to 3.413 s^{-1}.

Table 3·2 - *Initial mixing ratios (ppb) applied to the full MCM and CRI v2-R5 mechanisms.*

Species	Chemical formula	Mixing ratio / ppb
Oxides of nitrogen	$NO_X = NO_2$	15; 120; 513
Ozone	O_3	40
Carbon monoxide	CO	200
Nitric acid	HNO_3	2
Methane	CH_4	1800
Water vapour	H_2O	2 % (volume - 1 s.f.)
VOCs		
Ethane	C_2H_6	3.61
Propane	C_3H_8	1.69
Butane	C_4H_{10}	0.97
Ethene	C_2H_4	0.83
Propene	C_3H_6	0.26
Trans-2-butene	C_4H_6	0.02
Ethyne	C_2H_2	0.70
Benzene	C_6H_6	0.24
Toluene	C_7H_8	0.50
O-xylene	C_8H_{10}	0.09
Formaldehyde	HCHO	2.85
Acetaldehyde	CH_3CHO	2.70
Propanal	C2H5CHO	0.18
Isoprene	C_5H_8	0.28
MEK	C_4H_8O	1.07
Acetone	CH_3COCH_3	4.06
α-pinene	$C_{10}H_{16}$	0.01
β-pinene	$C_{10}H_{16}$	0.01
Methanol	CH_3OH	6.70
Ethanol	C_2H_5OH	1.07
Peroxyacetyl nitrate	PAN	0.42

3·4·6 Box model A simulation

Initially box model A was run over a four hour period (240 minutes) which started at 12.00 UTC and ended at 16.00 UTC. Concentrations were output at 10 second intervals throughout the simulation with photolysis rates recalculated at equivalent intervals.

3·5 Mechanism reduction

Prior to mechanism reduction the important species to be modelled first needed to be identified. In terms of street canyon atmospheric chemistry and the time scales of interest in this work the important species were defined as OH, HO_2, NO, NO_2, O_3 and CH_3O_2. The requirement was therefore that these species were modelled accurately using the reduced chemical scheme when compared to the near explicit MCM and full CRI v2-R5 mechanisms (§3·2). As a standard for further mechanism reduction the concentration of OH needed to be maintained to within an arbitrary $\pm$ 20 % of the full MCM over a relatively short time period (30 minutes) and a range of suitable conditions.

As discussed in §2·1·2, chemical mechanisms may be reduced automatically however this thesis uses a manual technique to carry out mechanism reduction. This approach was used in favour of alternative automatic techniques, as the CRI v2-R5 represents an already reduced chemical scheme of suitable size (when compared to larger and more complex near explicit chemical mechanisms) to apply this method within which VOC degradation largely follows parallel uncoupled pathways particularly under the typical (relatively high) NO_X conditions observed within street canyons.

With a large number of VOCs included in the CRI v2-R5 not significantly coupled to those chemical species (hence the removal of which has little or no effect on their concentration) deemed to be important within the canyon environment (Table 3·3), a manual approach to mechanism reduction could be applied.

A number of key stages were involved in the further reduction of the CRI v2-R5 these are included in Table 3·3. Figure 3·7 below illustrates the change in the number of species and reactions following each stage in mechanism reduction (Table 3·3). Figure 3·8 illustrates the mixing ratio of OH simulated using the box model over a 240 minute period whilst including the chemical scheme following each of the four stages in mechanism reduction and compared to the full MCM and CRI mechanisms. A 20 % error in the mixing ratio of OH when compared to the MCM is represented as the grey area included in the figures.

The typical residence time of a parcel of air within the canyon may be calculated using the height of the canyon and the rate of exchange between the canyon itself and the overlying background atmosphere *i.e.*: z/ω_t . In the case of Baker *et al*. (2004) z/ω_t is estimated to range from 19 to 43 minutes and is therefore in the same order as the chemical lifetimes of shorter lived species considered here.

The first 30 minutes (reflecting an average of residence times calculated) of the model simulation is that considered for evaluation of the chemical scheme following each phase in reduction as this period reflects the short residence time (in the order of minutes) of a street canyon air parcel. In addition, evaluation of the chemical scheme was also carried out at 50 minutes as a conservative approach to reflect an upper limit of the residence time estimates given above. One caveat of using the timescales typical of street canyons above is that if additional scenarios were to be simulated in different environments using the reduced chemical scheme

developed here, confirmation of the reduction over extended periods would be required.

In order to allow a sufficient period of time in which to initialise the mixing ratios of the short lived HO_X radicals the model spin up must be considered. The spin up time of the box model runs (Figure 3·8) in which OH concentrations reach 95 % of their steady state values varies between ≈ 1 to 2 minutes where NO_2 = 513 ppb and NO_2 = 120 ppb to approximately 20 minutes where NO_2 = 15 ppb. Therefore a 30 minute spin-up time was used as a conservative and consistent limit across all simulations. For all cases, OH concentrations simulated using the box model, steady state is established at t = 30 minutes.

Table 3·3 - *Key stages of mechanism reduction.*

	Stage	Description
R1	Identification and removal of less important species and associated reactions.	Determination of chemical species needed to accurately simulate concentrations of OH, HO_2, NO, NO_2, O_3 and CH_3O_2 and subsequent removal of unnecessary species and associated reactions.
R2	Determine specific conditions to be considered.	Scenarios limited to street canyon and daytime, afternoon period only when solar radiation is at its greatest and when key photo-chemical processes can be observed.
R3	Removal of any further redundant reactions.	Further reactions with limited or no effect on the concentration of OH, HO_2, NO, NO_2, O_3 and CH_3O_2 over the time period of interest are removed.
R4	Application of Quasi-steady state approximation (QSSA) and combination of reactions.	Assumption of QSSA allowed the removal of any fast reversible reactions as the concentration of these species can be represented algebraically in relation to other species. Reactions with the same reactants and fractional rates of reaction were combined to form a single reaction.

The prime stage in the reduction of the CRI v2-R5 involved identifying and subsequently eliminating those parent compounds, and their unique daughter products, which had little effect on the key chemical intermediates under street canyon conditions. In order to achieve this each individual VOC was removed in

turn, whilst scaling the abundance of others to retain the same reactivity (§3·4·5) and then examining the effect of removal on the important species stated above.

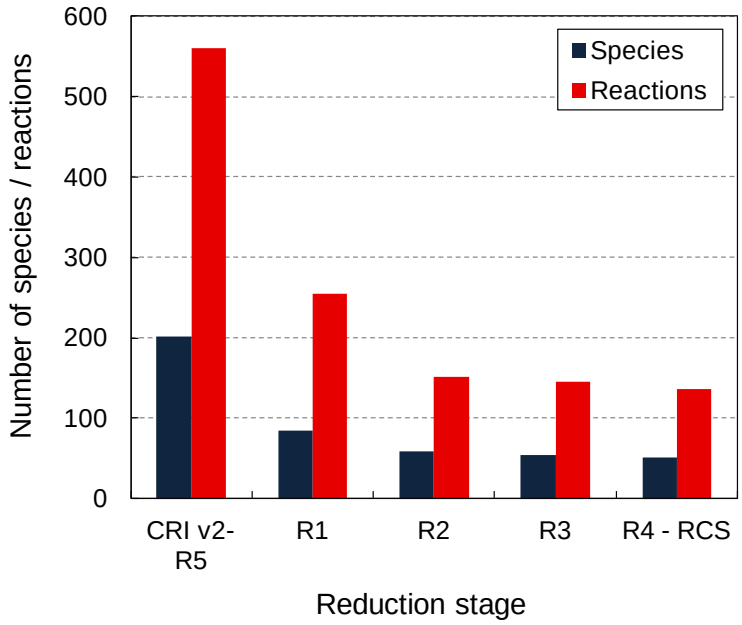

Figure 3·7 - *The number of species and reactions of the full CRI v2-R5 compared to each stage in mechanism reduction. The final reduced chemical scheme (RCS) was achieved at stage 4 in the reduction process with 51 chemical species and 136 reactions included in the mechanism.*

Those species that had a large effect on concentrations as a consequence of their removal were deemed a necessary component of the mechanism and were retained. A number of VOCs that had the smallest effect on concentrations once removed were then permanently eliminated from the mechanism simultaneously. This included the removal of the alkanes: ethane (C_2H_6), propane (C_3H_8) and butane (C_4H_{10}); the alkene: ethyne (C_2H_2) and aromatics benzene (C_6H_6) and o-xylene (C_8H_{10}). The aldehyde: propanal (C_2H_5CHO) was also removed together with the ketone: acetone (CH_3COCH_3). Finally, both monoterpenes: α-pinene and β-pinene (both $C_{10}H_{16}$) were removed from the mechanism with their respective concentrations represented by the surrogate species isoprene (C_5H_8) instead.

Following this elimination stage each of the remaining VOCs were removed in turn in order to test the sensitivity of the mechanism to their elimination. This allowed three additional VOCs to be removed from the mechanism that included: the alkene trans-2-butene (C_4H_8), the remaining aromatic, toluene (C_7H_8) and finally the ketone, MEK (C_4H_8O) which was represented in the reduced scheme by the surrogate species ethanol (C_2H_5OH).

After the first stage in mechanism reduction the CRI v2-R5 was reduced from 202 species and 560 reactions to 85 species and 254 chemical reactions, a reduction of 58 % of the species and 55 % of the reactions from the full CRI v2-R5 mechanism (Figure 3·8). Following this stage in reduction errors of less than 8 % for the concentration of OH existed (Table 3·4) when comparing the concentrations of important species simulated using the reduced scheme to that of the full MCM over a 30 minute period under intermediate NO_X levels (NO_2 = 120 ppb). There is also excellent agreement of the reduced scheme after the first phase in reduction (R1) with the MCM under the less polluted, low NO_X conditions (NO_2 = 15 ppb) where the maximum percentage difference in [OH] ≈ 1 % and the maximum difference between both mechanisms is observed for $[CH_3O_2]$ ≈ 2 %. In the more polluted high NO_X environment ($[NO_2]$ = 513 ppb), maximum differences observed between the R1 scheme and the MCM are considerably greater, reaching up to 29 % over short timescales, however as these conditions are extreme in terms of observed NO_X levels mechanism R1 was deemed suitable for further reduction.

To reduce the CRI v2-R5 further, the second phase in mechanism reduction involved limiting the scope of simulations to daytime scenarios, allowing night time only chemistry to be removed (VOC degradation by NO_3 and inorganic NO_3 / NO_y reactions were retained). This stage in reduction allowed an additional 26 species

and 102 reactions to be eliminated from the mechanism with reductions of 71 % and 73 % respectively when compared to the full CRI.

In this case, the maximum errors were again observed under the extreme case with high NO_X levels leading to a 29 % overestimation in [OH] when simulated using the reduced scheme after this stage in reduction. Under the intermediate and low NO_X scenarios the results of the reduced scheme were in closer agreement with the MCM with observed errors well within 20 % of the explicit mechanism.

The third stage in reduction was achieved by eliminating any further redundant species and reactions. This included the removal of 5 species and 6 reactions associated with SO_2 chemistry and gas phase particle reactions that were deemed unimportant in this research. This phase in reduction represents a cumulative 73 % and 74 % reduction in the number of species and reactions respectively when compared to the full CRI v2-R5. A maximum error of up to 29 % is observed under high NO_X conditions following this stage in reduction when compared to intermediate and low NO_X conditions where maximum errors remained below 8 %.

Further changes to the RCS mechanism were made following the third stage (R3) of reduction *i.e.* to fully reproduce the inorganic chemistry within the CRI whilst discounting surface processes. Firstly, the thermal gas-phase reaction: $NO_2 + O_3 \longrightarrow NO_3 + O_2$, (removed at stage 1), was re-added to the mechanism as a potential source of daytime NO_3 and to maintain the full daytime inorganic chemistry of the CRI V2-R5 (R3 (a) in Figure 3.8). Following this addition, a further reaction included in the full CRI v2-R5 was removed namely, the heterogeneous surface reaction of NO_2 and H_2O that provides a source of HONO at night but has a minimal effect in the presence of sunlight thus reflecting the constraint of chemistry to the daytime and gas phase alone.

The fourth and final stage in mechanism reduction involved the application of the quasi-steady state approximation (QSSA; section 2·1·2). QSSA species were identified as those species with an atmospheric lifetime, τ (defined in Equation 1·2), of less than 1×10^{-4} seconds and included $O(^3P)$ and $O(^1D)$ atoms. This allowed the removal of fast reversible reactions and the combination of reactions that include the same reactants. For example, $O(^3P)$ atoms were found to overwhelmingly react with O_2 (due to its abundance in the atmosphere) when compared to other atmospheric constituents, allowing less important chemical reactions involving $O(^3P)$ to be removed. The rate of production of $O(^3P)$ through the photolysis of O_3 was also found to be approximately equal to its rate of consumption through reaction (with O_2 and N_2) *i.e.* $dc_{O(^3P)}/dt \approx 0$. Thus $O(^3P)$ is in steady state with O_3, allowing the removal of three additional reactions and its substitution by O_3. The fraction of $O(^1D)$ that forms OH was also calculated, to give a composite photolysis reaction that includes $O(^1D)$ quenching (see notes 1 of Appendix A).

Following the fourth stage in reduction, the RCS was compared with the full MCM simulation, the latter providing the standard for evaluation of the new scheme with the explicit inorganic chemistry from the MCM fully retained. As shown in Figure 3·8 and Table 3·4, the difference between the MCM and R4 observed under high NO_X conditions are highest with these differences for O_3 and OH approximately equal to 11 % and 5 % respectively at t = 30 minutes. Under intermediate NO_X conditions, the difference observed for OH is reduced to 0.2 % after this stage in reduction with differences between the R4 scheme and the MCM less than ≈ 11 % for the important species defined under a range of atmospheric conditions.

In addition, considering the more conservative residence time of air within the canyon estimated above, the concentration of all key chemical species at t = 50 min

remain within 15 % of the MCM for the high NO_X case and within 6 % and 3 % for the intermediate and low NO_X cases considered respectively.

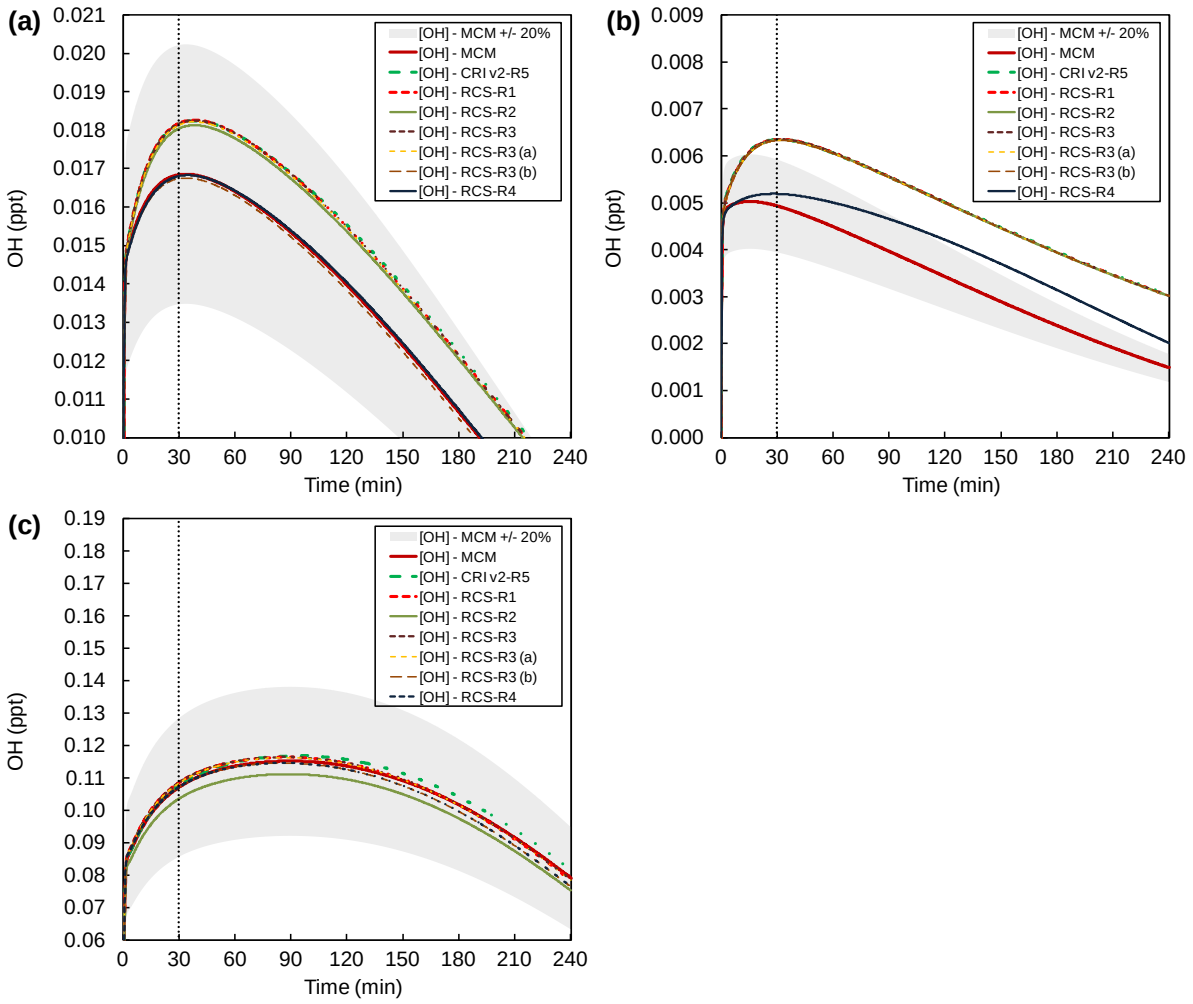

Figure 3·8 - *Temporal changes in the mixing ratio of OH (ppt) simulated by box model A under a range of NO_X conditions and over a four hour period with the full MCM, full CRI v2-R5 and reduced chemical schemes applied after each stage in reduction (R1-R4) for (a) NO_2 = 120 ppb, (b) NO_2 = 513 ppb and (c) NO_2 = 15 ppb. The vertical line represents the 30 minute period of importance when evaluating the chemical schemes reflecting the relatively short residence time of a street canyon air parcel.*

The reduced scheme after the fourth and final stage in reduction, referred to as the **Reduced Chemical Scheme** (**RCS**), includes 51 chemical species and 136 reactions. VOCs included in the RCS mechanism are outlined in section 3·6·2 below.

Table 3·4 - *Percentage differences between the full CRI v2-R5 and reduced chemical scheme (following each stage in mechanism reduction) when compared to the master chemical mechanism, tested under three scenarios at t = 30 min.*

Intermediate NO_X (120 ppb)							
	CRI v2-R5	R1	R2	R3	R3 (a)	R3 (b)	R4
OH	7.9	7.9	7.1	7.9	7.7	-0.6	-0.2
HO_2	1.1	2.2	-0.2	1.4	1.7	-0.4	0.4
CH_3O_2	-0.2	-5.5	-6.0	-5.7	-5.6	-7.7	-7.2
NO	0.0	0.0	0.4	0.4	0.0	0.0	-0.7
NO_2	-0.1	-0.1	-0.1	-0.1	0.0	0.1	0.3
O_3	-0.1	-0.1	0.1	0.2	0.0	0.0	1.0
High NO_X (513 ppb)							
	CRI v2-R5	R1	R2	R3	R3 (a)	R3 (b)	R4
OH	28.7	28.7	28.5	28.7	28.2	-0.9	5.2
HO_2	1.0	2.5	0.2	0.8	1.2	-1.3	7.8
CH_3O_2	0.9	-7.6	-8.0	-7.9	-7.8	-10.2	-4.8
NO	0.1	0.1	0.5	0.5	0.0	-0.1	-8.5
NO_2	-0.1	-0.1	0.0	0.0	0.1	0.2	1.7
O_3	-0.2	-0.2	0.6	0.6	0.1	0.3	11.1
Low NO_X (15 ppb)							
	CRI v2-R5	R1	R2	R3	R3 (a)	R3 (b)	R4
OH	0.6	1.3	-3.3	1.3	1.2	0.0	0.0
HO_2	0.0	0.2	-6.7	-0.1	0.0	-0.8	-0.8
CH_3O_2	-1.9	-2.0	-5.9	-2.2	-2.2	-3.0	-3.0
NO	0.0	0.1	0.6	0.5	0.2	0.3	0.2
NO_2	0.0	0.0	-0.1	-0.1	0.0	0.1	0.1
O_3	0.0	-0.1	-0.2	-0.1	-0.1	-0.1	-0.1

3·6 RCS input parameters

3·6·1 Initial conditions included in the RCS

Physical parameters included in the RCS are the same as those outlined in section 3·4·1. The initial mixing ratios of those species included in the RCS with a defined background concentration are listed in Table 3·5. The mixing ratio of all species

(excluding NO, NO_2 and VOCs) were kept the same as those included in Table 3·2 (discussed in §3·4·2 and §3·4·3). TORCH data was used to determine representative concentrations of NO and NO_2 typical at midday, under non-heatwave conditions and representative of levels observed in the urban background.

3·6·2 Representation of Volatile Organic Compounds (VOCs) in the RCS

Within the final RCS there are 8 VOCs in total that represent the speciation of anthropogenic and biogenic VOCs including: ethene, propene, formaldehyde, acetaldehyde, methanol, ethanol, peroxyacetylnitrate and isoprene. To ensure the adequate representation of VOCs within the RCS, the concentrations of those VOCs included were adjusted (in the same manner as outlined in section 3·4·4) to maintain the same overall OH reactivity as measured during the TORCH campaign when including the monoterpenes. This was achieved by applying an equal scaling factor to the measured concentrations of each of the 8 remaining parent VOCs in order to maintain the observed total reactivity of 3.396 s^{-1}(calculated as the sum total of the product of the OH reaction coefficient and the scaled concentration of each VOC *i.e.* Equation 3·7 whilst maintaining the (relative) measured ratios (and relative OH reactivity) of each retained VOC. The monoterpenes α and β-pinene were included at levels of 5 ppt, represented as isoprene in the final RCS, increasing the reactivity slightly to 3.413 s^{-1}.

Table 3·5 - *Initial mixing ratios (ppb) applied to the RCS.*

	Chemical formula	Mixing ratio / ppb
Nitric oxide	NO	2
Nitrogen dioxide	NO_2	8
Ozone	O_3	40
Carbon monoxide	CO	200
Nitric acid	HNO_3	2
Methane	CH_4	1800
Water vapour	H_2O	2 % (volume — 1 s.f.)
VOCs		
Ethene	C_2H_4	0.91
Propene	C_3H_6	0.29
Formaldehyde	HCHO	3.14
Acetaldehyde	CH_3CHO	2.98
Isoprene	C_5H_8	0.28
Methanol	CH_3OH	7.38
Ethanol	C_2H_5OH	2.37
Peroxyacetyl nitrate	PAN	0.46

3·6·3 Photolysis parameters

The photolysis frequencies used in the models were calculated offline using the **Tropospheric Ultraviolet and Visible (TUV)** Radiation Model v4.1 (Madronich and Flocke, 1998). The TUV model allows the combined effects of absorption, scattering and reflectivity (due to atmospheric constituents including: O_3, NO_2, SO_2; cloud, aerosol and surface albedo) on photolysis rate parameters to be determined through a number of user defined parameters. The parameters defined here were representative of those for a street canyon in Birmingham, UK (located at 52 ^{o} 29' N; -1 ^{o} 54$^{'}$ W; Figure 3·3) at 12.00 UTC on 1st August, 2010 giving a calculated solar zenith angle of 34 ^{o}. Column O_3 was calculated at 300 Dobson Units (DU) whilst SO_2 and NO_2 columns were negligible. The ground elevation was specified as 0.12 km and the atmosphere was assumed to be cloud free. A surface albedo of 0.15 was defined *i.e.* typical of an urban street surface (DFT, 2009, Liu *et al.*, 2011).

The rate of photolysis for NO_2 determined using the TUV Radiation Model is equal to j_{NO_2} = 0.009 s^{-1} with additional TUV derived photolysis rate constants highlighted in Appendix A. The rate constants for a number of reactions have also been derived using TUV model derived j_{NO_2} by relating the fraction of each rate constant to j_{NO_2} used within the MCM and then scaling the rate constant of each reaction using this fraction and the updated j_{NO_2} TUV value (Appendix A). Photolysis rates were held constant (at their calculated values obtained at 12 UTC) over the modelling period in order to reduce the computational expense once implemented in the LES, reflecting the short residence time (minutes) of a typical street canyon air parcel (Vardoulakis *et al.*, 2003, Baker *et al.*, 2004, Bright *et al.*, 2011).

3·7 Evaluation of the RCS

The RCS was compared with the full MCM simulation, the latter providing the standard for evaluation of the new scheme. Using both schemes and box model A within which the air is assumed to be well-mixed and pollutant concentrations are homogenous and therefore a function of chemistry alone, the accuracy of the RCS was assessed using the time variation of primarily OH together with other important species using the initial conditions in Table 3·5 (Bright *et al.*, 2011).

Photolysis rates were also fixed at the calculated 12 UTC value with the TUV derived rate constants applied to the RCS also included in the MCM (where applicable) for comparison. Figure 3·9 and Figure 3·10 show the change in concentration of important species to be modelled using the RCS. The left hand panels included in both figures represent temporal changes in the mixing ratio of species under typical urban background conditions (Table 3.5) where NO = 2 ppb and NO_2 = 8 ppb. Whilst the right hand panels represent high NO_X conditions (where NO = 1000 ppb and NO_2 = 120 ppb) such as those in close proximity to vehicle exhausts.

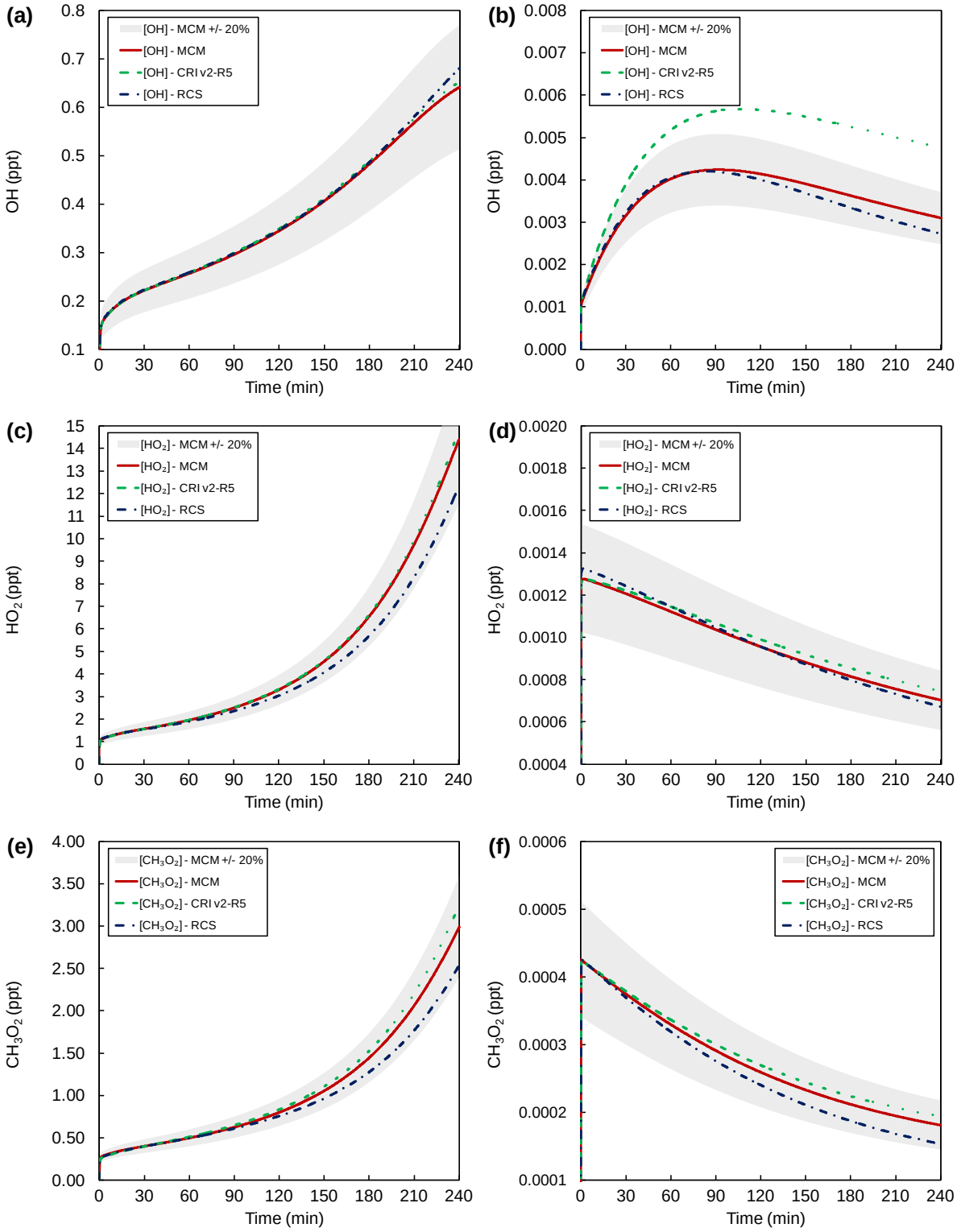

Figure 3·9 - *Temporal changes in the mixing ratio of (a; b) OH, (b; c) HO_2 and (d; e) CH_3O_2 (ppt) simulated by box model A under background conditions (left hand panels where NO = 2 ppb; NO_2 = 8 ppb) and high NO_X conditions (right hand panels where NO = 1000 ppb; NO_2 = 120 ppb) over a four hour period with the full MCM, full CRI v2-R5 and RCS mechanisms applied.*

The time taken for the box model simulations to achieve equilibrium (spin up) as shown in Figure 3·9a and b above (within which OH levels reach 95 % of their steady state values) are in the order of 1 to 2 minutes.

For the urban background case, the maximum difference in the mixing ratio of OH between the RCS and the MCM over a four hour period was approximately 6 % which is within the bounds of the smallest errors associated with the measurement of OH (7-16 %) (Heard and Pilling, 2003). For NO, NO_2, O_3 and HO_2, the largest differences between the RCS and the MCM, which occur toward the end of the four hour time period, are approximately 15 %, 7 %, 4 % and 14 % respectively. At the 30 minute time point, more relevant to canyon residence times, smaller respective differences of 0.4 %, 0.1 %, 0.2 %, 1.1 % and 0.7 % for OH are observed (Table 3·6) (Bright *et al.*, 2011).

The RCS and MCM were also compared under high NO_X conditions (NO = 1000 ppb and NO_2 = 120 ppb) such as those that may be experienced near to vehicle exhausts. The temporal change in observed mixing ratios of chemical species under high NO_X conditions are illustrated in the right hand panels of Figure 3·9 and Figure 3·10.

Table 3·6 - *Percentage differences between the RCS and MCM under background (NO = 2 ppb; NO_2 = 8 ppb) and (b) high NO_X conditions (NO = 1000 ppb; NO_2 = 120 ppb) at t = 30, 120 and 240 min.*

Difference between the RCS and MCM [%]						
	Background NO_X			High NO_X		
	30	120	240	30	120	240
OH	0.73	0.61	6.10	2.35	-3.32	-11.96
HO_2	-1.12	-7.95	-14.30	2.99	0.04	-4.31
CH_3O_2	-0.37	-5.24	-15.00	-1.31	-7.34	-15.29
NO	0.42	3.35	15.16	-0.28	-1.25	-2.76
NO_2	0.09	1.16	7.41	1.67	6.57	13.02
O_3	-0.19	-1.52	-4.05	2.10	8.07	16.39

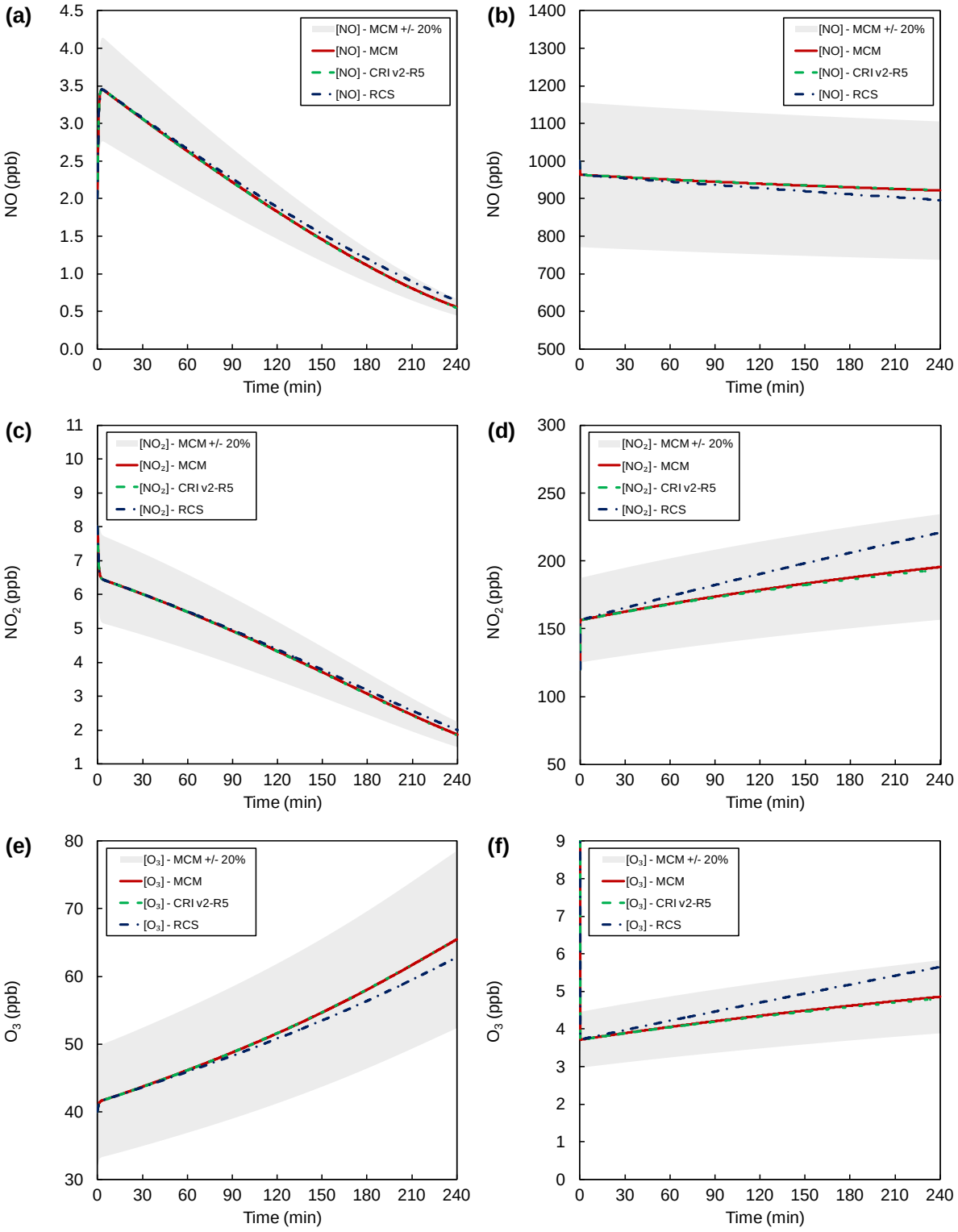

Figure 3·10 - *Temporal changes in the mixing ratio of NO, NO_2 and O_3 (ppb) simulated by the box model A under (a) background conditions (NO = 2 ppb; NO_2 = 8 ppb) and (b) high NO_X conditions (NO = 1000 ppb; NO_2 = 120 ppb) over a four hour period with the full MCM, full CRI v2-R5 and RCS mechanisms applied.*

The maximum differences observed over a four hour period are 3 %, 13 %, 16 %, and 4 % for NO, NO_2, O_3 and HO_2 respectively with 12 % for OH. At t = 30 minutes the simulated differences are 0.3 %, 1.7 %, 2.1 %, 3.0 % and 2.4 % for NO, NO_2, O_3, HO_2 and OH respectively (Table 3·6) (Derwent and Middleton, 1996). These values are significantly smaller than the uncertainty associated with emissions and with the measurement of such pollutants (Lee *et al.*, 2006, Boulter *et al.*, 2009). Under the more polluted conditions, that may be encountered by an air parcel within an urban street canyon, and over the shorter timescales that such parcels may reside within this domain, the RCS performs better than the CRI v2-R5 mechanism particularly in the case of the short lived species and in particular OH for which the MCM mechanism is replicated closely by the RCS.

Conversely, O_3 levels simulated using the CRI v2-R5 follow those of the MCM more closely than the RCS under high NO_X conditions particularly over the extended simulation period beyond t = 30 minutes. The high level of skill inherent in the CRI v2-R5 mechanism in its ability to emulate O_3 levels simulated by the MCM was also demonstrated over a 5 day period and under a range of conditions by Emmerson and Evans (2009).

Under low NO_X, background conditions, the RCS, CRI v2-R5 and MCM are in close agreement in simulating OH levels as are NO levels. Under these conditions, NO levels exhibit a decrease over time whilst OH levels increase as a result of VOC oxidation. Under high NO_X conditions OH levels increase up to a point with increasing NO_X (~ 90-120 minutes) prior to their decrease at a slower rate.

The differences between the CRI and MCM for RO_2 under both high and low NO_X conditions have been observed previously with RO_2 overestimated in both the CRI v1 and CRI v2 mechanisms (Watson, 2007, Jenkin *et al.*, 2008b).

Such differences, a likely result of the simplified representation of VOCs within the CRI mechanism (therefore fewer routes to HO_X loss *e.g.* reduced scope for alkyl nitrate formation compared with the MCM) were observed by Watson (2007) with the poorest agreement between the MCM and CRI v2-R5 evident for all anthropogenic VOCs under high NO_2 conditions albeit over a 4 day period. Lumping of species within the CRI is also likely to result in a more direct route of CH_3O_2 and HO_2 formation when compared to the full MCM.

As a result of the observed difference in CH_3O_2 it is clear that (particularly in the high NO_X case) HO_2 has subsequently increased, increasing the rate at which HO_2 + NO driven OH production occurs, hence a large increase in OH observed in the CRI particularly under high NO_X conditions.

In contrast to the CRI, CH_3O_2 is slightly underestimated by the RCS scheme when compared to the MCM with an increase in the deviation between mechanisms over time. As a result, radical cycling to OH is likely to be reduced with slower NO to NO_2 conversion and hence slower O_3 production when compared to the MCM and CRI schemes under background conditions. Under high NO_X conditions despite RO_2 levels being lower for the RCS than the MCM and CRI there is an increase in the rate of production of both NO_2 and O_3 (in line with decreasing NO levels) over time indicating a more direct route of production for the RCS under these conditions.

Under high NO_X conditions, as RCS simulated NO_2 increases and NO decreases over time, the OH sink (predominantly due to the termination reaction with NO_2) increases at a faster rate than its production (the major source represented by the HO_2 and NO reaction) with a larger decrease in OH over time when compared to the MCM and CRI schemes.

3·8 Box model B

Box model A (§3·3) was adapted to become more representative of the street canyon environment and ultimately to allow comparison with the LES model (Chapter 5).

Through the application of emissions and background mixing **box model B** was derived. In this case, the equation governing the change in concentration of species within the box model over time is now represented generically as:

$$\frac{d[c_i]}{dt} = \frac{q}{H} + S_i + \frac{\omega_t}{H}(c_B - c), \qquad (3\cdot8)$$

$$i = 1, 2, \ldots, N,$$

where the first term in the equation represents emissions, q is the amount emitted per unit time and per unit surface area of the box (molecules cm^{-2} s^{-1}), H is the characteristic length of the box, S_i is the photochemical source or loss term for species i and background mixing is represented by the final term in the equation where ω_t is the transfer velocity (m s^{-1}), c_B is the background concentration and c is the concentration of species within the box. Thus the rate of change in the concentration of a chemical species is determined through the integration of Equation 3·8 at each time step, Δt.

The exchange of species from within the box with those of the overlying background atmosphere is initiated after 30 minutes of the model simulation that included chemistry alone. The concentration of background species was then set to equal the concentration of all species simulated by the box model at t = 30 minutes following the chemical 'spin up'. After this initial half hour period the chemical species within the box are then mixed with background concentrations outside of the box (representing the background atmosphere above the canyon) that remain constant throughout the rest of the box model simulation. The rate of exchange between the background environment and the box itself is dependent on the difference between the concentration of species outside of the box and that inside

the box itself. The initial value of ω_t applied to the box model was taken to equal to 0.010 m s^{-1}, obtained by averaging the range of ω_t determined by Baker *et al.* (2004).

The change in concentration of NO and NO_2 as simulated by box models A and B, over a 210 minute period is illustrated in Figure 3·11 below with emissions and background mixing in box model B implemented from t = 30 minutes onwards with a large increase in NO_X levels evident as a result *.

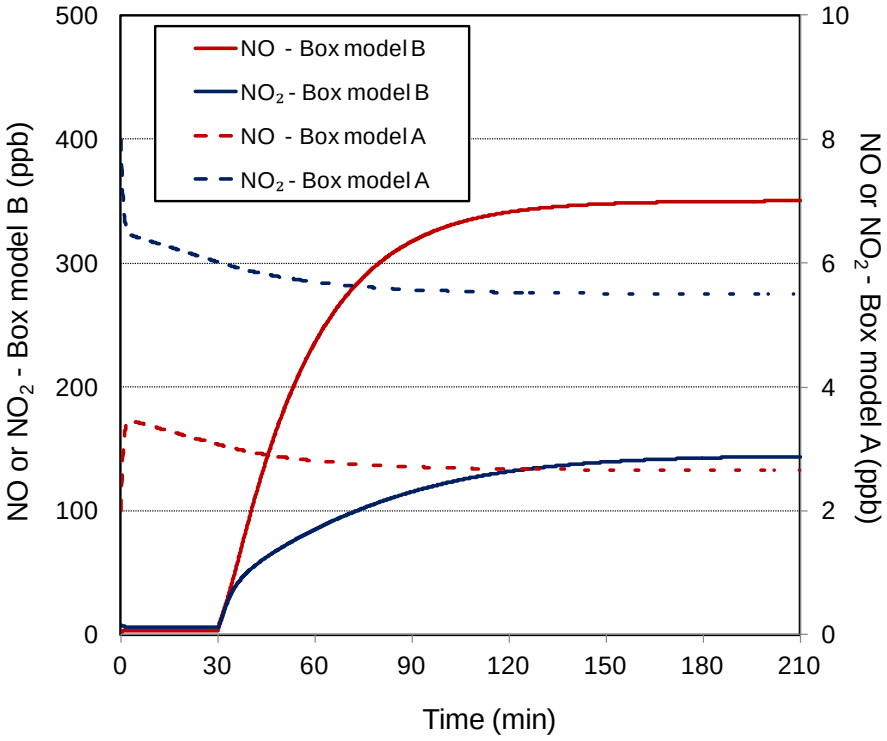

Figure 3·11 - *The change in mixing ratio of NO and NO_2 (ppb) simulated using photochemical box models A and B. Emissions and background mixing are initiated at t = 30 minutes within box model B.*

3·9 Emissions and Scenario development

3·9·1 Determination of representative vehicle emissions

As discussed in Chapter 1, emissions are of prime importance in controlling street canyon atmospheric composition. Within urban areas emissions are dominated primarily by road transport (Vardoulakis *et al.*, 2003). The emission rates to be

applied to the photochemical box model were determined using the UK Road Vehicle Emission Factors, 2009 (Boulter *et al.*, 2009) and are based on the National Atmospheric Emissions Inventory (NAEI). Vehicle emissions are calculated using vehicle speed emission factors, vehicle fleet composition data and total activity over the period of interest *i.e.*: Emissions (g km^{-1} hr^{-1}) = Emissions Factor (g km^{-1} veh^{-1}) × Activity (Volume of traffic (vehicles hr^{-1})).

Traffic data

In order to develop a number of suitable and realistic scenarios that can be applied to investigate the effect of emissions on atmospheric composition on the street canyon scale, traffic count data was utilised. Using Annual Average Daily Flows (AADF) that represent the average annual number of vehicles passing a point in the road network each day during 2008 (DFT, 2009), an average number of vehicles per hour was deduced for a representative site located on the A38 Bristol Road (52 ^{o} 29' N, -1 ^{o} 54' W). This road is a principal urban A road that has four lanes of traffic in total. The average diurnal variation in traffic on a typical weekday was then deduced using the traffic distribution by time of day on a Monday for all UK roads (DFT, 2009).

To determine the diurnal variation in number of vehicles per hour of an urban road with less traffic for comparison, 2008 road statistics were used to give an estimate of 2,400 vehicles per day (DFT, 2009) on a minor urban road. Figure 3·12a illustrates the calculated diurnal variation in hourly traffic deduced for the two road classes described above. The number of vehicles per hour for the principal urban A road was rounded down to the nearest 500 to give 1500 vehicles per hour and taken to represent moderate traffic which was then included in the base case scenario. In the case of the minor urban road the number of vehicles per hour was equivalent to 150 and equal to that calculated.

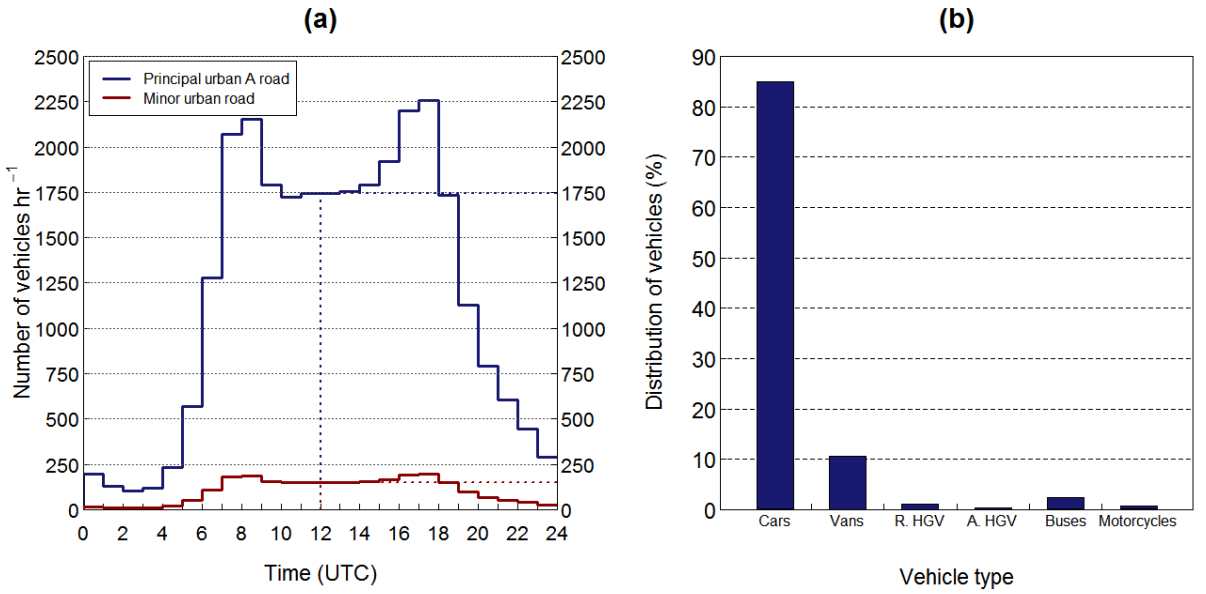

Figure 3·12 - *A graphic illustration of (a) the diurnal variation in the number of vehicles per hour observed on a typical weekday for a principal urban A road (four lanes of traffic) and a minor urban road (typically 1-2 lanes of traffic) where dashed lines represent the calculated values at midday; (b) the typical daily vehicle mix (%) observed on a principal urban A road.*

3·9·2 Vehicle speed emission factors

In order to determine representative emissions, typical moderate weekday traffic flow by vehicle type observed on the A38 Bristol road was used to calculate the percentage daily vehicle mix observed on a typical urban road (Figure 3·12b). Subsequently this was used to calculate the number of vehicles per hour for each vehicle type. Using fleet composition data for 2010 (Boulter *et al.*, 2009) and an average speed of 30 mph (representative of moderately free-flowing traffic), fleet weighted emission factors (Appendix B) per vehicle were calculated for the vehicle mix observed on the A38 Bristol Road (Appendix B) and for those pollutants applied to the RCS including: CO, total hydrocarbons (HC) and NO_X. The total hydrocarbons analyser that measures HC utilises flame ionisation detection that effectively counts the number of all carbon atoms present in an air sample. As a result, the composition of species and relative quantities of each included cannot be identified from such measurements (Latham *et al.*, 2001).

To determine a realistic representation of the VOC emissions to be applied to the model simulations the most important VOCs (in terms of their role in the chemical processes taking place on the street canyons scale) and their relative proportions were calculated. In order to establish the most important VOCs to be emitted along with their respective mass fractions, the VOCs were ranked according to their mass, Photochemical Ozone Creation Potential (POCP) and OH reactivity. The mass of each VOC was determined using the estimated annual mass emissions of VOCs (tonnes) originating from road transport during 2006 (Defra, 2008d). VOCs were then ranked in terms of their annual mass emissions into the atmosphere (Table 3·7). Using POCP values calculated after day 1 (Derwent *et al.*, 1996) VOCs were subsequently ranked in terms of their ozone creation potential weighted quantities (Table 3·7) where:

$$POCP_{weighted} = \left(\frac{POCP}{100} \right) \times mass \,. \qquad (3{\cdot}9)$$

Using evaluated kinetic data and the number of molecules emitted of each VOC, the OH reactivity of each species was then determined (Appendix C).

Table 3·7 - *The most important VOC emissions ranked in terms of annual mass emissions [t], Photochemical Ozone Creation Potential (POCP) and OH reactivity [$cm^3 s^{-1}$].*

Mass [t]		$POCP_{weighted}$ [t]		OH reactivity [$cm^3 s^{-1}$]	
2-methylbutane	7838	Ethylene (ethene)	6823	Propylene	1.23×10^{21}
Ethylene	6823	Propylene (propene)	2952	Ethylene	1.16×10^{21}
Toluene	6760	Toluene	2380	2-methylpropene	1.12×10^{21}
Butane	6017	2-methylpropene	2305	1,3-butadiene	1.04×10^{21}
Formaldehyde	3859	1,2,4-trimethylbenzene	1712	Formaldehyde	6.58×10^{20}
Pentane	3733	Formaldehyde	1644	Acetaldehyde	3.96×10^{20}
Hexane	3421	2-methylbutane	1599	1,2,4-trimethylbenzene	3.82×10^{20}
Propylene	2952	m-xylene	1436	m-xylene	2.66×10^{20}
Benzene	2592	Butane	1227	1,3,5-trimethylbenzene	2.48×10^{20}
2-methylpropane	2592	p-xylene	876	Toluene	2.47×10^{20}

VOC emission factors

Initially VOCs were ranked according to mass, POCP weighted mass and OH reactivity (Table 3·7). Following each stage in the ranking process, each VOC was assigned a score that indicated its significance in terms of each independent classification. A total score was then assigned to each VOC that combined the scores of each classification with the four most important emitted VOCs determined using these. Of these, three were included in the RCS namely ethylene (ethene), propylene (propene) and formaldehyde. Although less important in terms of mass emissions, a source term was also included for acetaldehyde.

Using the estimated annual mass of VOCs emitted in tonnes from road transport (Defra, 2008d), the relative proportion of each VOC deemed to be emitted in the urban environment was determined with the assumption that these species constitute total hydrocarbon emissions. Biogenic emissions, alcohols and PAN were negated from those VOCs emitted into the urban canyon environment by vehicles.

For the base case scenario, the fraction of total VOC emissions that each VOC included in the RCS contributes is illustrated in Figure 3·13.

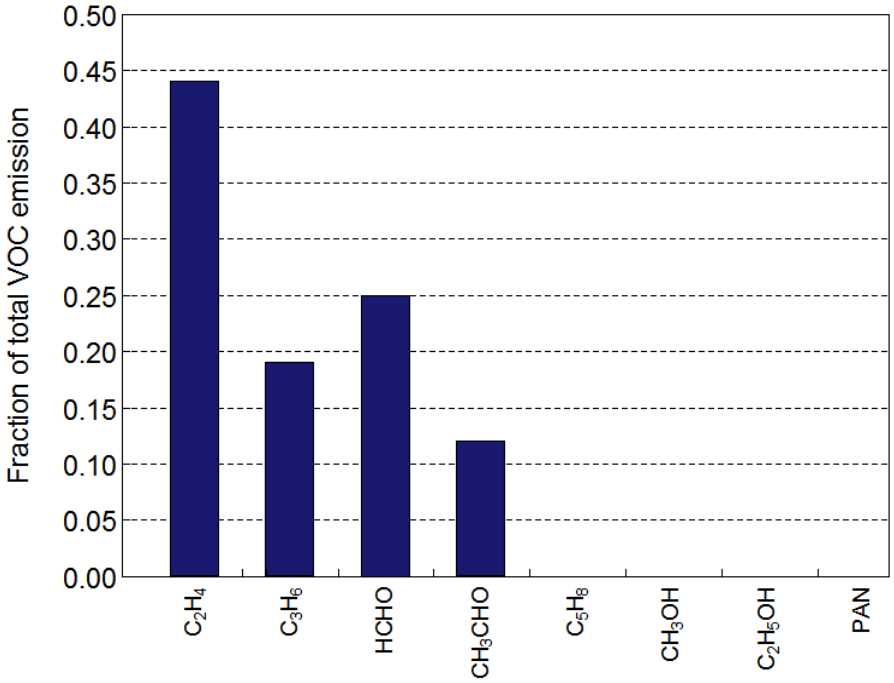

Figure 3·13 - *VOC emission fractions for VOCs included in the RCS and the base case model scenario.*

Using the calculated total hydrocarbon emissions rate for all vehicles of approximately 128 g km^{-1} hr^{-1}, total HC emissions were then converted to 3.56×10^{-7} g cm^{-1} s^{-1} (Table 3·8).

Table 3·8 - *Total emission rates to be applied to the photochemical box model.*

					Emission rates		
Pollutant emitted	Chemical formula	Molar mass [g mol^{-1}]	[g km^{-1} hr^{-1}]	[g cm^{-1} s^{-1}]	Moles cm^{-1} s^{-1}	Molecules cm^{-1} s^{-1}	Molecules cm^{-3} s^{-1}*
NO_X	NO_2	46.01	620	1.72×10^{-6}	3.74×10^{-8}	2.25×10^{16}	6.94×10^{9}
CO	CO	28.01	1356	3.77×10^{-6}	1.35×10^{-7}	8.10×10^{16}	2.50×10^{10}
HC	C	12.01	128	3.56×10^{-7}	2.97×10^{-8}	1.79×10^{16}	5.52×10^{9}

* Averaged over the area of box model B (3.24×10^{6} cm^{2}).

NO_X and CO emission factors

NO_X and CO emissions were also calculated using the UK Road Vehicle Emission Factors, 2009 (Boulter *et al.*, 2009) for typical weekday traffic and an average speed of 30 mph (§3·9·1). The total emission rates calculated for all vehicles was 620 g km^{-1} hr^{-1} for NO_X and 1356 g km^{-1} hr^{-1} for CO (Table 3·8).

Model emissions

In order to apply emissions to the photochemical box model, the amounts of NO_X, CO and VOCs emitted were calculated. Using the respective molar masses for NO_2 (46.01 g mol^{-1}), CO (28.04 g mol^{-1}) and carbon, C (12.01 g mol^{-1}), emissions were converted to the number of molecules cm^{-1} s^{-1}. These values were then applied to box model B where the emission rate of NO_X (ENO_X) was equal to 6.94×10^9 cm^{-3} s^{-1}, the emission rate of CO (ECO) was 2.5×10^{10} cm^{-3} s^{-1} and that of VOCs (EVOC) 5.52×10^9 cm^{-3} s^{-1} when emitted into the volume of the box (3.24×10^6 cm^3). For the base case scenario the fraction of NO_X emitted as NO was taken as 0.9 whilst NO_2 was equal to 0.1 *i.e.* within the mid range of the proportion of NO_X emitted as primary NO_2 which has seen an increase over recent decades (AQEG, 2007).

3·9·3 Emission scenario development

Variation in vehicle speed and traffic

In addition to the base case scenario of 1500 vehicles hr^{-1} moving at 30 mph, emission factors were also calculated for slow moving traffic (10 mph) and fast flowing traffic (60 mph) whilst the number of vehicles per hour was kept constant. For the urban minor road case with 150 vehicles hr^{-1} the speed of traffic was also varied between 30 mph and 10 mph to determine emission factors. As a worst case scenario, typical weekday traffic data (Defra, 2008a) observed at midday on a Monday (06/08/2007) for the six lane Marylebone Road in central London was used to determine an hourly flow of traffic of approximately 4000 vehicles hr^{-1}. As this

figure represents a wider street with six lanes of traffic it was reduced by a third to 2500 vehicles hr^{-1} to represent a total of four lanes of traffic. Vehicles moving at speeds of 30 and 10 mph were included in the calculation of emission factors in this heavy traffic case (Appendix D).

Changing the nature of NO_X emissions

The fraction of NO_X emitted as primary NO_2 (f-NO_2) can be considerably greater than the 5 % often commonly assumed with values ranging between 20 and 70 % for Euro III diesel cars (AQEG, 2007). A value of f-NO_2 equal to 0.3 is now evident in a number of locations (Jenkin *et al.*, 2008a). To study the effect of changing the proportion of NO_X emitted as NO_2 on atmospheric composition, f-NO_2 was varied between 0 and 0.3 (Appendix D).

The emission of HONO as a fraction of total NO_X (f-HONO) was also considered as an emission scenario to be applied to the photochemical box model. Small fractions of NO_X emitted as HONO have been observed and range from 0.005 to 0.01 (Gutzwiller *et al.*, 2002, AQEG, 2007, Jenkin *et al.*, 2008a). An increasing proportion of HONO is thought to be emitted into the urban environment by traffic with f-HONO increasing in line with the fraction of NO_X emitted as primary NO_2 (Jenkin *et al.*, 2008a). Although present as a small fraction of emitted NO_X such emissions of HONO can have a considerable effect on atmospheric composition particularly during pollution episodes (Jenkin *et al.*, 2008a). Within this study, f-HONO was varied between 0 and 0.05 to account for recent increases in the percentage of NO_X emitted as NO_2 and the likely associated increase in f-HONO.

VOC to NO_X ratios

To investigate the effect of varying emissions on canyon atmospheric composition the VOC to NO_X ratio was varied between 0.4 and 1.58 by either doubling NO_X or VOC emissions separately or by halving the amount of NO_X or VOC emitted. This

will allow the effect of varying to VOC to NO_X emission ratio to be explored, providing some insight into O_3 control regimes as discussed in Chapter 1 (§1·6·2).

Table 3·9 - *Emission scenarios that include variations in vehicle speed and traffic, the proportion of NO_X emitted as NO_2 or HONO and the ratio of VOC to NO_X emissions.*

Vehicle speed and traffic	**Base**	**A**	**B**	**C**	**D**	**E**	**F**
Vehicles hr^{-1}	1500	1500	1500	150	150	2500	2500
Speed (mph)	30	10	60	30	10	30	10
Primary NO_2 emissions	**Base**	**G**	**H**	**I**			
f-NO	0.9	0.7	0.8	1.0			
f-NO_2	0.1	0.3	0.2	0.0			
NO_2 emitted as HONO	**Base**	**J**	**K**	**L**	**M**		
f-NO	0.90	0.80	0.80	0.90	0.90		
f-NO_2	0.10	0.19	0.15	0.09	0.05		
f-HONO	0.00	0.01	0.05	0.01	0.05		
VOC to NO_X ratios	**Base**	**N**	**O**	**P**	**Q**		
VOC / NO_X	1	1	2	0.5	1		
VOC ×	1	2	1	1	0.5		
NO_X ×	0.79	0.40	1.58	0.40	1.58		

Future projections in vehicle fleet composition

As well as the vehicle fleet projections for 2010 included in the base case scenario, future projections of fleet composition for 2015 (case R) and 2025 (case S) have also been used to calculate vehicle speed emission factors (Boulter *et al.*, 2009).

Changes in urban background conditions

In addition to the base case scenario where urban background conditions were obtained using TORCH campaign data during the non-heatwave period, a scenario was also developed that included the more polluted conditions experienced during the heatwave period of the campaign between 6-10 August (§3·4·2) during which O_3, CO, NO_2 and VOC levels had increased. The total OH reactivity observed during the

heatwave period had increased to 6.612 s^{-1} (Lee *et al.*, 2006). Using the mixing ratios of chemical species measured during the heatwave period of the campaign (Lee *et al.*, 2006) once again an equal scaling factor was applied to the mixing ratio of each of the 8 VOCs to be included in the RCS in order to maintain the observed total reactivity of 6.612 s^{-1} whilst maintaining the (relative) measured ratios of each VOC. The monoterpenes α and β-pinene were included at levels (following scaling) of 10 ppt, represented as isoprene in the RCS, increasing the reactivity slightly to 6.628 s^{-1} (Table 3·10).

Table 3·10 - *Mixing ratios (ppb) of chemical species included in the RCS observed during non heatwave conditions, polluted conditions and less polluted conditions of the 2003 TORCH measurement campaign.*

Mixing ratios of RCS chemical species [ppb]	Base case — Non-heatwave conditions	Polluted heatwave conditions	Less polluted conditions
CH_4	1800	1800	1800
O_3	40	80	20
CO	200	300	200
NO	2	2	1
NO_2	8	12	7
HNO_3	2	2	2
C_2H_4	0.91	1.54	0.91
C_3H_6	0.29	0.42	0.29
HCHO	3.14	5.93	3.14
CH_3CHO	2.98	5.46	2.98
C_5H_8	0.28	0.70	0.28
CH_3OH	7.38	9.17	7.38
C_2H_5OH	2.37	5.13	2.37
PAN	0.46	1.16	0.46
Total OH reactivity	3.413	6.628	3.413

The background concentration of species during the less polluted conditions that occurred during the campaign between 1-3 August and 21-24 August when the air mass was Atlantic in its origin were determined utilising TORCH data once again. Total OH reactivity was not measured during this period therefore was kept the same as during the non-heatwave conditions. O_3, NO and NO_2 were compared to the

base case scenario. CH_4 and HNO_3 were held constant for all three scenarios. By scaling the VOCs using this methodology, the relative ratios of VOC abundances measured during the TORCH campaign under non-heatwave and heatwave conditions is maintained to within 14 %. The emission scenarios discussed above will be investigated using box model B and the combined LES-RCS model, the results of which are discussed in Chapter 6.

4: The LES-RCS model

4·1 Background

Following the development of the RCS using a photochemical box model of atmospheric chemistry, the chemical scheme was then implemented into a dynamical model known as a **Large Eddy Simulation (LES) model** introduced in section 2·2·5. This chapter provides further detail on the LES model used to simulate the fluid dynamics and turbulent flow within and above an **idealised street canyon**, and the implementation of the RCS into the LES. The configuration of the combined model, model simulation and finally model validation are also discussed.

4·2 Introduction to the Large Eddy Simulation (LES) model

The LES model used in this study is based on the **Regional Atmospheric Modelling System (RAMS)**, detailed in Cui *et al.* (2004) and discussed in section 2·2·6. The LES model resolves larger scale eddies that contain a large proportion of turbulent kinetic energy (TKE) and are the principal mechanism accountable for turbulent transport. The non-hydrostatic Reynolds-averaged primitive equations are the governing equations included in the RAMS used in this study and include those that apply to the conservation of mass, momentum, heat and scalars including pollutants.

4·2·1 LES model domain

Figure 4·1 illustrates the street canyon domain included in the LES model whilst Table 4·1 summarises the parameters included in all of the model simulations. An idealised street canyon with an aspect (*H*/*W*) ratio of 1 is used in the LES model

simulations where the height (H) of the canyon is equal to 18 m with the width of the street separating two buildings (W) also equal to 18 m. The mesh resolution in the x and y directions were set to equal Δx = 0.3 m and Δy = 1.0 m respectively.

The total width of the model domain in the x direction was equal to 24 m (including buildings of 3 m in width on either side of the street) with the length of the canyon in the y direction equal to 40 m. In the z direction, Δz = 0.3 m within the canyon which was gradually stretched by a factor of 1.15 above roof level (z = 18.0 m) to a maximum of 5.0 m at the top of the domain (z = 94 m). There were 288,000 grid points in total included in the model domain where N_x = 80, N_y = 40 and N_z = 90. The within canyon sub-domain was represented by 144,000 grid points where N_x = 60, N_y = 40 and N_z = 60.

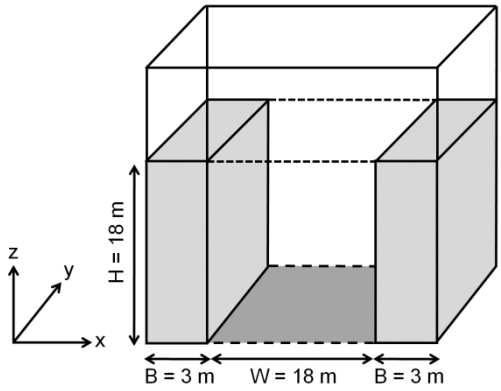

Figure 4·1 - *A schematic illustration of the LES model domain where x = 24 m, y = 40 m and z = 94 m with canyon dimensions of W = 18 m, H = 18 m and B = 3 m.*

4·2·2 Sub-grid scale parameterisation

Small, sub-grid scale (SGS) eddies that cannot be resolved explicitly by the RAMS model are parameterised using a first order closure model known as the Smagorinsky eddy viscosity model, where:

$$\tau_{ij} - \frac{1}{3}\delta_{ij}\tau_{kk} = 2\nu_s \bar{S}_{ij} \; ; \qquad (4\cdot1)$$

$$\bar{S}_{ij} = \frac{1}{2}\left(\bar{u}_{i,j} + \bar{u}_{j,i}\right); \tag{4·2}$$

$$\nu_s = l^2\sqrt{2\bar{S}_{ij}\bar{S}_{ij}}\,. \tag{4·3}$$

The indices i or j refer to the coordinates $i, j, k = x, y, z$ respectively; τ_{ij} denotes the SGS stress tensor; ν_s is the SGS eddy viscosity; δ_{ij} is the Kronecker symbol; $\bar{S}_{ij}$ is the rate of SGS deformation and l is the turbulent characteristic length scale defined as:

$$C_S = l/\left(\Delta x\Delta y\Delta z\right)^{\frac{1}{3}}, \tag{4·4}$$

where C_S is known as the Smagorinsky constant. For a scalar ϕ, its kinematic SGS flux $h_i^{(\phi)}$ is parameterised as:

$$h_i^{(\phi)} = -D_S\frac{\partial\phi}{\partial x_i}, \tag{4·5}$$

where D_S is the SGS eddy diffusivity and can be any chemical component. In this study $D_S = 3.0\ \nu_s$ is adopted.

Table 4·1 -*Experimental parameters used in LES model simulations.*

Parameter	L_x [m]	L_y [m]	L_z [m]	N_x	N_y	N_z	Δ_x [m]	Δ_y [m]	Δ_z* [m]
LES value	24	40	94	80	40	90	0.3	1.0	0.3*
Parameter	B [m]	W [m]	H [m]	Re	C_s (z/H < 0.9)	C_s (z/H > 1.1)	U_{max} [m s^{-1}]	T_{canyon} [K]	
LES value	6	18	18	10^6	0.08	0.1	2.5	293	

For the street canyon domain used in this study, the Reynolds number of the flow defined as $Re = U_{max}H/\nu$ is approximately 10^6, where U_{max} represents the free stream velocity at the top of the domain and ν represents the dynamic molecular viscosity. The Smagorinsky constant, C_s defined in Equation 4·4 above is consistent with the previous LES simulations of street canyon dynamics of Cui *et al.* (2004) and Cai *et al.* (2008) and taken to equal 0.08 where $z/H < 0.9$ and 0.1 where $z/H > 1.1$, with a linear

* Δ_z = 0.3 within canyon increasing by a factor of 1.15 from grid point 63 to a maximum of 5 m.

interpolation between these values applied where 0.9 < *z*/*H* < 1.1. Both previous LES studies were evaluated using wind tunnel data.

4·2·3 Flow characteristics on the street canyon scale

As previously discussed in section 2·2·1, the characteristics of the canyon dynamics are dependent on both wind direction and canyon geometry. When the direction of the prevailing wind is perpendicular to the canyon and the street canyon aspect ratio is approximately one (*H*/*W* = 1), skimming flow is observed (§2·2·1). This flow regime results in the formation of a large primary canyon vortex (Figure 4·2) that re-circulates the air and effectively decouples the canyons' atmosphere from the background air above resulting in reduced exchange, and poor ventilation. As a result, skimming flow is relatively ineffective in removing pollutants from within the street (Hunter *et al.*, 1992).

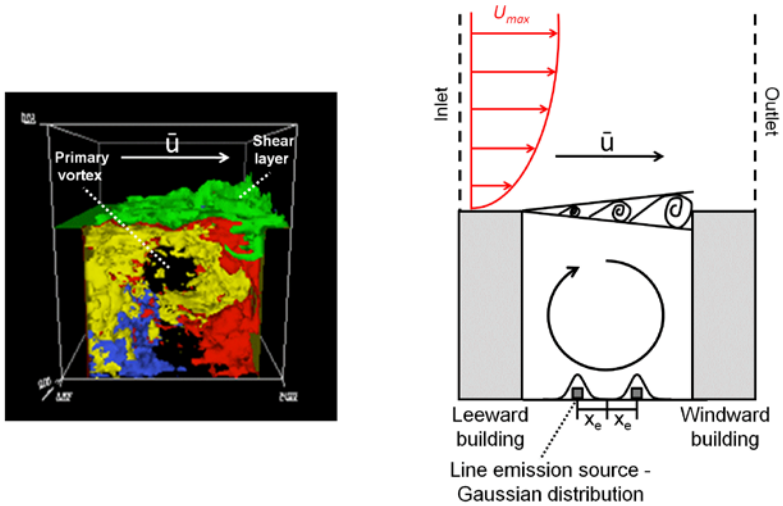

Figure 4·2 - *A 3-D and schematic illustration of the flow characteristics and emission sources within and above the idealised street canyon used in this study with an aspect (H/W) ratio of one.*

Strong intermittency in the street canyon re-circulation was observed using roof level measurements by Louka *et al.* (2000) who concluded that the mean flow within the canyon was merely a residual of an unsteady turbulent re-circulation. It was

proposed that the strong intermittency observed in the recirculation may be due to the intermittent nature of the mechanism that couples the flow within the canyon with that above *i.e.* the shear layer at roof level (Figure 4·2). This provides an effective ventilation mechanism allowing air to escape and efficient mixing to occur when the shear layer moves to an upward position. Such events, sweep and ejection events (§2·2·2), are major turbulent processes that govern pollutant removal from street level to the background atmosphere above (Cheng and Liu, 2011).

4·2·4 Mean flow fields and boundary conditions

Mean flow fields

The prevailing wind direction included in the LES model remains constant and perpendicular to the canyon axis (*i.e.* in the x direction), which is representative of a worst case scenario from the perspective of pollutant accumulation, in which canyon ventilation is limited. The wind speed is initially set to zero within the canyon and increases logarithmically above roof level to a maximum speed, U_{max}, of 2.5 m s^{-1} at the top of the domain at 94 m ($z/H \approx 5.2$). The variation in mean wind speed, $\bar{u}$ with height under the neutral conditions represented in this study (when wind shear has the predominant effect on turbulence when compared to buoyancy) can be expressed using the logarithmic relationship:

$$\bar{u}(z) = \frac{u_*}{k} \ln\left[\frac{(z-d)}{z_0}\right], \tag{4·6}$$

where u_* is the friction velocity (0.23 m s^{-1} where z = 94 m), k is von Karman's constant (0.41), z_0 is the surface roughness length (z_0 = 0.9 m where $z > 3H$), and d is the zero-plane displacement height (15 m). The values of z_0 and d applied to the LES-RCS model are representative of those of tall and high density residential areas (Table 1·2) (Grimmond and Oke, 1999).

The initial wind profile includes zero values within the canyon with the logarithmic wind profile (4·6) above roof level height (Figure 4·3). The initial wind profile of horizontal velocity applied above the canyon to the model simulations, $\bar{u}$ is shown in Figure 4·3.

Boundary conditions

The lateral boundary conditions were specified as cyclic for the velocity components u, v and w *i.e.* in the x, y and z direction. This condition implies that there are an infinite number of canyons included in the model domain in the x direction and that the canyon is infinitely long in the y direction. At the top of the domain (where $z/H \approx 5.2$) the upper boundary condition was determined by defining the normal velocity component as zero which meant that there was no flow of air out of the upper limit of the domain. As cyclic lateral boundary conditions are specified, the details of the initial wind profile become unimportant once dynamical equilibrium is established.

As discussed in section 2·2·5 this represents an idealised case with a more realistic representation of the incoming canyon flow likely to be achieved using field or numerical model (*e.g.* the Met Office Unified Model) input to account for the heterogeneous nature of the urban canopy and variability in the prevailing meteorological conditions over time.

Potential temperature is defined as 293 K for the entire model domain, representative of neutral conditions with no thermal effects on flow fields.

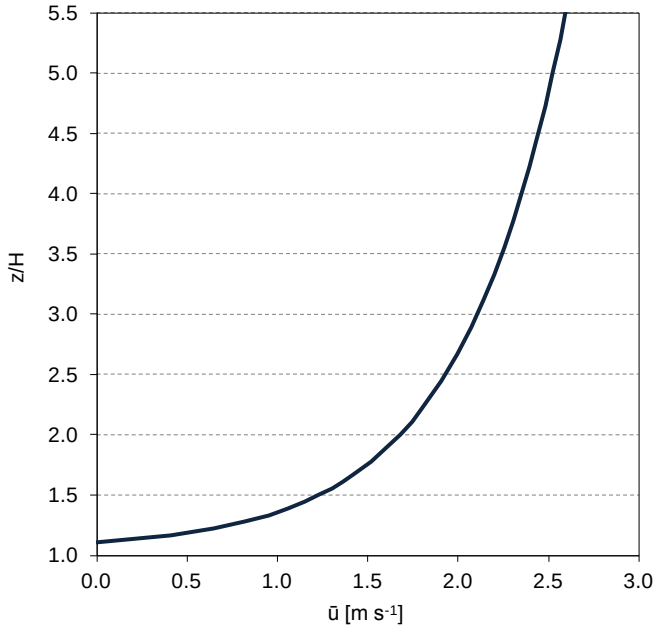

Figure 4·3 - *Initial wind profile of horizontal velocity [m s^{-1}] above the street canyon.*

Figure 4·4a illustrates the mean, spatially (in the *y* direction) and temporally averaged, wind vectors (*u, w*) observed within and above the canyon, indicating the presence of a primary vortex that spans the width of the canyon and the free flowing background atmosphere above. The presence of a small secondary eddy is also evident near street level toward the lower windward wall. The increase in horizontal velocity above the canyon is seen in Figure 4·4b as well as a point of inflection present at roof level due to the presence of the shear layer also observed at this height.

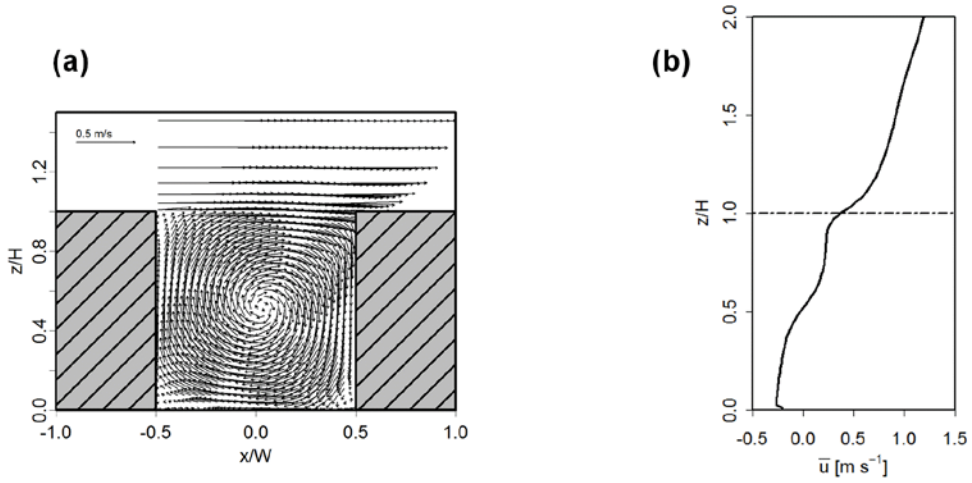

Figure 4·4 - *Temporally and spatially (along the y axis) averaged (a) wind vectors (u, w) and (b) vertical profile of horizontal velocity ($\overline{u}$) [m s^{-1}] at x/W = 0 where positive values represent movement from left to right. Averages are taken over the last hour of the model simulation (150 ≤ t ≤ 210 min).*

Horizontal and vertical velocity flow fields are illustrated in Figure 4·5. Air flows from left to right above the canyon with an increase in wind speed with height. Within the canyon, horizontal velocity exhibits a significant decrease, becoming negative toward street level indicating the flow of air toward the leeward wall. In contrast, within the upper portion of the canyon air flows in the opposite direction as a result of the primary canyon vortex, albeit at a similar speed to that near the surface below.

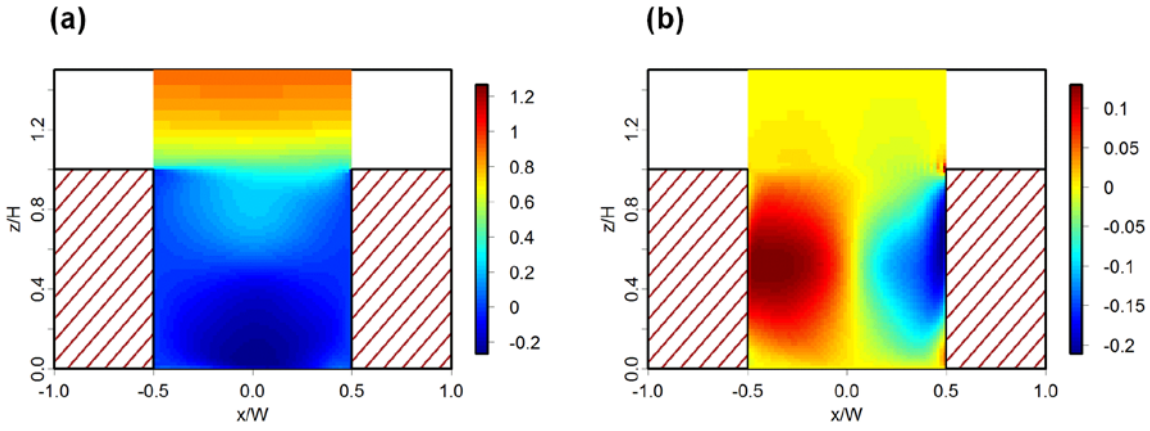

Figure 4·5 - *Temporally and spatially (along the y axis) averaged (a) horizontal velocity [m s^{-1}] where positive values represent movement to the right and (b) vertical velocity [m s^{-1}] where positive values represent movement upwards.*

On the approach to the free flowing background atmosphere above the canyon vertical velocity is close to zero. Maxima in mean vertical velocity are observed at mid level within the canyon toward the windward and leeward walls. On average an updraught is observed toward the leeward wall and a downdraught toward street level near the windward wall, again the result of the primary vortex within the canyon. The maximum strength of the downdraught is 0.15 m s^{-1} stronger than that of the updraught which reaches a maximum speed of 0.23 m s^{-1}.

4·3 The LES-RCS model

4·3·1 Introduction

As discussed in Chapter 2 the LES model described above has been previously used to investigate the dispersion and three-reaction NO_X-O_3 photochemical steady state (Baker *et al.*, 2004, Grawe *et al.*, 2007) and subsequently to study the effects of shading on pollutant concentrations (Grawe *et al.*, 2007). This section of work details the implementation of the RCS into the LES model, the development of which is detailed in Chapter 3. Apart from the application of the RCS and the introduction of vehicle emissions, the configuration of the combined model remains identical to that of the LES model described above (§4·3·4).

4·3·2 Code implementation

Prior to the addition of a chemical scheme within the LES, 52 tracers were added to the model for each of the 51 chemical species included within the RCS as well as a non-reactive passive scalar for which the continuity equation and the advection-diffusion equation are solved at each time step. The definition of these tracers and

their model initialisation is included within the subroutines `ZEROTRC` and `TRCINIT` of Appendix G.

In order to implement the RCS into the LES model, a chemical subroutine was written using FORTRAN code (and extract of which is included in Appendix E and in full within digital Appendix G). Firstly, each of the 51 chemical species to be included were declared as real variables within the program. The rate constants for each of the 136 chemical reactions included in the RCS were then expressed in terms of mixing ratios in ppb as opposed to concentrations (molecules cm^{-3}) simulated using the photochemical box model discussed in section 3·3. For the second order rate constant for the bimolecular reaction: $NO + O_3 \longrightarrow NO_2$ for example, where $k_{NO+O_3} = 1.60 \times 10^{-14}$ cm^3 $molecules^{-1}$ s^{-1}, k_{NO+O_3} was expressed as 4.01×10^{-4} ppb s^{-1} for the given temperature and pressure (T = 293 K and p = 1013.25 hPa).

The rates of each of the 136 reactions included in the RCS were calculated. As with the photochemical box model run using FACSIMILE, the rate of change of chemical species included in the chemical subroutine is given by:

$$\frac{d[c_i]}{dt} = P_i - L_i = S_i \,, \qquad (4{\cdot}7)$$

$$i = 1, 2, \ldots, N$$

where, P_i is the production term in which species i is a product, L_i is the loss term in which i is the reactant and S_i is the total photochemical source or loss term for species, i. Subsequently for each of the 51 chemical species included, the reactions that contribute to its production or loss were determined. The concentration of chemical species within the FORTRAN box model after each time step expressed as:

$$c_{i,t+\Delta t} = c_{i,t} + \left(P_{i,t+\Delta t} - L_{i,t+\Delta t}\right)\Delta t \,. \qquad (4{\cdot}8)$$

For the reactions involving intermediate- and longer lived chemical species included in the chemical mechanism, for example, NO, NO_2, O_3 and CO (Appendix E and

Appendix G) a time step of 0.01 s (DTLONG) was used in the numerical integration to determine the change in concentration of such species. To calculate the change in shorter lived species such as OH, HO_2 and RO_2 that are involved in faster chemical reactions, the time step for integration (DTSHORT) was reduced by an order of magnitude to 0.001 s. These time step values were empirically chosen (for fast and slow reactions respectively) to balance the requirement for stable output / convergence against integration time and thus ensure numerical stability.

The total concentration of all peroxy radicals included in the chemical mechanism (Appendix E) was also calculated after each time step in order to determine rate constants included in the RO_2 permutation reactions.

A zero-dimensional photochemical box model, equivalent to that implemented using FACSIMILE that includes the chemical reactions outlined above was written using FORTRAN code and run for a 30 minute period with chemistry alone, with fixed photolysis rates and without emissions, external mixing or deposition. At t = 30 minutes, a set of concentrations of all 51 chemical species, parent compounds and intermediate species were derived from the box model. The box model was compiled prior to being run with each simulation completed in the order of one to two minutes to determine the change in concentration of chemical species over a four hour period.

The Leapfrog integration method was the numerical scheme used for time advancement within the LES-RCS model. This method is advantageous over other alternatives as it is second order accurate and relatively simple to apply.

At this time the concentrations of all species included in the RCS that were derived using the box model at t = 30 minutes were inserted in the whole model domain. This set of values is also used as the inlet boundary conditions above the upwind

building. At the outlet boundary, the advective condition, $\frac{\partial c_i}{\partial t} + u\frac{\partial c_i}{\partial x} = 0$, is applied to all chemical species for the duration of the simulation.

4·3·3 Emissions

Emissions within the canyon are represented by two line sources centred at 2.5 m to the left and right of the canyon centre, signifying two lanes of traffic. Each of the line sources is considered to have a Gaussian distribution (where σ_x = 3 m and σ_y = 1 m), to be continuous in nature and is located at 1.0 m above the road as illustrated in Figure 4.2 above. As discussed in section 3·9·1, the emission rates to be included in the model were determined using the UK Road Vehicle Emission Factors, 2009 (Boulter *et al.*, 2009) and for the base case scenario, vehicle emissions are representative of moderate weekday traffic (1500 vehicles per hour) for an urban road with cars travelling at an average speed of 30 mph. The total emissions for NO, NO_2, CO, ethene (C_2H_4), propene (C_3H_6), formaldehyde (HCHO) and acetaldehyde (CH_3CHO) are equal to 900, 100, 3593, 347, 150, 96 and 98 ppb s^{-1} respectively emitted into one LES model cell (0.3 m × 1 m × 0.3 m). These emissions equate to total emissions of 101, 17, 377, 36, 24, 11 and 16 µg m^{-1} s^{-1} which are added to the LES at t = 30 minutes.

4·3·4 Running the LES-RCS model

The initial stage in the LES-RCS model simulation process was to specify the initial conditions and vehicle emissions to be applied to the LES-RCS model and included in the initial canyon chemistry input file. This initial input file was then compiled using a UNIX based platform in order to generate an executable file to be used to initiate the model simulation, with the compilation completed in approximately 10 seconds. The start and end time of the input RAMS file to be used in the LES

simulation was then specified *e.g.* beginning at t = 30 minutes and ending at t = 45 minutes for the initial 15 minute period of the model run. Once compiled the model was tested by running the executable file on a local node in order to assess any errors that may have arisen during the compilation process. Once the code was deemed to be running successfully a job was submitted to the University of Birmingham's BlueBEAR High Performance Computing (HPC) service (`http://www.bear.bham.ac.uk`). The model computations were carried out on nodes that had 64 bit and 2.6 GHz processors with either 8 or 16 GB of memory available. Using BlueBEAR, model simulations would take typically 4 - 5 days in terms of real time to compute 15 minutes of the run with a full, 3 hour combined chemistry and dynamics simulation completed in 6 - 8 weeks with each output data file representing a 3 minute interval and 1841 MB in size.

4·4 Model validation

The dynamical component of the LES model used in this study has been validated in Cui *et al*. (2004) using wind tunnel measurements of Brown *et al*. (2000) that demonstrated that both the mean flow fields and the RS-TKE simulated were in good agreement with the observations obtained, carried out for an idealised street canyon where H/W = 1. Reasonable agreement between LES model and wind tunnel data was found for skewness and kurtosis and a number of the flow characteristics evident in the wind-tunnel experiments were found to be replicated using the results of the LES model simulation. The LES model has also been further validated by (Cai *et al.*, 2008) through comparison of results to wind tunnel experiments in which the capability of the LES in simulating the spatial variation of mean concentrations in 2D (with line sources of emissions applied) was demonstrated.

Prior to the implementation of the RCS into the LES model, the accuracy of the chemical scheme coded in FORTRAN included in the photochemical box model was evaluated against the results obtained using the equivalent chemistry case simulated using FACSIMILE. Figure 4.6 illustrates the change in the mixing ratio of OH over a 240 minute (4 hour) period simulated with the RCS applied to the photochemical box model integrated using FASIMILE and once coded using FORTRAN run on a UNIX platform.

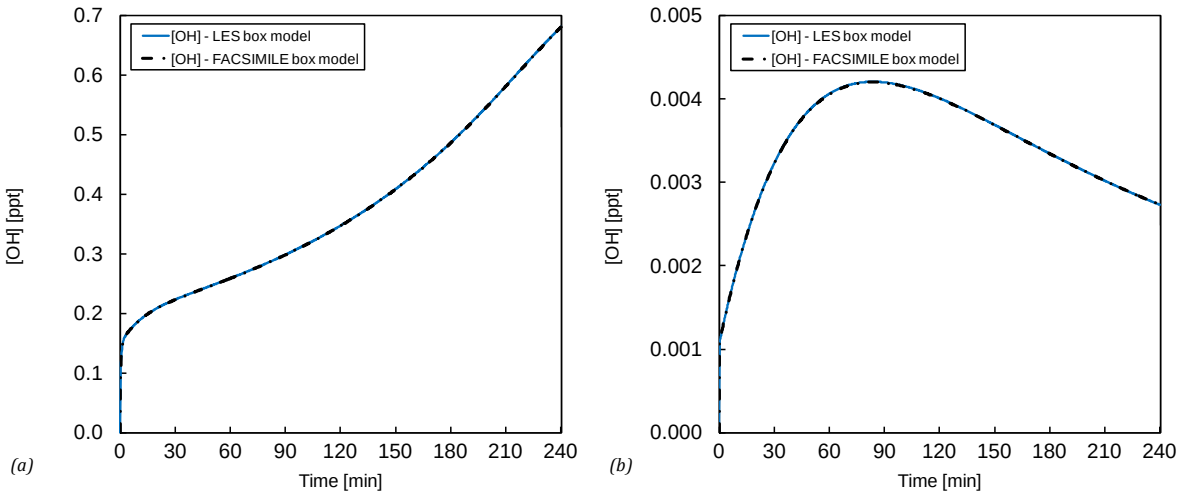

Figure 4·6 - *Temporal changes in the mixing ratio of OH (ppt) simulated by the box model run using FACSIMILE compared to that coded using FORTRAN 77 and run in UNIX under (a) background conditions (NO = 2 ppb; NO_2 = 8 ppb) and (b) high NO_X conditions (NO = 1000 ppb; NO_2 = 120 ppb) over a four hour period with the RCS mechanism applied.*

Figure 4·6 illustrates that the change in the mixing ratio of OH simulated by the box model run using both methods is near identical; a maximum difference of 0.09 % under background conditions and 0.17 % under high NO_X conditions thus providing suitable validation of the chemical scheme once coded using FORTRAN and the differential time step approach. As discussed in section 3·7 of this thesis, the RCS was evaluated against the near explicit MCM under a range of NO_X conditions thus providing confidence in the representation of chemical processes included in the LES-RCS.

Following the development of the LES-RCS model, the combined effects of emission, mixing and chemical processing on atmospheric composition could be simulated by the enhanced model, the results of which are presented in the subsequent chapters of this thesis.

5: Coupling dynamics, chemistry and atmospheric pre-processing

5·1 Introduction

In this chapter, the combined **LES-RCS** model (the development of which was outlined in the preceding chapters) will be used to investigate the combined effects of mixing and chemical processing upon air quality within an idealised street canyon. The results of LES and box model simulations will be used to examine urban atmospheric composition. A comparison of **oxidant levels** and the abundance of key reactive intermediates OH and HO_2 within the canyon calculated using the LES model, *i.e.* integrating both dynamics and chemistry, is made with those determined using a zero-dimensional box model (§3·3) providing further insight into the interaction of canyon dynamics and mixing on chemical processes and composition. The results will also be used to investigate the extent of **within-canyon processing** of exhaust emissions before their escape to the wider atmosphere. Subsequently, a representative **flux of pollutants** out of the urban canopy into the overlying boundary layer will be determined.

5·2 Analysis

Using the LES, 3-D composition model output was obtained from time-points 30 to 210 minutes at 5 s time intervals. The LES results were averaged along the *y*-axis over the length of the canyon (L_y - along which the resolved-scale turbulence is homogeneous), across the width of the canyon (the *x*-axis; *W*) and over the height of the canyon (the *z*-axis; *H*) to give a volume averaged (0-D) within-canyon concentration as a function of time, *i.e.*:

$$\overline{c_i}(t) = \frac{1}{W \cdot H \cdot L_y} \int_{-0.5W}^{0.5W} \int_{0}^{H} \int_{0}^{L_y} c_i(x, y, z, t)\, dx\, dy\, dz \quad , \tag{5·1}$$

As one aim of this work is to compare canyon-average concentrations predicted by the full RCS-LES model using Equation 5·1, with their equivalents determined using a zero-dimensional box model, under identical chemical and emission conditions, treatment for the exchange between the street canyon and the overlying boundary layer was required (§3·8). In the case of the LES-RCS model, the modelled domain (Figure 4·2) includes both within-canyon and above-canyon regions, and so implicitly incorporates exchange between the canyon and the overlying boundary layer. For the box model scenario, mixing with an overlying boundary layer was achieved by implementing a suitable **exchange velocity** (ω_t) within the model, defined as:

$$\omega_t = \frac{F_c}{\overline{c} - \overline{c}_B}, \tag{5·2}$$

where F_c is the pollutant flux at roof level (z/H = 1) and the denominator is the difference between the mean concentration within the canyon ($\overline{c}$) and the mean background concentration above the canyon ($\overline{c}_B$).

The value of ω_t was determined using LES simulations of a passive scalar (a non-reactive emitted species which is conserved within the model, and whose concentrations are therefore determined by dynamics alone) to evaluate the mean rate of exchange between the canyon and boundary layer above. A mean value of ω_t = 0.021 m s^{-1} was determined, averaged over the final hour of the simulation (150 ≤ t ≤ 210 min). Use of a single mean value removes the variability in the LES simulations (arising from periodic sweep / ejection events) that are evident in the comparisons of mean concentrations discussed below.

Volume averaged within canyon concentrations were then averaged over the final hour of the simulation (150 ≤ t ≤ 210 min, *i.e.* after 30 minutes of dynamical and 120 minutes of chemical spin up) to give a time and volume averaged (0-D) within canyon concentration *i.e.*:

$$\langle \phi \rangle = \frac{1}{W \cdot H \cdot L_y \cdot (t_2 - t_1)} \int_{t_1}^{t_2} \int_{-0.5W}^{0.5W} \int_{0}^{H} \int_{0}^{L_y} \phi(x, y, z, t) dx dy dz dt \quad . \tag{5·3}$$

where φ can be w or c_i. Over the same period, the concentration of the passive scalar (calculated using ω_t = 0.021 m s^{-1}) simulated by the box model was found to be within ± 0.04 % of its final concentration at 210 minutes *i.e.* to ensure this value is sufficiently close to final values.

The LES results were then averaged along the length of the canyon in the y axis (L_y) and over the final 60 minutes of the averaging period to give 2-D time averaged concentrations (150 ≤ t ≤ 210 min) *i.e.*:

$$\langle \varphi \rangle (x, z) = \frac{1}{L_y \cdot (t_2 - t_1)} \int_{t_1}^{t_2} \int_{0}^{L_y} \varphi(x, y, z, t) dy dt \quad , \tag{5·4}$$

where φ can be w or c_i. Following Equation 5·4, $\tilde{\varphi} = \varphi - \langle \varphi \rangle$ represents the resolved fluctuations of φ about $\langle \varphi \rangle$. Thus the following quantities are defined: the resolved-scale vertical turbulent flux, $F_{turb} = \langle \tilde{w} \tilde{c}_i \rangle$, the vertical advective flux, $F_{adv} = \langle w \rangle \langle c_i \rangle$, and total resolved-scale vertical flux $F_{total} = F_{turb} + F_{adv}$. These are 2-D quantities showing the spatial pattern of these variables in the x and z domain. For the purpose of analysis, vertical mixing ratio profiles were extracted from the 2-D time averaged concentrations at five sites across the canyon. In addition, the horizontally-averaged vertical profile of the flux of any advected quantity inside and above the canyon is derived from the following equation:

$$F(z) = \frac{1}{W} \int_{-0.5W}^{0.5W} F(x, z) dx \quad . \tag{5·5}$$

5·3 Results

5·3·1 Spatial variation in key atmospheric species

Figure 5·1 illustrates the mean mixing ratios of the passive scalar (subject only to dispersion/mixing) and a number of chemical species averaged over the final 60 minutes of the 210 minute simulation (with logarithmic colour scales included for O_3, OH and HO_2). Major features are the concentration patterns associated with the primary vortex within the canyon and the shear layer at roof level. The shear layer increases in amplitude and becomes increasingly turbulent downwind, effectively trapping pollutants toward the leeward wall and allowing greater exchange toward the windward wall.

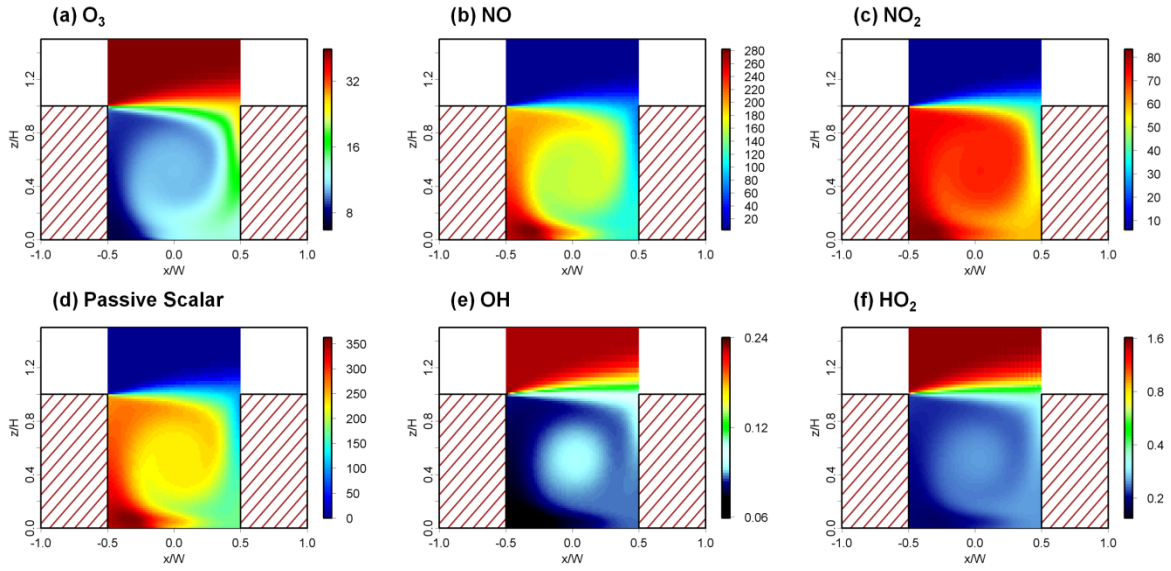

Figure 5·1 - *Mean (time averaged) mixing ratios (ppb) of (a) O_3, (b) NO, (c) NO_2, (d) passive scalar, (e) OH (ppt) and (f) HO_2 (ppt)*. Average taken over the last hour of the model simulation ($150 \leq t \leq 210$ min).*

As expected, increased levels of NO, NO_2 and the passive scalar are observed within the street canyon compared to the background atmosphere above roof level. The highest concentrations of these species are found at low level toward the leeward

* Logarithmic colour scales are plotted for O_3, OH and HO_2.

wall, a result of the dispersion and chemical processing of emissions as they are transported by the wind from their source located in the centre of the street. These findings are in agreement with those of Baker *et al*. (2004) and Kwak and Baik (2012).

For NO_2 increased levels observed toward the leeward wall at street level arise through secondary formation through reaction of NO with entrained O_3, *i.e.* through the oxidation of emitted NO, in addition to that emitted directly. HO_X levels are much lower within the canyon than in the background air, with a local maximum in the centre of the vortex, a semi-isolated region of entrained background air. Elevated OH within this region (relative to the periphery of the canyon) primarily reflects a reduced OH sink compared with the rest of the canyon, in particular with respect to reaction with NO (see below).

Figure 5·2 illustrates the (horizontally and temporally averaged) vertical profiles of O_3, NO, NO_2, OH and HO_2 using a logarithmic scale at five across-street locations within and just above the canyon ($z/H \leq 2$). The concentrations of O_3, OH and HO_2 increase near roof level on the approach to the less polluted background atmosphere above.

The smallest transition between within canyon and background concentrations of all chemical species occurs toward the windward wall due to the increase in exchange of air between the canyon and the background air above in this region associated with the turbulent nature of the shear layer at this point. Towards the leeward wall a sharp contrast exists between the canyon and the background atmosphere, demonstrated by a large change in concentration with height at roof level as pollutants become effectively trapped by the relatively impermeable shear layer that exists in this region.

Figure 5·2a illustrates a significant change in the concentration of NO and NO_2 across the canyon with the concentration of NO at street level toward the leeward wall more than double that observed on the windward side and with NO_2 over a third higher. In terms of O_3 the highest concentrations within the canyon are evident toward the windward wall, particularly toward roof level where ozone-rich air is brought into the canyon from aloft.

Toward the leeward wall of the canyon the mixing ratios of both NO and NO_2 show a significant decrease with height above roof level where levels rapidly approach those of the background atmosphere. Moving toward the windward wall again results in a much more gradual transition between within canyon and the background atmosphere as the influence of the shear layer spans a greater distance in this region causing the air well above the canyon to be mixed with that escaping from within.

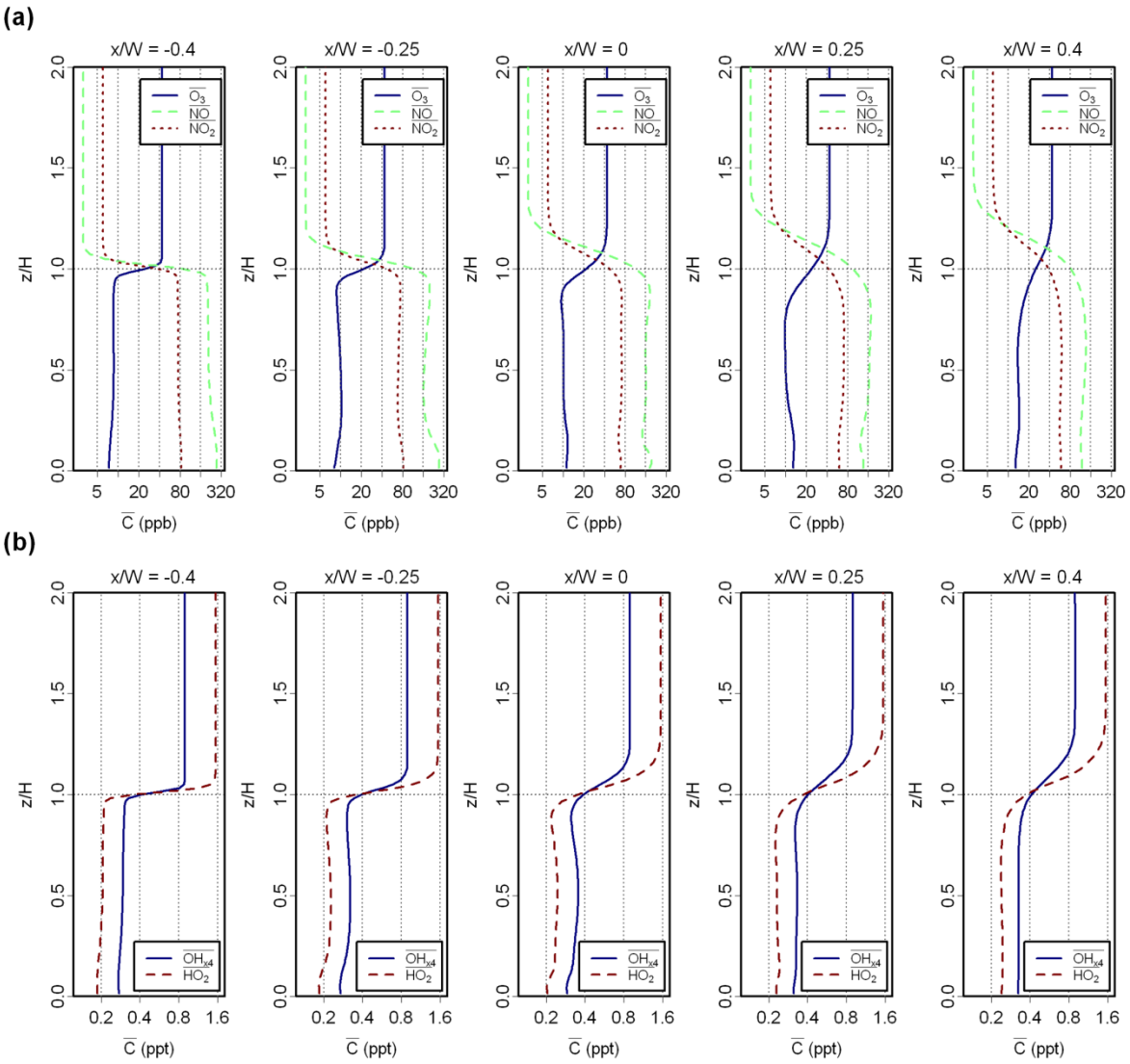

Figure 5·2 - *Variation in the mean and time averaged mixing ratios on a logarithmic scale of (a) O_3, NO, NO_2, and (b) OH_{x4} (4 × OH) and HO_2 with height within the canyon ($0.0 \leq z/H \leq 2.0$) at x/W= -0.4, 0.25, 0.0, 0.25, 0.4. Average taken over the last hour of the model simulation ($(150 \leq t \leq 210$ min).*

The change in mixing ratio of OH and HO_2 is illustrated in Figure 5·2b. Within the canyon the greatest concentrations of both OH and HO_2 are observed toward roof level at the windward wall where concentrations are slightly higher for OH and over a third greater for HO_2 when compared to those at street level toward the leeward wall. Within the centre of the street an increase in OH and HO_2 is also observed within the primary canyon vortex. As for NO, NO_2 and O_3, there is also a rapid transition in the concentration of HO_X radicals with height toward the leeward wall with a more gradual transition observed toward the windward wall. Close to roof

level ($z/H \approx 1.1$) toward the leeward wall of the canyon OH and HO_2 approach their background mixing ratios of 0.22 and 1.54 ppt respectively while these levels are only achieved at $z/H \approx 1.5$ on the windward side of the canyon.

The contrast between background and within canyon concentrations of NO_X, O_3 and HO_X is clear. Average within canyon levels of NO and NO_2 of 168 and 68 ppb respectively (Table 5·2) are considerably greater than the overlying urban boundary layer. A significant reduction in O_3 averaged within the canyon (where $O_3 \approx 11.2$ ppb) compared to that of the background atmosphere is also observed. In terms of HO_X, the reduction in OH and HO_2 within the canyon compared to the background atmosphere is ≈ 64 % and ≈ 85 % respectively. Short lived HO_X radicals are significantly depleted within the canyon due to the local chemical processes that are occurring.

Figure 5·3a illustrates the mixing ratio of the sum of organic peroxy radicals (*i.e.* RO_2, excluding HO_2) included in the RCS averaged over the last 60 minutes of the model simulation (logarithmic colour scale). The concentration of RO_2 exhibits a similar pattern to that of OH with a local minimum toward the lower leeward wall and maxima observed within the primary vortex, close to the mixing layer at roof level and toward the windward wall, and a swathe of elevated RO_2 accompanying the entrained air into the vortex on the windward side.

OH sources and sinks

To investigate the importance of OH sources and sinks within and above the canyon, the rate of production and loss of OH was studied using the rate constants and time averaged ($150 \leq t \leq 210$ min) concentration of reactants for each OH reaction taken at three locations as illustrated in Figure 5·3a: (V) within the vortex ($z/H = 0.5$, $x/W = 0$), (L) toward the leeward wall ($z/H \approx 0.08$, $x/W \approx -0.3$) and (B) in the background atmosphere above the canyon ($z/H \approx 1.2$, $x/W \approx -0.3$). The change in OH

with respect to time is governed by the rate of production and loss, as below (neglecting transport and turbulent dispersion at roof level):

$$\frac{\partial[OH]}{\partial t} = P_{OH} - k[OH][X] \,. \qquad (5{\cdot}6)$$

Where P_{OH} is the rate of production of OH, and $-k\,[OH]\,[X]$ represents the loss of OH through sinks such as the reaction of OH with a co-reactant, $[X]$ such as NO_2. The dominant OH chemical production and loss terms (rates, here expressed in ppt s^{-1} (see Table F1, Appendix F)) are given in Table 5·1. Primary OH production (O_3 photolysis) predictably falls with reduced O_3 abundance (NO titration) from the background into the canyon, but comprises a small fraction of the total production rate. NO-driven radical cycling dominates OH production, with modest (up to 22 %) contribution from HONO photolysis (under the non-shaded conditions simulated *i.e.* uniform illumination within the street canyon). The lifetime of HONO is comparable to the timescale of the vortex circulation and mixing (photolysis lifetime of 8 minutes), thus HONO must be explicitly considered in understanding OH abundance (cannot be assumed to be in steady state).

Going from the background to leeward (within-canyon) locations, the dominant OH sink increases from 2.8 s^{-1} to 96 s^{-1} (*i.e.* by over a factor of 30), while the dominant OH production rate, HO_2 + NO, increases from 1.1 to 11.7 ppt s^{-1} (total OH production increases by a factor of 8.8); accordingly within-canyon OH levels a much lower than in the overlying boundary layer. The local maximum in OH in the vortex centre arises from the semi-isolated nature of this part of the domain; at the centre, OH production rates are comparable with those at the leeward site (total production rate of 11.4 vs 13.5 ppt s^{-1}, dominated by HO_2 + NO), but the OH sink is much lower than directly downwind of the emission source — 61 vs 96 s^{-1} — and OH levels are correspondingly 31 % higher.

Table 5·1 - *The dominant OH production and loss rates calculated for the LES-RCS simulation. Average concentrations taken over the last hour of the model simulation (150 ≤ t ≤ 210 min) and at three locations (Figure 5·3): within the canyon vortex (V), toward the lower leeward wall (L) and in the background atmosphere (B).*

	A. Vortex (V)	**B. Lower leeward wall (L)**	**C. Background atmosphere (B)**
	Rate of production / loss (s^{-1})		
Production			
$HO_2 + NO \longrightarrow OH + NO_2$	100	174	4.8
$HONO + h\nu \longrightarrow OH + NO$	27	25	0.74
$O_3 + h\nu \longrightarrow OH + OH$	0.79	0.78	1.3
$O_3 + VOC^{\dagger} \longrightarrow OH + products$	0.35	0.57	0.0060
Loss			
$OH + VOC^{\ddagger} \longrightarrow products$	-61	-96	-2.8
$OH + NO \longrightarrow HONO$	-41	-71	-0.78
$OH + NO_2 \longrightarrow HNO_3$	-22	-26	-1.9
$OH + CO \longrightarrow HO_2$	-5.0	-7.4	-1.0

Figure 5·3b and c illustrates the spatial variation in NO_X and O_X (= O_3 + NO_2) within and above the canyon domain. Within the street canyon, gas phase chemistry is dominated by NO_X which to a first approximation is conserved. As such it is often useful to consider the temporal and spatial variation in NO_X levels. The chemical interaction of NO_X with O_3 plays a key role in determining NO_2 levels observed in the urban environment. As a result of this interaction, another useful measure to consider is defined as the total oxidant (O_X = O_3 + NO_2). Considering only NO-NO_2-O_3 reactions, O_X is conserved whilst partitioning between the component forms of O_3 and NO_2 is determined by the overall levels of NO_X, O_3 and solar radiation. The concentrations of NO_X and O_X are both greater within the canyon (236 and 79 ppb respectively) compared to the background atmosphere where NO_X = 9 ppb and O_X = 50 ppb. The spatial distribution of NO_X (Figure 5·3b) is similar to that of the passive

† C_2H_4; C_3H_6; C_5H_8.

‡ C_2H_4; C_3H_6; C_5H_8; HCHO; CH_3CHO; CH_3OH; C_2H_5OH; PAN.

scalar (Figure 5·1d) demonstrating the effective conservation of NO_X on the canyon residence timescale. The chemical lifetime of NO_X governed by the reaction of OH and NO_2 can be determined (using the mean concentration of OH within the canyon) by:

$$\tau_{NO_x} = \tau_{NO_2} = \frac{1}{k[OH]} , \qquad (5{\cdot}7)$$

to give τ_{NO_x} of 11.3 hours. When τ_{NO_x} is compared to a canyon residence time (calculated as z/ω_t = 18 m / 0.021 m s^{-1} = 857 s) of ~ 14 minutes the conservation of NO_X on such timescales is demonstrated.

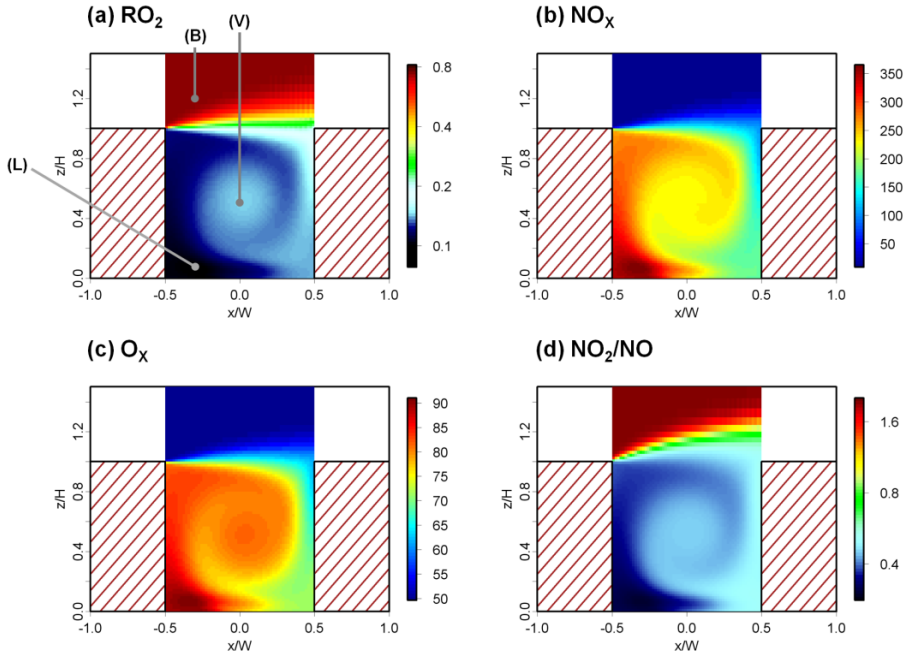

Figure 5·3 - *Mean and time averaged mixing ratios of (a) RO_2 (ppt), (b) NO_X (ppb), (c) O_X (ppb) and (d) NO_2/NO. Average taken over the last hour of the model simulation (150 ≤ t ≤ 210 min)* [§].

The change in mixing ratio of NO_X and O_X with height within the canyon (0.0 ≤ *z/H* ≤ 2.0) at five sites across the street is illustrated in Figure 5·4 using a logarithmic scale on the abscissa axis. The highest concentration of NO_X occurs at street level

[§] Logarithmic colour scales are included for RO_2 and NO_2/NO

toward the leeward wall downwind of the two line emission sources located in the centre of the street. Figures 5·3 and 5·4 also indicate that the lowest levels of O_X occur toward street level on the upper windward wall with the highest concentrations close to street level toward the leeward wall. Elevated O_X in this region results from the 5 % primary NO_2 emission within the NO_X source term. The lowest ratios of NO_2 to NO (Figure 5·3d where the colour scale for NO_2/NO is logarithmic) occur at street level downwind of the emission sources toward the leeward wall. The decrease in NO_2/NO reflects a larger increase in NO through primary emission when compared to NO_2.

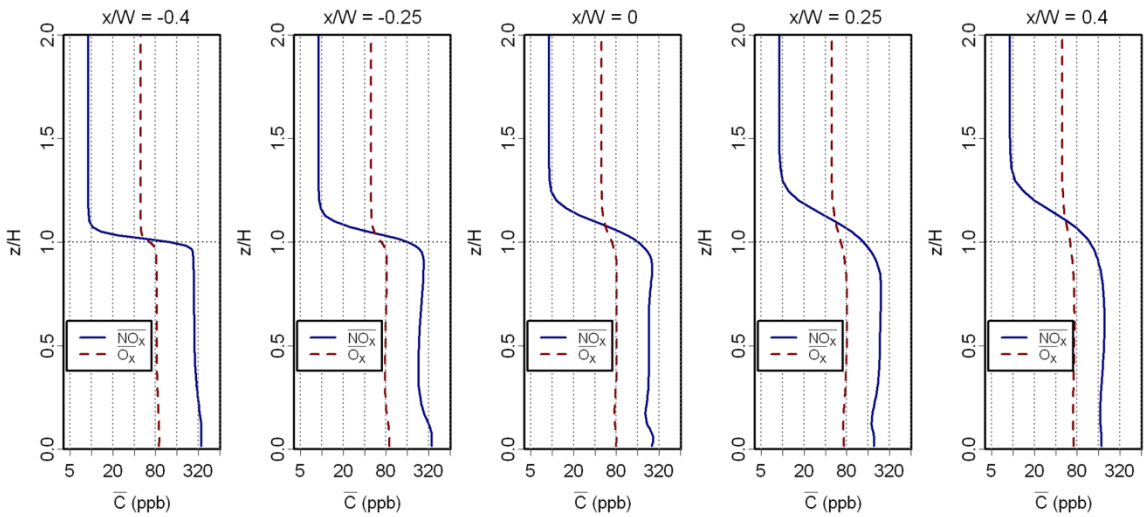

Figure 5·4 - *Time averaged vertical mixing ratio profiles on a logarithmic scale of NO_X and O_X at x/W= -0.4, -0.25, 0.0, 0.25, 0.4 within and above the canyon (0.0 ≤ z/H ≤ 2.0). Averages taken over the last hour of the model simulation (150 ≤ t ≤ 210 min).*

Table 5·2 illustrates that the ratio of NO_2 to NO is higher for the box model case indicating greater (mean) simulated conversion of NO to NO_2 when dynamical effects are neglected (*i.e.* assuming instant mixing). This arises as a number of cells within the LES model have very little or no O_3 present (Figure 5·1) hence NO-to-NO_2 conversion is precluded at many locations. Table 5·2 also shows that the time averaged mixing ratio of the passive scalar simulated by the box model is higher than that of the LES. As the passive scalar is unreactive, this small difference

(< 2.2 %) arises due to the reliance of the box model on the empirical value determined using Equation 5.2.

Table 5·2 - *Canyon and time averaged mixing ratios calculated using the LES and box model approaches. Averages taken over the last hour of the model simulation (150 ≤ t ≤ 210 min). ω_t = 0.021 m s^{-1} applied to the box model.*

	(a) LES	(b) Box	(b) - (a)	[(b) - (a)] / (a)
	Mixing ratio (ppb) [**]			%
O_3	11.2	10.5	-0.7	-5.9
NO	168	170	2	1.2
NO_2	68	74	6	9.5
OH	0.08	0.09	0.01	11.3
HO_2	0.23	0.25	0.02	8.1
NO_X	236	244	8	3.3
O_X	79	85	6	8.0
PS	233	238	5	2.2
NO_2/NO	0.40	0.44		

5·3·2 Atmospheric composition and exchange rate effects

The change in the canyon averaged concentration of the passive scalar over time is compared between the LES and box model results (Figure 5·5). Fluctuations in the concentration of the (spatially) averaged passive scalar inherent in the LES results are caused by large scale variations of the flow and the variable nature of canyon ventilation caused by the unsteady fluctuations in the shear layer at roof level, as observed by Louka *et al.* (2000) and replicated by the model.

The optimum value of exchange velocity, ω_t, to be applied to the box model simulations can be determined by minimising the difference between the passive scalar results for the LES and box model. As shown in Figure 5·5, for the final 60 minute averaging period a value of ω_t = 0.021 m s^{-1} applied to the box model best

[**] Mixing ratios of OH and HO_2 given in ppt

represents the mean LES value and is therefore a suitable value to allow comparison with canyon averaged LES results of other chemical species.

The sensitivity of canyon averaged concentrations from the box model output to the exchange velocity, ω_t between the canyon air and the background atmosphere was investigated. The effect of increasing ω_t from 0.021 m s^{-1} to 0.022 m s^{-1} is illustrated in Table **5·3**. The increase in the exchange velocity results in a decrease in mean within canyon averages of NO_X and O_X by 4.5 % and 2 % respectively. Increasing ω_t decreases the concentration of NO by 5 % and NO_2 by 3 %, indicating an increase in the exchange of air between the high NO_X canyon air and the low NO_X background air, decreasing the simulated build-up of such pollutants within the canyon.

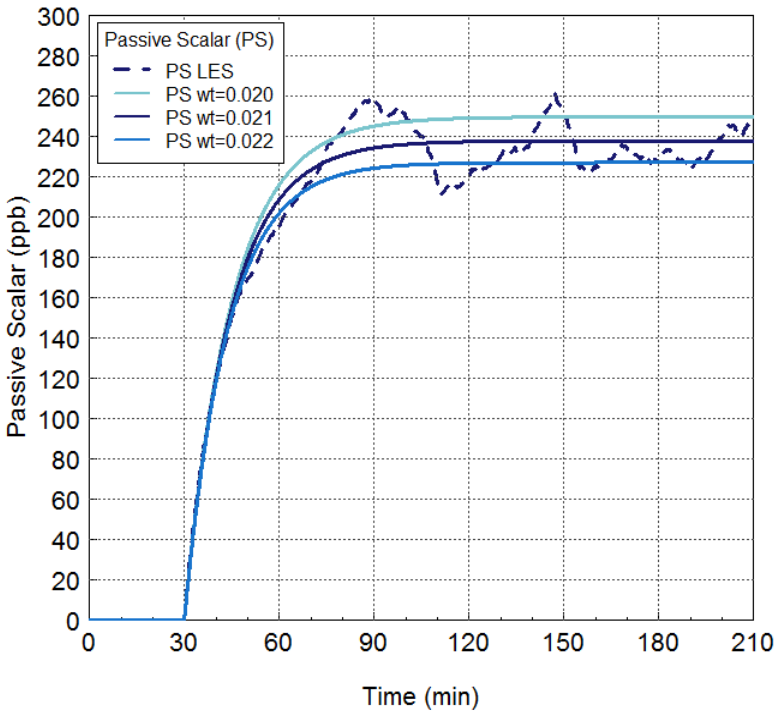

Figure 5·5 - *Time evolution of the canyon averaged mixing ratio of a passive scalar calculated using the LES and box model simulations.*

The concentration of O_3 increases with ω_t, partially due to an increase in O_3 rich background air entering the canyon from above and partly due to lower NO levels (due to an increase in ventilation), thereby reducing the effective titration of O_3. For

OH and HO_2, increasing ω_t reduces the modelled levels due to a reduction in the concentration of VOCs, as increased mixing leads to the increased ventilation of such emissions out of the canyon. In the case of the passive scalar, the flux at roof level is constant and therefore according to Equation 5·2 we have $\omega_t \cdot \left(\overline{c} - c_B\right) = constant$, and thus

$$\frac{\overline{c^{(b)}} - c_B}{\overline{c^{(a)}} - c_B} = \frac{\omega_a}{\omega_b} - 1, \text{ and } \frac{\overline{c^{(b)}} - \overline{c^{(a)}}}{\overline{c^{(a)}}} \cong -0.045.$$

Where $\overline{c^{(a)}}$ and $\overline{c^{(b)}}$ are the mean concentrations of pollutant within the canyon when exchange velocity is ω_a and ω_b respectively.

For NO_X where the concentration is considerably larger within the canyon when compared to the overlying background atmosphere *i.e.* $c_B << \overline{c^{(a)}}$ then $\frac{\overline{c^{(b)}} - \overline{c^{(a)}}}{\overline{c^{(a)}}} \cong -\frac{\omega_b - \omega_a}{\omega_b} = -0.045.$

The similarity of these results (and those in Table 5·2 and Table 5·3) indicates that (on this timescale) NO_X is approximately passive in nature.

Table 5·3 - *Canyon and time averaged mixing ratios for the box model simulation with $\omega_t = 0.021 m\ s^{-1}$ and $\omega_t = 0.022\ m\ s^{-1}$ applied. Averages taken over the last hour of the model simulation ($150 \leq t \leq 210$ min).*

	(a) Box ω_t = 0.021 m s^{-1}	**(b) Box ω_t = 0.022 m s^{-1}**	**(b) - (a)**	**[(b) - (a)] / (a)**
	Mixing ratio (ppb)[††]			%
O_3	10.54	10.76	0.22	2.1
NO	169.9	161.8	-8	-4.8
NO_2	74.0	71.6	-2	-3.2
OH	0.089	0.088	-0.0012	-1.3
HO_2	0.247	0.246	-0.0006	-0.3
NO_X	244	233	-11	-4.5
O_X	85	82	-3	-3.5

5·3·3 Temporal changes in key atmospheric species and segregation effects within the canyon

A comparison is made between the temporal variation in spatially averaged 'within canyon' concentrations of a number of species simulated by the LES model, with their equivalents simulated using the box model (with equal emissions and net external mixing applied), in Figure 5·6. Significant differences between the concentrations of key chemical species simulated using the box and LES models are apparent. In general, the LES results show dynamically-driven variability, but with some deviations from the within-canyon mixing ratios taken from the box model.

[††] Mixing ratios of OH and HO_2 given in ppt

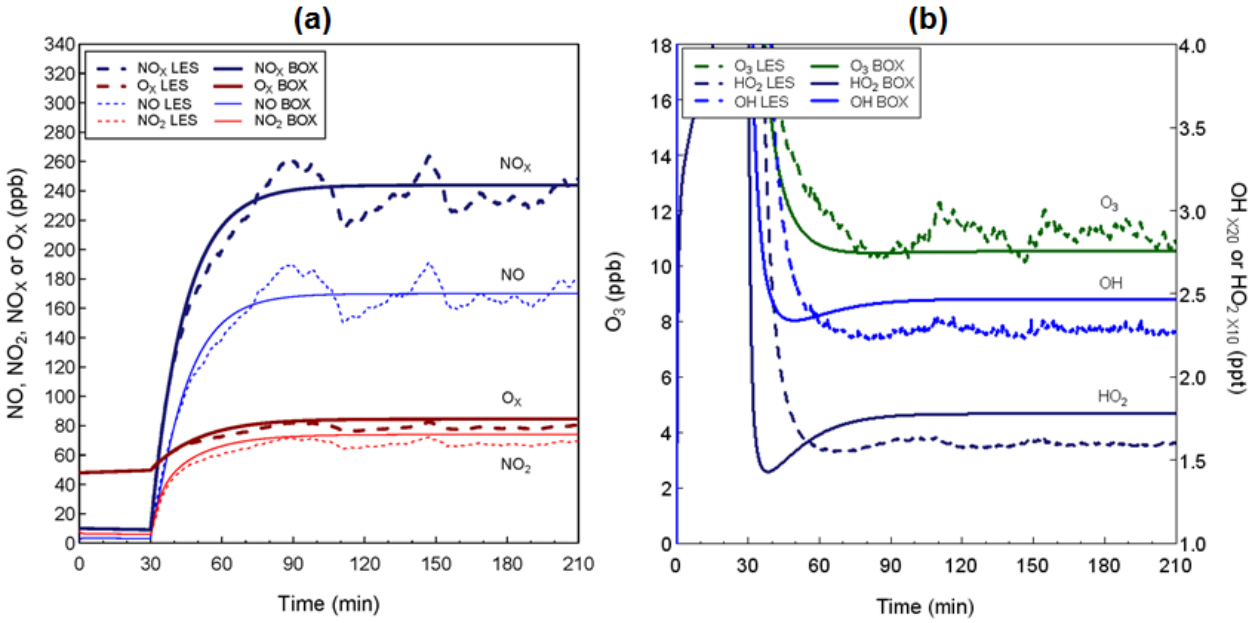

Figure 5·6 - *Time evolution of the canyon averaged mixing ratio of (a) NO_X, O_X, NO, NO_2 (ppb) and (b) O_3 (ppb), OH_{x20} (20 × OH) (ppt), HO_{2x10} (10 × HO_2) (ppt), calculated using the LES and box model simulations.*

For NO, over the final 60 minutes of the simulation, the box model results are around 1 % higher than those of the LES simulation, however this change is of the same order as the differences in the passive scalar resulting from the dynamical processes simulated by the LES and thus may not be attributed to chemistry alone. Levels of NO_2 are also higher in the box model than the LES, throughout the simulation, with a mean difference of 10 % over the final hour of the modelled period ($150 \leq t \leq 210$ min), while ozone levels are correspondingly lower, by 6 % over the final hour of the simulation.

Figure 5·6a illustrates the change in mixing ratio of NO_X and O_X over time. Over the last hour of the model run NO_X and O_X simulated by the box model are higher than the LES by approximately 3 % and 8 % respectively (Table 5·2). Thus the changes in abundance reflect chemical impacts upon NO_X and O_X levels, rather than simply differences in the NO-NO_2-O_3 photochemical steady state partitioning.

Following the initial spin up of each model run, OH and HO_2 levels increase steadily over the first 30 minutes of the model run as background chemistry (without emissions and mixing) is simulated over this period. This is followed by a large peak in both OH and HO_2 is observed directly after emissions are introduced. These peaks are followed by a rapid decline to equilibrium achieved *ca*. 30 minutes after the emissions were added. In contrast to the LES, the box model simulations show equilibrium to be approached significantly more rapidly, reflecting the slower mixing processes inherent in the LES when compared to the instantaneously and perfectly mixed conditions of the box model. Segregation effects therefore cause a reduction in the rate at which canyon-averaged concentrations approach the equilibrium levels simulated in a single-compartment model, *i.e.* street canyons respond more slowly to perturbations than a single-box model would suggest. OH and HO_2 levels simulated by the box model in steady state are higher than those in the LES simulation, with respective average differences of approximately 11 % and 8 % respectively over the final 60 minutes of the simulation.

* * * * *

The assumption of instant mixing inherent to the box model leads to overestimates of the concentrations of NO_2, O_X, OH and HO_2 and an underestimate for O_3, relative to the (more accurate) LES approach. Segregation effects, due to spatial inhomogeneity in composition due to incomplete mixing, reducing the canyon-averaged rate at which O_3 reacts with NO to produce NO_2 (*i.e.* the dominant pathway for NO-to-NO_2 conversion), due to limited quantities of O_3 in a number of cells within the LES model domain as is apparent in Figure 5·1. In terms of HO_X, it is clear that segregation effects also play an important role in determining composition; the higher OH abundance within the box model implies an overestimate of the extent of OH-driven processing of reactive emissions within the

canyon, compared with the more accurate LES scheme. While the comparison shown in Figure 5·6b suggests a deviation of the order of 11 %, the actual difference will be greater, as the OH levels experienced by the majority of emitted air parcels within the canyon will reflect those around the circumference of the vortex, rather than the centre (where OH levels are approximately 30 % higher - *see* Figure 5·1e).

5·3·4 VOC oxidation chemistry and atmospheric composition: RCS vs a simple chemistry case

To further ascertain the effect of the detailed VOC oxidation chemistry, a simplified chemical scheme was applied to both the box and LES models for comparison. This elementary chemical scheme comprised the NO_X photochemical steady state reactions only (as used by Baik *et al*. (2007); Baker *et al*. (2004); Grawe *et al*. (2007)):

$$NO_2 + h\nu \longrightarrow NO + O; \quad (5·8)$$

$$O + O_2 + M \longrightarrow O_3 + M; \quad (5·9)$$

$$NO + O_3 \longrightarrow NO_2 + O_2. \quad (5·10)$$

The initial conditions specified for the simple case were identical to those applied to the full RCS case, and in the LES construct the simulated dynamics were identical to those used with the full chemical scheme. Figure 5·7 shows a comparison of the simple chemistry case with the full RCS reaction scheme. Going from the simple to the full scheme, levels of NO_2 and O_3 are higher and NO lower, reflecting additional NO-to-NO_2 conversion (and net ozone production) in the more detailed chemistry.

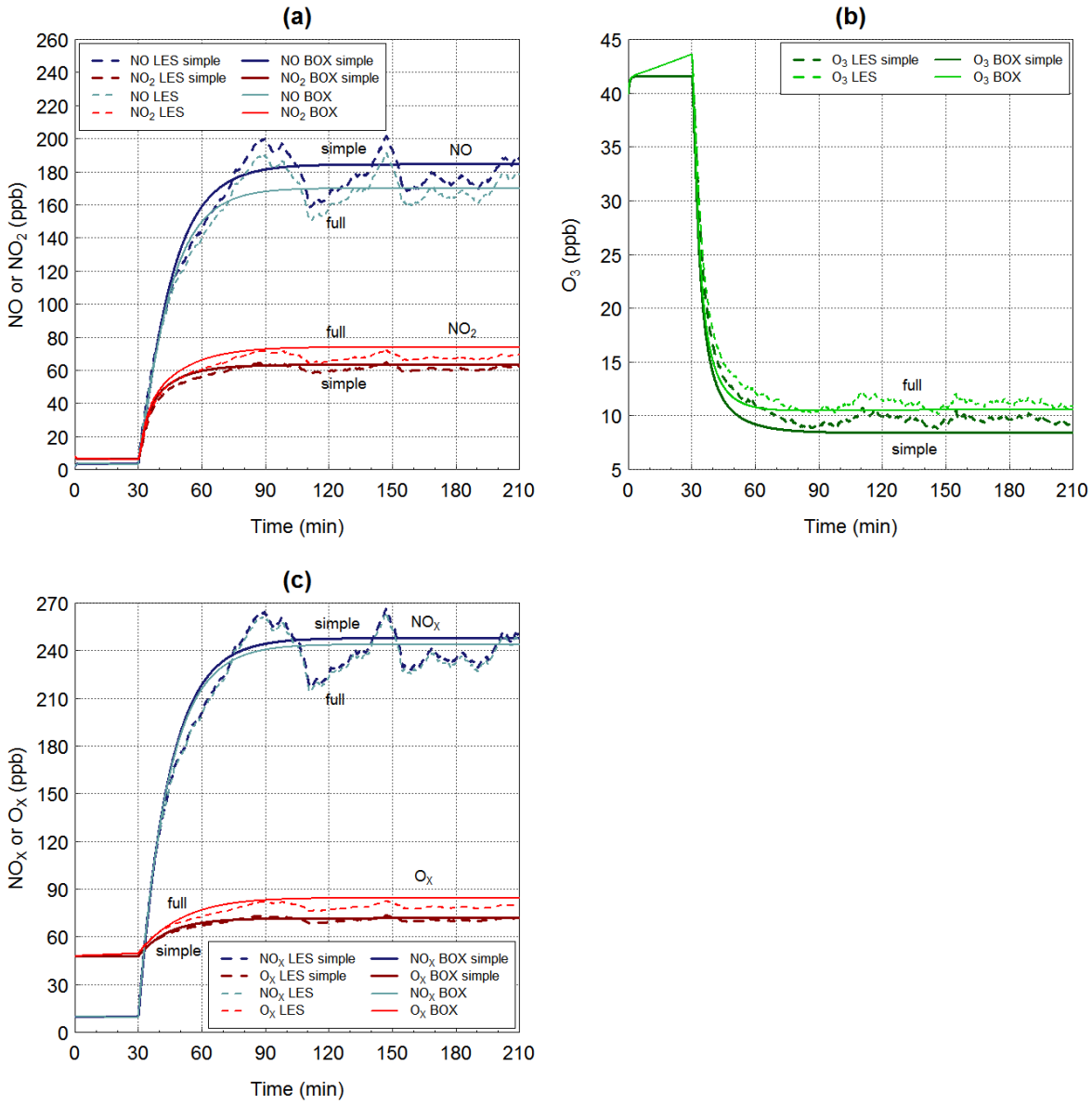

Figure 5·7 - *Time evolution of canyon averaged mixing ratio (ppb) of (a) NO, NO_2; (b) O_3 and (c) NO_X, O_X, using the LES and box model simulations and the simple and RCS chemistry cases.*

In agreement with the results presented here, when comparing steady state chemistry to the more detailed GEOS-Chem mechanism, Kim *et al.* (2012) also found O_3 levels (simulated using a CFD model) to increase significantly (up to 150 %) within the canyon with the additional VOC oxidation chemistry of the latter applied.

Correspondingly, levels of O_X are higher, while NO_X levels are slightly lower (again, going from the simple to the full scheme), reflecting the presence of NO_X loss

processes (*e.g.* formation of nitric acid, HNO_3) and partitioning to other NO_y species (*e.g.* HONO, HO_2NO_2). The differences between the full RCS scheme, and simple chemistry scheme, are similar but not identical between the box and LES dynamical frameworks — the changes in NO, NO_2, NO_X, O_3 and O_X are all less between the two LES models (dashed lines in Figure 5·7), than the two box models (solid lines in Figure 5·7).

For example, for NO the box models show a decrease of *ca*. 8 % (Table 5·4) from the simple to full chemical approaches, while the reduction is only 5 % for the LES models. For NO_2, the corresponding increases are *ca*. 18 % for the box models and 12 % for the LES approaches; changes in ozone are (proportionately) similar.

Table 5·4 - *Canyon and time averaged LES and box model mixing ratios for the full RCS and simple chemistry cases. Averages taken over the last hour of the model simulation ($150 \leq t \leq 210$ min). $\omega_t = 0.021$ m s^{-1} applied to the box model. The concentration of the passive scalar is included here to highlight that the dynamical processes within each simulation are constrained.*

	(a) LES RCS	**(b) Box RCS**	**(c) LES Simple**	**(d) Box Simple**	**LES [(a) - (c)] / (c)**	**Box [(b) - (d)] / (d)**
	Mixing ratio (ppb)				**%**	
O_3	11.2	10.5	9.7	8.4	15.5	25.0
NO	168	170	177	185	-5.1	-8.1
NO_2	68	74	61	63	11.5	17.5
NO_X	236	244	238	248	-0.8	-1.6
O_X	79	85	70.7	71.4	11.7	19.0
PS	233	238	233	238	0.0	0.0
NO_2/NO	0.40	0.44	0.34	0.34		

Within the LES dynamical framework, the system is less sensitive to the additional chemical processes included in the RCS, when compared with the simple scheme. In much of the domain, O_3 levels are very low / zero, such that the NO: NO_2 ratio is increased, and impacts of NO_X removal and partitioning in the full chemical scheme are reduced, while ozone production is immediately repartitioned into NO_2.

Effectively, segregation effects in the LES simulations make the canyon-averaged model composition less sensitive to the chemical simplifications when moving from the RCS to the simple chemical model.

5·3·5 Atmospheric pre-processing within the canyon

Figure 5·8 illustrates the change in mixing ratio of O_3, NO, NO_2, NO_X and O_X with height at the canyon inlet (x/W = -0.5) and canyon outlet (x/W = 0.5). Increases are observed in the levels of NO, NO_2, NO_X and O_X leaving the canyon, indicating the combined effect of primary emissions and atmospheric pre-processing on the concentration of pollutants escaping to the wider background atmosphere.

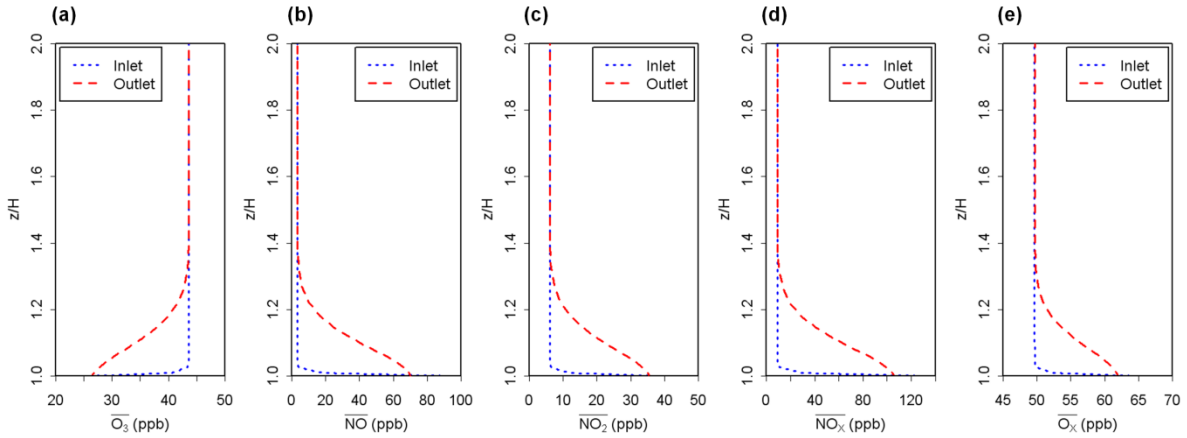

Figure 5·8 - *Time averaged vertical mixing ratio profiles ($1.0 \leq z/H \leq 2.0$) of (a) O_3, (b) NO, (c) NO_2, (d) NO_X and (e) O_X (ppb) at the canyon inlet (x/W = -0.5) and canyon outlet (x/W = 0.5). Average taken over the last hour of the model simulation ($150 \leq t \leq 210$ min).*

In order to evaluate the extent of pre-processing further, the change in vertical flux of a number of species with height was calculated based on Equation 5·5 for the last hour of the model simulation (shown in Figure 5·9) with comparison made to the primary emissions of NO, NO_2 and NO_X (ppb s^{-1} emitted into a single cell of 0.3 m × 1 m × 0.3 m). The calculated resolved-scale flux near roof level (z/H = 1) can be used to determine a representative flux of pollutants out of the canyon and into

the background atmosphere. This may then be compared with raw emission rates to evaluate within-canyon processing (although given the turbulent nature of the canyon-background interface (*e.g.* Figure 4·2) the choice of height at which to evaluate this is somewhat arbitrary). To account for the numerical effects that cause a small overestimation of the maximum total flux of passive scalar in comparison to its raw emission rate, a correction factor is applied to the flux of passive scalar. All other flux profiles included in Figure 5·9 were also scaled with this factor.

A peak in the resolved-scale turbulent flux profile is observed at $z/H \approx 0.1$ and a decrease in total flux is seen for $z/H < 0.1$ in all flux profiles. This is the result of the elevated line emission source located within the centre of the canyon being 1 m above street level. For the passive scalar, the profile differs from that expected a priori for a conserved quantity which should remain constant with height. At roof level ($z/H \approx 1$) the flux of the passive scalar into the background atmosphere is equal to 933 ppb m^{-2} s^{-1} *i.e.* 93 % of that emitted is escaping into the wider atmosphere.

The maximum flux of the passive scalar of 1000 ppb m^{-2} s^{-1} is observed slightly below roof level. This observed decrease in the flux of passive scalar with height arises from the sub-grid scale turbulent dispersion not resolved explicitly within the LES model (the sub-grid scale flux is not included here). Because of this, the fluxes of NO_X and O_X out of the canyon discussed below are obtained at a height slightly below the roof level, $z_f = 0.933\ H$, where the contribution of sub-grid scale dispersion is minimised and at which height the flux of passive scalar reaches 99.5 % of its theoretical value.

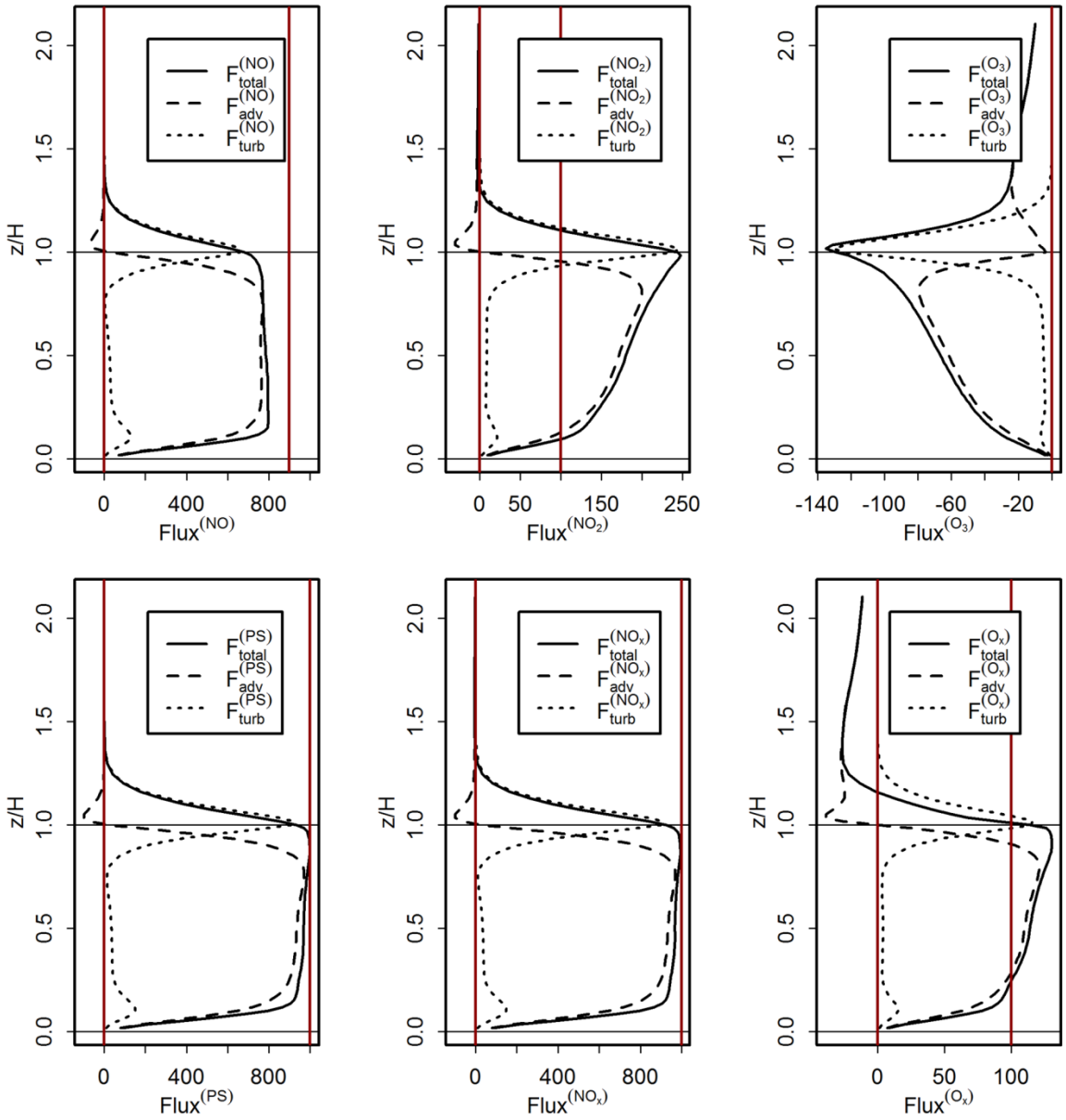

Figure 5·9 - *Vertical profiles of advective (F_{adv}), turbulent (F_{turb}) and total flux (F_{total}) (all ppb m^{-2} s^{-1}) averaged across the canyon ($-0.5 \leq x/W \leq 0.5$) and over the last 60 minutes of the model simulation. Red lines represent zero flux and raw emissions into one grid cell of 0.3 m x 1 m x 0.3 m.*

A significant effect of the within-canyon spatially resolved chemical processing on pollutant flux is observed for NO and NO_2. A positive upward total flux of both NO and NO_2 from within the street to the overlying background atmosphere is observed with a negative (downward) flux of O_3. The maximum total flux of NO (798 ppb m^{-2} s^{-1}) occurs near street level ($z/H \approx 0.2$). At $z = z_f$, the flux of NO is equal to 752 ppb m^{-2} s^{-1} compared to a raw emission rate equivalent to 900 ppb s^{-1}.

Therefore there is an approximately 17 % conversion of NO to NO_2 (and other NO_y components) within the canyon when compared to the raw emission rate.

The maximum flux of NO_2 (248 ppb m^{-2} s^{-1}) occurs just below roof level and is approximately 2.5 times that of the raw emission rate of 100 ppb s^{-1}, indicating a significant effect of atmospheric pre-processing on the level of NO_2 escaping into the wider urban boundary layer. In terms of O_3 the maximum downward flux into the canyon of 135 ppb m^{-2} s^{-1} occurs just above roof level as O_3 rich background air enters the canyon from above, and O_3 is removed within the canyon by reaction with NO. At $z = z_f$ (near roof level), the flux of NO_X is 989 ppb m^{-2} s^{-1} or 1.1 % lower than that emitted; O_X is 130 ppb m^{-2} s^{-1} at $z = z_f$, or 30 % higher than the 100 ppb s^{-1} of NO_2 emitted. Therefore NO_X release into the boundary layer is almost the same as that emitted, but oxidant release increases significantly, in part as a result of the chemical processing taking place within the canyon.

As seen in Figure 5·9, the dominant vertical flux observed within the canyon until $z/H \approx 0.8$ is the mean advective flux which transports all pollutants (except for O_3) upwards toward roof level throughout the canyon. Between $z/H \approx 0.8$ and roof level, the mean advective flux decreases rapidly to become negative just above the top of the canyon ($1.0 \leq z/H \leq 1.2$) indicating that the mean flow (averaged across the domain) acts to entrain pollutants downwards toward the canyon at this height. For all species included in Figure 5·9, a large increase in the resolved-scale turbulent flux is observed toward roof level indicating the importance of the shear layer associated turbulent processes in pollutant exchange at this level.

For all species considered in Figure 5·9, except O_3, the resolved-scale turbulent flux at roof level is at a maximum and is positive, indicating that there is more pollutant escaping out of the canyon at this height through turbulent transport than entering

from the background atmosphere above. The mean flux of all species excluding O_3 and O_X becomes close to zero at a height of $z/H \approx 1.4$ *i.e.* toward the free flowing boundary layer above, which is unaffected by the dynamical processes taking place within and just above the canyon itself. For O_3 however, a negative mean flux is observed until well above the canyon indicating net downward transport of O_3 rich air towards the canyon.

5·4 Discussion

The **LES-RCS** model has been used to investigate urban street canyon atmospheric composition by simulating the combined effects of emissions, mixing and chemical processing on pollutant concentration within an idealised canyon. The key questions that have been addressed in this chapter include: *How different is the air quality within the street canyon from the immediately overlying background atmosphere and how does this depend on dynamics? To what degree do key atmospheric species vary spatially within the canyon? To what extent are pollutants processed within street canyons before they escape to the wider atmosphere?*

* * * * *

Pollutants within and above the canyon were found to show a **clear spatial variation**, with NO_X levels close to the leeward wall over double those of the windward wall; such variations are of importance in assessing the potential exposure of receptors to air pollutants. Through comparison of simulations using the LES dynamical framework with those using a simple zero-dimensional box model approach, the effects of **segregation** on canyon atmospheric chemistry and composition are evident.

Compared with a single-box canyon model, the LES scheme responds more slowly to chemical perturbations, and (after quasi-equilibrium is established) the **box model simulated** levels of NO, NO_2 and OH were found to be higher than their (canyon-averaged) equivalents in the more realistic LES scheme, while **levels of O_3 were underestimated** (by the box model) compared with the LES approach. The assumption of instant mixing inherent to the box model leads to overestimates of the concentrations of NO, NO_2 and OH, and an underestimate for O_3, relative to the LES approach.

Segregation effects, due to spatial inhomogeneity in composition due to incomplete mixing, reduce the canyon-averaged rate at which O_3 reacts with NO to produce NO_2 (*i.e.* the dominant pathway for NO-to-NO_2 conversion), due to limited quantities of O_3 present in a number of cells within the LES model domain apparent in Figure 5·1. Segregation effects also affect HO_x levels; the higher OH abundance within the box model implies an overestimate of the extent of OH-driven processing of reactive emissions within the canyon, compared with the more realistic LES approach. While the comparison included in Figure 5·6b suggests a deviation of the order of 11 %, the actual difference will be greater, as the OH levels experienced by the majority of emitted air parcels within the canyon will reflect the circumference of the vortex, rather than the centre (where OH levels are approximately 30 % higher).

Through comparison of the comprehensive RCS and PSS-only chemical mechanisms, a clear effect of the inclusion of **detailed oxidation chemistry** is also evident. Going from the PSS-only to the RCS mechanisms, levels of NO_2 and O_3 are higher and NO lower, reflecting additional NO-to-NO_2 conversion (and net ozone production) under the more detailed chemistry. Segregation effects reduced the

sensitivity of the model outputs to the increase in chemical complexity when comparing the box model dynamical framework to the LES approach.

Chemical processing of emissions takes place within the canyon, contributing to an increase in O_x (O_3 + NO_2) of 30 % (compared to the primary NO_2 component of the emission source), for the moderately polluted emission scenario considered. This result shows that the atmospheric "pre-processing" of primary emissions taking place within street canyons can be significant in terms of atmospheric composition and the flux of pollutants from street canyon level to the wider urban boundary layer above.

6: Modelling atmospheric composition using the LES-RCS model

6·1 Introduction

This chapter further investigates atmospheric composition on the street canyon scale using the LES-RCS model. Within street canyons, adverse health effects and an increase in hospital admissions can result from higher pollutant levels with a significant increase in personal exposure often experienced (Vardoulakis *et al.*, 2003). The concentration of atmospheric pollutants of particular concern in terms of their adverse effects on public health will provide the initial focus of this chapter. The latter sections of this chapter (§6·3 onwards) consider the effect of varying emissions upon canyon atmospheric composition (via the application of a number of emission scenarios applied to the LES-RCS model) in addition to segregation effects and the role of canyon dynamics in turbulent transport within an above the canyon.

As detailed in Chapter 1, the atmospheric pollutants studied here, both emitted directly by vehicles and formed through photochemical reaction within the canyon, can have serious effects on human health. The exposure related health risks to receptors are of particular concern within the street canyon where it has been demonstrated that significant spatial and temporal variations exist.

In order to attribute the health effects of air pollution through epidemiological studies it is crucial to accurately quantify the personal exposure of receptors to atmospheric pollutants released in the atmosphere (Jensen, 1999, Vardoulakis *et al.*,

2005, Zou *et al.*, 2009). The health effects of air pollution in epidemiology studies have often been better characterised than the exposure themselves which presents difficulties in determining the correlation between health effect and exposure (Jensen, 1999).

In order to assess population exposure, fixed monitoring stations are often utilised, these however may provide a poor representation of individual exposure and as a single point spatial measurement are often assumed to be representative of the exposure of the urban population as a whole (Fenger, 1999, Vardoulakis *et al.*, 2002). A number of studies (*e.g.* Berkowicz *et al.* (1996), Vardoulakis *et al.* (2002) (2005) and Zou *et al.* (2009)) have highlighted the need for more detailed measurements / model output in order to provide a more accurate representation of personal exposure or inform the location of monitoring sites used to assess compliance with EU and UK legislation.

Vardoulakis *et al.* (2002) (2005) assessed the spatial variability in pollution levels within street canyons in Paris highlighting the implication of such measurements for exposure studies. Vardoulakis *et al.* (2002) demonstrated that a strong spatial variation in pollutants exists within the canyon with exposure significantly higher on the leeward side of the canyon when compared to the windward under perpendicular winds and suggested that the side of the street should be considered when linking health effects to traffic related air pollution.

Vardoulakis *et al.* (2005) demonstrated that measurements taken at a fixed monitoring site within the vicinity of their measurement campaign may not provide an adequate representation of air quality within the surrounding area and may therefore be -inappropriate for use within population exposure studies.

Factors that lead to an augment of the exposure of individuals to atmospheric pollutants include increasing concentrations and the duration of exposure, though in some instances effects may be immediate (Walters and Ayres, 2001). Those regions of the canyon in which pedestrians are likely to be affected by pollutant levels are of prime importance in terms of personal exposure.

With regard to air pollution and related health effects (Chapter 1) the pollutants of main concern in terms of public health are NO_2 and O_3. NO may also be of concern if chemically processed to produce NO_2. It is these pollutants that will be focused upon here.*

As presented in §5·3·1 and discussed in Chapter 2 of this thesis, a strong spatial variation in pollutants is observed within the canyon. As a result of the relatively short distance between source and receptor only very fast chemical reactions have a significant influence on concentrations observed within street canyons (Costabile and Allegrini, 2007).

Longer-lived chemical species emitted within the canyon such as VOCs and CO may be considered inert on such timescales (limited by the rate of chemical reaction) whilst for species including NO, NO_2 and O_3, the timescales of these chemical reactions is in the same order as the residence times of pollutants within the canyon resulting in complex and non-linear interactions between chemical and dynamical processes (Costabile and Allegrini, 2007).

To explore the variation in the potential exposure of individuals to harmful atmospheric constituents further statistical analysis is carried out. The health effects related to increasing concentrations of atmospheric pollutants may be non-linear

* Particulate matter is also a major concern in terms of the health effects (see Fenger (1999)) related to air pollution however this is not considered within this thesis.

therefore statistical measures such as skewness may be more valuable than using the mean alone in predicting such effects.

As discussed in §1·5·1, pollutants are often regulated with respect to exposure times, with the standards set within the EU daughter directive and the UK National Air Quality Strategy. Exposure limits for a number of pollutants are derived on an hourly interval with a number of exceedences permitted annually. Such guidelines are likely to be set on the basis of an underlying statistical distribution of such pollutants.

Li *et al*. (2013) outline that concentration distributions (for VOCs in this case) that may have multiple modes and extended tails are not well represented by normal distributions. Thus, with implications in terms of pollutant exposure presenting challenges to parametric distribution models. The need for information on full distributions of exposure levels in order to determine exposure, estimate health risks and conduct probability analysis is also stressed (Li *et al.*, 2013).

For NO_2 an hourly limit of 105 ppb is set under both the UK's N.A.Q. guidelines and the EU daughter directive with 18 exceedences of this limit permitted on an annual basis.

In order to estimate the likelihood of concentrations exceeding a certain threshold, or the number of occasions that this may occur it is necessary to consider the statistical properties of concentration data with respect to time (Seinfeld and Pandis, 1998). Hypothetical normal and positively skewed distributions of the concentration of atmospheric pollutants where both distributions have an equal arithmetic mean are presented in Figure 6·1. For atmospheric pollutant data with a normal distribution a threshold concentration is unlikely to be exceeded. If the observed distribution is positively skewed however, it is probable that the threshold

concentration is exceeded due to the extended tail to the right of the distribution at high concentrations.

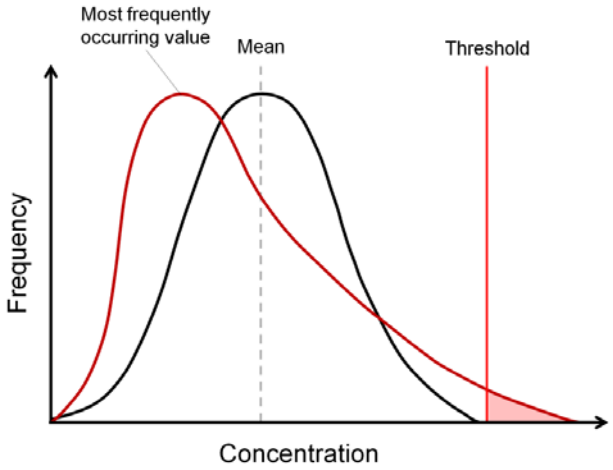

Figure 6·1 - *Hypothetical normal and positively skewed continuous distributions with the same mean illustrating possible exceedances of a threshold value.*

It is useful to consider the pollutant dose response to increasing levels of pollutants when examining the potential implication of the statistical analysis carried out in section 6·2 as such relationships are being used extensively for health impact assessment. Figure 6·2 illustrates three hypothetical dose response curves for consideration. The linear response shown in (a) illustrates that evaluating the mean concentration is appropriate and that further statistical insight is not required. However, using the mean concentration alone to determine pollutant concentration levels is not sufficient in correctly describing the expected health effects depicted in (b) and (c). Health effects become prevalent in (b) above a threshold concentration whilst in (c) adverse health effects increase exponentially with increasing pollutant concentration.

A large number of physiological studies have demonstrated curvilinear relationships (Figure 6·2) between O_3 concentration and respiratory lung function. Such studies have also shown that increasing inhaled O_3 concentration had a

greater effect than increasing the duration of exposure (Walters and Ayres, 2001).As such it is better, in terms of the associated health effects that may arise, to breath in reduced levels of O_3 over an extended period than higher concentrations for just a short period of the time. An increasingly positively skewed distribution of atmospheric pollutants, such as that of O_3 observed within the pedestrian right zone of the canyon, could therefore have a greater negative effect on human health.

Receptors are less likely to be exposed to higher concentrations above a certain threshold where atmospheric pollutants exhibit near Gaussian distributions, thus highlighting the importance of the study of statistical distributions of concentration and their potential use as tools in predicting pollution levels, public exposure and informing policy.

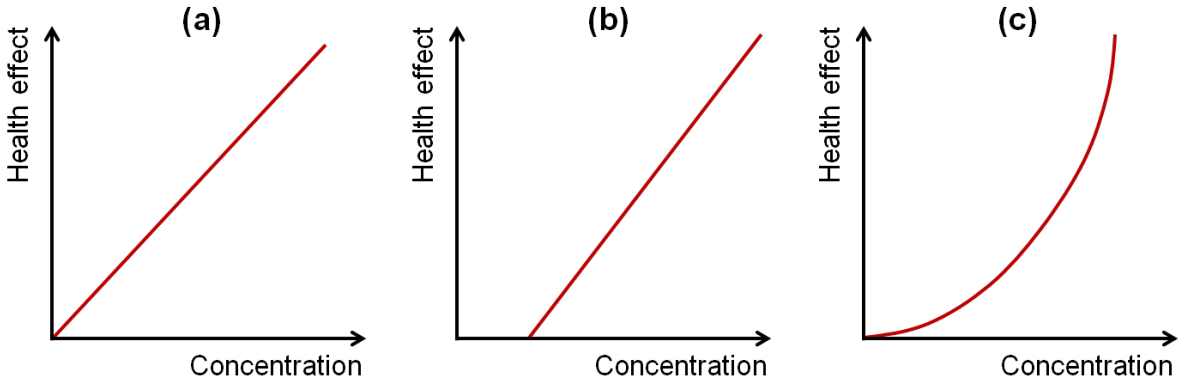

Figure 6·2 - *Hypothetical dose response curves to illustrate the potential effect of increasing pollutant concentration on health. A linear response to increasing pollutant concentration is illustrated in (a) and (b) whilst a curvilinear response is demonstrated in (c).*

In terms of health effects, the above findings are also of prime concern for the potential exposure of pedestrians to elevated levels of NO_2 that may be above a certain threshold within the canyon. However, the dose response curve for NO_2 has received relatively little attention (Samoli *et al.*, 2003). Although Samoli *et al.* (2003) found that NO_2 mortality dose-response association may be adequately represented by a linear model, the results showed that there was clear heterogeneity in the dose

response curves observed in a number of EU cities with some demonstrating a clearly curve-linear relationship.

6·2 Potential exposure to key atmospheric pollutants within the canyon

Analysis was carried out on 3-D model output obtained using the LES-RCS with the base case scenario applied. These data have been averaged in the *y*-axis over the length of the canyon (L_y) (see §5·2) and are output at 5 second intervals over a 3 hour period ($30 \leq t \leq 210$ min).

Initially, data were averaged over the final hour of the model simulation ($150 \leq t \leq 210$ min) to investigate the spatial variability of pollutants within the canyon (§6·2·1). Data were extracted from street level to the top of the canyon where $z = 18$ m ($0 \leq z/H \leq 1$) at 1.8 m to the right and left hand side of the leeward and windward canyon walls (Figure 6·3a) to give vertical mixing ratio profiles. The change in concentration of pollutants across the canyon at a typical pedestrian height was determined by extracting the horizontal mixing ratio profile ($-0.5 \leq x/W$ 0.5) at a height of 1.8 m ($z/H \approx 0.1$) as shown in Figure 6·3a.

To study the temporal variability in pollutant levels on either side of the street (within the region where pedestrians are predominantly exposed to harmful pollutants) averages were calculated within two 9 m^3 boxes (*i.e.* $\Delta x \times \Delta y \times \Delta z = 3$ m × 1 m × 3 m). These were situated next to the leeward ($-0.5 \leq x/W \leq -0.33$) and windward ($0.33 \leq x/W \leq 0.5$) walls ($0 \leq z/H \leq 0.17$) as shown in Figure 6.1b and referred to hereafter as the *pedestrian left (PL)* and *pedestrian right (PR)* cases.

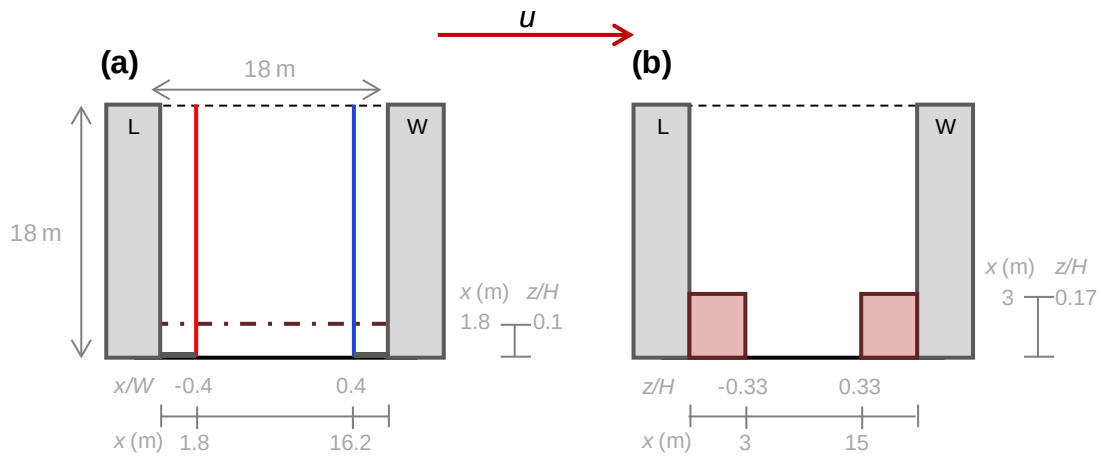

Figure 6·3 - *Schematic diagram (not drawn to scale) of the locations at which data have been extracted. The dashed purple, solid red and blue lines in (a) represent the locations at which mixing ratio profiles were extracted. The red boxes in (b) represent the 9 m^3 volume over which data were averaged. L and W refer to the leeward and windward walls respectively.*

The data output at 5 s intervals over the last hour of the model simulation ($150 \leq t \leq 210$ min) was analysed for this purpose, hence for each chemical species there were 720 entities in total. Hourly averaged mixing ratios for NO, NO_2 and O_3 were also calculated over the last 60 minutes of the simulation ($150 \leq t \leq 210$ min) using data obtained for each pedestrian zone. Comparison was also made to volume averaged within canyon concentrations (§5·2) output at equal intervals and over the same period. R© version 2.13.1 (`http://www.r-project.org/`) was used to process data and carry out all statistical tests and analysis included in this chapter.

6·2·1 The spatial variation in pollutant levels at pedestrian level within the canyon

A clear spatial variation in a number of key chemical species was previously found to exist within the street canyon, a full discussion of which is given in Chapter 5. Such variability particularly at the lower levels of the canyon (*i.e.* that region where individuals are predominantly exposed to atmospheric pollutants) will be quantified further here. The mixing ratio of NO, NO_2 and O_3 in close proximity to the leeward (x/W = -0.4; x = 1.8 m) and windward (x/W = 0.4; x = 16.2 m) walls of the canyon are illustrated in Figure 6·4.

Concentrations of NO and NO_2 are considerably higher toward the lee (x/W = -0.4) of the canyon where levels at typical pedestrian height (z = 1.8 m) are over two times (58 %) and approximately a third higher (30 %) respectively. Conversely, O_3 concentrations are highest toward the windward wall (up to 86 %).

A significant change in the concentration of NO_2 and O_3 is evident across the canyon (Figure 6·5) at pedestrian height (z/H = 0.1). A peak in the concentration NO_2 of 83 ppb is observed 2.4 m from the leeward wall with receptors likely to be exposed to similarly high levels throughout the *PL* zone. Moving toward the windward side of the street, NO_2 levels decrease to a minimum of 58 ppb, 2.4 m from the windward wall ($x/W \approx 0.37$). Maximum NO_2 levels on the leeward side of the canyon, in that region where pedestrians may be exposed to such harmful pollutants, are approximately 42 % higher than the windward side of the street.

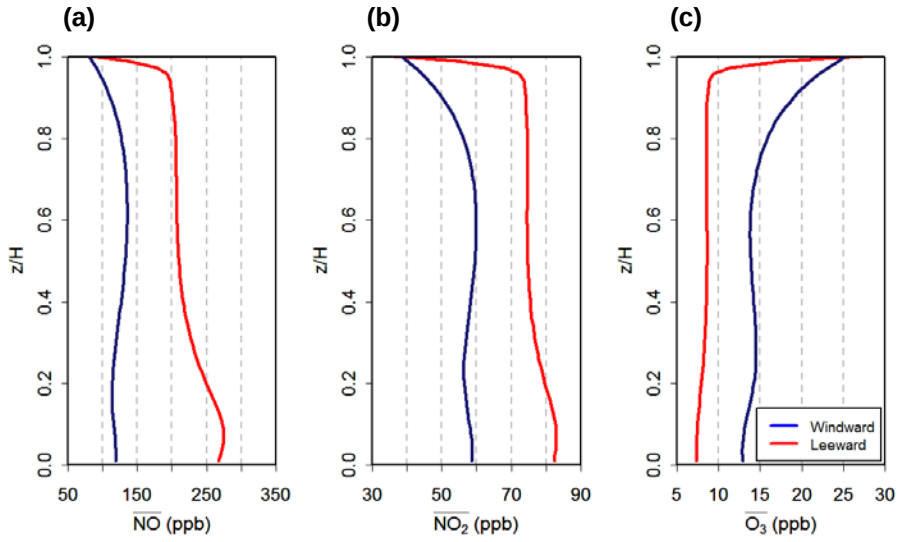

Figure 6·4 - *Time averaged vertical mixing ratio profiles within the canyon ($0.0 \leq z/H \leq 1.0$) of (a) NO, (b) NO_2 and (c) O_3 (ppb) on the leeward (red lines; $x/W = -0.4$) and windward (blue lines; $x/W = 0.4$) sides of the canyon. Averages taken over the last hour of the model simulation ($150 \leq t \leq 210$ min).*

The variation in O_3 across the canyon at pedestrian height (Figure 6·5) shows that a maximum concentration occurs 3 m from the windward wall (upwind of the emission source) where O_3 = 13 ppb ($x/W \approx 0.33$). A minimum level of O_3 is reached in close proximity the leeward wall of the street ($x/W \approx -0.45$) where the mixing ratio decreases to 7 ppb.

As discussed in the previous chapter, the observations made above can be explained by the mixing and transport of primary emissions (from their source in the centre of the street) by the primary canyon vortex (Figure 5·1) as well as the chemical processing of pollutants within the canyon.

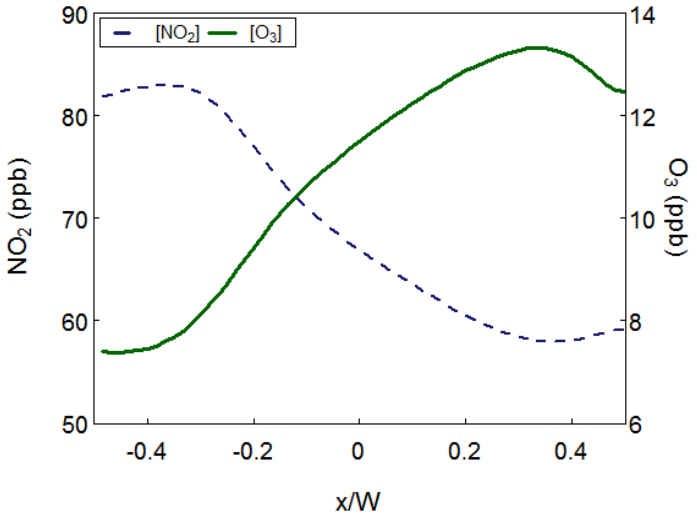

Figure 6·5 - *Time averaged horizontal mixing ratio profiles of NO_2 (dashed line) and O_3 (solid line) across the street canyon ($-0.5 \leq x/W \leq 0.5$) at a typical pedestrian height of 1.8 m ($z/H = 0.1$). Averages taken over the last hour of the model simulation ($150 \leq t \leq 210$ min).*

In addition to that emitted directly into the canyon, increased NO_2 levels and a minimum in O_3 toward the leeward wall can be explained by the oxidation of emitted NO that effectively titrates O_3 to produce NO_2. Higher levels of O_3 encountered toward the windward wall can be accounted for (in part) by the entrainment of O_3 rich air into the canyon from aloft.

6·2·2 The temporal variability of pollutant levels within the street canyon

An investigation into the short term pollutant levels experienced within the canyon was carried out with comparison made to hourly averages that represent those reported at fixed monitoring stations (*i.e.* those that form the UK Automatic Urban and Rural Network (AURN)). Mixing ratios observed within a single cell at z = 1.8 m (typical roadside / kerbside monitoring station height), 1.5 m from the canyon wall were within a few ppb of hourly means calculated for the *PL* and *PR* cases, therefore comparison is made to these values alone hereafter.

Time series analysis

The fluctuation in the concentration of NO, NO_2 and O_3 for the *PL* and *PR* cases at 5 s intervals over a 60 minute period ($150 \leq t \leq 210$ min) is illustrated in Figure 6.4[†]. The inherently random nature of short term variations in pollutant concentrations is evident, the result of their dependence on highly variable canyon dynamics, turbulence, emissions and non-linear chemical processes. For the emission scenarios considered here, emissions are constant and therefore may under-estimate the true temporal variability in pollutant levels.

In comparison with the *PR* and *CAN* averages, NO and NO_2 mixing ratios are considerably higher (268 and 82 ppb respectively, shown in Figure 6·6) and exhibit the greatest variability on the left hand side of the street (with respective standard deviations, σ, of 14 and 2 ppb). When expressing standard deviation as a percentage of the mean (Table 6·1), the variability in NO and NO_2 levels is almost equal for the *PL* and *PR* cases, the latter being slightly higher. In both cases however, the variability relative to the mean is significantly higher than that of the canyon average.

O_3 is most variable to the right of the canyon (σ_{O_3} = 0.6 ppb and 4.6 % relative to the mean) whilst fluctuations from the mean on the left hand side appear to be relatively damped (σ_{O_3} = 0.3 ppb) in comparison. Within the pedestrian right region, short term variability in O_3 may be significant with some large fluctuations (up to 3 ppb > $\overline{O_3}$) observed.

[†] It must be noted here that the results presented in this section of work are based on model output averaged along the *y* axis; this combined with a constant emission source may cause the true variability in pollutant levels to be reduced.

An insight into the distributions of data-set was gained by calculating a non-dimensional third order moment about the mean known as **skewness**:

$$sk_a = \frac{\overline{a'^3}}{\sigma_a^3}\ , \tag{6.1}$$

where $\overline{a'^3} = \frac{\Sigma\left(a-\bar{a}\right)^3}{n}$ and σ_a is the standard deviation, $\sigma_a = \sqrt{\overline{a'^2}}$.‡

The results presented in Table 6·1 indicate a low level of skewness (-0.5 ≤ sk_a ≤ 0.5) for all pedestrian left and pedestrian right samples, indicating that the data are approximately normally distributed (Bulmer, 1979).

Table 6·1 - *Summary statistics for NO, NO_2 and O_3 data-sets for the pedestrian left (PL), pedestrian right (PR) and canyon average (CAN) cases calculated over the last hour of the model simulation (150 ≤ t ≤ 210 min).*

	A. NO			B. NO_2			C. O_3		
	PL	**PR**	**CAN**	**PL**	**PR**	**CAN**	**PL**	**PR**	**CAN**
Mean (ppb)	268	117	168	82	58	68	8	13	11
Median (ppb)	265	116	166	82	58	67	8	13	11
S.d. (ppb)§	14.4	6.5	5.8	2.2	1.7	1.1	0.3	0.6	0.3
S.d. (% of mean)	5.4	5.6	3.5	2.7	2.9	1.6	3.8	4.6	2.7
Skewness	0.39	0.08	0.73	0.36	-0.14	0.74	0.05	0.45	0.10

For canyon averaged NO and NO_2, the data are moderately positively skewed ($sk \approx$ 0.7) whilst O_3 is approximately Gaussian in distribution and only slightly positively skewed (sk_{O_3} = 0.10). The highest degree of (positive) skewness is inherent in O_3 data in the pedestrian right case where sk_{O_3} = 0.45.

‡ Normally distributed data that are perfectly symmetrical have a skewness = 0. For skewness values between 0.5 and 0.5 the distribution is approximately normal. If the skew of the data is greater than -1 or +1 the data is said to be highly negatively or positively skewed respectively (Bulmer, 1979).

§ S.d. refers to the standard deviation, σ

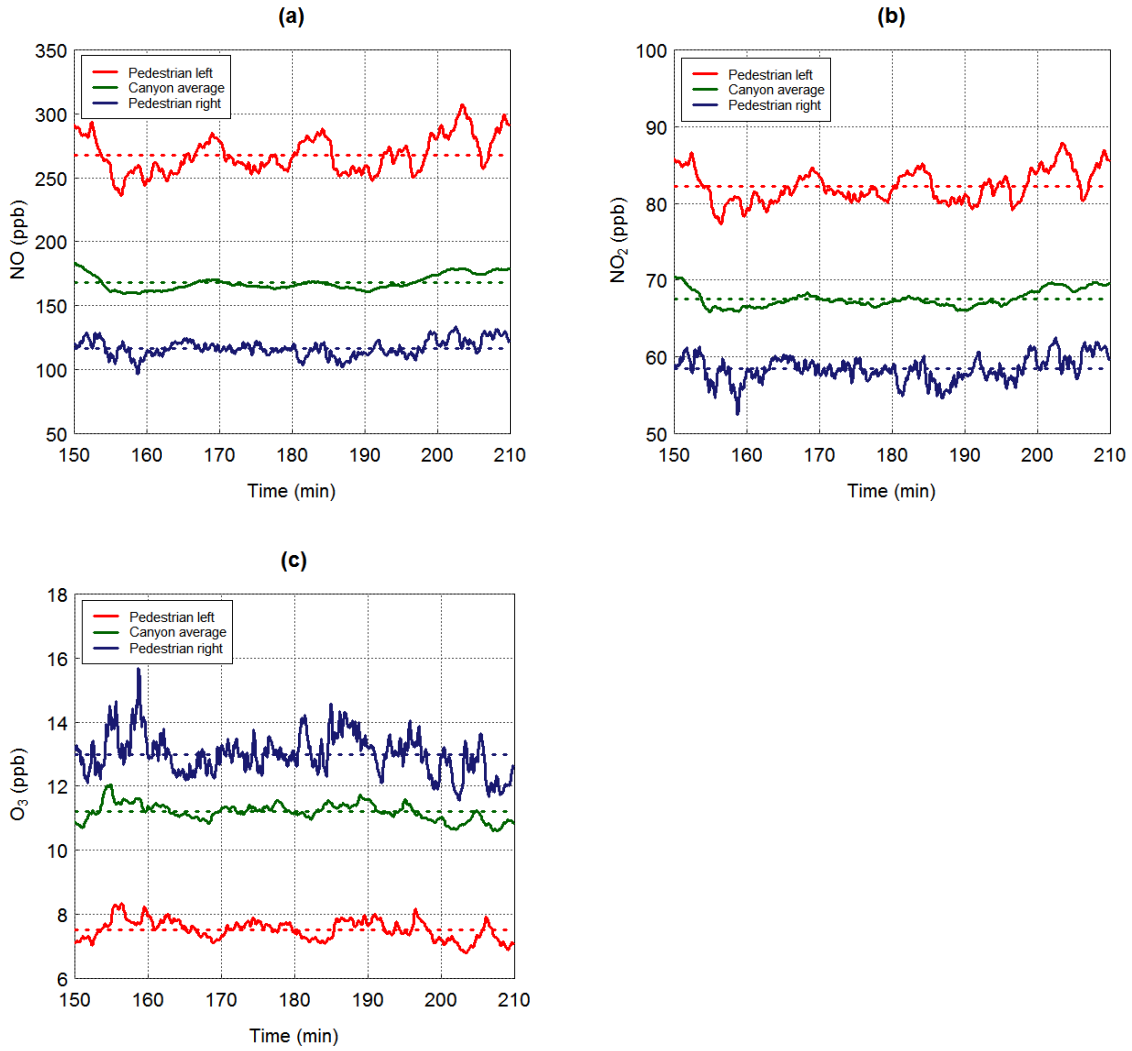

Figure 6·6 - *Time series of mixing ratios for (a) NO, (b) NO_2 and (c) O_3 at 5 second intervals (solid lines) and hourly averages (dashed lines) taken over the last hour of the model simulation ($150 \leq t \leq 210$ min). Spatial averages taken within a 9 m^3 (3 m × 1 m × 3 m) box to the left and right (pedestrian right) of the street shown together with the canyon average.*

Figure 6·7 shows a clear shift in the distributions of mixing ratio data in the pedestrian left and right zones, with higher levels of NO and NO_2 observed for the former and O_3 in the latter. The greatest spread of NO (interquartile range, IQR = 24 ppb) and NO_2 (IQR = 3 ppb) data is evident for mixing ratios observed to the left hand side of the canyon. For O_3 the largest spread (IQR = 0.8 ppb) is evident to the right hand side of the street with extremes observed at high mixing ratios and a maximum of approximately 16 ppb.

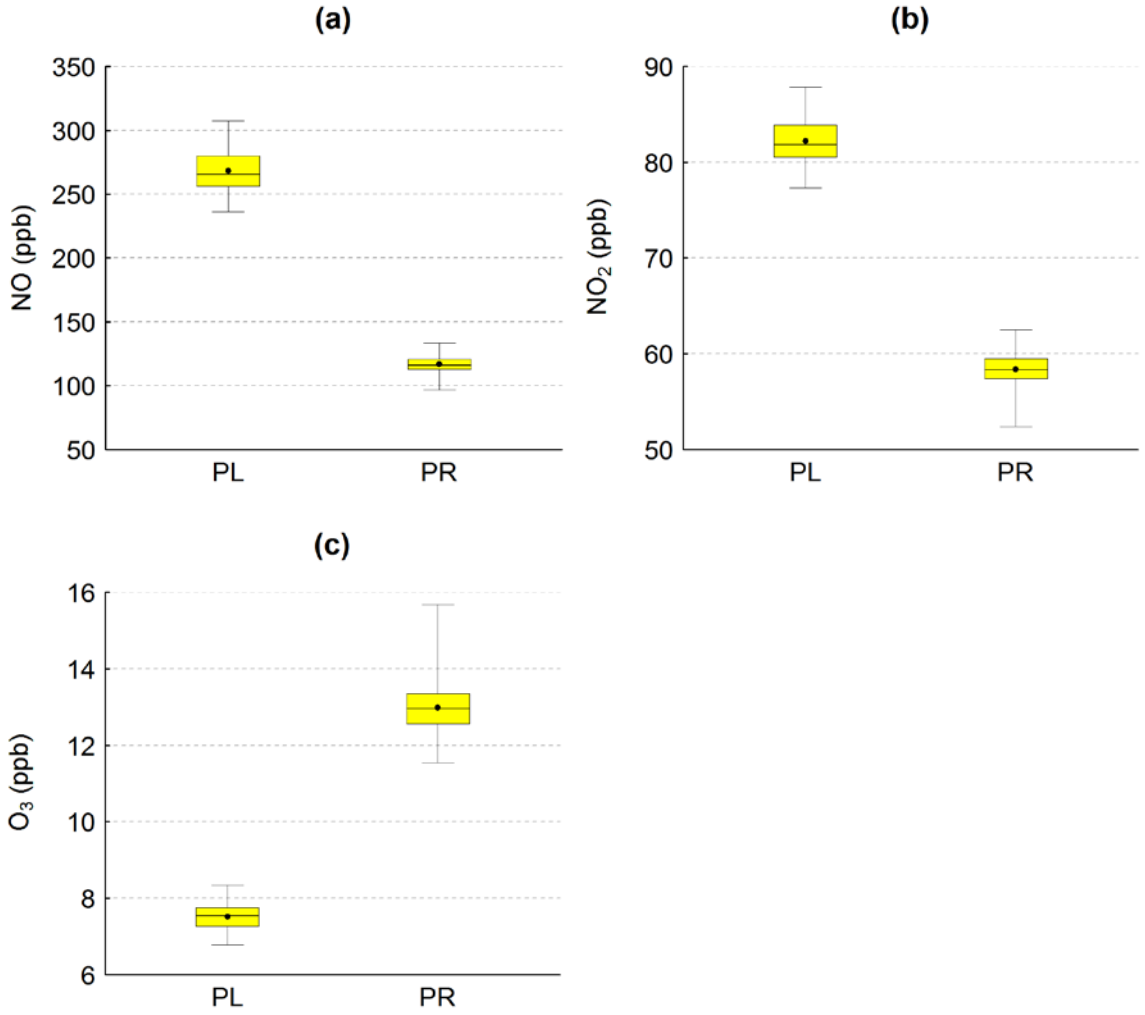

Figure 6·7 - *Box-plots of (a) NO, (b) NO_2 and (c) O_3 mixing ratios with data averaged spatially over the pedestrian left (PL) and pedestrian right (PR) zones and output at 5 s intervals over the last hour of the model simulation ($150 \leq t \leq 210$ min). The dot represents the mean, the bar is the median, the box is the inter-quartile range (25^{th} and 75^{th} percentiles) and the whiskers encompass the minimum and maximum concentrations.*

There is therefore, strong evidence to suggest that pollutant levels of NO and NO_2 are significantly higher (by 151 ppb and 24 ppb on average respectively) toward the lee of the canyon when compared to the windward side, downwind of the emission source in the centre of the street.

O_3 levels are also significantly lower (≈ 5 ppb) toward the leeward wall when compared to the windward wall. Such observations reflect the contribution of primary emissions and their chemical processing (as they are transported from their

street source) together with the exchange of pollutants from within the canyon with the overlying boundary layer that increases toward the windward wall of the canyon.

The high level of variability in O_3 to the right of the canyon is evident once again with mixing ratios greater than or equal to 3 standard deviations higher than the mean observed (albeit on a small number of occasions). There is a clear correlation between NO and NO_2 levels observed on either side of the canyon with peaks in NO_2 coinciding with peaks in NO. The highest levels of NO and NO_2 ($\geq 2\sigma$ from the mean observed) occur toward the end of the 60 minute observational period.

To investigate the underlying statistical distribution of pollutants observed within each pedestrian zone to the left and right of the street canyon further, histograms of the frequency of occurrence versus mixing ratio of NO_2 are presented in Figure 6·8.

It is clear that to the right of the canyon there are two peaks in the frequency histogram for NO_2, thus indicating a bi-modal distribution. Such bi-modality may be explained by both primary emissions and chemical processing raking place within the canyon. The first (higher frequency) peak of approximately 80 ppb is likely to reflect re-circulated pollutants that have undergone mixing and chemical processing within the canyon *i.e.* NO + O_3 titration whilst the secondary higher concentration peak at approximately 84 ppb (observed at a lower frequency) may represent primary NO_2 released in the centre of the canyon.

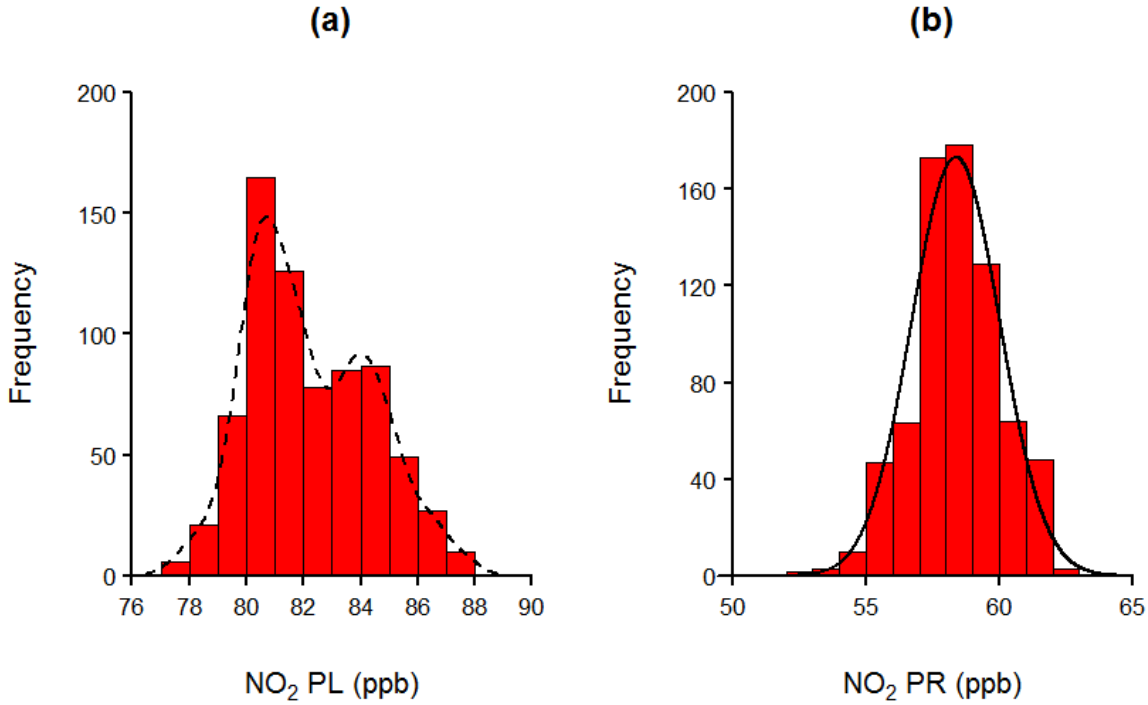

Figure 6·8 - *Frequency histograms of NO_2 mixing ratios (ppb) observed ($150 \leq t \leq 210$ min) on the left (PL) and right (PR) hand sides of the street canyon.*

The statistical distributions of atmospheric pollutants are explored further in Figure 6·9. The primary modes of NO concentrations occur in the lower portion of the histograms at mixing ratios that are less than the mean within the pedestrian left and right zones with a smaller secondary mode observed for the pedestrian left zone that is greater than the mean. Once again, it is evident that both NO and NO_2 concentrations are highest and most variable to the left hand side of the street with an increase in extreme concentrations.

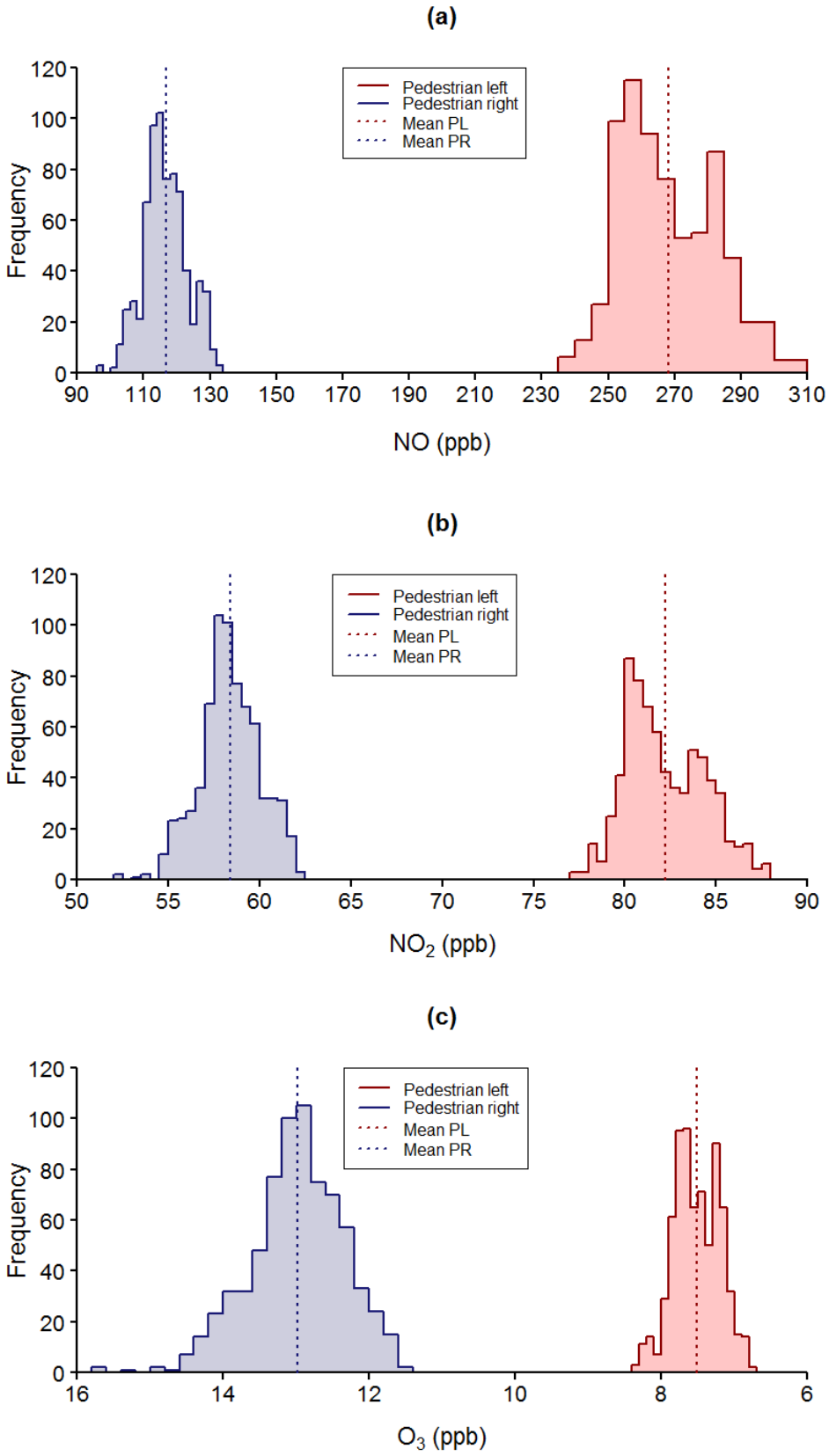

Figure 6·9 - *Frequency histograms of (a) NO (b) NO_2 and (c) O_3 mixing ratios (ppb) for the pedestrian left (PL; red lines) and pedestrian right cases (PR; blue lines). Mean mixing ratios are illustrated by the dashed lines.*

There is also some degree of bimodality observed for O_3 to the left of the street canyon however the peak mode is observed at higher concentrations of O_3 (~ 7.6 to 7.8 ppb) with a secondary mode at slightly lower concentration (~ 7.2 to 7.3 ppb). In this case the distribution of O_3 within the canyon is due solely to mixing and chemical processing within the canyon. The most frequent mode at higher concentrations is likely to be the result of mixing of higher background O_3 values originating from the windward side of the street with the secondary mode at lower concentrations attributable to chemical processing within the canyon.

As shown in Table 6·1, Figure 6·6 and Figure 6·7, the highest concentrations of O_3 are encountered to the right of the canyon with a discernible increase in the spread of mixing ratios indicating its increased variability. An extended tail towards higher O_3 concentrations also indicates the potential increase in exposure to higher O_3 levels, within the pedestrian right zone, that are considerably greater than the mean.

Figure 6·10 shows the statistical distribution of mixing ratios of NO_X and the passive scalar to the left and right of the street canyon. It is clear that bimodality is inherent in the concentrations observed for the passive scalar thereby highlighting the importance of canyon dynamics and emissions in determining the statistical distribution in each case. Once again, the first mode may be attributed to recirculated canyon air that has undergone mixing whilst the secondary mode (at higher concentrations) is likely to be the result of the entrainment of fresh emissions. Toward the windward wall of the canyon where the air is relatively well mixed and there are negligible effects of the street level emission source, the distribution of mixing ratios of the passive scalar is near Gaussian.

When comparing these observations to the underlying NO_X distribution that is subject to the same emissions and mixing, despite the distributions being similar to those of the passive scalar to both the left and right of the canyon, there is a slight shift in the modes to higher concentrations highlighting a slight effect of chemical processing within the canyon in causing a small increase in the modal concentration of NO_X.

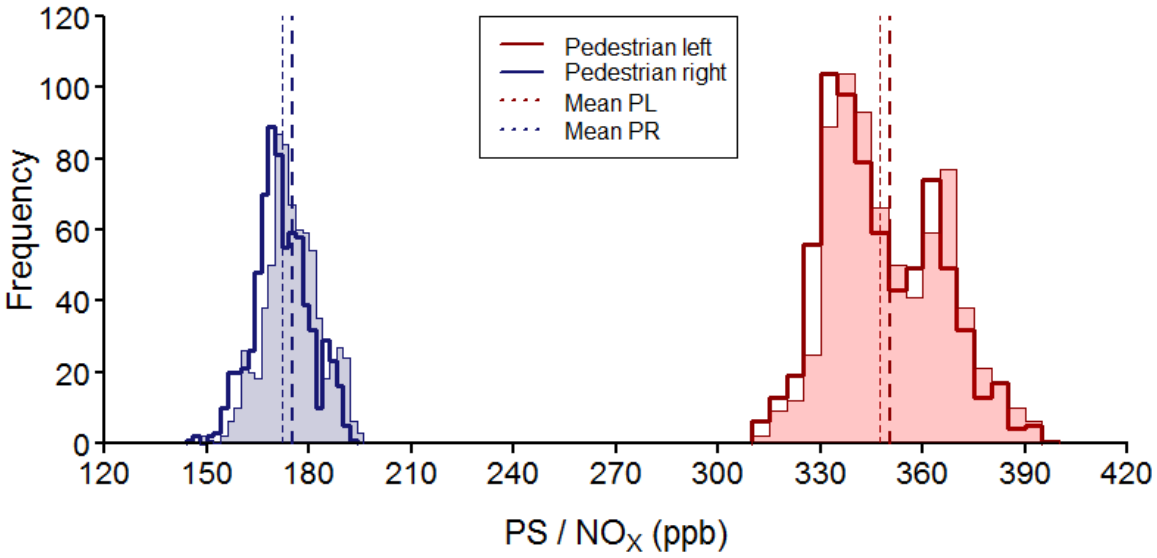

Figure 6·10 - *Frequency histograms of NO_X (filled histograms) and a passive scalar (outlined histogram), mixing ratios (ppb) for the pedestrian left (PL; red lines) and pedestrian right cases (PR; blue lines). Mean mixing ratios for NO_X and P.S. are illustrated by the thin and thick dashed lines respectively.*

In terms of the potential exposure of individuals to these pollutants and the health effects dose-response relationships (see §1·5·1) these results are likely to be of some importance. In addition, the results presented here highlight the importance of the dose-response curve when determining guideline values.

NO + O_3 titration

The extent to which NO + O_3 titration is taking place within limited parts of the canyon domain may be determined by investigating the concentrations of O_3 within individual LES-RCS model cells. As seen in Figure 5·1a, the lowest concentrations of

O_3 are found to the left hand (leeward) side of the street canyon with average levels of O_3 within the pedestrian left region approximately 8 ppb (Table 6·1). The minimum concentrations of O_3 obtained using 5 s output for the last hour of the model simulation ($150 \leq t \leq 210$ min) were calculated for each model cell within the pedestrian left region of the canyon. The lowest O_3 mixing ratio observed was equal to 6.6 ppb for the LES-RCS model cell where $x = 2.7$ m, $y = 2.4$ m, the PDF of which is presented in Figure 6·11.

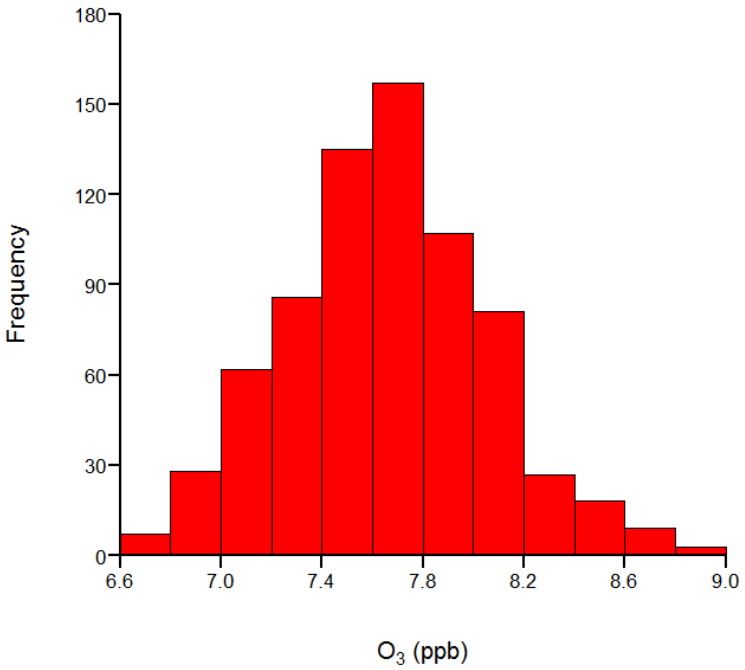

Figure 6·11 - *Frequency histogram of O_3 mixing ratios (ppb) for a single LES-RCS computational cell (left corner of 0.9 m^3 cell at $x = 2.7$ m, $y = 2.4$ m) within the pedestrian left region of the canyon with data obtained over the last hour of the model simulation ($150 \leq t \leq 210$ min).*

Thus, it is clear although there is substantial O_3 titration within this region of the canyon, O_3 is not or even close to being fully titrated on these timescales and under the conditions studied here.

The timescale for O_3 titration can be estimated from its lifetime with respect to reaction with NO:

$$\frac{d[O_3]}{dt} = -k[NO][O_3] = -k'[O_3] \ , \tag{6.2}$$

and

$$k' = k[NO] \ . \tag{6.3}$$

Therefore within the pedestrian left region of the canyon (where NO is highest and O_3 least), $[O_3]$ = 8 ppb, and [NO] = 268 ppb, NO >> O_3, thus the pseudo-first order approach may be applied. Where $k_{[NO + O3]}$ = 4.01×10^{-04} ppb s^{-1} and thus k'=0.107 s^{-1} corresponding to a chemical lifetime for O_3 with respect to reaction with NO of $1/k'$ = 9.3 s.

This timescale is shorter than the mixing timescale of NO emissions within this region of the canyon, thus total O_3 loss does not take place *i.e.* chemical species mixing and chemical processing timescales are comparable and segregation effects may be important. In addition, there is a continuous source of air with higher O_3 mixing ratios brought down into the canyon from the overlying background atmosphere thus preventing full O_3 removal from taking place.

6·3 The effect of varying emissions on canyon atmospheric composition

As discussed in section 3·9 of this thesis, 21 emission scenarios were developed in order to investigate the effect of changing emissions on canyon atmospheric composition. Tables D1 to D5 of Appendix D quantify the emissions applied to the LES-RCS model for each of the scenarios considered, with the equivalent emissions also applied to the box model simulations discussed here.

To investigate further the importance of NO_2 and O_3 sources and sinks in determining the change in concentration of these species within the canyon (for each of the scenarios considered and models evaluated, neglecting transport), the chemical rates of production and loss for the species were considered using time averaged ($150 \leq t \leq 210$ min) mixing ratios of the reactants averaged within the canyon.

6·3·1 Vehicle emissions and average within canyon concentrations

Initially, the effect of changing traffic characteristics on the level of pollutants emitted into the canyon and atmospheric composition is considered, the scenarios for which are introduced in Chapter 3, section 3·9. Table 6·2 includes the mixing ratios of O_3, NO, NO_2 and NO_X averaged over the last hour of the model simulations ($150 \leq t \leq 210$ min) and within the canyon in the case of the LES-RCS.

The worst case scenario in terms of pollutant emitted is case F which represents heavy (2500 vehicles hr^{-1}) and slow moving traffic (10 mph) with NO_X emissions of 2976 ppb s^{-1}. Under this scenario, there is a large and disproportionate increase in average NO and NO_2 for both the LES and box model cases in response to increasing emissions. Average O_3 levels for case F simulated by both models are lower (approximately 34 % for the LES-RCS model) when compared to the base scenario.

Table 6·2 - *Emissions, canyon and time averaged mixing ratios calculated using the LES-RCS and Box model (with the equivalent emissions applied) for the base case pollution scenario and cases A to F. Averages taken over the last hour of the model simulation ($150 \leq t \leq 210$ min).*

Case	Base	A	B	C	D	E	F
Number and speed of vehicles							
Vehicles hr^{-1}	1500	1500	1500	150	150	2500	2500
Speed [mph]	30	10	60	30	10	30	10
Emissions (ppb s^{-1})[**]							
NO_X	1000	1786	1139	100	179	1667	2976
CO	3593	9286	4031	359	929	5989	15476
VOCs	791	2161	577	80	217	1320	3601
Mixing ratio – LES-RCS model (ppb)							
O_3	11.2	9.2	9.8	35	30	8.3	7.4
NO	168	309	199	12.9	22	299	536
NO_2	68	105	70	17.6	26	90	153
NO_X	236	415	268	31	48	389	688
Mixing ratio – Box model (ppb)							
O_3	10.5	9.7	8.8	35	30	8.0	8.2
NO	170	303	204	13.2	23	301	522
NO_2	74	123	74	18.9	28	101	183
NO_X	244	426	279	32	50	402	705
Emissions							
$ENO_{X\text{-}CASE}/ENO_{X\text{-}BASE}$		1.79	1.14	0.10	0.18	1.67	2.98
$ECO_{\text{-}CASE}/ECO_{\text{-}BASE}$		2.58	1.12	0.10	0.26	1.67	4.31
$EVOC_{\text{-}CASE}/EVOC_{\text{-}BASE}$		2.73	0.73	0.10	0.27	1.67	4.55
LES-RCS model							
$[NO_{2\text{-}CASE}/NO_{2\text{-}BASE}]$		1.54	1.03	0.26	0.38	1.32	2.25

In terms of NO_2, Table 6·2 shows that the increase in the within canyon average concentration is not equal to that of raw emissions, highlighting a degree of non-linearity in chemical processing taking place within the canyon. The level of NO_2 within the canyon, averaged over the last 60 minutes of the LES-RCS model

[**] Emitted into one LES model cell (0.3 m × 1 m × 0.3 m).

simulation has increased by 2.3 × (in case F) when compared to the base case scenario, a result of a 3 fold increase in NO_2 emissions within the more polluted environment. As such, primary NO_2 emissions undergo chemical processing within the canyon predominantly through photolysis to form NO and O_3 and to a lesser degree through reaction with OH to form HNO_3.

Similarly for case A, increasing levels of NO and NO_2 and decreasing O_3 were observed in line with increasing emissions of NO_X, CO and VOCs, in comparison with the base case. An increase in the canyon average rate of O_3 production is observed for both cases A and F from 0.62 ppb s^{-1} of the base case to 0.97 ppb s^{-1} for case A and 1.40 ppb s^{-1} for Case F, with this increase fundamentally the result of NO_2 photolysis. This increase however is offset by increases in the loss of O_3 for these high emission cases increasing from 0.75 ppb s^{-1} for the base scenario to 1.14 ppb s^{-1} of case A and 1.60 ppb s^{-1} of case F.

As anticipated, loss of O_3 occurs primarily through the NO + O_3 titration reaction, at close to equivalent rates. Overall for these cases, there is a sink of O_3 with the rate of at which O_3 is removed increasing from 0.17 ppb s^{-1} for case A and 0.20 ppb s^{-1} for case F when compared to the base scenario (0.13 ppb s^{-1}).

In terms of NO_2, for cases A and F, increasing average levels of NO_2 within the canyon can be attributed to an increase in the source term of NO_2 (primarily the result of NO + O_3 titration) under these conditions (0.21 ppb s^{-1} and 0.39 ppb s^{-1} respectively) in comparison to the base scenario (0.15 ppb s^{-1}). Note that for these scenarios (A-F), $f(NO_2)$ was held constant at a value of 0.1, the effect of this assumption is considered further below.

Considering vehicle emissions, the lowest emissions occur when there are less than 150 vehicles per hour, moving at 30 mph (90 % reduction in NO_X, CO and VOCs

when compared to the base case). Under this scenario (case C), there is a substantial decrease in NO_2 (≈ 55 ppb) within the canyon when compared to the base pollution scenario. Decreasing emissions in this case have also elicited a large increase in average O_3 levels within the canyon that are over 3 times that of the base pollution scenario. This is also the case for scenario D where low levels of traffic exist also. Under these scenarios a significant degree of non-linearity is also observed. While NO_X levels largely track emission changes (but with some deviation), the partitioning between NO and NO_2 changes substantially, such that (for example) between the base case and case D, a reduction in NO_X emissions to 18 % of the base case only leads to NO_2 falling to 38 % of the base case value. This non-linearity is summarised across all cases, and discussed further, in section 6·3·8 below.

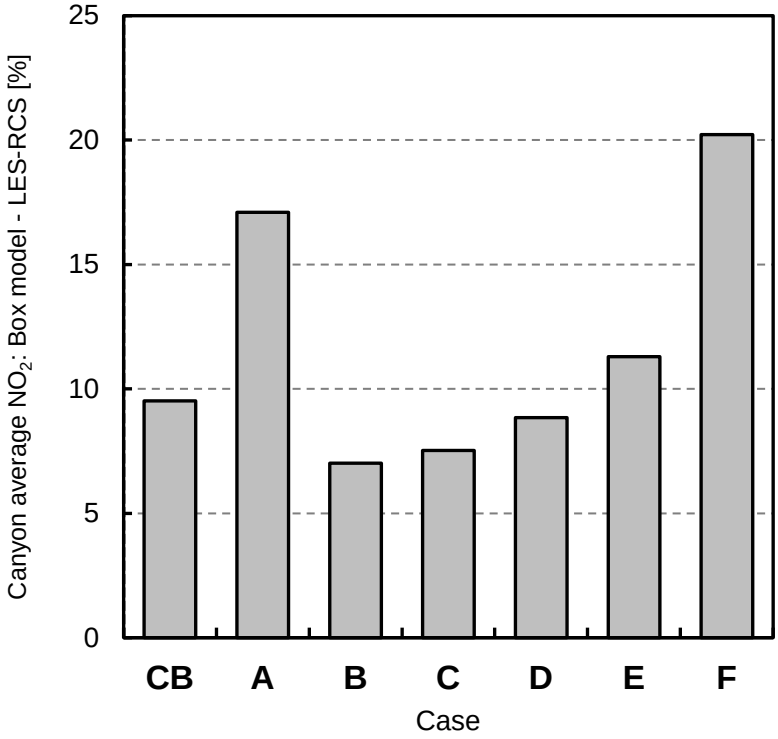

Figure 6·12 - *Percentage difference of NO_2 simulated by the box model and canyon averaged NO_2 simulated by the LES-RCS for the base scenario (CB) and cases A to F. Data output at 5 second intervals over the last hour of the model simulation ($150 \leq t \leq 210$ min).*

For case C, under a low emission scenario, a large reduction in NO_2 levels may be explained by a decrease in its overall rate of change of concentration (production - loss) term from 0.02 ppb s^{-1} for case C when compared to 0.15 ppb s^{-1}. The dominant mechanisms of NO_2 production being NO + O_3 titration (0.18 ppb s^{-1} for case C and 0.75 ppb s^{-1} for the base scenario), only partly offset by the reaction of HO_2 + NO (0.009 ppb s^{-1} and 0.002 ppb s^{-1} for the base case and case C respectively).

An increase in canyon average O_3 levels may be attributed to a decrease in overall O_3 loss term for case C (0.02 ppb s^{-1}) when compared to the base scenario (0.13 ppb s^{-1}). Production of O_3 is higher for the base scenario (0.62 ppb s^{-1}) when compared to case C (0.16 ppb s^{-1}) primarily through NO_2 photolysis. Loss rates of O_3 are higher for the base scenario mainly the result of NO + O_3 titration (0.75 ppb s^{-1} when compared to 0.18 ppb s^{-1} for case C) and to a significantly less extent reaction with NO_2 (0.0006 ppb s^{-1} compared to 0.0005 ppb s^{-1} for case C) and VOCs which is considerably higher for the base scenario (0.0001 ppb s^{-1}) when compared to case C (0.00004 ppb s^{-1}).

For the pollution scenarios considered here, it can therefore be summarised that the lowest within-canyon levels of O_3 are experienced where vehicle emissions have increased and associated NO_2 levels are at their highest.

As shown in Figure 6·12, the largest differences between NO_2 simulated using the zero dimensional box model and the LES-RCS simulations exist for case F and case A *i.e.* those cases in which slow moving traffic leads to the largest amount of vehicular pollutant being released into the canyon domain. Increasing emissions in these cases leads to an overestimation in average NO_2 levels using the zero-dimensional box model when compared to the more realistic LES-RCS model simulations.

As highlighted previously for the base scenario, segregation effects inherent in the LES-RCS model act to reduce the canyon averaged rate of NO + O_3 titration in comparison to the box model due to limited amounts of O_3 in a number of individual model cells. As vehicle emissions increase it is evident that these effects become more pronounced in line with lower O_3 levels for case A and F and an increase in the rate of NO + O_3 titration (1.14 and 1.60 ppb s^{-1} respectively) when compared to the box model (0.75 ppb s^{-1}).

For cases A and F it is also evident that segregation effects have resulted in levels of canyon average O_3 for the LES-RCS model that are between 5 and 10 % lower than the box model. This is explained by an increase in overall loss rates of O_3 as a result of segregation. The loss term of O_3 however is smaller as a result of segregation effects (*e.g.* 1.6 ppb s^{-1} for the LES-RCS when compared to 1.7 ppb s^{-1} of the box model for case F) largely a result of segregation effects on NO + O_3 titration but also the NO_2 + O_3, O_3 + alkene reactions and radical propagation initiated by the OH + VOC reaction.

Conversely, in the case of scenarios C and D where emissions are reduced relative to the base case, a smaller difference between the box model and LES simulations is observed. In these cases less NO is emitted within the canyon, therefore segregation effects become less pronounced in terms of NO + O_3 titration (see section 6·3·7). The smallest difference between the box and LES-RCS models is observed for case B (Figure 6·12). In this case although both NO_X and CO emissions have undergone a slight increase in comparison to the base scenario (approximately 14 % and 12 % respectively) VOC emissions have been reduced (27 %). As a result segregation effects are less pronounced; highlighting the importance of reducing VOC emissions relative to those of NO_X and CO in reducing the effects of incomplete mixing on canyon averaged NO_2 mixing ratios.

6·3·2 The effect of changing proportions of NO_X emitted as NO_2

As discussed in section 1·5·1, technological advances have led to changes in the relative proportion of NO_2 to NO_X emissions with the potential for significant effects of such changes on atmospheric composition. For the base scenario, the proportion of NO_X emitted as NO was equal to 0.9 whilst for NO_2 this was equal to 0.1 (*i.e.* *f*-NO = 0.9; *f*-NO_2 = 0.1). To consider the effect of changing the proportion of NO_X emitted as NO_2 on atmospheric composition, *f*-NO_2 was varied between 0 and 0.3.

Figure 6·13a and b illustrate the spatial variation in mean O_3 and NO_2 levels for the base case scenario and case G within and above the canyon averaged over the last 60 minutes of the LES-RCS model simulation. A significant increase in both O_3 and NO_2 is observed within the canyon for case G with O_3 near street level toward the leeward wall approximately double that of the base scenario.

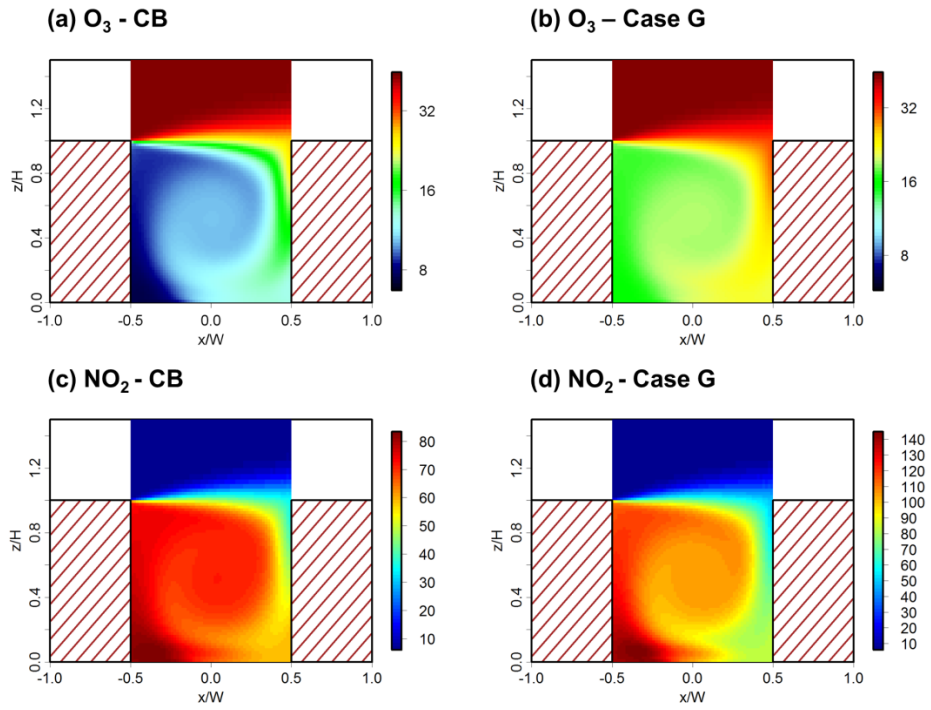

Figure 6·13 - *Mean and time averaged mixing ratios of ozone for (a) the case base scenario (CB) and (b) case G; nitrogen dioxide for (c) the base case scenario and (d) case G. Temporal averages taken over the last hour of the model simulations (150 ≤ t ≤ 210 min). N.B. the increase in the mixing ratios of NO_2 for the equivalent colour scale in (d).*

Table 6·3 illustrates that for scenario G (that represents the case with the highest proportion of NO_X is emitted as NO_2) average within canyon O_3 and NO_2 levels are highest whilst for the case where there are no primary emissions of NO_2 with all NO_X emitted as NO (case I) the mixing ratios of these chemical species is lowest (29 % and 27 % reductions in O_3 and NO_2 when compared to the base case scenario respectively).

Table 6·3 - *Canyon and time averaged mixing ratios calculated using the LES-RCS and Box models (with the equivalent emissions applied) for the base case pollution scenario and cases G to H. Averages taken over the last hour of the model simulation ($150 \leq t \leq 210$ min).*

Case	Base	G	H	I
Fraction of emissions as NO or NO_2				
f-NO	0.90	0.70	0.80	1.00
f-NO_2	0.10	0.30	0.20	0.00
Mixing ratio – LES-RCS model (ppb)				
O_3	11.2	19.7	15.1	8.0
NO	168	132	149	187
NO_2	68	103	86	49
NO_X	236	235	235	236
Mixing ratio – Box model (ppb)				
O_3	10.5	19.4	14.5	7.3
NO	170	134	151	189
NO_2	74	110	92	55
NO_X	244	244	244	244
Emissions				
$ENO_{2\text{-CASE}}/ENO_{2\text{-BASE}}$	3.00	2.00	0.00	
LES-RCS model				
$[NO_{2\text{-CASE}}/NO_{2\text{-BASE}}]$	1.49	1.24	0.74	

Table 6·3 shows that increasing *f*-NO_2 leads to a significant increase in average O_3 levels observed within the canyon with a 76 % increase for scenario G (*f*-NO_2 = 0.3) when compared to the base scenario (*f*-NO_2 = 0.1). Non-linear changes in average

NO_2 and O_3 levels within the canyon are observed as a result of increasing NO_2 emissions.

Such changes in average NO_2 and O_3 levels may be explained by considering changes in rate of production and loss of NO_2 and O_3 in these cases. NO + O_3 titration (that is the predominant source of NO_2) takes place at a considerably higher rate for case G (1.04 ppb s^{-1}) when compared to the base case (0.75 ppb s^{-1}) further increasing NO_2 levels through chemical processing in addition to raw emissions. The O_3 production term is higher for case G (0.95 ppb s^{-1}) when compared to the base case scenario (0.62 ppb s^{-1}), however overall O_3 loss is higher for the later as discussed above due to NO + O_3 titration (0.13 ppb s^{-1} for the base case compared to 0.09 ppb s^{-1} for case G).

Table 6·3 also shows reducing the *f*-NO_2 to 0, results in a disproportionate decrease in both canyon average NO_2 and O_3 when compared to the base case scenario as there is a reduction in primary NO_2, resulting in an overall decrease in average levels and a decrease in the amount of O_3 present within the canyon (through NO + O_3 titration). Despite production of NO_2 increasing for case G through NO + O_3, loss rates of NO_2 have also increased, thereby decreasing overall NO_2 production. Thus increasing or decreasing primary NO_2 emissions has a notable effect on canyon atmospheric composition.

Figure 6·14 shows the differences in average NO_2 observed when simulated using the box and LES-RCS models. The figure shows that the largest differences (in excess of 12 %) between these models arise when there are no primary emissions of NO_2 released into the street canyon, whilst the smallest differences arise when a higher proportion of NO_X is directly emitted as NO_2.

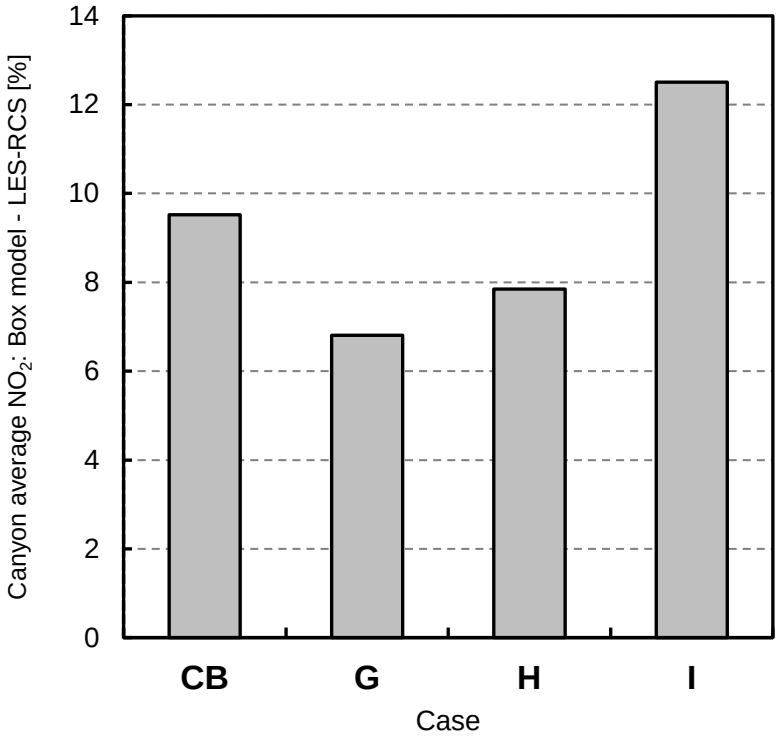

Figure 6·14 - *Percentage difference between NO_2 simulated by the box model and canyon averaged NO_2 simulated by the LES-RCS for the base scenario (CB) and cases G to H. Data output at 5 second intervals over the last hour of the model simulation ($150 \leq t \leq 210$ min).*

This again highlights the effect of segregation on the average rate of NO + O_3 titration and hence NO_2 production, where if there increased levels of NO directly released within the canyon, the effect of limited levels of O_3 within parts of the model domain become more pronounced.

Referring back to Table 6·3, it is evident that increasing f-NO_2 leads to a significant increase in average O_3 levels observed within the canyon (76 % increase for scenario G where f-NO_2 = 0.3 in comparison to the base scenario (f-NO_2 = 0.1)). It is clear that non-linear changes in average within-canyon NO_2 and O_3 levels are observed in response to increasing primary NO_2 emissions.

6·3·3 The potential impacts of emissions of nitrous acid (HONO)

An important consideration relating to atmospheric composition is the potential impact of HONO emissions (from traffic and the use of materials such as self-cleaning window glass) within street canyons. Scenarios J to M consider the effect of such emissions on canyon atmospheric composition. When increasing emissions of HONO, emissions of NO_X were reduced by an equal amount, thus the quantity NO + NO_2 + HONO emitted as molecules are conserved.

Table 6·4 - *Canyon and time averaged mixing ratios calculated using the LES-RCS and Box model (with the equivalent emissions applied) for the base case pollution scenario and cases J to M. Averages taken over the last hour of the model simulation ($150 \leq t \leq 210$ min).*

Case	Base	J	K	L	M
Fraction of emissions as NO, NO_2 or HONO					
f-NO	0.90	0.80	0.80	0.90	0.90
f-NO_2	0.10	0.19	0.15	0.09	0.05
f-HONO	0.00	0.01	0.05	0.01	0.05
Mixing ratio – LES-RCS model (ppb)					
O_3	11.2	15.4	16.7	11.5	12.9
NO	168	147	136	165	152
NO_2	68	86	87	68	71
NO_X	236	233	223	233	224
Mixing ratio – Box model (ppb)					
O_3	10.5	14.9	16.3	10.9	12.3
NO	170	149	137	166	153
NO_2	74	93	94	75	78
NO_X	244	241	232	241	232
Emissions					
$ENO_{\text{-CASE}}/ENO_{\text{-BASE}}$		0.89	0.89	1.00	1.00
$ENO_{2\text{-CASE}}/ENO_{2\text{-BASE}}$		1.90	1.50	0.90	0.50
LES-RCS model					
$[NO_{2\text{-CASE}}/NO_{2\text{-BASE}}]$		1.26	1.28	1.00	1.04

Large increases in both NO_2 and O_3 are observed as a result of increased HONO emissions particularly in the instance where *f*-HONO = 0.05. A decrease in NO is observed with an increasing proportion of HONO emitted (~ 2 % for case L and ~ 9 % for case M) when compared to the base scenario whilst NO_2 shows a slight increase (1 % for case L and 4 % for case M). For case M, increasing HONO emissions has resulted in a 5 fold increase in OH (0.40 ppt for case M) when compared to the reference base case scenario (0.08 ppt) through photodissociation of HONO to form OH and NO.

A slight increase in NO_2 for the cases in which an increasing proportion of NO_2 is emitted as HONO can be attributed to an increase in O_3 levels under these conditions *e.g.* the rate of NO + O_3 reaction (to produce NO_2) increases from 0.75 ppb s^{-1} for the base scenario to 0.79 ppb s^{-1} for case M. In addition, NO_2 production through the HO_2 + NO reaction has also increased to 0.03 ppb s^{-1} when compared to 0.009 ppb s^{-1} of the base scenario. Loss rates of NO_2 also show an increase for case M, mainly due to photolysis (0.67 ppb s^{-1} when compared to 0.62 ppb s^{-1} for the base case), whilst the overall source term for NO_2 increases to 0.18 ppb s^{-1} for case M when compared to 0.15 ppb s^{-1} for the base scenario.

One might expect increasing levels of HONO and hence OH to increase VOC oxidation, thereby increasing NO to NO_2 conversion and thus increasing within canyon levels of NO_2 significantly. Evidence for such an increase in VOC oxidation and hence NO to NO_2 conversion is provided by comparing the average levels of RO_2 (0.13 ppt for the base case and 0.64 for case M) and HO_2 (0.23 ppt for the base case and 0.87 for case M) over the last 60 minutes of the LES-RCS model simulation. However if VOC conditions become limiting the OH + NO_2 $\longrightarrow$ HNO_3 reaction becomes the termination reaction for NO_2, the loss rate of NO_2 through this sink increasing for case M (0.009 ppb s^{-1}) compared to the base case (0.002 ppb s^{-1}).

In line with the increase in NO_2 loss rates discussed above, O_3 production has also increased for case M whilst loss of O_3 has also increased to 0.79 ppb s^{-1} compared to 0.75 ppb s^{-1} for the base scenario through reaction with NO and NO_2 with the resultant overall loss of O_3 slightly lower for case M.

Table 6·4 and Figure 6·16 show that there is a small but significant increase in canyon average O_3 levels as a result of increasing HONO emissions within the canyon. There is an 8 % increase in O_3 where *f*-NO = 0.8 and *f*-HONO increases from 0.01 to 0.05. Where *f*-NO = 0.9, increases in O_3 of 3 % and 15 % are observed for scenario L (*f*-HONO = 0.01) and scenario M (*f*-HONO = 0.05) respectively when compared to the base case (*f*-HONO = 0.00).

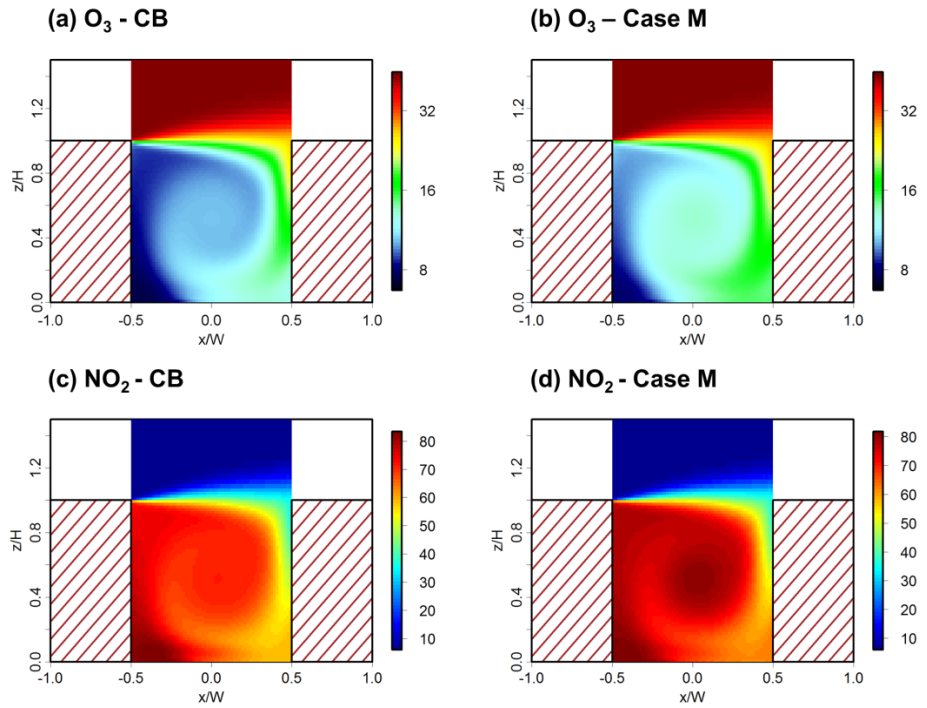

Figure 6·15 - *Mean and time averaged mixing ratios of ozone for (a) the case base scenario (CB) and (b) case M; nitrogen dioxide for (c) the base case scenario and (d) case M. Temporal averages taken over the last hour of the model simulations (150 ≤ t ≤ 210 min).*

Figure 6·15 illustrates the spatial variation in mean O_3 and NO_2 for case M within and above the canyon averaged over the last 60 minutes of the model simulation in

comparison to the base case scenario. When compared to the base emission scenario, O_3 and NO_2 levels are both higher for case M.

The distribution of NO_2 within the canyon has changed for case M with an increase in NO_2 mixing ratios observed within the primary vortex. These observations show that increasing the proportion of NO_X emitted as HONO reduces the amount of NO within the canyon and indicates that HONO (that has a photolysis lifetime of 8 minutes) emissions may not be photolysed completely to OH + NO over the time periods considered here. These changes are also the result of increased OH production with average OH levels observed to be 75 % ($[OH]_{Case\ L}$ = 0.14 ppt) and fourfold ($[OH]_{Case\ M}$ = 0.40 ppt) higher than that of the base case scenario ($[OH]_{Base}$ = 0.08 ppt) in addition to an increase in VOC oxidation and NO to NO_2 conversion (indicated by increases in average RO_2 and HO_2 levels within the canyon for case M). Non-linearity in the chemical processing of emissions is once again evident in the results presented in Table 6·4.

Figure 6·16 shows that NO_2 levels simulated using the box model are higher than the LES-RCS model and that once again, increasing primary NO_2 emissions relative to the base case scenario (cases J and K) reduces the differences in NO_2 observed between each model. Increasing the fraction of NO_2 emitted as HONO in these cases also acts to increase the observed effect of segregation.

When comparing the LES-RCS model results to those of the box model, for the cases where *f*-NO is equal to that of the base scenario, increasing the proportion of NO_2 emitted as HONO can be seen to increase the effects of segregation and thus difference between the box and LES-RCS model simulations (up to 10 % for scenario M) when compared to the base case scenario.

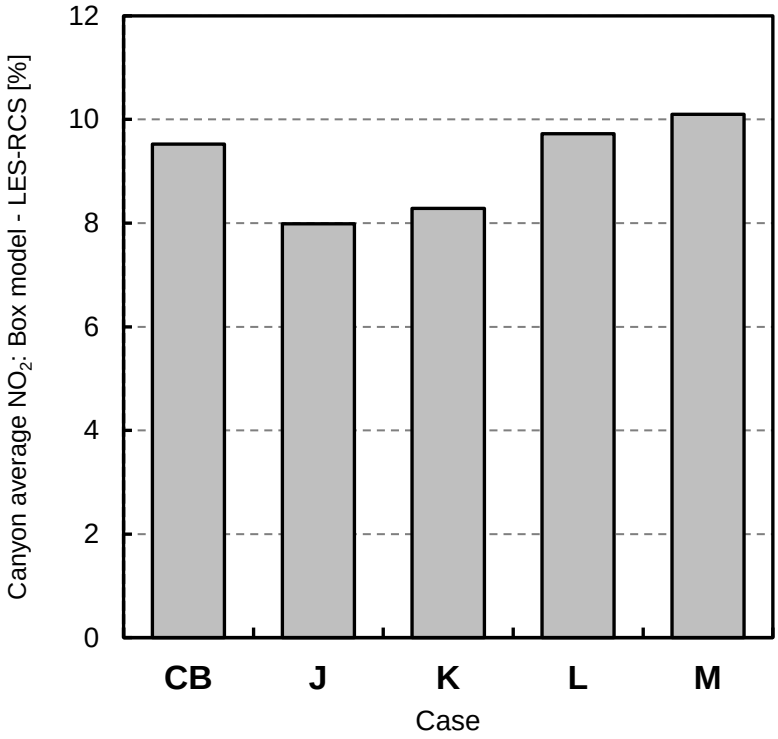

Figure 6·16 - *Percentage difference between NO_2 simulated by the box model and canyon averaged NO_2 simulated by the LES-RCS for the base scenario (CB) and cases J to M. Data output at 5 second intervals over the last hour of the model simulation ($150 \leq t \leq 210$ min).*

6·3·4 The effect of changing VOC to NO_X emission ratios on canyon atmospheric composition

As discussed in §1·6·2, within the wider urban environment, changing the VOC to NO_X ratio has an influence on the O_3 production regime yet within the canyon VOC limited conditions govern. To study the effect of changing NO_X and VOC emissions on O_3 levels within the canyon, a number of emission scenarios were developed in which the VOC to NO_X ratio was varied between 0.4 and 1.6.

Increasing the VOC to NO_X ratio from 0.8 to 1.6 by reducing NO_X emissions by 50 % within the canyon (case Q) leads to a small but significant increase in canyon average O_3 levels (75 %) when compared to the base case scenario (Table 6·5). A corresponding decrease in NO_2 (25 %) is observed for scenario Q when compared to the base case pollution scenario, once more the likely result of NO + O_3 titration.

Table 6·5 - *Emissions, canyon and time averaged mixing ratios calculated using the LES-RCS and Box model (with the equivalent emissions applied) for the base case pollution scenario and cases N to Q. Averages taken over the last hour of the model simulation (150 ≤ t ≤ 210 min).*

Case	Base	N	O	p	Q
VOC to NO_X emission ratio					
VOC ×	1	1	2	0.5	1
NO_X ×	1	2	1	1	0.5
VOC / NO_X	0.79	0.40	1.58	0.40	1.58
Emissions (ppb s^{-1})[††]					
NO_X	1000	2000	1000	1000	500
VOCs	791	791	1586	396	791
Mixing ratio – LES-RCS model (ppb)					
O_3	11.2	8.4	14.0	10.5	20
NO	168	348	153	172	69
NO_2	68	109	80	64	50
NO_X	236	457	233	236	120
Mixing ratio – Box model (ppb)					
O_3	10.5	6.2	14.5	9.4	20
NO	170	384	150	177	68
NO_2	74	99	91	68	57
NO_X	244	483	241	245	125
Emissions					
$ENO_{X\text{-}CASE}/ENO_{X\text{-}BASE}$	2.00	1.00	1.00	0.50	
$EVOC_{\text{-}CASE}/EVOC_{\text{-}BASE}$	1.00	2.01	0.50	1.00	
LES-RCS model					
$[NO_{2\text{-}CASE}/NO_{2\text{-}BASE}]$	1.60	1.18	0.94	0.74	

When considering the nature of the response of average within canyon concentrations to increased emissions of VOCs or NO_X it is once again evident that there is a high level of non-linearity observed in the case of NO_2 when compared to raw emissions.

[††] Emitted into one LES model cell (0.3 m × 1 m × 0.3 m).

An 18 % increase in within canyon levels of NO_2 in addition to a 25 % increase in O_3 was observed for case O, whilst NO has decreased by 10 % due to altered NO/NO_2 partitioning as a result of higher O_3 levels. For case O, the overall rate of NO_2 production has increased to 0.17 ppb s^{-1} in comparison to that of the base case of 0.15 ppb s^{-1} with increases in production of NO_2 have resulted from increasing the rates of the NO + O_3 and HO_2 + NO reactions. Photolysis of NO_2 is also enhanced for case O increasing its loss when compared to the base scenario whilst contributing to a slight decrease in the overall loss rate of O_3 in this case (0.129 ppb s^{-1}) when compared to the base scenario (0.133 ppb s^{-1}).

The highest loss rates of O_3 result through reaction with NO and NO_2 in addition to reaction with alkenes (increasing to 0.0003 ppb s^{-1} from 0.0001 ppb s^{-1} of the base case). Despite the effect of increasing removal of O_3 through reaction with increased alkene emissions, RO_2 radicals derived from VOC oxidation (canyon average RO_2 levels of 0.13 ppt for the base case and 0.50 for case O) remain dominant in increasing NO to NO_2 conversion (in comparison to the base case) and hence subsequently increasing O_3 production through NO_2 photolysis.

Figure 6·17 shows that the largest differences between the box and LES-RCS models are observed for cases O and Q *i.e.* those in which the VOC/NO_X emission ratio has increased relative to the base scenario.

In terms of case O, VOC emissions have been doubled when compared to the base case scenario. The effect of increasing VOC emissions upon increasing NO_2 levels is over-estimated by the zero-dimensional box model, highlighting the role of segregation in reducing the effective rate at which radical propagation occurs (initiated by the OH + VOC reaction) and alkenes react to form NO_2.

In a similar manner, for case Q, where NO_X emissions have been halved whilst VOC emissions are maintained (relative to the base case), segregation effects result in a larger differences in the amount of canyon average NO_2 relative to the box model simulation.

In terms of case N where NO_X emissions are doubled when compared to the base case scenario, there is a larger increase in canyon averaged NO_2 for the LES-RCS model when compared to box model simulation. Thus under such high NO_X conditions, segregation effects act to increase the rate of NO_2 production whilst maintaining higher O_3 levels and reducing NO when compared to the box model in this case.

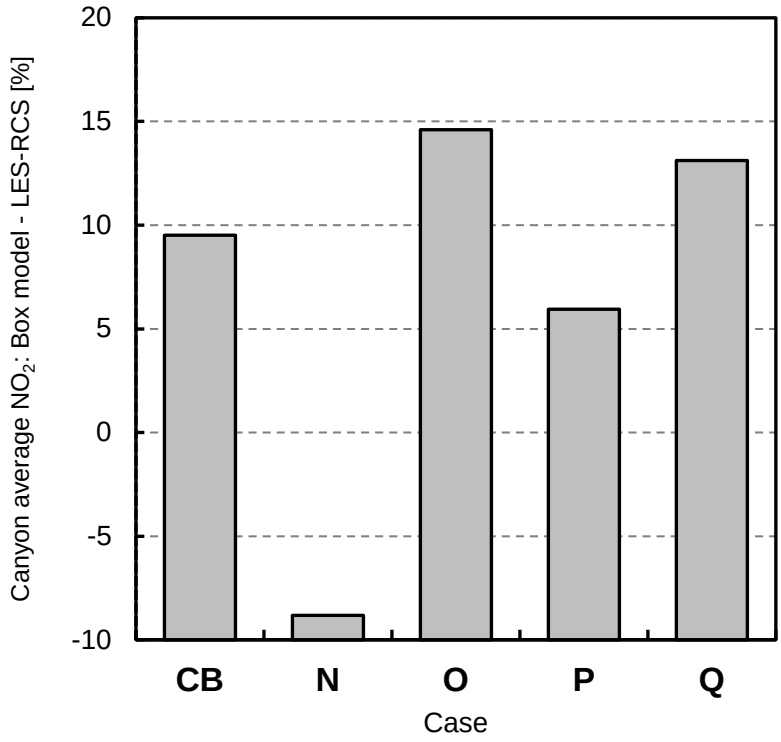

Figure 6·17 - *Percentage difference between NO_2 simulated by the box model and canyon averaged NO_2 simulated by the LES-RCS for the base scenario (CB) and cases N to Q. Data output at 5 second intervals over the last hour of the model simulation ($150 \leq t \leq 210$ min).*

When considering the most important processes involved in NO_2 production or loss under this scenario, for both models, there is a discernible increase in NO + O_3

titration for the LES-RCS model (1.17 ppb s^{-1}) when compared to the box model (0.96 ppb s^{-1}) with both production and loss rates higher for the former and overall production of NO_2 increased to 0.20 ppb s^{-1} for the LES-RCS simulation when compared to the box model (0.05 ppb s^{-1}).

6·3·5 -The effect of changing fleet composition

Table 6·6 shows that changing the fleet composition has a significant impact on emissions of NO_X; CO and VOCs.

Table 6·6 - *Emissions, canyon and time averaged mixing ratios calculated using the LES-RCS and Box model (with the equivalent emissions applied) for the base case pollution scenario and cases R to S. Averages taken over the last hour of the model simulation (150 ≤ t ≤ 210 min).*

Case	**Base**	**R**	**S**
Year	2010	2015	2025
Emissions (ppb s^{-1})‡‡			
NO_X	1000	642	322
CO	3593	3250	3797
VOCs	791	662	812
Mixing ratio – LES-RCS model (ppb)			
O_3	11.2	15.4	27.7
NO	168	98	38
NO_2	68	55	41
NO_X	236	153	79
Mixing ratio – Box model (ppb)			
O_3	10.5	14.8	30.2
NO	170	99	36
NO_2	74	60	46
NO_X	244	160	82
Emissions			
$ENO_{X\text{-}CASE}/ENO_{X\text{-}BASE}$		0.64	0.32
$ECO_{\text{-}CASE}/ECO_{\text{-}BASE}$		0.90	1.06
$EVOC_{\text{-}CASE}/EVOC_{\text{-}BASE}$		0.84	1.03
LES-RCS model			
$[NO_{2\text{-}CASE}/NO_{2\text{-}BASE}]$		0.81	0.60

‡‡ Emitted into one LES model cell (0.3 m × 1 m × 0.3 m).

A substantial reduction in NO_X emissions is anticipated for the 2015 and 2025 vehicle fleets with the largest reduction achieved in the latter case. The 2025 fleet however shows an increase in CO and VOC emissions when compared to the conditions simulated under the base and case S scenarios. The reduction in NO_X emissions for cases R and S is evident in reduced canyon average levels of NO and NO_2 of 77 % and 40 % respectively when compared to the base scenario whilst a significant increase in O_3 (2.5 times that of the base scenario for case S) is observed.

Decreasing emissions of NO_X, CO and VOCs for case R has resulted in a small increase in O_3 and decrease in NO_2, as a result of lower levels of NO and VOCs to titrate O_3 and less NO_2 production through these processes. Decreasing NO_X emissions further whilst increasing VOCs and CO for case S has resulted in an increase in canyon average O_3 levels whilst decreasing NO_2, a likely result of a reduced rate of NO + O_3 titration and therefore an increase in O_3 levels. Increasing VOC emissions will also act to increase the rate at which at which radical propagation and O_3 + alkene reactions occur, however these have a considerably smaller effect upon O_3 concentrations when compared to NO + O_3 titration.

Figure 6·18 illustrates the differences in simulated NO_2 levels between the box model and LES-RCS model simulations. It is clear that the largest difference is observed for case S *i.e.* where NO_X emissions have decreased whilst CO and VOCs have increased. Thus segregation effects are once again contributing to a decreased in the average rate of NO_2 formation through NO + O_3 titration.

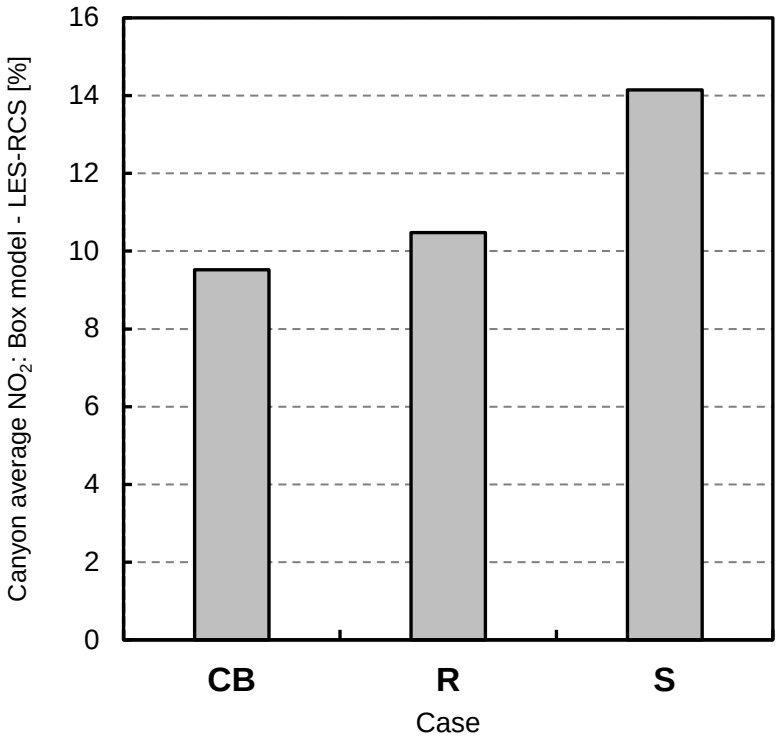

Figure 6·18 - *Percentage difference between NO_2 simulated by the box model and canyon averaged NO_2 simulated by the LES-RCS for the base scenario (CB), cases R and S. Data output at 5 second intervals over the last hour of the model simulation ($150 \leq t \leq 210$ min).*

6·3·6 Changing urban background conditions

As discussed in Chapter 3 (§3·9), a number of scenarios were developed in which the background concentrations of pollutants in the overlying urban boundary layer were varied. In addition to the TORCH campaign data used to represent the base case (§3·6), scenarios representative of more and less polluted conditions were devised using select periods of the campaign.

Table 6·7 and Figure 6·19 show that in terms of O_3 the worst case scenario is that of the polluted case where O_3 shows a significant increase (96 %) when compared to the base case scenario whilst a decrease in O_3 of 33 % is observed for the less polluted cleaner background conditions where there is a decrease in O_3 rich air mixed down into the canyon. These large changes in within canyon O_3 reflect the significant influence of background changes of O_3.

Table 6·7 - *Canyon and time averaged mixing ratios calculated using the LES-RCS and Box model (with the equivalent emissions applied) for the base case pollution scenario (non heatwave background conditions (NHW)), cases T (polluted, heatwave background conditions (HW)) and case U (less polluted conditions (LPC)). M.R. refers to mixing ratio (ppb). Averages taken over the last hour of the model simulation (150 ≤ t ≤ 210 min).*

Case	**Base**	**T**	**U**	**Case**	**Base**	**T**	**U**
C_B (ppb)	NHW	HW	LPC		NHW	HW	LPC
CH_4	1800	1800	1800				
O_3	40	80	20	**Mixing ratio – LES-RCS model (ppb)**			
CO	200	300	200	O_3	11.2	21.9	7.5
NO	2	2	1	NO	168	136	182
NO_2	8	12	7	NO_2	68	102	52
HNO_3	2	2	2	NO_X	236	238	234
C_2H_4	0.91	1.54	0.91				
C_3H_6	0.29	0.42	0.29				
HCHO	3.14	5.93	3.14	**Mixing ratio – Box model (ppb)**			
CH_3CHO	2.98	5.46	2.98	O_3	10.5	19.4	7.5
C_5H_8	0.28	0.70	0.28	NO	170	138	184
CH_3OH	7.38	9.17	7.38	NO_2	74	109	58
C_2H_5OH	2.37	5.13	2.37	NO_X	244	247	242
PAN	0.46	1.16	0.46				
k'_{OH}	3.413	6.628	3.413				

A significant increase in NO_2 (51 %) is evident in the more polluted conditions relative to the base scenario whilst under the less polluted conditions, NO_2 levels decreases by 24 %.

For case T, the increase in NO_2 arises under heat-wave conditions in which background levels of O_3, CO, NO_2 and VOCs have increased. In terms of NO_2 although there is a small increase in background levels from 4 ppb to 12 ppb, there is a significant increase in NO_2 observed within the canyon (34 ppb) despite emissions into the canyon being equal to the base case scenario. An increase in O_3 within the canyon in this case is likely to have contributed to a large increase in

NO_2 observed also indicated by a decrease in NO that demonstrates the importance of NO + O_3 titration in this case.

For case T, a large increase in NO_2 production is observed particularly through NO + O_3 titration (1.2 ppb s^{-1}) when compared to the base case scenario (0.75 ppb s^{-1}). Despite increasing loss rates for case T (overwhelmingly through photo-dissociation of NO_2), there remains an overall increase in NO_2 production (to 0.27 ppb s^{-1}) from the base scenario (0.15 ppb s^{-1}. For case U, there is a decrease in the overall rate of NO_2 production (0.09 ppb s^{-1}) primarily the result of a decreasing rate of NO + O_3 reaction whereas the rate of production through HO_2 + NO reaction exhibits a slight increase in this instance.

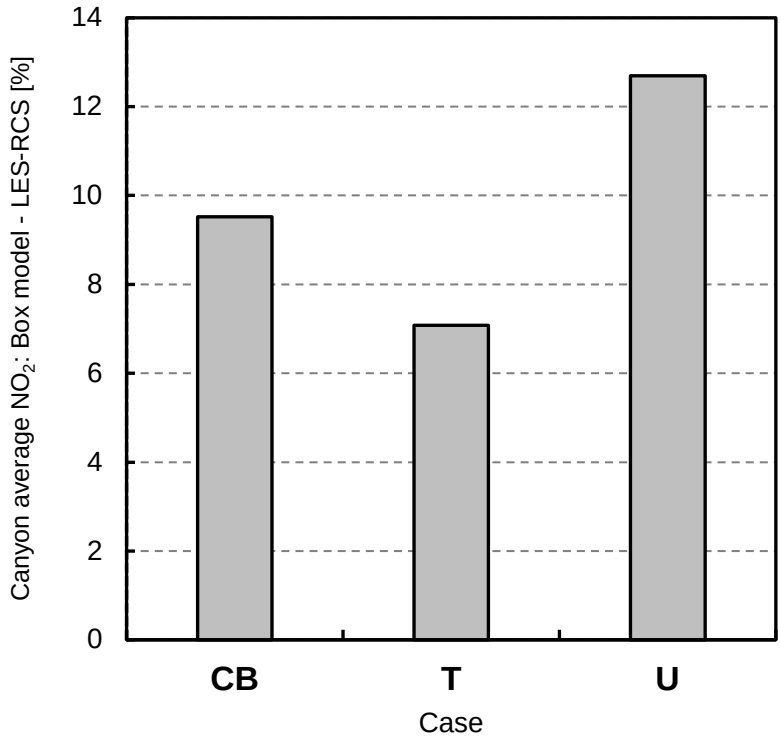

Figure 6·19 - *Percentage difference between NO_2 simulated by the box model and canyon averaged NO_2 simulated by the LES-RCS for the base scenario (CB), cases T and U. Data output at 5 second intervals over the last hour of the model simulation ($150 \leq t \leq 210$ min).*

Figure 6·19 shows that under heat wave (more polluted) conditions (case T) there is a reduction in the difference between the box model and LES-RCS model simulations

relative to the base scenario and hence a reduction in the effect of segregation under these conditions a result of an increase in O_3 within the canyon due to increased background levels.

Conversely, when there are lower background levels of pollution a larger effect of segregation is observed, likely to be a reflection of the effect of reducing above canyon levels of O_3, thus within some regions of the model domain O_3 concentrations will be limited and thus further reduce the effective rate of NO + O_3 reaction.

6·3·7 Emission scenarios and segregation effects

In terms of segregation, the largest effects on canyon average NO_2 are observed for cases A and F where the box model simulations are 17 and 20 % higher than the LES-RCS model Table 6·8. Under these conditions emissions of NO_X, CO and VOCs have increased relative to the base case scenario.

Table 6·8 - *Canyon and time averaged NO_2 mixing ratios calculated using the LES-RCS and Box model (with the equivalent emissions applied) for the base case pollution scenario (non heatwave background conditions (NHW)), cases T (polluted, heatwave background conditions (HW)) and case U (less polluted conditions (LPC)). M.R. refers to mixing ratio (ppb). Averages taken over the last hour of the model simulation ($150 \leq t \leq 210$ min).*

	CB	**A**	**B**	**C**	**D**	**E**	**F**	**G**
% Box-LES-RCS	9.5	17.1	7.0	7.5	8.8	11.3	20.2	6.8
	H	**I**	**J**	**K**	**L**	**M**	**N**	**O**
% Box-LES-RCS	7.8	12.5	8.0	8.3	9.7	10.1	-8.8	14.6
	P	**Q**	**R**	**S**	**T**	**U**		
% Box-LES-RCS	6.0	13.1	10.5	14.1	7.1	12.7		

As discussed above, increasing NO_X emissions may result in an increase in the effect of segregation on NO + O_3 titration, a result of decreasing average canyon O_3 and increasing NO_X in these cases. In addition an increase in VOCs emitted also enhances the effect of segregation reducing the effective rate at which radical propagation and O_3 + alkene reactions take place in the case of the LES-RCS.

The smallest difference between NO_2 levels simulated using the box and LES-RCS models is observed for scenario P where primary emissions of VOCs are reduced to 50 % of that of the base case scenario (*i.e.* 396 ppb s^{-1} of VOCs is emitted into one LES-RCS model cell). As all other emission conditions are the same as those for the base case scenario, the smaller difference between model simulations provides further evidence of the role of segregation in predominantly reducing the rate at which radical propagation and the O_3 + alkene reactions occur. For this case, individual production and loss rates of NO_2 calculated using both the LES-RCS and box model simulations are similar mainly due to a decrease in the rate of NO + O_3 for the box model case when compared to the base case scenario. In additions there is a considerably smaller difference in the rate of radical propagation and O_3 + alkene reactions between each model for case P when compared to the base scenario.

For case N, the average concentration of NO_2 within the canyon is approximately 9 % higher for the LES-RCS model simulation when compared to the box model. In this case, NO_X emissions have been doubled and segregation effects act to increase the rate of NO_2 production primarily through the NO + O_3 → NO_2 + O_2 reaction in this case in comparison to the box model simulation.

6·3·8 Chemical processing of emissions within the canyon

The variation in within canyon processing under different emission scenarios is addressed here with the level of pollution escaping from the canyon to the wider urban atmosphere reflecting the combined effects of primary emissions and chemical processing on pollutant levels. The calculated resolved-scale flux (§5·3·5) is used to determine a representative flux of pollutants into the background atmosphere overlying the street canyon. Table 6·9 illustrates the flux of NO, NO_2, O_3, NO_X, and O_X calculated at $z = z_f = 0.933\ H$ (unless otherwise stated) in order to minimise the contribution of sub-grid scale dispersion (§5·3·5).

Table 6·9 - *The total flux (ppb m^{-2} s^{-1}) at $z = z_f = 0.933\ H$ (unless otherwise stated) and emissions (ppb s^{-1}) into one LES model cell (0.3 m × 1 m × 0.3 m) within the canyon for the base case pollution scenario, case F (slow moving, heavy traffic) and case K (f-HONO = 0.05; where NO_X emissions include HONO). Averages taken over the last hour of the model simulation (150 ≤ t ≤ 210 min).*

Case	Base	F	K	Base	F	K	Base	F	K
	(a) Flux (ppb m^{-2} s^{-1})			(b) Emissions (ppb s^{-1})[§§]			[(a) - (b)] / (b) (%)		
NO	752	2385	610	900	2678	800	-17	-11	-24
NO_2[***]	248	574	334	100	298	150	149	93	123
NO_X	989	2935	939	1000	2976	1000	- 1.1	-1.4	-1.2
O_3[†††]	-135	-145	-116	—	—	—	—	—	—
O_X	130	464	235	100	298	150	30	56	57
HONO	—	—	—	—	—	50	—	—	—

The flux of pollutants observed for the base case scenario has been discussed in detail in section §5·3·5. Here, comparison is made to a number of selected cases including case F (slow moving heavy traffic), and case K (where a proportion of primary NO_2 emissions are released as HONO).

[§§] Emitted into one LES model cell (0.3 m × 1 m × 0.3 m).
[***] Total flux of NO_2 calculated at $z_f = 0.983\ H$.
[†††] Total flux of O_3 calculated at $z_f = 1.016\ H$.

As shown in §5·3·5, the flux of O_3 is negative *i.e.* downwards into the canyon from the overlying background atmosphere even where the highest levels of O_3 within the canyon domain are present. The largest flux of O_3 is observed for case F in which average within canyon concentrations are lowest when compared to the other scenarios evaluated.

When considering slow moving heavy traffic (case F) there is a decrease in the total flux of NO out of the canyon when compared to raw emissions however this difference is less pronounced than that observed for the base case. When compared to raw emissions, the total flux of NO_2 out of the canyon in case F represents an approximate 93 % increase. The most notable difference between the base case scenario and case F is observed in the percentage difference between O_X and raw NO_2 emissions whilst the amount of NO_X released compared to raw emissions remains almost equal. In both cases there is a large increase in the difference between the flux of O_X out of the canyon when compared to primary emissions of NO_2.

For case F the level of O_X escaping from the canyon is 55.7 % higher than the 298 ppb of NO_2 emitted, thus highlighting the importance of chemical processing taking place within the canyon prior to release into the background atmosphere. These findings are also likely to reflect differences in NO + O_3 titration under the different scenarios considered In terms of case K, despite NO_X release being almost equivalent to that emitted there is a large increase in O_X released into the atmosphere compared to raw emissions of NO_2 equal to 150 ppb.

When examining the average within canyon concentrations for case F (Table 6·2), the increase in O_X relative to the base case scenario is the result of increasing NO_2 as O_3 levels have decreased. When considering the rate of production and loss of NO_2

(calculated for OH in §5·3·1), NO + O_3 driven NO_2 production increases with increasing NO emissions (1.60 ppb s^{-1} when compared to 0.75 ppb s^{-1} of the base case) and the NO_2 source increasing by a factor of 4.8 when going from the base scenario to case F. In addition, there is a significant increase in the rate of NO_2 production through the reaction: NO + NO ⟶ NO_2 + NO_2 (0.00151 ppb s^{-1} for case F when compared to 0.00015 ppb s^{-1} of the base case) with this source of NO_2 for case F increasing by over a factor of 20 in comparison to the base scenario.

In spite of the difference between the total flux of NO_2 out of the canyon when compared to raw emissions being lower for case K than the base case, the difference between the flux of O_X out of the canyon and raw emissions of NO_2 is considerably higher (56.7 %). Table 6·9 shows that for the more polluted scenarios there is a large change in the percentage difference between the flux of pollutants out of the canyon when compared to the base scenario. Whilst the flux of O_X out of the canyon compared to raw emissions increases in both of these cases, the flux of NO_2 compared to raw emissions is reduced.

Inter-comparison of scenarios

To intercompare the scenarios considered in the preceding sections, Figure 6·20 shows the ratio of emissions of NO_2 for each case to NO_2 for the base scenario plotted against the ratio average canyon averaged NO_2 levels (simulated by the LES-RCS model) for each case when compared to the base scenario.

Figure 6·20 illustrates that there are a number of pollution scenarios which have resulted in significant increases in NO_2 relative to the base case. In terms of health effects and policy-making it is these scenarios that are considered most important. Significant increases in canyon average NO_2 are observed for cases F, A, N, T and G (discussed in detail above).

In terms of case A, an increase in emissions of NO_X, CO and VOCs as a result of decreasing the average speed of traffic to 10 mph compared to 30 mph as simulated in the base case has contributed to an increase in within canyon NO_2 of 54 % (primary emissions increasing by 78 %). In contrast, for case N, primary emission of NO_X were doubled (ENO_X = 2000 ppb s^{-1}; ENO_2 = 200 ppb s^{-1} emitted into one LES-RCS model cell) whilst emissions of CO and VOCs were held as those specified for the base case scenario. Under these conditions, within canyon NO_2 levels simulated by the LES-RCS exhibit a 60 % increase. Therefore comparing cases A and N, a larger increase in primary emissions of NO_2 (20 % higher for the latter) leads to only a slight increase in NO_2 of 4 ppb for case N over case A, thus the effect of the additional increase in emissions of CO and VOCs in case A is deemed important in determining within canyon NO_2 levels.

For case T and G in addition to an increase in NO_2, O_3 which is also a concern in terms of health effects has also shown a considerable increase ≥ 70 % higher than the base case scenario.

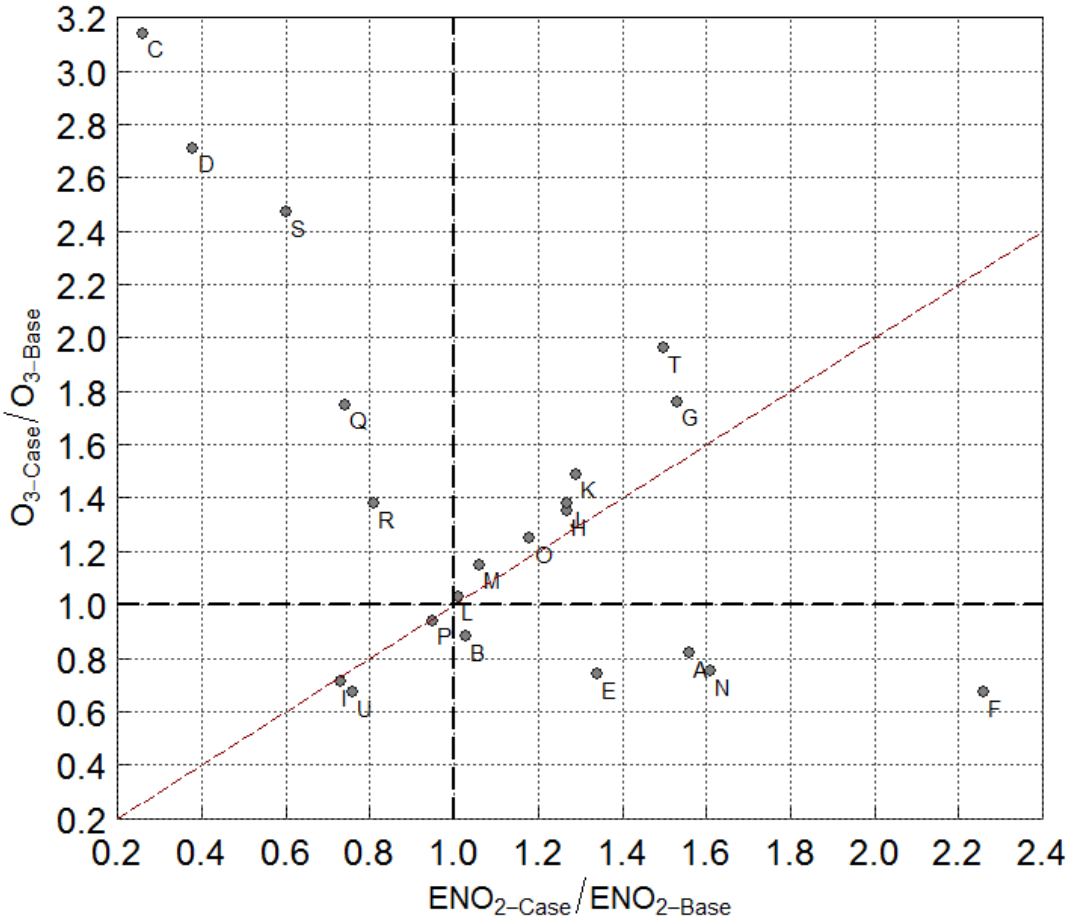

Figure 6·20 - *Scatter plot of the ratio of NO_2 emissions for each scenario to NO_2 emissions of the base scenario against the ratio of average within-canyon concentration of O_3 for each case to the base scenario as simulated by the LES-RCS model and over the last hour of the model simulation ($150 \leq t \leq 210$ min). The red dashed line represents a 1:1 ratio.*

The different scenarios considered above have been integrated by plotting the modelled canyon and time averaged ($150 \leq t \leq 210$ min) levels of NO_X, NO_2 and O_3, relative to the base case, as a function of the emitted NO_X ratio, relative to the base case, for both the box model and LES-RCS methodologies (see Figure 6·21 to Figure 6·23). These figures include those runs with altered $f(NO_2)$, HONO emissions and differing background concentrations — as labelled.

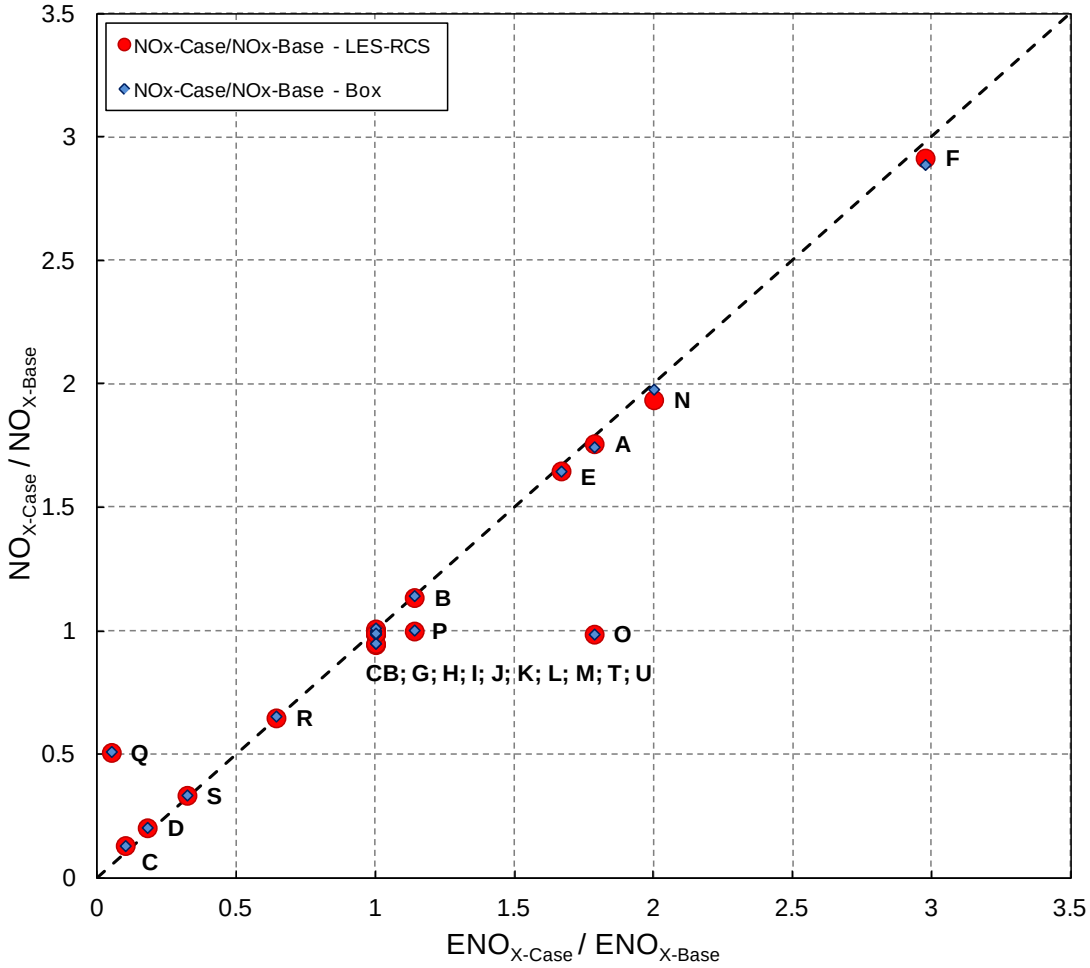

Figure 6·21 - *Scatter plot of the ratio of NO_X emissions for each scenario to NO_X emissions of the base scenario against the ratio of average within-canyon concentration of NO_X for each case to the base scenario as simulated by the LES-RCS model and over the last hour of the model simulation ($150 \leq t \leq 210$ min). The black dashed line represents a 1:1 ratio.*

Figure 6·21 shows that across all scenarios there is a near-uniform increase in canyon-average NO_X levels with those emitted, however some deviations from the 1:1 line are apparent, resulting from chemical transformation of NO_X into other forms of NO_y such as HNO_3, as shown in Table 6.9, which summarises the conservation of NO_X and O_X for selected scenarios.

When considered in more detail however (Figure 6·22 and Figure 6·23), differences in behaviour for NO_2 and O_3 are apparent.

For NO_2, concentrations increase at a lower rate (with a lower gradient with respect to $ENO_{X\text{-}Case}$/ $ENO_{X\text{-}Base}$) than those of NO_X, that is, the modelling predicts that within-canyon NO_2 concentrations show a less-than-unity dependence upon emitted NO_X. NO_2 levels are in general lower (at higher emitted NO_X) for the LES-RCS than the box reflecting segregation limitations upon O_3 mediated NO-to-NO_2 conversion.

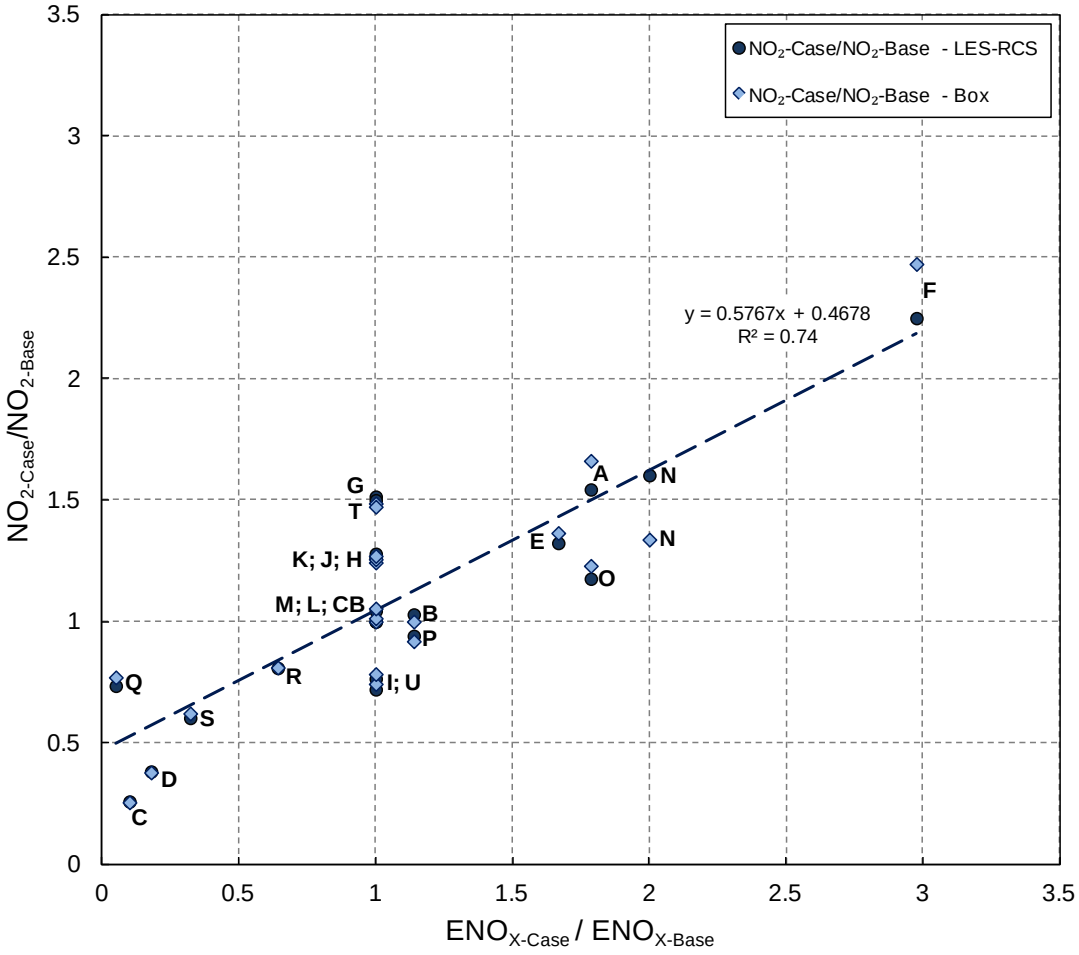

Figure 6·22 - *Scatter plot of the ratio of NO_X emissions for each scenario to NO_X emissions of the base scenario against the ratio of average within-canyon concentration of NO_2 for each case to the base scenario as simulated by the LES-RCS model and over the last hour of the model simulation ($150 \leq t \leq 210$ min). The blue dashed line represents a linear fit applied to the LES-RCS modelled ratio of $NO_{2\text{-}Case}/NO_{2\text{-}Base}$.*

For O_3, an inverse relationship with NO_X emissions is observed as anticipated (when considering the NO + O_3 = NO_2 + O_2 process); however substantial curvature is evident — at the lowest NO_X levels. This reflects the importance of this process in

governing O_3 levels within the canyon under low NO_X conditions. For cases G, I, T and U large deviations a linear response of O_3 to changing NO_X emissions are observed highlighting the importance of both changing the proportion of primary NO_2 emissions within the canyon (cases G and I) and background sources of O_3 from outside the canyon in determining canyon average O_3 levels.

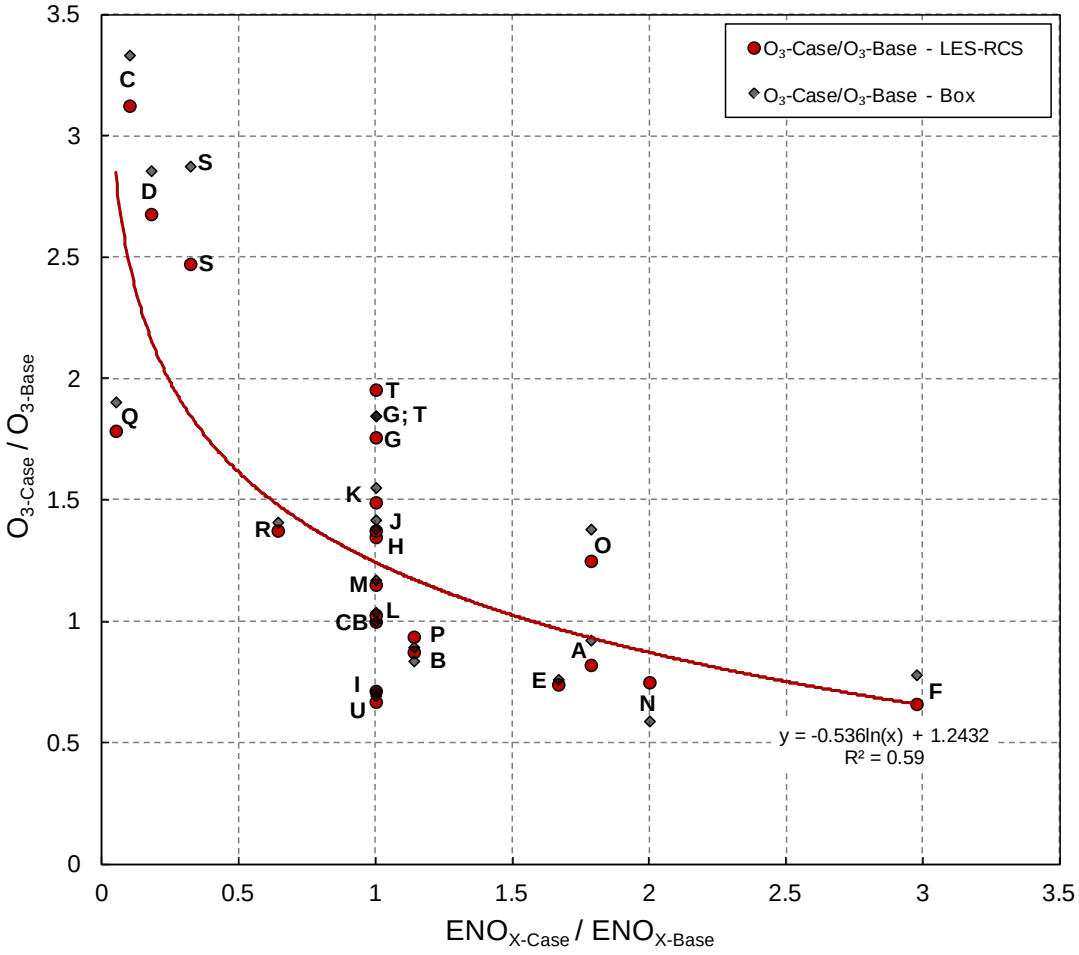

Figure 6·23 - *Scatter plot of the ratio of NO_X emissions for each scenario to NO_X emissions of the base scenario against the ratio of average within-canyon concentration of O_3 for each case to the base scenario as simulated by the LES-RCS model and over the last hour of the model simulation ($150 \leq t \leq 210$ min). The red line represents a logarithmic fit applied to the LES-RCS modelled ratio of $O_{3\text{-}Case}/O_{3\text{-}Base}$.*

At higher NO_X levels the anticipated anticorrelation with NO_X emerges, but with a gradient significantly less than -1 — that is, the model shows clearly the non-linearity in the "urban decrement" in O_3 with respect to NO_X at higher NO_X.

Implications for Air Quality Policy

In terms of the implications of the above findings for policy-making, it is evident that those scenarios in which there is a large increase in average within canyon NO_2 require particular attention. Decreasing the speed of traffic (scenarios A and F) as well as increase in the number of vehicles per hour (case F) lead to a significant increase in NO_2. Thus the focus of policy making should be on reducing traffic within urban areas in addition to improving traffic flow.

There is also a clear implication of increasing primary emissions of NO_2 in such environments that not only contributes to a large increase in within-canyon NO_2 but also results in an additional increase in O_3 observed. Thus to reduce such effects, direct emissions of NO_2 from vehicles must be controlled and consideration given to the effects of increasing the use of diesel vehicles that increase primary NO_2 emissions, such as EURO III light duty diesel vehicles in addition to fitting of catalytically regenerating particle traps both of which increasing f-NO_2 (up to 0.3) may be attributed to (Jenkin *et al.*, 2008a).

The use of certain building materials such self-cleaning window glass that increase HONO and a reduction in its emissions in addition to decreasing VOCs must also be of prime important in terms of policy making in order to reduce NO_2 levels, risk of exposure and associated health effects.

Future reductions in NO_X emissions (from new fleet) are also likely to lead to proportionately greater within-canyon O_3 levels, and so greater O_3 exposure.

Within-canyon processing has been found to substantially alter the partitioning of NO_X and O_X (Table 6·9), compared with those emitted and also leads to modest reductions in NO_X when compared to emissions (Table 6·9) with such findings likely

to be of some importance when considering emissions to be applied to larger scale regional models.

6·4 Canyon dynamics and turbulent transport processes

Intensity of segregation

As was shown in Chapter 5 the interaction between dynamical and chemical processes can have a significant effect on atmospheric composition. In order to quantify such effects further, a measure known as the **intensity of segregation**, I_S, can be derived. The intensity of segregation quantifies the deviation from chemical equilibrium due to incomplete mixing and represents the extent to which reactants are mixed within a particular environment, the volume averaged intensity of segregation $\langle I_S \rangle$ is defined as (Krol *et al.*, 2000):

$$\left\langle I_{S(A+B)} \right\rangle = \frac{\langle A'B' \rangle}{\langle A \rangle \langle B \rangle} \ , \tag{6.4}$$

where *A'B'* represents the spatial covariance between species *A* and *B*, spatial averages are denoted by angle brackets and a prime represents the deviation from the mean[‡‡‡]. In the case where atmospheric species are perfectly mixed (spatially homogeneous), the intensity of segregation will tend to zero whilst values of I_s greater than and less than 0 (ranging from -1 to 1) are indicative of incomplete mixing.

The sign of I_S is always equal to the sign of the spatial covariance, <*A' B'*> upon which both chemistry and dynamics have an effect (Ouwersloot *et al.*, 2011). In terms of mixing, those species that exhibit similar behaviour (*e.g.* greater values of one variable correspond to greater values of another) *i.e.* both emitted or entrained

[‡‡‡] In the case of the LES model the intensity of segregation is defined as a function of (*x, z*) *i.e.*: <*A' B'*>(*x, z*), <*A*>*(x, z)* and <*B*>(*x, z*).

from the background atmosphere will be positively correlated and I_S will remain positive.

Conversely, if the chemical species show opposite behaviour *e.g.* one chemical species is emitted whilst another is entrained from the overlying background atmosphere; chemical species will be negatively correlated and thus I_S will be negative. From a chemistry perspective, two reactive chemical species will be negatively correlated with an associated effect on the correlation coefficient between these species. As

Where $A = B$, the result becomes the autocovariance of A and thus must be greater than 0 if A is not constant in space within the 2D domain, thus I_S is greater than 0 and may be interpreted as the spatial autocovariance of a chemical species normalised by the square of its mean concentration.

As discussed above, $<I_S>$ provides a measure of imperfect mixing on chemical transformation and hence atmospheric composition, with the analysis presented here used to assess the applicability of the box model in simulating street canyon atmospheric composition. From chemical perspective, for the second order chemical reaction between A and B for a single-box model of the street canyon chemistry for a complete mixing case:

$$\frac{d < C >}{dt} = k < A >< B > . \tag{6.5}$$

Whilst for an incomplete mixing case:

$$\frac{d < C >}{dt} = k(< A > + A')(< B > + B'). \tag{6.6}$$

Therefore, for the box model of the incomplete mixing case:

$$\frac{d < C >}{dt} = k(< A >< B > + < A'B' >) = k < A >< B > (1 + I_S). \quad (6.7)$$

Thus, Equation 6.7 leads to the definition of the intensity of segregation. Only if <*A'B'*> is much smaller than <*A*><*B*> *i.e.* I_S << ± 1 % are the box model results reliable where segregation effects are negligible. The magnitude of the calculated values of I_S (Table 6·10) therefore may be important in terms of the reliability of the box model simulated levels of chemical species.

In box-modelling methods, the canyon averaged reaction rate of chemical species (*R*) may be defined as (Vinuesa and VilÃ -Guerau de Arellano, 2005, Ouwersloot *et al.*, 2011):

$$[R] = k\left(\frac{1 + < A'B' >}{< A >< B >}\right) < A >< B > , \quad (6.8)$$

where k represents the rate coefficient for the complete mixing, and $k_{eff,}$ represents the effective rate of chemical reaction for incomplete mixing may be expressed as:

$$k_{eff} = k(1 + \langle I_S \rangle) . \quad (6.9)$$

Thus,

$$[R] = k_{eff} \langle A \rangle \langle B \rangle . \quad (6.10)$$

When considering the effective rate of chemical reaction, it is evident from Equation 6.9 that negative intensities of segregation between chemical species will act to reduce the canyon average chemical reaction rate when compared to those species that are perfectly mixed. Conversely, positive intensities of segregation will act to increase the canyon average chemical reaction rate by increasing the effective rate of chemical reaction.

In terms of the magnitude of segregation effects, large values are those that are of importance as these indicate that dynamical processes and non-uniform emissions have the largest effect on the rate of chemical reaction. However, even segregation effects in the order of 0.5 to 1 % may be considered significant as small changes in the production or loss rates may have a considerable effect on average concentrations (Auger and Legras, 2007).

Significant large negative values may result for example in the case of a reaction: $A + B \longrightarrow C$, where species A is emitted and B is distributed throughout the domain and a local positive fluctuation in A leaves less B after undergoing chemical reaction (Auger and Legras, 2007). Negative segregation is also observed for reaction of VOCs with short-lived species including OH and HO_2 where slowly varying species such as VOCs are mostly concentrated in updrafts whilst shorter lived species remain better mixed within the domain and upon reaction with VOCs become less abundant within updraughts when compared to surrounding regions of the domain (Auger and Legras, 2007).

Canyon averaged intensities of segregation (calculated using Equation 6.4 and expressed as a percentage) between a number of chemical species as simulated by the LES model using the base scenario are presented in Table 6·10. The calculations here are performed using mixing ratios averaged along the y-axis and over the last 60 minutes of the 3.5 hour model simulation ($150 \leq t \leq 210$ minutes). Thus, the calculations presented here are both time and spatially averaged in the y direction and therefore spatially variability in two dimensions is of concern.

Table 6·10 - *Canyon and time averaged intensities of segregation between chemical species expressed as percentages. Chemical species shown in bold and underlined represent those that undergo direct chemical reaction. Temporal averages have been taken over the last hour of the model simulation ($150 \leq t \leq 210$ min).*

	O_3	NO	NO_2	OH	HO_2	VOC
O_3	8.3	—	—	—	—	—
NO	**-5.5**	**5.7**	—	—	—	—
NO_2	**-3.5**	2.8	1.6	—	—	—
OH	**1.3**	**-1.4**	**-0.6**	0.5	—	—
HO_2	**2.7**	**-2.2**	**-1.2**	**0.7**	**1.8**	—
VOC	**-4.7**	4.6	2.3	**-1.1**	-1.8	3.7

Table 6·10 shows that positive intensities of segregation are observed between VOCs, NO and NO_2 thus indicating that emitted species are carried upwards within the canyon by the canyon vortex whilst depleted levels of VOCs, NO and NO_2 are carried toward street level by downward vertical transport due to loss through chemical reaction and exchange with the background atmosphere.

Positive segregation effects are also observed between O_3, OH and HO_2 as these species are all observed to be highest in the background atmosphere than within the canyon itself with depleted levels transported in updraughts and higher concentrations entrained into the canyon from the background atmosphere. The largest (positive) values of I_S are observed between O_3 / O_3 as its covariance is large when compared to the mean values.

Negative segregation effects are observed between those species emitted within the canyon (NO, NO_2 and VOCs) and those species that are in higher concentrations in the background atmosphere (OH, HO_2 and O_3), entrained into the canyon where there concentrations are lower.

Large negative segregation effects are observed between selected reaction partners O_3, NO, NO_2 and VOCs (Table 6·10) where incomplete mixing acts to decelerate the

canyon average rate of chemical reaction between these species. Segregation effects between these species reflect inhomogeneity in both emissions and their average concentrations (§5·3·1 and Figure 6·25) within the canyon due to chemical and dynamical processes (discussed fully in section 5·3·3).

The effective rate of chemical reaction between OH and VOCs is diminished by ~ 1 % (when compared to perfectly mixed conditions) as a result of segregation effects, the result of large fluctuations in long-lived VOCs due to spatial inhomogeneity in emissions following transport from their source in the centre of the street as well as minimal concentrations of OH in regions of the canyon where VOC concentrations are high (Figure 6·25b). Negative (slightly larger) segregation effects for the reaction of OH with VOCs were also observed by Krol *et al.* (2000).

Table 6·10 shows that the magnitude of the intensity of segregation may be reduced when the flux of two chemical species is closer to equal and when the lifetime of chemical species is reduced as the lowest values of $<I_S>$ are observed for those short lived chemical species. In this case, local equilibrium reached at a faster rate than the flow can perform redistribution.

When the chemical and dynamical timescales are of the same order, or chemical timescales are shorter than those of the dynamics, segregation effects will be enhanced and the rate of chemical processing is limited by the dynamics. In this case one would expect complex non-linear effects of dynamical processes upon chemistry, as observed here for NO + O_3 titration and NO_2 production. This indicates that the interaction between chemistry and dynamical is important and that segregation effects must be accounted for.

Figure 6·24 shows the spatial variability in the intensity of segregation within the canyon ($z/H \leq 1$) between (a) OH and NO, (b) OH and NO_2, (c) OH and VOCs and (d) O_3 and VOCs. Large negative values of I_S are observed for all pairs of reacting species downwind of the emission source located within the centre of the street canyon. Such emissions generate large horizontal variations in emitted species and result in the largest segregation effects being observed at the surface which act to reduce the rate of reaction between these species.

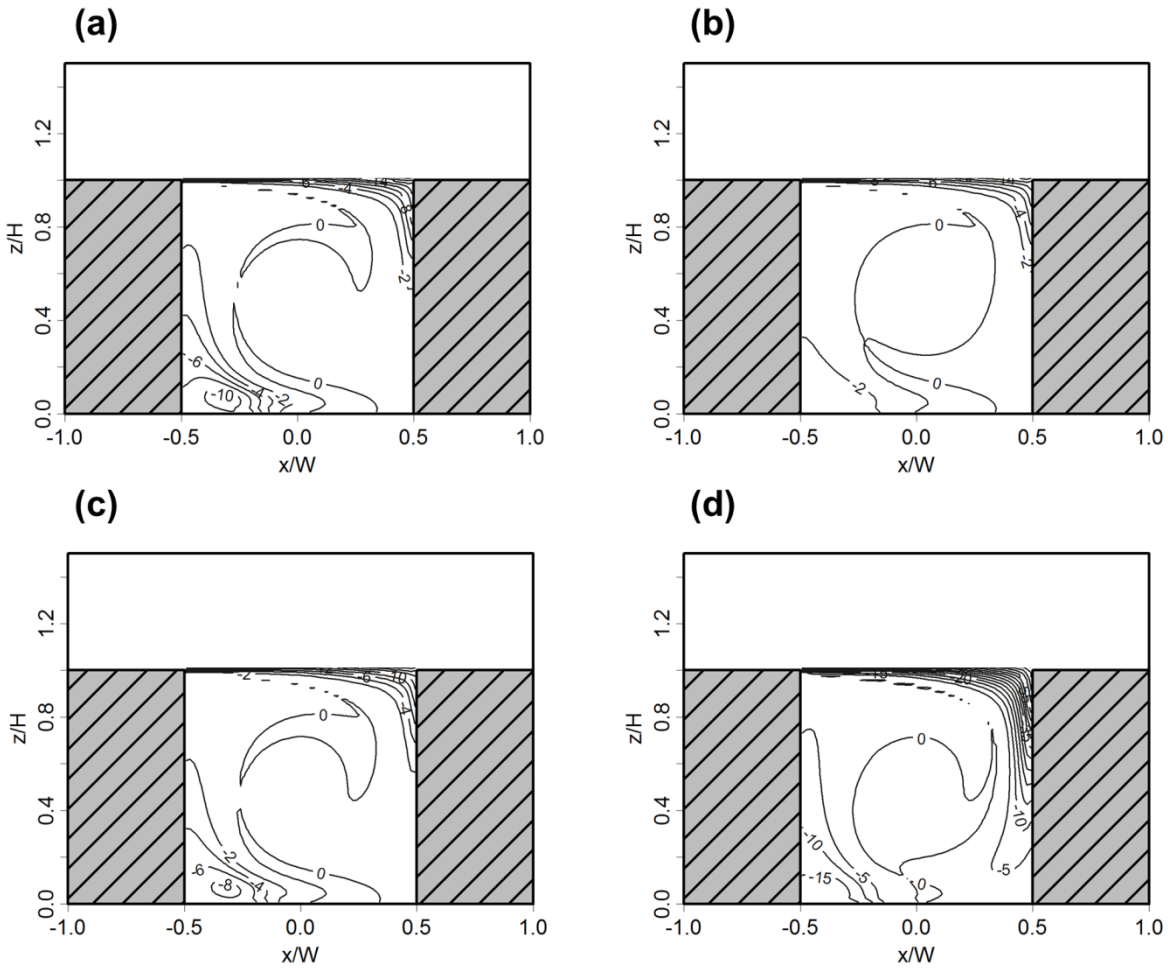

Figure 6·24 - *Mean and time averaged intensities of segregation between (a) OH and NO; (b) OH and NO_2; (c) OH and VOCs; (d) O_3 and VOCs. Averages taken over the last hour of the model simulations ($150 \leq t \leq 210$ min). Contours are given in intervals of 2 % for (a) to (c) and 5 % for (d).*

Moving toward roof level close to the leeward wall of the canyon, segregation effects quickly diminish as emissions become well mixed. The intensity of segregation is

minimised within the canyon vortex reflecting the extended time period over which emissions undergo mixing and chemical processing within this region of the canyon. Toward the leeward wall at roof level, large segregation effects are observed once again due to the fast downward transport of relatively 'clean' air from the background atmosphere which mixes with the more polluted air within the canyon. Horizontal mixing that occurs over longer time periods when compared to vertical updraughts and downdraughts, acts to weaken horizontal concentration gradients and hence reduces horizontal segregation.

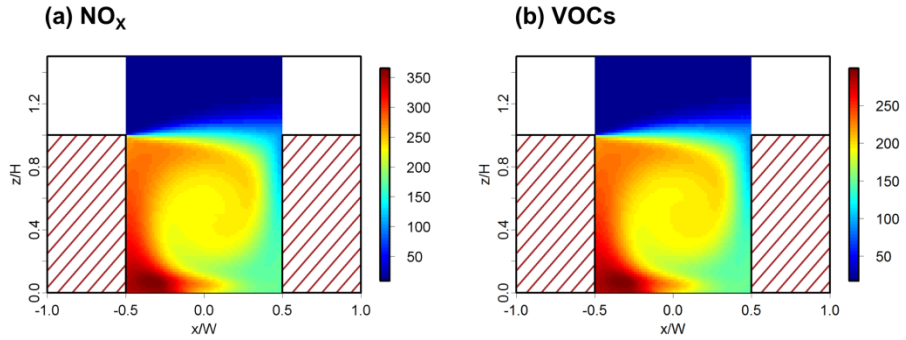

Figure 6·25 - *Mean and time averaged mixing ratios of (a) NO_X and (b) VOCs[§§§] (ppb). Temporal averages taken over the last hour of the model simulations (150 ≤ t ≤ 210 min).*

Turbulent transport processes

The RAMS based LES-RCS model used in this study that provides high-resolution data on both temporal and spatial scales may also give a more accurate insight into the turbulent processes and concentration fluctuations presented here and when used to investigate segregation effects in comparison to RANS models as discussed in section 4·2. The LES-RCS model has the advantage over its RANS based counterparts in that the model provides a more realistic representation of turbulence within and above the canyon itself in its ability to resolve larger scale turbulent eddies that contain a large proportion of TKE and are the principal

[§§§] Including: C_2H_4, C_3H_6, HCHO, CH_3CHO, C_5H_8, CH_3OH, C_2H_5OH and PAN.

mechanism accountable for turbulent transport. As such, this data can be used to investigate the characteristics of turbulent transport processes taking place within the canyon. Section 6·2·2 showed that the mixing ratios of chemical species within the canyon exhibit a large degree of variability over time. Such variability may be attributed to 'sweep' and 'ejection' events that are important in terms of turbulence characteristics and the transport of quantities such as chemical species (§2·2·2).

To investigate the dominance of large coherent structures in characterising turbulence and determine their role in turbulent transport, data was extracted at 5 second intervals at two locations, both in the centre of the canyon (x/W = 0.5) at z/H = 0.5 and the other at roof level (z/H =1) with data averaged along the y axis (§5·2).

In order to investigate turbulent transport processes, turbulent fluctuations (§1·4) were calculated, averaged along the y axis *i.e.* for horizontal velocity:

$$u'(x,z,t) = u(x,z,t) - \overline{u}(x,z) \ , \qquad (6{\cdot}11)$$

where $u'(t)$ is the turbulent fluctuation in horizontal velocity, $u(t)$ is the instantaneous horizontal velocity as a function of time and $\overline{u}$ is the mean wind speed. It is worth noting however that as u' is calculated following averaging along the y axis some degree of variability in u' along this axis will be reduced and it is likely that the following analysis will underestimate such fluctuations. As such, this analysis will provide a qualitative insight into such processes rather than quantitative assessment.

Quadrant analysis and Joint Probability Density Functions (JPDFs)

Quadrant analysis is a conditional sampling method that is used to detect the relative importance of different turbulent events. The relative contributions to momentum flux originate from four quadrants defined by u' and w'. The quadrants identified are illustrated in Figure 6·26 for (a) momentum flux and (b) vertical fluxes

of NO. Both momentum flux ($\overline{u'w'}$) and vertical O_3 flux ($\overline{w'O_3'}$) act toward the surface whilst vertical fluxes of NO ($\overline{w'NO'}$) and NO_2 ($\overline{w'NO_2'}$) act to transport such pollutants away. As such, quadrants have been labelled in a manner that mean the vertical wind gradient is opposite to the vertical gradient of these species and as such correspond to the quadrants illustrated in Figure 6·26b whilst vertical O_3 flux is represented by those included in Figure 6·26a (Christen, 2005).

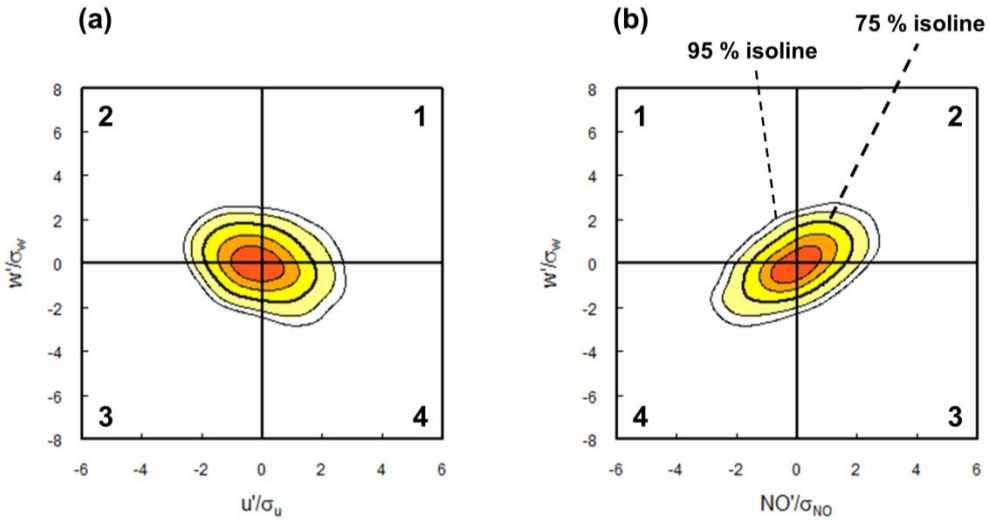

Figure 6·26 - *Schematic to showing sample joint probability density functions for (a) P(u'w') and (b) P(w'NO') illustrating the definitions of each quadrant used in analysis and the locations of the 75 and 95 % isolines.*

Sweep, ejection, outward and inward interaction events are discussed fully in section 2·2·2. In Figure 6·26 above each quadrant is defined (according to Cheng and Liu (Cheng and Liu, 2011) as follows:

Q1 - represents outward interactions: $u' \geq 0, w' \geq 0; c' \leq 0, w' \geq 0;$

Q2 - ejections: $u' \leq 0, w' \geq 0; c' \geq 0, w' \geq 0;$

Q3 - inward interactions: $u' \leq 0, w' \leq 0; c' \geq 0, w' \leq 0;$

Q4 - sweeps or gusts: $u' \geq 0, w' \leq 0; c' \leq 0, w' \leq 0;$

where *u'* may represent the quantities *u'* or O_3' (*dC/dz* = +ve) and *c'* either *NO'* or NO_2' (*dC/dz* = -ve). Thus, for ejection events there are negative fluctuations (*c'*-) in both u and O_3 (*i.e.* lower values transported upwards within the canyon compared to the overlying boundary layer) and a positive fluctuations (*c'*+) of NO and NO_2 (higher values within the canyon than above transported upwards).

Conversely for sweep events there is a positive downward fluctuations of u and O_3 and negative fluctuations of NO and NO_2. For inward interactions there are positive fluctuations of both u and O_3 whilst for NO and NO_2 the opposite is true (*c'*-). In the case of inward interactions there are negative fluctuations of u and O_3 and positive fluctuations of NO and NO_2.

For both sweep and inward interaction events the direction of vertical transport (*w*) acts towards the surface *i.e.* downward transport of high concentrations of O_3 and low concentration NO and NO_2 toward the surface. Conversely, for ejections and outward interactions vertical transport acts away from the surface *i.e.* against the concentration gradient of O_3 and in the same direction as those of NO and NO_2. As such, sweep and ejection events contribute to the normal flux (from higher to lower mean concentrations) whilst both interaction events act to reduce the normal flux of pollutants. Scatter plots of the fluctuations of *u'* and *w'* normalised by the standard deviation of horizontal velocity (σ_u) are shown in Figure 6·27 both (a) within the canyon and (b) at roof level with data taken over the last hour of the model simulation ($150 \leq t \leq 210$ minutes). Within the canyon, turbulence appears to show a higher degree of symmetry and is relatively isotropic when compared to that at roof level.

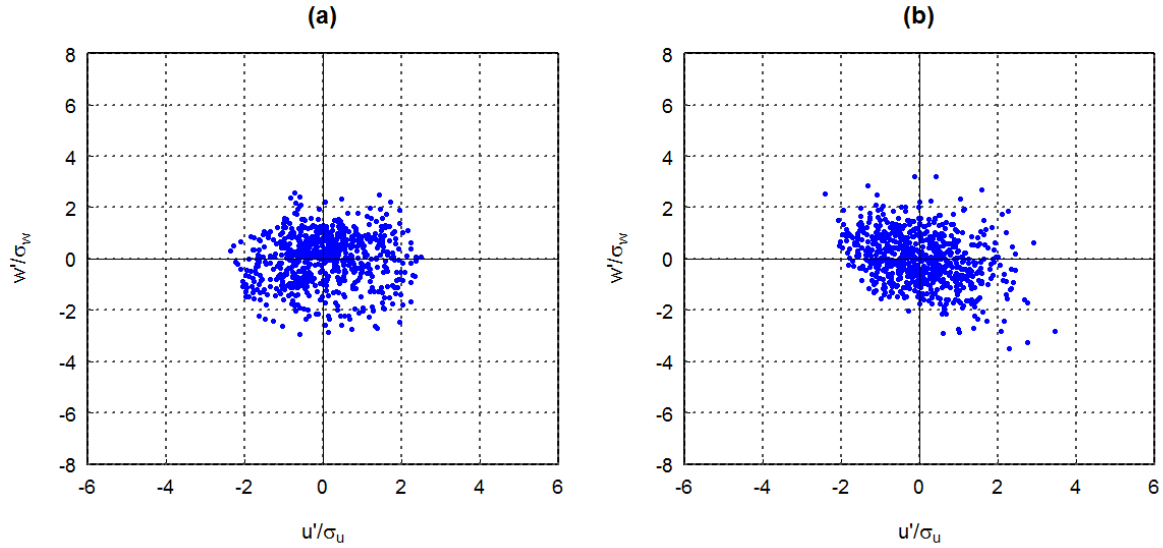

Figure 6·27 - *Scatter plots of normalised vertical velocity fluctuations within the centre of the canyon (x/W = 0.5) at (a) z/H = 0.5 and (b) z/H = 1. Data extracted at 5 second intervals over the last hour of the model simulation (150 ≤ t ≤ 210 min).*

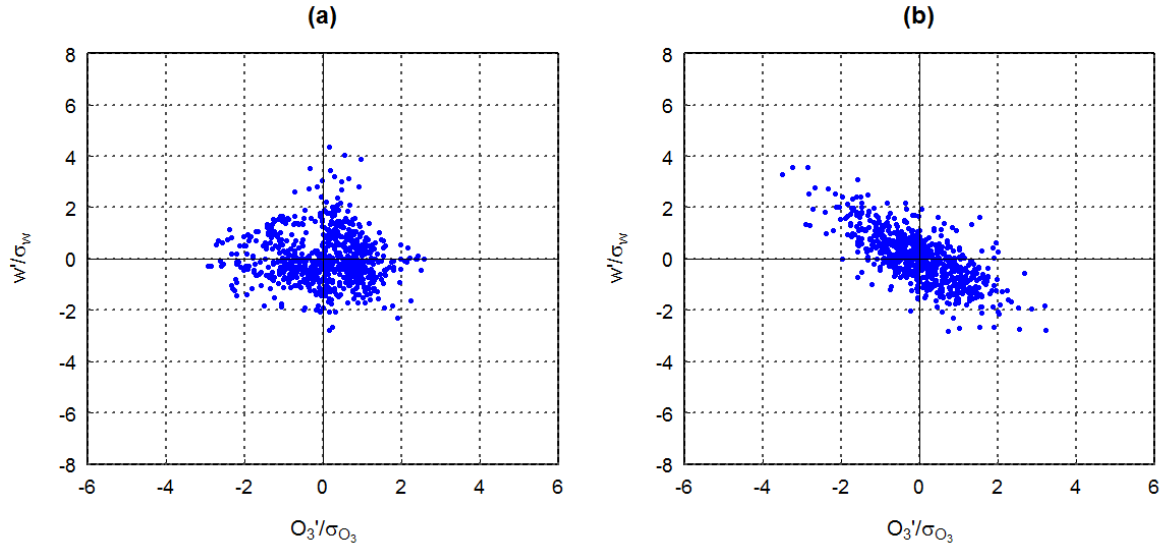

Figure 6·28 - *Scatter plots of normalised vertical O_3 fluctuations within the centre of the canyon (x/W = 0.5) at (a) z/H = 0.5 and (b) z/H = 1. Data extracted at 5 second intervals over the last hour of the model simulation (150 ≤ t ≤ 210 min).*

Table 6·11 quantifies the percentage frequency of the occurrence of each of the four events falling in each quadrant both within the canyon and at roof level. At roof level the scatter plot extends into the fourth quadrant in which $u' \geq 0$ and $w' \leq 0$ with 29 % of events falling within this sector. Table 6·11 also shows the near

symmetric distribution of *u'w'* between each quadrant within the centre of the canyon (*x*/*W* = 0.5; *z*/*H* = 0.5).

Sweeps and ejections at roof level appear to be equal in terms of their frequency of occurrence (29 and 30 % respectively). This is also true for the flux of O_3 at roof level where the occurrence of events in the second and fourth quadrants are equal to 37 %. In terms of the flux of O_3 within the canyon, the scatter plot appears to possess a degree of asymmetry with the highest frequency of events in Q2 and Q3 indicating the predominance of ejections (31 %) and inward interactions (28 %) in the turbulent transport of O_3 within the canyon.

Table 6·11 – *Percentage frequency of occurrence of turbulent fluctuations in each quadrant within the centre of the canyon (x/W = 0.5) at both (a) z/H = 0.5 and (b) z/H =1. Data extracted at 5 second intervals over the last hour of the model simulation (150 ≤ t ≤ 210 min).*

Quadrant	*u'w'*		*w'O₃'*		*w'NO'*		*w'NO₂'*	
	a	b	a	b	a	b	a	b
1	29	19	18	12	28	13	25	11.5
2	26	30	31	37	21	36	24	37.5
3	25	22	28	14	21	14	26	14
4	20	29	23	37	30	37	25	37

At roof level, the scatter plots of both the vertical flux of NO and NO_2 show a high degree of asymmetry with extended tails in the second and third quadrants illustrating the dominance of these processes in the turbulent transport of these pollutants (also shown in Table 6·11). Within the canyon, a symmetrical pattern in the scatter plot for NO and NO_2 is observed with a slight increase in the frequency of events observed for Q1 and Q4 in the case of NO (Table 6·11).

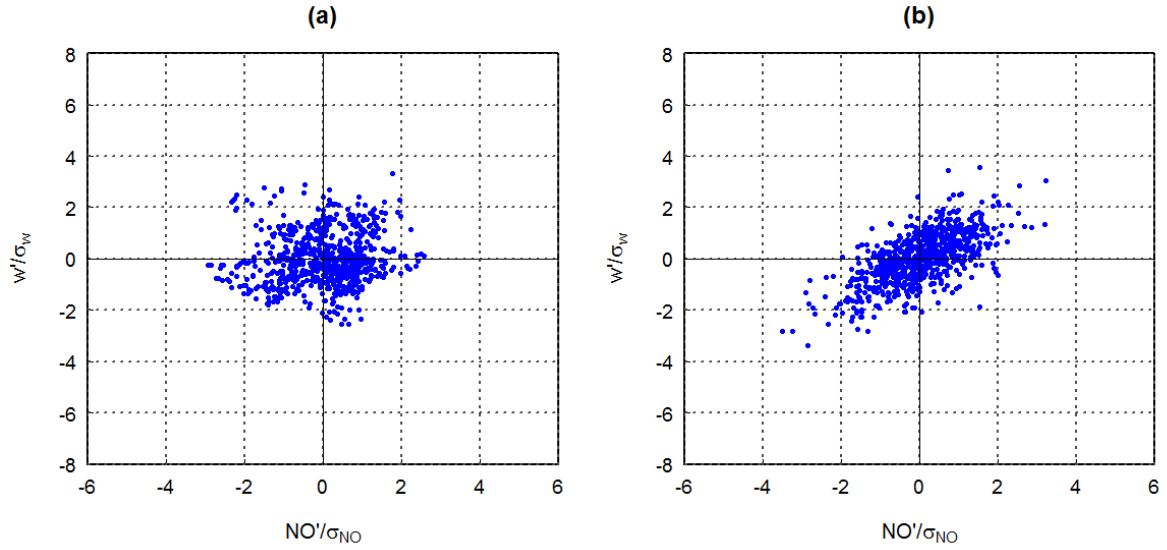

Figure 6·29 - *Scatter plots of normalised vertical NO fluctuations within the centre of the canyon (x/W = 0.5) at (a) z/H = 0.5 and (b) z/H = 1. Data extracted at 5 second intervals over the last hour of the model simulation (150 ≤ t ≤ 210 min).*

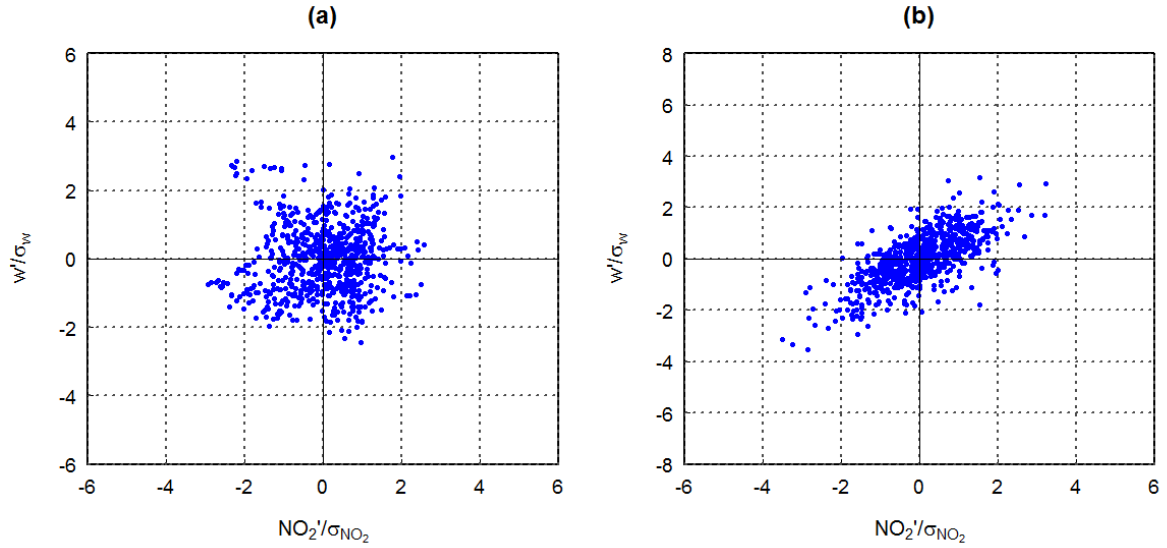

Figure 6·30 - *Scatter plots of normalised vertical NO_2 fluctuations within the centre of the canyon (x/W = 0.5) at (a) z/H = 0.5 and (b) z/H = 1. Data extracted at 5 second intervals over the last hour of the model simulation (150 ≤ t ≤ 210 min).*

The results above demonstrate that ejections are the dominant mechanism of turbulent transport of O_3 within the canyon whilst at roof level both sweeps and ejections are prevalent. Thus O_3 within the canyon is transported at low velocity in an upward motion (from low to high concentrations) whilst at roof level above, high

velocity downward moving air also contributes bringing O_3 rich air into the canyon in addition to ejection events during which within canyon air is released to the overlying boundary layer.

For both NO and NO_2, sweeps and ejections are the most significant events in terms of the turbulent transport of pollutants above the canyon (contributing to the normal flux of these pollutants) whilst equal contributions from all events exist for NO_2 within the canyon. Turbulent transport of NO within the canyon is governed by both outward interactions (that reduce the normal flux) and sweep events (that enhance the normal flux).

A further insight into the nature of turbulent processes taking place within the canyon can also be gained by calculating **joint probability density functions** (**JPDFs**) *i.e.* P(*u'w'*) and P(*w'c'*) as shown in Figure 6·26 above. Normalised JPDFs for *u'w'* are presented in Figure 6·31 below, these clarify that within the canyon there is almost equilibrium between sweeps and ejection events. At roof level however, momentum flux is skewed toward sweep events that transport less polluted background air into the street canyon from above.

In terms of the flux of O_3 (Figure 6·32) at roof level (b) the data is clearly skewed toward the fourth quadrant indicating that sweep events act to transport higher concentration O_3 air into the street canyon from the overlying background atmosphere. The dominance of such sweep events is also observed at roof level for NO (Figure 6·33) and NO_2 (Figure 6·34) where the data are highly skewed toward the fourth quadrant in both cases thus signifying the predominance of sweep events that act to transport less polluted overlying background air into the street canyon at this level. These results show that sweep events are the most important mechanism

in controlling the exchange of air from within the canyon with that of the overlying urban boundary layer above.

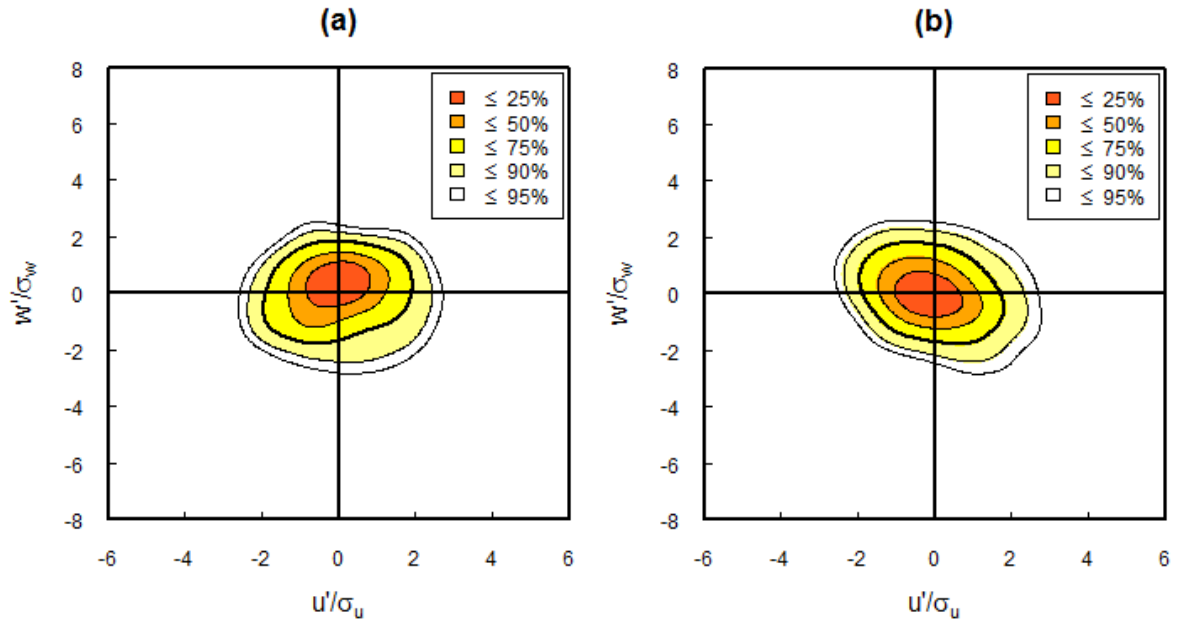

Figure 6·31 - *Normalised joint probability density functions of vertical velocity fluctuations, P(u'w') within the centre of the canyon (x/W = 0.5) at (a) z/H = 0.5 and (b) z/H = 1. Data taken at 5 second intervals over the last hour of the model simulation (150 ≤ t ≤ 210 min).*

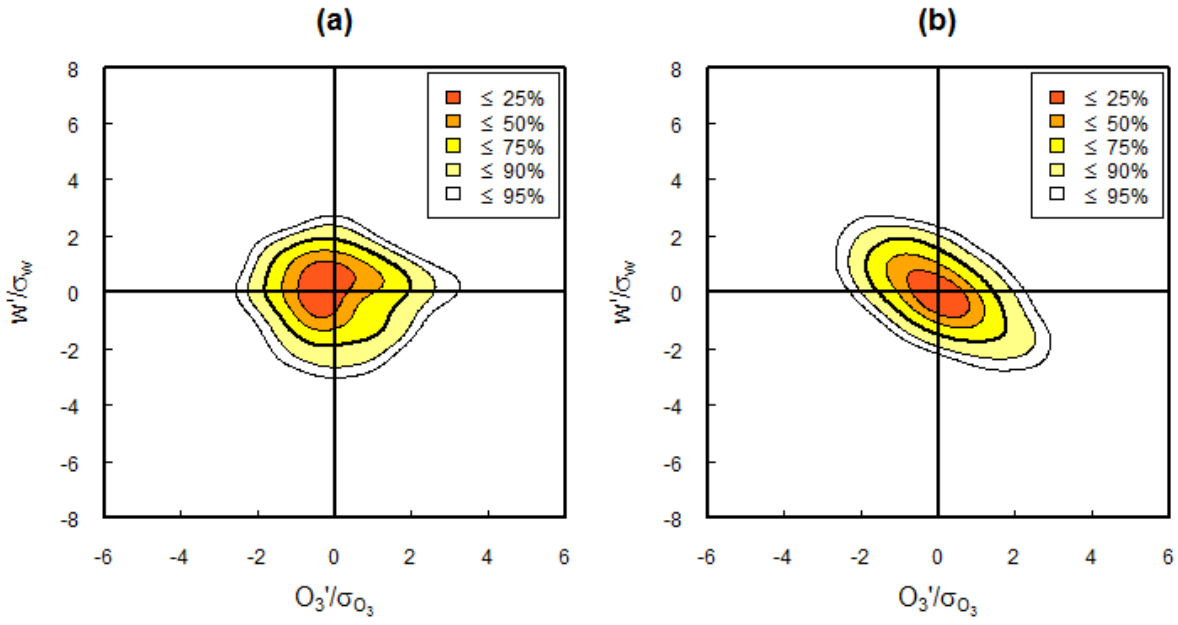

Figure 6·32 - *Normalised joint probability density functions of vertical O_3 fluctuations, P(w'O_3') within the centre of the canyon (x/W = 0.5) at (a) z/H = 0.5 and (b) z/H = 1. Data taken at 5 second intervals over the last hour of the model simulation (150 ≤ t ≤ 210 min).*

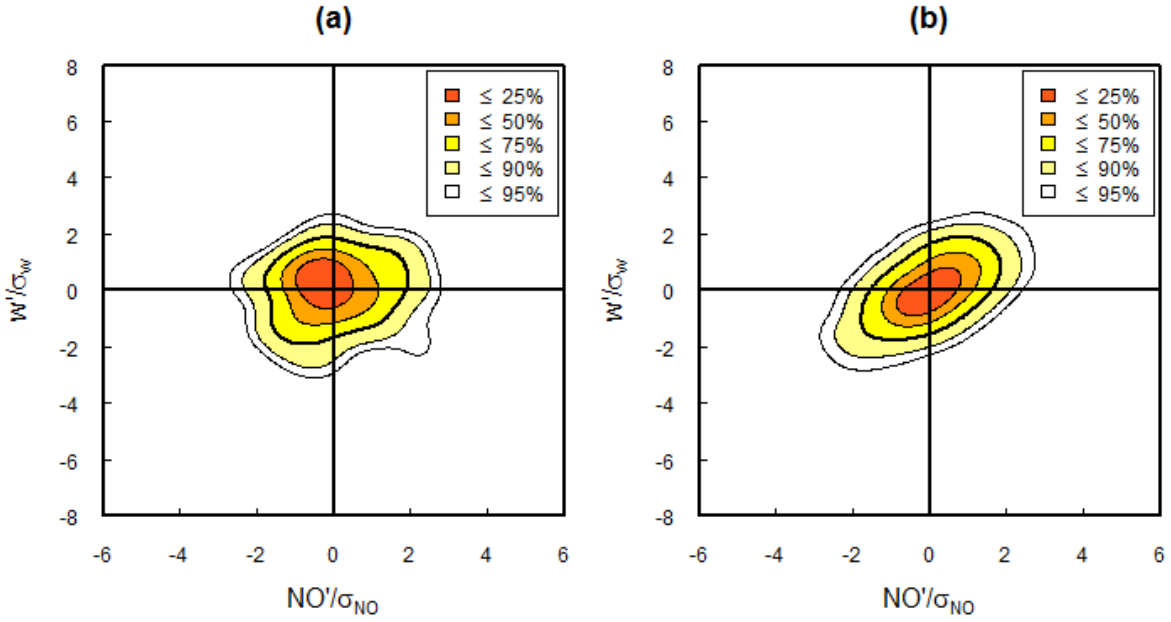

Figure 6·33 - *Normalised joint probability density functions of vertical NO fluctuations, P(u'w') within the centre of the canyon (x/W = 0.5) at (a) z/H = 0.5 and (b) z/H = 1. Data taken at 5 second intervals over the last hour of the model simulation (150 ≤ t ≤ 210 min).*

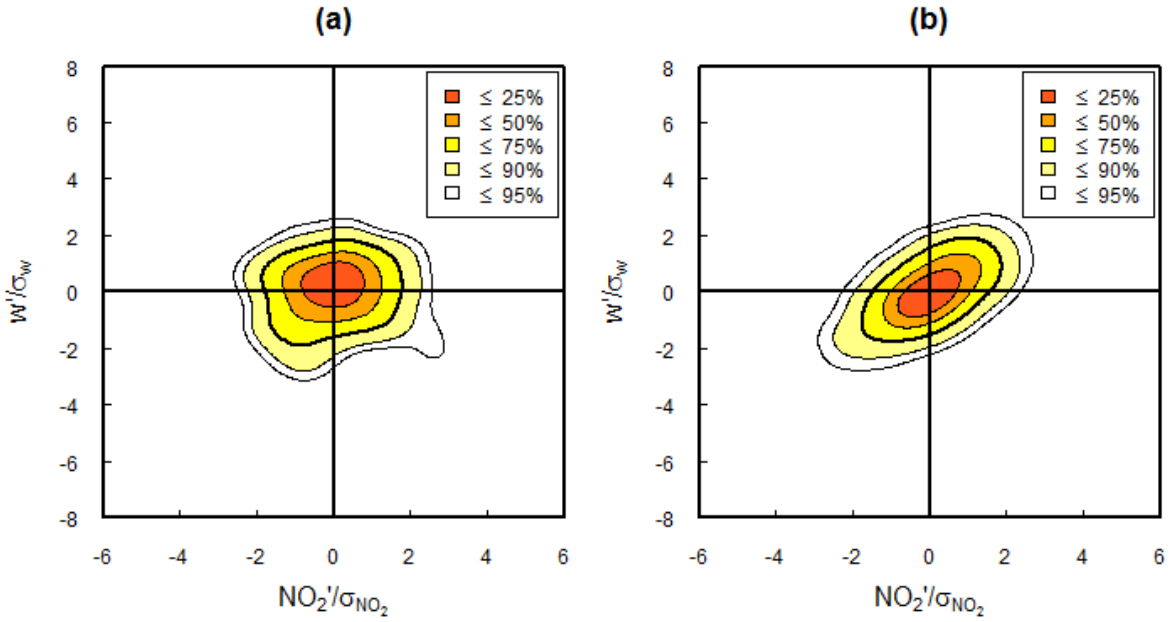

Figure 6·34 - *Normalised joint probability density functions of vertical NO_2 fluctuations, P(w'NO_2') within the centre of the canyon (x/W = 0.5) at (a) z/H = 0.5 and (b) z/H = 1. Data taken at 5 second intervals over the last hour of the model simulation (150 ≤ t ≤ 210 min).*

6·5 Discussion

The key questions posed in the initial sections of this chapter are: *What is the spatial and temporal variation in pollutant levels within the street canyon in terms of pollutant exposure? Secondly, what are the short term (in the order of seconds) pollutant levels experienced within street canyons and how do these compare with single point measurements recorded at fixed monitoring stations?*

As first explored in Chapter 5 (under the scenario and environmental conditions applied), large spatial gradients in atmospheric pollutants exist within the canyon. Higher concentrations of NO and NO_2 are observed to the left hand side of the street when compared to the right. The opposite is true for O_3 with the highest levels observed on the windward side of the canyon. These findings have clear implications relating to the personal exposure of receptors to atmospheric pollutants which is dependent upon their location within the canyon.

An investigation carried out into the short term temporal variation in pollutant levels has shown that the (absolute) variability observed to the left of the canyon within the pedestrian left zone is far greater than that to the right for NO and NO_2 however the reverse being true in the case of O_3. Such observations have clear implications in relation to the procedures employed in air quality monitoring and the frequency at which sampling should take place.

Significant differences that exist in the mean hourly concentrations of atmospheric pollutants observed in the pedestrian left and right zones are fundamental in terms of the selection of monitoring locations within the canyon itself. NO and NO_2 were observed to be 151 and 24 ppb higher, on average, on the left hand side of the canyon whilst O_3 was 5 ppb lower. Sampling on the right hand side of the street could therefore result in lower NO and NO_2 and higher O_3 levels being recorded

when compared to the lee of the canyon (over the 60 minute period sampled here). It is within these regions of the canyon that the population is increasing likely to be exposed to pollutant levels that exceed air quality regulations / standards.

The assumption that pollution concentrations are spatially homogenous within the street canyon made in many population exposure models clearly does not apply. As Vardoulakis *et al.* (2003) and Baker *et al.* (2004) state, exposure calculations must be refined to account for such spatial variation within the canyon.

In terms of the standard one hour sampling frequency used at the majority of air quality monitoring stations (or hour long averages calculated from higher resolution temporal measurements) or even longer time average in-situ measurements made using diffusion tubes, such measurements do not appear adequate in terms of capturing the true variability in pollutant levels within the canyon, that can deviate substantially from the calculated hourly mean. Failure to observe such exceedances of the mean may result in important air quality targets (aimed to reduce pollutant exposure) such as local, national or even international air quality objectives/standards being met when in reality concentrations may exceed them substantially for some period of time. As such, the importance of adopting suitable averaging times over which pollutants are monitored has also been highlighted.

Concentration data-sets for NO and NO_2 examined to the right of the canyon and O_3 to the right of the left of the canyon are reasonably well approximated by near-normal distributions (indicated by a low level of skewness).

The highest level of skewness (sk_{O_3} = 0.45) was inherent in raw O_3 concentration data extracted for the pedestrian right case where O_3 levels observed are commonly relatively low but where extremes at higher concentrations may also be

experienced. In terms of pollutant exposure such findings have important implications in regard to the related health effects that may result.

The distributions of NO, NO_2 mixing ratios for the pedestrian left case were found to be positively skewed. The results presented in section 6·2·2 also show that there are bi-modal distributions of NO and NO_2 to the left of the canyon whilst for O_3 this is observed on the right hand side of the street. For NO and NO_2, these results may be explained by the entrainment of vehicle emissions in addition to recirculated canyon air. In the case of O_3, entrainment of higher O_3 concentrated background air in addition to chemical processing of canyon air may explain the bi-modal distribution observed.

* * * * *

The latter sections of this chapter have provided an insight into the effect of varying emissions on canyon atmospheric composition. The effects of incomplete mixing on the rates of chemical reaction and the dominant processes governing turbulent transport within the canyon have also been explored. This section of work also provides the scope for further work which is discussed in the concluding chapter of this thesis.

Changing emissions and atmospheric composition

Varying emissions within the canyon has a notable effect on average canyon atmospheric composition. Slow moving (10 mph), heavy traffic (2500 veh hr^{-1}) represented in case F results in a substantial increase in NO_X, CO and VOCs emitted into the canyon when compared to the base pollution scenario. As such, a large increase in canyon averaged NO_2 is observed that is ~ 2.2 times higher for case F than the base case.

Changing the nature of emissions within the canyon whilst maintaining the amount of NO_X emitted also has a pronounced effect on canyon averaged composition. Increasing the proportion of NO_X released as NO_2 leads to a significant increase in average within canyon levels of NO_2 (51 %) and O_3 (up to 76 % for f-NO_2 = 0.3) in comparison to the base scenario (f-NO_2 = 0.1).

The effect of increasing the proportion of NO_X emitted into the canyon as HONO is also clearly evident with an increase in O_3 of 15 % (f-HONO = 0.05 and f-NO = 0.9) and NO_2 up to 4 % in comparison to the base case where there are zero emissions of HONO. These observations highlight the importance of changing the proportion of NO_X emitted as NO_2 and HONO, a potential future impact of changing the vehicle fleet and introducing materials such as self-cleaning window glass into the canyon environment. For the cases discussed above it was also clear that there is a degree of non-linearity evident in the LES-RCS simulated within canyon concentrations that show a disproportionate change with increased emissions due to the combined effects of chemistry and segregation.

The findings discussed above highlight that policy-making should focus on reducing traffic as well as improving traffic flow within urban areas in addition to reducing primary emissions of NO_2 and HONO through consideration of vehicle type and building materials in order to reduce the health effects associated with elevated NO_2 concentrations.

Under the pollution scenarios considered, the largest effects of segregation were observed for case A and F where box model simulated NO_2 levels were up to 20 % of that of the LES-RCS model where segregation may reduce the effective rate of NO + O_3 titration in addition to radical propagation and O_3 + alkene reactions in the case of the LES-RCS.

In contrast the smallest difference between the model simulations was observed for case P where VOC emissions had been halved whilst maintaining all other emissions as those specified for the base case scenario thus providing further evidence of the role of segregation in reducing the rate at which radical propagation and the O_3 + alkene reactions occur.

Under the 2 × NO_X conditions of case N, the average concentration of NO_2 within the canyon was higher for the LES-RCS model simulation when compared to the box model where segregation acts to increase the rate of NO_2 production primarily through the NO + O_3 reaction.

Increasing emissions also have a pronounced effect on the flux of a number of pollutants escaping from the canyon, a combined effect of both increased emissions themselves and within canyon chemical processing whilst average within canyon NO_X is conserved. In those cases where there is an increase in NO_X emissions, a disproportionate increase in the amount of total oxidant is evident indicating the non-linearity of chemical processes within the canyon. The flux of NO_X out of the canyon is almost equal to raw emissions whilst O_X is significantly higher as a result of chemical processing prior to release into the background atmosphere. The significance of atmospheric "pre-processing" of primary emissions within the canyon is highlighted as well as the dependence of such processes on the emission / pollution scenario applied. For the most polluted conditions considered (case F), the LES-RCS simulated results diverged significantly from the single box case in which O_3 levels may be overestimated (assuming perfectly mixed conditions) in comparison to the more realistic LES-RCS case.

Canyon dynamics and turbulent transport processes

Considering the intensity of segregation, further evidence of the effects of canyon dynamics processes on atmospheric composition has been provided. The intensity of

segregation can also be used to assess the applicability of the box model in simulating street canyon atmospheric composition where only if $\langle A'B' \rangle$ is much smaller than $\langle A \rangle \langle B \rangle$ *i.e.* $I_S << \pm 1$ % are the box model results reliable and segregation effects minimal.

Segregation effects were observed to be largest for the reaction of O_3 with NO and NO_2 where mixing within the canyon acts to decrease the rate of average within canyon chemical reactions between these species.

Quadrant analysis and joint probability density functions provided and insight into the turbulent transport processes at roof level and within the canyon. At roof level, sweep events were observed to dominate exchange between the background atmosphere and the canyon itself, transporting higher levels of O_3 and lower concentrations of NO_X into the canyon from above.

7: Conclusions

7·1 Summary

The work included in this thesis concerns the study of atmospheric composition on the street canyon scale. Specifically, the objectives of this thesis were to:

- Develop and evaluate a suitably reduced chemical scheme.
- Develop a combined chemical-dynamical model following the implementation of the reduced chemical scheme into the LES model.
- Investigate atmospheric composition and chemical processing on the street canyon scale.
- Explore the potential exposure of receptors to harmful atmospheric pollutants within the canyon whilst assessing the representativeness of measurements made by for example local authorities.
- Investigate the effect of changing emissions upon atmospheric composition within the canyon.
- Consider the effect of incomplete mixing on the rates of chemical reaction and thus atmospheric composition as well as the nature of turbulent transport processes taking place within the canyon.

A reduced chemical scheme has been developed (using a closed zero-dimensional box model), appropriate in terms of its size and complexity for inclusion in a canyon dynamical model.

Using the CRI v2-R5 mechanism as a basis for development, the reduced chemical scheme was evaluated following each stage in reduction over a range of atmospheric conditions with comparison made to the near-explicit Master Chemical

Mechanism (v3.1). It was demonstrated that for OH, HO_2, NO, NO_2 and O_3, the RCS emulated the MCM well, particularly over the shorter time periods of up to 30 minutes that are of more relevance in terms of canyon residence times. In the case of the RCS, simulated OH provided a very close fit to levels simulated by the MCM over these timescales. Comparison made between the RCS and the MCM gave model differences of less than 3 % under typical urban background and high NO_X conditions, these values being significantly lower than the uncertainty associated with emissions and measurements of such pollutants.

Emissions within the canyon for the base pollution scenario considered were determined using UK road vehicle emission factors, with the relative mass emission of each VOC calculated using the UK National Atmospheric Emissions Inventory (NAEI). For the model base case scenario, emissions were representative of moderate weekday traffic (1500 vehicles per hour) for an urban road with cars travelling at an average speed of 30 mph. To investigate the effect of emissions on atmospheric composition within the canyon further, a number of pollution scenarios were developed. These included varying the speed of vehicles, volume of traffic and the fraction of NO_X emitted as NO_2 or HONO.

Subsequent to its development, the RCS was implemented into the LES model. The combined LES-RCS model provided a novel approach to study the processing of pollutants within the street canyon as relatively few studies (reviewed in Chapter 2) have applied full oxidation chemistry to dynamical models such as the LES. The LES-RCS model was used to investigate urban street canyon atmospheric composition by simulating the combined effects of emissions, mixing and chemical processing on pollutant concentration within an idealised urban street canyon.

7·2 Discussion

The LES-RCS model was used to investigate the spatial and temporal variability in pollutants levels within the canyon (Chapter 5). In addition to the LES-RCS model, the photo-chemical box model (outlined in section 3·8) was used to explore exchange rate effects and atmospheric composition (§5·3·2). Comparing the results simulated using both models, segregation effects were investigated. The effect of VOC oxidation chemistry upon within canyon atmospheric composition through comparison of the RCS with a three reaction NO_X-photochemical steady state chemical scheme was also considered. The within canyon processing of emissions was explored in Chapter 5 of this thesis.

7·2·1 Spatial and temporal variability

Analysis of LES-RCS model output has proved that a clear spatial variation in pollutant levels exists within and above the idealised street canyon studied. Towards the windward wall of the canyon levels of NO_X were observed to be over two times those of the leeward wall. Distinct features in the canyon dynamical regime were apparent including the primary canyon vortex and a shear layer at roof level that becomes increasingly more turbulent moving downwind from the leeward wall whilst increasing in amplitude.

Due to their increased emissions from vehicle exhaust at street level, mixing ratios of NO, NO_2 and the passive scalar were significantly higher within the canyon when compared to the overlying urban background atmosphere above. Elevated levels of these species were observed toward the leeward wall of the canyon following transport and chemical processing of primary emissions as they are carried by the primary vortex downwind from their emission source in the centre of the canyon.

The oxidation of primary emissions of NO (through the reaction: $NO + O_3 \rightarrow NO_2 + O_2$) contributes to increased concentrations of NO_2 being observed toward the leeward wall in addition to primary emissions of NO_2 alone.

The concentration of peroxy radicals are lower within the canyon compared to the background atmosphere. A local maximum of HO_X is observed within the canyon vortex that represents a relatively isolated region of entrained background air. OH levels are also observed to be highest in this region of the canyon, a reflection of the diminished OH sink here, in particular due to reaction with NO.

Towards the leeward wall of the canyon a sharp contrast in pollutant levels exists between the canyon itself and the background atmosphere due to the impermeable nature of the shear layer at this point. Moving downwind, on the approach to the windward wall, the concentration gradient between the within canyon and background atmosphere diminishes due to an increase in exchange in this region.

LES-RCS model simulated results provided the focus of Chapter 6 that were used to investigate the potential exposure of individuals to pollution within the canyon. The spatial and temporal variation of key pollutants (of prime concern in terms of health effects) within the canyon were investigated in those regions were pedestrians are likely to be located.

Analysis of pollutant concentrations within in these regions showed that NO and NO_2 are highest toward the leeward wall, whilst the opposite is true for O_3 with the highest levels observed toward the windward wall (when the wind blows perpendicular to the canyon's axis and from left to right across the canyon). Thus the exposure of individuals to pollutants at typical pedestrian height is highly dependent upon their location within the canyon. An investigation into the short term temporal variation in pollutant levels has revealed that the absolute variability

in both NO and NO_2 toward the leeward wall of the canyon is far greater than the windward wall, the reverse being true for O_3 with implications in terms of the characteristics of the dose-response relationship.

Such findings are of some significance in terms of locating fixed monitoring stations such as the UK Automatic Urban and Rural Network for example as measurements made at one location within the street may not be representative of the true variability in pollutant levels within the canyon.

The statistical distribution of NO, NO_2 to the left of the canyon and O_3 data to the right were all found to be positively skewed with important implications in terms of the related health effects that may arise from individual exposure. Bi-modal distributions in concentration data were also observed in these cases highlighting the existence of an emission and recirculated air component of the observations.

7·2·2 VOC oxidation chemistry and atmospheric composition

To study the effect of detailed VOC chemistry upon atmospheric composition, the RCS chemical scheme (that includes 51 species and 136 reactions) and a NO_X photochemical steady state (PSS-only) three reaction chemical scheme were inter-compared. This comparison showed a clear effect of including the more detailed VOC oxidation chemistry that resulted in increased levels of NO_2 and O_3 and a decrease in NO. Such observations indicate the importance of the NO-to-NO_2 conversion processes that result in net ozone production in the VOC oxidation case. As a result, O_X levels are also higher whilst NO_X levels remain lower due to the additional processes that lead to the loss of NO_X (*e.g.* HNO_3 formation) and NO_X partitioning to NO_y species including HONO.

7·2·3 Changing emissions within the canyon

Using the pollution scenarios developed in Chapter 3, the effect of varying emissions upon atmospheric composition and chemical processing within the canyon was considered.

Increasing the level of vehicle emissions within the canyon has a clear effect on atmospheric composition. Increases in both the volume of traffic in addition to a reduction in vehicle speed lead to a large increase in NO_2 levels within the canyon whilst decreasing canyon average O_3.

Changing the nature of emissions within the canyon by increasing the proportion of NO_X emitted as either NO_2 or HONO has a clear effect on canyon average composition. Increasing the fraction of NO_X emitted as NO_2 by as little as 20 % contributes to a 51 % increase in canyon average NO_2 and a 76 % increase in canyon average O_3 highlighting the highly non-linear effect of increasing primary NO_2 emissions on atmospheric composition due to chemical processing taking place within the canyon prior to the release of pollutants into the background atmosphere.

Similarly, introducing HONO emissions by increasing proportions whilst maintaining NO_X emissions into the canyon leads to a pronounced effect on average within canyon atmospheric composition, increasing O_3 levels to 15 % and NO_2 of 4 % where 5 % of NO_X is emitted as HONO (where *f*-NO = 0.9) in comparison to zero emissions of the base scenario, providing evidence of its role in reducing NO + O_3 driven O_3 removal.

Increasing vehicle emissions (of NO_X, CO and VOCs) within the canyon by increasing the number of vehicles whilst reducing their speed under case F resulted in a

significant increase in average O_X levels observed within the canyon attributed to increasing NO_2 levels as O_3 levels decreased. Under this scenario, a significant increase in NO + O_3 driven NO_2 production was observed when compared to the base case scenario in addition to a significant increase in production through the $NO + NO \longrightarrow NO_2 + NO_2$ reaction (increasing by over a factor of 20).

7·2·4 Within canyon chemical processing

It was evident in Chapter 5 that the amount of NO, NO_2, NO_X and O_X escaping from the canyon was far greater than that entering the canyon from the urban atmosphere signifying the combined effects of primary emissions and within canyon processing of pollutants prior to release into the background atmosphere. The calculated resolved-scale flux was used to determine a representative flux of pollutants into the overlying urban boundary layer.

Positive fluxes of NO and NO_2 from the canyon into the overlying atmosphere were evident with a negative downward flux of O_3 into the canyon. A clear influence of within canyon processing of emissions on the level of NO_X escaping was observed. For the base scenario, the chemical processing of emissions lead to a 30 % increase in O_X (O_3 + NO) escaping from the canyon when compared to raw emissions of NO_2 thus demonstrating the importance of within canyon processing on atmospheric composition.

Large increases in the levels of O_X escaping from the canyon when compared to raw NO_2 emissions were also observed for the additional pollution scenarios considered in Chapter 6.

A near-uniform increase in average NO_X levels with increasing NO_X emissions was observed, however a small number of deviations from this provide some evidence of the effect of chemical transformation of NO_X into other forms of NO_y such as HNO_3.

NO_2 concentrations were observed to increase at a lower rate than those of NO_X as a result of increasing levels of NO_X emitted within the canyon with NO_2 concentrations exhibiting a less than unity dependence on such emissions.

An inverse relationship was also observed between increasing NO_X levels and average O_3 levels due to NO + O_3 titration within the canyon, however with substantial curvature evident particularly at low NO_X levels highlighting the importance of this process under such conditions in determining average O_3 levels within the canyon. At higher NO_X levels, non-linearity in the urban decrement in O_3 with respect to NO_X at higher NO_X levels was also evident.

7·2·5 Segregation effects and turbulence characteristics

Comparison of the LES-RCS model simulation with that of the zero-dimensional box model demonstrates the effects of incomplete mixing upon canyon average atmospheric composition and chemistry. In comparison to the box model within which emissions are homogeneous and well mixed, the LES-RCS model shows a delayed response to chemical perturbations.

Levels of NO, NO_2 and OH simulated by the box model were lower than those simulated using the more realistic LES-RCS model whilst O_3 mixing ratios are lower in the box model case when compared to the LES-RCS approach. Thus assuming instantaneous mixing inherent in the box model simulations results in an underestimation of O_3 levels. Segregation effects due to spatial inhomogeneity in composition, a result of dispersion and incomplete mixing, lead to a reduction in

the canyon average rate at which O_3 reacts with NO to produce NO_2 due to limited O_3 being present in a number of cells within the LES model.

Partial NO + O_3 titration was evident upon investigating the statistical distribution of O_3 for one computational cell with mixing ratios observed down to 6.6 ppb when compared to an average of 8 ppb within that region of the canyon.

HO_X levels are also affected by segregation with OH levels highest in the box model case and the extent of OH driven processing of reactive emissions overestimated in comparison to the more realistic LES-RCS model. Average within canyon mixing ratios of OH deviate by up to 11 % from the box model case over the last hour of the model simulation. This difference is likely to be far greater in reality due to the spatial variability in OH levels within the canyon with OH levels up to 30 % higher within the canyon vortex itself.

Under the pollution scenarios considered, the largest effects of segregation were observed for case A and F where box model simulated NO_2 levels were up to 20 % of that of the LES-RCS model. Segregation effects may therefore diminish the effective rate of NO + O_3 titration in addition to radical propagation and O_3 + alkene reactions in the case of the LES-RCS.

When comparing changing background conditions, differences between the LES-RCS and box model simulations were observed. Under heat wave (more polluted) conditions, the difference between the box model and LES-RCS model simulations was reduced compared to the base scenario with the effect of segregation minimised, a result of an increase in O_3 within the canyon due to increased levels above the canyon.

In contrast, when background O_3 levels were reduced a larger effect of segregation is observed (when compared to the base scenario), thus within some regions of the model domain O_3 concentrations were further limited resulting in a reduction of the effective rate of NO + O_3 reaction.

The intensity of segregation was calculated in order to further study the effect of incomplete mixing on the rates of chemical reaction between certain species within the canyon. Large segregation effects were observed between the reaction of O_3 with NO, NO_2 and VOCs where incomplete mixing and spatial inhomogeneity in chemical species act to reduce the canyon average rate of chemical reaction. Conversely, incomplete mixing inherent in the LES model acts to increase the rate of reaction of VOCs with NO and NO_2.

Quadrant analysis and joint probability density functions were used to investigate turbulence characteristics and the dominant mechanisms in pollutant transport within the street canyon as simulated by the LES-RCS model.

The characteristics of turbulent transport processes simulated by the LES-RCS model were explored using quadrant analysis and joint probability density functions. At roof level sweep events are observed to be the dominant mechanism that acts to transport NO and NO_2 out of the canyon whilst O_3 is transported downwards.

7·3 Further research

The processes discussed above are likely to be dependent upon the nature of the canyon domain (canyon aspect ratio), prevailing meteorology and emission / pollution scenario considered. Further research to average the extent of these effects across a representative parameter space will determine the modification to raw

emission rates which might be applied to account for within canyon processing of raw emissions in larger scale regional and neighbourhood models.

The effect of changing canyon characteristics on both canyon dynamics and atmospheric composition using the LES-RCS model was not addressed within this thesis. In addition to the LES-RCS approach, additional modelling techniques such as Computational Fluid Dynamics (CFD) may be utilised with the RCS chemical scheme applied. The use of CFD would allow objects such as trees (*e.g.* Salim *et al*. (2011)) and barriers (*e.g.* Finn *et al.* (2010)) and even green infrastructure (*e.g.* Pugh *et al.* (2012)) to be introduced into the canyon as well as changing roof type (*e.g.* Huang *et al.* (2009)) and building characteristics with clear applications in terms of planning and building design.

Analysis of the effect of dynamical processes on atmospheric composition could also be extended by using additional measures such as the Damköhler number, *Da* (see §2·3). Further insight into turbulent transport within the canyon may also be gained by studying the co-variance of chemical species and conducting spectral analysis.

Most importantly future research directed towards validation of the combined LES-RCS model using high spatial and temporal resolution measurements of atmospheric species and meteorological variables (*e.g.* Mead *et al.* (2013)) within the canyon environment would strengthen the conclusions drawn in this thesis, an area of research which has been relatively limited to date.

7·4 Concluding remarks

Although a number of studies that relate to street canyon atmospheric composition have been conducted, relatively few have included detailed chemical schemes. Much research until more recently has involved the application of photo-chemical steady state chemistry (with a limited number of reactions included) to dynamical models. Such research therefore is questionable in terms of its adequacy in representing the true complexity of the photo-chemical reactions taking place within the canyon, governed by the oxidation of VOCs present in such domains.

The work included in this thesis represents a substantial analysis into the spatial and temporal variability of pollutants within the canyon, providing a detailed assessment of the likely exposure of receptors to harmful pollutants within the canyon. This has important implications in terms of local air quality measurement and the adequacy of measurements employed in risk assessment.

This thesis has revealed that the inclusion of a more comprehensive chemical reaction scheme, that represents VOC oxidation processes, has a clear effect on canyon atmospheric chemistry that results in net ozone production reflecting the additional NO-to-NO_2 conversion that takes place.

Analysis has demonstrated that the chemical processing of emissions within the canyon prior to release into the background atmosphere is significant. In addition, segregation effects have been shown to influence the rate of chemical reaction between a number of species, with O_3 levels likely to be underestimated in zero-dimensional models that assume instantaneous mixing and homogeneous pollutant concentrations.

The development of a number of pollution scenarios in which the quantity and characteristics of emissions are varied has shown that such variations have a considerable effect on average within canyon concentrations and the flux of pollutants out of the canyon into the urban background environment. Such observations emphasize the need to modify raw emissions when used in larger neighbourhood and regional models and the potential impact of technological advances in both vehicles and materials that may be introduced into the canyon environment.

Publications arising as a result of this thesis

Bright, V.B, Bloss, W. J. & Cai, X. M. (2013). Urban street canyons: Coupling dynamics, chemistry and within-canyon chemical processing of emissions. *Atmos. Environ*, **68,** 127-142.

Bright, V.B, Bloss, W. J. & Cai, X. M. (2011). Modelling atmospheric composition in urban street canyons. *Weather,* **66**, 106-110.

Bright, V.B, Bloss, W. J. & Cai, X. M. (2011). Street canyon atmospheric composition: Coupling dynamics and chemistry. *In:* Steyn, D.G. & Castelli, S.T. (eds.) *Air Pollution Modeling and its Application XXI.* NATO Science for Peace and Security Series C: Environmental security. 63-68.

Appendix A: RCS mechanism

Table A1 - *All reactions included in the Reduced Chemical Scheme (RCS). All reactions and rate constants are taken from the MCM v3.1 (§2·1·1) unless otherwise stated. Rate constants highlighted in red are those updated using TUV Radiation Model values with those highlighted in green derived from TUV values. Complex (bold) and simple (italics) rate co-efficients are calculated according to the MCM v3.1 protocol and are presented in Table A2.*

Inorganic Reactions		Rate Constant, k		Reaction type[1]
1.	$O_3 \longrightarrow OH + OH$	3.40×10^{-6}	JFAC[2]	P[3]
2.	$NO + O_3 \longrightarrow NO_2$	1.40×10^{-12}	exp(-1310/T)	B
3.	$NO + NO \longrightarrow NO_2 + NO_2$	3.30×10^{-39}	exp(530/T)*O_2	T
4.	$NO + NO_3 \longrightarrow NO_2 + NO_2$	1.80×10^{-11}	exp(110/T)	B
5.	$OH + O_3 \longrightarrow HO_2$	1.70×10^{-12}	exp(-940/T)	B
6.	$OH + H_2 \longrightarrow HO_2$	7.70×10^{-12}	exp(-2100/T)	B
7.	$OH + CO \longrightarrow HO_2$	1.30×10^{-13}	**KMT05**	C
8.	$OH + H_2O_2 \longrightarrow HO_2$	2.90×10^{-12}	exp(-160/T)	B
9.	$HO_2 + O_3 \longrightarrow OH$	2.03×10^{-16}	$(T/300)^{4.57}$exp(693/T)	B
10.	$OH + HO_2 \longrightarrow$	4.80×10^{-11}	exp(250/T)	B
11.	$HO_2 + HO_2 \longrightarrow H_2O_2$	2.20×10^{-13}	**KMT06*** exp(600/T)	C
12.	$HO_2 + HO_2 \longrightarrow H_2O_2$	1.90×10^{-33}	M***KMT06***exp (980/T)	T
13.	$OH + NO \longrightarrow HONO$		**KMT07**	T
14.	$OH + NO_2 \longrightarrow HNO_3$		**KMT08**	T
15.	$OH + NO_3 \longrightarrow HO_2 + NO_2$	2.00×10^{-11}		B
16.	$HO_2 + NO \longrightarrow OH + NO_2$	3.60×10^{-12}	exp(270/T)	B
17.	$HO_2 + NO_2 \longrightarrow HO_2NO_2$		**KMT09**	T
18.	$HO_2NO_2 \longrightarrow HO_2 + NO_2$		**KMT10**	B
19.	$OH + HO_2NO_2 \longrightarrow NO_2$	1.90×10^{-12}	exp(270/T)	B
20.	$OH + HONO \longrightarrow NO_2$	2.50×10^{-12}	exp(-260/T)	B
21.	$NO_2 + O_3 \longrightarrow NO_3$	1.40×10^{-13}	exp(-2470/T)	B
22.	$OH + HNO_3 \longrightarrow NO_3$		**KMT11**	C

[1] Reaction type: (P) Photolysis; (B) Bimolecular; (C) Bimolecular reactions involving complex rate coefficients that may have a termolecular component and (T) Termolecular.

[2] JFAC is a scaling factor that can be applied to photolysis rate constants in order to account for variations in cloud cover however under the scenarios considered in this thesis JFAC is equal to 1.0 i.e. under clear sky conditions.

[3] This is a composite photolysis reaction that includes $O(^1D)$ quenching (see notes 1).

	Photolysis Reactions	Rate Constant, k		Reaction type[4]
23.	$H_2O_2 + h\nu \longrightarrow OH + OH$	7.11×10^{-6}	JFAC	P
24.	$NO_2 + h\nu \longrightarrow NO + O_3$	9.20×10^{-3}	JFAC	P
25.	$NO_3 + h\nu \longrightarrow NO$	2.34×10^{-2}	JFAC	P
26.	$NO_3 + h\nu \longrightarrow NO_2 + O_3$	1.83×10^{-1}	JFAC	P
27.	$HONO + h\nu \longrightarrow OH + NO$	2.02×10^{-3}	JFAC	P
28.	$HNO_3 + h\nu \longrightarrow OH + NO_2$	6.30×10^{-7}	JFAC	P
	Organic Reactions			
29.	$OH + CH_4 = CH_3O_2$	9.65×10^{-20}	$T^{2.58}\exp(-1082/T)$	B
30.	$OH + C_2H_4 = HOCH_2CH_2O_2$		**KMT15**	T
31.	$OH + C_3H_6 = RN9O2$		**KMT16**	T
32.	$O_3 + C_2H_4 = HCHO + CO + HO_2 + OH$	9.14×10^{-15}	exp(-2580/T)*0.13	B
33.	$O_3 + C_2H_4 = HCHO + HCOOH$	9.14×10^{-15}	exp(-2580/T)*0.87	B
34.	$O_3 + C_3H_6 = HCHO + CO + CH_3O_2 + OH$	5.51×10^{-15}	exp(-1878/T)*0.36	B
35.	$O_3 + C_3H_6 = HCHO + CH_3CO_2H$	5.51×10^{-15}	exp(-1878/T)*0.64	B
36.	$OH + C_5H_8 = RU14O2$	2.54×10^{-11}	exp(410/T)	B
37.	$O_3 + C_5H_8 = UCARB10 + CO + HO_2 + OH$	7.86×10^{-15}	exp(-1913/T)*0.27	B
38.	$O_3 + C_5H_8 = UCARB10 + HCOOH$	7.86×10^{-15}	exp(-1913/T)*0.73	B
39.	$HCHO = CO + HO_2 + HO_2$	3.05×10^{-5}	JFAC	P
40.	$HCHO = H_2 + CO$	4.61×10^{-5}	JFAC	P
41.	$CH_3CHO = CH_3O_2 + HO_2 + CO$	5.07×10^{-6}	JFAC	P
42.	$OH + HCHO = HO_2 + CO$	1.20×10^{-14}	T*exp(287/T)	B
43.	$OH + CH_3CHO = CH_3CO_3$	5.55×10^{-12}	exp(311/T)	B
44.	$OH + CH_3OH = HO_2 + HCHO$	6.01×10^{-18}	T^{2}* exp(170/T)	B
45.	$OH + C_2H_5OH = CH_3CHO + HO_2$	6.18×10^{-18}	T^{2}*exp(532/T)*0.887	B
46.	$OH + C_2H_5OH = HOCH_2CH_2O_2$	6.18×10^{-18}	T^{2}*exp(532/T)*0.113	B
47.	$HCOOH + OH = HO_2$	4.50×10^{-13}		B
48.	$CH_3CO_2H + OH = CH_3O_2$	8.00×10^{-13}		B
49.	$CH_3O_2 + NO = HCHO + HO_2 + NO_2$	3.00×10^{-12}	exp(280/T)*0.999	B
50.	$HOCH_2CH_2O_2 + NO = HCHO + HCHO + HO_2 + NO_2$		*KRO2NO*0.995*0.776	B
51.	$HOCH_2CH_2O_2 + NO = HOCH_2CHO + HO_2 + NO_2$		*KRO2NO*0.995*0.224	B
52.	$RN_9O_2 + NO = CH_3CHO + HCHO + HO_2 + NO_2$		*KRO2NO*0.979	B
53.	$CH_3CO_3 + NO = CH_3O_2 + NO_2$		*KAPNO*	B
54.	$HOCH_2CO_3 + NO = HO_2 + HCHO + NO_2$		*KAPNO*	B
55.	$RU14O2 + NO = UCARB12 + HO_2 + NO_2$		*KRO2NO*0.900*0.252	B
56.	$RU14O2 + NO = UCARB10 + HCHO + HO_2 + NO_2$		*KRO2NO*0.900*0.748	B

[4] Reaction action type: (P) Photolysis; (B) Bimolecular and (T) Termolecular.

	Organic Reactions	Rate Constant, k		Reaction type[5]
57.	RU12O2 + NO = CH3CO3 + HOCH2CHO + NO_2		*KRO2NO**0.7	B
58.	RU12O2 + NO = CARB7 + CO + HO_2 + NO_2		*KRO2NO**0.3	B
59.	RU10O2 + NO = CH_3CO_3 + $HOCH_2CHO$ + NO_2		*KRO2NO**0.5	B
60.	RU10O2 + NO = CARB6 + HCHO + HO_2 + NO_2		*KRO2NO**0.3	B
61.	RU10O2 + NO = CARB7 + HCHO + HO_2 + NO_2		*KRO2NO**0.2	B
62.	CH_3O_2 + NO = CH_3NO_3	3.00×10^{-12}	exp(280/T)*0.001	B
63.	$HOCH_2CH_2O_2$ + NO = $HOC_2H_4NO_3$		*KRO2NO**0.005	B
64.	RN9O2 + NO = RN9NO3		*KRO2NO**0.021	B
65.	RU14O2 + NO = RU14NO3		*KRO2NO**0.100	B
66.	CH_3O_2 + HO_2 = CH_3OOH	4.10×10^{-13}	exp(790/T)	B
67.	$HOCH_2CH_2O_2$ + HO_2 = HOC_2H_4OOH	2.03×10^{-13}	exp(1250/T)	B
68.	RN9O2 + HO_2 = RN9OOH		*KRO2H02**0.520	B
69.	CH_3CO_3 + HO_2 = CH_3CO_3H		*KAPH02*	B
70.	$HOCH_2CO_3$ + HO_2 = $HOCH_2CO_3H$		*KAPH02*	B
71.	RU14O2 + HO_2 = RU14OOH		*KRO2H02**0.770	B
72.	RU12O2 + HO_2 = RU12OOH		*KRO2H02**0.706	B
73.	RU10O2 + HO_2 = RU10OOH		*KRO2H02**0.625	B
74.	CH_3O_2 = HCHO + HO_2	1.82×10^{-12}	exp(416/T)*0.33*RO_2	R
75.	CH_3O_2 = HCHO	1.82×10^{-13}	exp(416/T)*0.335*RO_2	R
76.	CH_3O_2 = CH_3OH	1.82×10^{-13}	exp(416/T)*0.335*RO_2	R
77.	$HOCH_2CH_2O_2$ = $HOCH_2CHO$ + HO_2	2.00×10^{-12}	RO_2*0.224	R
78.	RN9O2 = CH_3CHO + HCHO + HO_2	8.80×10^{-13}	RO_2	R
79.	CH_3CO_3 = CH_3O_2	1.00×10^{-11}	RO_2	R
80.	$HOCH_2CO_3$ = HCHO + HO_2	1.00×10^{-11}	RO_2	R
81.	RU14O2 = UCARB12 + HO_2	1.71×10^{-12}	RO_2*0.252	R
82.	RU14O2 = UCARB10 + HCHO + HO_2	1.71×10^{-12}	RO_2*0.748	R
83.	RU12O2 = CH_3CO_3 + $HOCH_2CHO$	2.00×10^{-12}	RO_2*0.7	R
84.	RU12O2 = CARB7 + $HOCH_2CHO$ + HO_2	2.00×10^{-12}	RO_2*0.3	R
85.	RU10O2 = CH_3CO_3 + $HOCH_2CHO$	2.00×10^{-12}	RO_2*0.5	R
86.	RU10O2 = CARB6 + HCHO + HO_2	2.00×10^{-12}	RO_2*0.3	R
87.	RU10O2 = CARB7 + HCHO + HO_2	2.00×10^{-12}	RO_2*0.2	R
88.	CARB7 = CH_3CO_3 + HCHO + HO_2	3.36×10^{-6}	JFAC	P
89.	$HOCH_2CHO$ = HCHO + CO + HO_2 + HO_2	1.77×10^{-5}	JFAC	P
90.	UCARB10 = CH_3CO_3 + HCHO + HO_2	1.62×10^{-5}	JFAC	P
91.	CARB6 = CH_3CO_3 + CO + HO_2	1.26×10^{-4}	JFAC	P
92.	UCARB12 = CH_3CO_3 + $HOCH_2CHO$ + CO + HO_2	1.62×10^{-5}	JFAC	P

[5] Reaction action type: (P) Photolysis; (B) Bimolecular and (T) Termolecular (R) RO_2 permutation reactions (see notes).

	Organic Reactions	Rate Constant, k		Reaction type[6]
93.	$OH + CARB7 = CARB6 + HO_2$	3.00×10^{-12}		B
94,	$OH + UCARB10 = RU10O2$	2.50×10^{-11}		B
95.	$O_3 + UCARB10 = HCHO + CH_3CO_3 + CO + OH$	2.85×10^{-18}	0.59	B
96.	$O_3 + UCARB10 = HCHO + CARB6 + H_2O_2$	2.85×10^{-18}	0.41	B
97.	$OH + HOCH_2CHO = HOCH_2CO_3$	1.00×10^{-11}		B
98.	$OH + CARB6 = CH_3CO_3 + CO$	1.72×10^{-11}		B
99.	$OH + UCARB12 = RU12O2$	4.52×10^{-11}		B
100.	$O_3 + UCARB12 = HOCH_2CHO + CH_3CO_3 + CO + OH$	2.40×10^{-17}	0.89	B
101.	$O_3 + UCARB12 = HOCH_2CHO + CARB6 + H_2O_2$	2.40×10^{-17}	0.11	B
102.	$CH_3NO_3 = HCHO + HO_2 + NO_2$	8.96×10^{-7}	JFAC	P
103.	$OH + CH_3NO_3 = HCHO + NO_2$	1.00×10^{-14}	exp(1060/T)	B
104.	$OH + HOC_2H_4NO_3 = HOCH_2CHO + NO_2$	1.09×10^{-12}		B
105.	$OH + RN9NO3 = CARB7 + NO_2$	1.31×10^{-12}		B
106.	$OH + RU14NO3 = UCARB12 + NO_2$	5.55×10^{-11}		B
107.	$CH_3OOH = HCHO + HO_2 + OH$	5.44×10^{-6}	JFAC	P
108.	$CH_3CO_3H = CH_3O_2 + OH$	5.44×10^{-6}	JFAC	P
109.	$HOCH_2CO_3H = HCHO + HO_2 + OH$	5.44×10^{-6}	JFAC	P
110.	$RU14OOH = UCARB12 + HO_2 + OH$	1.37×10^{-6}	JFAC	P
111.	$RU14OOH = UCARB10 + HCHO + HO_2 + OH$	4.07×10^{-6}	JFAC	P
112.	$RU12OOH = CARB6 + HOCH_2CHO + HO_2 + OH$	5.44×10^{-6}	JFAC	P
113.	$RU10OOH = CH_3CO_3 + HOCH_2CHO + OH$	5.44×10^{-6}	JFAC	P
114.	$HOC_2H_4OOH = HCHO + HCHO + HO_2 + OH$	5.44×10^{-6}	JFAC	P
115.	$RN9OOH = CH_3CHO + HCHO + HO_2 + OH$	5.44×10^{-6}	JFAC	P
116.	$OH + CH_3OOH = CH_3O_2$	1.90×10^{-11}	exp(190/T)	B
117.	$OH + CH_3OOH = HCHO + OH$	1.00×10^{-11}	exp(190/T)	B
118.	$OH + CH_3CO_3H = CH_3CO_3$	3.70×10^{-12}		B
119.	$OH + HOCH_2CO_3H = HOCH_2CO_3$	6.19×10^{-12}		B
120.	$OH + RU14OOH = UCARB12 + OH$	7.51×10^{-11}		B
121.	$OH + RU12OOH = RU12O2$	3.00×10^{-11}		B
122.	$OH + RU10OOH = RU10O2$	3.00×10^{-11}		B
123.	$OH + HOC_2H_4OOH = HOCH_2CHO + OH$	2.13×10^{-11}		B
124.	$OH + RN9OOH = CARB7 + OH$	2.50×10^{-11}		B
125.	$CH_3CO_3 + NO_2 = PAN$		**KFPAN**	T
126.	$PAN = CH_3CO_3 + NO_2$		**KBPAN**	T
127.	$HOCH_2CO_3 + NO_2 = PHAN$		**KFPAN**	T
128.	$PHAN = HOCH_2CO_3 + NO_2$		**KBPAN**	T
129.	$OH + PAN = HCHO + CO + NO_2$	9.50×10^{-13}	exp(-650/T)	B

[6] Reaction action type: (P) Photolysis; (B) Bimolecular and (T) Termolecular.

Organic Reactions		Rate Constant, k		Reaction type[7]
130.	OH + PHAN = HCHO + CO + NO_2	1.12×10^{-12}		B
131.	RU12O2 + NO_2 = RU12PAN		**KFPAN***0.061	T
132.	RU12PAN = RU12O2 + NO_2		**KBPAN**	T
133.	RU10O2 + NO_2 = MPAN		**KFPAN***0.041	T
134.	MPAN = RU10O2 + NO_2		**KBPAN**	T
135.	OH + MPAN = CARB7 + CO + NO_2	3.60×10^{-12}		B
136.	OH + RU12PAN = UCARB10 + NO_2	2.52×10^{-11}		B

Table A2 - *Complex and simple rate coefficients calculated according to the MCM v3.1 protocol.*

Complex rate coefficients		Simple rate coefficients		
KMT05	1.55	KRO2NO	2.54×10^{-12}	exp(360/T)
KMT06	2.05	KAPNO	8.10×10^{-12}	exp(270/T)
KMT07	1.01×10^{-11}	KRO2HO2	2.91×10^{-13}	exp(1300/T)
KMT08	1.23×10^{-11}	KAPHO2	4.30×10^{-13}	exp(1040/T)
KMT09	1.43×10^{-12}			
KMT10	3.74×10^{-2}			
KMT11	1.63×10^{-13}			
KMT15	7.99×10^{-12}			
KMT16	2.87×10^{-11}			
KFPAN	1.07×10^{-11}			
KBPAN	1.51×10^{-4}			

Notes

1. The rate constant is given as $j_1 \times f$ where j_1 is the photolysis rate constant for the reaction: $O_3 + h\nu \longrightarrow O(^1D) + O_2$ and f is:

$$f = \frac{k_3[H_2O]}{k_1[N_2]+k_2[O_2]+k_3[H_2O]}$$

where: $k_1 = 1.80\times10^{-11}\exp(107/T)$;

$k_2 = 3.20\times10^{-11}\exp(67/T)$;

$k_3 = 2.20\times10^{-10}$.

[7] Reaction type: (P) Photolysis; (B) Bimolecular and (T) Termolecular.

2. The **peroxy radical summation** applied to the RO_2 permutation reactions is calculated at each time step as:

$[RO_2] = [CH_3O_2] + [HOCH_2CH_2O_2] + [RN9O2] + [CH_3CO_3] + [HOCH_2CO_3] + [RU14O2] + [RU12O2] + [RU10O2]$

Appendix B: Emission factors

The following tables included in this Appendix present the vehicle emissions applied to the box and LES-RCS models calculated using vehicle speed emission factors (Boulter et al., 2009).

Table B1 - *Fleet weighted emission rates (CO, HC and NO_X) per vehicle (g km^{-1}) for the year 2010 for vehicles travelling at 30 mph.*

Vehicle type	CO	HC	NO_X
		g km^{-1}	
Cars	0.869	0.070	0.213
Taxis	0.266	0.048	0.454
Vans	0.341	0.040	0.326
Rigid HGVs	0.780	0.135	3.668
Artic HGVs	1.000	0.182	6.263
Buses	0.974	0.221	5.749
Coaches	1.174	0.310	6.391
Moped	8.840	8.068	0.026
Motorcycles	13.513	2.043	0.186
All types	0.900	0.090	0.410

Table B2 - *Fractions of traffic flows by vehicle type on urban roads[1] and calculated total emission rates for CO, HC and NO_X (g km^{-1} hr^{-1}) for the year 2010.*

Vehicle type	Relative proportion of vehicle type [%]	Number of vehicles hr^{-1}	CO	HC	NO_X
			Total emission rate g km^{-1} hr^{-1}		
Cars	84.9	1273	1106	89	272
Taxis	0.0	0	0	0	0
Vans	10.6	159	54	6	52
Rigid HGVs	1.1	17	13	2	61
Artic HGVs	0.4	6	6	1	38
Buses	2.3	34	33	8	197
Coaches	0.0	0	0	0.000	0.00
Moped	0.0	0	0	0.000	0.00
Motorcycles	0.7	11	144	22	2
All types	100	1500	1356	128	620

[1] The relative proportion of each vehicle type observed on urban roads was calculated using DFT count data (count point 36401) on the Bristol Road, Birmingham, UK (http://www.dft.gov.uk/traffic-counts/cp.php?la=Birmingham#countpointstable).

Table B3 - *Calculated vehicle emission rates of CO, HC and NO_X (2010).*

	CO[2]	**HC**[3]	**NO_X**[4]
g km^{-1} hr^{-1}	1356	128	620
g cm^{-1} s^{-1}	3.77×10^{-6}	3.56×10^{-7}	1.72×10^{-6}
No. of moles cm^{-1} s^{-1}	1.35×10^{-7}	2.97×10^{-8}	3.74×10^{-8}
No. of molecules cm^{-1} s^{-1}	8.10×10^{16}	1.79×10^{16}	2.25×10^{16}
No. of molecules cm^{-3} s^{-1}	2.50×10^{10}	5.52×10^{9}	6.94×10^{9}

[2] Molar mass of CO = 28.01 g mol^{-1}.

[3] Molar mass of HC determined as C = 12.01 g mol^{-1}.

[4] Molar mass of NO_X determined as NO_2 = 46.01 g mol^{-1}.

Appendix C: VOCs emitted from road transport

Table C1 - *The annual mass emissions (in tonnes and number of molecules emitted) of VOCs from UK road transport (Defra, 2008d), their Photochemical Ozone Creation Potential (POCP) for day 1 (Derwent et al., 1996, calculated OH reactivity [$cm^3\ s^{-1}$] and k_{OH} (molec.$^{-1}$ $cm^3\ s^{-1}$).*

Species	OH Reactivity [$cm^3\ s^{-1}$]	Molar Mass [g mol^{-1}]	Mass [t]	No. of molec. emitted	POCP		k_{OH} x 10^{12} [molec.$^{-1}$ $cm^3\ s^{-1}$]
					Day 1	Weighted [t]	
Alkanes							
ethane C_2H_6	7.56×10^{18}	30.07	1,573	3.15×10^{31}	3.7	58	0.24[5]
propane C_3H_8	8.07×10^{18}	44.09	537	7.34×10^{30}	13.0	70	1.1[1]
butane C_4H_{10}	1.43×10^{20}	58.12	6,017	6.23×10^{31}	20.4	1,227	2.3[1]
2-methylpropane C_4H_{10}	5.64×10^{19}	58.12	2,592	2.69×10^{31}	20.4	529	2.1[6]
pentane C_5H_{12}	1.18×10^{20}	72.15	3,733	3.12×10^{31}	14.8	552	3.8[7]
2-methylbutane C_5H_{12}	2.36×10^{20}	72.15	7,838	6.54×10^{31}	20.4	1,599	3.6[3]
hexane C_6H_{14}	1.24×10^{20}	86.17	3,421	2.39×10^{31}	20.4	698	5.2[3]
heptane C_7H_{16}	3.16×10^{19}	100.20	773	4.65×10^{30}	24.1	186	6.8[3]
octane C_8H_{18}	1.41×10^{19}	114.22	329	1.73×10^{30}	24.1	79	8.1[3]
nonane C_9H_{20}	6.34×10^{18}	128.25	139	6.54×10^{29}	20.4	28	9.7[3]
decane $C_{12}H_{22}$	2.31×10^{19}	166.30	580	2.10×10^{30}	20.4	118	11.0[3]

[5] Atkinson *et al.* (2006)
[6] IUPAC (2009b)
[7] Atkinson (2003)

Species	OH Reactivity [$cm^3\ s^{-1}$]	Molar Mass [$g\ mol^{-1}$]	Mass [t]	No. of molec. emitted	POCP Day 1	POCP Weighted [t]	k_{OH} x 10^{12} [$molec.^{-1}\ cm^3\ s^{-1}$]
Alkenes							
ethylene C_2H_4	1.16E+21	28.05	6,823	1.46×10^{32}	100.0	6,823	7.9[1]
propylene C_3H_6	1.23E+21	42.08	2,952	4.23×10^{31}	100.0	2,952	29.0[1]
2-methylpropene C_4H_8	1.12E+21	56.10	2,040	2.19×10^{31}	113.0	2,305	51.0[8]
Alkynes							
acetylene C_2H_2	4.49E+19	26.04	2,488	5.75×10^{31}	13.0	323	0.78[1]
Aromatics							
benzene C_6H_6	2.40E+19	78.11	2,592	2.00×10^{31}	11.1	288	1.2[9]
toluene C_7H_8	2.47E+20	92.13	6,760	4.42×10^{31}	35.2	2,380	5.6[10]
o-xylene C_8H_{10}	1.41E+20	106.16	1,771	1.00×10^{31}	38.9	689	14.0[11]
m-xylene C_8H_{10}	2.66E+20	106.16	2,039	1.16×10^{31}	70.4	1,436	23.0[12]
p-xylene C_8H_{10}	1.25E+20	106.16	1,576	8.94×10^{30}	55.6	876	14.0[13]
ethylbenzene C_8H_{10}	6.33E+19	106.16	1,595	9.05×10^{30}	37.0	590	7.0[7]
trimethylbenzene							
1,2,3- C_9H_{12}	8.64E+19	120.19	522	2.62×10^{30}	72.2	377	33.0[7]
1,2,4- C_9H_{12}	3.82E+20	120.19	2,311	1.16×10^{31}	74.1	1,712	33.0[7]
1,3,5 C_9H_{12}	2.48E+20	120.19	867	4.34×10^{30}	75.9	658	57.0[8]
Aldehydes							
formaldehyde CH_2O	6.58E+20	30.03	3,859	7.74×10^{31}	42.6	1,644	8.5[1]
acetaldehyde C_2H_4O	3.96E+20	44.05	1,932	2.64×10^{31}	-20.4	-394	15.0[1]

[8] IUPAC (2009a)
[9] IUPAC (2008a)
[10] IUPAC (2008b)
[11] MCM (2009)
[12] Atkinson and Arey (2003)
[13] Calvert *et al.* (2002)

Species	OH Reactivity [cm^3 s^{-1}]	Molar Mass [g mol^{-1}]	Mass [t]	No. of molec. emitted	POCP Day 1	POCP Weighted [t]	k_{OH} x 10^{12} [$molec.^{-1}$ cm^3 s^{-1}]
Ketones							
acetone **C_3H_6O**	1.06E+18	58.08	566	5.87×10^{30}	1.9	11	0.18[1]
2-butanone **C_4H_8O**	3.15E+19	72.10	157	1.31×10^{30}	7.4	12	24.0[14]
Dialkenes							
1,3-butadiene **C_4H_6**	1.04E+21	54.09	1,398	1.56×10^{31}			67.0[15]

[14] IUPAC (2007)
[15] Atkinson (1997)

Appendix D: Emission scenarios

Table D1 - *Air pollution scenarios and emission rates to be applied to the LES derived from variations in vehicle speed and traffic.*

Case	Base	A	B	C	D	E	F
Number and speed of vehicles							
Vehicles hr^{-1}	1500	1500	1500	150	150	2500	2500
Speed (mph)	30	10	60	30	10	30	10
Emissions (ppb s^{-1})*							
NO	900	1607	1025	90	161	1500	2678
NO_2	100	179	114	10	18	167	298
HONO	0	0	0	0	0	0	0
CO	3593	9286	4031	359	929	5989	15476
C_2H_4	347	947	253	35	95	579	1578
C_3H_6	150	410	109	15	41	250	683
CH_3CHO	98	268	72	10	27	164	447
HCHO	196	536	143	20	54	327	893

Table D2 - *Air pollution scenarios and emission rates to be applied to the LES derived from variations in the fraction of NO_X emitted as NO and NO_2.*

Case	Base	G	H	I
Fraction of emissions as NO or NO_2				
f-NO	0.90	0.70	0.80	1.00
f-NO_2	0.10	0.30	0.20	0.00
Emissions (ppb s^{-1})				
NO	900	700	800	1000
NO_2	100	300	200	0
HONO	0	0	0	0
CO	3593	3593	3593	3593
C_2H_4	347	347	347	347
C_3H_6	150	150	150	150
CH_3CHO	98	98	98	98
HCHO	196	196	196	196

* All emission rates reflect those emitted into one LES model cell (0.3 m × 1 m × 0.3 m).

Table D3 - *Air pollution scenarios and emission rates to be applied to the LES derived from variations in the fraction of NO_X emitted as NO, NO_2 and HONO.*

Case	Base	J	K	L	M
Fraction of emissions as NO, NO_2 or HONO					
f-NO	0.90	0.80	0.80	0.90	0.90
f-NO_2	0.10	0.19	0.15	0.09	0.05
f-HONO	0.00	0.01	0.05	0.01	0.05
Emissions (ppb s^{-1})					
NO	900	800	800	900	900
NO_2	100	190	150	90	50
HONO	0	10	50	10	50
CO	3593	3593	3593	3593	3593
C_2H_4	347	347	347	347	347
C_3H_6	150	150	150	150	150
CH_3CHO	98	98	98	98	98
HCHO	196	196	196	196	196

Table D4 - *Air pollution scenarios and emission rates to be applied to the LES derived from variations in the VOC to NO_X emission ratios.*

Case	Base	N	O	p	Q
VOC to NO_X emission ratio					
VOC / NO_X	1	1	2	0.5	1
VOC ×	1	2	1	1	0.5
NO_X ×	0.79	0.40	1.58	0.40	1.58
Emissions (ppb s^{-1})					
NO	900	1800	900	900	450
NO_2	100	200	100	100	50
HONO	0	0	0	0	0
CO	3593	3593	3593	3593	3593
C_2H_4	347	347	695	174	347
C_3H_6	150	150	301	75	150
CH_3CHO	98	98	197	49	98
HCHO	196	196	393	98	196

Table D5 - *Air pollution scenarios and emission rates to be applied to the LES derived from changes in projections of the future composition of the UK vehicle fleet.*

Case	**Base**	**R**	**S**
Year	2010	2015	2025
Emissions (ppb s^{-1})			
NO	900	578	290
NO_2	100	64	32
HONO	0	0	0
CO	3593	3250	3797
C_2H_4	347	290	356
C_3H_6	150	126	154
CH_3CHO	98	82	101
HCHO	196	164	201

Appendix E: Fortran code extracts

As discussed in Chapter 4, the LES model was coded using FORTRAN. An extract from the LES-RCS model subroutine used to specify Gaussian source emissions emitted into one LES model cell (0.3 m × 1 m × 0.3 m) within the canyon (the GAUSSTRCE subroutine used to formulate a Gaussian distribution of line source emissions) is included below[†]. The 51 chemical species of the RCS were listed and assigned (elsewhere) a species number (ITRCE) in the same order of the list of chemical variables, *i.e.* NO_2 is assigned as (ITRCE):

```
C-------------------------------------------------------------------------
C Gaussian sources
C-------------------------------------------------------------------------
      CALL GAUSSTRCE(NZP,NXP,NYP,A(ITRCE2  ),900.)  ! ENO     ppb/s
      CALL GAUSSTRCE(NZP,NXP,NYP,A(ITRCE3  ),100.)  ! ENO2    ppb/s
      CALL GAUSSTRCE(NZP,NXP,NYP,A(ITRCE8  ),3593.) ! ECO     ppb/s
      CALL GAUSSTRCE(NZP,NXP,NYP,A(ITRCE16 ),347.)  ! EC2H4   ppb/s
      CALL GAUSSTRCE(NZP,NXP,NYP,A(ITRCE17 ),150.)  ! EC3H6   ppb/s
      CALL GAUSSTRCE(NZP,NXP,NYP,A(ITRCE20 ),98.)   ! ECH3CHO ppb/s
      CALL GAUSSTRCE(NZP,NXP,NYP,A(ITRCE24 ),196.)  ! EHCHO   ppb/s
      CALL GAUSSTRCE(NZP,NXP,NYP,A(ITRCE52 ),1000.) ! EPS     ppb/s
C-------------------------------------------------------------------------


C-------------------------------------------------------------------------
C List of Chemical variables (Vivien Bright, 2009)
C-------------------------------------------------------------------------
C 1  2  3  4  5  6  7  8  9  10
C 11  12  13  14  15  16  17  18  19  20
C 21  22  23  24  25  26  27  28  29  30
C 31  32  33  34  35
C 36  37  38  39  40
C 41  42  43  44  45
C 46  47  48  49  50  51
C
C O3, NO, NO2, NO3, OH, HO2, H2, CO, H2O2, HONO,
C HNO3,HO2NO2,CH3O2,CH3OH,CH4,C2H4,C3H6,HOCH2CH2O2,CH3CO2H,CH3CHO,
C C5H8,RU14O2,UCARB10,HCHO,CH3CO3,HOCH2CHO,C2H5OH,RN9O2,HCOOH,CARB6,
C UCARB12,RU12O2,CARB7,RU10O2,CH3NO3,
C HOC2H4NO3,RN9NO3,RU14NO3,CH3OOH,HOC2H4OOH,
C CH3CO3H,HOCH2CO3H,RU14OOH,RU12OOH,RU10OOH,
C HOCH2CO3,PAN,PHAN,RU12PAN,RN9OOH,
C MPAN
C-------------------------------------------------------------------------
```

[†] The emissions shown here are those of the base case scenario. EPS represents the emission of the passive scalar into the canyon included within the LES code as species 52.

The following extracts (for the first 20 reactions) of LES-RCS code illustrate the implementation of the RCS chemistry into the chemical subroutine included in the LES model.

```
C-----------------------------------------------------------------------
C Reaction rate constants
C-----------------------------------------------------------------------
      data ak1/3.40E-6/,ck2/4.01E-4/,ck3/2.63E-9/,ck4/6.56E-1/,
     +  ck5/1.72E-3/,ck6/1.49E-4/,ck7/5.06E-3/,ck8/4.21E-2/,
     +  ck9/4.86E-5/,ck10/2.82E+0/,ck11/8.74E-2/,ck12/6.92E-2/,
     +  ck13/2.54E-1/,ck14/3.08E-1/,ck15/5.01E-1/,ck16/2.27E-1/,
     +  ck17/3.59E-2/,ck18/3.74E-2/,ck19/1.20E-1/,ck20/2.58E-2/,
C-----------------------------------------------------------------------


C-----------------------------------------------------------------------
C Photolysis rate constants
C-----------------------------------------------------------------------
data CJFAC/1.0/           ! Units of s-1
ck1   = ak1*CJFAC
C-----------------------------------------------------------------------


C-----------------------------------------------------------------------
C RO2 summation calculated at each time step for RO2 permutation rxns
C-----------------------------------------------------------------------
RO2 = CH3O2(k,i,j) + HOCH2CH2O2(k,i,j) + RN9O2(k,i,j)
   +        + CH3CO3(k,i,j) + HOCH2CO3(k,i,j) + RU14O2(k,i,j)
   +        + RU12O2(k,i,j) + RU10O2(k,i,j)
C-----------------------------------------------------------------------


C-----------------------------------------------------------------------
C Chemical reactions
C-----------------------------------------------------------------------
s1 =ck1 *O3(k,i,j)
             s2 =ck2 *NO(k,i,j)*O3(k,i,j)
             s3 =ck3 *NO(k,i,j)*NO(k,i,j)
             s4 =ck4 *NO(k,i,j)*NO3(k,i,j)
             s5 =ck5 *OH(k,i,j)*O3(k,i,j)
             s6 =ck6 *OH(k,i,j)*H2(k,i,j)
             s7 =ck7 *OH(k,i,j)*CO(k,i,j)
             s8 =ck8 *OH(k,i,j)*H2O2(k,i,j)
             s9 =ck9 *HO2(k,i,j)*O3(k,i,j)
             s10=ck10*OH(k,i,j)*HO2(k,i,j)
             s11=ck11*HO2(k,i,j)*HO2(k,i,j)
             s12=ck12*HO2(k,i,j)*HO2(k,i,j)
             s13=ck13*OH(k,i,j)*NO(k,i,j)
             s14=ck14*OH(k,i,j)*NO2(k,i,j)
             s15=ck15*OH(k,i,j)*NO3(k,i,j)
             s16=ck16*HO2(k,i,j)*NO(k,i,j)
             s17=ck17*HO2(k,i,j)*NO2(k,i,j)
             s18=ck18*HO2NO2(k,i,j)
             s19=ck19*OH(k,i,j)*HO2NO2(k,i,j)
             s20=ck20*OH(k,i,j)*HONO(k,i,j)
C-----------------------------------------------------------------------
```

The following extracts are for illustration purposes alone and only include the first 20 reactions in the calculations presented here with the full LES-RCS including all 136 reactions.

```
C-------------------------------------------------------------------------
C Slower reactions
C-------------------------------------------------------------------------
            SNO=-S2-2*S3-S4-S13-S16

            NO(K,I,J)=NO(K,I,J)+DTLONG*SNO
C-------------------------------------------------------------------------


C-------------------------------------------------------------------------
C Faster reactions
C-------------------------------------------------------------------------
do ic=1,nshort
                s5 =ck5*OH(k,i,j)*O3(k,i,j)
                s6 =ck6*OH(k,i,j)*H2(k,i,j)
                s7 =ck7*OH(k,i,j)*CO(k,i,j)
                s8 =ck8*OH(k,i,j)*H2O2(k,i,j)
                s9 =ck9*HO2(k,i,j)*O3(k,i,j)
                s10=ck10*OH(k,i,j)*HO2(k,i,j)
                s11=ck11*HO2(k,i,j)*HO2(k,i,j)
                s12=ck12*HO2(k,i,j)*HO2(k,i,j)
                s13=ck13*OH(k,i,j)*NO(k,i,j)
                s14=ck14*OH(k,i,j)*NO2(k,i,j)
                s15=ck15*OH(k,i,j)*NO3(k,i,j)
                s16=ck16*HO2(k,i,j)*NO(k,i,j)
                s17=ck17*HO2(k,i,j)*NO2(k,i,j)
                s19=ck19*OH(k,i,j)*HO2NO2(k,i,j)
                s20=ck20*OH(k,i,j)*HONO(k,i,j)


                SOH=+2*S1-S5-S6-S7-S8+S9-S10-S13-S14-S15+S16
     +              -S19-S20

                OH(K,I,J)=OH(K,I,J)+DTSHORT*SOH

            enddo
C-------------------------------------------------------------------------
```

The following extract of code illustrates the initial conditions of the LES-RCS, including a selection of chemical species with those not included here set to zero.

```
C-------------------------------------------------------------------------
C Upwind inlet initial conditions – run the 0-dimensional model for 30 C
minutes.
C-------------------------------------------------------------------------
      nint = 180000
C----   initial conditions
      O3          =40.00
      NO          =2.00
      NO2         =8.00
      NO3         =0
      OH          =0
      HO2         =0
      H2          =0
      CO          =200.00
      H2O2        =0
      HONO        =0
      HNO3        =2.00
      HO2NO2      =0
      CH3O2       =0
      CH3OH       =7.38
      CH4         =1800.00
      C2H4        =0.91
      C3H6        =0.29
      HOCH2CH2O2  =0
      CH3CO2H     =0
      CH3CHO      =2.98
      C5H8        =0.28
      HCHO        =3.14
      C2H5OH      =2.37
      PAN         =0.46
C-------------------------------------------------------------------------
```

Appendix F: OH production and loss mechanisms

Table F1 - *The most dominant rates of OH production and loss (ppt s^{-1}) and the average OH concentrations calculated for the LES-RCS base case simulation at three locations above and within the canyon. Average concentrations taken over the last hour of the model simulation ($150 \leq t \leq 210$ min). Locations as outlined in §5·3·1 above.*

	A. Vortex (V)	**B. Lower leeward wall (L)**	**C. Background atmosphere (B)**
	Rate of production / loss (ppt s^{-1})		
Production			
$HO_2 + NO \longrightarrow OH + NO_2$	8.9	11.7	1.1
$HONO + h\nu \longrightarrow OH + NO$	2.4	1.7	0.17
$O_3 + h\nu \longrightarrow OH + OH$	0.07	0.05	0.30
$O_3 + VOC^{\ddagger} \longrightarrow OH + products$	0.03	0.04	0.001
Loss			
$OH + VOC^{\S} \longrightarrow products$	-5.39	-6.44	-0.63
$OH + NO \longrightarrow HONO$	-3.60	-4.79	-0.17
$OH + NO_2 \longrightarrow HNO_3$	-1.94	-1.72	-0.41
$OH + CO \longrightarrow HO_2$	-0.44	-0.49	-0.23
Mixing ratio (ppb)			
OH	0.088	0.067	0.223

‡ C_2H_4; C_3H_6; C_5H_8.

§ C_2H_4; C_3H_6; C_5H_8; HCHO; CH_3CHO; CH_3OH; C_2H_5OH; PAN.

Appendix G: LES code digital appendix

The full LES code used in this research is included within a digital appendix at the end of this thesis.

References

AQEG (2007). Trends in Primary Nitrogen Dioxide in the UK. Report of the UK Air Quality Expert Group, AQEG. Prepared for the Department for Environment, Food and Rural Affairs, the Scottish Executive, the Welsh Assembly Government and the Department of the Environment in Northern Ireland

AQEG (2009). Ozone in the United Kingdom. Report of the UK Air Quality Expert Group, AQEG. Prepared for the Department for Environment, Food and Rural Affairs, the Scottish Executive, the Welsh Assembly Government and the Department of the Environment in Northern Ireland.

Arya, S. P. (1999). *Air pollution meteorology and dispersion.* Oxford University Press, New York.

Assimakopoulos, V. D., ApSimon, H. M. & Moussiopoulos, N. (2003). A numerical study of atmospheric pollutant dispersion in different two-dimensional street canyon configurations. *Atmos. Environ.,* **37**, 4037-4049.

Atkinson, R. (1997). Gas-phase tropospheric chemistry of volatile organic compounds .1. Alkanes and alkenes. *Journal of Physical and Chemical Reference Data,* **26**, 215-290.

Atkinson, R. (2003). Kinetics of the gas-phase reactions of OH radicals with alkanes and cycloalkanes. *Atmos. Chem. Phys.,* **3**, 2233-2307.

Atkinson, R. & Arey, J. (2003). Atmospheric degradation of volatile organic compounds. *Chemical Reviews,* **103**, 4605-4638.

Atkinson, R., Baulch, D. L., Cox, R. A., Crowley, J. N., Hampson, R. F., Hynes, R. G., Jenkin, M. E., Rossi, M. J., Troe, J. & Subcommittee., I. (2006). Evaluated kinetic and photochemical data for atmospheric chemistry: Volume II - gas phase reactions of organic species. *Atmos. Chem. Phys.,* **6**, 3625-4055.

Auger, L. & Legras, B. (2007). Chemical segregation by heterogeneous emissions. *Atmos. Environ.,* **41**, 2303-2318.

Aumont, B., Szopa, S. & Madronich, S. (2005). Modelling the evolution of organic carbon during its gas-phase tropospheric oxidation: development of an explicit model based on a self generating approach. *Atmos. Chem. Phys.,* **5**, 2497-2517.

BADC. (2004). *NO_X and O_3 measured at Writtle, Essex during the TORCH campaign*. URL: http://cmip-dap.badc.rl.ac.uk/badc/polluted-tropo/data/torch/torch1_2003/.

Baik, J. J., Kang, Y. S. & Kim, J. J. (2007). Modeling reactive pollutant dispersion in an urban street canyon. *Atmos. Environ.,* **41**, 934-949.

Baker, J., Walker, H. L. & Cai, X. M. (2004). A study of the dispersion and transport of reactive pollutants in and above street canyons - a large eddy simulation. *Atmos. Environ.,* **38**, 6883-6892.

Barlow, J. (2009). Boundary layer meteorology and atmospheric dispersion. *In:* Hewitt, C. N. & Jackson, A. V. (eds.) *Atmospheric science for environmental scientists.* Wiley-Blackwell, Chichester.

Belcher, S. E. (2005). Mixing and transport in urban areas. *Philosophical Transactions of the Royal Society. Mathematical Physical and Engineering Sciences,* **363**, 2947-2968.

Bell, M. L., Davis, D. L. & Fletcher, T. (2004). A retrospective assessment of mortality from the London smog episode of 1952: The role of influenza and pollution. *Environmental Health Perspectives,* **112**, 6-8.

Benson, J., Ziehn, T., Dixon, N. S. & Tomlin, A. S. (2008). Global sensitivity analysis of a 3D street canyon model—Part II: Application and physical insight using sensitivity analysis. *Atmos. Environ.,* **42**, 1874-1891.

Berkowicz, R. (2000). OSPM - A parameterised street pollution model. *Environmental Monitoring and Assessment,* **65**, 323-331.

Berkowicz, R., Ketzel, M., Vachon, G., Louka, P., Rosant, J. M., Mestayer, P. G. & Sini, J. F. (2002). Examination of Traffic Pollution Distribution in a Street Canyon Using the Nantes'99 Experimental Data and Comparison with Model Results. *Water, Air, & Soil Pollution: Focus,* **2**, 311-324.

Berkowicz, R., Palmgren, F., Hertel, O. & Vignati, E. (1996). Using measurements of air pollution in streets for evaluation of urban air quality -- meterological analysis and model calculations. *Science of The Total Environment,* **189-190**, 259-265.

Bloss, C., Wagner, V., Bonzanini, A., Jenkin, M. E., Wirtz, K., Martin-Reviejo, M. & Pilling, M. J. (2005a). Evaluation of detailed aromatic mechanisms (MCMv3 and MCMv3.1) against environmental chamber data. *Atmos. Chem. Phys.,* **5**, 623-639.

Bloss, C., Wagner, V., Jenkin, M. E., Volkamer, R., Bloss, W. J., Lee, J. D., Heard, D. E., Wirtz, K., Martin-Reviejo, M., Rea, G., Wenger, J. C. & Pilling, M. J. (2005b). Development of a detailed chemical mechanism (MCMv3.1) for the atmospheric oxidation of aromatic hydrocarbons. *Atmos. Chem. Phys.,* **5**, 641-664.

Bloss, W. J. (2009). Atmospheric Chemical Processes of Importance in Cities. *In:* Harrison, R. M. & Hester, R. E. (eds.) *Air Quality in Urban Environments.* The Royal Society of Chemistry, Cambridge.

Boddy, J. W. D., Smalley, R. J., Dixon, N. S., Tate, J. E. & Tomlin, A. S. (2005). The spatial variability in concentrations of a traffic-related pollutant in two street canyons in York, UK—Part I: The influence of background winds. *Atmos. Environ.,* **39**, 3147-3161.

Boulter, P. G., Barlow, T. J., Latham, S. & McCrae, I. S. (2009). Emission Factors 2009: Report 1 - a review of methods for determining hot exhaust emission factors for road vehicles. TRL, Wokingham.

Bright, V., Bloss, W. & Cai, X. (2011). Modelling atmospheric composition in urban street canyons. *Weather,* **66**, 106-110.

Brimblecombe, P. (1987). *The big smoke.* Methuen, London.

Brimblecombe, P. (1999). History of urban air pollution. *In:* Fenger, J., Hertel, O. & Palmgren, F. (eds.) *Urban Air Pollution: European Aspects.* Kluwer Academic Publishers, Dordrecht.

Britter, R. E. & Hanna, S. R. (2003). Flow and dispersion in urban areas. *Annual Review of Fluid Mechanics,* **35**, 469-496.

Brown, M. L., Lawson, R.E., Decroix, D.S., Lee, R.L. (2000). Mean flow and turbulence measurements around a 2-D array of buildings in a wind tunnel. *11th Joint AMS/AWMA Conference on Applied Air Pollution.* Long Beach, CA.

Buckland, A. T. (1998). Validation of a street canyon model in two cities. *Environmental Monitoring and Assessment,* **52**, 255-267.

Buckland, A. T. & Middleton, D. R. (1999). Nomograms for calculating pollution within street canyons. *Atmos. Environ.,* **33**, 1017-1036.

Bulmer, M. G. (1979). *Principles of statistics.* Dover Publications, New York.

Ca, V. T., Asaeda, T., Ito, M. & Armfield, S. (1995). Characteristics of wind-field in a street canyon. *Journal of Wind Engineering and Industrial Aerodynamics,* **57**, 63-80.

Cai, X.-M. (2012a). Effects of differential wall heating in street canyons on dispersion and ventilation characteristics of a passive scalar. *Atmos. Environ.,* **51**, 268-277.

Cai, X.-M. (2012b). Effects of wall heating on flow characteristics in a street canyon. *Boundary-Layer Meteorol,* **142**, 443-467.

Cai, X. M., Barlow, J. F. & Belcher, S. E. (2008). Dispersion and transfer of passive scalars in and above street canyons - Large-eddy simulations. *Atmos. Environ.,* **42**, 5885-5895.

Calogirou, A., Larsen, B. R. & Kotzias, D. (1999). Gas-phase terpene oxidation products: a review. *Atmos. Environ.,* **33**, 1423-1439.

Calvert, J. G., Atkinson, R., Becker, K. H., Kamens, R. M., Seinfeld, J. H., Wallington, T. J. & Yarwood, G. (2002). *The Mechanisms of Atmospheric Oxidation of Aromatic Hydrocarbons.* Oxford University Press, New York.

Carslaw, N. & Carslaw, D. (2001). The gas-phase chemistry of urban atmospheres. *Surveys in Geophysics,* **22**, 31-53.

Cheng, W. & Liu, C.-H. (2011). Large-Eddy Simulation of Flow and Pollutant Transports in and Above Two-Dimensional Idealized Street Canyons. *Boundary-Layer Meteorol*, **139**, 411-437.

Christen, A. (2005). *Atmospheric turbulence and surface energy exchange in urban environments. Results from the Basel Urban Boundary Layer Experiment (BUBBLE). Ph.D. Thesis.* University of Basel, Switzerland.

Costabile, F. & Allegrini, I. (2007). Measurements and analyses of nitrogen oxides and ozone in the yard and on the roof of a street-canyon in Suzhou. *Atmos. Environ.,* **41**, 6637-6647.

Criegee, R. (1975). Mechanism of Ozonolysis. *Angewandte Chemie International Edition in English,* **14**, 745-752.

Crowther, J. M. & Hassan, A. (Year). Three-dimensional numerical simulation of air pollutant dispersion in street canyons. *In:* Sokhi, R. S. & Bartzis, J. G., eds. 3rd International Conference on Urban Air Quality - Measurement, Modeling and Management, Mar 20-23 2002 Loutraki, Greece. 279-295.

Cui, Z. Q., Cai, X. M. & Baker, C. J. (2004). Large-eddy simulation of turbulent flow in a street canyon. *Quarterly Journal of the Royal Meteorological Society,* **130**, 1373-1394.

Curtis, A. R. & Sweetenham, W. P. (1987). *FACSIMILE/CHECKMAT user's manual*, UKAEA Atomic Energy Research Establishment Computer Science and Systems Division.

Dabberdt, W. F., Ludwig, F. L. & Johnson, W. B. (1973). Validation and applications of an urban diffusion model for vehicular pollutants. *Atmos. Environ.,* **7**, 603-618.

Defra. (2003). *NOx monitoring data for Marylebone Road during August 2003*. URL: **http://uk-air.defra.gov.uk/data/**.

Defra. (2007). The Air Quality Strategy for England, Scotland, Wales and Northern Ireland. Volume 1. HMSO.

Defra. (2008a). *Data Archive: Marylebone Road, London - Non-Automatic Data. Traffic count data 2007*. URL: **http://uk-air.defra.gov.uk/data/maryleboneroad**.

Defra. (2008b). *Emissions of carbon monoxide (CO): 1970-2008*. URL: **http://archive.defra.gov.uk/evidence/statistics/environment/airqual/alltables.htm**.

Defra. (2008c). *Emissions of nitrogen oxides (NOx) including for large combustion plants (LCPs): 1970-2008*. URL: http://archive.defra.gov.uk/evidence/statistics/environment/airqual/alltables.htm.

Defra. (2008d). *Estimated emissions of volatile organic compounds (VOCs) by species and by source: 2006*. URL: http://archive.defra.gov.uk/evidence/statistics/environment/airqual/alltables.htm.

Defra. (2008e). *UK Pollutant Deposition. Ammonia, Acid Gases and Aerosols, and Heavy Metals Monitoring Networks for the UK*. URL: http://pollutantdeposition.defra.gov.uk/networks.

Defra. (2012). Air Pollution in the UK 2011. Defra.

DePaul, F. T. & Sheih, C. M. (1985). A tracer study of dispersion in an urban street canyon. *Atmos. Environ. (1967),* **19**, 555-559.

Derwent, R. G. (1995). Sources, Distributions, and Fates of VOCs in the Atmosphere. *In:* Hester, R. E. & Harrison, R. M. (eds.) *Volatile Organic Compounds in the Atmosphere.* Cambridge: Royal Society of Chemistry.

Derwent, R. G., Jenkin, M. E. & Saunders, S. M. (1996). Photochemical ozone creation potentials for a large number of reactive hydrocarbons under European conditions. *Atmos. Environ.,* **30**, 181-199.

Derwent, R. G. & Middleton, D. R. (1996). An empirical function for the ratio NO_2 : NO_X. Clean Air 26 (3). National Society for Clean Air and Environmental Protection. Brighton, UK.

DFT (2009). Transport Statistics Bulletin. *Road Statistics 2008: Traffic, Speeds and Congestion.* Department for Transport.

Dobre, A., Arnold, S. J., Smalley, R. J., Boddy, J. W. D., Barlow, J. F., Tomlin, A. S. & Belcher, S. E. (2005). Flow field measurements in the proximity of an urban intersection in London, UK. *Atmos. Environ.,* **39**, 4647-4657.

Dodge, M. C. (2000). Chemical oxidant mechanisms for air quality modeling: critical review. *Atmos. Environ.,* **34**, 2103-2130.

Emmerson, K. M. & Evans, M. J. (2009). Comparison of tropospheric gas-phase chemistry schemes for use within global models. *Atmos. Chem. Phys.,* **9**, 1831-1845.

EU (2008). DIRECTIVE 2008/50/EC OF THE EUROPEAN PARLIAMENT AND OF THE COUNCIL of 21 May 2008 on ambient air quality and cleaner air for Europe. *Official Journal of the European Union*.

Feigenwinter, C. & Vogt, R. (2005). Detection and analysis of coherent structures in urban turbulence. *Theor. Appl. Climatol.,* **81**, 219-230.

Feigenwinter, C., Vogt, R. & Parlow, E. (1999). Vertical structure of selected turbulence characteristics above an urban canopy. *Theor. Appl. Climatol.,* **62**, 51-63.

Fenger, J. (1999). Urban air quality. *Atmos. Environ.,* **33**, 4877-4900.

Finlayson-Pitts, B. J. & Pitts Jr, J. N. (2000). *Chemistry of the Upper and Lower Atmosphere: Theory, Experiments and Applications,* San Diego, Academic Press.

Finn, D., Clawson, K. L., Carter, R. G., Rich, J. D., Eckman, R. M., Perry, S. G., Isakov, V. & Heist, D. K. (2010). Tracer studies to characterize the effects of roadside noise barriers on near-road pollutant dispersion under varying atmospheric stability conditions. *Atmos. Environ.,* **44**, 204-214.

Finnigan, J. (2000). Turbulence in plant canopies. *Annual Review of Fluid Mechanics,* **32**, 519-571.

Frampton, M. W., Morrow, P. E., Cox, C., Gibb, F. R., Speers, D. M. & Utell, M. J. (1991). Effects of Nitrogen Dioxide Exposure on Pulmonary function and Airway Reactivity in Normal Humans. *American Journal of Respiratory and Critical Care Medicine,* **143**, 522-527.

Garmory, A., Kim, I. S., Britter, R. E. & Mastorakos, E. (2009). Simulations of the dispersion of reactive pollutants in a street canyon, considering different chemical mechanisms and micromixing. *Atmos. Environ.,* **43**, 4670-4680.

Garmory, A., Richardson, E. S. & Mastorakos, E. (2006). Micromixing effects in a reacting plume by the Stochastic Fields method. *Atmos. Environ.,* **40**, 1078-1091.

Garratt, J. R. (1992). *The atmospheric boundary layer*. Cambridge University Press, Cambridge.

Gauderman, W. J., Avol, E., Lurmann, F., Kuenzli, N., Gilliland, F., Peters, J. & McConnell, R. (2005). Childhood Asthma and Exposure to Traffic and Nitrogen Dioxide. *Epidemiology,* **16**, 737-743.

Gery, M. W., Whitten, G. Z., Killus, J. P. & Dodge, M. C. (1989). A photochemical kinetics mechanism for urban and regional scale computer modeling. *Journal of Geophysical Research-Atmospheres,* **94**, 12925-12956.

Grawe, D., Cai, X. M. & Harrison, R. M. (2007). Large eddy simulation of shading effects on NO2 and O-3 concentrations within an idealised street canyon. *Atmos. Environ.,* **41**, 7304-7314.

Grimmond, C. S. B. & Oke, T. R. (1999). Aerodynamic properties of urban areas derived from analysis of surface form. *Journal of Applied Meteorology,* **38**, 1262-1292.

Gromke, C., Buccolieri, R., Di Sabatino, S. & Ruck, B. (2008). Dispersion study in a street canyon with tree planting by means of wind tunnel and numerical investigations - Evaluation of CFD data with experimental data. *Atmos. Environ.,* **42**, 8640-8650.

Gutzwiller, L., Arens, F., Baltensperger, U., Gaggeler, H. W. & Ammann, M. (2002). Significance of semivolatile diesel exhaust organics for secondary HONO formation. *Environmental Science & Technology,* **36**, 677-682.

Harrison, R. M. (2001a). Chemistry and Climate Change in the Troposphere. *In:* Harrison, R. M. (ed.) *Pollution: Causes, Effects and Control.* 4th ed. The Royal Society of Chemistry, Cambridge.

Harrison, R. M. (2001b). Air Pollution: Sources, Concentrations and Measurements. *In:* Harrison, R. M. (ed.) *Pollution: Causes, Effects and Control.* 4th ed. The Royal Society of Chemistry, Cambridge.

Hassan, A. A. & Crowther, J. M. (1998). A simple model of pollutant concentrations in a street canyon. *Environmental Monitoring and Assessment,* **52**, 269-280.

Hassoun, S., Pilling, M. J. & Bartle, K. D. (1999). A catalogue of urban hydrocarbons for the city of Leeds: atmospheric monitoring of volatile organic compounds by thermal desorption-gas chromatography. *Journal of Environmental Monitoring,* **1**, 453-458.

Heard, A. C., Pilling, M. J. & Tomlin, A. S. (1998). Mechanism reduction techniques applied to tropospheric chemistry. *Atmos. Environ.,* **32**, 1059-1073.

Heard, D. E. & Pilling, M. J. (2003). Measurement of OH and HO2 in the troposphere. *Chemical Reviews,* **103**, 5163-5198.

Holmes, N. S. & Morawska, L. (2006). A review of dispersion modelling and its application to the dispersion of particles: An overview of different dispersion models available. *Atmos. Environ.,* **40**, 5902-5928.

Hough, A. M. (1988). The calculation of photolysis rates for use in global tropospheric modelling studies. *AERE Report R-13259 (HMSO) London.*

Huang, Y., Hu, X. & Zeng, N. (2009). Impact of wedge-shaped roofs on airflow and pollutant dispersion inside urban street canyons. *Building and Environment,* **44**, 2335-2347.

Hunter, L. J., Johnson, G. T. & Watson, I. D. (1992). An investigation of three-dimensional characteristics of flow regimes within the urban canyon. *Atmos. Environ. Part B. Urban Atmosphere,* **26**, 425-432.

Hynes, R. G., Angove, D. E., Saunders, S. M., Haverd, V. & Azzi, M. (2005). Evaluation of two MCM v3.1 alkene mechanisms using indoor environmental chamber data. *Atmos. Environ.,* **39**, 7251-7262.

IUPAC. (2007). IUPAC Subcommittee on Gas Kinetic Data Evaluation - Data Sheet HOx_VOC14. URL: http://www.iupac-kinetic.ch.cam.ac.uk/.

IUPAC. (2008a). IUPAC Subcommittee on Gas Kinetic Data Evaluation - Data Sheet HOx_AROM1. URL: http://www.iupac-kinetic.ch.cam.ac.uk.

IUPAC. (2008b). IUPAC Subcommittee on Gas Kinetic Data Evaluation - Data Sheet HOx_AROM2. URL: http://www.iupac-kinetic.ch.cam.ac.uk/.

IUPAC. (2009a). IUPAC Subcommittee on Gas Kinetic Data Evaluation - Data Sheet HOx_VOC61. URL: http://www.iupac-kinetic.ch.cam.ac.uk/.

IUPAC. (2009b). IUPAC Subcommitteee on Gas Kintetic Data Evaluation - Data Sheet HOx_VOC60. URL: http://www.iupac-kinetic.ch.cam.ac.uk/.

Jacob, D. J. (2000). *Introduction to atmospheric chemistry.* Princeton University Press, Chichester.

Jacobson, M. Z. (2002). *Atmospheric pollution : history, science, and regulation.* Cambridge University Press, Cambridge.

Jacobson, M. Z. (2005). *Fundamentals of atmospheric modeling.* Cambridge University Press, Cambridge.

Jenkin, M. E. & Clemitshaw, K. C. (2000). Ozone and other secondary photochemical pollutants: chemical processes governing their formation in the planetary boundary layer. *Atmos. Environ.,* **34**, 2499-2527.

Jenkin, M. E., Davies, T. J. & Stedman, J. R. (2002). The origin and day-of-week dependence of photochemical ozone episodes in the UK. *Atmos. Environ.,* **36**, 999-1012.

Jenkin, M. E., Saunders, S. M., Derwent, R. G. & Pilling, M. J. (1997a). Construction and application of a master chemical mechanism (MCM) for modelling tropospheric chemistry. *Abstracts of Papers of the American Chemical Society,* **214**, 116-COLL.

Jenkin, M. E., Saunders, S. M. & Pilling, M. J. (1997b). The tropospheric degradation of volatile organic compounds: a protocol for mechanism development. *Atmos. Environ.,* **31**, 81-104.

Jenkin, M. E., Saunders, S. M., Wagner, V. & Pilling, M. J. (2003). Protocol for the development of the Master Chemical Mechanism, MCM v3 (Part B): tropospheric degradation of aromatic volatile organic compounds. *Atmos. Chem. Phys.,* **3**, 181-193.

Jenkin, M. E., Utembe, S. R. & Derwent, R. G. (2008a). Modelling the impact of elevated primary NO2 and HONO emissions on regional scale oxidant formation in the UK. *Atmos. Environ.,* **42**, 323-336.

Jenkin, M. E., Watson, L. A., Utembe, S. R. & Shallcross, D. E. (2008b). A Common Representative Intermediates (CRI) mechanism for VOC degradation. Part 1: Gas phase mechanism development. *Atmos. Environ.,* **42**, 7185-7195.

Jensen, S. S. (1999). *A Geographic Approach to Modelling Human Exposure to Traffic Air Pollution using GIS. Ph.D. Thesis.* University of Roskilde, Denmark.

Johnson, G. T. & Hunter, L. J. (1995). A numerical study of dispersion of passive scalars in city canyons. *Boundary-Layer Meteorol,* **75**, 235-262.

Johnson, W. B., Ludwig, F. L., Dabberdt, W. F. & Allen, R. J. (1973). Urban diffusion simulation model for carbon-monoxide. *Journal of the Air Pollution Control Association,* **23**, 490-498.

Jones, A. P. (1999). Indoor air quality and health. *Atmos. Environ.,* **33**, 4535-4564.

Kaimal, J. C. & Finnigan, J. J. (1994). *Atmospheric boundary layer flows: Their structure and measurement.* Oxford University Press, Oxford.

Kastner-Klein, P. & Plate, E. J. (1999). Wind-tunnel study of concentration fields in street canyons. *Atmos. Environ.,* **33**, 3973-3979.

Kastner-Klein, P. & Rotach, M. W. (2004). Mean flow and turbulence characteristics in an urban roughness sublayer. *Boundary-Layer Meteorol,* **111**, 55-84.

Kikumoto, H. & Ooka, R. (2012). A numerical study of air pollutant dispersion with bimolecular chemical reactions in an urban street canyon using large-eddy simulation. *Atmos. Environ.,* **54**, 456-464.

Kim, M. J., Park, R. J. & Kim, J.-J. (2012). Urban air quality modeling with full O3—NOx—VOC chemistry: Implications for O3 and PM air quality in a street canyon. *Atmos. Environ.,* **47**, 330-340.

Kitto, A.-M. N. & Harrison, R. M. (1992). Nitrous and nitric acid measurements at sites in South-East England. *Atmos. Environ. Part A. General Topics,* **26**, 235-241.

Krol, M. C., Molemaker, M. J. & de Arellano, J. V. G. (2000). Effects of turbulence and heterogeneous emissions on photochemically active species in the convective boundary layer. *Journal of Geophysical Research-Atmospheres,* **105**, 6871-6884.

Kwak, K.-H. & Baik, J.-J. (2012). A CFD modeling study of the impacts of NOx and VOC emissions on reactive pollutant dispersion in and above a street canyon. *Atmos. Environ.,* **46**, 71-80.

Kwok, E. S. C. & Atkinson, R. (1995). Estimation of hydroxyl radical reaction rate constants for gas-phase organic compounds using a structure-reactivity relationship: An update. *Atmos. Environ.,* **29**, 1685-1695.

Langridge, J. M., Gustafsson, R. J., Griffiths, P. T., Cox, R. A., Lambert, R. M. & Jones, R. L. (2009). Solar driven nitrous acid formation on building material surfaces containing titanium dioxide: A concern for air quality in urban areas? *Atmos. Environ.,* **43**, 5128-5131.

Latham, S., Kollamthodi, S., Boulter, P. G., Nelson, P. M. & Hickman, A. J. (2001). Assessment of primary NO_2 emissions, hydrocarbon speciation and particulate sizing on a range of road vehicles. TRL, Wokingham.

Lee, J. D., Lewis, A. C., Monks, P. S., Jacob, M., Hamilton, J. F., Hopkins, J. R., Watson, N. M., Saxton, J. E., Ennis, C., Carpenter, L. J., Carslaw, N., Fleming, Z., Bandy, B. J., Oram, D. E., Penkett, S. A., Slemr, J., Norton, E., Rickard, A. R., Whalley, L. K., Heard, D. E., Bloss, W. J., Gravestock, T., Smith, S. C., Stanton, J., Pilling, M. J. & Jenkin, M. E. (2006). Ozone photochemistry and elevated isoprene during the UK heatwave of August 2003. *Atmos. Environ.,* **40**, 7598-7613.

Li, S., Batterman, S., Su, F.-C. & Mukherjee, B. (2013). Addressing extrema and censoring in pollutant and exposure data using mixture of normal distributions. *Atmos. Environ.,* **77**, 464-473.

Li, X.-X., Liu, C.-H. & Leung, D. (2008). Large-Eddy Simulation of Flow and Pollutant Dispersion in High-Aspect-Ratio Urban Street Canyons with Wall Model. *Boundary-Layer Meteorol,* **129**, 249-268.

Li, X.-X., Liu, C. H. & Leung, D. Y. C. (2009). Numerical investigation of pollutant transport characteristics inside deep urban street canyons. *Atmos. Environ.,* **43**, 2410-2418.

Li, X. X., Liu, C. H., Leung, D. Y. C. & Lam, K. M. (2006). Recent progress in CFD modelling of wind field and pollutant transport in street canyons. *Atmos. Environ.,* **40**, 5640-5658.

Liu, C.-H., Cheng, W. C., Leung, T. C. Y. & Leung, D. Y. C. (2011). On the mechanism of air pollutant re-entrainment in two-dimensional idealized street canyons. *Atmos. Environ.,* **45**, 4763-4769.

Liu, C. H. & Barth, M. C. (2002). Large-eddy simulation of flow and scalar transport in a modeled street canyon. *Journal of Applied Meteorology,* **41**, 660-673.

Liu, C. H., Barth, M. C. & Leung, D. Y. C. (2004). Large-eddy simulation of flow and pollutant transport in street canyons of different building-height-to-street-width ratios. *Journal of Applied Meteorology,* **43**, 1410-1424.

Liu, C. H., Leung, D. Y. C. & Barth, M. C. (2005). On the prediction of air and pollutant exchange rates in street canyons of different aspect ratios using large-eddy simulation. *Atmos. Environ.,* **39**, 1567-1574.

Longley, I. D., Gallagher, M. W., Dorsey, J. R., Flynn, M. & Barlow, J. F. (2004). Short-term measurements of airflow and turbulence in two street canyons in Manchester. *Atmos. Environ.,* **38**, 69-79.

Louka, P., Belcher, S. E. & Harrison, R. G. (2000). Coupling between air flow in streets and the well-developed boundary layer aloft. *Atmos. Environ.,* **34**, 2613-2621.

Madronich, S. & Flocke, S. (1998). The role of solar radiation in atmospheric chemistry. *In: Boule, P. (ed.). Handbook of Environmental Chemistry.* Springer, New York.

McConnell, R., Berhane, K., Gilliland, F., Molitor, J., Thomas, D., Lurmann, F., Avol, E., Gauderman, W. J. & Peters, J. M. (2003). Prospective study of air pollution and bronchitic symptoms in children with asthma. *American Journal of Respiratory and Critical Care Medicine,* **168**, 790-797.

MCM. (2009). *The Master Chemical Mechanism Web Page*. URL: http://mcm.leeds.ac.uk/MCMv3.1/.

MCM. (2012). *The Master Chemical Mechanism Web Page: Construction method.* URL: http://mcm.leeds.ac.uk/MCM/project.htt.

McNabola, A., Broderick, B. M. & Gill, L. W. (2009). A numerical investigation of the impact of low boundary walls on pedestrian exposure to air pollutants in urban street canyons. *Science of the Total Environment,* **407**, 760-769.

Mead, M. I., Popoola, O. A. M., Stewart, G. B., Landshoff, P., Calleja, M., Hayes, M., Baldovi, J. J., McLeod, M. W., Hodgson, T. F., Dicks, J., Lewis, A., Cohen, J., Baron, R., Saffell, J. R. & Jones, R. L. (2013). The use of electrochemical sensors for monitoring urban air quality in low-cost, high-density networks. *Atmos. Environ.,* **70**, 186-203.

Monks, P. S. (2005). Gas-phase radical chemistry in the troposphere. *Chemical Society Reviews,* **34**, 376-395.

Murena, F., Favale, G., Vardoulakis, S. & Solazzo, E. (2009). Modelling dispersion of traffic pollution in a deep street canyon: Application of CFD and operational models. *Atmos. Environ.,* **43**, 2303-2311.

Nagy, T. & Turányi, T. (2009). Reduction of very large reaction mechanisms using methods based on simulation error minimization. *Combustion and Flame,* **156**, 417-428.

Nakamura, Y. & Oke, T. R. (1988). Wind, temperature and stability conditions in an east-west oriented urban canyon. *Atmos. Environ.,* **22**, 2691-2700.

Nicholson, S. E. (1975). Pollution model for street-level air. *Atmos. Environ.,* **9**, 19-31.

Oikawa, S. & Meng, Y. (1995). Turbulence characteristics and organized motion in a suburban roughness sublayer. *Boundary-Layer Meteorol,* **74**, 289-312.

Oke, T. R. (1987). *Boundary layer climates.* Methuen, London.

Ouwersloot, H. G., Vilà-Guerau de Arellano, J., van Heerwaarden, C. C., Ganzeveld, L. N., Krol, M. C. & Lelieveld, J. (2011). On the segregation of chemical species in a clear boundary layer over heterogeneous land surfaces. *Atmos. Chem. Phys.,* **11**, 10681-10704.

Pavageau, M. & Schatzmann, M. (1999). Wind tunnel measurements of concentration fluctuations in an urban street canyon. *Atmos. Environ.,* **33**, 3961-3971.

Pilotto, L. S., Douglas, R. M., Attewell, R. G. & Wilson, S. R. (1997). Respiratory effects associated with indoor nitrogen dioxide exposure in children. *International journal of epidemiology,* **26**, 788-96.

Pinho, P., Pio, C., Carter, W. & Jenkin, M. (2006). Evaluation of alkene degradation in the detailed tropospheric chemistry mechanism, MCM v3, using environmental chamber data. *Journal of Atmospheric Chemistry,* **55**, 55-79.

Pinho, P., Pio, C., Carter, W. & Jenkin, M. (2007). Evaluation of α- and β-pinene degradation in the detailed tropospheric chemistry mechanism, MCM v3.1, using environmental chamber data. *Journal of Atmospheric Chemistry,* **57**, 171-202.

Pugh, T. A. M., MacKenzie, A. R., Langford, B., Nemitz, E., Misztal, P. K. & Hewitt, C. N. (2011). The influence of small-scale variations in isoprene concentrations on atmospheric chemistry over a tropical rainforest. *Atmos. Chem. Phys.,* **11**, 4121-4134.

Pugh, T. A. M., MacKenzie, A. R., Whyatt, J. D. & Hewitt, C. N. (2012). Effectiveness of Green Infrastructure for Improvement of Air Quality in Urban Street Canyons. *Environ. Sci. Technol.,* **46**, 7692-7699.

Raupach, M. R., Antonia, R. A. & Rajagopalan, S. (1991). Rough-wall turbulent boundary layers. *Appl. Mech. Rev.,* **44**, 1-25.

Raupach, M. R., Finnigan, J. J. & Brunet, Y. (1996). Coherent eddies and turbulence in vegetation canopies: The mixing-layer analogy. *Boundary-Layer Meteorol,* **78**, 351-382.

Raupach, M. R., Thom, A. S. & Edwards, I. (1980). A wind-tunnel study of turbulent flow close to regularly arrayed rough surfaces. *Boundary-Layer Meteorol,* **18**, 373-397.

Rickard, A. R., Whitehouse, L., Pilling, M. J., Pascoe, S. & Jenkin, M. E. (2006). The Master Chemical Mechanism (MCM) - Updates and Improvements. *Geophysical Research Abstracts,* 8.

Rotach, M. W. (1993). Turbulence close to a rough urban surface. 1. Reynolds stress. *Boundary-Layer Meteorol,* **65**, 1-28.

Rotach, M. W. (1995). Profiles of turbulence statistics in and above an urban street canyon. *Atmos. Environ.,* **29**, 1473-1486.

Salim, S. M., Buccolieri, R., Chan, A. & Di Sabatino, S. (2011). Numerical simulation of atmospheric pollutant dispersion in an urban street canyon: Comparison between RANS and LES. *Journal of Wind Engineering and Industrial Aerodynamics,* **99**, 103-113.

Salizzoni, P., Soulhac, L. & Mejean, P. (2009). Street canyon ventilation and atmospheric turbulence. *Atmos. Environ.,* **43**, 5056-5067.

Samoli, E., Touloumi, G., Zanobetti, A., Le Tertre, A., Schindler, C., Atkinson, R., Vonk, J., Rossi, G., Saez, M., Rabczenko, D., Schwartz, J. & Katsouyanni, K. (2003). Investigating the dose-response relation between air pollution and total mortality in the APHEA-2 multicity project. *Occupational and environmental medicine,* **60**, 977-82.

Saunders, S. M., Jenkin, M. E., Derwent, R. G. & Pilling, M. J. (2003). Protocol for the development of the Master Chemical Mechanism, MCM v3 (Part A): tropospheric degradation of non-aromatic volatile organic compounds. *Atmos. Chem. Phys.,* **3**, 161-180.

Seinfeld, J. H. & Pandis, S. N. (1998). *Atmospheric chemistry and physics : from air pollution to climate change.* J. Wiley, New Jersey.

So, E. S. P., Chan, A. T. Y. & Wong, A. Y. T. (2005). Large-eddy simulations of wind flow and pollutant dispersion in a street canyon. *Atmos. Environ.,* **39**, 3573-3582.

Stedman, J. R. (2004). The predicted number of air pollution related deaths in the UK during the August 2003 heatwave. *Atmos. Environ.,* **38**, 1087-1090.

Stull, R. B. (1988). *An introduction to boundary layer meteorology.* Kluwer Academic Publishers, Dordrecht.

Stull, R. B. (2000). *Meteorology for Scientists and Engineers*. Brooks/Cole.

Tomlin, A. S., Smalley, R. J., Tate, J. E., Barlow, J. F., Belcher, S. E., Arnold, S. J., Dobre, A. & Robins, A. (2009). A field study of factors influencing the concentrations of a traffic-related pollutant in the vicinity of a complex urban junction. *Atmos. Environ.,* **43**, 5027-5037.

UKMO (1991). Meteorological Glossary. *In:* Lewis, R. P. W. (ed.) 6th ed. London: HMSO.

Vardoulakis, S., Fisher, B. E. A., Pericleous, K. & Gonzalez-Flesca, N. (2003). Modelling air quality in street canyons: a review. *Atmos. Environ.,* **37**, 155-182.

Vardoulakis, S., Gonzalez-Flesca, N. & Fisher, B. E. A. (2002). Assessment of traffic-related air pollution in two street canyons in Paris: implications for exposure studies. *Atmos. Environ.,* **36**, 1025-1039.

Vardoulakis, S., Gonzalez-Flesca, N., Fisher, B. E. A. & Pericleous, K. (2005). Spatial variability of air pollution in the vicinity of a permanent monitoring station in central Paris. *Atmos. Environ.,* **39**, 2725-2736.

Vardoulakis, S., Valiantis, M., Milner, J. & ApSimon, H. (2007). Operational air pollution modelling in the UK - Street canyon applications and challenges. *Atmos. Environ.,* **41**, 4622-4637.

Vinuesa, J. F. & VilÃ -Guerau de Arellano, J. (2005). Introducing effective reaction rates to account for the inefficient mixing of the convective boundary layer. *Atmos. Environ.,* **39**, 445-461.

Walters, S. & Ayres, J. (2001). The Health Effects of Air Pollution. *In:* Harrison, R. M. (ed.) *Pollution: Causes, Effects and Control.* 4th ed. Cambridge: Royal Society of Chemistry.

Wang, P. & Mu, H. L. (2010). Analysis of Reactive Pollutants Distribution in Damaging Street Canyon Architectures. *In:* Luo, Q. (ed.) *Information Technology for Manufacturing Systems, Pts 1 and 2.*

Watson, L. A. (2007). *Development and Application of Chemical Mechanisms in Atmospheric Modelling. Ph.D. Thesis.* University of Bristol, UK.

Watson, L. A., Shallcross, D. E., Utembe, S. R. & Jenkin, M. E. (2008). A Common Representative Intermediates (CRI) mechanism for VOC degradation. Part 2: Gas phase mechanism reduction. *Atmos. Environ.,* **42**, 7196-7204.

Wayne, R. P. (1991). *Chemistry of atmospheres : an introduction to the chemistry of the atmospheres of earth, the planets, and their satellites / Richard P. Wayne,* Oxford, Clarendon Press.

Whitehouse, L. E., Tomlin, A. S. & Pilling, M. J. (2004a). Systematic reduction of complex tropospheric chemical mechanisms, Part I: sensitivity and time-scale analyses. *Atmos. Chem. Phys.,* **4**, 2025-2056.

Whitehouse, L. E., Tomlin, A. S. & Pilling, M. J. (2004b). Systematic reduction of complex tropospheric chemical mechanisms, Part II: Lumping using a time-scale based approach. *Atmos. Chem Phys.,* **4**, 2057-2081.

WHO (2000). Air Quality Guidelines for Europe. *WHO Regional Publications, Europen series, No. 91.* Second ed.

WHO (2006). WHO Air quality guidelines for particulate matter, ozone, nitrogen and sulfur dioxide. Global update 2005. Summary of risk assessment. *World Health Organisation.*

Wood, C. R., Lacser, A., Barlow, J. F., Padhra, A., Belcher, S. E., Nemitz, E., Helfter, C., Famulari, D. & Grimmond, C. S. B. (2010). Turbulent Flow at 190 m Height Above London During 2006—2008: A Climatology and the Applicability of Similarity Theory. *Boundary-Layer Meteorol,* **137**, 77-96.

Xie, S. D., Zhang, Y. H., Li, Q. & Tang, X. Y. (2003). Spatial distribution of traffic-related pollutant concentrations in street canyons. *Atmos. Environ.,* **37**, 3213-3224.

Xie, Z.-T. (2011). Modelling Street-Scale Flow and Dispersion in Realistic Winds—Towards Coupling with Mesoscale Meteorological Models. *Boundary-Layer Meteorol,* **141**, 53-75.

Xie, Z.-T. & Castro, I. P. (2009). Large-eddy simulation for flow and dispersion in urban streets. *Atmos. Environ.,* **43**, 2174-2185.

Xie, Z.-T., Hayden, P. & Wood, C. R. (2013). Large-eddy simulation of approaching-flow stratification on dispersion over arrays of buildings. *Atmos. Environ.,* **71**, 64-74.

Yu, J. Z., Cocker, D. R., Griffin, R. J., Flagan, R. C. & Seinfeld, J. H. (1999). Gas-phase ozone oxidation of monoterpenes: Gaseous and particulate products. *Journal of Atmospheric Chemistry,* **34**, 207-258.

Ziehn, T. & Tomlin, A. S. (2008). Global sensitivity analysis of a 3D street canyon model—Part I: The development of high dimensional model representations. *Atmos. Environ.,* **42**, 1857-1873.

Zou, B., Wilson, J. G., Zhan, F. B. & Zeng, Y. (2009). Air pollution exposure assessment methods utilized in epidemiological studies. *Journal of Environmental Monitoring,* **11**, 475-490.

LES code digital appendix

```
C##########################################
C  For different canyon geometry, the following lines marked with '*'
C  in the given subroutines need change:
C------------------------------------------
c      SUBROUTINE CNSTBLDG(NZP,NXP,NYP,VAR,PLUSONE,CNST)
c * set a value to inside buildings
C------------------------------------------
C      SUBROUTINE WALLBCTR(NZP,NXP,NYP,TRP)
c - set zero inside building: C_bldg=0
c * set zero gradient on walls: dC/dn|walls = 0
C------------------------------------------
c      SUBROUTINE WALLTH(NZP,NXP,NYP,TRP)
c * set Tmean
c * set all Twall according to DTs in canyon.h
C------------------------------------------
C      SUBROUTINE XWLLBCT(N1,N2,N3,TRP)
C - call WALLBCTR for all scalars
C - call WALLTH to set wall temperatures
c * set Cwall values for all VERTICAL x-walls
C------------------------------------------
c      SUBROUTINE YWLLBCT(N1,N2,N3,TRP)
C - call WALLBCTR for all scalars
C - call WALLTH to set wall temperatures
c * set Cwall values for all VERTICAL y-walls
C------------------------------------------
c      SUBROUTINE ZWLLBCT(N1,N2,N3,TRP)
C - call WALLBCTR for all scalars
C - call WALLTH to set wall temperatures
c * set Cwall values for all HORIZONTAL z-walls
C------------------------------------------
c      SUBROUTINE XWLLFLXT(N1,N2,N3,FLX,DN0)
c * calculate HEAT FLUX at all VERTICAL x-walls
c * calculate SCALAR FLUX at all VERTICAL x-walls
C------------------------------------------
c      SUBROUTINE YWLLFLXT(N1,N2,N3,FLX,DN0)
c * calculate HEAT FLUX at all VERTICAL y-walls
c * calculate SCALAR FLUX at all VERTICAL y-walls
C------------------------------------------
c      SUBROUTINE ZWLLFLXT(N1,N2,N3,FLX,DN0)
c * calculate HEAT FLUX at all HORIZONTAL z-walls
c * calculate SCALAR FLUX at all HORIZONTAL z-walls
C------------------------------------------
c      SUBROUTINE WALLUTS(NZP,NXP,NYP,UP,VP,WP,THP)
c * calculate u*, T*, Q* for all surfaces
C------------------------------------------
c      SUBROUTINE XWLLFLXV(N1,N2,N3,FLX,DN0)
c * calculate V-FLUX at all VERTICAL x-walls
C------------------------------------------
c      SUBROUTINE XWLLFLXW(N1,N2,N3,FLX,DN0)
c * calculate W-FLUX at all VERTICAL x-walls
C------------------------------------------
c      SUBROUTINE YWLLFLXW(N1,N2,N3,FLX,DN0)
c * calculate W-FLUX at all VERTICAL y-walls
C------------------------------------------
c      SUBROUTINE YWLLFLXU(N1,N2,N3,FLX,DN0)
c * calculate U-FLUX at all VERTICAL y-walls
C------------------------------------------
c      SUBROUTINE ZWLLFLXU(N1,N2,N3,FLX,DN0)
c * calculate U-FLUX at all HORIZONTAL z-walls
C------------------------------------------
c      SUBROUTINE ZWLLFLXV(N1,N2,N3,FLX,DN0)
c * calculate V-FLUX at all HORIZONTAL z-walls
C------------------------------------------
c     ~/rams/compile/str1can2d.h
c * specify memory for U*, T* and Q*
C------------------------------------------
c      SUBROUTINE ZWALLBC(NZP,NXP,NYP,UP,VP,THP,FLX,NSF,KSF,ISGNSF
c        entry ZWALLUTS --- U*, T* and Q*
c        entry ZWALLU   --- U-FLUX/Z
c        entry ZWALLV   --- V-FLUX/Z
c        entry ZWALLT   --- T-FLUX/Z
c        entry ZWALLQ   --- Q-FLUX/Z
c - general routine for any-flux at a HORIZONTAL z-wall
c * number of surfaces for ISTRZSVE(1:?)
C------------------------------------------
c      SUBROUTINE XWALLBC(NZP,NXP,NYP,VP,WP,THP,FLX,NSF,ISF,ISGNSF
c        entry XWALLUTS --- U*, T* and Q*
c        entry XWALLU   --- U-FLUX/X
c        entry XWALLV   --- V-FLUX/X
c        entry XWALLT   --- T-FLUX/X
c        entry XWALLQ   --- Q-FLUX/X
c - general routine for any-flux at a VERTICAL x-wall
c * number of surfaces for ISTRXSVE(1:?)
C------------------------------------------
c      SUBROUTINE YWALLBC(NZP,NXP,NYP,WP,UP,THP,FLX,NSF,JSF,ISGNSF
c        entry YWALLUTS --- U*, T* and Q*
c        entry YWALLU   --- U-FLUX/Y
c        entry YWALLV   --- V-FLUX/Y
c        entry YWALLT   --- T-FLUX/Y
```

```
c        entry YWALLQ   --- Q-FLUX/Y
c - general routine for any-flux at a VERTICAL y-wall
c * number of surfaces for ISTRYSVE(1:?)
C-----------------------------------------
c      SUBROUTINE WLLBCUVW
c - set U=V=W=0 inside building
C=========================================
C
C
      FUNCTION DKRGRID(NGRID)
      character*80 rcsid,sccsid
      data rcsid/
     +'$Id: rauxn2a.model,v 1.18 1998/05/25 19:18:41 ming Exp ming $'
     +/
      data sccsid/
     +'@(#)rauxn2a.model        1.15 95/07/21'
     +/
      IF(NGRID.EQ.1) DKRGRID=0.1
      IF(NGRID.EQ.2) DKRGRID=0.1
      RETURN
      END
C
C     ************************************************************
      SUBROUTINE CTFZ(N2,N3,TFZ,QFZ)
.IN   STORAGE
      DIMENSION TFZ(N2,N3),QFZ(N2,N3)
      CHARACTER*10 TFZFN,QFZFN,CHNGRID*1
C specify the surface heat flux with random perturbations
      IF(ISTP.EQ.1)THEN
        WRITE(CHNGRID,'(I1)')NGRID
        TFZFN='TFZ.g'//CHNGRID
        QFZFN='QFZ.g'//CHNGRID
        PRINT*,'---- GRID',NGRID,': TFZ filename:',TFZFN
        PRINT*,'---- GRID',NGRID,': QFZ filename:',QFZFN
C        OPEN(UNIT=58,FILE=TFZFN,STATUS='OLD')
C        READ(58,*)((TFZ(I,J),I=1,N2),J=1,N3)
C        CLOSE(58)
C        OPEN(UNIT=58,FILE=QFZFN,STATUS='OLD')
C        READ(58,*)((QFZ(I,J),I=1,N2),J=1,N3)
C        CLOSE(58)
      ENDIF
      IF(TIME.LT.TIMTFZ)THEN
        DO(J=N2Y,NY)
        DO(I=N2X,NX)
          RDN=RAMRAN()
          TFZ(I,J)=TFZ(I,J)+2.*(RDN-0.5)*AMPTFZ
        ENDDO
        ENDDO
      ENDIF
      RETURN
      END
C
C     ************************************************************
C
      SUBROUTINE DEGALN(N1,N2,N3,UP,VP)
.IN   STORAGE
      DIMENSION UP(N1,N2,N3),VP(N1,N2,N3)
      DO(J=1,NYP)
      DO(I=1,NXP)
      DO(K=1,NZP)
        UP(K,I,J)=UP(K,I,J)-U01D(1)
        VP(K,I,J)=VP(K,I,J)-V01D(1)
      ENDDO
      ENDDO
      ENDDO
C
      RETURN
      END
C
      SUBROUTINE GALN(N1,N2,N3,UP,VP)
.IN   STORAGE
      DIMENSION UP(N1,N2,N3),VP(N1,N2,N3)
      DO(J=1,NYP)
      DO(I=1,NXP)
      DO(K=1,NZP)
        UP(K,I,J)=UP(K,I,J)+U01D(1)
        VP(K,I,J)=VP(K,I,J)+V01D(1)
      ENDDO
      ENDDO
      ENDDO
C
      RETURN
      END
C     ************************************************************
C
      SUBROUTINE PERTURB(N1,N2,N3,UP,VP,WP,THP)
.IN   STORAGE
      DIMENSION UP(N1,N2,N3),VP(N1,N2,N3),WP(N1,N2,N3),THP(N1,N2,N3)
C
```

```
C +--------------------------------------------------------------------
C _    This routine disturbs the 3-D velocity fields
C +--------------------------------------------------------------------
C
C      HEKMAN=0.2*(0.05*(UP(NZP-1,1,1)-UP(2,1,1))/0.0001)
C      Hekman1=12.5
       Hekman1=0.0
       HEKMAN2=100.0
       hekman=hekman2-hekman1
C modified on 920328: change initial perturbation profile (more shallow)
       DO(K=2,NZP-1)
C            FACTOR=4.*(K-2)*(NZP-1-K)/((NZP-2)*(NZP-2))
         IF(Z(K).GE.HEKMAN1 .and. Z(K).LE.HEKMAN2)THEN
           ZZKK=z(k)-hekman1
           FACTOR=9.0/4.0*ZZKK/HEKMAN*(1.0-ZZKK/HEKMAN)**2
         ELSE
           FACTOR=0.
         ENDIF
         DO(J=1,NYP)
           DO(I=1,NXP)
             UP(K,I,J)= UP(K,I,J)+2.*(RAMRAN()-0.5)*PERUP*FACTOR
             VP(K,I,J)= VP(K,I,J)+2.*(RAMRAN()-0.5)*PERVP*FACTOR
             WP(K,I,J)= WP(K,I,J)+2.*(RAMRAN()-0.5)*PERWP*FACTOR
             THP(K,I,J)=THP(K,I,J)+2.*(RAMRAN()-0.5)*PERTHP*FACTOR
           ENDDO
         ENDDO
       ENDDO
C
       RETURN
       END
C      *****************************************************************
C
       SUBROUTINE CE0PS1(NPTS,C,C0,A)
       DIMENSION A(NPTS)
       C=C0
       DO(I=1,NPTS)
         C=C+A(I)
       ENDDO
       RETURN
       END
C
C=======================================
       SUBROUTINE TRACINI(N1,N2,N3,TRACE,JEMISN,ZEMISN)
.IN    STORAGE
       DIMENSION TRACE(N1,N2,N3)
C
C specifying gaussian distribution
C
C LINE SOURCE OF NXPxGaussian centred at Jemission, Kemission
C jemisn=1  9 17 25 33 41 49 57
C
C      JEMISN=1
C      ZEMISN=Z(18)
       PRINT*,'IN TRACINI: JEMISN,ZEMISN=',JEMISN,ZEMISN
       SGMY=DELTAY
       SGMZ=0.5*DELTAY
       EMISRATE=100.
       YEMISN=FLOAT(JEMISN)*DELTAY
C number of
       NYCYCL=NYP-3
       LYCYCL=FLOAT(NYCYCL)*DELTAY
       DO(J=1,N3)
          DO(I=1,N2)
             DO(K=2,N1)
                YTOYS=ABS(FLOAT(J)*DELTAY-YEMISN)
                IF(YTOYS.GT.(LYCYCL/2)) YTOYS=LYCYCL-YTOYS
                TRACE(K,I,J)=EMISRATE/(2.*3.1416*SGMY*SGMZ)
     +              *EXP(-0.5*(YTOYS /SGMY)**2)
     +              *EXP(-0.5*((Z(K)-ZEMISN)/SGMZ)**2)
             ENDDO
          ENDDO
       ENDDO
       RETURN
       END
C=======================================
       SUBROUTINE GAUSSTRCE(N1,N2,N3,TRACE,EMISRATE)
.IN    STORAGE
       DIMENSION CEMSN(NZPMAX,NXPMAX)
       DIMENSION TRACE(N1,N2,N3)
       DATA IHORZTRC/0/
C
       IHORZTRC=IHORZTRC+1
       IF(IHORZTRC.GE.2)GOTO 777
C-------------------------------------------------------------
C only for 1st steps
C-------------------------------------------------------------
C
C-------------------------------------------------------------
C specifying key parameters
```

```
C-------------------------------------------------------------
C
C      HCAR=1.5                  ! height of car is 1.5 m
      NPLUMES=2                 ! 2 PLUMES
      XEMSNL=-2.5               !  left-lane emsn centre is -2.5 m
      XEMSNR= 2.5               ! right-lane emsn centre is  2.5 m
      XEMSN=0.0                 !   one-lane emsn centre is  0.0 m
      ZEMSN=1.0                 ! emsn height centre is 1.0 m
      SGMX=3.0                  ! sgmx=3.0 m
      SGMZ=1.0                  ! sgmz=1.0 m
C
C-------------------------------------------------------------
C to get Gaussian profile for either 1 plume or 2 plumes
C-------------------------------------------------------------
      IF(NPLUMES.EQ.1)THEN
         DO(I=1,N2)
            DO(K=2,N1)
               CEMSN(K,I)=EXP(-( (X(I)-XEMSN)/SGMX )**2
     +                        -( (Z(K)-ZEMSN)/SGMZ )**2)
            ENDDO
         ENDDO
      ELSE IF(NPLUMES.EQ.2)THEN
         DO(I=1,N2)
            DO(K=2,N1)
               CEMSN(K,I)=EXP(-( (X(I)-XEMSNL)/SGMX )**2
     +                        -( (Z(K)-ZEMSN )/SGMZ )**2)
     +                  +EXP(-( (X(I)-XEMSNR)/SGMX )**2
     +                        -( (Z(K)-ZEMSN )/SGMZ )**2)
            ENDDO
         ENDDO
      ELSE
         STOP 'NPLUMES MUST BE 1 OR 2'
      ENDIF
C-------------------------------------------------------------
C to normalise trace so that sum(trace)=1.0
C-------------------------------------------------------------
      CSUM=0.0
      DO(I=1,N2)
         DO(K=2,N1)
            CSUM=CSUM+CEMSN(K,I)
         ENDDO
      ENDDO
      DO(I=1,N2)
         DO(K=2,N1)
            CEMSN(K,I)=CEMSN(K,I)/CSUM
         ENDDO
      ENDDO

      WRITE(*,*)'IN GAUSSTRCE: XEMSNL,XEMSNR,ZEMSN,SGMX,SGMZ,EMISRATE'
      WRITE(*,20)XEMSNL,XEMSNR,ZEMSN,SGMX,SGMZ,EMISRATE
 20   FORMAT(5F5.1,F10.2)
      WRITE(*,10)((CEMSN(K,I),I=1,N2),K=2,N1)
 10   FORMAT(81(1Pe11.3))

C-------------------------------------------------------------
C for all steps
C-------------------------------------------------------------
 777  CONTINUE
      DO(J=1,N3)
         DO(I=1,N2)
            DO(K=2,N1)
               TRACE(K,I,J)=TRACE(K,I,J)+EMISRATE*DTLONG*CEMSN(K,I)
            ENDDO
         ENDDO
      ENDDO

      RETURN
      END
C=======================================
      SUBROUTINE HORZTRCE(N1,N2,N3,TRACE,KEMISN,KDPTH,EMISRATE,
     +   ILEFT,IRIGHT)
.IN   STORAGE
      DIMENSION TRACE(N1,N2,N3)
      DATA IHORZTRC/0/
C equivalent amount of flux out of canyon for rauxn2a.model.constc (an area source with
C a constant concentraion at the emission surface of 1 g/m3) is about Qs=0.003 g/s/m2.
C This corresponds to an emission rate of 0.003 g/s/m2 near the source when an equilibrium
C state is reached.  For a line source in a canyon with its width of W=(L4-L3+1)*DELTAX,
C the strength of the source would be Qs*W=0.003 g/s/m2 * 20m = 0.06 g/s/m.
C ---------- Therefore,
C at one grid point which represents a volume of DX*DY*DZ, if emission from this volume
C is q1 (in g/s), the increment concentration assigned to the grid point is dC (g/m3), then
C dC*DX*DY*DZ=q1*DT.  Because Qs=0.003 g/s/m2, q1=Qs*DX*DY; where q1 is the emissions rate
C for one horizontal grid at the top [g/s]. So,
C  dC=q1*DT/(DX*DY*DZ)=Qs*DX*DY*DT/(DX*DY*DZ)=Qs*DT/DZ
C ===> source strength Q=Qs*Lx*Ly/Nx=EMISRATE*Nx*DELTAX*Ny*DELTAY/Nx=EMISRATE*DELTAX*Ny*DELTAY
C ----------
C 020702: The above argument (from 'Therefore...') contains an error: q1=Qs*DX*DY ==>
q1dyW=Qs*W*DY
```

```
C because q1dyW [g/s] is the total emissions rate for a stripe with a depth of DY at the top.
So,
C  dC=q1dyW*DT/(DX*DY*DZ)=Qs*W*DY*DT/(DX*DY*DZ)=Qs*W*DT/(DX*DZ). If Qs=0.003 g/s/m2,
C  dC=Qs*20*DT/(0.5*0.5)=80*Qs*DT=40*Qs*DT/DZ
C ===> source strength Q=q1dyW*Ny=Qs*W*Ly=EMISRATE*Nx*DELTAX*Ny*DELTAY
C
C      DATA EMISRATE/0.003/
C
C
C    |
C    +----------+               +------------+ <- IH
C               |               |
C               |               |
C               |               |
C               |               |
C               |               |
C               |               |
C               |   #########   |
C    +          +---------------+            + <- L1
C                    |       |
C   L2          L3   |       |    L4          L5
C                  ILEFT    IRIGHT
C
C
C
C specifying gaussian distribution
C
C LINE SOURCE OF NXPxGaussian centred at Jemission, Kemission

      NEMCELLS=(IRIGHT-ILEFT+1)*KDPTH
      EMSN1STP=EMISRATE*DTLONG/nemcells
      IHORZTRC=IHORZTRC+1
      IF(IHORZTRC.le.6)
     +PRINT*,'IN HORZTRCE: KEMISN,KDPTH,ZEMISN,ILEFT,IRIGHT,EMSN1STP,EMS
     +RATE,NEMCELLS,EmsRate/Cell=',KEMISN,KDPTH,Z(KEMISN),ILEFT,IRIGHT
     +,EMSN1STP,EMISRATE,nemcells,emisrate/nemcells
C
C      ZEMISN=Z(KEMISN)
C number of
C      DO(J=1,N3)
C         DO(I=ILEFT,IRIGHT)
C            DO(K=2,N1)
C               TRACE(K,I,J)=EMISRATE/(SQRT(2.*3.1416)*SGMZ)
C     +              *EXP(-0.5*((Z(K)-ZEMISN)/SGMZ)**2)
C            ENDDO
C         ENDDO
C      ENDDO
      DO(J=1,N3)
         DO(I=ILEFT,IRIGHT)
           DO(K=KEMISN,KEMISN+KDPTH-1)
             TRACE(K,I,J)=TRACE(K,I,J)+EMSN1STP
           ENDDO
         ENDDO
      ENDDO
      RETURN
      END
C~~~~~~~~~~~~~~~~~~~~~~~~~~~~~~~~~~~~~~~~~~~~~~~~~~~~
C=======================================
      SUBROUTINE VERTTRCE(N1,N2,N3,TRACE,IEMISN,IDPTH,KBOT,KTOP)
.IN   STORAGE
      DIMENSION TRACE(N1,N2,N3)
      DATA IVERTTRC/0/
C equivalent amount of flux out of canyon for rauxn2a.model.constc (an area source with
C a constant concentraion at the emission surface of 1 g/m3) is about Qs=0.003 g/s/m2.
C This corresponds to an emission rate of 0.003 g/s/m2 near the source when an equilibrium
C state is reached.  For a line source in a canyon with its width of W=(L4-L3+1)*DELTAX,
C the strength of the source would be Qs*W=0.003 g/s/m2 * 20m = 0.06 g/s/m. Therefore,
C at one grid point which represents a volume of DX*DY*DZ, if emission from this volume
C is q1 (in g/s), the increment concentration assigned to the grid point is dC (g/m3), then
C dC*DX*DY*DZ=q1*DT.  Because Qs=0.003 g/s/m2, q1=Qs*DZ*DY; so
C  dC=q1*DT/(DX*DY*DZ)=Qs*DZ*DY*DT/(DX*DY*DZ)=Qs*DT/DX
C
      DATA EMISRATE/0.003/
C
C
C    |
C    +----------+               +------------+ <- IH
C               |               |
C     KTOP ---> |  #            |
C               |  #            |
C               |  #            |
C               |  #            |
C     KBOT ---> |  #            |
C               |               |
C    +          +---------------+            + <- L1
C                   |
C   L2          L3  |            L4          L5
C                IEMISN
C
```

```
C
C specifying gaussian distribution
C
C LINE SOURCE OF NXPxGaussian centred at Jemission, Kemission

      EMSN1STP=EMISRATE*DTLONG/DELTAX

      IVERTTRC=IVERTTRC+1
      IF(IVERTTRC.EQ.1)
     +PRINT*,'IN VERTTRCE: IEMISN,IDPTH,KBOT,KTOP,ZBBOT,ZTOP,EMSN1STP=',
     +     IEMISN,IDPTH,KBOT,KTOP,Z(KBOT),Z(KTOP),EMSN1STP
C
C number of
C      DO(J=1,N3)
C         DO(I=1,N2)
C            DO(K=KBOT,KTOP)
C               TRACE(K,I,J)=EMISRATE/(SQRT(2.*3.1416)*SGMX)
C     +              *EXP(-0.5*((I-IEMISN)*DELTAX/SGMX)**2)
C            ENDDO
C          ENDDO
C       ENDDO
      DO(J=1,N3)
         DO(K=KBOT,KTOP)
           DO(I=IEMISN,IEMISN+IDPTH-1)
             TRACE(K,I,J)=TRACE(K,I,J)+EMSN1STP
           ENDDO
         ENDDO
      ENDDO
      RETURN
      END
C~~~~~~~~~~~~~~~~~~~~~~~~~~~~~~~~~~~~~~~~~~~~~~~~~~~~
C modified on 980220: add a printing subroutine:
      subroutine pr3dvar(nz,nx,ny,kb,ke,ib,ie,jb,je,var,iunit,fmt)
      real var(nz,nx,ny)
      character*30 fmt
      write(iunit,fmt)(((var(k,i,j),k=kb,ke),i=ib,ie),j=jb,je)
      return
      end

C=======================================
      SUBROUTINE ZEROTRC
.IN   STORAGE
C zero all the tracers
      CALL AZERO(NXYZP,A(ITRCE1 ))
      CALL AZERO(NXYZP,A(ITRCE2 ))
      CALL AZERO(NXYZP,A(ITRCE3 ))
      CALL AZERO(NXYZP,A(ITRCE4 ))
      CALL AZERO(NXYZP,A(ITRCE5 ))
      CALL AZERO(NXYZP,A(ITRCE6 ))
      CALL AZERO(NXYZP,A(ITRCE7 ))
      CALL AZERO(NXYZP,A(ITRCE8 ))
      CALL AZERO(NXYZP,A(ITRCE9  ))
      CALL AZERO(NXYZP,A(ITRCE10 ))
      CALL AZERO(NXYZP,A(ITRCE11 ))
      CALL AZERO(NXYZP,A(ITRCE12 ))
      CALL AZERO(NXYZP,A(ITRCE13 ))
      CALL AZERO(NXYZP,A(ITRCE14 ))
      CALL AZERO(NXYZP,A(ITRCE15 ))
      CALL AZERO(NXYZP,A(ITRCE16 ))
      CALL AZERO(NXYZP,A(ITRCE17 ))
      CALL AZERO(NXYZP,A(ITRCE18 ))
      CALL AZERO(NXYZP,A(ITRCE19 ))
      CALL AZERO(NXYZP,A(ITRCE20 ))
      CALL AZERO(NXYZP,A(ITRCE21 ))
      CALL AZERO(NXYZP,A(ITRCE22 ))
      CALL AZERO(NXYZP,A(ITRCE23 ))
      CALL AZERO(NXYZP,A(ITRCE24 ))
      CALL AZERO(NXYZP,A(ITRCE25 ))
      CALL AZERO(NXYZP,A(ITRCE26 ))
      CALL AZERO(NXYZP,A(ITRCE27 ))
      CALL AZERO(NXYZP,A(ITRCE28 ))
      CALL AZERO(NXYZP,A(ITRCE29 ))
      CALL AZERO(NXYZP,A(ITRCE30 ))
      CALL AZERO(NXYZP,A(ITRCE31 ))
      CALL AZERO(NXYZP,A(ITRCE32 ))
      CALL AZERO(NXYZP,A(ITRCE33 ))
      CALL AZERO(NXYZP,A(ITRCE34 ))
      CALL AZERO(NXYZP,A(ITRCE35 ))
      CALL AZERO(NXYZP,A(ITRCE36 ))
      CALL AZERO(NXYZP,A(ITRCE37 ))
      CALL AZERO(NXYZP,A(ITRCE38 ))
      CALL AZERO(NXYZP,A(ITRCE39 ))
      CALL AZERO(NXYZP,A(ITRCE40 ))
      CALL AZERO(NXYZP,A(ITRCE41 ))
      CALL AZERO(NXYZP,A(ITRCE42 ))
      CALL AZERO(NXYZP,A(ITRCE43 ))
      CALL AZERO(NXYZP,A(ITRCE44 ))
      CALL AZERO(NXYZP,A(ITRCE45 ))
      CALL AZERO(NXYZP,A(ITRCE46 ))
```

```
      CALL AZERO(NXYZP,A(ITRCE47 ))
      CALL AZERO(NXYZP,A(ITRCE48 ))
      CALL AZERO(NXYZP,A(ITRCE49 ))
      CALL AZERO(NXYZP,A(ITRCE50 ))
      CALL AZERO(NXYZP,A(ITRCE51 ))
      CALL AZERO(NXYZP,A(ITRCE52 ))

      CALL AZERO(NXYZP,A(ITRCE1C))
      CALL AZERO(NXYZP,A(ITRCE2C))
      CALL AZERO(NXYZP,A(ITRCE3C))
      CALL AZERO(NXYZP,A(ITRCE4C))
      CALL AZERO(NXYZP,A(ITRCE5C))
      CALL AZERO(NXYZP,A(ITRCE6C))
      CALL AZERO(NXYZP,A(ITRCE7C))
      CALL AZERO(NXYZP,A(ITRCE8C))
      CALL AZERO(NXYZP,A(ITRCE9C))
      CALL AZERO(NXYZP,A(ITRCE10C))
      CALL AZERO(NXYZP,A(ITRCE11C))
      CALL AZERO(NXYZP,A(ITRCE12C))
      CALL AZERO(NXYZP,A(ITRCE13C))
      CALL AZERO(NXYZP,A(ITRCE14C))
      CALL AZERO(NXYZP,A(ITRCE15C))
      CALL AZERO(NXYZP,A(ITRCE16C))
      CALL AZERO(NXYZP,A(ITRCE17C))
      CALL AZERO(NXYZP,A(ITRCE18C))
      CALL AZERO(NXYZP,A(ITRCE19C))
      CALL AZERO(NXYZP,A(ITRCE20C))
      CALL AZERO(NXYZP,A(ITRCE21C))
      CALL AZERO(NXYZP,A(ITRCE22C))
      CALL AZERO(NXYZP,A(ITRCE23C))
      CALL AZERO(NXYZP,A(ITRCE24C))
      CALL AZERO(NXYZP,A(ITRCE25C))
      CALL AZERO(NXYZP,A(ITRCE26C))
      CALL AZERO(NXYZP,A(ITRCE27C))
      CALL AZERO(NXYZP,A(ITRCE28C))
      CALL AZERO(NXYZP,A(ITRCE29C))
      CALL AZERO(NXYZP,A(ITRCE30C))
      CALL AZERO(NXYZP,A(ITRCE31C))
      CALL AZERO(NXYZP,A(ITRCE32C))
      CALL AZERO(NXYZP,A(ITRCE33C))
      CALL AZERO(NXYZP,A(ITRCE34C))
      CALL AZERO(NXYZP,A(ITRCE35C))
      CALL AZERO(NXYZP,A(ITRCE36C))
      CALL AZERO(NXYZP,A(ITRCE37C))
      CALL AZERO(NXYZP,A(ITRCE38C))
      CALL AZERO(NXYZP,A(ITRCE39C))
      CALL AZERO(NXYZP,A(ITRCE40C))
      CALL AZERO(NXYZP,A(ITRCE41C))
      CALL AZERO(NXYZP,A(ITRCE42C))
      CALL AZERO(NXYZP,A(ITRCE43C))
      CALL AZERO(NXYZP,A(ITRCE44C))
      CALL AZERO(NXYZP,A(ITRCE45C))
      CALL AZERO(NXYZP,A(ITRCE46C))
      CALL AZERO(NXYZP,A(ITRCE47C))
      CALL AZERO(NXYZP,A(ITRCE48C))
      CALL AZERO(NXYZP,A(ITRCE49C))
      CALL AZERO(NXYZP,A(ITRCE50C))
      CALL AZERO(NXYZP,A(ITRCE51C))
      CALL AZERO(NXYZP,A(ITRCE52C))
      RETURN
      END
C=======================================
      SUBROUTINE TRCINIT
.IN   STORAGE
      include 'canyon.h'
      real NO_0,NO2_0,NO3_0,NA_0,MPAN_0
        common /chems/ O3_0,NO_0,NO2_0,NO3_0,OH_0,HO2_0,
     +  H2_0,CO_0,H2O2_0,HONO_0,HNO3_0,HO2NO2_0,CH3O2_0,CH3OH_0,
     +  CH4_0,C2H4_0,C3H6_0,HOCH2CH2O2_0,CH3CO2H_0,CH3CHO_0,
     +  C5H8_0,RU14O2_0,UCARB10_0,HCHO_0,CH3CO3_0,HOCH2CHO_0,
     +  C2H5OH_0,RN9O2_0,HCOOH_0,CARB6_0,UCARB12_0,RU12O2_0,
     +  CARB7_0,RU10O2_0,CH3NO3_0,HOC2H4NO3_0,RN9NO3_0,
     +  RU14NO3_0,CH3OOH_0,HOC2H4OOH_0,RN9OOH_0,CH3CO3H_0,
     +  HOCH2CO3H_0,RU14OOH_0,RU12OOH_0,RU10OOH_0,HOCH2CO3_0,
     +  PAN_0,PHAN_0,RU12PAN_0,MPAN_0
      DATA NSHORT/5/  ! number of steps for faster chemistry
C
C modified on 040401: add the cyclic B.C. for temperature
C     CALL BEGPRO('/THP/THC/UP/UC/VP/VC')
      CALL NONCYCLIC(NZP,NXP,NYP,A(ITHP),293.0)
      CALL NONCYCLIC(NZP,NXP,NYP,A(ITHC),293.0)
      CALL RDBTNDC(NZP,NXP,NYP,A(IUP),A(IUC),A(IVP),A(IVC)
     +     ,A(ITHP),A(ITHC))

C-------------------------------------------------------
C Gaussian sources:
C-------------------------------------------------------
      CALL GAUSSTRCE(NZP,NXP,NYP,A(ITRCE2  ),900.)  ! NO's emission ppb/s
      CALL GAUSSTRCE(NZP,NXP,NYP,A(ITRCE3  ),100.)  ! NO2's emission
```

```
      CALL GAUSSTRCE(NZP,NXP,NYP,A(ITRCE8  ),3593.) ! CO's emission
      CALL GAUSSTRCE(NZP,NXP,NYP,A(ITRCE16 ),347.)  ! C2H4's emission
      CALL GAUSSTRCE(NZP,NXP,NYP,A(ITRCE17 ),150.)  ! C3H6's emission
      CALL GAUSSTRCE(NZP,NXP,NYP,A(ITRCE20 ),98.)   ! CH3CHO's emission
      CALL GAUSSTRCE(NZP,NXP,NYP,A(ITRCE24 ),196.)  ! HCHO's emission
C a passive tracer: TRCE52
      CALL GAUSSTRCE(NZP,NXP,NYP,A(ITRCE52 ),1000.)  ! a passive tracer's emission ppb/s
C-----------------------------------------------------
C modified on 20100610: add the emissions to ITRCE?C
C-----------------------------------------------------
      CALL GAUSSTRCE(NZP,NXP,NYP,A(ITRCE2C ),900.)  ! NO's emission ppb/s
      CALL GAUSSTRCE(NZP,NXP,NYP,A(ITRCE3C ),100.)  ! NO2's emission
      CALL GAUSSTRCE(NZP,NXP,NYP,A(ITRCE8C ),3593.) ! CO's emission
      CALL GAUSSTRCE(NZP,NXP,NYP,A(ITRCE16C),347.)  ! C2H4's emission
      CALL GAUSSTRCE(NZP,NXP,NYP,A(ITRCE17C),150.)  ! C3H6's emission
      CALL GAUSSTRCE(NZP,NXP,NYP,A(ITRCE20C),98.)   ! CH3CHO's emission
      CALL GAUSSTRCE(NZP,NXP,NYP,A(ITRCE24C),196.)  ! HCHO's emission
C a passive tracer: TRCE52
      CALL GAUSSTRCE(NZP,NXP,NYP,A(ITRCE52C),1000.)  ! a passive tracer's emission ppb/s
C-----------------------------------------------------

C-----------------------------------------------------------
C call chemical module
C-----------------------------------------------------------
c      idx=nzp*nyp*20+nzp*4+65
c      print*,'--- at an inlet (k,i,j)=(65,4,20)'
c     +     ,A(ITRCE1+idx),A(ITRCE2+idx),A(ITRCE3+idx),A(ITRCE4+idx)
c     +     ,A(ITRCE5+idx),A(ITRCE6+idx),A(ITRCE7+idx),A(ITRCE8+idx)
c     +     ,A(ITRCE9+idx),A(ITRCE10+idx),A(ITRCE11+idx),A(ITRCE12+idx)
c     +     ,A(ITRCE13+idx),A(ITRCE14+idx)
      CALL OHCHM(NZP,NXP,NYP
     +          ,A(ITRCE1 ),A(ITRCE2 ),A(ITRCE3 ),A(ITRCE4 ),A(ITRCE5 )
     +          ,A(ITRCE6 ),A(ITRCE7 ),A(ITRCE8 ),A(ITRCE9 ),A(ITRCE10)
     +          ,A(ITRCE11),A(ITRCE12),A(ITRCE13),A(ITRCE14),A(ITRCE15)
     +          ,A(ITRCE16),A(ITRCE17),A(ITRCE18),A(ITRCE19),A(ITRCE20)
     +          ,A(ITRCE21),A(ITRCE22),A(ITRCE23),A(ITRCE24),A(ITRCE25)
     +          ,A(ITRCE26),A(ITRCE27),A(ITRCE28),A(ITRCE29),A(ITRCE30)
     +          ,A(ITRCE31),A(ITRCE32),A(ITRCE33),A(ITRCE34),A(ITRCE35)
     +          ,A(ITRCE36),A(ITRCE37),A(ITRCE38),A(ITRCE39),A(ITRCE40)
     +          ,A(ITRCE41),A(ITRCE42),A(ITRCE43),A(ITRCE44),A(ITRCE45)
     +          ,A(ITRCE46),A(ITRCE47),A(ITRCE48),A(ITRCE49),A(ITRCE50)
     +          ,A(ITRCE51)
     +     ,A(ITHETA),DTLONG,NSHORT)
c      idx=nzp*nyp*20+nzp*4+65
c      print*,'+++ at an inlet (k,i,j)=(65,4,20)'
c     +     ,A(ITRCE1+idx),A(ITRCE2+idx),A(ITRCE3+idx),A(ITRCE4+idx)
c     +     ,A(ITRCE5+idx),A(ITRCE6+idx),A(ITRCE7+idx),A(ITRCE8+idx)
c     +     ,A(ITRCE9+idx),A(ITRCE10+idx),A(ITRCE11+idx),A(ITRCE12+idx)
c     +     ,A(ITRCE13+idx),A(ITRCE14+idx)
C-------------------------------------------------------------------
C LIST OF Chemical variables (William Bloss, 2007)
C  1     2   3   4    5     6    7     8      9      10    11    12      13     14
C CNO, CNO2, O3, OH, HO2, CH3O2, HONO, HNO3, HO2NO2, PERP, H2O2, HCHO, CH3O2NO2, CO
C-------------------------------------------------------------------
      CALL NONCYCLIC(NZP,NXP,NYP,A(ITRCE 1),O3_0          )
      CALL NONCYCLIC(NZP,NXP,NYP,A(ITRCE 2),NO_0          )
      CALL NONCYCLIC(NZP,NXP,NYP,A(ITRCE 3),NO2_0         )
      CALL NONCYCLIC(NZP,NXP,NYP,A(ITRCE 4),NO3_0         )
      CALL NONCYCLIC(NZP,NXP,NYP,A(ITRCE 5),OH_0          )
      CALL NONCYCLIC(NZP,NXP,NYP,A(ITRCE 6),HO2_0         )
      CALL NONCYCLIC(NZP,NXP,NYP,A(ITRCE 7),H2_0          )
      CALL NONCYCLIC(NZP,NXP,NYP,A(ITRCE 8),CO_0          )
      CALL NONCYCLIC(NZP,NXP,NYP,A(ITRCE 9),H2O2_0        )
      CALL NONCYCLIC(NZP,NXP,NYP,A(ITRCE10),HONO_0        )
      CALL NONCYCLIC(NZP,NXP,NYP,A(ITRCE11),HNO3_0        )
      CALL NONCYCLIC(NZP,NXP,NYP,A(ITRCE12),HO2NO2_0      )
      CALL NONCYCLIC(NZP,NXP,NYP,A(ITRCE13),CH3O2_0       )
      CALL NONCYCLIC(NZP,NXP,NYP,A(ITRCE14),CH3OH_0       )
      CALL NONCYCLIC(NZP,NXP,NYP,A(ITRCE15),CH4_0         )
      CALL NONCYCLIC(NZP,NXP,NYP,A(ITRCE16),C2H4_0        )
      CALL NONCYCLIC(NZP,NXP,NYP,A(ITRCE17),C3H6_0        )
      CALL NONCYCLIC(NZP,NXP,NYP,A(ITRCE18),HOCH2CH2O2_0  )
      CALL NONCYCLIC(NZP,NXP,NYP,A(ITRCE19),CH3CO2H_0     )
      CALL NONCYCLIC(NZP,NXP,NYP,A(ITRCE20),CH3CHO_0      )
      CALL NONCYCLIC(NZP,NXP,NYP,A(ITRCE21),C5H8_0        )
      CALL NONCYCLIC(NZP,NXP,NYP,A(ITRCE22),RU14O2_0      )
      CALL NONCYCLIC(NZP,NXP,NYP,A(ITRCE23),UCARB10_0     )
      CALL NONCYCLIC(NZP,NXP,NYP,A(ITRCE24),HCHO_0        )
      CALL NONCYCLIC(NZP,NXP,NYP,A(ITRCE25),CH3CO3_0      )
      CALL NONCYCLIC(NZP,NXP,NYP,A(ITRCE26),HOCH2CHO_0    )
      CALL NONCYCLIC(NZP,NXP,NYP,A(ITRCE27),C2H5OH_0      )
      CALL NONCYCLIC(NZP,NXP,NYP,A(ITRCE28),RN9O2_0       )
      CALL NONCYCLIC(NZP,NXP,NYP,A(ITRCE29),HCOOH_0       )
      CALL NONCYCLIC(NZP,NXP,NYP,A(ITRCE30),CARB6_0       )
      CALL NONCYCLIC(NZP,NXP,NYP,A(ITRCE31),UCARB12_0     )
      CALL NONCYCLIC(NZP,NXP,NYP,A(ITRCE32),RU12O2_0      )
      CALL NONCYCLIC(NZP,NXP,NYP,A(ITRCE33),CARB7_0       )
      CALL NONCYCLIC(NZP,NXP,NYP,A(ITRCE34),RU10O2_0      )
      CALL NONCYCLIC(NZP,NXP,NYP,A(ITRCE35),CH3NO3_0      )
```

```
      CALL NONCYCLIC(NZP,NXP,NYP,A(ITRCE36),HOC2H4NO3_0  )
      CALL NONCYCLIC(NZP,NXP,NYP,A(ITRCE37),RN9NO3_0     )
      CALL NONCYCLIC(NZP,NXP,NYP,A(ITRCE38),RU14NO3_0    )
      CALL NONCYCLIC(NZP,NXP,NYP,A(ITRCE39),CH3OOH_0     )
      CALL NONCYCLIC(NZP,NXP,NYP,A(ITRCE40),HOC2H4OOH_0  )
      CALL NONCYCLIC(NZP,NXP,NYP,A(ITRCE41),RN9OOH_0     )
      CALL NONCYCLIC(NZP,NXP,NYP,A(ITRCE42),CH3CO3H_0    )
      CALL NONCYCLIC(NZP,NXP,NYP,A(ITRCE43),HOCH2CO3H_0  )
      CALL NONCYCLIC(NZP,NXP,NYP,A(ITRCE44),RU14OOH_0    )
      CALL NONCYCLIC(NZP,NXP,NYP,A(ITRCE45),RU12OOH_0    )
      CALL NONCYCLIC(NZP,NXP,NYP,A(ITRCE46),RU10OOH_0    )
      CALL NONCYCLIC(NZP,NXP,NYP,A(ITRCE47),HOCH2CO3_0   )
      CALL NONCYCLIC(NZP,NXP,NYP,A(ITRCE48),PAN_0        )
      CALL NONCYCLIC(NZP,NXP,NYP,A(ITRCE49),PHAN_0       )
      CALL NONCYCLIC(NZP,NXP,NYP,A(ITRCE50),RU12PAN_0    )
      CALL NONCYCLIC(NZP,NXP,NYP,A(ITRCE51),MPAN_0       )
      CALL NONCYCLIC(NZP,NXP,NYP,A(ITRCE52),0.0          )

      CALL NONCYCLIC(NZP,NXP,NYP,A(ITRCE 1C),O3_0        )
      CALL NONCYCLIC(NZP,NXP,NYP,A(ITRCE 2C),NO_0        )
      CALL NONCYCLIC(NZP,NXP,NYP,A(ITRCE 3C),NO2_0       )
      CALL NONCYCLIC(NZP,NXP,NYP,A(ITRCE 4C),NO3_0       )
      CALL NONCYCLIC(NZP,NXP,NYP,A(ITRCE 5C),OH_0        )
      CALL NONCYCLIC(NZP,NXP,NYP,A(ITRCE 6C),HO2_0       )
      CALL NONCYCLIC(NZP,NXP,NYP,A(ITRCE 7C),H2_0        )
      CALL NONCYCLIC(NZP,NXP,NYP,A(ITRCE 8C),CO_0        )
      CALL NONCYCLIC(NZP,NXP,NYP,A(ITRCE 9C),H2O2_0      )
      CALL NONCYCLIC(NZP,NXP,NYP,A(ITRCE10C),HONO_0      )
      CALL NONCYCLIC(NZP,NXP,NYP,A(ITRCE11C),HNO3_0      )
      CALL NONCYCLIC(NZP,NXP,NYP,A(ITRCE12C),HO2NO2_0    )
      CALL NONCYCLIC(NZP,NXP,NYP,A(ITRCE13C),CH3O2_0     )
      CALL NONCYCLIC(NZP,NXP,NYP,A(ITRCE14C),CH3OH_0     )
      CALL NONCYCLIC(NZP,NXP,NYP,A(ITRCE15C),CH4_0       )
      CALL NONCYCLIC(NZP,NXP,NYP,A(ITRCE16C),C2H4_0      )
      CALL NONCYCLIC(NZP,NXP,NYP,A(ITRCE17C),C3H6_0      )
      CALL NONCYCLIC(NZP,NXP,NYP,A(ITRCE18C),HOCH2CH2O2_0)
      CALL NONCYCLIC(NZP,NXP,NYP,A(ITRCE19C),CH3CO2H_0   )
      CALL NONCYCLIC(NZP,NXP,NYP,A(ITRCE20C),CH3CHO_0    )
      CALL NONCYCLIC(NZP,NXP,NYP,A(ITRCE21C),C5H8_0      )
      CALL NONCYCLIC(NZP,NXP,NYP,A(ITRCE22C),RU14O2_0    )
      CALL NONCYCLIC(NZP,NXP,NYP,A(ITRCE23C),UCARB10_0   )
      CALL NONCYCLIC(NZP,NXP,NYP,A(ITRCE24C),HCHO_0      )
      CALL NONCYCLIC(NZP,NXP,NYP,A(ITRCE25C),CH3CO3_0    )
      CALL NONCYCLIC(NZP,NXP,NYP,A(ITRCE26C),HOCH2CHO_0  )
      CALL NONCYCLIC(NZP,NXP,NYP,A(ITRCE27C),C2H5OH_0    )
      CALL NONCYCLIC(NZP,NXP,NYP,A(ITRCE28C),RN9O2_0     )
      CALL NONCYCLIC(NZP,NXP,NYP,A(ITRCE29C),HCOOH_0     )
      CALL NONCYCLIC(NZP,NXP,NYP,A(ITRCE30C),CARB6_0     )
      CALL NONCYCLIC(NZP,NXP,NYP,A(ITRCE31C),UCARB12_0   )
      CALL NONCYCLIC(NZP,NXP,NYP,A(ITRCE32C),RU12O2_0    )
      CALL NONCYCLIC(NZP,NXP,NYP,A(ITRCE33C),CARB7_0     )
      CALL NONCYCLIC(NZP,NXP,NYP,A(ITRCE34C),RU10O2_0    )
      CALL NONCYCLIC(NZP,NXP,NYP,A(ITRCE35C),CH3NO3_0    )
      CALL NONCYCLIC(NZP,NXP,NYP,A(ITRCE36C),HOC2H4NO3_0 )
      CALL NONCYCLIC(NZP,NXP,NYP,A(ITRCE37C),RN9NO3_0    )
      CALL NONCYCLIC(NZP,NXP,NYP,A(ITRCE38C),RU14NO3_0   )
      CALL NONCYCLIC(NZP,NXP,NYP,A(ITRCE39C),CH3OOH_0    )
      CALL NONCYCLIC(NZP,NXP,NYP,A(ITRCE40C),HOC2H4OOH_0 )
      CALL NONCYCLIC(NZP,NXP,NYP,A(ITRCE41C),RN9OOH_0    )
      CALL NONCYCLIC(NZP,NXP,NYP,A(ITRCE42C),CH3CO3H_0   )
      CALL NONCYCLIC(NZP,NXP,NYP,A(ITRCE43C),HOCH2CO3H_0 )
      CALL NONCYCLIC(NZP,NXP,NYP,A(ITRCE44C),RU14OOH_0   )
      CALL NONCYCLIC(NZP,NXP,NYP,A(ITRCE45C),RU12OOH_0   )
      CALL NONCYCLIC(NZP,NXP,NYP,A(ITRCE46C),RU10OOH_0   )
      CALL NONCYCLIC(NZP,NXP,NYP,A(ITRCE47C),HOCH2CO3_0  )
      CALL NONCYCLIC(NZP,NXP,NYP,A(ITRCE48C),PAN_0       )
      CALL NONCYCLIC(NZP,NXP,NYP,A(ITRCE49C),PHAN_0      )
      CALL NONCYCLIC(NZP,NXP,NYP,A(ITRCE50C),RU12PAN_0   )
      CALL NONCYCLIC(NZP,NXP,NYP,A(ITRCE51C),MPAN_0      )
      CALL NONCYCLIC(NZP,NXP,NYP,A(ITRCE52C),0.0         )


C
C-------------------------------------------------------
C advective downwind B.C.
C-------------------------------------------------------
      CALL RDBTNDC(NZP,NXP,NYP,A(IUP),A(IUC),A(IVP),A(IVC),
     +            A(ITRCE1),A(ITRCE1C))
      CALL RDBTNDC(NZP,NXP,NYP,A(IUP),A(IUC),A(IVP),A(IVC),
     +            A(ITRCE2),A(ITRCE2C))
      CALL RDBTNDC(NZP,NXP,NYP,A(IUP),A(IUC),A(IVP),A(IVC),
     +            A(ITRCE3),A(ITRCE3C))
      CALL RDBTNDC(NZP,NXP,NYP,A(IUP),A(IUC),A(IVP),A(IVC),
     +            A(ITRCE4),A(ITRCE4C))
      CALL RDBTNDC(NZP,NXP,NYP,A(IUP),A(IUC),A(IVP),A(IVC),
     +            A(ITRCE5),A(ITRCE5C))
      CALL RDBTNDC(NZP,NXP,NYP,A(IUP),A(IUC),A(IVP),A(IVC),
     +            A(ITRCE6),A(ITRCE6C))
      CALL RDBTNDC(NZP,NXP,NYP,A(IUP),A(IUC),A(IVP),A(IVC),
```

```
+            A(ITRCE7),A(ITRCE7C))
 CALL RDBTNDC(NZP,NXP,NYP,A(IUP),A(IUC),A(IVP),A(IVC),
+            A(ITRCE8),A(ITRCE8C))
 CALL RDBTNDC(NZP,NXP,NYP,A(IUP),A(IUC),A(IVP),A(IVC),
+            A(ITRCE9),A(ITRCE9C))
 CALL RDBTNDC(NZP,NXP,NYP,A(IUP),A(IUC),A(IVP),A(IVC),
+            A(ITRCE10),A(ITRCE10C))
 CALL RDBTNDC(NZP,NXP,NYP,A(IUP),A(IUC),A(IVP),A(IVC),
+            A(ITRCE11),A(ITRCE11C))
 CALL RDBTNDC(NZP,NXP,NYP,A(IUP),A(IUC),A(IVP),A(IVC),
+            A(ITRCE12),A(ITRCE12C))
 CALL RDBTNDC(NZP,NXP,NYP,A(IUP),A(IUC),A(IVP),A(IVC),
+            A(ITRCE13),A(ITRCE13C))
 CALL RDBTNDC(NZP,NXP,NYP,A(IUP),A(IUC),A(IVP),A(IVC),
+            A(ITRCE14),A(ITRCE14C))
 CALL RDBTNDC(NZP,NXP,NYP,A(IUP),A(IUC),A(IVP),A(IVC),
+            A(ITRCE15),A(ITRCE15C))
 CALL RDBTNDC(NZP,NXP,NYP,A(IUP),A(IUC),A(IVP),A(IVC),
+            A(ITRCE16),A(ITRCE16C))
 CALL RDBTNDC(NZP,NXP,NYP,A(IUP),A(IUC),A(IVP),A(IVC),
+            A(ITRCE17),A(ITRCE17C))
 CALL RDBTNDC(NZP,NXP,NYP,A(IUP),A(IUC),A(IVP),A(IVC),
+            A(ITRCE18),A(ITRCE18C))
 CALL RDBTNDC(NZP,NXP,NYP,A(IUP),A(IUC),A(IVP),A(IVC),
+            A(ITRCE19),A(ITRCE19C))
 CALL RDBTNDC(NZP,NXP,NYP,A(IUP),A(IUC),A(IVP),A(IVC),
+            A(ITRCE20),A(ITRCE20C))
 CALL RDBTNDC(NZP,NXP,NYP,A(IUP),A(IUC),A(IVP),A(IVC),
+            A(ITRCE21),A(ITRCE21C))
 CALL RDBTNDC(NZP,NXP,NYP,A(IUP),A(IUC),A(IVP),A(IVC),
+            A(ITRCE22),A(ITRCE22C))
 CALL RDBTNDC(NZP,NXP,NYP,A(IUP),A(IUC),A(IVP),A(IVC),
+            A(ITRCE23),A(ITRCE23C))
 CALL RDBTNDC(NZP,NXP,NYP,A(IUP),A(IUC),A(IVP),A(IVC),
+            A(ITRCE24),A(ITRCE24C))
 CALL RDBTNDC(NZP,NXP,NYP,A(IUP),A(IUC),A(IVP),A(IVC),
+            A(ITRCE25),A(ITRCE25C))
 CALL RDBTNDC(NZP,NXP,NYP,A(IUP),A(IUC),A(IVP),A(IVC),
+            A(ITRCE26),A(ITRCE26C))
 CALL RDBTNDC(NZP,NXP,NYP,A(IUP),A(IUC),A(IVP),A(IVC),
+            A(ITRCE27),A(ITRCE27C))
 CALL RDBTNDC(NZP,NXP,NYP,A(IUP),A(IUC),A(IVP),A(IVC),
+            A(ITRCE28),A(ITRCE28C))
 CALL RDBTNDC(NZP,NXP,NYP,A(IUP),A(IUC),A(IVP),A(IVC),
+            A(ITRCE29),A(ITRCE29C))
 CALL RDBTNDC(NZP,NXP,NYP,A(IUP),A(IUC),A(IVP),A(IVC),
+            A(ITRCE30),A(ITRCE30C))
 CALL RDBTNDC(NZP,NXP,NYP,A(IUP),A(IUC),A(IVP),A(IVC),
+            A(ITRCE31),A(ITRCE31C))
 CALL RDBTNDC(NZP,NXP,NYP,A(IUP),A(IUC),A(IVP),A(IVC),
+            A(ITRCE32),A(ITRCE32C))
 CALL RDBTNDC(NZP,NXP,NYP,A(IUP),A(IUC),A(IVP),A(IVC),
+            A(ITRCE33),A(ITRCE33C))
 CALL RDBTNDC(NZP,NXP,NYP,A(IUP),A(IUC),A(IVP),A(IVC),
+            A(ITRCE34),A(ITRCE34C))
 CALL RDBTNDC(NZP,NXP,NYP,A(IUP),A(IUC),A(IVP),A(IVC),
+            A(ITRCE35),A(ITRCE35C))
 CALL RDBTNDC(NZP,NXP,NYP,A(IUP),A(IUC),A(IVP),A(IVC),
+            A(ITRCE36),A(ITRCE36C))
 CALL RDBTNDC(NZP,NXP,NYP,A(IUP),A(IUC),A(IVP),A(IVC),
+            A(ITRCE37),A(ITRCE37C))
 CALL RDBTNDC(NZP,NXP,NYP,A(IUP),A(IUC),A(IVP),A(IVC),
+            A(ITRCE38),A(ITRCE38C))
 CALL RDBTNDC(NZP,NXP,NYP,A(IUP),A(IUC),A(IVP),A(IVC),
+            A(ITRCE39),A(ITRCE39C))
 CALL RDBTNDC(NZP,NXP,NYP,A(IUP),A(IUC),A(IVP),A(IVC),
+            A(ITRCE40),A(ITRCE40C))
 CALL RDBTNDC(NZP,NXP,NYP,A(IUP),A(IUC),A(IVP),A(IVC),
+            A(ITRCE41),A(ITRCE41C))
 CALL RDBTNDC(NZP,NXP,NYP,A(IUP),A(IUC),A(IVP),A(IVC),
+            A(ITRCE42),A(ITRCE42C))
 CALL RDBTNDC(NZP,NXP,NYP,A(IUP),A(IUC),A(IVP),A(IVC),
+            A(ITRCE43),A(ITRCE43C))
 CALL RDBTNDC(NZP,NXP,NYP,A(IUP),A(IUC),A(IVP),A(IVC),
+            A(ITRCE44),A(ITRCE44C))
 CALL RDBTNDC(NZP,NXP,NYP,A(IUP),A(IUC),A(IVP),A(IVC),
+            A(ITRCE45),A(ITRCE45C))
 CALL RDBTNDC(NZP,NXP,NYP,A(IUP),A(IUC),A(IVP),A(IVC),
+            A(ITRCE46),A(ITRCE46C))
 CALL RDBTNDC(NZP,NXP,NYP,A(IUP),A(IUC),A(IVP),A(IVC),
+            A(ITRCE47),A(ITRCE47C))
 CALL RDBTNDC(NZP,NXP,NYP,A(IUP),A(IUC),A(IVP),A(IVC),
+            A(ITRCE48),A(ITRCE48C))
 CALL RDBTNDC(NZP,NXP,NYP,A(IUP),A(IUC),A(IVP),A(IVC),
+            A(ITRCE49),A(ITRCE49C))
 CALL RDBTNDC(NZP,NXP,NYP,A(IUP),A(IUC),A(IVP),A(IVC),
+            A(ITRCE50),A(ITRCE50C))
 CALL RDBTNDC(NZP,NXP,NYP,A(IUP),A(IUC),A(IVP),A(IVC),
+            A(ITRCE51),A(ITRCE51C))
```

```
      CALL RDBTNDC(NZP,NXP,NYP,A(IUP),A(IUC),A(IVP),A(IVC),
     +            A(ITRCE52),A(ITRCE52C))
C-------------------------------------------------------
      RETURN
      END

C=======================================
      SUBROUTINE NONCYCLIC(NZP,NXP,NYP,C,CVAL)
      DIMENSION C(NZP,NXP,NYP)
      include 'canyon.h'
      DO(J=1,NYP)
         DO(K=IH,NZP)
            C(K,1,J)=CVAL
            C(K,2,J)=CVAL
            C(K,3,J)=CVAL
         ENDDO
      ENDDO
      RETURN
      END
C=======================================
      SUBROUTINE VARYLR(N1,N2,N3,THP,THC)
.IN   STORAGE
      DIMENSION THP(N1,N2,N3),THC(N1,N2,N3),THAVERZ(100)
C disable this function
C      RETURN
C STARTING HEIGHT
C      ZINV0=700.
C LAPSE RATE
      THLR=0.009
C AVERAGE TEMPERATURE PROFILE
      DO(K=1,N1)
        THAVER=0.
        DO(I=1,N2)
          DO(J=1,N3)
            THAVER=THAVER+THP(K,I,J)/FLOAT(N2*N3)
          ENDDO
        ENDDO
        THAVERZ(K)=THAVER
      ENDDO
C DETERMINE ZI
      DO(K=4,N1)
        THLRK1=(THAVERZ(K)-THAVERZ(K-1))/(Z(K)-Z(K-1))
        THLRK2=(THAVERZ(K-1)-THAVERZ(K-2))/(Z(K-1)-Z(K-2))
        THLRK3=(THAVERZ(K-2)-THAVERZ(K-3))/(Z(K-2)-Z(K-3))
        IF(THLRK1.GT.0.001.AND.THLRK2.GT.0.001
     +       .AND.THLRK3.GT.0.001)THEN
          KZINV0=K-2
          GOTO 100
        ENDIF
      ENDDO
 100  CONTINUE
      ZINV0=Z(KZINV0)
C DETERMINE THETA WITHIN THE BOUNDARY LAYER
      THINBL=0.
      KTHINBL=0
      DO(K=1,N1)
        IF(Z(K).GT.100. .AND. Z(K).LT.ZINV0) THEN
          THINBL=THINBL+THAVERZ(K)
          KTHINBL=KTHINBL+1
          PRINT*,'K,Z(K),THAVER(K):',K,Z(K),THAVERZ(K)
C          KZINV0=Z(K)
        ENDIF
      ENDDO
      THINBL=THINBL/FLOAT(KTHINBL)
C
      PRINT*,'Z(K):'
      WRITE(*,777)(Z(K),K=1,N1)
      PRINT*,'THAVER(K):'
      WRITE(*,777)(THAVERZ(K),K=1,N1)
      PRINT*,'TH IN BL:',THINBL
      PRINT*,'K-INDEX AND HEIGHT OF INVERSION:',KZINV0,ZINV0
C SPECIFY TEMPERATURE PROFILE ABOVE THE BL
      DO(I=1,N2)
        DO(J=1,N3)
          DO(K=KZINV0+1,N1)
            THP(K,I,J)=THAVERZ(KZINV0)+(Z(K)-ZINV0)*THLR
            THC(K,I,J)=THP(K,I,J)
          ENDDO
        ENDDO
      ENDDO
      DO(K=KZINV0+1,N1)
        TH01D(K)=THP(K,1,1)
        TH01DN(K,1)=THP(K,1,1)
      ENDDO
      PRINT*,'*** new profile:'
      WRITE(*,777)(TH01D(K),K=1,N1)
 777  FORMAT(10(F10.3,','))
      RETURN
      END
```

```
C================================================
      SUBROUTINE ZWALLBC(NZP,NXP,NYP,UP,VP,THP,FLX,NSF,KSF,ISGNSF
     +     ,I1,I2,J1,J2,DN0,DN01D,ITOPO)
C------------------------------------------------
C This programme sets the B.C. of u,v,w,T for a surface
C   with the z-normal direction based on MOST theory
C------------------------------------------------
C --- here give surface parameters to provide characteristics of the surface
C NSF: number of surface (No.1=1, No.2=2, Maxsfc=2 here for 2 surfaces)
C KSF: grid index of the surface (at K=IH, or at K=2)
C ISGNSF: +1=when normal direction of the surface is same as +direction of the axis
C ISGNSF: -1=when normal direction of the surface is opposite to +direction of the axis
C J1,J2: starting and ending indices of J
C I1,I2: starting and ending indices of I
      include 'canyon.h'
      DIMENSION VP(NZP,NXP,NYP),UP(NZP,NXP,NYP),FLX(NZP,NXP,NYP)
     +   ,THP(NZP,NXP,NYP),DN0(NZP,NXP,NYP),DN01D(NZP)
      DATA IACESS/1/
C ------------- calculation of U* and T*
      ENTRY ZWALLUTS(NZP,NXP,NYP,UP,VP,THP,FLX,NSF,KSF,ISGNSF
     +     ,I1,I2,J1,J2)
C
C cell index of the surface: e.g. a street surface with KSF=1,  KAIR=2,  KWLL=1
C cell index of the surface: e.g. a roof   surface with KSF=61, KAIR=62, KWLL=61
      KAIR=KSF+(1+ISGNSF)/2
      KWLL=KSF+(1-ISGNSF)/2
C
C memory indices for saved T* & U*
      IF(IACESS.EQ.1)THEN
         ISTRZSVE(1)=1
         ISTRZSVE(2)=ISTRZSVE(1)+NZSVE1
         ISTRZSVE(3)=ISTRZSVE(2)+NZSVE2
C--------------------------------
C     for 2 canyons: uncomment the two lines
C--------------------------------
C         ISTRZSVE(4)=ISTRZSVE(3)+NZSVE3
C         ISTRZSVE(5)=ISTRZSVE(4)+NZSVE4
         IACCESS=2
      ENDIF
      ISTRSV=ISTRZSVE(NSF)
C loop over the cells on the surface
      DO(I=I1,I2)
         DO(J=J1,J2)
            UAIR= UP(KAIR,I,J)
            VAIR= VP(KAIR,I,J)
            TWLL=THP(KWLL,I,J)
            TAIR=THP(KAIR,I,J)
C
C assign initial values of u* and T*
            USOLD=USTRZSVE(ISTRSV)
            TSOLD=TSTRZSVE(ISTRSV)
C calculate new values of u* and T* based on MOST -
C ISFCL  = 1: DTH=TAIR-TWALL=variable => Businger or Louis
C ISTARS = 2: Louis' scheme (1: Businger's scheme)
            CALL WALLSTAR(1,2,UAIR,VAIR,DELTAH,TWLL
     +           ,TAIR,DTH,WTH0,USOLD,TSOLD,USTAR,TSTAR
     +           ,RWALL,RAIR,DRT,WRT0,RSOLD,RSTAR,CHU,CQU)
C         the output of CHU will suffice calculation of scalar flux: F_C=-CHU*deltaC
C         deltaC = C_air - C_wall & CHU >0
C assign the new values of T*
            TSTRZSVE(ISTRSV)=CHU
C assign the new values of T*
            QSTRZSVE(ISTRSV)=CQU
C assign the new values of u*
            USTRZSVE(ISTRSV)=ABS(USTAR)
C increment memory index by 1
            ISTRSV=ISTRSV+1
         ENDDO
      ENDDO
      RETURN
C ------------- FOR U-FLUX
      ENTRY ZWALLU(NZP,NXP,NYP,UP,VP,THP,FLX,NSF,KSF,ISGNSF
     +     ,I1,I2,J1,J2,DN0,DN01D,ITOPO)
C
C cell index of the surface: e.g. a street surface with KSF=1,  KAIR=2,  KWLL=1
C cell index of the surface: e.g. a roof   surface with KSF=61, KAIR=62, KWLL=61
      KAIR=KSF+(1+ISGNSF)/2
C
C memory indices for saved T* & U*
      ISTRSV=ISTRZSVE(NSF)
C loop over the cells on the surface
      DO(I=I1,I2)
         DO(J=J1,J2)
            UAIR= UP(KAIR,I,J)
            VAIR= VP(KAIR,I,J)
            UBAR2=SQRT(UAIR*UAIR+VAIR*VAIR)
            COSTHE=UAIR/(UBAR2+1.0E-30)
C for an up-facing wall: flx=-u*^2 if U>0 (what about density?)
            FLX(KSF,I,J)=-ISGNSF*USTRZSVE(ISTRSV)*USTRZSVE(ISTRSV)
```

```
     +           *COSTHE
Y    +                 *DN01D(KAIR)
Z    +                 *DN0(KAIR,I,J)
C             if(j.eq.LY2/2 .and. (i.eq.(L2+(L3-L2)/2) .or.
C     +           i.eq.(L3+L34/10) .or. i.eq.(L3+L34/10*5)
C     +           .or. i.eq.(L3+L34/10*9) .or. i.eq.(L4+L45/2)))then
C               print*,'&&&& ',ih,ksf,uair,vair,ubar2,costhe,isgnsf
C               print*,'-----',ISTRSV,USTRZSVE(ISTRSV),flx(ksf,i,j)
C             endif
C increment memory index by 1
            ISTRSV=ISTRSV+1
         ENDDO
      ENDDO
      RETURN
C
C ------------- FOR V-FLUX
      ENTRY ZWALLV(NZP,NXP,NYP,UP,VP,THP,FLX,NSF,KSF,ISGNSF
     +     ,I1,I2,J1,J2,DN0,DN01D,ITOPO)
C
C cell index of the surface: e.g. a street surface with KSF=1,  KAIR=2,  KWLL=1
C cell index of the surface: e.g. a roof   surface with KSF=61, KAIR=62, KWLL=61
      KAIR=KSF+(1+ISGNSF)/2
C
C memory indices for saved T* & U*
      ISTRSV=ISTRZSVE(NSF)
C loop over the cells on the surface
      DO(I=I1,I2)
         DO(J=J1,J2)
            UAIR= UP(KAIR,I,J)
            VAIR= VP(KAIR,I,J)
            UBAR2=SQRT(UAIR*UAIR+VAIR*VAIR)
            SINTHE=VAIR/(UBAR2+1.0E-30)
C for an up-facing wall: flx=-u*^2 if V>0 (what about density?)
C            FLX(KSF,I,J)=-ISGNSF*SIGN(USTRZSVE(ISTRSV),VAIR)
C     +           *SINTHE*USTRZSVE(ISTRSV)
            FLX(KSF,I,J)=-ISGNSF*USTRZSVE(ISTRSV)*USTRZSVE(ISTRSV)
     +           *SINTHE
Y    +                 *DN01D(KAIR)
Z    +                 *DN0(KAIR,I,J)
C increment memory index by 1
            ISTRSV=ISTRSV+1
         ENDDO
      ENDDO
      RETURN
C ------------- FOR T-FLUX at a z-facing wall
C --- This subroutine can also be called for any tracer TRCE?
C For example, for TRCE1, a street surface No.2 with KSF=1,  ISGNSF=1, (L3+1,L4;LY1-LY2)
C          CALL ZWALLT(NZP,NXP,NYP,A(IUP),A(IVP),A(ITRCE1)
C     +  ,FLX,2, 1,1,L3+1,L4,LY1,LY2,DN0,DN01D,ITOPO)
C ---------------------------------------------------------------
      ENTRY ZWALLT(NZP,NXP,NYP,UP,VP,THP,FLX,NSF,KSF,ISGNSF
     +     ,I1,I2,J1,J2,DN0,DN01D,ITOPO)
C
C cell index of the surface: e.g. a street surface with KSF=1,  KAIR=2,  KWLL=1
C cell index of the surface: e.g. a roof   surface with KSF=61, KAIR=62, KWLL=61
      KAIR=KSF+(1+ISGNSF)/2
      KWLL=KSF+(1-ISGNSF)/2
      ISTRSV=ISTRZSVE(NSF)
      DO(I=I1,I2)
         DO(J=J1,J2)
            TWLL=THP(KWLL,I,J)
            TAIR=THP(KAIR,I,J)
C for an up-facing wall: flx=-u*T* if T0-Tair>0 (what about density and Cp?)
C for an up-facing wall: flx=-CHU*deltaC, deltaC = C_air - C_wall & CHU >0
            FLX(KSF,I,J)=-ISGNSF*TSTRZSVE(ISTRSV)*(TAIR-TWLL)
Y    +                 *DN01D(KAIR)
Z    +                 *DN0(KAIR,I,J)
            ISTRSV=ISTRSV+1
         ENDDO
      ENDDO
C ---------------------------------------------------------------
      ENTRY ZWALLQ(NZP,NXP,NYP,UP,VP,THP,FLX,NSF,KSF,ISGNSF
     +     ,I1,I2,J1,J2,DN0,DN01D,ITOPO)
C
C cell index of the surface: e.g. a street surface with KSF=1,  KAIR=2,  KWLL=1
C cell index of the surface: e.g. a roof   surface with KSF=61, KAIR=62, KWLL=61
      KAIR=KSF+(1+ISGNSF)/2
      KWLL=KSF+(1-ISGNSF)/2
      ISTRSV=ISTRZSVE(NSF)
      DO(I=I1,I2)
         DO(J=J1,J2)
            TWLL=THP(KWLL,I,J)
            TAIR=THP(KAIR,I,J)
C for an up-facing wall: flx=-u*T* if T0-Tair>0 (what about density and Cp?)
C for an up-facing wall: flx=-CHU*deltaC, deltaC = C_air - C_wall & CHU >0
            FLX(KSF,I,J)=-ISGNSF*QSTRZSVE(ISTRSV)*(TAIR-TWLL)
Y    +                 *DN01D(KAIR)
Z    +                 *DN0(KAIR,I,J)
            ISTRSV=ISTRSV+1
```

```
         ENDDO
      ENDDO
      RETURN
      END
C================================================
      SUBROUTINE XWALLBC(NZP,NXP,NYP,VP,WP,THP,FLX,NSF,ISF,ISGNSF
     +     ,J1,J2,K1,K2,DN0,DN01D,ITOPO)
C------------------------------------------------
C This programme sets the B.C. of u,v,w,T for a surface
C   with the z-normal direction based on MOST theory
C------------------------------------------------
C --- here give surface parameters to provide characteristics of the surface
C NSF: number of surface (No.1=1, No.2=2, Maxxsf=2 here for 2 surfaces)
C ISF: grid index of the surface (at K=IH, or at K=2)
C ISGNSF: +1=when normal direction of the surface is same as +direction of the axis
C ISGNSF: -1=when normal direction of the surface is opposite to +direction of the axis
C J1,J2: starting and ending indices of J
C I1,I2: starting and ending indices of I
      include 'canyon.h'
      DIMENSION WP(NZP,NXP,NYP),VP(NZP,NXP,NYP),FLX(NZP,NXP,NYP)
     +   ,THP(NZP,NXP,NYP),DN0(NZP,NXP,NYP),DN01D(NZP)
      DATA IACESS/1/
C ------------- calculation of U* and T*
      ENTRY XWALLUTS(NZP,NXP,NYP,VP,WP,THP,FLX,NSF,ISF,ISGNSF
     +     ,J1,J2,K1,K2)
C
C cell index of the surface: e.g. a  left-wall with ISF=L3, IAIR=L3+1,  IWLL=L3
C cell index of the surface: e.g. a right-wall with ISF=L4, IAIR=L4,    IWLL=L4+1
      IAIR=ISF+(1+ISGNSF)/2
      IWLL=ISF+(1-ISGNSF)/2
C
C memory indices for saved T* & U*
      IF(IACESS.EQ.1)THEN
         ISTRXSVE(1)=1
         ISTRXSVE(2)=ISTRXSVE(1)+NXSVE1
C---------------------------------
C     for 2 canyons: uncomment the two lines
C---------------------------------
C          ISTRXSVE(3)=ISTRXSVE(2)+NXSVE2
C          ISTRXSVE(4)=ISTRXSVE(3)+NXSVE3
         IACCESS=2
      ENDIF
      ISTRSV=ISTRXSVE(NSF)
C loop over the cells on the surface
      DO(K=K1,K2)
         DO(J=J1,J2)
            VAIR= VP(K,IAIR,J)
            WAIR= WP(K,IAIR,J)
            TWLL=THP(K,IWLL,J)
            TAIR=THP(K,IAIR,J)
C
C assign initial values of u* and T*
            USOLD=USTRXSVE(ISTRSV)
            TSOLD=TSTRXSVE(ISTRSV)
C calculate new values of u* and T* based on MOST
            CALL WALLSTAR(1,2,VAIR,WAIR,DELTAH,TWLL
     +           ,TAIR,DTH,WTH0,USOLD,TSOLD,USTAR,TSTAR
     +           ,RWALL,RAIR,DRT,WRT0,RSOLD,RSTAR,CHU,CQU)
C         the output of CHU will suffice calculation of scalar flux: F_C=-CHU*deltaC
C         deltaC = C_air - C_wall
C assign the new values of T*
            TSTRXSVE(ISTRSV)=CHU
C assign the new values of Q*
            QSTRXSVE(ISTRSV)=CQU
C assign the new values of u*
            USTRXSVE(ISTRSV)=ABS(USTAR)
C increment memory index by 1
            ISTRSV=ISTRSV+1
         ENDDO
      ENDDO
      RETURN
C ------------- FOR V-FLUX
      ENTRY XWALLV(NZP,NXP,NYP,VP,WP,THP,FLX,NSF,ISF,ISGNSF
     +     ,J1,J2,K1,K2,DN0,DN01D,ITOPO)
C
C cell index of the surface: e.g. a  left-wall with ISF=L3, IAIR=L3+1,  IWLL=L3
C cell index of the surface: e.g. a right-wall with ISF=L4, IAIR=L4,    IWLL=L4+1
      IAIR=ISF+(1+ISGNSF)/2
C
C memory indices for saved T* & U*
      ISTRSV=ISTRXSVE(NSF)
C loop over the cells on the surface
      DO(K=K1,K2)
         DO(J=J1,J2)
            VAIR= VP(K,IAIR,J)
            WAIR= WP(K,IAIR,J)
            UBAR2=SQRT(VAIR*VAIR+WAIR*WAIR)
            COSTHE=VAIR/(UBAR2+1.0E-30)
C for an up-facing wall: flx=-u*^2 if V>0 (what about density?)
```

```
            FLX(K,ISF,J)=-ISGNSF*USTRXSVE(ISTRSV)*USTRXSVE(ISTRSV)
     +           *COSTHE
Y    +                 *DN01D(K)
Z    +                 *DN0(K,IAIR,J)
C increment memory index by 1
            ISTRSV=ISTRSV+1
         ENDDO
      ENDDO
      RETURN
C
C ------------- FOR W-FLUX
      ENTRY XWALLW(NZP,NXP,NYP,VP,WP,THP,FLX,NSF,ISF,ISGNSF
     +     ,J1,J2,K1,K2,DN0,DN01D,ITOPO)
C
C cell index of the surface: e.g. a  left-wall with ISF=L3, IAIR=L3+1,  IWLL=L3
C cell index of the surface: e.g. a right-wall with ISF=L4, IAIR=L4,    IWLL=L4+1
      IAIR=ISF+(1+ISGNSF)/2
C
C memory indices for sved T* & U*
      ISTRSV=ISTRXSVE(NSF)
C loop over the cells on the surface
      DO(K=K1,K2)
         DO(J=J1,J2)
            VAIR= VP(K,IAIR,J)
            WAIR= WP(K,IAIR,J)
            UBAR2=SQRT(VAIR*VAIR+WAIR*WAIR)
            SINTHE=WAIR/(UBAR2+1.0E-30)
C for an up-facing wall: flx=-u*^2 if W>0 (what about density?)
            FLX(K,ISF,J)=-ISGNSF*USTRXSVE(ISTRSV)*USTRXSVE(ISTRSV)
     +           *SINTHE
Y    +                 *DN01D(K)
Z    +                 *DN0(K,IAIR,J)
C increment memory index by 1
            ISTRSV=ISTRSV+1
         ENDDO
      ENDDO
      RETURN
C ------------- FOR T-FLUX
      ENTRY XWALLT(NZP,NXP,NYP,VP,WP,THP,FLX,NSF,ISF,ISGNSF
     +     ,J1,J2,K1,K2,DN0,DN01D,ITOPO)
C
      IAIR=ISF+(1+ISGNSF)/2
      IWLL=ISF+(1-ISGNSF)/2
      ISTRSV=ISTRXSVE(NSF)
      DO(K=K1,K2)
         DO(J=J1,J2)
            TWLL=THP(K,IWLL,J)
            TAIR=THP(K,IAIR,J)
C for an right-facing wall: flx=-u*T* if T0-Tair>0 (what about density and Cp?)
C for an right-facing wall: flx=-CHU*deltaC, deltaC = C_air - C_wall & CHU >0
            FLX(K,ISF,J)=-ISGNSF*TSTRXSVE(ISTRSV)*(TAIR-TWLL)
Y    +                 *DN01D(K)
Z    +                 *DN0(K,IAIR,J)
            ISTRSV=ISTRSV+1
         ENDDO
      ENDDO
C ------------- FOR T-FLUX
      ENTRY XWALLQ(NZP,NXP,NYP,VP,WP,THP,FLX,NSF,ISF,ISGNSF
     +     ,J1,J2,K1,K2,DN0,DN01D,ITOPO)
C
      IAIR=ISF+(1+ISGNSF)/2
      IWLL=ISF+(1-ISGNSF)/2
      ISTRSV=ISTRXSVE(NSF)
      DO(K=K1,K2)
         DO(J=J1,J2)
            TWLL=THP(K,IWLL,J)
            TAIR=THP(K,IAIR,J)
C for an right-facing wall: flx=-u*T* if T0-Tair>0 (what about density and Cp?)
C for an right-facing wall: flx=-CHU*deltaC, deltaC = C_air - C_wall & CHU >0
            FLX(K,ISF,J)=-ISGNSF*QSTRXSVE(ISTRSV)*(TAIR-TWLL)
Y    +                 *DN01D(K)
Z    +                 *DN0(K,IAIR,J)
            ISTRSV=ISTRSV+1
         ENDDO
      ENDDO
      RETURN
      END
C================================================
      SUBROUTINE YWALLBC(NZP,NXP,NYP,WP,UP,THP,FLX,NSF,JSF,ISGNSF
     +     ,K1,K2,I1,I2,DN0,DN01D,ITOPO)
C------------------------------------------------
C This programme sets the B.C. of u,v,w,T for a surface
C   with the z-normal direction based on MOST theory
C------------------------------------------------
C --- here give surface parameters to provide characteristics of the surface
C NSF: number of surface (No.1=1, No.2=2, Maxysf=2 here for 2 surfaces)
C JSF: grid index of the surface (at K=IH, or at K=2)
C ISGNSF: +1=when normal direction of the surface is same as +direction of the axis
C ISGNSF: -1=when normal direction of the surface is opposite to +direction of the axis
```

```
C I1,I2: starting and ending indices of I
C K1,K2: starting and ending indices of K
      include 'canyon.h'
      DIMENSION UP(NZP,NXP,NYP),WP(NZP,NXP,NYP),FLX(NZP,NXP,NYP)
     +   ,THP(NZP,NXP,NYP),DN0(NZP,NXP,NYP),DN01D(NZP)
      DATA IACESS/1/
C ------------- calculation of U* and T*
      ENTRY YWALLUTS(NZP,NXP,NYP,WP,UP,THP,FLX,NSF,JSF,ISGNSF
     +     ,K1,K2,I1,I2)
C
C cell index of the surface: e.g. a  back-wall with JSF=30, JAIR=31, JWLL=30
C cell index of the surface: e.g. a front-wall with JSF=10, JAIR=10, JWLL=11
      JAIR=JSF+(1+ISGNSF)/2
      JWLL=JSF+(1-ISGNSF)/2
C
C memory indices for saved T* & U*
      IF(IACESS.EQ.1)THEN
         ISTRYSVE(1)=1
         ISTRYSVE(2)=ISTRYSVE(1)+NYSVE1
         ISTRYSVE(3)=ISTRYSVE(2)+NYSVE2
         ISTRYSVE(4)=ISTRYSVE(3)+NYSVE3
         IACCESS=2
      ENDIF
      ISTRSV=ISTRYSVE(NSF)
C loop over the cells on the surface
      DO(K=K1,K2)
         DO(I=I1,I2)
            WAIR= WP(K,I,JAIR)
            UAIR= UP(K,I,JAIR)
            TWLL=THP(K,I,JWLL)
            TAIR=THP(K,I,JAIR)
C
C assign initial values of u* and T*
            USOLD=USTRYSVE(ISTRSV)
            TSOLD=TSTRYSVE(ISTRSV)
C calculate new values of u* and T* based on MOST
            CALL WALLSTAR(1,2,WAIR,UAIR,DELTAH,TWLL
     +           ,TAIR,DTH,WTH0,USOLD,TSOLD,USTAR,TSTAR
     +           ,RWALL,RAIR,DRT,WRT0,RSOLD,RSTAR,CHU,CQU)
C         the output of CHU will suffice calculation of scalar flux: F_C=CHU*deltaC
C         deltaC = C_air - C_wall
C assign the new values of T*
            TSTRYSVE(ISTRSV)=CHU
C assign the new values of Q*
            QSTRYSVE(ISTRSV)=CQU
C assign the new values of u*
            USTRYSVE(ISTRSV)=ABS(USTAR)
C increment memory index by 1
            ISTRSV=ISTRSV+1
         ENDDO
      ENDDO
      RETURN
C ------------- FOR W-FLUX
      ENTRY YWALLW(NZP,NXP,NYP,WP,UP,THP,FLX,NSF,JSF,ISGNSF
     +     ,K1,K2,I1,I2,DN0,DN01D,ITOPO)
C
C cell index of the surface: e.g. a street surface with JSF=1,  JAIR=2,  JWLL=1
C cell index of the surface: e.g. a roof   surface with JSF=60, JAIR=61, JWLL=60
      JAIR=JSF+(1+ISGNSF)/2
C
C memory indices for saved T* & U*
      ISTRSV=ISTRYSVE(NSF)
C loop over the cells on the surface
      DO(K=K1,K2)
         DO(I=I1,I2)
            WAIR= WP(K,I,JAIR)
            UAIR= UP(K,I,JAIR)
            UBAR2=SQRT(WAIR*WAIR+UAIR*UAIR)
            COSTHE=WAIR/(UBAR2+1.0E-30)
C for an up-facing wall: flx=-u*^2 if W>0 (what about density?)
            FLX(K,I,JSF)=-ISGNSF*USTRYSVE(ISTRSV)*USTRYSVE(ISTRSV)
     +           *COSTHE
Y    +                 *DN01D(K)
Z    +                 *DN0(K,I,JAIR)
C increment memory index by 1
            ISTRSV=ISTRSV+1
         ENDDO
      ENDDO
      RETURN
C
C ------------- FOR U-FLUX
      ENTRY YWALLU(NZP,NXP,NYP,WP,UP,THP,FLX,NSF,JSF,ISGNSF
     +     ,K1,K2,I1,I2,DN0,DN01D,ITOPO)
C
C cell index of the surface: e.g. a street surface with JSF=1,  JAIR=2,  JWLL=1
C cell index of the surface: e.g. a roof   surface with JSF=60, JAIR=61, JWLL=60
      JAIR=JSF+(1+ISGNSF)/2
C
C memory indices for sved T* & U*
```

```
      ISTRSV=ISTRYSVE(NSF)
C loop over the cells on the surface
      DO(K=K1,K2)
         DO(I=I1,I2)
            WAIR= WP(K,I,JAIR)
            UAIR= UP(K,I,JAIR)
            UBAR2=SQRT(WAIR*WAIR+UAIR*UAIR)
            SINTHE=UAIR/(UBAR2+1.0E-30)
C for an up-facing wall: flx=-u*^2 if U>0 (what about density?)
            FLX(K,I,JSF)=-ISGNSF*USTRYSVE(ISTRSV)*USTRYSVE(ISTRSV)
     +           *SINTHE
Y    +                *DN01D(K)
Z    +                *DN0(K,I,JAIR)
C increment memory index by 1
            ISTRSV=ISTRSV+1
         ENDDO
      ENDDO
      RETURN
C ------------- FOR T-FLUX
      ENTRY YWALLT(NZP,NXP,NYP,WP,UP,THP,FLX,NSF,JSF,ISGNSF
     +     ,K1,K2,I1,I2,DN0,DN01D,ITOPO)
C
C cell index of the surface: e.g. a street surface with JSF=1,  JAIR=2,  JWLL=1
C cell index of the surface: e.g. a roof   surface with JSF=60, JAIR=61, JWLL=60
      JAIR=JSF+(1+ISGNSF)/2
      JWLL=JSF+(1-ISGNSF)/2
      ISTRSV=ISTRYSVE(NSF)
      DO(K=K1,K2)
         DO(I=I1,I2)
            TWLL=THP(K,I,JWLL)
            TAIR=THP(K,I,JAIR)
C for an y-facing wall: flx=-u*T* if T0-Tair>0 (what about density and Cp?)
C for an y-facing wall: flx=-CHU*deltaC, deltaC = C_air - C_wall & CHU >0
            FLX(K,I,JSF)=-ISGNSF*TSTRYSVE(ISTRSV)*(TAIR-TWLL)
Y    +                *DN01D(K)
Z    +                *DN0(K,I,JAIR)
            ISTRSV=ISTRSV+1
         ENDDO
      ENDDO
C ------------- FOR T-FLUX
      ENTRY YWALLQ(NZP,NXP,NYP,WP,UP,THP,FLX,NSF,JSF,ISGNSF
     +     ,K1,K2,I1,I2,DN0,DN01D,ITOPO)
C
C cell index of the surface: e.g. a street surface with JSF=1,  JAIR=2,  JWLL=1
C cell index of the surface: e.g. a roof   surface with JSF=60, JAIR=61, JWLL=60
      JAIR=JSF+(1+ISGNSF)/2
      JWLL=JSF+(1-ISGNSF)/2
      ISTRSV=ISTRYSVE(NSF)
      DO(K=K1,K2)
         DO(I=I1,I2)
            TWLL=THP(K,I,JWLL)
            TAIR=THP(K,I,JAIR)
C for an y-facing wall: flx=-u*T* if T0-Tair>0 (what about density and Cp?)
C for an y-facing wall: flx=-CHU*deltaC, deltaC = C_air - C_wall & CHU >0
            FLX(K,I,JSF)=-ISGNSF*QSTRYSVE(ISTRSV)*(TAIR-TWLL)
Y    +                *DN01D(K)
Z    +                *DN0(K,I,JAIR)
            ISTRSV=ISTRSV+1
         ENDDO
      ENDDO
      RETURN
      END
C=================================================
      SUBROUTINE WALLUTS(NZP,NXP,NYP,UP,VP,WP,THP)
      include 'canyon.h'
      DIMENSION UP(NZP,NXP,NYP),VP(NZP,NXP,NYP),WP(NZP,NXP,NYP)
     +   ,THP(NZP,NXP,NYP)
C---------------------------
C for 1 canyon case
C---------------------------
C a roof   surface No.1 with KSF=60, ISGNSF=1, (L2,L3;LY1,LY2)
      CALL ZWALLUTS(NZP,NXP,NYP,UP,VP,THP
     +  ,FLX,1,IH,1,L2,L3,LY1,LY2)
C a street surface No.2 with KSF=1,  ISGNSF=1, (L3+1,L4;LY1-LY2)
      CALL ZWALLUTS(NZP,NXP,NYP,UP,VP,THP
     +  ,FLX,2, 1,1,L3+1,L4,LY1,LY2)
C a roof   surface No.3 with KSF=60, ISGNSF=1, (L2,L3;LY1,LY2)
      CALL ZWALLUTS(NZP,NXP,NYP,UP,VP,THP
     +  ,FLX,3,IH,1,L4+1,L5,LY1,LY2)
C  left wall: No.1 with ISF=L3, ISGNSF=1, (LY1,LY2;1,IH)
      CALL XWALLUTS(NZP,NXP,NYP,VP,WP,THP
     +  ,FLX,1,L3, 1,LY1,LY2,1,IH)
C right wall: No.2 with ISF=L4, ISGNSF=-1, (LY1,LY2;1,IH)
      CALL XWALLUTS(NZP,NXP,NYP,VP,WP,THP
     +  ,FLX,2,L4,-1,LY1,LY2,1,IH)
C~~~~~~~~~~~~~~~~~~~~~~~~~~~~~~~~
      RETURN
      END
C=================================================
```

```
      SUBROUTINE XWLLFLXV(N1,N2,N3,FLX,DN0)
.IN   STORAGE
      include 'canyon.h'
      DIMENSION FLX(N1,N2,N3),DN0(N1,N2,N3)
C---------------------------
C for 1 canyon case
C---------------------------
C
C for 1 canyon case
C
C  left wall: No.1 with ISF=L3, ISGNSF=1, (LY1,LY2;1,IH)
      CALL XWALLV(NZP,NXP,NYP,A(IVP),A(IWP),A(ITHP)
     +  ,FLX,1,L3, 1,LY1,LY2,1,IH,DN0,DN01D,ITOPO)
C right wall: No.2 with ISF=L4, ISGNSF=-1, (LY1,LY2;1,IH)
      CALL XWALLV(NZP,NXP,NYP,A(IVP),A(IWP),A(ITHP)
     +  ,FLX,2,L4,-1,LY1,LY2,1,IH,DN0,DN01D,ITOPO)
      RETURN
      END
C=================================================
      SUBROUTINE XWLLFLXW(N1,N2,N3,FLX,DN0)
.IN   STORAGE
      include 'canyon.h'
      DIMENSION FLX(N1,N2,N3),DN0(N1,N2,N3)
C---------------------------
C for 1 canyon case
C---------------------------
C
C for 1 canyon case
C
C  left wall: No.1 with ISF=L3, ISGNSF=1, (LY1,LY2;1,IH)
      CALL XWALLW(NZP,NXP,NYP,A(IVP),A(IWP),A(ITHP)
     +  ,FLX,1,L3, 1,LY1,LY2,1,IH,DN0,DN01D,ITOPO)
C right wall: No.2 with ISF=L4, ISGNSF=-1, (LY1,LY2;1,IH)
      CALL XWALLW(NZP,NXP,NYP,A(IVP),A(IWP),A(ITHP)
     +  ,FLX,2,L4,-1,LY1,LY2,1,IH,DN0,DN01D,ITOPO)
      RETURN
      END
C=================================================
      SUBROUTINE YWLLFLXW(N1,N2,N3,FLX,DN0)
.IN   STORAGE
      include 'canyon.h'
      DIMENSION FLX(N1,N2,N3),DN0(N1,N2,N3)
C---------------------------
C for 1 canyon case
C---------------------------
C
C for 1 canyon case
C
C modified by ming on 040809: for future y-wall-W
C      CALL YWALLW(NZP,NXP,NYP,A(IWP),A(IUP),A(ITHP)
C     +  ,FLX,1,ISF, 1,K1,K2,I1,I2,DN0,DN01D,ITOPO)
C      CALL YWALLW(NZP,NXP,NYP,A(IWP),A(IUP),A(ITHP)
C     +  ,FLX,2,ISF,-1,K1,K2,I1,I2,DN0,DN01D,ITOPO)
C end
      RETURN
      END
C=================================================
      SUBROUTINE YWLLFLXU(N1,N2,N3,FLX,DN0)
.IN   STORAGE
      include 'canyon.h'
      DIMENSION FLX(N1,N2,N3),DN0(N1,N2,N3)
C---------------------------
C for 1 canyon case
C---------------------------
C
C for 1 canyon case
C
C modified by ming on 040809: for future y-wall-U
C      CALL YWALLU(NZP,NXP,NYP,A(IWP),A(IUP),A(ITHP)
C     +  ,FLX,1,ISF, 1,K1,K2,I1,I2,DN0,DN01D,ITOPO)
C      CALL YWALLU(NZP,NXP,NYP,A(IWP),A(IUP),A(ITHP)
C     +  ,FLX,2,ISF,-1,K1,K2,I1,I2,DN0,DN01D,ITOPO)
C end
      RETURN
      END
C=================================================
      SUBROUTINE ZWLLFLXU(N1,N2,N3,FLX,DN0)
.IN   STORAGE
      include 'canyon.h'
      DIMENSION FLX(N1,N2,N3),DN0(N1,N2,N3)
C---------------------------
C for 1 canyon case
C---------------------------
C
C for 1 canyon case
C
C a roof   surface No.1 with KSF=60, ISGNSF=1, (L2,L3;LY1,LY2)
      CALL ZWALLU(NZP,NXP,NYP,A(IUP),A(IVP),A(ITHP)
     +     ,FLX,1,IH,1,L2,L3,LY1,LY2,DN0,DN01D,ITOPO)
```

```
C     a street surface No.2 with KSF=1,  ISGNSF=1, (L3+1,L4;LY1-LY2)
      CALL ZWALLU(NZP,NXP,NYP,A(IUP),A(IVP),A(ITHP)
     +     ,FLX,2, 1,1,L3+1,L4,LY1,LY2,DN0,DN01D,ITOPO)
C     a roof   surface No.3 with KSF=60, ISGNSF=1, (L2,L3;LY1,LY2)
      CALL ZWALLU(NZP,NXP,NYP,A(IUP),A(IVP),A(ITHP)
     +     ,FLX,3,IH,1,L4+1,L5,LY1,LY2,DN0,DN01D,ITOPO)
      RETURN
      END
C================================================
      SUBROUTINE ZWLLFLXV(N1,N2,N3,FLX,DN0)
.IN   STORAGE
      include 'canyon.h'
      DIMENSION FLX(N1,N2,N3),DN0(N1,N2,N3)
C----------------------------
C for 1 canyon case
C----------------------------
C
C for 1 canyon case
C
C a roof   surface No.1 with KSF=60, ISGNSF=1, (L2,L3;LY1,LY2)
      CALL ZWALLV(NZP,NXP,NYP,A(IUP),A(IVP),A(ITHP)
     +  ,FLX,1,IH,1,L2,L3,LY1,LY2,DN0,DN01D,ITOPO)
C a street surface No.2 with KSF=1,  ISGNSF=1, (L3+1,L4;LY1-LY2)
      CALL ZWALLV(NZP,NXP,NYP,A(IUP),A(IVP),A(ITHP)
     +  ,FLX,2, 1,1,L3+1,L4,LY1,LY2,DN0,DN01D,ITOPO)
C a roof   surface No.3 with KSF=60, ISGNSF=1, (L2,L3;LY1,LY2)
      CALL ZWALLV(NZP,NXP,NYP,A(IUP),A(IVP),A(ITHP)
     +  ,FLX,3,IH,1,L4+1,L5,LY1,LY2,DN0,DN01D,ITOPO)
      RETURN
      END
C================================================
      SUBROUTINE XWLLFLXT(N1,N2,N3,FLX,DN0)
.IN   STORAGE
      include 'canyon.h'
      DIMENSION FLX(N1,N2,N3),DN0(N1,N2,N3)
C----------------------------
C for 1 canyon case
C----------------------------
C
C for 1 canyon case
C
C temperature at Upstream-wall surface
      IF(CHTRP(1:3).EQ.'THP')THEN
         CALL XWALLT(NZP,NXP,NYP,A(IVP),A(IWP),A(ITHP)
     +        ,FLX,1,L3, 1,LY1,LY2,1,IH,DN0,DN01D,ITOPO)
C     temperature at Downstream wall: No.2 with ISF=L4, ISGNSF=-1, (LY1,LY2;1,IH)
         CALL XWALLT(NZP,NXP,NYP,A(IVP),A(IWP),A(ITHP)
     +        ,FLX,2,L4,-1,LY1,LY2,1,IH,DN0,DN01D,ITOPO)
      ENDIF

C modified on 20071030: delete all "IF(CHTRP(1:5).EQ.'TRCE?') CALL ZWALLQ"
C   for all scalars on z-walls ==> equivalent to setting FLX=0 (set in rturb)

      RETURN
      END
C================================================
      SUBROUTINE YWLLFLXT(N1,N2,N3,FLX,DN0)
.IN   STORAGE
      include 'canyon.h'
      DIMENSION FLX(N1,N2,N3),DN0(N1,N2,N3)
C
C for 1 canyon case
C
C temperature at Upstream-wall surface
C      IF(CHTRP(1:3).EQ.'THP')THEN
C     modified by ming on 040809: for future y-wall-T
C     CALL YWALLT(NZP,NXP,NYP,A(IWP),A(IUP),A(ITHP)
C     +  ,FLX,1,ISF, 1,K1,K2,I1,I2,DN0,DN01D,ITOPO)
C     CALL YWALLT(NZP,NXP,NYP,A(IWP),A(IUP),A(ITHP)
C     +  ,FLX,2,ISF,-1,K1,K2,I1,I2,DN0,DN01D,ITOPO)
      RETURN
      END
C================================================
      SUBROUTINE ZWLLFLXT(N1,N2,N3,FLX,DN0)
.IN   STORAGE
      include 'canyon.h'
      DIMENSION FLX(N1,N2,N3),DN0(N1,N2,N3)
C
C for 1 canyon case
C
C temperature at the left-roof: surface No.1 with KSF=60, ISGNSF=1, (L2,L3;LY1,LY2)
      IF(CHTRP(1:3).EQ.'THP')THEN
         CALL ZWALLT(NZP,NXP,NYP,A(IUP),A(IVP),A(ITHP)
     +        ,FLX,1,IH,1,L2,L3,LY1,LY2,DN0,DN01D,ITOPO)
C     temperature at the street: surface No.2 with KSF=1,  ISGNSF=1, (L3+1,L4;LY1-LY2)
         CALL ZWALLT(NZP,NXP,NYP,A(IUP),A(IVP),A(ITHP)
     +        ,FLX,2, 1,1,L3+1,L4,LY1,LY2,DN0,DN01D,ITOPO)
C     temperature at the right-roof:   surface No.3 with KSF=60, ISGNSF=1, (L2,L3;LY1,LY2)
         CALL ZWALLT(NZP,NXP,NYP,A(IUP),A(IVP),A(ITHP)
```

```
     +        ,FLX,3,IH,1,L4+1,L5,LY1,LY2,DN0,DN01D,ITOPO)
      ENDIF

C modified on 20071030: delete all "IF(CHTRP(1:5).EQ.'TRCE?') CALL ZWALLQ"
C   for all scalars on z-walls ==> equivalent to setting FLX=0 (set in rturb)
      RETURN
      END
C================================================
      SUBROUTINE XWLLBCT(N1,N2,N3,TRP)
.IN   STORAGE
      include 'canyon.h'
      DIMENSION TRP(N1,N2,N3)
C
C for 1 canyon case
C
C----------------------------------------
C modified on 061103: set BC for TRP on the wall and zero it in wall !!!
      IF(CHTRP(1:3).NE.'THP')CALL WALLBCTR(NZP,NXP,NYP,TRP)
C modified by ming on 020418: set BC for TRP on the wall and zero it in wall !!!
      IF(CHTRP(1:3).EQ.'THP')CALL WALLTH(NZP,NXP,NYP,TRP)
      IF(CHTRP(1:3).EQ.'THP')CALL WALLTH(NZP,NXP,NYP,A(ITHC))
      RETURN
      END
C================================================
      SUBROUTINE YWLLBCT(N1,N2,N3,TRP)
.IN   STORAGE
      include 'canyon.h'
      DIMENSION TRP(N1,N2,N3)
C
C for 1 canyon case
C
C----------------------------------------
C modified by ming on 020418: set BC for TRP on the wall and zero it in wall !!!
      IF(CHTRP(1:3).NE.'THP')CALL WALLBCTR(NZP,NXP,NYP,TRP)
      IF(CHTRP(1:3).EQ.'THP')CALL WALLTH(NZP,NXP,NYP,TRP)
      IF(CHTRP(1:3).EQ.'THP')CALL WALLTH(NZP,NXP,NYP,A(ITHC))
      RETURN
      END
C================================================
      SUBROUTINE ZWLLBCT(N1,N2,N3,TRP)
.IN   STORAGE
      include 'canyon.h'
      DIMENSION TRP(N1,N2,N3)
C
C for 1 canyon case
C
C modified on 061103: set BC for TRP on the wall and zero it in wall !!!
      IF(CHTRP(1:3).NE.'THP')CALL WALLBCTR(NZP,NXP,NYP,TRP)
      IF(CHTRP(1:3).EQ.'THP')CALL WALLTH(NZP,NXP,NYP,TRP)
      IF(CHTRP(1:3).EQ.'THP')CALL WALLTH(NZP,NXP,NYP,A(ITHC))
      RETURN
      END
C================================================
      SUBROUTINE WLLBCUVW
.IN   STORAGE
C
C modified by ming on 020418: zero wall again
C
      CALL DEGALN(NZP,NXP,NYP,A(IUP),A(IVP))
      IF(NGRID.EQ.1)CALL ZEROBLDG(NZP,NXP,NYP,A(IUP),'N')
      IF(NGRID.EQ.1)CALL ZEROBLDG(NZP,NXP,NYP,A(IVP),'Y')
      IF(NGRID.EQ.1)CALL ZEROBLDG(NZP,NXP,NYP,A(IWP),'Y')
      CALL GALN(NZP,NXP,NYP,A(IUP),A(IVP))
      RETURN
      END
C================================================
      SUBROUTINE ZEROBLDG(NZP,NXP,NYP,VAR,PLUSONE)
C------------------------------------------------
C This programme sets the value of a variable as 0 inside the walls
C------------------------------------------------
      DIMENSION VAR(NZP,NXP,NYP)
      CHARACTER*20 PLUSONE
      include 'canyon.h'
C
C      front and back wall boundary condition
C
      CALL CNSTBLDG(NZP,NXP,NYP,VAR,PLUSONE,0.)
C
      RETURN
      END
C================================================
      SUBROUTINE CNSTBLDG(NZP,NXP,NYP,VAR,PLUSONE,CNST)
C------------------------------------------------
C This programme sets the value of a variable as CNST inside the walls
C------------------------------------------------
      DIMENSION VAR(NZP,NXP,NYP)
      CHARACTER*20 PLUSONE
      include 'canyon.h'
C
```

```
C for some components, we need to shift one grid to the right:
C  'Y'  ===>  VP, WP, T or other scalars; FLX in ZDIFF? and YDIFF?;
C     'N'  ===>  UP; FLX in XDIFF?;
      IF(PLUSONE(1:1) .EQ. 'Y') THEN
         LR4=L4+1
         LR14=L14+1
      ELSE
         LR4=L4
         LR14=L14
      ENDIF
C
C     for 1 canyon
C
      CALL CNSTWALL(NZP,NXP,NYP,VAR,CNST,L2,L3,LY1,LY2,1,IH)
      CALL CNSTWALL(NZP,NXP,NYP,VAR,CNST,LR4,L5,LY1,LY2,1,IH)
C--------------------------------
C     for 2 canyons
C--------------------------------
C     CALL CNSTWALL(NZP,NXP,NYP,VAR,CNST,L2,L3,LY1,LY2,1,IH)
C     CALL CNSTWALL(NZP,NXP,NYP,VAR,CNST,LR4,L13,LY1,LY2,1,IH)
C     CALL CNSTWALL(NZP,NXP,NYP,VAR,CNST,LR14,L15,LY1,LY2,1,IH)
C--------------------------------
C
      RETURN
      END
C================================================
      SUBROUTINE CNSTWALL(NZP,NXP,NYP,VAR,CNST,I1,I2,J1,J2,K1,K2)
C------------------------------------------------
C This programme sets the value of a variable as CNST on the walls
C *** set temperature on the street
C     CALL CNSTWALL(NZP,NXP,NYP,A(ITHP),293.+DTROAD,L3+1,L4,LY1,LY2,1,1)
C *** set temperature at the left wall (2 layers)
C     CALL CNSTWALL(NZP,NXP,NYP,A(ITHP),293.+DTLWALL,L3-1,L3,LY1,LY2,1,IH)
C *** set tracer concentraion on the right wall (2 layers)
C     CALL CNSTWALL(NZP,NXP,NYP,A(ITRCE3),1.,L4+1,L4+2,LY1,LY2,1,IH)
C *** set tracer concentraion on the right ROOF (2 layers)
C     CALL CNSTWALL(NZP,NXP,NYP,A(ITRCE6),1.,L4+1,L5,LY1,LY2,IH-1,IH)
C------------------------------------------------
      DIMENSION VAR(NZP,NXP,NYP)
      DO(I=I1,I2)
         DO(J=J1,J2)
            DO(K=K1,K2)
               VAR(K,I,J)=CNST
            ENDDO
         ENDDO
      ENDDO
      RETURN
      END
C================================================
      SUBROUTINE WALLBCTR(NZP,NXP,NYP,TRP)
C------------------------------------------------
C This programme sets the wall B.C.s of 0 gradient:
C    dC/dn = 0.  for a variable (all tracers in practice)
C------------------------------------------------
      include 'canyon.h'
      DIMENSION TRP(NZP,NXP,NYP)
C zero wall
      CALL ZEROBLDG(NZP,NXP,NYP,TRP,'Y')
C-------------------------------------
C one-canyon
C
C road
      CALL ZEROGRAD(NZP,NXP,NYP,TRP, 3,L3+1,L4,LY1,LY2,1,1)
C left roof
      CALL ZEROGRAD(NZP,NXP,NYP,TRP, 3,L2,L3,LY1,LY2,IH,IH)
C right roof
      CALL ZEROGRAD(NZP,NXP,NYP,TRP, 3,L4+1,L5,LY1,LY2,IH,IH)
C left wall
      CALL ZEROGRAD(NZP,NXP,NYP,TRP, 1,L3,L3,LY1,LY2,1,IH)
C right wall
      CALL ZEROGRAD(NZP,NXP,NYP,TRP,-1,L4,L4,LY1,LY2,1,IH)
C
C-------------------------------------
C 1 canyon
C left road
C      CALL ZEROGRAD(NZP,NXP,NYP,TRP, 3,L3+1,L4,LY1,LY2,1,1)
C left roof
C      CALL ZEROGRAD(NZP,NXP,NYP,TRP, 3,L2,L3,LY1,LY2,IH,IH)
C middle roof
C      CALL ZEROGRAD(NZP,NXP,NYP,TRP, 3,L4+1,L13,LY1,LY2,IH,IH)
C right roof
C      CALL ZEROGRAD(NZP,NXP,NYP,TRP, 3,L14+1,L15,LY1,LY2,IH,IH)
C 1st left wall
C      CALL ZEROGRAD(NZP,NXP,NYP,TRP, 1,L3,L3,LY1,LY2,1,IH)
C 1st right wall
C      CALL ZEROGRAD(NZP,NXP,NYP,TRP,-1,L4,L4,LY1,LY2,1,IH)
C 2nd left wall
C      CALL ZEROGRAD(NZP,NXP,NYP,TRP, 1,L13,L13,LY1,LY2,1,IH)
C 2nd right wall
```

```
C      CALL ZEROGRAD(NZP,NXP,NYP,TRP,-1,L14,L14,LY1,LY2,1,IH)

      RETURN
      END
C=================================================
      SUBROUTINE ZEROGRAD(NZP,NXP,NYP,VAR,IAXIS,I1,I2,J1,J2,K1,K2)
C-------------------------------------------------
C This programme sets the value of a variable as CNST on the walls
C IAXIS=1: for a surface normal to x-axis
C IAXIS=2: for a surface normal to y-axis
C IAXIS=3: for a surface normal to z-axis
C *** set zero gradient for temperature on the street
C     CALL ZEROGRAD(NZP,NXP,NYP,A(ITHP),+3,L3+1,L4,LY1,LY2,1,1)
C *** set zero gradient for temperature at the left wall
C     CALL ZEROGRAD(NZP,NXP,NYP,A(ITRCE3),+1,L3,L3,LY1,LY2,1,IH)
C *** set tracer concentraion on the right wall (2 layers)
C     CALL ZEROGRAD(NZP,NXP,NYP,A(ITRCE3),-1,L4,L4,LY1,LY2,1,IH)
C *** set tracer concentraion on the right ROOF (2 layers)
C     CALL ZEROGRAD(NZP,NXP,NYP,A(ITRCE2),+3,L4+1,L5,LY1,LY2,IH,IH)
C-------------------------------------------------
      DIMENSION VAR(NZP,NXP,NYP)

C      ISGNSF=SIGN(1,IAXIS)
C      INCP=(1+ISGNSF)/2         ! +IAXIS: 1;  -IAXIS: 0
C      INCN=(1-ISGNSF)/2         ! +IAXIS: 0;  -IAXIS: 1
C               VAR(K,I1+INCN,J)=VAR(K,I1+INCP,J)

      IF(IAXIS.EQ.1)THEN
         DO(J=J1,J2)
            DO(K=K1,K2)
               VAR(K,I1,J)=VAR(K,I1+1,J)
            ENDDO
         ENDDO
      ELSEIF(IAXIS.EQ.-1)THEN
         DO(J=J1,J2)
            DO(K=K1,K2)
               VAR(K,I1+1,J)=VAR(K,I1,J)
            ENDDO
         ENDDO
      ELSEIF(IAXIS.EQ.2)THEN
         DO(I=I1,I2)
            DO(K=K1,K2)
               VAR(K,I,J1)=VAR(K,I,J1+1)
            ENDDO
         ENDDO
      ELSEIF(IAXIS.EQ.-2)THEN
         DO(I=I1,I2)
            DO(K=K1,K2)
               VAR(K,I,J1+1)=VAR(K,I,J1)
            ENDDO
         ENDDO
      ELSEIF(IAXIS.EQ.3)THEN
         DO(I=I1,I2)
            DO(J=J1,J2)
               VAR(K1,I,J)=VAR(K1+1,I,J)
            ENDDO
         ENDDO
      ELSEIF(IAXIS.EQ.-3)THEN
         DO(I=I1,I2)
            DO(J=J1,J2)
               VAR(K1+1,I,J)=VAR(K1,I,J)
            ENDDO
         ENDDO
      ENDIF
      RETURN
      END
C=================================================
      SUBROUTINE WALLTH(NZP,NXP,NYP,TRP)
C-------------------------------------------------
C This programme sets the wall temperature values at 293K
C-------------------------------------------------
      include 'canyon.h'
      DIMENSION TRP(NZP,NXP,NYP)
C      DATA ITSTEP/1/
      DATA TMEAN/293./
C calculate mean air temperature in canyon
C      IF(ITSTEP.EQ.1)THEN
C         TMEAN=0.
C         DO(K=1,IH)
C            DO(I=L3+1,L4)
C               DO(J=Ly1,Ly2)
C                  TMEAN=TMEAN+TRP(K,I,NYP/2)
C               ENDDO
C            ENDDO
C         ENDDO
C         TMEAN=TMEAN/(IH*(L4-L3)*Ly2)
C         ITSTEP=ITSTEP+1
C      ENDIF
C one-canyon
```

```
C road
      CALL CNSTWALL(NZP,NXP,NYP,TRP,TMEAN+DTROAD,L3+1,L4,LY1,LY2,1,1)
C left roof
      CALL CNSTWALL(NZP,NXP,NYP,TRP,TMEAN+DTLROOF,L2,L3,LY1,LY2,IH-1,IH)
C right roof
      CALL CNSTWALL(NZP,NXP,NYP,TRP,TMEAN+DTRROOF
     +     ,L4+1,L5,LY1,LY2,IH-1,IH)
C left wall
      CALL CNSTWALL(NZP,NXP,NYP,TRP,TMEAN+DTLWALL
     +     ,L3-1,L3,LY1,LY2,1,IH)
C right wall
      CALL CNSTWALL(NZP,NXP,NYP,TRP,TMEAN+DTRWALL
     +     ,L4+1,L4+2,LY1,LY2,1,IH)
C----------
C 2 canyons
C left building
C      CALL CNSTWALL(NZP,NXP,NYP,TRP,TMEAN+DTLWALL
C     +     ,L2,L3,LY1,LY2,1,IH)
C middle building
C      CALL CNSTWALL(NZP,NXP,NYP,TRP,TMEAN+DTRWALL
C     +     ,L4+1,L13,LY1,LY2,1,IH)
C right building
C      CALL CNSTWALL(NZP,NXP,NYP,TRP,TMEAN+DTRWALL
C     +     ,L14+1,L15,LY1,LY2,1,IH)
      RETURN
      END
C=======================================
      SUBROUTINE RDBTNDC(N1,N2,N3,UP,UC,VP,VC,BBP,BBC)
      DIMENSION UP(N1,N2,N3),UC(N1,N2,N3),BBC(N1,N2,N3)
     +         ,VP(N1,N2,N3),VC(N1,N2,N3),BBP(N1,N2,N3)
.IN   STORAGE
      SAVE
      DATA NCALL/0/
      data ibndc,jbndc/3,4/
C
C     This routine ultimately updates tendencies at lateral boundaries
C     after first diagnosing appropriate phase speeds.
C
C     IBND and JBND are flags for the radiative type in the X and Y
C     direction. Their meaning is:
C
C        IBND=1......Klemp-Wilhelmson (1978) type; phase speed given
C                    by CPHAS
C        IBND=2......Klemp-Lilly (1980) type; doppler shifted phase
C                    speed constant with height and diagnosed from
C                    average of Orlanski speeds, i.e. function of
C                    only (X,Y)
C        IBND=3......Orlanski(1974) type; Phase speeds diagnosed
C                    from local conditions and function of (x,y,z)
C
C     The first order of business is to calculate the diagnostic phase
C     speed. The Orlanski(1976) leapfrog method is to use three time
C     levels of information, namely the T-2, T-1, and T level to
C     evaluate the phase speed given by - du/dt / du/dx = u + C.
C     If this is to be an Orlanski or Klemp-Lilly type boundary in the x
C     direction then this following diagnostic procedure is necessary.
C
C     If this is the first call to a routine, initialize the phase
C       speed arrays if necessary.
C
C      cphas=1.3
      IF ((INITIAL.EQ.2).AND.(IBCFLG.EQ.0)) RETURN
      IF(NCALL.EQ.0)THEN
        NCALL=1
        IF(ITMDIFF.EQ.1)THEN
          DTLBC=DTL
          DTLBCI=DTLI
        ELSE
          DTLBC=DTL2
          DTLBCI=DTL2I
        ENDIF
        IF(JDIM.EQ.1.AND.JBNDC.NE.1) THEN
          DO(I=1,NXP)
            DO(K=1,NZP)
              CPHY(K,I,1)=VP(K,I,N2YM)
              CPHY(K,I,2)=VP(K,I,NY1M)
              CPHY(K,I,3)=VP(K,I,N3YM)
              CPHY(K,I,4)=VP(K,I,NY2M)
            ENDDO
          ENDDO
        ENDIF
        IF(IDIM.EQ.1.AND.IBNDC.NE.1) THEN
          DO(J=1,NYP)
            DO(K=1,NZP)
              CPHX(K,J,1)=UP(K,N2XM,J)
              CPHX(K,J,2)=UP(K,NX1M,J)
              CPHX(K,J,3)=UP(K,N3XM,J)
              CPHX(K,J,4)=UP(K,NX2M,J)
            ENDDO
```

```
          ENDDO
        ENDIF
      ENDIF
C
C     First compute "X" boundaries.
C
      IF(IDIM.EQ.1) THEN
        IBD=IBNDC/3
        FBD=1./FLOAT(IBD+1)
C
        DO(J=N2Y,NY)
C
C         East and west boundaries
C
          IF(IBNDC.GT.1)THEN
C
            IF(ITMDIFF.EQ.2) THEN
              DO(K=2,NZ)
                VCTR2(K)=(UP(K,N3XM,J)-.5*(UC(K,N2XM,J)+CPHX(K,J,1)))
     +            *FBD
                VCTR12(K)=-(UP(K,NX2M,J)-.5*(UC(K,NX1M,J)+CPHX(K,J,2)))
     +            *FBD
              ENDDO
            ELSEIF(ITMDIFF.EQ.1) THEN
              DO(K=2,NZ)
                VCTR2(K)=(CPHX(K,J,3)-CPHX(K,J,1))
                VCTR12(K)=(CPHX(K,J,2)-CPHX(K,J,4))
              ENDDO
            ENDIF
            DO(K=2,NZ)
              VCTR1(K)=MIN(0.,MAX(-1.,-(UC(K,N2XM,J)-CPHX(K,J,1))
     *          /(VCTR2(K)+1.E-30)))
              VCTR11(K)=MAX(0.,MIN(1.,-(UC(K,NX1M,J)-CPHX(K,J,2))
     *          /(VCTR12(K)+1.E-30)))
            ENDDO
C
            IF(IBNDC.EQ.2) THEN
              DO(K=2,NZ)
                VCTR3(K)=ABS(VCTR2(K))/DZZM(K)
                CPHX(K,J,1)=VCTR1(K)*VCTR3(K)
                VCTR13(K)=ABS(VCTR12(K))/DZZM(K)
                CPHX(K,J,2)=VCTR11(K)*VCTR13(K)
              ENDDO
              CPHX(1,J,1)=.8*CPHX(1,J,1)+.2*SSUM(NZ1,CPHX(2,J,1),1)
     *          /((SSUM(NZ1,VCTR3(2),1)+1.E-30)*DXXM(N3XM)*DTLBC)
              CPHX(1,J,2)=.8*CPHX(1,J,2)+.2*SSUM(NZ1,CPHX(2,J,2),1)
     *          /((SSUM(NZ1,VCTR13(2),1)+1.E-30)*DXXM(NX1M)*DTLBC)
            ELSE
              DO(K=2,NZ)
                CPHX(K,J,1)=VCTR1(K)
                CPHX(K,J,2)=VCTR11(K)
              ENDDO
            ENDIF
          ENDIF
C
          IF(IBNDC.EQ.1) THEN
            DO(K=2,NZ)
              BBP(K,N1XM,J)=BBP(K,N1XM,J)
     *      -MIN(0.,MAX(-1.,(UC(K,N1XM,J)-CPHAS)
C modified on 020704: multiply DTLONG for time advancing (the original code was for FU, which
does
C  not need this DTLONG until the final advancing, but here the time advancing is for tracer
C)
C     *      *DTLBC*DXXM(N2XM)))*(BBP(K,N2XM,J)-BBP(K,N1XM,J))*DTLBCI
C     *      *DTLBC*DXXM(N2XM)))*(BBP(K,N2XM,J)-BBP(K,N1XM,J))*DTLBCI*DTL
     *   *DTLBC*DXXM(N2XM)))*(BBP(K,N2XM,J)-BBP(K,N1XM,J))*DXXM(NXM)*DTL
              BBP(K,NXM,J)=BBP(K,NXM,J)
     *      -MAX(0.,MIN(1.,(UC(K,NXM,J)+CPHAS)
C     *      *DTLBC*DXXM(NXM)))*(BBP(K,NXM,J)-BBP(K,NX1M,J))*DTLBCI
C     *      *DTLBC*DXXM(NXM)))*(BBP(K,NXM,J)-BBP(K,NX1M,J))*DTLBCI*DTL
     *    *DTLBC*DXXM(NXM)))*(BBP(K,NXM,J)-BBP(K,NX1M,J))*DXXM(NXM)*DTL
            ENDDO
C
C         Second case: Klemp-Lilly type:
C
          ELSEIF(IBNDC.EQ.2) THEN
            DO(K=2,NZ)
              BBP(K,N1XM,J)=BBP(K,N1XM,J)-CPHX(1,J,1)*(BBP(K,N2XM,J)
C     *          -BBP(K,N1XM,J))*DXXM(N2XM)
     *          -BBP(K,N1XM,J))*DXXM(N2XM)*DTL
              BBP(K,NXM,J)=BBP(K,NXM,J)-CPHX(1,J,2)*(BBP(K,NXM,J)
C     *          -BBP(K,NX1M,J))*DXXM(NXM)
     *          -BBP(K,NX1M,J))*DXXM(NXM)*DTL
            ENDDO
C
C         Third case: Orlanski type:
C
          ELSEIF(IBNDC.EQ.3) THEN
            IF(ITMDIFF.EQ.2) THEN
```

```
              DO(K=2,NZ)
C               BBP(K,N1XM,J)=BBP(K,N1XM,J)-2.*CPHX(K,J,1)
C               BBP(K,N1XM,J)=BBP(K,N1XM,J)-2.*CPHX(K,J,1)*DTL
C     *          /(1.-CPHX(K,J,1))*(BBC(K,N2XM,J)-BBP(K,N1XM,J))*DTLBCI
                BBC(K,N1XM,J)=BBC(K,N1XM,J)-UP(K,N1XM,J)
      *         *(BBP(K,N2XM,J)-BBP(K,N1XM,J))*DXXM(N2XM)*DTL
                BBP(K,N1XM,J)=BBC(K,N1XM,J)
C                BBP(K,NXM,J)=BBP(K,NXM,J)-2.*CPHX(K,J,2)
C                BBP(K,NXM,J)=BBP(K,NXM,J)-2.*CPHX(K,J,2)*DTL
C     *          /(1.+CPHX(K,J,2))*(BBP(K,NXM,J)-BBC(K,NX1M,J))*DTLBCI
                BBC(K,NXM,J)=BBC(K,NXM,J)-UP(K,NXM,J)
      *         *(BBP(K,NXM,J)-BBP(K,NX1M,J))*DXXM(NXM)*DTL
                BBP(K,NXM,J)=BBC(K,NXM,J)
              ENDDO
            ELSEIF(ITMDIFF.EQ.1) THEN
              DO(K=2,NZ)
C               BBP(K,N1XM,J)=BBP(K,N1XM,J)-CPHX(K,J,1)
                BBP(K,N1XM,J)=BBP(K,N1XM,J)-CPHX(K,J,1)*DTL
      *           *(BBP(K,N2XM,J)-BBP(K,N1XM,J))*DTLBCI
C                BBP(K,NXM,J)=BBP(K,NXM,J)-CPHX(K,J,2)
                BBP(K,NXM,J)=BBP(K,NXM,J)-CPHX(K,J,2)*DTL
      *           *(BBP(K,NXM,J)-BBP(K,NX1M,J))*DTLBCI
              ENDDO
            ENDIF
          ENDIF
C
        ENDDO
       ENDIF
C
C       Print some phase speeds if interested here.
C
C      IF(MOD(ISTP,10).EQ.0.AND.IBNDC.EQ.2) THEN
C        PRINT 123,(J,CPHX(1,J,1),CPHX(1,J,2),J=N2Y,NY)
C123     FORMAT(' JD=',I5,' X PHASE SPEEDS AT (M/S)',-2P2F10.5)
C      ENDIF
C
C     If this is to be a Orlanski or Klemp-Lilly type boundary in the y
C     direction then this following diagnostic procedure is necessary.
C
C     South and north boundaries.
C
      IF(JBNDC.EQ.4)GOTO 777
      IF(JDIM.EQ.1) THEN
        JBD=JBNDC/3
        FBD=1./FLOAT(JBD+1)
        DO(I=N2X,NX)
C
          IF(JBNDC.GT.1) THEN
            IF(ITMDIFF.EQ.2) THEN
              DO(K=2,NZ)
                VCTR2(K)=(VP(K,I,N3YM)-.5*(VC(K,I,N2YM)+CPHY(K,I,1)))
     +            *FBD
                VCTR12(K)=-(VP(K,I,NY2M)-.5*(VC(K,I,NY1M)+CPHY(K,I,2)))
     +            *FBD
              ENDDO
            ELSEIF(ITMDIFF.EQ.1) THEN
              DO(K=2,NZ)
                VCTR2(K)=(CPHY(K,I,3)-CPHY(K,I,1))
                VCTR12(K)=(CPHY(K,I,2)-CPHY(K,I,4))
              ENDDO
            ENDIF
            DO(K=2,NZ)
              VCTR1(K)=MIN(0.,MAX(-1.,-(VC(K,I,N2YM)-CPHY(K,I,1))
      *         /(VCTR2(K)+1.E-30)))
              VCTR11(K)=MAX(0.,MIN(1.,-(VC(K,I,NY1M)-CPHY(K,I,2))
      *         /(VCTR12(K)+1.E-30)))
            ENDDO
            IF(JBNDC.EQ.2) THEN
              DO(K=2,NZ)
                VCTR3(K)=ABS(VCTR2(K))/DZZM(K)
                CPHY(K,I,1)=VCTR1(K)*VCTR3(K)
                VCTR13(K)=ABS(VCTR12(K))/DZZM(K)
                CPHY(K,I,2)=VCTR11(K)*VCTR13(K)
              ENDDO
              CPHY(1,I,2)=.8*CPHY(1,I,2)+.2*SSUM(NZ1,CPHY(2,I,2),1)
      *         /((SSUM(NZ1,VCTR13(2),1)+1.E-30)*DYYM(NY1M)*DTLBC)
              CPHY(1,I,1)=.8*CPHY(1,I,1)+.2*SSUM(NZ1,CPHY(2,I,1),1)
      *         /((SSUM(NZ1,VCTR3(2),1)+1.E-30)*DYYM(N3YM)*DTLBC)
            ELSE
              DO(K=2,NZ)
                CPHY(K,I,1)=VCTR1(K)
                CPHY(K,I,2)=VCTR11(K)
              ENDDO
            ENDIF
          ENDIF
C
C          IF(MOD(ISTP,10).EQ.0.AND.JBNDC.EQ.2) THEN
C            PRINT 124,(II,CPHY(1,II,1),CPHY(1,II,2),II=N2X,NX)
C124         FORMAT(' I=',I5,'Y PHASE SPEEDS (M/S)',-2P2F10.5)
```

```
C          ENDIF
C
C         First case: Klemp-Wilhelmson type
C
          IF(JBNDC.EQ.1) THEN
            DO(K=2,NZ)
               BBP(K,I,N1YM)= BBP(K,I,N1YM)
     *        -MIN(0.,MAX(-1.,(VC(K,I,N1YM)-CPHAS)
     *        *DTLBC*DYYM(N2YM)))*(BBP(K,I,N2YM)-BBP(K,I,N1YM))*DTLBCI
               BBP(K,I,NYM)= BBP(K,I,NYM)
     *           -MAX(0.,MIN(1.,(VC(K,I,NYM)+CPHAS)
     *        *DTLBC*DYYM(NYM)))*(BBP(K,I,NYM)-BBP(K,I,NY1M))*DTLBCI
            ENDDO
C
C         Second case: Klemp-Lilly type:
C
          ELSEIF(JBNDC.EQ.2) THEN
            DO(K=2,NZ)
               BBP(K,I,N1YM)= BBP(K,I,N1YM)-CPHY(1,I,1)*(BBP(K,I,N2YM)
     *           -BBP(K,I,N1YM))*DYYM(N2YM)
               BBP(K,I,NYM)= BBP(K,I,NYM)-CPHY(1,I,2)*(BBP(K,I,NYM)
     *           -BBP(K,I,NY1M))*DYYM(NYM)
            ENDDO
C
C         Third case: Orlanski type:
C
          ELSEIF(JBNDC.EQ.3) THEN
            IF(ITMDIFF.EQ.2) THEN
              DO(K=2,NZ)
                 BBP(K,I,N1YM)= BBP(K,I,N1YM)-2.*CPHY(K,I,1)
     *          /(1.-CPHY(K,I,1))*(BBC(K,I,N2YM)-BBP(K,I,N1YM))*DTLBCI
                 BBP(K,I,NYM)= BBP(K,I,NYM)-2.*CPHY(K,I,2)
     *          /(1.+CPHY(K,I,2))*(BBP(K,I,NYM)-BBC(K,I,NY1M))*DTLBCI
              ENDDO
            ELSEIF(ITMDIFF.EQ.1) THEN
              DO(K=2,NZ)
                 BBP(K,I,N1YM)= BBP(K,I,N1YM)-CPHY(K,I,1)
     *             *(BBC(K,I,N2YM)-BBP(K,I,N1YM))*DTLBCI
                 BBP(K,I,NYM)= BBP(K,I,NYM)-CPHY(K,I,2)
     *             *(BBP(K,I,NYM)-BBC(K,I,NY1M))*DTLBCI
              ENDDO
            ENDIF
          ENDIF
C
        ENDDO
      ENDIF
C
C     Now  save past arrays in CPH arrays for use on next time step
C     evaluating the phase speed. Next step this will be the T-2 time
C     level.
C
C     First set the "X" boundary velocities
C
 777  CONTINUE
      IF((IBNDC.EQ.2.OR.IBNDC.EQ.3).AND.IDIM.EQ.1) THEN
        DO(J=N2Y,NY)
          DO(K=2,NZ)
            CPHX(K,J,1)=UP(K,N2XM,J)
            CPHX(K,J,2)=UP(K,NX1M,J)
            CPHX(K,J,3)=UP(K,N3XM,J)
            CPHX(K,J,4)=UP(K,NX2M,J)
          ENDDO
        ENDDO
      ENDIF
C
C     Now set the "Y" boundary velocities.
C
      IF((JBNDC.EQ.2.OR.JBNDC.EQ.3).AND.JDIM.EQ.1) THEN
        DO(I=N2X,NX)
          DO(K=2,NZ)
            CPHY(K,I,1)=VP(K,I,N2YM)
            CPHY(K,I,2)=VP(K,I,NY1M)
            CPHY(K,I,3)=VP(K,I,N3YM)
            CPHY(K,I,4)=VP(K,I,NY2M)
          ENDDO
        ENDDO
      ENDIF
C
      RETURN
      END
C
C     ****************************************************************
C
      SUBROUTINE WALLSTAR(ISFCL,ISTARS,UAIR,VAIR,ZABOVE
     +     ,TWALL,TAIR,DTH,WTH0,USOLD,TSOLD,USTAR,TSTAR
     +     ,RWALL,RAIR,DRT,WRT0,RSOLD,RSTAR,CHU,CQU)
C      DATA ISFCL/1/              ! ISFCL=-1: wth0=constant           => using Businger's
scheme
C                                 ! ISFCL= 0: DTH=TAIR-TWALL=contant  => not impleted yet on
```

```
20061927
C                               ! ISFCL= 1: DTH=TAIR-TWALL=variable => Businger or Louis
C      DATA ISTARS/1/           ! 1: Businger's scheme; 2: Louis' scheme
C   +---------------------------------------------------------------+
C   \    This routine computes USTAR, TSTAR, and RSTAR based on the   \
C   \    iterative scheme using Businger profile functions or the     \
C   \    Louis(1979) analytic functions.                              \
C   +---------------------------------------------------------------+
C **** ISFCL=-1: wth0=constant          => using Businger's scheme
C input : UAIR,VAIR,ZABOVE,TAIR,WTH0,USOLD,TSOLD,RWALL,RAIR,WRT0,RSOLD
C output: USTAR,TSTAR,DTH,TWALL,RSTAR,RWALL
C **** ISFCL= 1: DTH=TAIR-TWALL=variable
C ++++ ISTARS= 1: DTH=TAIR-TWALL=variable => Businger
C input : UAIR,VAIR,ZABOVE,TAIR,TWALL,RWALL,RAIR,USOLD,TSOLD,RSOLD
C output: USTAR,TSTAR,RSTAR,WTH0,WRT0
C ++++ ISTARS= 2: DTH=TAIR-TWALL=variable => Louis
C input : UAIR,VAIR,ZABOVE,TAIR,TWALL,RWALL,RAIR
C output: USTAR,TSTAR,RSTAR,WTH0,WRT0,CHU,CQU
C         the output of CHU will suffice calculation of scalar flux: F_C=CHU*deltaC
C         deltaC = C_air - C_wall
      include 'canyon.h'
      DATA BO/9.4/,CSTMO/7.4/,CSTHO/5.3/
      DATA VONK,G/0.4,9.8/
      data UBMIN,USTMIN,TSMIN,VISCOS/0.01,0.001,0.005,0.000015/         ! min of u*, T*
      DATA USTARINI,THINI/0.01,0.05/
      DATA LEVEL/1/
C
C     COMPUTE THE MEAN WIND SPEED
C
      UBAR2=UAIR**2+VAIR**2
      UBAR=SQRT(UBAR2)
      IF (UBAR.LT.UBMIN)THEN
        UBAR=UBMIN
        UBAR2=UBAR**2
      ENDIF
      IF(USOLD.LT.UBMIN)USOLD=0.01
      IF(TSOLD.LT.TSMIN)TSOLD=0.05
      BZ=ZABOVE
c the case of specifying TFZ through ISFCL=-1
      IF(ISFCL.EQ.-1) THEN
C +++++++++++++++++++++++++++++++++++++++++++++++
C      ISFCL=-1: wth0=constant
C +++++++++++++++++++++++++++++++++++++++++++++++
C
C     The Businger iterative solution technique with wth0, wq0 from input data
C
C     START ITERATION
C
         DO 210 NNTER=1,50
C
C                            If TSTAR is near zero, Monin-obukhov length
C                            is large, so set   Z/L   to zero.
C                            Otherwise compute  Z/L  .
            IF(ABS(TSOLD).LT.1E-30)THEN
               ZL=0.
            ELSE
               THTM=(TAIR+TWALL)*.5
               ZL=BZ*VONK*G*TSOLD/(THTM*USOLD*USOLD)
               ZL=MIN( .5,ZL)
               ZL=MAX(  -25.,ZL)
            ENDIF
C
C                            Compute profile functions for stable or
C                            unstable cases.
            IF(ZL.GE.0.)THEN
               PSY1=-4.7*ZL
            ELSEIF(ZL.LT.0.)THEN
               PHIM=(1.-15.*ZL)**(.25)
               PSY1=2.*LOG((1.+PHIM)*.5)
     +              +LOG((1.+PHIM*PHIM)*.5)-2.*ATAN(PHIM)+1.57
            ENDIF
C
C    Finally, compute USTAR and
C    check iteration for convergence.  Note
C    these computations include the conversion
C    of ground theta to theta at Zo.
            C1=LOG(BZ/RL)
            USTAR=VONK*UBAR/(C1-PSY1)
            USTAR=MAX(USTMIN,USTAR)
            IF(ABS(USOLD-USTAR).LT.0.001)
     +           GO TO 212
            IF(NNTER.GT.10)THEN
               WTFCT=.3
               USOLD=USOLD+WTFCT*(USTAR-USOLD)
            ELSE
               USOLD=USTAR
            ENDIF
 210     CONTINUE
C     modified on 910816: when STOP 210, output some data
```

```
         PRINT*,'UBAR=',UBAR,'  Z(2)=',BZ,'  TH(2)=',THTM
         PRINT*,'U*  =',USTAR,'  T* =',TSTAR
         STOP ' STARS  STOP 210'
 212     CONTINUE
C     modified on 960205: WTH should be assigned by TFZ(i,j)
         TSTAR=-WTH0/USTAR
         RSTAR=-WRT0/USTAR
C     TSTAR=-TWFLUX/USTAR
C     RSTAR=-QWFLUX/USTAR
         IF(ZL.GE.0.)THEN
            PSY2=-6.35*ZL
         ELSEIF(ZL.LT.0.)THEN
            PHIH=SQRT(1.-9.*ZL)
            PSY2=2.*LOG((1.+PHIH)*.5)
         ENDIF
         C2=.74*(C1-PSY2)
         C3=.0962*(USTAR*RL/VISCOS)**.45
         DTH=TSTAR/VONK*(C2+C3)
         DRT=RSTAR/VONK*(C2+C3)
         TWALL=TAIR-DTH
         RWALL=RAIR-DRT
      ENDIF
C +++++++++++++++++++++++++++++++++++++++++++++++++++
C ===  ISFCL=1: DTH=TAIR-TWALL=variable => Businger or Louis
C +++++++++++++++++++++++++++++++++++++++++++++++++++
C     the case of specifying wall temperature
      IF(ISFCL.EQ.1) THEN
         DTH=TAIR-TWALL
         DRT=RAIR-RWALL
C
C     Chose the actual computation scheme to compute the surface layer
C       parameters.
C
c if Louis scheme is requested
         IF(ISTARS.EQ.2) THEN
C ----------------------------------------
C      ISTARS=2: Louis scheme
c ----------------------------------------
C
C     This is the computation technique of Louis (1979) which
C       replaces the iterative equations with analytic functions.
C
C     Compute the Richardson number and the empirical functions F for
C     the stable (DTH.GT.0) and the unstable (DTH.LT.0) cases
C
            THT2 = TAIR
            BZ = (G/THT2)*ZABOVE
            ZOZ=ZABOVE/RL
            ZL=1./LOG(ZOZ)
C modified on 20061226: add z0_T and z0_q
            ZOTZ=ZABOVE/RLT
            ZLT=1./LOG(ZOTZ)
            ZOQZ=ZABOVE/RLQ
            ZLQ=1./LOG(ZOQZ)
C
            AO2=VONK*VONK*ZL*ZL
            AOM=VONK*ZL
            AOT=VONK*ZLT
            AOQ=VONK*ZLQ
            RI=BZ*DTH/UBAR2
            IF (DTH.LT.0.0)THEN
               CM=CSTMO*AO2*BO*SQRT(ZOZ)
               CH=CSTHO*AO2*BO*SQRT(ZOZ)
               FM = 1. - BO*RI/(1.+CM*SQRT(-RI))
               FH = 1. - BO*RI/(1.+CH*SQRT(-RI))
            ELSE
               CM=1.+.5*BO*RI
               FM=1./(CM*CM)
               FH=FM
            ENDIF
C
C     Compute USTAR**2 and USTAR*TSTAR, then get USTAR, TSTAR, RSTAR
C
            USTR2=AO2*UBAR2*FM
            WTH0=-1.35*AOM*AOT*UBAR*DTH*FH
            WRT0=-1.35*AOM*AOQ*UBAR*DRT*FH
C
            USTAR=SQRT(USTR2)
            USTAR=MAX(USTMIN,USTAR)
            TSTAR=-WTH0/USTAR
            RSTAR=-WRT0/USTAR
C
            CHU=1.35*AOM*AOT*UBAR*FH ! the output will suffice calculation of scalar flux:
F_C=-CHU*deltaC
            CQU=1.35*AOM*AOQ*UBAR*FH ! the output will suffice calculation of scalar flux:
F_C=-CHU*deltaC
                                ! deltaC = C_air - C_wall & CHU > 0
         ENDIF                  ! end of IF(ISTARS.EQ.2) THEN
```

```
C
        IF(ISTARS.EQ.1) THEN
C ----------------------------------------
C      ISTARS=2: The Businger iterative solution technique has been chosen.
c ----------------------------------------
C
C     START ITERATION
C      USOLD=UBAR*0.05
C      TSOLD=DTH*0.05
           DO 10 NNTER=1,50
C
C     If TSTAR is near zero, Monin-obukhov length
C     is large, so set   Z/L   to zero.
C     Otherwise compute  Z/L  .
              IF(ABS(TSOLD).LT.1E-30)THEN
                 ZL=0.
              ELSE
                 THTM=(TAIR+TWALL)*.5
                 ZL=BZ*VONK*G*TSOLD/(THTM*USOLD*USOLD)
                 ZL=MIN( .5,ZL)
                 ZL=MAX(  -25.,ZL)
              ENDIF
C
C     Compute profile functions for stable or
C     unstable cases.
              IF(ZL.GE.0.)THEN
                 PSY1=-4.7*ZL
                 PSY2=-6.35*ZL
              ELSEIF(ZL.LT.0.)THEN
                 PHIM=(1.-15.*ZL)**(.25)
                 PHIH=SQRT(1.-9.*ZL)
                 PSY1=2.*LOG((1.+PHIM)*.5)
     +               +LOG((1.+PHIM*PHIM)*.5)-2.*ATAN(PHIM)+1.57
                 PSY2=2.*LOG((1.+PHIH)*.5)
              ENDIF
C
C     Finally, compute USTAR,TSTAR,RSTAR and
C     check iteration for convergence.  Note
C     these computations include the conversion
C     of ground theta to theta at Zo.
              C1=LOG(BZ/RL)
              USTAR=VONK*UBAR/(C1-PSY1)
              USTAR=MAX(USTMIN,USTAR)
              C2=.74*(C1-PSY2)
              C3=.0962*(USTAR*RL/VISCOS)**.45
              TSTAR=VONK*DTH/(C2+C3)
              RSTAR=VONK*DRT/(C2+C3)
              IF(ABS(USOLD-USTAR).LT.0.001.OR.ABS(TSOLD-TSTAR).LT.0.01)
     +           GO TO 12
              IF(NNTER.GT.10)THEN
                 WTFCT=.3
                 USOLD=USOLD+WTFCT*(USTAR-USOLD)
                 TSOLD=TSOLD+WTFCT*(TSTAR-TSOLD)
              ELSE
                 USOLD=USTAR
                 TSOLD=TSTAR
              ENDIF
 10         CONTINUE
C     modified on 910816: when STOP 10, output some data
           PRINT*,'UBAR=',UBAR,'  Z(2)=',BZ,'  TH(2)=',THTM
           PRINT*,'U*  =',USTAR,'  T* =',TSTAR
           STOP ' STARS  STOP 10'
 12         CONTINUE
           WTH0=-TSTAR*USTAR
           WRT0=-RSTAR*USTAR
           CHU=VONK*USTAR/(C2+C3) ! the output will suffice calculation of scalar flux:
F_C=-CHU*deltaC
                                  ! deltaC = C_air - C_wall & CHU > 0
C     PRINT*,'U*=',USTAR,' T*=',TSTAR,' Niter=',NNTER,DTH,TAIR,TWALL
C
        ENDIF                     ! end of IF(ISTARS.EQ.1) THEN
      ENDIF                       ! end of IF(ISFCL.EQ.1) THEN
C
C
      RETURN
      END
C=================================================
      SUBROUTINE PRNWALL(N1,N2,N3,VAR,IPRNTYPE,CHTRP)
      include 'canyon.h'
      CHARACTER*10 CHTRP
      DIMENSION VAR(N1,N2,N3)
C-------------------------------------------------
C This programme prints the values of a variable along the walls
C ***
C
C    |    1       12    13    14       5
C    +----------+              +------------+ <- IH
C               |8             11|
C               |                |
```

```
C              |                 |
C              |7             10|
C              |                 |
C              |                 |
C              |6              9|
C    +         +-----------------+           + <- L1
C                 2     3     4
C
C  if IPRNTYPE=1   --> prints 1-5
C  if IPRNTYPE=2   --> prints 6-11
C
C  if IPRNTYPE=11   --> prints 1-5
C  if IPRNTYPE=12   --> prints 6-11

C for horizontal surfaces
      IF(IPRNTYPE.EQ.11)THEN
         IF(CHTRP(1:6).EQ.'TRCE1 ' .OR. CHTRP(1:6).EQ.'TRCE2 '
     +        .OR. CHTRP(1:6).EQ.'TRCE3 ' .OR. CHTRP(1:6).EQ.'TRCE5 ')
     +       write(*,'(a5,a,3(1pe12.4))')chtrp(1:5),' at (12-14):'
     +       ,VAR(IH,L3+L34/10,LY2/2),VAR(IH,L3+L34/10*5,LY2/2)
     +       ,VAR(IH,L3+L34/10*9,LY2/2)

C         IF(CHTRP(1:6).EQ.'TRCE1 ' .OR. CHTRP(1:5).EQ.'TRCE5'
C     +        .OR. CHTRP(1:5).EQ.'TRCE6' .OR. CHTRP(1:5).EQ.'TRCE8')
C     +       write(*,'(a5,a,3(1pe12.4))')chtrp(1:5),' at (2-4):'
C     +       ,VAR(1,L3+L34/10,LY2/2),VAR(1,L3+L34/10*5,LY2/2)
C     +       ,VAR(1,L3+L34/10*9,LY2/2)
C         IF(CHTRP(1:5).EQ.'TRCE4')
C     +       write(*,'(a5,a,5(1pe12.4))')chtrp(1:5),' at (5):'
C     +       ,VAR(IH,L4+L45/4,LY2/2),VAR(IH,L4+L45/2,LY2/2)
C     +       ,VAR(IH,L4+L45*3/4,LY2/2)
C         IF(CHTRP(1:5).EQ.'TRCE7' .OR. CHTRP(1:5).EQ.'TRCE8')
C     +       write(*,'(a5,a,5(1pe12.4))')chtrp(1:5),' at (1):'
C     +       ,VAR(IH,L2+(L3-L2)/4,LY2/2)
C     +       ,VAR(IH,L2+(L3-L2)/2,LY2/2)
C     +       ,VAR(IH,L2+(L3-L2)*3/4,LY2/2)
      ENDIF

C for vertical surfaces
      IF(IPRNTYPE.EQ.12)THEN
C         IF(CHTRP(1:5).EQ.'TRCE2' .OR. CHTRP(1:5).EQ.'TRCE5')
C     +       write(*,'(a5,a,3(1pe12.4))')chtrp(1:5),' at (6-8):'
C     +       ,VAR(IH/10,L3,LY2/2),VAR(IH/10*5,L3,LY2/2)
C     +       ,VAR(IH/10*9,L3,LY2/2)
C         IF(CHTRP(1:5).EQ.'TRCE3' .OR. CHTRP(1:5).EQ.'TRCE6')
C     +       write(*,'(a5,a,3(1pe12.4))')chtrp(1:5),' at (9-11):'
C     +       ,VAR(IH/10,L4,LY2/2)
C     +       ,VAR(IH/10*5,L4,LY2/2),VAR(IH/10*9,L4,LY2/2)
      ENDIF


      IF(IPRNTYPE.EQ.21)THEN
C         IF(CHTRP(1:6).EQ.'TRCE1 ' .OR. CHTRP(1:5).EQ.'TRCE5'
C     +        .OR. CHTRP(1:5).EQ.'TRCE6' .OR. CHTRP(1:5).EQ.'TRCE8')
C     +       write(*,'(a5,a,3(1pe12.4))')chtrp(1:5),' Can2 at (2-4):'
C     +       ,VAR(1,L13+L34/10,LY2/2),VAR(1,L13+L34/10*5,LY2/2)
C     +       ,VAR(1,L13+L34/10*9,LY2/2)
C         IF(CHTRP(1:5).EQ.'TRCE4')
C     +       write(*,'(a5,a,5(1pe12.4))')chtrp(1:5),' Can2 at (5):'
C     +       ,VAR(IH,L14+L45/4,LY2/2),VAR(IH,L14+L45/2,LY2/2)
C     +       ,VAR(IH,L14+L45*3/4,LY2/2)
C         IF(CHTRP(1:5).EQ.'TRCE7' .OR. CHTRP(1:5).EQ.'TRCE8')
C     +       write(*,'(a5,a,5(1pe12.4))')chtrp(1:5),' Can2 at (1):'
C     +       ,VAR(IH,L12+(L13-L12)/4,LY2/2)
C     +       ,VAR(IH,L12+(L13-L12)/2,LY2/2)
C     +       ,VAR(IH,L12+(L13-L12)*3/4,LY2/2)
      ENDIF

C for vertical surfaces
      IF(IPRNTYPE.EQ.22)THEN
C         IF(CHTRP(1:6).EQ.'TRCE2 ' .OR. CHTRP(1:5).EQ.'TRCE5')
C     +       write(*,'(a5,a,3(1pe12.4))')chtrp(1:5),' Can2 at (6-8):'
C     +       ,VAR(IH/10,L13,LY2/2),VAR(IH/10*5,L13,LY2/2)
C     +       ,VAR(IH/10*9,L13,LY2/2)
C         IF(CHTRP(1:5).EQ.'TRCE3' .OR. CHTRP(1:5).EQ.'TRCE6')
C     +       write(*,'(a5,a,3(1pe12.4))')chtrp(1:5),' Can2 at (9-11):'
C     +       ,VAR(IH/10,L14,LY2/2)
C     +       ,VAR(IH/10*5,L14,LY2/2),VAR(IH/10*9,L14,LY2/2)
      ENDIF

      IF(IPRNTYPE.EQ.1)
     +     write(*,'(a5,a,5(1pe12.4))')chtrp(1:5),' at (1-5):'
     +     ,VAR(IH,L2+(L3-L2)/2,LY2/2)
     +     ,VAR(1,L3+L34/10,LY2/2),VAR(1,L3+L34/10*5,LY2/2)
     +     ,VAR(1,L3+L34/10*9,LY2/2),VAR(IH,L4+L45/2,LY2/2)
      IF(IPRNTYPE.EQ.2)
     +     write(*,'(a5,a,6(1pe12.4))')chtrp(1:5),' at (6-11):'
     +     ,VAR(IH/10,L3,LY2/2),VAR(IH/10*5,L3,LY2/2)
     +     ,VAR(IH/10*9,L3,LY2/2),VAR(IH/10,L4,LY2/2)
```

```
     +     ,VAR(IH/10*5,L4,LY2/2),VAR(IH/10*9,L4,LY2/2)
      RETURN
      END
C================================================
      SUBROUTINE NONEGTVE(N1,N2,N3,VAR)
      DIMENSION VAR(N1,N2,N3)
      DO(K=1,N1)
        DO(I=1,N2)
          DO(J=1,N3)
            IF(VAR(K,I,J).LT.0.0) VAR(K,I,J)=0.
          ENDDO
        ENDDO
      ENDDO
      RETURN
      END
C================================================================================
C List of Chemical variables (Vivien Bright, 2009)
C 1  2  3  4   5   6   7  8  9  10  11   12   13    14   15
C 16 17 18 19 20 21 22 23 24 25
C 26 27 28 29 30 31 32 33 34 35
C 36 37 38 39 40 41 42 43 44
C 45 46 47 48 49 50 51 52 53 54
C O3,NO,NO2,NO3,OH,HO2,H2,CO,H2O2,HONO,HNO3,HO2NO2,
C CH3O2,CH3OH,CH4,C2H4,C3H6,HOCH2CH2O2,CH3CO2H,CH3CHO,C5H8,RU14O2,
C UCARB10,HCHO,CH3CO3,HOCH2CHO,C2H5OH,RN9O2,HCOOH,CARB6,UCARB12,RU12O2,
C CARB7,RU10O2,CH3NO3,HOC2H4NO3,RN9NO3,RU14NO3,CH3OOH,HOC2H4OOH,RN9OOH,
C CH3CO3H,HOCH2CO3H,RU14OOH,RU12OOH,RU10OOH,HOCH2CO3,PAN,PHAN,RU12PAN,MPAN
C--------------------------------------------------------------------------------
      subroutine OHchm (nzp,nxp,nyp,O3,NO,NO2,NO3,OH,
     +  HO2,H2,CO,H2O2,HONO,HNO3,HO2NO2,CH3O2,
     +  CH3OH,CH4,C2H4,C3H6,HOCH2CH2O2,CH3CO2H,
     +  CH3CHO,C5H8,RU14O2,UCARB10,HCHO,CH3CO3,
     +  HOCH2CHO,C2H5OH,RN9O2,HCOOH,CARB6,UCARB12,
     +  RU12O2,CARB7,RU10O2,CH3NO3,HOC2H4NO3,
     +  RN9NO3,RU14NO3,CH3OOH,HOC2H4OOH,RN9OOH,
     +  CH3CO3H,HOCH2CO3H,RU14OOH,RU12OOH,RU10OOH,
     +  HOCH2CO3,PAN,PHAN,RU12PAN,MPAN,theta,dtlong,nshort)
      real O3(nzp,nxp,nyp),NO(nzp,nxp,nyp),
     +  NO2(nzp,nxp,nyp),NO3(nzp,nxp,nyp),
     +  OH(nzp,nxp,nyp),HO2(nzp,nxp,nyp),H2(nzp,nxp,nyp),
     +  CO(nzp,nxp,nyp),H2O2(nzp,nxp,nyp),HONO(nzp,nxp,nyp),
     +  HNO3(nzp,nxp,nyp),HO2NO2(nzp,nxp,nyp),
     +  CH3O2(nzp,nxp,nyp),CH3OH(nzp,nxp,nyp),CH4(nzp,nxp,nyp),
     +  C2H4(nzp,nxp,nyp),C3H6(nzp,nxp,nyp),HOCH2CH2O2(nzp,nxp,nyp),
     +  CH3CO2H(nzp,nxp,nyp),CH3CHO(nzp,nxp,nyp),C5H8(nzp,nxp,nyp),
     +  RU14O2(nzp,nxp,nyp),UCARB10(nzp,nxp,nyp),HCHO(nzp,nxp,nyp),
     +  CH3CO3(nzp,nxp,nyp),HOCH2CHO(nzp,nxp,nyp),C2H5OH(nzp,nxp,nyp),
     +  RN9O2(nzp,nxp,nyp),HCOOH(nzp,nxp,nyp),CARB6(nzp,nxp,nyp),
     +  UCARB12(nzp,nxp,nyp),RU12O2(nzp,nxp,nyp),CARB7(nzp,nxp,nyp),
     +  RU10O2(nzp,nxp,nyp),CH3NO3(nzp,nxp,nyp),HOC2H4NO3(nzp,nxp,nyp),
     +  RN9NO3(nzp,nxp,nyp),RU14NO3(nzp,nxp,nyp),CH3OOH(nzp,nxp,nyp),
     +  HOC2H4OOH(nzp,nxp,nyp),RN9OOH(nzp,nxp,nyp),CH3CO3H(nzp,nxp,nyp),
     +  HOCH2CO3H(nzp,nxp,nyp),RU14OOH(nzp,nxp,nyp),
     +  RU12OOH(nzp,nxp,nyp),RU10OOH(nzp,nxp,nyp),HOCH2CO3(nzp,nxp,nyp),
     +  PAN(nzp,nxp,nyp),PHAN(nzp,nxp,nyp),RU12PAN(nzp,nxp,nyp),
     +  MPAN(nzp,nxp,nyp)
      real theta(nzp,nxp,nyp)
C--------------------------------------------------------------------------------
      DATA PPB2MOLEC/2.50474E+10/ ! conversion rate: 1ppb=2.5x10^10 molecules
      common /JFAC/CJFAC
C     data cjno2/0.009/,CJFAC/1.0/   ! in unit of 1/sec
      data ak1/3.40E-6/,ck2/4.01E-4/,ck3/2.63E-9/,
     +  ck4/6.56E-1/,ck5/1.72E-3/,ck6/1.49E-4/,ck7/5.06E-3/,
     +  ck8/4.21E-2/,ck9/4.86E-5/,ck10/2.82E+0/,ck11/8.74E-2/,
     +  ck12/6.92E-2/,ck13/2.54E-1/,ck14/3.08E-1/,
     +  ck15/5.01E-1/,ck16/2.27E-1/,ck17/3.59E-2/,ck18/3.74E-2/,
     +  ck19/1.20E-1/,ck20/2.58E-2/,ck21/4.08E-3/,
     +  ak22/7.11E-6/,ak23/9.20E-3/,ak24/2.34E-2/,ak25/1.83E-1/,
     +  ak26/2.02E-3/,ak27/6.30E-7/,ck28/1.39E-4/,
     +  ck29/2.00E-1/,ck30/7.19E-1/,ck31/4.46E-9/,ck32/2.99E-8/,
     +  ck33/8.18E-8/,ck34/1.45E-7/,ck35/2.58E+0/,ck36/7.76E-8/,
     +  ck37/2.10E-7/,ak38/3.05E-5/,ak39/4.61E-5/,ak40/5.07E-6/,
     +  ck41/2.35E-1/,ck42/4.02E-1/,ck43/2.31E-2/,ck44/7.24E-2/,
     +  ck45/9.23E-3/,ck46/1.13E-2/,ck47/2.00E-2/,ck48/1.95E-1/,
     +  ck49/1.68E-1/,ck50/4.84E-2/,ck51/2.13E-1/,ck52/5.10E-1/,
     +  ck53/5.10E-1/,ck54/4.93E-2/,ck55/1.46E-1/,ck56/1.52E-1/,
     +  ck57/6.52E-2/,ck58/1.09E-1/,ck59/6.52E-2/,ck60/4.35E-2/,
     +  ck61/1.95E-4/,ck62/1.09E-3/,ck63/4.56E-3/,ck64/2.17E-2/,
     +  ck65/1.52E-1/,ck66/3.62E-1/,ck67/3.20E-1/,ck68/3.75E-1/,
     +  ck69/3.75E-1/,ck70/4.74E-1/,ck71/4.35E-1/,ck72/3.85E-1/,
     +  rk73/6.22E-3/,rk74/6.32E-3/,rk75/6.32E-3/,rk76/1.12E-2/,
     +  rk77/2.20E-2/,rk78/2.50E-1/,rk79/2.50E-1/,rk80/1.08E-2/,
     +  rk81/3.20E-2/,rk82/3.51E-2/,rk83/1.50E-2/,rk84/2.50E-2/,
     +  rk85/1.50E-2/,rk86/1.00E-2/,ak87/3.36E-6/,ak88/1.77E-5/,
     +  ak89/1.62E-5/,ak90/1.26E-4/,ak91/1.62E-5/,ck92/7.51E-2/,
     +  ck93/6.26E-1/,ck94/4.21E-8/,ck95/2.93E-8/,ck96/2.50E-1/,
     +  ck97/4.31E-1/,ck98/1.13E+0/,ck99/5.35E-7/,ck100/6.61E-8/,
     +  ak101/8.96E-7/,ck102/9.33E-3/,ck103/2.73E-2/,ck104/3.28E-2/,
     +  ck105/1.39E+0/,ak106/5.44E-6/,ak107/5.44E-6/,ak108/5.44E-6/,
```

```
     +  ak109/1.37E-6/,ak110/4.07E-6/,ak111/5.44E-6/,ak112/5.44E-6/,
     +  ak113/5.44E-6/,ak114/5.44E-6/,ck115/9.10E-1/,ck116/4.79E-1/,
     +  ck117/9.27E-2/,ck118/1.55E-1/,ck119/1.88E+0/,ck120/7.51E-1/,
     +  ck121/7.51E-1/,ck122/5.34E-1/,ck123/6.26E-1/,ck124/2.68E-1/,
     +  ck125/1.51E-4/,ck126/2.68E-1/,ck127/1.51E-4/,ck128/2.59E-3/,
     +  ck129/2.81E-2/,ck130/1.63E-2/,ck131/1.51E-4/,ck132/1.10E-2/,
     +  ck133/1.51E-4/,ck134/9.02E-2/,ck135/6.31E-1/,
     +  ck136/7.65E-7/
C-------------------------------------------------------------------------------
        DTSHORT=DTLONG/NSHORT
        ck1   = ak1*CJFAC
        ck22  = ak22*CJFAC
        ck23  = ak23*CJFAC
        ck24  = ak24*CJFAC
        ck25  = ak25*CJFAC
        ck26  = ak26*CJFAC
        ck27  = ak27*CJFAC
        ck38  = ak38*CJFAC
        ck39  = ak39*CJFAC
        ck40  = ak40*CJFAC
        ck87  = ak87*CJFAC
        ck88  = ak88*CJFAC
        ck89  = ak89*CJFAC
        ck90  = ak90*CJFAC
        ck91  = ak91*CJFAC
        ck101 = ak101*CJFAC
        ck106 = ak106*CJFAC
        ck107 = ak107*CJFAC
        ck108 = ak108*CJFAC
        ck109 = ak109*CJFAC
        ck110 = ak110*CJFAC
        ck111 = ak111*CJFAC
        ck112 = ak112*CJFAC
        ck113 = ak113*CJFAC
        ck114 = ak114*CJFAC


        do j=1,nyp
           do i =1,nxp
              do k=1,nzp
        ! The peroxy radical summation- this needs to be calculated at each timestep

        RO2 = CH3O2(k,i,j) + HOCH2CH2O2(k,i,j) + RN9O2(k,i,j)
     +  + CH3CO3(k,i,j) + HOCH2CO3(k,i,j) + RU14O2(k,i,j)
     +  + RU12O2(k,i,j) + RU10O2(k,i,j)

        ! RO2 permutation reactions

        ck73  = rk73*RO2
        ck74  = rk74*RO2
        ck75  = rk75*RO2
        ck76  = rk76*RO2
        ck77  = rk77*RO2
        ck78  = rk78*RO2
        ck79  = rk79*RO2
        ck80  = rk80*RO2
        ck81  = rk81*RO2
        ck82  = rk82*RO2
        ck83  = rk83*RO2
        ck84  = rk84*RO2
        ck85  = rk85*RO2
        ck86  = rk86*RO2

                 s1 =ck1 *O3(k,i,j)
                 s2 =ck2 *NO(k,i,j)*O3(k,i,j)
                 s3 =ck3 *NO(k,i,j)*NO(k,i,j)
                 s4 =ck4 *NO(k,i,j)*NO3(k,i,j)
                 s5 =ck5 *OH(k,i,j)*O3(k,i,j)
                 s6 =ck6 *OH(k,i,j)*H2(k,i,j)
                 s7 =ck7 *OH(k,i,j)*CO(k,i,j)
                 s8 =ck8 *OH(k,i,j)*H2O2(k,i,j)
                 s9 =ck9 *HO2(k,i,j)*O3(k,i,j)
                 s10=ck10*OH(k,i,j)*HO2(k,i,j)
                 s11=ck11*HO2(k,i,j)*HO2(k,i,j)
                 s12=ck12*HO2(k,i,j)*HO2(k,i,j)
                 s13=ck13*OH(k,i,j)*NO(k,i,j)
                 s14=ck14*OH(k,i,j)*NO2(k,i,j)
                 s15=ck15*OH(k,i,j)*NO3(k,i,j)
                 s16=ck16*HO2(k,i,j)*NO(k,i,j)
                 s17=ck17*HO2(k,i,j)*NO2(k,i,j)
                 s18=ck18*HO2NO2(k,i,j)
                 s19=ck19*OH(k,i,j)*HO2NO2(k,i,j)
                 s20=ck20*OH(k,i,j)*HONO(k,i,j)
                 s21=ck21*OH(k,i,j)*HNO3(k,i,j)
                 s22=ck22*H2O2(k,i,j)
                 s23=ck23*NO2(k,i,j)
                 s24=ck24*NO3(k,i,j)
                 s25=ck25*NO3(k,i,j)
                 s26=ck26*HONO(k,i,j)
```

```
s27=ck27*HNO3(k,i,j)
s28=ck28*OH(k,i,j)*CH4(k,i,j)
s29=ck29*OH(k,i,j)*C2H4(k,i,j)
s30=ck30*OH(k,i,j)*C3H6(k,i,j)
s31=ck31*O3(k,i,j)*C2H4(k,i,j)
s32=ck32*O3(k,i,j)*C2H4(k,i,j)
s33=ck33*O3(k,i,j)*C3H6(k,i,j)
s34=ck34*O3(k,i,j)*C3H6(k,i,j)
s35=ck35*OH(k,i,j)*C5H8(k,i,j)
s36=ck36*O3(k,i,j)*C5H8(k,i,j)
s37=ck37*O3(k,i,j)*C5H8(k,i,j)
s38=ck38*HCHO(k,i,j)
s39=ck39*HCHO(k,i,j)
s40=ck40*CH3CHO(k,i,j)
s41=ck41*OH(k,i,j)*HCHO(k,i,j)
s42=ck42*OH(k,i,j)*CH3CHO(k,i,j)
s43=ck43*OH(k,i,j)*CH3OH(k,i,j)
s44=ck44*OH(k,i,j)*C2H5OH(k,i,j)
s45=ck45*OH(k,i,j)*C2H5OH(k,i,j)
s46=ck46*HCOOH(k,i,j)*OH(k,i,j)
s47=ck47*CH3CO2H(k,i,j)*OH(k,i,j)
s48=ck48*CH3O2(k,i,j)*NO(k,i,j)
s49=ck49*HOCH2CH2O2(k,i,j)*NO(k,i,j)
s50=ck50*HOCH2CH2O2(k,i,j)*NO(k,i,j)
s51=ck51*RN9O2(k,i,j)*NO(k,i,j)
s52=ck52*CH3CO3(k,i,j)*NO(k,i,j)
s53=ck53*HOCH2CO3(k,i,j)*NO(k,i,j)
s54=ck54*RU14O2(k,i,j)*NO(k,i,j)
s55=ck55*RU14O2(k,i,j)*NO(k,i,j)
s56=ck56*RU12O2(k,i,j)*NO(k,i,j)
s57=ck57*RU12O2(k,i,j)*NO(k,i,j)
s58=ck58*RU10O2(k,i,j)*NO(k,i,j)
s59=ck59*RU10O2(k,i,j)*NO(k,i,j)
s60=ck60*RU10O2(k,i,j)*NO(k,i,j)
s61=ck61*CH3O2(k,i,j)*NO(k,i,j)
s62=ck62*HOCH2CH2O2(k,i,j)*NO(k,i,j)
s63=ck63*RN9O2(k,i,j)*NO(k,i,j)
s64=ck64*RU14O2(k,i,j)*NO(k,i,j)
s65=ck65*CH3O2(k,i,j)*HO2(k,i,j)
s66=ck66*HOCH2CH2O2(k,i,j)*HO2(k,i,j)
s67=ck67*RN9O2(k,i,j)*HO2(k,i,j)
s68=ck68*CH3CO3(k,i,j)*HO2(k,i,j)
s69=ck69*HOCH2CO3(k,i,j)*HO2(k,i,j)
s70=ck70*RU14O2(k,i,j)*HO2(k,i,j)
s71=ck71*RU12O2(k,i,j)*HO2(k,i,j)
s72=ck72*RU10O2(k,i,j)*HO2(k,i,j)
s73=ck73*CH3O2(k,i,j)
s74=ck74*CH3O2(k,i,j)
s75=ck75*CH3O2(k,i,j)
s76=ck76*HOCH2CH2O2(k,i,j)
s77=ck77*RN9O2(k,i,j)
s78=ck78*CH3CO3(k,i,j)
s79=ck79*HOCH2CO3(k,i,j)
s80=ck80*RU14O2(k,i,j)
s81=ck81*RU14O2(k,i,j)
s82=ck82*RU12O2(k,i,j)
s83=ck83*RU12O2(k,i,j)
s84=ck84*RU10O2(k,i,j)
s85=ck85*RU10O2(k,i,j)
s86=ck86*RU10O2(k,i,j)
s87=ck87*CARB7(k,i,j)
s88=ck88*HOCH2CHO(k,i,j)
s89=ck89*UCARB10(k,i,j)
s90=ck90*CARB6(k,i,j)
s91=ck91*UCARB12(k,i,j)
s92=ck92*OH(k,i,j)*CARB7(k,i,j)
s93=ck93*OH(k,i,j)*UCARB10(k,i,j)
s94=ck94*O3(k,i,j)*UCARB10(k,i,j)
s95=ck95*O3(k,i,j)*UCARB10(k,i,j)
s96=ck96*OH(k,i,j)*HOCH2CHO(k,i,j)
s97=ck97*OH(k,i,j)*CARB6(k,i,j)
s98=ck98*OH(k,i,j)*UCARB12(k,i,j)
s99=ck99*O3(k,i,j)*UCARB12(k,i,j)
s100=ck100*O3(k,i,j)*UCARB12(k,i,j)
s101=ck101*CH3NO3(k,i,j)
s102=ck102*OH(k,i,j)*CH3NO3(k,i,j)
s103=ck103*OH(k,i,j)*HOC2H4NO3(k,i,j)
s104=ck104*OH(k,i,j)*RN9NO3(k,i,j)
s105=ck105*OH(k,i,j)*RU14NO3(k,i,j)
s106=ck106*CH3OOH(k,i,j)
s107=ck107*CH3CO3H(k,i,j)
s108=ck108*HOCH2CO3H(k,i,j)
s109=ck109*RU14OOH(k,i,j)
s110=ck110*RU14OOH(k,i,j)
s111=ck111*RU12OOH(k,i,j)
s112=ck112*RU10OOH(k,i,j)
s113=ck113*HOC2H4OOH(k,i,j)
s114=ck114*RN9OOH(k,i,j)
s115=ck115*OH(k,i,j)*CH3OOH(k,i,j)
```

```
                  s116=ck116*OH(k,i,j)*CH3OOH(k,i,j)
                  s117=ck117*OH(k,i,j)*CH3CO3H(k,i,j)
                  s118=ck118*OH(k,i,j)*HOCH2CO3H(k,i,j)
                  s119=ck119*OH(k,i,j)*RU14OOH(k,i,j)
                  s120=ck120*OH(k,i,j)*RU12OOH(k,i,j)
                  s121=ck121*OH(k,i,j)*RU10OOH(k,i,j)
                  s122=ck122*OH(k,i,j)*HOC2H4OOH(k,i,j)
                  s123=ck123*OH(k,i,j)*RN9OOH(k,i,j)
                  s124=ck124*CH3CO3(k,i,j)*NO2(k,i,j)
                  s125=ck125*PAN(k,i,j)
                  s126=ck126*HOCH2CO3(k,i,j)*NO2(k,i,j)
                  s127=ck127*PHAN(k,i,j)
                  s128=ck128*OH(k,i,j)*PAN(k,i,j)
                  s129=ck129*OH(k,i,j)*PHAN(k,i,j)
                  s130=ck130*RU12O2(k,i,j)*NO2(k,i,j)
                  s131=ck131*RU12PAN(k,i,j)
                  s132=ck132*RU10O2(k,i,j)*NO2(k,i,j)
                  s133=ck133*MPAN(k,i,j)
                  s134=ck134*OH(k,i,j)*MPAN(k,i,j)
                  s135=ck135*OH(k,i,j)*RU12PAN(k,i,j)
                  s136=ck136*NO2(k,i,j)*O3(k,i,j)

c --------------------------
c slower reactions
c --------------------------

                  SNO=-S2-2*S3-S4-S13-S16+S23+S24+S26-S48-S49-S50
     +            -S51-S52-S53-S54-S55-S56-S57-S58-S59-S60-S61-S62-S63
     +            -S64
c Changed 24.02.2010
                  SNO2=+S2+2*S3+2*S4-S14+S15+S16-S17+S18-S136
c                 SNO2=+S2+2*S3+2*S4-S14+S15+S16-S17+S18
     +            +S19+S20-S23+S25+S27+S48+S49+S50+S51+S52+S53+S54+S55
     +            +S56+S57+S58+S59+S60+S101+S102+S103+S104+S105-S124+S125
     +            -S126+S127+S128+S129-S130+S131-S132+S133+S134+S135
c Changed 24.02.2010
c                  SNO3=-S4-S15+S21-S24-S25+S136
c                 SNO3=-S4-S15+S21-S24-S25
c Changed 24.02.2010
                  SO3=-S1-S2-S5-S9+S23+S25-S31-S32-S33-S34-S136
c                 SO3=-S1-S2-S5-S9+S23+S25-S31-S32-S33-S34
     +            -S36-S37-S94-S95-S99-S100
                  SH2=-S6+S39
                  SCO=-S7+S31+S33+S36+S38+S39+S40+S41+S57+S88+S90+S91
     +            +S94+S97+S99+S128+S129+S134
                  SH2O2=-S8+S11+S12-S22+S95+S100
                  SHONO=+S13-S20-S26
                  SHNO3=+S14-S21-S27
                  SHO2NO2=+S17-S18-S19
                  SCH4=-S28
                  SC2H4=-S29-S31-S32
                  SC3H6=-S30-S33-S34
                  SC5H8=-S35-S36-S37
                  SC2H5OH=-S44-S45
                  SCH3NO3=+S61-S101-S102


                  NO(K,I,J)=NO(K,I,J)+DTLONG*SNO
                  NO2(K,I,J)=NO2(K,I,J)+DTLONG*SNO2
c                 NO3(K,I,J)=NO3(K,I,J)+DTLONG*SNO3
                  O3(K,I,J)=O3(K,I,J)+DTLONG*SO3
                  H2(K,I,J)=H2(K,I,J)+DTLONG*SH2
                  CO(K,I,J)=CO(K,I,J)+DTLONG*SCO
                  H2O2(K,I,J)=H2O2(K,I,J)+DTLONG*SH2O2
                  HONO(K,I,J)=HONO(K,I,J)+DTLONG*SHONO
                  HNO3(K,I,J)=HNO3(K,I,J)+DTLONG*SHNO3
                  HO2NO2(K,I,J)=HO2NO2(K,I,J)+DTLONG*SHO2NO2
                  CH4(K,I,J)=CH4(K,I,J)+DTLONG*SCH4
                  C2H4(K,I,J)=C2H4(K,I,J)+DTLONG*SC2H4
                  C3H6(K,I,J)=C3H6(K,I,J)+DTLONG*SC3H6
                  C5H8(K,I,J)=C5H8(K,I,J)+DTLONG*SC5H8
                  C2H5OH(K,I,J)=C2H5OH(K,I,J)+DTLONG*SC2H5OH
                  CH3NO3(K,I,J)=CH3NO3(K,I,J)+DTLONG*SCH3NO3

c --------------------------
c NO3 faster reactions
c --------------------------
                  SNO3=-S4-S15+S21-S24-S25+S136
c                 SNO3=-S4-S15+S21-S24-S25
                  DTsno3=0.2*ABS(NO3(K,I,J)/(SNO3+1.e-30))
                  Nsno3=min(10.0,amax1(DTLONG/(DTsno3+1.e-30) ,1.0))
                  DTsno3=DTLONG/Nsno3
c                 print*,'nsno3:',nsno3,no3(k,i,j)
                  do ic=1,Nsno3
                     s4 =ck4 *NO(k,i,j)*NO3(k,i,j)
                     s15=ck15*OH(k,i,j)*NO3(k,i,j)
                     s24=ck24*NO3(k,i,j)
                     s25=ck25*NO3(k,i,j)
                     SNO3=-S4-S15+S21-S24-S25+S136
```

```
c                  SNO3=-S4-S15+S21-S24-S25
                   NO3(K,I,J)=NO3(K,I,J)+DTSNO3*SNO3
c                print*,'no3:',nsno3,sno3,no3(k,i,j),s4,s15,s24,s25,s136
                 enddo
c       WRITE(*,77)'NO3   :',NO3   (K,I,J),DTSNO3*SNO3   /NO3   (K,I,J)

c --------------------------
c faster reactions
c --------------------------

                 do ic=1,nshort
                    s5 =ck5*OH(k,i,j)*O3(k,i,j)
                    s6 =ck6*OH(k,i,j)*H2(k,i,j)
                    s7 =ck7*OH(k,i,j)*CO(k,i,j)
                    s8 =ck8*OH(k,i,j)*H2O2(k,i,j)
                    s9 =ck9*HO2(k,i,j)*O3(k,i,j)
                    s10=ck10*OH(k,i,j)*HO2(k,i,j)
                    s11=ck11*HO2(k,i,j)*HO2(k,i,j)
                    s12=ck12*HO2(k,i,j)*HO2(k,i,j)
                    s13=ck13*OH(k,i,j)*NO(k,i,j)
                    s14=ck14*OH(k,i,j)*NO2(k,i,j)
                    s15=ck15*OH(k,i,j)*NO3(k,i,j)
                    s16=ck16*HO2(k,i,j)*NO(k,i,j)
                    s17=ck17*HO2(k,i,j)*NO2(k,i,j)
                    s19=ck19*OH(k,i,j)*HO2NO2(k,i,j)
                    s20=ck20*OH(k,i,j)*HONO(k,i,j)
                    s21=ck21*OH(k,i,j)*HNO3(k,i,j)
                    s28=ck28*OH(k,i,j)*CH4(k,i,j)
                    s29=ck29*OH(k,i,j)*C2H4(k,i,j)
                    s30=ck30*OH(k,i,j)*C3H6(k,i,j)
                    s35=ck35*OH(k,i,j)*C5H8(k,i,j)
                    s38=ck38*HCHO(k,i,j)
                    s39=ck39*HCHO(k,i,j)
                    s40=ck40*CH3CHO(k,i,j)
                    s41=ck41*OH(k,i,j)*HCHO(k,i,j)
                    s42=ck42*OH(k,i,j)*CH3CHO(k,i,j)
                    s43=ck43*OH(k,i,j)*CH3OH(k,i,j)
                    s44=ck44*OH(k,i,j)*C2H5OH(k,i,j)
                    s45=ck45*OH(k,i,j)*C2H5OH(k,i,j)
                    s46=ck46*HCOOH(k,i,j)*OH(k,i,j)
                    s47=ck47*CH3CO2H(k,i,j)*OH(k,i,j)
                    s48=ck48*CH3O2(k,i,j)*NO(k,i,j)
                    s49=ck49*HOCH2CH2O2(k,i,j)*NO(k,i,j)
                    s50=ck50*HOCH2CH2O2(k,i,j)*NO(k,i,j)
                    s51=ck51*RN9O2(k,i,j)*NO(k,i,j)
                    s52=ck52*CH3CO3(k,i,j)*NO(k,i,j)
                    s53=ck53*HOCH2CO3(k,i,j)*NO(k,i,j)
                    s54=ck54*RU14O2(k,i,j)*NO(k,i,j)
                    s55=ck55*RU14O2(k,i,j)*NO(k,i,j)
                    s56=ck56*RU12O2(k,i,j)*NO(k,i,j)
                    s57=ck57*RU12O2(k,i,j)*NO(k,i,j)
                    s58=ck58*RU10O2(k,i,j)*NO(k,i,j)
                    s59=ck59*RU10O2(k,i,j)*NO(k,i,j)
                    s60=ck60*RU10O2(k,i,j)*NO(k,i,j)
                    s61=ck61*CH3O2(k,i,j)*NO(k,i,j)
                    s62=ck62*HOCH2CH2O2(k,i,j)*NO(k,i,j)
                    s63=ck63*RN9O2(k,i,j)*NO(k,i,j)
                    s64=ck64*RU14O2(k,i,j)*NO(k,i,j)
                    s65=ck65*CH3O2(k,i,j)*HO2(k,i,j)
                    s66=ck66*HOCH2CH2O2(k,i,j)*HO2(k,i,j)
                    s67=ck67*RN9O2(k,i,j)*HO2(k,i,j)
                    s68=ck68*CH3CO3(k,i,j)*HO2(k,i,j)
                    s69=ck69*HOCH2CO3(k,i,j)*HO2(k,i,j)
                    s70=ck70*RU14O2(k,i,j)*HO2(k,i,j)
                    s71=ck71*RU12O2(k,i,j)*HO2(k,i,j)
                    s72=ck72*RU10O2(k,i,j)*HO2(k,i,j)
                    s73=ck73*CH3O2(k,i,j)
                    s74=ck74*CH3O2(k,i,j)
                    s75=ck75*CH3O2(k,i,j)
                    s76=ck76*HOCH2CH2O2(k,i,j)
                    s77=ck77*RN9O2(k,i,j)
                    s78=ck78*CH3CO3(k,i,j)
                    s79=ck79*HOCH2CO3(k,i,j)
                    s80=ck80*RU14O2(k,i,j)
                    s81=ck81*RU14O2(k,i,j)
                    s82=ck82*RU12O2(k,i,j)
                    s83=ck83*RU12O2(k,i,j)
                    s84=ck84*RU10O2(k,i,j)
                    s85=ck85*RU10O2(k,i,j)
                    s86=ck86*RU10O2(k,i,j)
                    s87=ck87*CARB7(k,i,j)
                    s88=ck88*HOCH2CHO(k,i,j)
                    s89=ck89*UCARB10(k,i,j)
                    s90=ck90*CARB6(k,i,j)
                    s91=ck91*UCARB12(k,i,j)
                    s92=ck92*OH(k,i,j)*CARB7(k,i,j)
                    s93=ck93*OH(k,i,j)*UCARB10(k,i,j)
                    s94=ck94*O3(k,i,j)*UCARB10(k,i,j)
                    s95=ck95*O3(k,i,j)*UCARB10(k,i,j)
```

```
                    s96=ck96*OH(k,i,j)*HOCH2CHO(k,i,j)
                    s97=ck97*OH(k,i,j)*CARB6(k,i,j)
                    s98=ck98*OH(k,i,j)*UCARB12(k,i,j)
                    s99=ck99*O3(k,i,j)*UCARB12(k,i,j)
                    s100=ck100*O3(k,i,j)*UCARB12(k,i,j)
                    s102=ck102*OH(k,i,j)*CH3NO3(k,i,j)
                    s103=ck103*OH(k,i,j)*HOC2H4NO3(k,i,j)
                    s104=ck104*OH(k,i,j)*RN9NO3(k,i,j)
                    s105=ck105*OH(k,i,j)*RU14NO3(k,i,j)
                    s106=ck106*CH3OOH(k,i,j)
                    s107=ck107*CH3CO3H(k,i,j)
                    s108=ck108*HOCH2CO3H(k,i,j)
                    s109=ck109*RU14OOH(k,i,j)
                    s110=ck110*RU14OOH(k,i,j)
                    s111=ck111*RU12OOH(k,i,j)
                    s112=ck112*RU10OOH(k,i,j)
                    s113=ck113*HOC2H4OOH(k,i,j)
                    s114=ck114*RN9OOH(k,i,j)
                    s115=ck115*OH(k,i,j)*CH3OOH(k,i,j)
                    s116=ck116*OH(k,i,j)*CH3OOH(k,i,j)
                    s117=ck117*OH(k,i,j)*CH3CO3H(k,i,j)
                    s118=ck118*OH(k,i,j)*HOCH2CO3H(k,i,j)
                    s119=ck119*OH(k,i,j)*RU14OOH(k,i,j)
                    s120=ck120*OH(k,i,j)*RU12OOH(k,i,j)
                    s121=ck121*OH(k,i,j)*RU10OOH(k,i,j)
                    s122=ck122*OH(k,i,j)*HOC2H4OOH(k,i,j)
                    s123=ck123*OH(k,i,j)*RN9OOH(k,i,j)
                    s124=ck124*CH3CO3(k,i,j)*NO2(k,i,j)
                    s125=ck125*PAN(k,i,j)
                    s126=ck126*HOCH2CO3(k,i,j)*NO2(k,i,j)
                    s127=ck127*PHAN(k,i,j)
                    s128=ck128*OH(k,i,j)*PAN(k,i,j)
                    s129=ck129*OH(k,i,j)*PHAN(k,i,j)
                    s130=ck130*RU12O2(k,i,j)*NO2(k,i,j)
                    s131=ck131*RU12PAN(k,i,j)
                    s132=ck132*RU10O2(k,i,j)*NO2(k,i,j)
                    s133=ck133*MPAN(k,i,j)
                    s134=ck134*OH(k,i,j)*MPAN(k,i,j)
                    s135=ck135*OH(k,i,j)*RU12PAN(k,i,j)


                    SOH=+2*S1-S5-S6-S7-S8+S9-S10-S13-S14-S15+S16
     +              -S19-S20-S21+2*S22+S26+S27-S28-S29-S30+S31+S33-S35
     +              +S36-S41-S42-S43-S44-S45-S46-S47-S92-S93+S94
     +              -S96-S97-S98+S99-S102-S103-S104-S105+S106+S107
     +              +S108+S109+S110+S111+S112+S113+S114-S115-S116+S116
     +              -S117-S118-S119+S119-S120-S121-S122+S122-S123+S123
     +              -S128-S129-S134-S135
                    SHO2=+S5+S6+S7+S8-S9-S10-2*S11-2*S12+S15-S16
     +              -S17+S18+S31+S36+2*S38+S40+S41+S43+S44+S46+S48
     +              +S49+S50+S51+S53+S54+S55+S57+S59+S60-S65-S66-S67
     +              -S68-S69-S70-S71-S72+S73+S76+S77+S79+S80+S81+S83
     +              +S85+S86+S87+2*S88+S89+S90+S91+S92+S101+S106
     +              +S108+S109+S110+S111+S113+S114
                    SCH3O2=+S28+S33+S40+S47-S48+S52-S61-S65-S73-S74-S75
     +              +S78+S107+S115
                    SCH3OH=-S43+S75
                    SHOCH2CH2O2=+S29+S45-S49-S50-S62-S66-S76
                    SCH3CO2H=+S34-S47
                    SCH3CHO=-S40-S42+S44+S51+S77+S114
                    SRU14O2=+S35-S54-S55-S64-S70-S80-S81
                    SUCARB10=+S36+S37+S55+S81-S89-S93-S94-S95+S110
     +              +S135
                    SHCHO=+S31+S32+S33+S34-S38-S39-S41+S43+S48+2*S49
     +              +S51+S53+S55+S59+S60+S73+S74+S77+S79+S81+S85+S86
     +              +S87+S88+S89+S94+S95+S101+S102+S106+S108+S110
     +              +2*S113+S114+S116+S128+S129
                    SCH3CO3=+S42-S52+S56+S58-S68-S78+S82+S84+S87+S89
     +              +S90+S91+S94+S97+S99+S112+S117-S124+S125
                    SHOCH2CHO=+S50+S56+S58+S76+S82+S83+S84-S88+S91
     +              -S96+S99+S100+S103+S111+S112+S122
c corrected on 20100122
c                   SRN9O2=-S51-S63-S67-S77
                    SRN9O2=+S30-S51-S63-S67-S77
                    SHCOOH=+S32+S37-S46
                    SCARB6=+S59+S85-S90+S92+S95-S97+S100+S111
                    SUCARB12=+S54+S80-S91-S98-S99-S100+S105+S109
     +              +S119
                    SRU12O2=-S56-S57-S71-S82-S83+S98+S120-S130+S131
                    SCARB7=+S57+S60+S83+S86-S87-S92+S104+S123+S134
                    SRU10O2=-S58-S59-S60-S72-S84-S85-S86+S93+S121
     +              -S132+S133
                    SHOC2H4NO3=+S62-S103
                    SRN9NO3=+S63-S104
                    SRU14NO3=+S64-S105
                    SCH3OOH=+S65-S106-S115-S116
                    SHOC2H4OOH=+S66-S113-S122
                    SRN9OOH=+S67-S114-S123
                    SCH3CO3H=+S68-S107-S117
```

```
                    SHOCH2CO3H=+S69-S108-S118
                    SRU14OOH=+S70-S109-S110-S119
                    SRU12OOH=+S71-S111-S120
                    SRU10OOH=+S72-S112-S121
                    SHOCH2CO3=-S53-S69-S79+S96+S118-S126+S127
                    SPAN=+S124-S125-S128
                    SPHAN=+S126-S127-S129
                    SRU12PAN=+S130-S131-S135
                    SMPAN=+S132-S133-S134

                    OH(K,I,J)=OH(K,I,J)+DTSHORT*SOH
                    HO2(K,I,J)=HO2(K,I,J)+DTSHORT*SHO2
                    CH3O2(K,I,J)=CH3O2(K,I,J)+DTSHORT*SCH3O2
                    CH3OH(K,I,J)=CH3OH(K,I,J)+DTSHORT*SCH3OH
                    HOCH2CH2O2(K,I,J)=HOCH2CH2O2(K,I,J)
     +              +DTSHORT*SHOCH2CH2O2
                    CH3CO2H(K,I,J)=CH3CO2H(K,I,J)
     +              +DTSHORT*SCH3CO2H
                    CH3CHO(K,I,J)=CH3CHO(K,I,J)+DTSHORT*SCH3CHO
                    RU14O2(K,I,J)=RU14O2(K,I,J)+DTSHORT*SRU14O2
                    UCARB10(K,I,J)=UCARB10(K,I,J)
     +              +DTSHORT*SUCARB10
                    HCHO(K,I,J)= HCHO(K,I,J)+DTSHORT*SHCHO
                    CH3CO3(K,I,J)=CH3CO3(K,I,J)+DTSHORT*SCH3CO3
                    HOCH2CHO(K,I,J)=HOCH2CHO(K,I,J)
     +              +DTSHORT*SHOCH2CHO
                    RN9O2(K,I,J)=RN9O2(K,I,J)+DTSHORT*SRN9O2
                    HCOOH(K,I,J)=HCOOH(K,I,J)+DTSHORT*SHCOOH
                    CARB6(K,I,J)=CARB6(K,I,J)+DTSHORT*SCARB6
                    UCARB12(K,I,J)=UCARB12(K,I,J)
     +              +DTSHORT*SUCARB12
                    RU12O2(K,I,J)=RU12O2(K,I,J)+DTSHORT*SRU12O2
                    CARB7(K,I,J)=CARB7(K,I,J)+DTSHORT*SCARB7
                    RU10O2(K,I,J)=RU10O2(K,I,J)
c corrected on 20100122
c     +              +DTSHORT*RU10O2(k,i,j)
     +              +DTSHORT*SRU10O2
                    HOC2H4NO3(K,I,J)=HOC2H4NO3(K,I,J)
     +              +DTSHORT*SHOC2H4NO3
                    RN9NO3(K,I,J)=RN9NO3(K,I,J)+DTSHORT*SRN9NO3
                    RU14NO3(K,I,J)=RU14NO3(K,I,J)
     +              +DTSHORT*SRU14NO3
                    CH3OOH(K,I,J)=CH3OOH(K,I,J)+DTSHORT*SCH3OOH
                    HOC2H4OOH(K,I,J)=HOC2H4OOH(K,I,J)
     +              +DTSHORT*SHOC2H4OOH
                    RN9OOH(K,I,J)=RN9OOH(K,I,J)+DTSHORT*SRN9OOH
                    CH3CO3H(K,I,J)=CH3CO3H(K,I,J)
     +              +DTSHORT*SCH3CO3H
                    HOCH2CO3H(K,I,J)=HOCH2CO3H(K,I,J)
     +              +DTSHORT*SHOCH2CO3H
                    RU14OOH(K,I,J)= RU14OOH(K,I,J)
     +              +DTSHORT*SRU14OOH
                    RU12OOH(K,I,J)=RU12OOH(K,I,J)
     +              +DTSHORT*SRU12OOH
                    RU10OOH(K,I,J)=RU10OOH(K,I,J)
     +              +DTSHORT*SRU10OOH
                    HOCH2CO3(K,I,J)=HOCH2CO3(K,I,J)
     +              +DTSHORT*SHOCH2CO3
                    PAN(K,I,J)=PAN(K,I,J)+DTSHORT*SPAN
                    PHAN(K,I,J)=PHAN(K,I,J)+DTSHORT*SPHAN
                    RU12PAN(K,I,J)=RU12PAN(K,I,J)
     +              +DTSHORT*SRU12PAN
                    MPAN(K,I,J)=MPAN(K,I,J)+DTSHORT*SMPAN

                  enddo
                enddo
              enddo
            enddo
            return
            end
c=============================================
      subroutine OHequi
      parameter (nchems=51)
      character*16 chems(nchems)
      real NO,NO2,NO3,NA,MPAN
      common /JFAC/CJFAC
      data CJFAC/1.0/           ! in unit of 1/sec
      data chems/'O3','NO','NO2','NO3',
     +  'OH','HO2','H2','CO','H2O2','HONO','HNO3',
     +  'HO2NO2','CH3O2','CH3OH','CH4','C2H4',
     +  'C3H6','HOCH2CH2O2','CH3CO2H','CH3CHO',
     +  'C5H8','RU14O2','UCARB10','HCHO','CH3CO3',
     +  'HOCH2CHO','C2H5OH','RN9O2','HCOOH',
     +  'CARB6','UCARB12','RU12O2','CARB7','RU10O2',
     +  'CH3NO3','HOC2H4NO3','RN9NO3','RU14NO3',
     +  'CH3OOH','HOC2H4OOH','RN9OOH','CH3CO3H',
     +  'HOCH2CO3H','RU14OOH','RU12OOH','RU10OOH',
     +  'HOCH2CO3','PAN','PHAN','RU12PAN','MPAN'/
        common /chems/ O3,NO,NO2,NO3,OH,HO2,
```

```
     +  H2,CO,H2O2,HONO,HNO3,HO2NO2,CH3O2,CH3OH,
     +  CH4,C2H4,C3H6,HOCH2CH2O2,CH3CO2H,CH3CHO,
     +  C5H8,RU14O2,UCARB10,HCHO,CH3CO3,HOCH2CHO,
     +  C2H5OH,RN9O2,HCOOH,CARB6,UCARB12,RU12O2,
     +  CARB7,RU10O2,CH3NO3,HOC2H4NO3,RN9NO3,
     +  RU14NO3,CH3OOH,HOC2H4OOH,RN9OOH,CH3CO3H,
     +  HOCH2CO3H,RU14OOH,RU12OOH,RU10OOH,HOCH2CO3,
     +  PAN,PHAN,RU12PAN,MPAN
        real chemvec(nchems),chemold(nchems)
        equivalence (chemvec,O3)
c-------------------------------------------------------
c several tests have been done in order to find optimal values
c of 'dtlong' and 'nshort' for this initial setting
c dtlong=0.1 and nshort=4 is probably the one
c-------------------------------------------------------
        dtlong=0.01
        nshort=10

C to run the 0-dim model for 30 mins; the results to be used as the
C upwind inlet conditions
        nint = 180000
C----   initial conditions
        O3         =40.00
        NO         =2.00
        NO2        =8.00
        NO3        =0
        OH         =0
        HO2        =0
        H2         =0
        CO         =200.00
        H2O2       =0
        HONO       =0
        HNO3       =2.00
        HO2NO2     =0
        CH3O2      =0
        CH3OH      =7.38
        CH4        =1800.00
        C2H4       =0.91
        C3H6       =0.29
        HOCH2CH2O2 =0
        CH3CO2H    =0
        CH3CHO     =2.98
        C5H8       =0.28
        RU14O2     =0
        UCARB10    =0
        HCHO       =3.14
        CH3CO3     =0
        HOCH2CHO   =0
        C2H5OH     =2.37
        RN9O2      =0
        HCOOH      =0
        CARB6      =0
        UCARB12    =0
        RU12O2     =0
        CARB7      =0
        RU10O2     =0
        CH3NO3     =0
        HOC2H4NO3  =0
        RN9NO3     =0
        RU14NO3    =0
        CH3OOH     =0
        HOC2H4OOH  =0
        RN9OOH     =0
        CH3CO3H    =0
        HOCH2CO3H  =0
        RU14OOH    =0
        RU12OOH    =0
        RU10OOH    =0
        HOCH2CO3   =0
        PAN        =0.46
        PHAN       =0
        RU12PAN    =0
        MPAN       =0

      print*,'=== OH Equilibrium...'
c       print*,'=== OH Initialization...'
        write(*,20)(chems(i),i=1,nchems)
 20     format(51a12)
        write(*,10)(chemvec(iv),iv=1,nchems)
        do i=1,nint
           do iv=1,nchems
              chemold(iv)=chemvec(iv)
           enddo
           call OHchm(1,1,1,O3,NO,NO2,NO3,OH,
     +  HO2,H2,CO,H2O2,HONO,HNO3,HO2NO2,CH3O2,
     +  CH3OH,CH4,C2H4,C3H6,HOCH2CH2O2,CH3CO2H,
     +  CH3CHO,C5H8,RU14O2,UCARB10,HCHO,CH3CO3,
     +  HOCH2CHO,C2H5OH,RN9O2,HCOOH,CARB6,UCARB12,
     +  RU12O2,CARB7,RU10O2,CH3NO3,HOC2H4NO3,
```

```
     +  RN9NO3,RU14NO3,CH3OOH,HOC2H4OOH,RN9OOH,
     +  CH3CO3H,HOCH2CO3H,RU14OOH,RU12OOH,RU10OOH,
     +  HOCH2CO3,PAN,PHAN,RU12PAN,MPAN,theta,
     +  dtlong,nshort)

c-------------------------------------------------------
c testing equilibrium
c          ipass=0
c          do iv=1,nchems
c             error=(chemold(iv)-chemvec(iv))/max(chemold(iv),1e-30)
c             if(error .le. 1e-4) ipass=ipass+1
c          enddo
c          if(ipass.ge.nchems) goto 777
        enddo
 777     continue
c       print*,'=== number of steps:',i
        write(*,10)(chemvec(iv),iv=1,nchems)
 10     format(51(1pe12.4))
        return
        end
c=============================================================
      subroutine OHinit(nzp,nxp,nyp,O3,NO,NO2,NO3,OH,
     +  HO2,H2,CO,H2O2,HONO,HNO3,HO2NO2,CH3O2,
     +  CH3OH,CH4,C2H4,C3H6,HOCH2CH2O2,CH3CO2H,
     +  CH3CHO,C5H8,RU14O2,UCARB10,HCHO,CH3CO3,
     +  HOCH2CHO,C2H5OH,RN9O2,HCOOH,CARB6,UCARB12,
     +  RU12O2,CARB7,RU10O2,CH3NO3,HOC2H4NO3,
     +  RN9NO3,RU14NO3,CH3OOH,HOC2H4OOH,RN9OOH,
     +  CH3CO3H,HOCH2CO3H,RU14OOH,RU12OOH,RU10OOH,
     +  HOCH2CO3,PAN,PHAN,RU12PAN,MPAN)

      real O3(nzp,nxp,nyp),NO(nzp,nxp,nyp),
     +  NO2(nzp,nxp,nyp),NO3(nzp,nxp,nyp),
     +  OH(nzp,nxp,nyp),HO2(nzp,nxp,nyp),H2(nzp,nxp,nyp),
     +  CO(nzp,nxp,nyp),H2O2(nzp,nxp,nyp),HONO(nzp,nxp,nyp),
     +  HNO3(nzp,nxp,nyp),HO2NO2(nzp,nxp,nyp),
     +  CH3O2(nzp,nxp,nyp),CH3OH(nzp,nxp,nyp),CH4(nzp,nxp,nyp),
     +  C2H4(nzp,nxp,nyp),C3H6(nzp,nxp,nyp),HOCH2CH2O2(nzp,nxp,nyp),
     +  CH3CO2H(nzp,nxp,nyp),CH3CHO(nzp,nxp,nyp),C5H8(nzp,nxp,nyp),
     +  RU14O2(nzp,nxp,nyp),UCARB10(nzp,nxp,nyp),HCHO(nzp,nxp,nyp),
     +  CH3CO3(nzp,nxp,nyp),HOCH2CHO(nzp,nxp,nyp),C2H5OH(nzp,nxp,nyp),
     +  RN9O2(nzp,nxp,nyp),HCOOH(nzp,nxp,nyp),CARB6(nzp,nxp,nyp),
     +  UCARB12(nzp,nxp,nyp),RU12O2(nzp,nxp,nyp),CARB7(nzp,nxp,nyp),
     +  RU10O2(nzp,nxp,nyp),CH3NO3(nzp,nxp,nyp),HOC2H4NO3(nzp,nxp,nyp),
     +  RN9NO3(nzp,nxp,nyp),RU14NO3(nzp,nxp,nyp),CH3OOH(nzp,nxp,nyp),
     +  HOC2H4OOH(nzp,nxp,nyp),RN9OOH(nzp,nxp,nyp),CH3CO3H(nzp,nxp,nyp),
     +  HOCH2CO3H(nzp,nxp,nyp),RU14OOH(nzp,nxp,nyp),
     +  RU12OOH(nzp,nxp,nyp),RU10OOH(nzp,nxp,nyp),HOCH2CO3(nzp,nxp,nyp),
     +  PAN(nzp,nxp,nyp),PHAN(nzp,nxp,nyp),RU12PAN(nzp,nxp,nyp),
     +  MPAN(nzp,nxp,nyp)
      parameter (nchems=51)
      real NO_0,NO2_0,NO3_0,NA_0,MPAN_0
        common /chems/ O3_0,NO_0,NO2_0,NO3_0,OH_0,HO2_0,
     +  H2_0,CO_0,H2O2_0,HONO_0,HNO3_0,HO2NO2_0,CH3O2_0,CH3OH_0,
     +  CH4_0,C2H4_0,C3H6_0,HOCH2CH2O2_0,CH3CO2H_0,CH3CHO_0,
     +  C5H8_0,RU14O2_0,UCARB10_0,HCHO_0,CH3CO3_0,HOCH2CHO_0,
     +  C2H5OH_0,RN9O2_0,HCOOH_0,CARB6_0,UCARB12_0,RU12O2_0,
     +  CARB7_0,RU10O2_0,CH3NO3_0,HOC2H4NO3_0,RN9NO3_0,
     +  RU14NO3_0,CH3OOH_0,HOC2H4OOH_0,RN9OOH_0,CH3CO3H_0,
     +  HOCH2CO3H_0,RU14OOH_0,RU12OOH_0,RU10OOH_0,HOCH2CO3_0,
     +  PAN_0,PHAN_0,RU12PAN_0,MPAN_0

C  modified on 100301: move the inlet/initial condition to 'rdriv2a.model.RCRI.v2'
c--- calculate the equilibrium values
c      call OHequi
c--- assign the equilibrium values to the whole field
      do j=1,nyp
         do i=1,nxp
            do k=1,nzp
        O3         (K,I,J)=O3_0
        NO         (K,I,J)=NO_0
        NO2        (K,I,J)=NO2_0
        NO3        (K,I,J)=NO3_0
        OH         (K,I,J)=OH_0
        HO2        (K,I,J)=HO2_0
        H2         (K,I,J)=H2_0
        CO         (K,I,J)=CO_0
        H2O2       (K,I,J)=H2O2_0
        HONO       (K,I,J)=HONO_0
        HNO3       (K,I,J)=HNO3_0
        HO2NO2     (K,I,J)=HO2NO2_0
        CH3O2      (K,I,J)=CH3O2_0
        CH3OH      (K,I,J)=CH3OH_0
        CH4        (K,I,J)=CH4_0
        C2H4       (K,I,J)=C2H4_0
        C3H6       (K,I,J)=C3H6_0
        HOCH2CH2O2 (K,I,J)=HOCH2CH2O2_0
        CH3CO2H    (K,I,J)=CH3CO2H_0
        CH3CHO     (K,I,J)=CH3CHO_0
```

```
        C5H8       (K,I,J)=C5H8_0
        RU14O2     (K,I,J)=RU14O2_0
        UCARB10    (K,I,J)=UCARB10_0
        HCHO       (K,I,J)=HCHO_0
        CH3CO3     (K,I,J)=CH3CO3_0
        HOCH2CHO   (K,I,J)=HOCH2CHO_0
        C2H5OH     (K,I,J)=C2H5OH_0
        RN9O2      (K,I,J)=RN9O2_0
        HCOOH      (K,I,J)=HCOOH_0
        CARB6      (K,I,J)=CARB6_0
        UCARB12    (K,I,J)=UCARB12_0
        RU12O2     (K,I,J)=RU12O2_0
        CARB7      (K,I,J)=CARB7_0
        RU10O2     (K,I,J)=RU10O2_0
        CH3NO3     (K,I,J)=CH3NO3_0
        HOC2H4NO3  (K,I,J)=HOC2H4NO3_0
        RN9NO3     (K,I,J)=RN9NO3_0
        RU14NO3    (K,I,J)=RU14NO3_0
        CH3OOH     (K,I,J)=CH3OOH_0
        HOC2H4OOH  (K,I,J)=HOC2H4OOH_0
        RN9OOH     (K,I,J)=RN9OOH_0
        CH3CO3H    (K,I,J)=CH3CO3H_0
        HOCH2CO3H  (K,I,J)=HOCH2CO3H_0
        RU14OOH    (K,I,J)=RU14OOH_0
        RU12OOH    (K,I,J)=RU12OOH_0
        RU10OOH    (K,I,J)=RU10OOH_0
        HOCH2CO3   (K,I,J)=HOCH2CO3_0
        PAN        (K,I,J)=PAN_0
        PHAN       (K,I,J)=PHAN_0
        RU12PAN    (K,I,J)=RU12PAN_0
        MPAN       (K,I,J)=MPAN_0
            enddo
          enddo
        enddo
C zero wall
      CALL ZEROBLDG(NZP,NXP,NYP,O3         ,'Y')
      CALL ZEROBLDG(NZP,NXP,NYP,NO         ,'Y')
      CALL ZEROBLDG(NZP,NXP,NYP,NO2        ,'Y')
      CALL ZEROBLDG(NZP,NXP,NYP,NO3        ,'Y')
      CALL ZEROBLDG(NZP,NXP,NYP,OH         ,'Y')
      CALL ZEROBLDG(NZP,NXP,NYP,HO2        ,'Y')
      CALL ZEROBLDG(NZP,NXP,NYP,H2         ,'Y')
      CALL ZEROBLDG(NZP,NXP,NYP,CO         ,'Y')
      CALL ZEROBLDG(NZP,NXP,NYP,H2O2       ,'Y')
      CALL ZEROBLDG(NZP,NXP,NYP,HONO       ,'Y')
      CALL ZEROBLDG(NZP,NXP,NYP,HNO3       ,'Y')
      CALL ZEROBLDG(NZP,NXP,NYP,HO2NO2     ,'Y')
      CALL ZEROBLDG(NZP,NXP,NYP,CH3O2      ,'Y')
      CALL ZEROBLDG(NZP,NXP,NYP,CH3OH      ,'Y')
      CALL ZEROBLDG(NZP,NXP,NYP,CH4        ,'Y')
      CALL ZEROBLDG(NZP,NXP,NYP,C2H4       ,'Y')
      CALL ZEROBLDG(NZP,NXP,NYP,C3H6       ,'Y')
      CALL ZEROBLDG(NZP,NXP,NYP,HOCH2CH2O2 ,'Y')
      CALL ZEROBLDG(NZP,NXP,NYP,CH3CO2H    ,'Y')
      CALL ZEROBLDG(NZP,NXP,NYP,CH3CHO     ,'Y')
      CALL ZEROBLDG(NZP,NXP,NYP,C5H8       ,'Y')
      CALL ZEROBLDG(NZP,NXP,NYP,RU14O2     ,'Y')
      CALL ZEROBLDG(NZP,NXP,NYP,UCARB10    ,'Y')
      CALL ZEROBLDG(NZP,NXP,NYP,HCHO       ,'Y')
      CALL ZEROBLDG(NZP,NXP,NYP,CH3CO3     ,'Y')
      CALL ZEROBLDG(NZP,NXP,NYP,HOCH2CHO   ,'Y')
      CALL ZEROBLDG(NZP,NXP,NYP,C2H5OH     ,'Y')
      CALL ZEROBLDG(NZP,NXP,NYP,RN9O2      ,'Y')
      CALL ZEROBLDG(NZP,NXP,NYP,HCOOH      ,'Y')
      CALL ZEROBLDG(NZP,NXP,NYP,CARB6      ,'Y')
      CALL ZEROBLDG(NZP,NXP,NYP,UCARB12    ,'Y')
      CALL ZEROBLDG(NZP,NXP,NYP,RU12O2     ,'Y')
      CALL ZEROBLDG(NZP,NXP,NYP,CARB7      ,'Y')
      CALL ZEROBLDG(NZP,NXP,NYP,RU10O2     ,'Y')
      CALL ZEROBLDG(NZP,NXP,NYP,CH3NO3     ,'Y')
      CALL ZEROBLDG(NZP,NXP,NYP,HOC2H4NO3  ,'Y')
      CALL ZEROBLDG(NZP,NXP,NYP,RN9NO3     ,'Y')
      CALL ZEROBLDG(NZP,NXP,NYP,RU14NO3    ,'Y')
      CALL ZEROBLDG(NZP,NXP,NYP,CH3OOH     ,'Y')
      CALL ZEROBLDG(NZP,NXP,NYP,HOC2H4OOH  ,'Y')
      CALL ZEROBLDG(NZP,NXP,NYP,RN9OOH     ,'Y')
      CALL ZEROBLDG(NZP,NXP,NYP,CH3CO3H    ,'Y')
      CALL ZEROBLDG(NZP,NXP,NYP,HOCH2CO3H  ,'Y')
      CALL ZEROBLDG(NZP,NXP,NYP,RU14OOH    ,'Y')
      CALL ZEROBLDG(NZP,NXP,NYP,RU12OOH    ,'Y')
      CALL ZEROBLDG(NZP,NXP,NYP,RU10OOH    ,'Y')
      CALL ZEROBLDG(NZP,NXP,NYP,HOCH2CO3   ,'Y')
      CALL ZEROBLDG(NZP,NXP,NYP,PAN        ,'Y')
      CALL ZEROBLDG(NZP,NXP,NYP,PHAN       ,'Y')
      CALL ZEROBLDG(NZP,NXP,NYP,RU12PAN    ,'Y')
      CALL ZEROBLDG(NZP,NXP,NYP,MPAN       ,'Y')
      return
      end
```